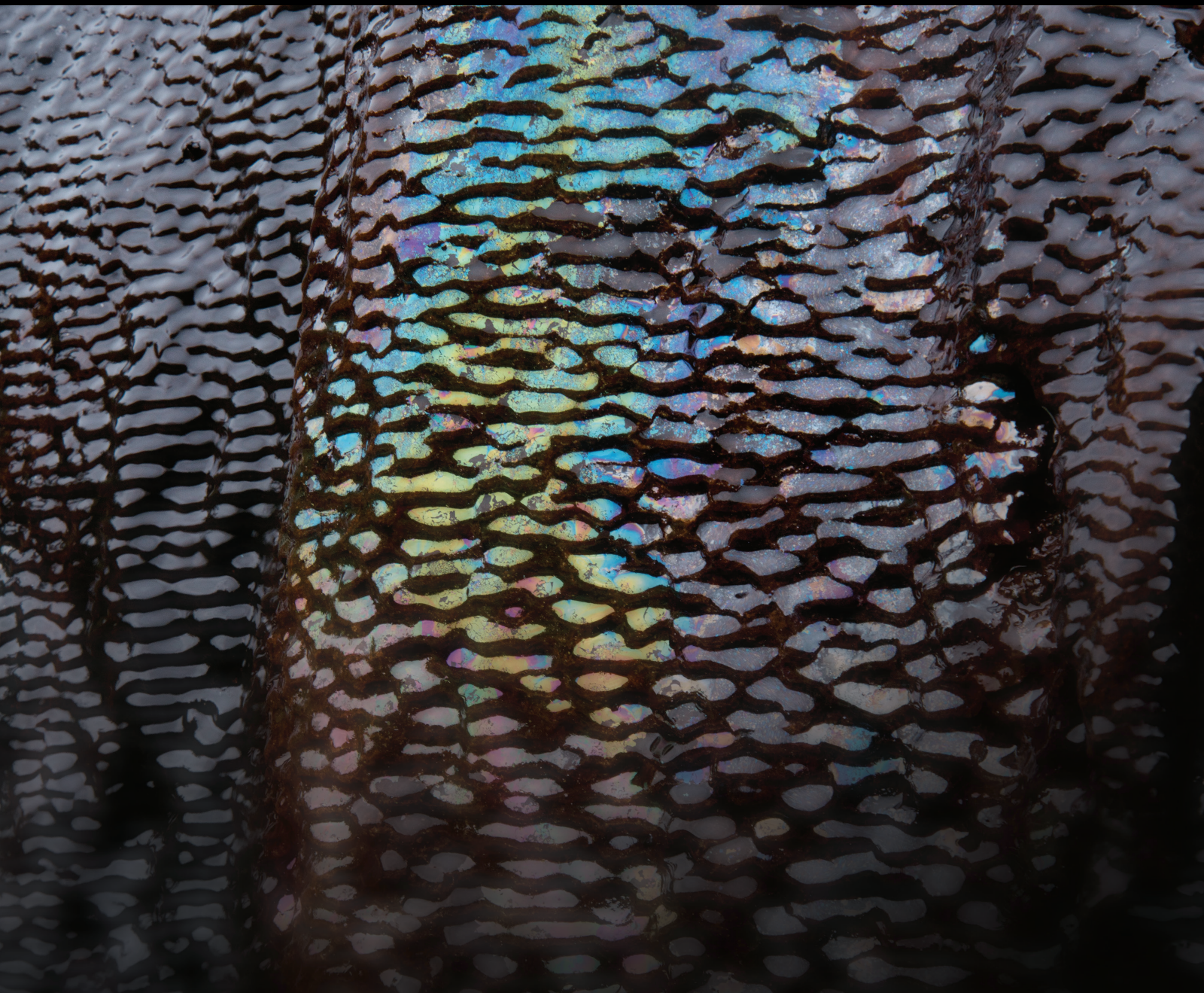


Fluid Flow in Unconventional Gas Reservoirs

Lead Guest Editor: Tongqiang Xia

Guest Editors: Egor Dontsov, Zhongwei Chen, Fengshou Zhang, Mingyao Wei,
and Xiangzhao Kong





Fluid Flow in Unconventional Gas Reservoirs

Geofluids

Fluid Flow in Unconventional Gas Reservoirs

Lead Guest Editor: Tongqiang Xia

Guest Editors: Egor Dontsov, Zhongwei Chen, Fengshou Zhang, Mi



Copyright © 2018 Hindawi. All rights reserved.

This is a special issue published in "Geofluids." All articles are open access articles distributed under the Creative Commons Attribution License, which permits unrestricted use, distribution, and reproduction in any medium, provided the original work is properly cited.

Editorial Board

Baojun Bai, USA
Maurizio Barbieri, Italy
Julien Bourdet, Australia
Mauro Cacace, Germany
Daniele Cinti, Italy
Timothy S. Collett, USA
Mercè Corbella, Spain
Henrik Drake, Sweden
Lionel Esteban, Australia
Cinzia Federico, Italy
Tobias P. Fischer, USA
Paulo Fonseca, Portugal
Francesco Frondini, Italy
Paolo Fulignati, Italy

Salvatore Inguaggiato, Italy
Francesco Italiano, Italy
Karsten Kroeger, New Zealand
Cornelius Langenbruch, USA
Huazhou Li, Canada
Stefano Lo Russo, Italy
Fabien Magri, Germany
Andrew H. Manning, USA
Lucie Mathieu, Canada
John A. Mavrogenes, Australia
Agnes Mazot, New Zealand
Jean-Luc Michelot, France
Ferenc Molnar, Finland
Julie K. Pearce, Australia

Daniele Pedretti, Finland
Marco Petitta, Italy
Christophe Renac, France
Reza Rezaee, Australia
Mohammad Sarmadivaleh, Australia
Christian Siebert, Germany
Ricardo L. Silva, Canada
Andri Stefansson, Iceland
Richard E. Swarbrick, UK
Rene Therrien, Canada
Umberta Tinivella, Italy
Tivadar M. Tóth, Hungary

Contents

Fluid Flow in Unconventional Gas Reservoirs

Tongqiang Xia , Egor Dontsov, Zhongwei Chen , Fengshou Zhang , Mingyao Wei , and Xiangzhao Kong

Editorial (2 pages), Article ID 2178582, Volume 2018 (2018)

Characteristics of Pores under the Influence of Cyclic Cryogenic Liquid Carbon Dioxide Using Low-Field Nuclear Magnetic Resonance

Jizhao Xu, Cheng Zhai , Lei Qin, Shangjian Wu, Yong Sun, and Ruowei Dong

Research Article (14 pages), Article ID 1682125, Volume 2018 (2018)

Effects of Formation Dip on Gas Production from Unconfined Marine Hydrate-Bearing Sediments through Depressurization

Yilong Yuan , Tianfu Xu , Yingli Xia, and Xin Xin 

Research Article (11 pages), Article ID 5836293, Volume 2018 (2018)

Effects of Maceral Compositions of Coal on Methane Adsorption Heat

Yingke Liu, Jianhong Kang , Fubao Zhou , Yanming Fan, and Haijian Li

Research Article (15 pages), Article ID 7596138, Volume 2018 (2018)

Triple-Porosity Modelling for the Simulation of Multiscale Flow Mechanisms in Shale Reservoirs

Mingyao Wei , Jishan Liu , Derek Elsworth, and Enyuan Wang

Research Article (11 pages), Article ID 6948726, Volume 2018 (2018)

A Two-Phase Flowback Model for Multiscale Diffusion and Flow in Fractured Shale Gas Reservoirs

Huimin Wang, J. G. Wang , Feng Gao , and Xiaolin Wang 

Research Article (15 pages), Article ID 5910437, Volume 2018 (2018)

Brittleness Evaluation of Shale Based on the Brazilian Splitting Test

Bing Hou, Yijin Zeng , Meng Fan, and Dandan Li

Research Article (11 pages), Article ID 3602852, Volume 2018 (2018)

Visualized Experimental Investigation on the Gas-Water Distribution Characteristics in Intersecting Fractures

Chen Wang , Yujing Jiang , Richeng Liu , and Changsheng Wang 

Research Article (10 pages), Article ID 4273450, Volume 2018 (2018)

Study on Pulse Characteristic of Produced Crude Composition in CO₂ Flooding Pilot Test

Pengxiang Diwu, Tongjing Liu , Zhenjiang You , Ganggang Hou, Runwei Qiao, and Lekun Zhao

Research Article (5 pages), Article ID 2968629, Volume 2018 (2018)

Investigating Multiphase Flow Phenomena in Fine-Grained Reservoir Rocks: Insights from Using Ethane Permeability Measurements over a Range of Pore Pressures

Eric Aidan Letham  and Robert Marc Bustin

Research Article (13 pages), Article ID 5098283, Volume 2018 (2018)

Methane Extraction from Abandoned Mines by Surface Vertical Wells: A Case Study in China

Shengyong Hu , Ao Zhang, Guorui Feng , Xiangqian Guo, Xuyang Miu, Chao Li, Dandan Han, Jin Wang, and Lixun Kang
Research Article (9 pages), Article ID 8043157, Volume 2018 (2018)

A Numerical Simulation Study of the Migration Law of Water-Sand Two-Phase Flow in Broken Rock Mass

Feng Du, Guanghui Jiang , and Zhanqing Chen 
Research Article (12 pages), Article ID 6418476, Volume 2018 (2018)

Lateral Percolation and Its Effect on Shale Gas Accumulation on the Basis of Complex Tectonic Background

Kun Zhang, Zhenxue Jiang , Xuelian Xie, Zhiye Gao , Tianlin Liu, Lishi Yin, Chengzao Jia, Yan Song, Chang'an Shan, Yinghui Wu, and Pengfei Wang
Research Article (11 pages), Article ID 5195469, Volume 2018 (2018)

Evolution of Friction and Permeability in a Propped Fracture under Shear

Fengshou Zhang, Yi Fang, Derek Elsworth, Chaoyi Wang, and Xiaofeng Yang
Research Article (13 pages), Article ID 2063747, Volume 2017 (2018)

Research on Rapid Identification and Evaluation Technology for Gas Formation during Underbalanced Drilling

Hao Wu, Ping Chen, Xiangyu Fan, Hongquan Xia, Junrui Wang, Junli Wang, and Jian Wu
Research Article (8 pages), Article ID 2742637, Volume 2017 (2018)

Back Analysis of Rock Hydraulic Fracturing by Coupling Numerical Model and Computational Intelligent Technology

Shaojun Li, Hongbo Zhao, Xiating Feng, Quan Jiang, and Qiancheng Sun
Research Article (16 pages), Article ID 5314628, Volume 2017 (2018)

Real-Time Pore Pressure Detection: Indicators and Improved Methods

Jincai Zhang and Shangxian Yin
Research Article (12 pages), Article ID 3179617, Volume 2017 (2018)

Editorial

Fluid Flow in Unconventional Gas Reservoirs

Tongqiang Xia ¹, **Egor Dontsov**,² **Zhongwei Chen** ³, **Fengshou Zhang** ⁴, **Mingyao Wei** ⁵,
and **Xiangzhao Kong**⁶

¹State Key Laboratory of Coal Resources and Safe Mining, China University of Mining and Technology, Xuzhou 221116, China

²Department of Civil and Environmental Engineering, University of Houston, Houston, TX 77004, USA

³School of Mechanical and Mining Engineering, The University of Queensland, St. Lucia, QLD 4072, Australia

⁴Department of Geotechnical Engineering, Tongji University, Shanghai 200092, China

⁵State Key Laboratory of Geomechanics and Geotechnical Engineering, Institute of Rock and Soil Mechanics, Chinese Academy of Sciences, Wuhan 430071, China

⁶Department of Earth Sciences Institute of Geophysics, ETH Zürich, 8092 Zurich, Switzerland

Correspondence should be addressed to Tongqiang Xia; tq.xia@cumt.edu.cn

Received 4 June 2018; Accepted 4 June 2018; Published 2 July 2018

Copyright © 2018 Tongqiang Xia et al. This is an open access article distributed under the Creative Commons Attribution License, which permits unrestricted use, distribution, and reproduction in any medium, provided the original work is properly cited.

Unconventional gas (including tight, shale, and coal seam gas) production has led to a drastic change of global energy landscape. The fundamental understanding of gas flow behaviours in unconventional gas reservoirs is essential to elevate the potential gas resource recovery. The behaviours of gas flow follow a chain of physicochemical processes in unconventional gas reservoirs, which can be labeled as “coupled processes” implying that one process affects the initiation and progress of another. This process chain is linked together through different disciplines, including geoscience, rock mechanics, multiphase flow, engineering chemistry, and thermodynamics, among others. Although progress on evaluation of migration, control, and recovery of unconventional gas has been achieved using mathematical models and physical experiments, the role of different fluids (e.g., CH₄ and other hydrocarbons, CO₂, and water) in unconventional gas flow is not well understood. Filling this knowledge gap is likely to play a critical impact on raising the potential of unconventional gas resource recovery and on reducing the environmental risks.

The overall theme of this special issue focuses on the impact of different fluids on flow behaviours and its impact on gas recovery. It serves as a platform for international researchers and practitioners from different disciplines to

develop innovative solutions and to explore emerging technologies in key areas of shale and coal seam gas extraction.

This special issue presented contains 16 peer-reviewed papers to address technical and scientific aspects in unconventional gas reservoirs, topics covering physical behaviour of gas reservoir (4 articles), multiphase flow mechanics (5 articles), hydraulic fracturing mechanics (3 articles), and gas production (4 articles).

This special issue is organized as follows:

- (1) Part A: physical behaviour of gas reservoir
 - (i) Triple-porosity modelling for the simulation of multiscale flow mechanisms in shale reservoirs
 - (ii) Effects of maceral compositions of coal on methane adsorption heat
 - (iii) Characteristics of pores under the influence of cyclic cryogenic liquid carbon dioxide using low-field nuclear magnetic resonance
 - (iv) Real-time pore pressure detection—indicators and improved methods
- (2) Part B: multiphase flow mechanics

- (i) A numerical simulation study of the migration law of water-sand two-phase flow in broken rock mass
 - (ii) A two-phase flowback model for multiscale diffusion and flow in fractured shale gas reservoirs
 - (iii) Visualized experimental investigation on the gas-water distribution characteristics in intersecting fractures
 - (iv) Study on pulse characteristic of produced crude composition in CO₂ flooding pilot test
 - (v) Investigating multiphase flow phenomena in fine-grained reservoir rocks: insights from using ethane permeability measurements over a range of pore pressures
- (3) Part C: hydraulic fracturing mechanics
- (i) Evolution of friction and permeability in a propped fracture under shear
 - (ii) Back analysis of rock hydraulic fracturing by coupling numerical model and computational intelligent technology
 - (iii) Brittleness evaluation of shale based on the Brazilian splitting test
- (4) Part D: issues related to gas production
- (i) Research on rapid identification and evaluation technology for gas formation while underbalanced drilling
 - (ii) Methane extraction from abandoned mines by surface vertical wells: a case study in China
 - (iii) Lateral percolation and its effect on shale gas accumulation on the basis of complex tectonic background
 - (iv) Effects of formation dip on gas production from unconfined marine hydrate-bearing sediments through depressurization

Acknowledgments

This special issue was supported by the Fundamental Research Funds for the Central Universities (2017QNA06). We would like to thank all authors for their valuable contributions and all reviewers for their collaboration in providing rigorous peer-reviewed comments that greatly improved the accepted articles in this special issue.

*Tongqiang Xia
Egor Dontsov
Zhongwei Chen
Fengshou Zhang
Mingyao Wei
Xiangzhao Kong*

Research Article

Characteristics of Pores under the Influence of Cyclic Cryogenic Liquid Carbon Dioxide Using Low-Field Nuclear Magnetic Resonance

Jizhao Xu,^{1,2,3} Cheng Zhai ,^{1,2,3} Lei Qin,^{1,2,3} Shangjian Wu,^{1,2,3} Yong Sun,^{1,2,3} and Ruowei Dong^{1,2,3}

¹State Key Laboratory of Coal Resources and Safe Mining, Xuzhou, Jiangsu 221116, China

²Key Laboratory of Coal Methane and Fire Control, Ministry of Education, China University of Mining and Technology, Xuzhou, Jiangsu 221116, China

³School of Safety Engineering, China University of Mining and Technology, Xuzhou 221116, China

Correspondence should be addressed to Cheng Zhai; greatzc@126.com

Received 25 October 2017; Revised 12 April 2018; Accepted 3 May 2018; Published 2 July 2018

Academic Editor: Fengshou Zhang

Copyright © 2018 Jizhao Xu et al. This is an open access article distributed under the Creative Commons Attribution License, which permits unrestricted use, distribution, and reproduction in any medium, provided the original work is properly cited.

The enhancement of coalbed methane extraction by repeatedly injecting CO₂ has been investigated for many decades, mostly focusing on the fracturing and flooding effect in numerous lab experiments, simulations, and field applications, whereas the effect of the accompanying heat transfer during cyclic liquid CO₂ (LCO₂) injection has rarely been studied. In this paper, the influence of the cyclic injection of cryogenic LCO₂ with different cycle numbers and time on the coal pore variation was explored using low-field nuclear magnetic resonance to extract the T_2 spectral information. The results have shown that as the cycle number increased, the adsorbed water (AW) decreased while the capillary water (CW) and bulk water (BW) values increased, and the pore volumes were magnified greatly based on the tendencies of fitted polynomial curves of I_{sa1} values and fitted exponential curve of I_{sa2} values. With increasing cycle time, the increase ratios of AW, CW, and BW were not independent but mutually influenced, and the I_{sa1} values approximately displayed a “rapid increase-slow increase” tendency, while I_{sa2} roughly showed fluctuating or “increase-decrease” tendencies. The changes in the IWS and FWS showed that the increased pore connectivity could allow more water to infiltrate into the pores at the saturation state and accelerate the removal of fluid water during the centrifugation state. The φ_e and φ_r variations indicated that longer cycle time coupled with a larger cycle number could cause damage generation and enhance the pore connectivity.

1. Introduction

Coalbed methane (CBM) is mainly formed during a long epoch of coalification stages and reserves in the coal seams under the effect of stratum sedimentation accompanied by high temperature and pressure [1–4]. The detectable CBM content in the reservoirs is abundant, and its recovery has attracted interests and concerns from many governments, researchers, and entrepreneurs, due to its higher calorific value, abundant content, and less environmentally damaging nature [5, 6]. However, the permeability of most Chinese coal seams is generally three orders of magnitude lower than that of the San Juan basin, which is unsatisfactory for effective gas

extraction merely based on its original conditions [7–9]. Therefore, it is necessary to explore possible ways to improve the permeability.

Enhanced CBM (ECBM) recovery by injecting CO₂ along with amounts of proppants into the reservoirs along the fracture wells has been proposed and developed in some countries such as the United States [10, 11], Canada [12, 13], China [14, 15], and Japan [16, 17]; the reported results have all suggested that CO₂-ECBM has a significant application feasibility and that this method could increase the extraction efficiency by enhancing the permeability of reservoirs. In particular, liquid CO₂ (LCO₂) has been widely applied in the field of ECBM recovery [18]. LCO₂ has a

large liquid gas expansion ratio of 1:557 at 273K and 1 atm, which can be used to generate huge gas pressures in confined spaces [19]. Cao et al. [20] studied the application of CO₂ gas fracturing in low-permeability gassy coal seams using the CARDOX system, which could cause the LCO₂ to form a high-pressure gas, and the results indicated that the permeability and methane drainage effectiveness were significantly improved. The larger adsorption capacity could help CO₂ compete with CH₄ to adsorb on the coal matrix, which finally converts a huge volume of adsorbed CH₄ to the free state [21, 22]. The complete compatibility with the matrix could avoid some reservoir damages, and the formed acidic species with lower pH values might prevent iron hydroxides from forming, buffer against clay reactions, and reduce the flow resistance of gas [23, 24]. Meanwhile, the geological sequestration of CO₂ could be achieved to some extent [25, 26].

Generally, the latent heat of evaporation for LCO₂ is 347 kJ/kg; therefore, it can adsorb a considerable amount of heat from the surroundings. When sufficient amounts of LCO₂ are injected in the boreholes, the heat transfer will occur at the contact surface between the LCO₂ and the coal matrix. A previous study has shown that the temperature of coals decreased obviously and even to less than -18°C when the core was contacted with LCO₂ media, causing the matrix to shrink [19]. A temperature gradient would be formed due to the high inherent temperature of the surrounding coal matrix, and a temperature stress was generated, accompanying one cycle of the “freeze-thaw” (“F-T”) process, which might induce some damage to occur in the coals [27]. The strengths of six sandstones under the effect of a cyclic F-T process deteriorated significantly [28]. Zhai et al. [29] studied consecutive F-T cycles on coal pore structure deterioration by using a compressor and a condenser, and the results from low-field nuclear magnetic resonance (LF-NMR) and scanning electron microscopy showed that the coal samples were significantly destroyed by F-T cycles, with numerous cracks generated on the coal surfaces. The F-T cycle number decreased the mechanical properties of rocks or cement materials, including shear strength [30], uniaxial compressive strength [31, 32], elastic modulus [33, 34], and P-wave velocity [35–37], and the integrity loss of the rocks was verified by a decay function [38]. Xu et al. proved the feasibility of cryogenic effects from cyclic LCO₂ fracturing [19] and investigated the influence of F-T effect on the pore variations of coal with different ranks [27], and the results all showed that the cyclic F-T process with LCO₂ had significant effects on the pore enhancement.

The mentioned publications mostly focused on the deterioration of the F-T effect with different cycle numbers, and rarely considering other cyclic parameters. In this paper, the influence of LCO₂ with different cycle numbers and time on the pore variation was studied, where the experimental subjects were six cores drilled from the same coal block. The methodology of pore measurement is introduced in Section 2, and some of the materials and equipment are described in Section 3. Finally, the experimental results are analyzed in Section 4.

2. Methodology

In general, the porous coal is composed of two subsystems, the coal matrix system and the fracture system, in which there are several states for CBM occurrence: trapped gas within the matrix pores, adsorption gas within micropores (<2 nm), and dissociative gas and dissolved gas in water within the fractures [39–41]. The diffusion phase in the matrix is determined by the concentration gradient, while the seepage phase in the cleats or fractures influences the gas extraction efficiency considerably [42, 43]. Porosity and permeability are two important evaluation indices to measure the volume of reserve gas and the seepage features of coals, respectively [44, 45]. Porosity is usually considered as the void spaces within the coal matrix and represents the capacity of coals to retain fluids, such as liquid or gas, which then indicates that a highly porous reservoir has a great potential to reserve abundant gas [46, 47]. The property determining the fluid flow ability through the coals via the interconnection of the pore spaces is known as permeability, which greatly influences the transport characteristics of CBM, such as migration within the matrix and flow from the matrix to the cleats or fractures [48].

Currently, the measurement methods for the petrophysical properties of coal, such as scanning electron microscopy (SEM) [49], optical microscopy, or transmission electron microscopy [50], usually display the surface morphology and pore size distribution qualitatively. The quantitative measurements, including gas adsorption [51], mercury intrusion porosimetry (MIP) [52], micro-X-ray tomography [53], and small-angle X-ray scattering or neutron scattering (SAXS/SANS) methods [54], could show the detailed information of the pores from a numerical aspect. However, these methods always have limited measurement ranges for the pore size as well as low efficiency and they cause damage to the pore structures [55]. Due to its properties of being nondestructive and highly efficient and having large test ranges, low-field nuclear magnetic resonance (LF-NMR) has been provided as an alternative measurement technique to obtain internal pore information for coal.

Water is generally the medium used to characterize the internal void spaces of porous media; the net magnetization of a hydrogen atom or proton ¹H from water-saturated coal placed in the sample chamber refers to an attenuation curve between signal amplitude and relaxation time using the Carr-Purcell-Meiboom-Gill (CPMG) spin-echo pulse sequence, which will be recorded by LF-NMR under the magnetic phenomenon [27, 52, 55] (shown in Figure 1). The signal amplitude is positively correlated to the proton ¹H number, which indirectly corresponds to the internal water content and therefore the pore spaces, that is, the porosity. Compared to the water kinetics from the T₂ spectra at the saturation condition, the kinetics from the T₂ spectra under the centrifugation condition are always different, and the longer T₂ values represent the mobile water molecules while the shorter values represent the irreducible water; thus, the entire T₂ spectrum could characterize the pore distribution. The amplitude values are proportional to

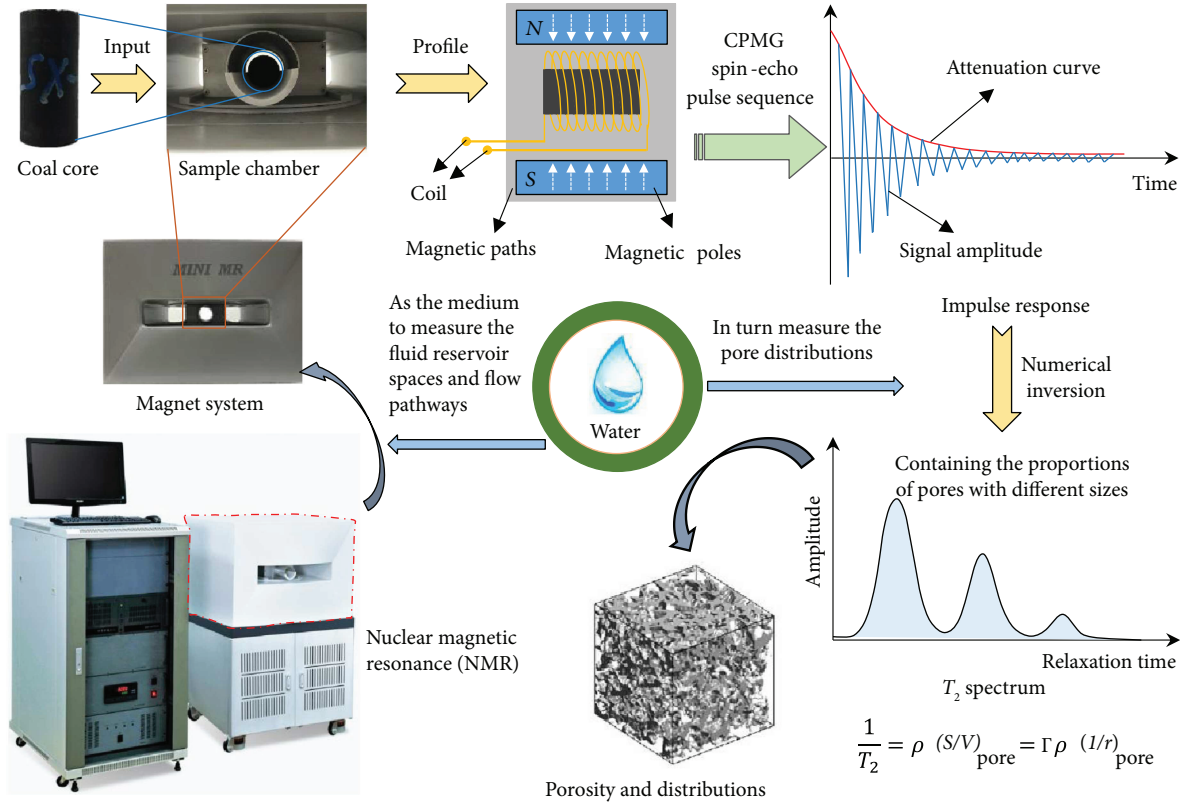


FIGURE 1: The measurement principle and process of LF-NMR.

the ratio of the pore surface to the pore volume according to Kleinberg et al. [56]:

$$\frac{1}{T_2} = \rho \left(\frac{S}{V} \right)_{\text{pore}} = \Gamma \rho \left(\frac{1}{r} \right)_{\text{pore}}, \quad (1)$$

where ρ is the surface relaxivity occurring at the mineral surface in $\mu\text{m/s}$; $(S/V)_{\text{pore}}$ is the surface to volume of the pore in μm^{-1} ; r is the pore radius in μm ; and Γ is a pore geometry constant.

3. Materials and Equipment

3.1. Coal Core Preparation. All six cores were drilled from the same coal block that came from Datong Coal Mine, Shanxi province, China, and their shapes are cylinders with an approximate diameter of 25 mm and an approximate length of 50 mm, as shown in Figure 2. These cores were labeled $sx-i$ ($i=1, 2, \dots, 6$). The proximate analysis results showed that cores $sx-i$ had a moisture value of 4.83%, ash yield value of 7.3%, volatile matter dry ash-free basis value of 29.64%, and fixed carbon content value of 58.23%. The $R_{o,\text{max}}$ value is 0.43, with values of 75.3% for vitrinite, 18.6% for inertinite, 2.7% for exinite, and 5.3% for minerals [57].

3.2. Experimental System and Procedures. According to previous studies [19, 27], an innovative experimental system (shown in Figure 3) comprised three components: a

cryogenic system, an LCO_2 injection system, and a data monitoring system. The first subsystem provides the cryogenic environment during the LCO_2 injection process, and the thermal insulation material around the chamber is used to maintain the internal low-temperature condition. The pressure relief valve is used to relieve the excess gas pressure for safety. The second subsystem could constantly inject LCO_2 into the chamber by using a pump. The function of the third subsystem mainly records the corresponding data during the experimental process with a pressure sensor and thermocouple to express the gas pressure and temperature, respectively.

During the pretest and posttest processing, the pore size and distributions of cores were tested by an LF-NMR (mini MR60) manufactured from Niumag Analytical Instrument Corporation, Suzhou, China, which has a magnetic field of 0.51 T, maximum sampling frequency of 333 kHz, and maximum echo number of 20000. Next, its auxiliary equipment, such as a vacuum drying oven (DHG-9023A), vacuum water saturation device (NEL-VJH), and rock centrifuge (TG16-WS), is also used to cause the cores to undergo the “drying-saturation-centrifugation” process for the purpose of obtaining the related T_2 spectra under the saturation and centrifugation conditions.

LF-NMR has a strict working temperature of 305 K for the purpose of accurate T_2 spectral measurement, and its sample scanning times were set at 64. The ambient (room) temperature and relative humidity were 298 K and 40%, respectively, and the drying temperature was set at 313 K.

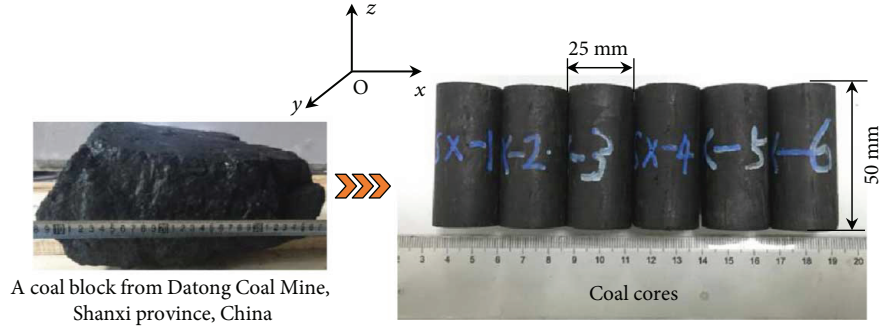


FIGURE 2: Images of coal block and drilled cores.

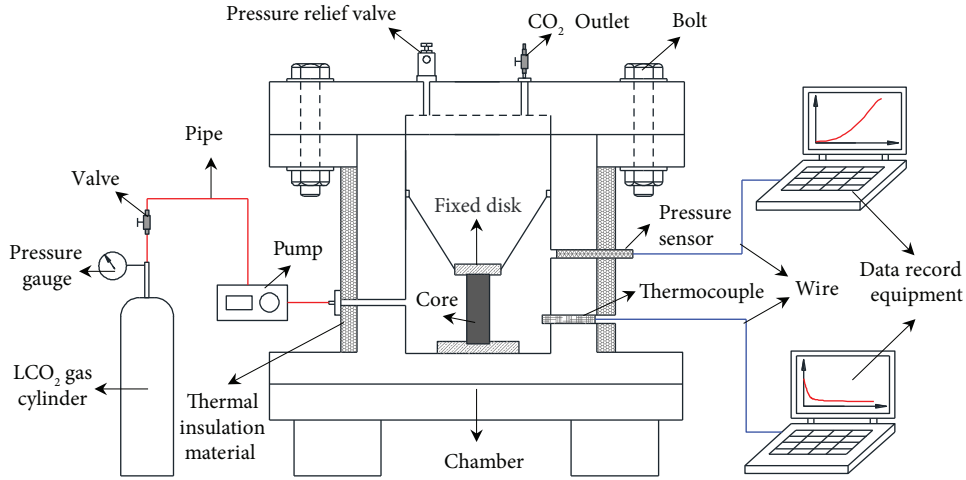


FIGURE 3: Sketch image of the experimental system.

TABLE 1: Experimental design of six cores.

Core number	Cycle number	LCO ₂ injection (min)	Normal temperature (min)	Total cycle time (min)
sx-1		5	5	10
sx-2		10	10	20
sx-3	5, 10, 15, 20,	15	15	30
sx-4	25	20	20	40
sx-5		25	25	50
sx-6		30	30	60

The experimental design is listed in Table 1, in which the cores were alternately placed in the cryogenic and the normal temperature environment to simulate the cyclic thermal interaction process. Initially, the weights of dried cores were tested by a balance, and then, they were immersed into distilled water for 24 hr to reach their saturation state. The saturated cores were measured by LF-NMR and a balance to obtain their original T_2 spectra and weights, respectively, for the saturation condition; next, the cores were centrifuged via rock centrifuge for 1.5 hr to remove the movable water and generate the centrifuged core state, and the original T_2 spectra and weights for the centrifugation condition

were measured by LF-NMR and a balance, respectively. Next, these cores were immersed into distilled water to ensure their saturation; then, they were packaged with a thin film and placed in a precooled chamber; LCO₂ was injected from the cylinder into the chamber; the cryogenic cores were then placed in a normal-temperature environment; and the durations for these steps are all listed in Table 1. Considering the water runoff, the cores affected by one cycle were then processed according to the flow path of “saturation-measurement-centrifugation-measurement.” Finally, the entire experiment was completed on the basis of the above testing process.

4. Results and Analysis

4.1. T_2 Spectral Analysis. Some T_2 spectra under the saturation and centrifugation conditions were obtained after different cycles of the LCO₂ injection process. Due to the similarity of the curves, core sx-1 was selected for the study of T_2 spectral changes along the relaxation time, and the distributions of the T_2 spectra at the initial state, after 15 cycles and after 25 cycles under two conditions, are shown in Figure 4. As seen in Figure 4(a), the amplitude peak values increased after different numbers of cycles of LCO₂ injection compared to those values at the initial state and

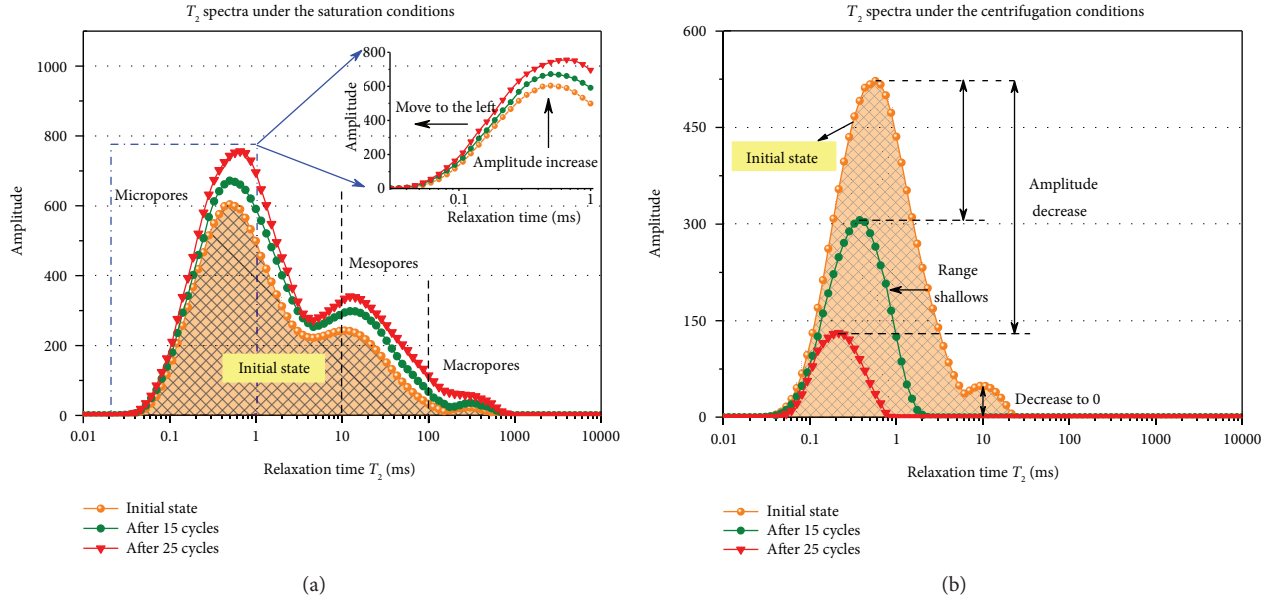


FIGURE 4: T_2 spectral curves of core sx-1 under the saturation and centrifugation conditions.

the amplitude increase was positively correlated to the cycle number; the amplitude values decreased with an increasing number of cycles of LCO₂ injection, and the decrement was negatively correlated to the cycle numbers. The T_2 spectra of the water-saturated cores expressed three distinct peaks, and from left to right, the corresponding pore sizes were micropores, mesopores, and macropores [19, 27, 55, 58], which indicated that the distilled water occupied approximately all the open or semiopen pores; the increased amplitude values and widened T_2 ranges all showed that the pore size and distributions varied greatly after different numbers of cycles of LCO₂ injection. The greater the amplitude increase and the larger the T_2 coverage, the greater the water volume and pore spaces. Meanwhile, the T_2 curves of the centrifuged cores showed two peaks or one peak, which indicated that the water in the larger pore sizes was removed and that the decreased amplitude value and the narrowing T_2 coverage all meant that the pore connectivity increased after different numbers of cycles of LCO₂ injection.

4.2. Variations of Three Types of Water in Cores. According to Dillinger and Esteban and Olatinsu et al. [59, 60], the T_2 curves of saturated cores usually contain some information about the relationship between water types and pores with different sizes; in general, the relaxation time less than 10 ms, dependent on the surface relaxation from the micropore walls, represents the adsorbed water (AW); the relaxation time from 10 ms to 100 ms, attributed to the surface relaxation in the mesopores, denotes the capillary water (CW); and the relaxation time larger than 100 ms (up to 10,000 ms), corresponding to the macropores, signifies the bulk water (BW). Figure 5(a) shows the variations of AW, CW, and BW for cores sx-1 and sx-4 with increasing cycle numbers. The three types of water proportions varied differently; for example, the proportions of BW all increased,

the CW proportion increased, and the AW proportion decreased for core sx-4, while the maximum CW proportion and the minimum AW proportion of core sx-1 were present after 20 cycles. Figures 5(b)–5(d) show the variations of AW, CW, and BW, respectively. As the cycle number increased, the AW of six cores all expressed decreasing trends of different amplitudes, and the cores' CW and BW increased in the opposite direction. The values of AW, CW, and BW were within the range of [0.812, 0.84], [0.143, 0.173], and [0.007, 0.017], respectively, at the initial state; then, the values correspondingly changed to the ranges of [0.759, 0.802], [0.172, 0.193], and [0.02, 0.05] after 15 cycles of LCO₂ injection and of [0.731, 0.791], [0.176, 0.202], and [0.033, 0.067] after 25 cycles of LCO₂ injection. The changes indicated that the water proportion variations were comprehensively impacted by the changes of pore sizes; additionally, the AW decrease did not mean that the micropore numbers decreased but rather that those pores transformed into mesopores under a cyclic “shrink-swell” effect, causing unallowable deformation generation and internal damage within the coal matrix. In the meantime, the partial CW freezing could enlarge the size of the mesopores to form macropores due to the ice-wedge effect. The longer LCO₂ injection time might cause the CW and BW to freeze completely, providing more opportunities for the macropore number to increase.

Figure 5 shows the distributions of the three types of water values; however, due to the different initial values, the subsequent values changed greatly on the basis of the larger values; thus, it is necessary to estimate the increase ratios of AW, CW, and BW compared to the initial values under different cycle numbers and cycle time, and their variations are each shown in Figure 6. On the one hand, the increase ratios of AW displayed “decrease-increase-decrease” trends, while those of CW showed an “increase-decrease-increase” tendency after 5 cycles and 10 cycles; on the other hand,

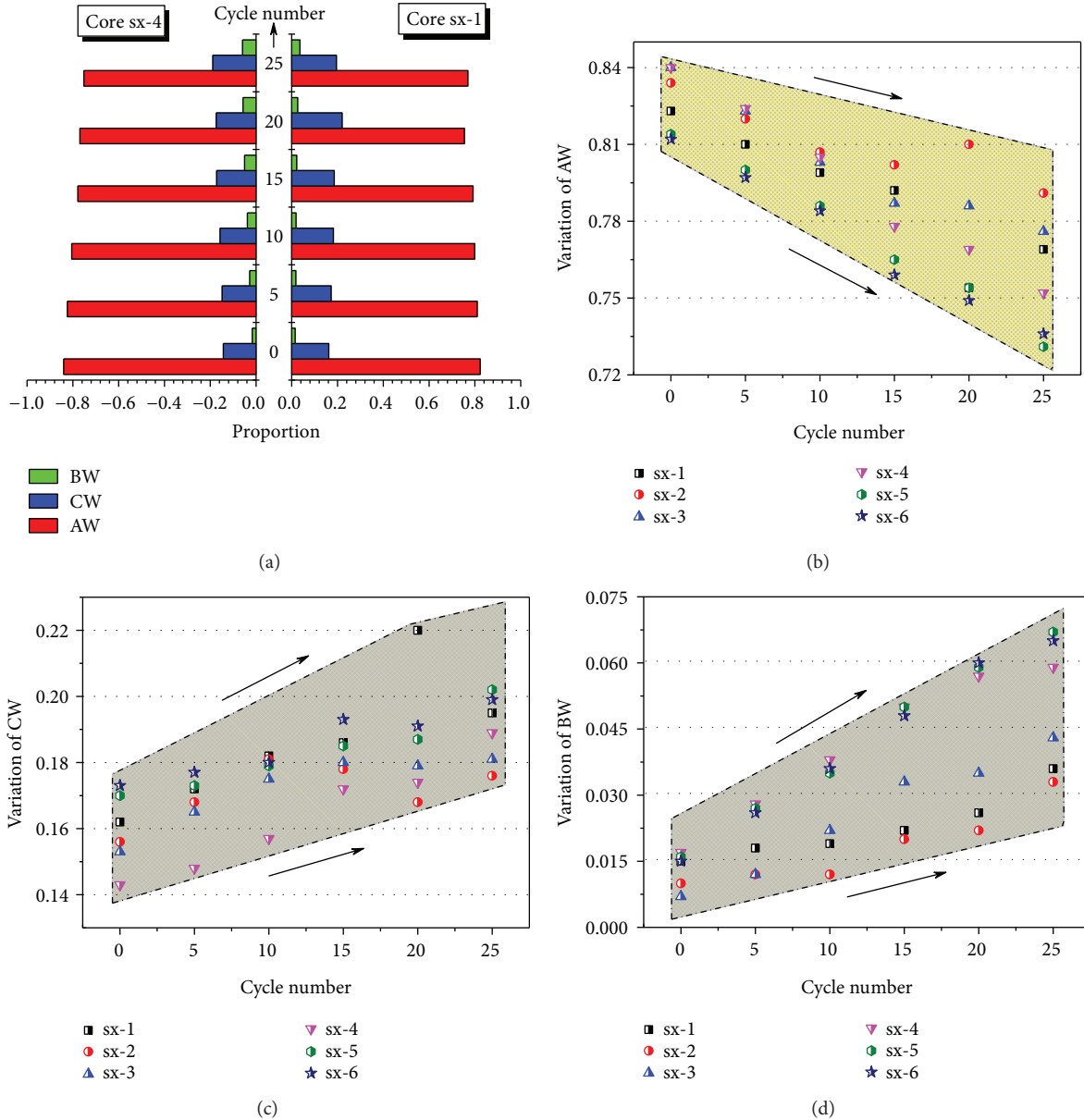


FIGURE 5: Changes of AW, CW, and BW for different cores: (a) proportion of AW, CW, and BW for cores sx-1 and sx-4; (b), (c), and (d) mean the variations of AW, CW, and BW, respectively, with increasing cycle number.

the increase ratios of AW and CW all changed adversely with higher cycle numbers; however, the increase ratios of BW approximately showed similar “increase-decrease-increase” changes as the cycle time increased.

As seen in Figures 6(a)–6(c), the largest increase ratios of AW (negative values) and the smallest increase ratios of CW and BW after 5 cycles all indicated that the lower cycle numbers could partly cause the internal pores with different sizes to change with small amplitude and that the increase ratios of three types of water varied greatly with large amplitudes after the longer cycle time. The increase ratios of water after 20 cycles and 25 cycles had the largest changes that accompanied the sharp increase or decrease. These variations and differences all indicated that the water increase ratios were positively correlated to the cycle number and that the larger

cycle numbers could freeze the saturated water and shrink the coal matrix for larger times, inducing more “unallowed damages or deformations” to form and accumulate with circulation, which would cause many transformations among pores with different sizes; thus, LCO₂ injection with more cycles had greater superiority to enhance the fracture results by producing many macropores to provide free pathways for fluids. Moreover, the three water increase ratio variations were not independent but were affected mutually, as shown in Figure 6(d). The greater BW increase ratios, representing the larger BW proportion, signified a larger transformation of mesopores due to the ice-wedge effect; meanwhile, the cyclic F-T process also facilitated the growing amount of mesopores and the corresponding CW proportions and increase ratios also increased. After the larger cycle numbers,

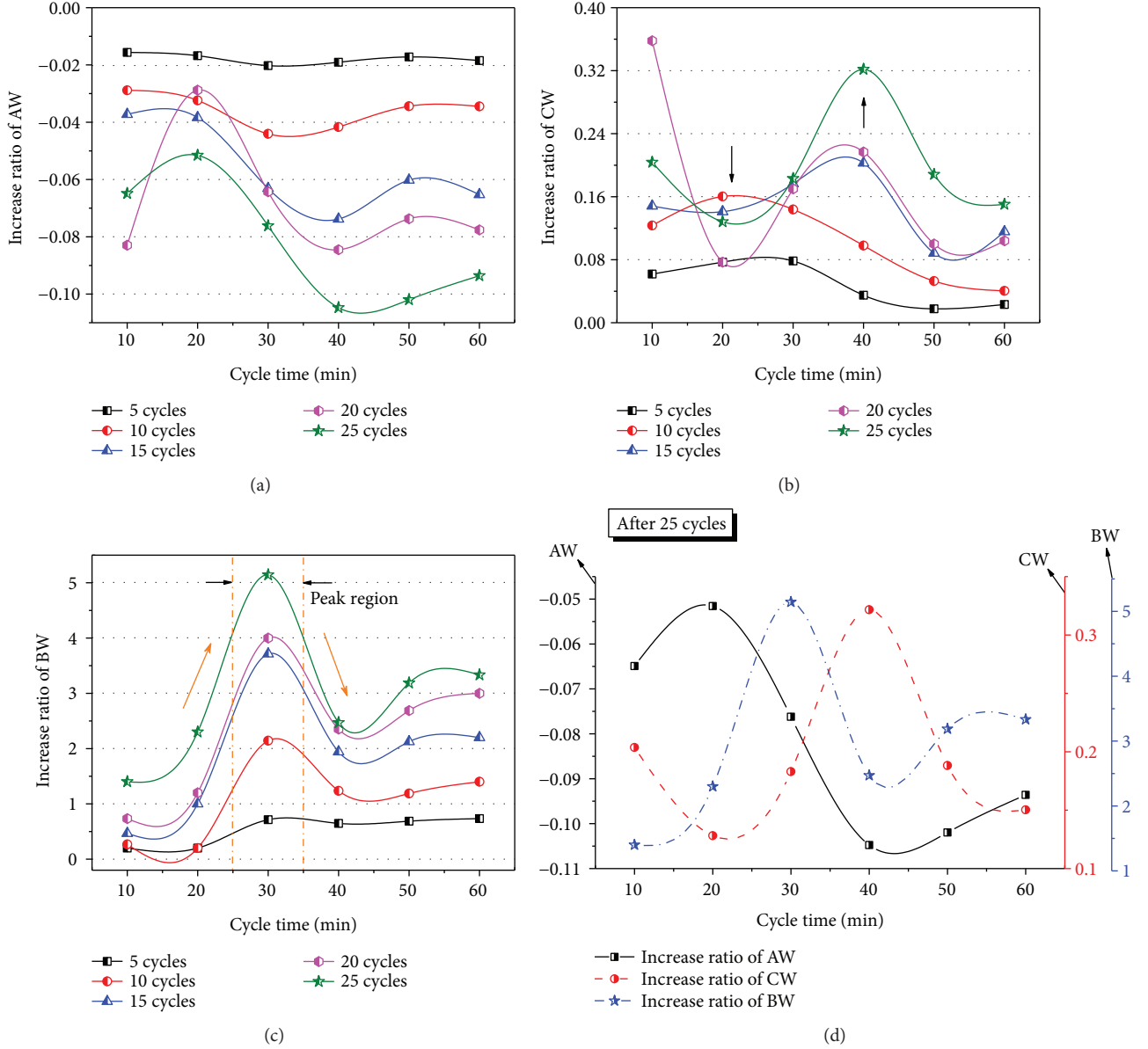


FIGURE 6: Increase ratio of AW, CW, and BW for six cores after different cycle time and cycle numbers.

the AW increase ratios (negative values) were minimized under the cycle time of 40 min, which was true for the maximum CW increase ratios as well, while the maximum increase ratios of BW were at the cycle time of 30 min. This enhancement analysis could provide some information to improve the LCO₂ cyclic injection process.

4.3. Analysis of Spectral Areas. The coverage under a T_2 spectrum commonly indicates the pore volumes including the pores with different sizes where water could infiltrate. The spectral area is calculated by an integration of the amplitude along the relaxation time, and a greater amplitude with wider range indicates a larger internal pore volume at a certain time duration. To obtain the information of pore volume changes from the T_2 spectra, an increase ratio of spectral area I_{saij} was adopted to characterize the area enhancement due to the

various initial values of the different cores. The function of I_{saij} was deduced as follows:

$$I_{saij} = \frac{\Delta S_{ij}}{S_{inj}} = \frac{S_{poij} - S_{inj}}{S_{inj}}, \quad i = 5, 10, \dots, 25, j = 1, 2, \quad (2)$$

where I_{saij} means the increase ratio of the spectral area under saturation and centrifugation states after the i th cycle injection; S_{poij} and S_{inj} represent the spectral areas after the i th cycle of LCO₂ injection and the initial areas, respectively; ΔS_{ij} is the difference between S_{poij} and S_{inj} ; and $j = 1, 2$ means the two states of saturation and centrifugation.

As seen in Figures 7(a) and 7(b), the I_{sa1} of six cores increased with different amplitudes with the increasing cycle number, which indicated that the internal pore volumes all

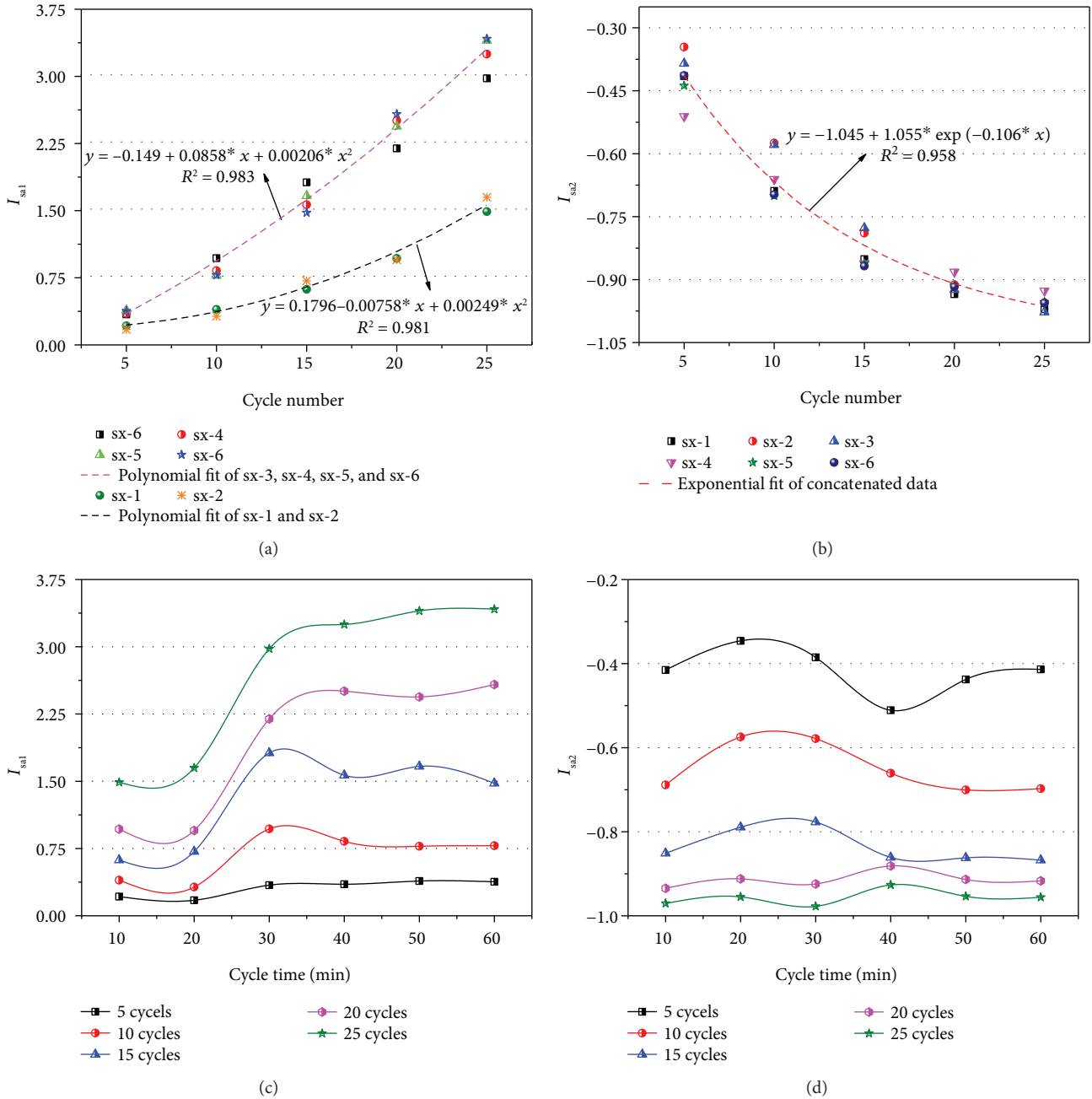


FIGURE 7: Variations of I_{sa1} and I_{sa2} with increasing cycle number and cycle time.

enlarged after the cyclic F-T effect from LCO₂ injection with different cycles. The connectivity among pores was enhanced in the form of uplifting amplitude peaks and widening curve coverage, enabling the water to immerse in the pore spaces, and the greater I_{sa1} meant the greater enhancement of pore volume and connectivity. Moreover, the I_{sa1} scatters were distributed with two different regions at the dividing cycle time of 20 min: the I_{sa1} scatters of cores affected for less than 20 min cycle time increased slowly, whereas those effected for more than 20 min cycle time increased greatly. Due to the fewer differences among their values at a certain cycle number within each region, the method of concatenated fit was

used to approximate the variation tendency. The data in the two regions were all fitted by polynomial curves with good fit coefficients larger than 0.98:

$$\begin{aligned} \text{Small } I_{sa1} \text{ region : } y &= -0.149 + 0.0858x \\ &+ 0.00206x^2 \quad (R^2 = 0.983), \\ \text{Large } I_{sa1} \text{ region : } y &= 0.1796 - 0.00758x \\ &+ 0.00249x^2 \quad (R^2 = 0.981). \end{aligned} \quad (3)$$

In contrast, the I_{sa2} values of the six cores in Figure 7(b) all decreased as the cycle number increased, and these

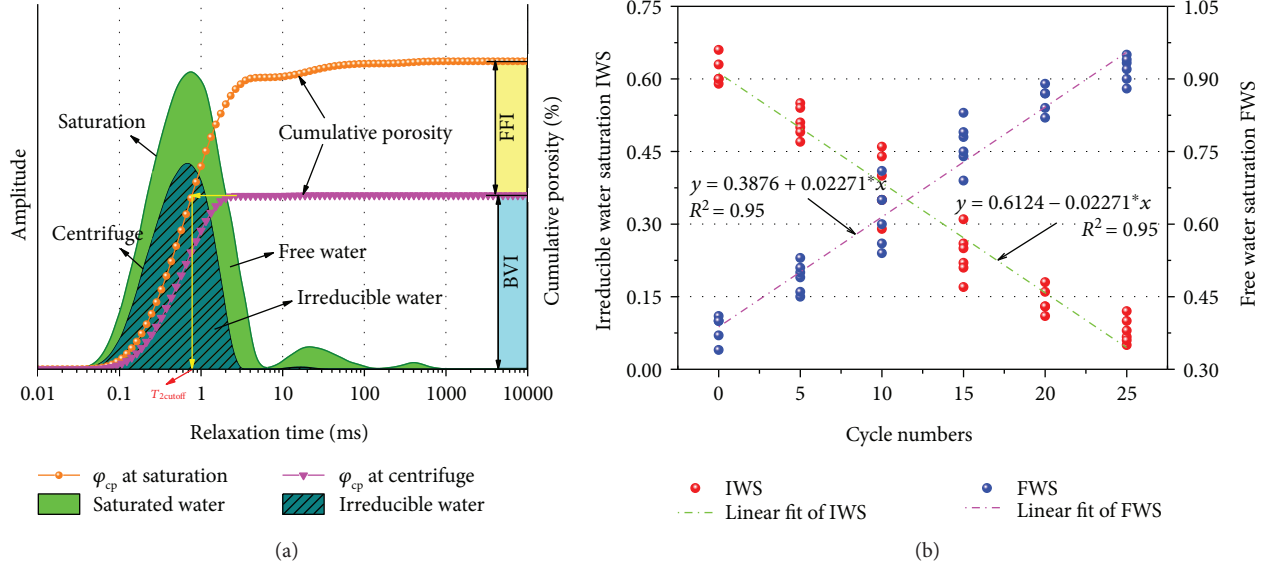


FIGURE 8: Diagram of the porosity division dependent on the T_2 spectra (a) and scatters and the fitting lines of IWS and FWS (b).

scatters were all fitted as exponential curves, with their concatenated data fit curve shown as follows:

$$y = -1.045 + 1.055 \cdot \exp(-0.1026 \cdot x) \quad (R^2 = 0.958). \quad (4)$$

The fit curves of the I_{sa1} and I_{sa2} values all indicated that the pore volumes magnified more greatly as the cycle number increased. The cyclic effect of the F-T process would cause many deformations or damage to be generated around the pore walls or tips, and the physical parameters of whole cores decreased; thus, the pore spaces will easily be enlarged under the coupled effect of temperature stress and ice extrusion, which would cause more water to occupy the pores under the saturation state and to be removed from the free spaces under the centrifugation condition.

Figures 7(c) and 7(d) both show the variations of I_{sa1} and I_{sa2} with increasing cycle time. On the whole, the I_{sa1} increments and I_{sa2} decrements after larger cycles of LCO₂ injection were all greater than those after LCO₂ injection with smaller cycles, which was well consistent with (3) and (4). Moreover, as the cycle time increased, the I_{sa1} values approximately displayed a “rapid increase-slow increase” tendency, while I_{sa2} roughly showed an “increase-decrease” tendency for short cycles and double “increase-decrease” trends for long cycles. In addition, the I_{sa1} values with longer cycle time increased much more than those with a shorter cycle time; both I_{sa2} variations indicated that the number of open or semiopen pores increased, causing more free water to be removed during the centrifugation process. The potentials indicated that the longer freezing time might cause the matrix to conduct the heat and cause the saturated water occupying the pores with different sizes to freeze into ice completely, after which the pore volumes would be magnified much more due to the ice-extrusion and ice-wedge effects.

4.4. Porosity Analysis. The weight method was used to calculate the porosity under the water saturation and centrifugation conditions. The original weight of the completely dried core was regarded as M_{dry} , and the water-saturated cores and centrifuged cores after LCO₂ treatment with different cycle parameters were regarded as M_{sat} and M_{cen} , respectively. Thus, the corresponding porosity ϕ could be calculated as follows [19, 27]:

$$\phi = \frac{V_{water}}{V_{core}} = \begin{cases} \frac{(M_{sat} - M_{dry})}{V_{core}} \text{ (saturation),} \\ \frac{(M_{cen} - M_{dry})}{V_{core}} \text{ (centrifuge),} \end{cases} \quad (5)$$

where V_{water} and V_{core} represent the water volume in pores and the core volume (cm^3), respectively, $(M_{sat} - M_{dry})/V_{core}$ is for saturation, $(M_{cen} - M_{dry})/V_{core}$ is for centrifugation, and the water density is 1 g/cm^3 .

According to [27, 57, 61, 62], the T_2 spectra under the saturation and centrifugation conditions also characterize the variation of three kinds of porosity, such as total porosity (ϕ_t), effective porosity (ϕ_e), and residual porosity (ϕ_r). Figure 8(a) shows the diagram of porosity division dependent on the T_2 spectra. All the amplitude values were processed using normalization calculation, and the cumulative porosity under saturation was deemed to be ϕ_t while the cumulative porosity under centrifugation was considered to be ϕ_r ; thus, the difference of ϕ_r from ϕ_t was ϕ_e . Moreover, the spectral area of the centrifuged core always represents the remaining water volume in the pores, namely, the bound pore volume; thus, the ratio of the spectral area at centrifugation to that at saturation, referred to as the irreducible water saturation (IWS), might be adopted to characterize the proportion variation of bound pore volume under the effect of the LCO₂ injection, which also expresses the volume changes of the

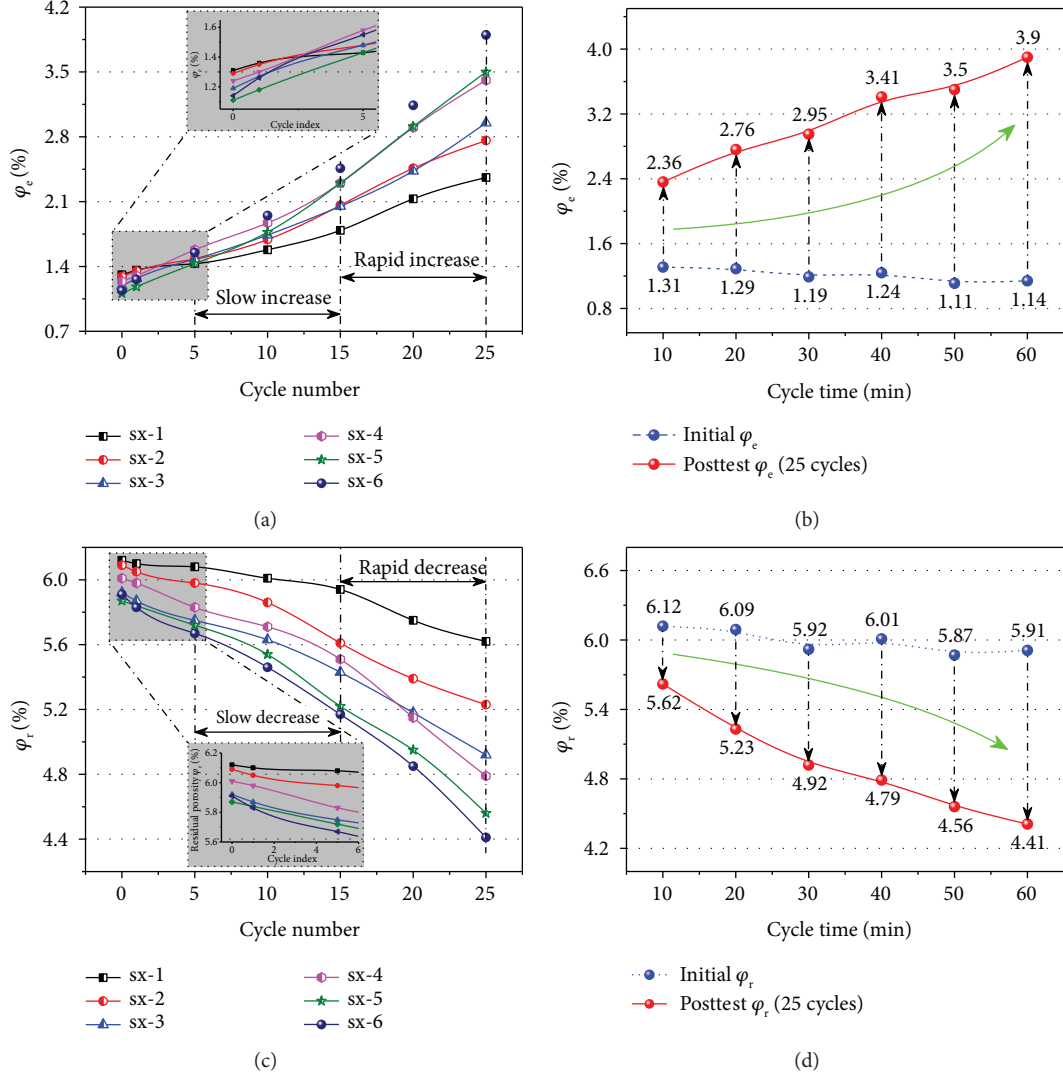


FIGURE 9: Variations in the φ_e and φ_r values of the six cores after different cycle time and cycle numbers.

connected pore. Thus, the equations of IWS and free water saturation (FWS) were deduced as follows:

$$\begin{aligned} \text{IWS} &= \frac{S_{\text{cen}}}{S_{\text{sat}}}, \\ \text{FWS} &= \frac{S_{\text{sat}} - S_{\text{cen}}}{S_{\text{sat}}} = 1 - \frac{S_{\text{cen}}}{S_{\text{sat}}}. \end{aligned} \quad (6)$$

As seen in Figure 8(b), all the IWS and FWS values of the six cores show similar changes with increasing cycle number. The IWS values decreased as the cycle number increased, which was consistent with the tendency of increased amplitude and widened T_2 spectral coverage under the saturation condition. Meanwhile, the FWS values were negatively correlated to the cycle number, which indicated that more fluid water was removed from the saturated cores, which in turn indicated that the free pore volume and space increased after the cyclic LCO₂ application. Moreover, there were linear

relationships between the two kinds of corresponding concatenated values and cycle number:

$$\begin{aligned} \text{IWS} : y &= 0.3876 + 0.02271 * x (R^2 = 0.95), \\ \text{FWS} : y &= 0.6124 - 0.02271 * x (R^2 = 0.95). \end{aligned} \quad (7)$$

These two linear fit curves all have great fit coefficients of 0.95, and the potentials of IWS and FWS indicated that the increments and decrements were relatively variable; as the total pore volume increased, the amounts of immersed water or removed water were also influenced by several factors, such as the chemical and physical properties of pore walls, the clay content, and the mineral distributions.

Dependent on (5) and Figure 8(a), the variations in φ_e and φ_r after LCO₂ treatment with different cycle parameters are shown in Figure 9. Figures 9(a) and 9(b) show that the φ_e values change with the increasing cycle parameters, and Figures 9(c) and 9(d) display the variations in the φ_r values as the cycle parameters increase. All the φ_e values positively

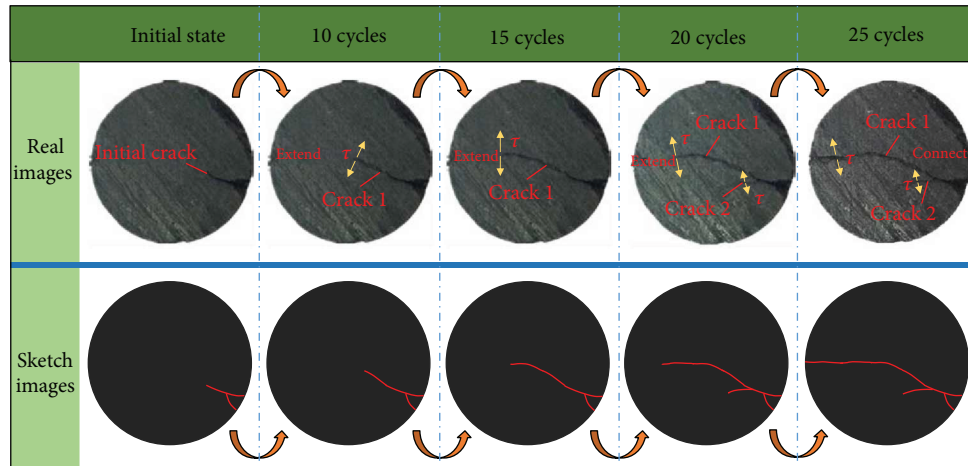


FIGURE 10: Propagation of a surface crack of sx-1 in forms of real images and sketch images.

correlated to the cycle parameters and had a “slow increase-rapid increase” tendency, whereas the φ_r values were negatively related to the cycle parameters and showed a “slow decrease-rapid decrease” trend. With a case study of core sx-3, the φ_e increment was 0.26% with an increase ratio of 46.2% after 10 cycle numbers, while it was 1.76% with an increase ratio of 176% after 25 cycle numbers. However, the φ_r decrement was 0.29% (decrease ratio of 4.9%) after 10 cycle numbers and 1% (decrease ratio of 16.9%) after 25 cycle numbers. The increased φ_e and the decreased φ_r all indicated that the cycle number had a great enhancement effect on the porosity alteration, which might increase the pore size and improve the connectivity. After the same number of cycles, the φ_e and φ_r values of the six cores exhibited different changes. Core sx-6 had the maximum φ_e increment of 2.76% (with an increase ratio of 243%) and φ_r decrement of 1.5% (with a decrease ratio of 25.4%), while core sx-1 had the minimum φ_e increment of 1.05% (with an 80.2% increase ratio) and φ_r decrement of 0.5% (with an 8.17% decrease ratio). This difference might be dependent on the cycle time, as the longer cycle time caused the matrix to completely shrink and swell to generate larger amounts of damage, eventually weakening the strength of the coal.

4.5. Crack Evolution Analysis. To intuitively characterize the results after some LCO₂ injection cycles, the photos and the corresponding sketch images of core sx-1 shown in Figure 10 were studied. A crack of small length was initially preexistent on the end surface; when the cycle number was 10 cycles, crack 1 had propagated for a certain distance under the effect of tension stress τ caused by the coupled mechanism between temperature stress and ice swelling force during the cyclic LCO₂ injection. As the cycle number increased, crack 1 extended continuously and crack 2 was generated at the weakened location along crack 1 when the cycle number reached 20 cycles. After the cycle number reached 25 cycles, crack 2 had propagated slowly, and crack 1 finally extended through the whole end surface. This process might be influenced by several factors: the mineral distribution, the petrological structure, and/or the water content

and its leakage quantity. The more uneven mineral distribution and the more complex petrological structure caused the cold to conduct less uniformly, resulting in some temperature stress to be produced among the contact points among the particles. The larger the amount of saturated water in the crack there is, the greater the ice volume preparation and the more violent the ice-wedge effect is. Under the cyclically coupled effect of temperature stress and ice-swelling force, the crack length was increased, and the connectivity between the cracks was enhanced; finally, the coal porosity was improved.

Analyses were performed regarding the variation in the different types of water, the change of spectral area, and the porosity, and some significant results were obtained. However, some research gaps still existed and were not explored, for instance, the relationship between the three types of water variation and the porosity, the relationships between the cycle parameters and the porosity, and the optimal application range of the different cycle parameters. Thus, many works will be carried out in future studies to improve the mechanistic understanding of these processes.

5. Conclusions

Several conclusions were made:

- (1) The T_2 spectra under saturation and centrifugation conditions obtained by LF-NMR with different cycle parameters were analyzed. As the cycle number increased, the AW values of all the cores decreased with different amplitudes while the CW and BW values increased adversely and their increase ratio variations were not independent but were influenced mutually.
- (2) The water increase ratios were positively correlated to the cycle number. Larger cycle numbers could freeze the saturated water and shrink the coal matrix more times, inducing more “unallowed damages or deformations” to form and accumulate with circulation,

which would cause many transformations to occur among pores with different sizes.

- (3) The concatenated I_{sa1} values were fitted as two different polynomial curves with fit coefficients more than 0.98, and the concatenated I_{sa2} values were fitted as an exponential curve with fit coefficient more than 0.95. The increased I_{sa1} and decreased I_{sa2} of the six cores all indicated that the pore volumes were magnified much more as the cycle number increased. Moreover, as the cycle time increased, I_{sa1} values approximately displayed a “rapid increase-slowly increase” tendency, while I_{sa2} approximately showed a singular “increase-decrease” tendency for short cycles and double “increase-decrease” trends for long cycles.
- (4) The positive relationship between the IWS values and cycle numbers was consistent with the tendency of increased amplitude and widened coverage of T_2 spectra under the saturation, whereas the negative relationship between the FWS value and cycle number indicated that free pore volume and space increased after the cyclic LCO₂ treatment. Moreover, the linear fit curves between the two corresponding concatenated values and cycle number were fitted well with a fit coefficient more than 0.95.
- (5) All the φ_e values were positively correlated to the cycle parameters and had a “slow increase-rapid increase” tendency whereas the φ_r values were negatively correlated to the cycle parameters and showed a “slow decrease-rapid decrease” trend. These variations indicated that the longer cycle time caused the matrix to completely shrink and swell, causing greater amounts of damages and weakening the strength of coals, and the cycle number also had a great enhancement effect on the porosity alteration, which might increase the pore size and improve the connectivity.

Conflicts of Interest

The authors declare that they have no conflicts of interest.

Acknowledgments

This work was financially supported by the National Natural Science Foundation of China (51774278, 51274195, and U1361106), the Natural Science Foundation of Jiangsu Province (BK20170001), the National Major Scientific Instrument and Equipment Development Project (2013YQ17046309), and the State Key Laboratory of Coal Resources and Safe Mining, China University of Mining and Technology (SKLRCRSM14X02).

References

- [1] T. A. Moore, “Coalbed methane: a review,” *International Journal of Coal Geology*, vol. 101, pp. 36–81, 2012.

- [2] I. Palmer, “Coalbed methane completions: a world view,” *International Journal of Coal Geology*, vol. 82, no. 3-4, pp. 184–195, 2010.
- [3] A. Shahtalebi, C. Khan, A. Dmyterko, P. Shukla, and V. Rudolph, “Investigation of thermal stimulation of coal seam gas fields for accelerated gas recovery,” *Fuel*, vol. 180, pp. 301–313, 2016.
- [4] D. Ritter, D. Vinson, E. Barnhart et al., “Enhanced microbial coalbed methane generation: a review of research, commercial activity, and remaining challenges,” *International Journal of Coal Geology*, vol. 146, pp. 28–41, 2015.
- [5] C. Ö. Karacan, F. A. Ruiz, M. Cotè, and S. Phipps, “Coal mine methane: a review of capture and utilization practices with benefits to mining safety and to greenhouse gas reduction,” *International Journal of Coal Geology*, vol. 86, no. 2-3, pp. 121–156, 2011.
- [6] J. Xu, C. Zhai, and L. Qin, “Mechanism and application of pulse hydraulic fracturing in improving drainage of coalbed methane,” *Journal of Natural Gas Science and Engineering*, vol. 40, pp. 79–90, 2017.
- [7] G. Ni, W. Cheng, B. Lin, and C. Zhai, “Experimental study on removing water blocking effect (WBE) from two aspects of the pore negative pressure and surfactants,” *Journal of Natural Gas Science and Engineering*, vol. 31, pp. 596–602, 2016.
- [8] T. Liu, B. Lin, and W. Yang, “Impact of matrix–fracture interactions on coal permeability: model development and analysis,” *Fuel*, vol. 207, pp. 522–532, 2017.
- [9] Q. I. Zou, B. q. Lin, T. Liu, X. c. Hu, and C. s. Zheng, “Variations in coalbed gas content, initial gas desorption property and coal strength after drilling-slotting integration technique and gas drainage: insight into pore characteristics,” *International Journal of Oil, Gas and Coal Technology*, vol. 15, no. 3, pp. 235–266, 2017.
- [10] J. C. Pashin, P. E. Clark, M. R. McIntyre-Redden et al., “SECARB CO₂ injection test in mature coalbed methane reservoirs of the Black Warrior basin, Blue Creek Field, Alabama,” *International Journal of Coal Geology*, vol. 144-145, pp. 71–87, 2015.
- [11] B. Meier and S. Sharma, “Using stable carbon isotopes to track potential leakage of carbon dioxide: example from an enhanced coal bed methane recovery site in West Virginia, USA,” *International Journal of Greenhouse Gas Control*, vol. 41, pp. 107–115, 2015.
- [12] W. D. Gunter, M. J. Mavor, and J. R. Robinson, “CO₂ storage and enhanced methane production: field testing at Fenn-Big Valley, Alberta, Canada, with application,” in *Proceeding of the 7th International Conference on Greenhouse Gas Control Technologies*, Vancouver, Canada, September 2004.
- [13] M. M. Reynolds, R. S. Ku, J. B. Vertz, and Z. D. Stashko, “First field application in Canada of carbon dioxide separation for hydraulic fracture flow back operations,” in *SPE 167197-MS, SPE Unconventional Resources Conference Canada*, Calgary, Alberta, Canada, November 2013.
- [14] S. Wong, D. Law, X. Deng et al., “Enhanced coalbed methane and CO₂ storage in anthracitic coals—micro-pilot test at south Qinshui, Shanxi, China,” *International Journal of Greenhouse Gas Control*, vol. 1, no. 2, pp. 215–222, 2007.
- [15] J. Liu, L. Sun, X. Wu, and J. Yao, “Feasibility of combination of CO₂ geological storage with geothermal-type water-soluble gas recovery in Yinggehai basin, China,” *International Journal of Greenhouse Gas Control*, vol. 45, pp. 139–149, 2016.

- [16] M. Fujioka, S. Yamaguchi, and M. Nako, "CO₂-ECBM field tests in the Ishikari Coal Basin of Japan," *International Journal of Coal Geology*, vol. 82, no. 3-4, pp. 287-298, 2010.
- [17] S. Yamaguchi, K. Ohga, M. Fujioka, and M. Nako, "History matching on micro-pilot tests of CO₂ sequestration and ECBM in the Ishikari Coal Field," *Journal of the Japan Institute of Energy*, vol. 86, no. 2, pp. 80-86, 2007.
- [18] H. Wen, Z. Li, J. Deng et al., "Influence on coal pore structure during liquid CO₂-ECBM process for CO₂ utilization," *Journal of CO₂ Utilization*, vol. 21, pp. 543-552, 2017.
- [19] J. Xu, C. Zhai, S. Liu, L. Qin, and Y. Sun, "Feasibility investigation of cryogenic effect from liquid carbon dioxide multi cycle fracturing technology in coalbed methane recovery," *Fuel*, vol. 206, pp. 371-380, 2017.
- [20] Y. Cao, J. Zhang, H. Zhai, G. Fu, L. Tian, and S. Liu, "CO₂ gas fracturing: a novel reservoir stimulation technology in low permeability gassy coal seams," *Fuel*, vol. 203, pp. 197-207, 2017.
- [21] R. Sander, L. D. Connell, Z. Pan, M. Camilleri, D. Heryanto, and N. Lupton, "Core flooding experiments of CO₂ enhanced coalbed methane recovery," *International Journal of Coal Geology*, vol. 131, pp. 113-125, 2014.
- [22] H. Xu, W. Chu, X. Huang, W. Sun, C. Jiang, and Z. Liu, "CO₂ adsorption-assisted CH₄ desorption on carbon models of coal surface: a DFT study," *Applied Surface Science*, vol. 375, pp. 196-206, 2016.
- [23] D. N. Espinoza and J. C. Santamarina, "Clay interaction with liquid and supercritical CO₂: the relevance of electrical and capillary forces," *International Journal of Greenhouse Gas Control*, vol. 10, pp. 351-362, 2012.
- [24] S. Gao, Y. Wang, L. Jia, H. Wang, J. Yuan, and X. Wang, "CO₂-H₂O-coal interaction of CO₂ storage in coal beds," *International Journal of Mining Science and Technology*, vol. 23, no. 4, pp. 525-529, 2013.
- [25] W. Li, P. L. Younger, Y. Cheng et al., "Addressing the CO₂ emissions of the world's largest coal producer and consumer: lessons from the Haishiwan Coalfield, China," *Energy*, vol. 80, pp. 400-413, 2015.
- [26] N. H. Mohd Yasin, T. Maeda, A. Hu, C.-P. Yu, and T. K. Wood, "CO₂ sequestration by methanogens in activated sludge for methane production," *Applied Energy*, vol. 142, pp. 426-434, 2015.
- [27] J. Xu, C. Zhai, S. Liu, L. Qin, and S. Wu, "Pore variation of three different metamorphic coals by multiple freezing-thawing cycles of liquid CO₂ injection for coalbed methane recovery," *Fuel*, vol. 208, pp. 41-51, 2017.
- [28] P. A. Hale and A. Shakoor, "A laboratory investigation of the effects of cyclic heating and cooling, wetting and drying, and freezing and thawing on the compressive strength of selected sandstones," *Environmental and Engineering Geoscience*, vol. 9, no. 2, pp. 117-130, 2003.
- [29] C. Zhai, S. Wu, S. Liu, L. Qin, and J. Xu, "Experimental study on coal pore structure deterioration under freeze-thaw cycles," *Environmental Earth Sciences*, vol. 76, no. 15, p. 507, 2017.
- [30] J. Q. Mu, X. J. Pei, R. Q. Huang, N. Rengers, and X. Q. Zou, "Degradation characteristics of shear strength of joints in three rock types due to cyclic freezing and thawing," *Cold Regions Science and Technology*, vol. 138, pp. 91-97, 2017.
- [31] Q. Liu, S. Huang, Y. Kang, and X. Liu, "A prediction model for uniaxial compressive strength of deteriorated rocks due to freeze-thaw," *Cold Regions Science and Technology*, vol. 120, pp. 96-107, 2015.
- [32] X. Zhang, L. Wang, and J. Zhang, "Mechanical behavior and chloride penetration of high strength concrete under freeze-thaw attack," *Cold Regions Science and Technology*, vol. 142, pp. 17-24, 2017.
- [33] L. Qin, C. Zhai, S. Liu, J. Xu, Z. Tang, and G. Yu, "Failure mechanism of coal after cryogenic freezing with cyclic liquid nitrogen and its influences on coalbed methane exploitation," *Energy & Fuels*, vol. 30, no. 10, pp. 8567-8578, 2016.
- [34] L. Liu, S. Wu, H. Chen, and Z. Haitao, "Numerical investigation of the effects of freezing on micro-internal damage and macro-mechanical properties of cement pastes," *Cold Regions Science and Technology*, vol. 106-107, pp. 141-152, 2014.
- [35] P. Wang, J. Xu, X. Fang, P. Wang, G. Zheng, and M. Wen, "Ultrasonic time-frequency method to evaluate the deterioration properties of rock suffered from freeze-thaw weathering," *Cold Regions Science and Technology*, vol. 143, pp. 13-22, 2017.
- [36] M. Molero, S. Aparicio, G. Al-Assadi, M. J. Casati, M. G. Hernández, and J. J. Anaya, "Evaluation of freeze-thaw damage in concrete by ultrasonic imaging," *NDT & E International*, vol. 52, pp. 86-94, 2012.
- [37] J. Park, C. U. Hyun, and H. D. Park, "Changes in microstructure and physical properties of rocks caused by artificial freeze-thaw action," *Bulletin of Engineering Geology and the Environment*, vol. 74, no. 2, pp. 555-565, 2015.
- [38] M. Mutluturk, R. Altindag, and G. Turk, "A decay function model for the integrity loss of rock when subjected to recurrent cycles of freezing-thawing and heating-cooling," *International Journal of Rock Mechanics and Mining Sciences*, vol. 41, no. 2, pp. 237-244, 2004.
- [39] J. Zhao, H. Xu, D. Tang, J. P. Mathews, S. Li, and S. Tao, "Coal seam porosity and fracture heterogeneity of macrolithotypes in the Hancheng Block, eastern margin, Ordos Basin, China," *International Journal of Coal Geology*, vol. 159, pp. 18-29, 2016.
- [40] Q. Li, B. Lin, and C. Zhai, "A new technique for preventing and controlling coal and gas outburst hazard with pulse hydraulic fracturing: a case study in Yuwu coal mine, China," *Natural Hazards*, vol. 75, no. 3, pp. 2931-2946, 2015.
- [41] Q. Zou and B. Lin, "Modeling the relationship between macro- and meso-parameters of coal using a combined optimization method," *Environmental Earth Sciences*, vol. 76, no. 14, p. 479, 2017.
- [42] T. Liu, B. Lin, W. Yang et al., "Dynamic diffusion-based multi-field coupling model for gas drainage," *Journal of Natural Gas Science and Engineering*, vol. 44, pp. 233-249, 2017.
- [43] T. Xia, F. Zhou, J. Liu, S. Hu, and Y. Liu, "A fully coupled coal deformation and compositional flow model for the control of the pre-mining coal seam gas extraction," *International Journal of Rock Mechanics and Mining Sciences*, vol. 72, pp. 138-148, 2014.
- [44] L. D. Connell, R. Sander, M. Camilleri, D. Heryanto, Z. Pan, and N. Lupton, "Nitrogen enhanced drainage of CO₂ rich coal seams for mining," *International Journal of Mining Science and Technology*, vol. 27, no. 5, pp. 755-761, 2017.
- [45] C. Zheng, M. Kizil, Z. Chen, and S. Aminossadati, "Effects of coal damage on permeability and gas drainage performance,"

- International Journal of Mining Science and Technology*, vol. 27, no. 5, pp. 783–786, 2017.
- [46] T. Teng, F. Gao, Y. N. Gao, and Z. Z. Zhang, “Experimental study of micro-damage and fracturing characteristics on raw coal under cyclic pneumatic hydraulic loading,” *Journal of China University of Mining & Technology*, vol. 46, pp. 306–311, 2017.
- [47] J. Yang, W. Chen, D. Yang, and H. Tian, “Investigating the permeability of marble under moderate pressure and temperature,” *Geofluids*, vol. 2017, 8 pages, 2017.
- [48] S. Chattaraj, D. Mohanty, T. Kumar, and G. Halder, “Thermodynamics, kinetics and modeling of sorption behaviour of coalbed methane – a review,” *Journal of Unconventional Oil and Gas Resources*, vol. 16, pp. 14–33, 2016.
- [49] S. Giffin, R. Littke, J. Klaver, and J. L. Urai, “Application of BIB-SEM technology to characterize macropore morphology in coal,” *International Journal of Coal Geology*, vol. 114, pp. 85–95, 2013.
- [50] W. Li, H. Liu, and X. Song, “Multifractal analysis of Hg pore size distributions of tectonically deformed coals,” *International Journal of Coal Geology*, vol. 144–145, pp. 138–152, 2015.
- [51] J. S. Bae, S. K. Bhatia, V. Rudolph, and P. Massarotto, “Pore accessibility of methane and carbon dioxide in coals,” *Energy & Fuels*, vol. 23, no. 6, pp. 3319–3327, 2009.
- [52] Y. Yao and D. Liu, “Comparison of low-field NMR and mercury intrusion porosimetry in characterizing pore size distributions of coals,” *Fuel*, vol. 95, pp. 152–158, 2012.
- [53] D. Wildenschild and A. P. Sheppard, “X-ray imaging and analysis techniques for quantifying pore-scale structure and processes in subsurface porous medium systems,” *Advances in Water Resources*, vol. 51, pp. 217–246, 2013.
- [54] A. P. Radlinski, M. Mastalerz, A. L. Hinde et al., “Application of SAXS and SANS in evaluation of porosity, pore size distribution and surface area of coal,” *International Journal of Coal Geology*, vol. 59, no. 3–4, pp. 245–271, 2004.
- [55] L. Qin, C. Zhai, S. Liu, J. Xu, G. Yu, and Y. Sun, “Changes in the petrophysical properties of coal subjected to liquid nitrogen freeze-thaw – a nuclear magnetic resonance investigation,” *Fuel*, vol. 194, pp. 102–114, 2017.
- [56] R. L. Kleinberg, W. E. Kenyon, and P. P. Mitra, “Mechanism of NMR relaxation of fluids in rock,” *Journal of Magnetic Resonance, Series A*, vol. 108, no. 2, pp. 206–214, 1994.
- [57] J. Xu, C. Zhai, S. Liu, L. Qin, and R. Dong, “Investigation of temperature effects from LCO₂ with different cycle parameters on the coal pore variation based on infrared thermal imagery and low-field nuclear magnetic resonance,” *Fuel*, vol. 215, pp. 528–540, 2018.
- [58] Y. Cai, D. Liu, Z. Pan, Y. Yao, J. Li, and Y. Qiu, “Petrophysical characterization of Chinese coal cores with heat treatment by nuclear magnetic resonance,” *Fuel*, vol. 108, pp. 292–302, 2013.
- [59] A. Dillinger and L. Esteban, “Experimental evaluation of reservoir quality in Mesozoic formations of the Perth Basin (Western Australia) by using a laboratory low field nuclear magnetic resonance,” *Marine and Petroleum Geology*, vol. 57, pp. 455–469, 2014.
- [60] O. B. Olatinsu, D. O. Olorode, B. Clennell, L. Esteban, and M. Josh, “Lithotype characterizations by nuclear magnetic resonance (NMR): a case study on limestone and associated rocks from the eastern Dahomey Basin, Nigeria,” *Journal of African Earth Sciences*, vol. 129, pp. 701–712, 2017.
- [61] C. X. Ning, Z. X. Jiang, and Z. Y. Gao, “Quantitative evaluation of pore connectivity with nuclear magnetic resonance and high pressure mercury injection: a case study of the lower section of E s3 in Zhanhua sag,” *Journal of China University of Mining & Technology*, vol. 46, pp. 559–566, 2017.
- [62] N. Golsanami, J. Sun, and Z. Zhang, “A review on the applications of the nuclear magnetic resonance (NMR) technology for investigating fractures,” *Journal of Applied Geophysics*, vol. 133, pp. 30–38, 2016.

Research Article

Effects of Formation Dip on Gas Production from Unconfined Marine Hydrate-Bearing Sediments through Depressurization

Yilong Yuan , Tianfu Xu , Yingli Xia, and Xin Xin 

Key Laboratory of Groundwater Resources and Environment, Ministry of Education, Jilin University, Changchun 130021, China

Correspondence should be addressed to Xin Xin; xxxx@jlu.edu.cn

Received 24 October 2017; Revised 30 January 2018; Accepted 13 February 2018; Published 26 June 2018

Academic Editor: Egor Dontsov

Copyright © 2018 Yilong Yuan et al. This is an open access article distributed under the Creative Commons Attribution License, which permits unrestricted use, distribution, and reproduction in any medium, provided the original work is properly cited.

The effects of geologic conditions and production methods on gas production from hydrate-bearing sediments (HBS) have been widely investigated. The reservoir was usually treated as horizontal distribution, whereas the sloping reservoir was not considered. In fact, most strata have gradients because of the effects of geological structure and diagenesis. In this study, based on currently available geological data from field measurements in Shenhu area of the South China Sea, the effects of formation dip on gas production were investigated through depressurization using a horizontal well. The modeling results indicate that the strategy of horizontal well is an effective production method from the unconfined Class 2 HBS. The predicted cumulative volume of methane produced at the 1000 m horizontal well was 4.51×10^7 ST m³ over 5-year period. The hydrate dissociation behavior of sloping formation is sensitive to changes in the reservoir pressure. As in unconfined marine hydrate reservoir, the sloping formation is not conducive to free methane gas recovery, which results in more dissolved methane produced at the horizontal well. The obvious issue for this challenging target is relatively low exploitation efficiency of methane because of the recovery of very large volumes of water. Consequently, the development of the favorable well completion method to prevent water production is significantly important for realizing large scale hydrate exploitation in the future.

1. Introduction

Natural gas hydrate (NGH) is crystalline solid composed of water and gas, typically including CH₄, C₂H₆, C₃H₈, CO₂, and H₂S [1, 2]. In nature, the dominant gas in hydrate is CH₄, which is expected to be a potential energy resource. The exploration results show that hydrates are widely distributed in the permafrost and in deep ocean sediments, where the necessary conditions of low temperature and high pressure exist for hydrate stability [3–5].

Gas production from hydrate-bearing sediments (HBS) could be realized by decomposing solid-state hydrate into fluid phases (e.g., gas and water) [4, 6, 7]. There are three main dissociation methods for gas recovery from the HBS: (1) depressurization [2, 5, 8–10], (2) thermal stimulation [11–13], and (3) the use of hydration inhibitors (such as salts and alcohols), which shifts the pressure-temperature equilibrium conditions to dissociate the hydrate [14]. Past field tests, experimental investigations, and numerical studies indicated that depressurization is the most promising method for gas

recovery from the HBS, while the other methods may be suitable for enhancing recovery or reservoir stimulation [2, 4, 7, 8, 15].

Up to now, many countries including the United States, Canada, Japan, India, South Korea, and China have launched extensive investigations and field production tests of the HBS [7, 16, 17]. Recently, significant gas hydrate deposits have been confirmed to exist in Shenhu area of the South China Sea (SCS), and this region was regarded as a potential target area [18–21]. In order to seek the most economically and technically feasible method for gas production from the HBS, numerical simulation for its economic, convenient, and flexible response to complex geological problems was considered as the best way to achieve this objective. Based on the available geological data in Shenhu area of the SCS, Zhang et al. [22] investigated the gas production performance by using two parallel horizontal wells to depressurize the HBS; Li et al. [13, 23] and Su et al. [24–26] fully investigated the gas production potential and efficiency through depressurization and the combination of depressurization and

thermal stimulation, respectively, employing both vertical and horizontal wells. Their results indicated low gas production rates and unsatisfied gas/water ratios because of low intrinsic permeability of the HBS and permeable overburden and underburden formations. To accelerate the gas hydrate dissociation and to enlarge the dissociation range, Jin et al. [10] investigated the gas production performance by using the joint depressurization and thermal stimulation based on three horizontal wells. They indicated lower efficiency of hot water injection compared with depressurization. Li et al. [5] and Sun et al. [27] investigated the effects of the permeability of the boundaries on the gas production potential in Shenhu area of the SCS. Their results indicated that the HBS with impermeable boundaries were expected to be the potential gas production target. Huang et al. [9, 28] and Yuan et al. [29] investigated the effects of different geologic conditions on the hydrate dissociation and gas production through depressurization. They indicated that permeability, porosity, and initial hydrate saturation have significant effects on gas production performance. Recently, on the basis of the available geological data from site GMGS3-W19 [20], the geomechanical behaviors for gas production in this area have been conducted and reported by Sun et al. [30]. They indicated that the balance between gas production and reservoir stability is needed to be optimized. The further investigation about the geomechanical behaviors of the HBS induced by gas production indicated that the spatial evolution of the temperature, pore pressure, hydrate saturation, and gas saturation are the most relevant factors [1, 30–35].

The above investigations have properly promoted the development of gas production from the HBS. The effects of production pressure, permeability, porosity, hydrate saturation, thickness, and initial temperature and pressure of HBS on gas production behavior have been widely carried out. Nevertheless, to the best knowledge of the authors, most of previous numerical simulations, the reservoir was usually treated as horizontal distribution, while the sloping reservoir was not considered. In fact, horizontal strata are not common in natural hydrate reservoirs, especially in the marine HBS. Most strata have gradients because of the effects of geological structure and diagenesis [36, 37]. The geologic formation in AT1 site of the Eastern Nankai Trough in Japan with slope angle of approximately 20° is determined based on the interpretations of formation resistivity image logs and drillings [38, 39]. Analysis of seismic and bathymetric data identified seventeen sublinear, near-parallel submarine canyons in Shenhu area of the SCS [19, 40]. The occurrence of gas hydrates was located along the flanks of these prominent canyons; as a consequence, the hydrate reservoirs have a varied dip angles between 6° and 17° in this area [19, 21, 41–43]. Due to influence of the formation dip, the gas production performance and the spatial distribution of reservoir physical characteristics could be different from those of horizontal reservoirs.

This study will look into the effects of the formation dip on the gas production performance in Shenhu area of the SCS, with a horizontal well through depressurization. We designed four simulation schemes with different dip angles of 0° (Base Case), 10° (Case A), 20° (Case B), and 30° (Case

C), respectively. In order to make a systematic comparison of the gas production performance in these cases, we used the two criteria, an absolute criterion and a relative criterion [5, 26, 44]. The absolute criterion includes the total methane production rate (Q_{PT}), methane release rate from hydrate dissociation (Q_R), water volumetric production rate (Q_W), and the cumulative volume of methane produced at the well (V_G) and released from hydrate dissociation (V_R). The relative criterion refers to the gas-to-water ratio ($R_{GW} = V_G/V_W$). The reason for considering Q_W and R_{GW} is that the accompanied water production from the borehole will waste a lot of energy and reduce the methane production efficiency. In addition, the practical production characteristics of HBS and multiphase movement behaviors of water and gas induced by depressurization under different dip angles were assessed.

2. Numerical Models and Simulation Approach

2.1. Geological Setting. Shenhu area is located in the Baiyun Sag, Pearl River Mouth Basin (PRMB) of the northern slope of the SCS (Figure 1). Geological, geophysical, geothermal, and geochemical investigations had suggested that Shenhu area is a beneficial district for the formation of NGH [18, 24, 26]. Gas hydrate samples were collected during a recent scientific expedition conducted by the China Geological Survey in this area in May 2007 and September 2015 [5, 19, 20, 45]. The drilling results indicated that the top of the hydrate layers is located 155–229 m below the seafloor (mbsf) and the water depths vary from 1108 m to 1245 m. The thickness of HBS is estimated to be 10–44 m. The average water temperature at the sea floor is measured at about 3.5°C . The in situ salinity measured from the pressure cores is 0.033. The hydrate disseminates in the sediments, mainly composed of fine-grained clay-silts, with the porosity varying from 0.33 to 0.48 and the maximum hydrate saturation of 0.48 [10, 19, 46]. The HBS is overlain and underlain by permeable strata, which have the similar lithology to that in HBS but lack hydrate. Consequently, the geological system of the HBS in this area is typical unconfined Class 2 deposits [10, 47].

2.2. Model Setup

2.2.1. Model Geometry and Spatial Discretization. The geometry of the rectangular 3D system we consider in this study is shown in Figure 2. The model size in x -axis is 200 m, assuming well spacing of 200 m in the future commercial field development with multiwells. The well is perforated in the horizontal part with the length of 1000 m along the y -axis, and the vertical part of the well is sealed to avoid water and gas leaking into the overlying formation and seawater. The thickness of HBS is 40 m, with 30 m overburden and underburden to allow heat exchange with the HBS during a 5-year production period. The 30 m thick boundary layers were sufficient to simulate the boundary effects of heat exchange [8, 17, 26]. The horizontal well is placed at the center of the HBS with a radius of 0.1 m. Assuming uniformity of property and behavior along the horizontal well [5, 32], only a single unit of length ($\Delta y = 1$ m) needs to be simulated.

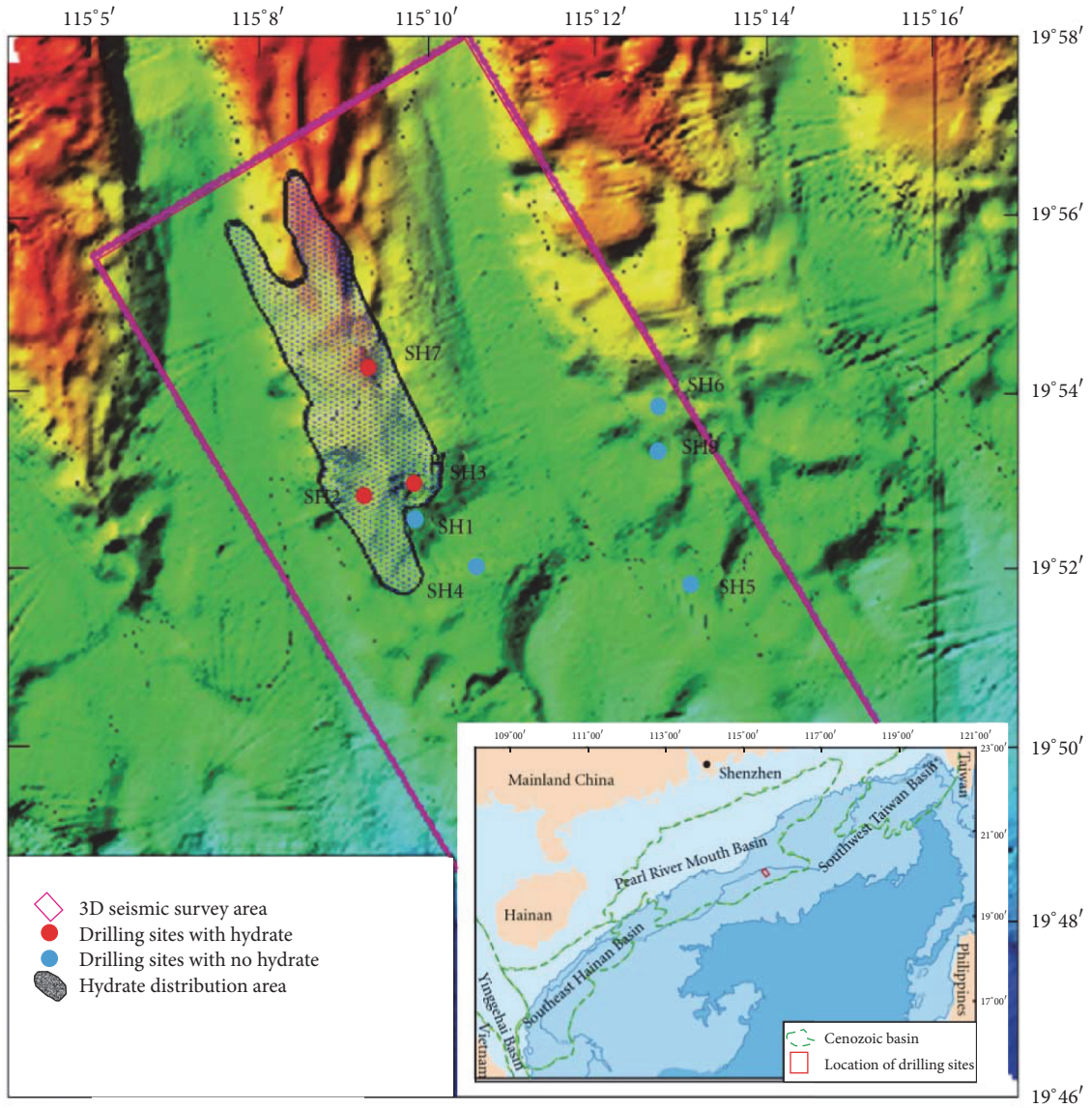


FIGURE 1: Location of study area, drilling sites, and the confirmed gas hydrate distribution in Shenhu area of the SCS [18].

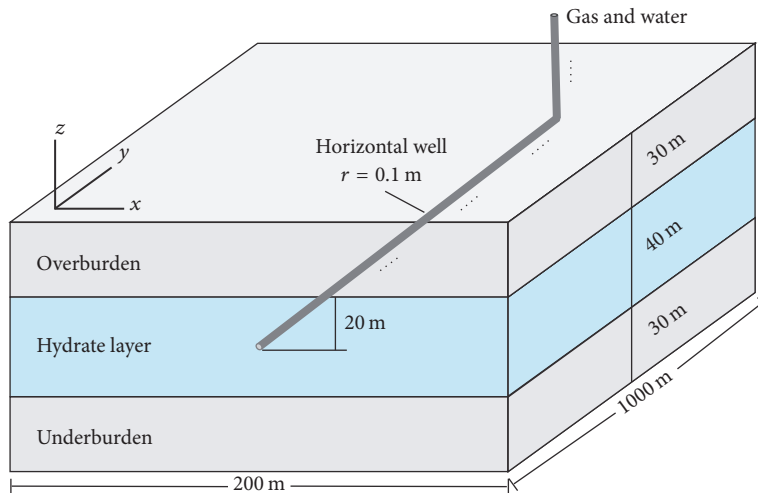


FIGURE 2: Model geometry and the configurations of horizontal well.

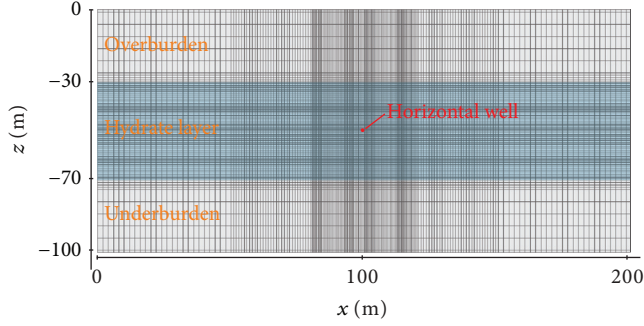


FIGURE 3: The corresponding grids used in the numerical models, with the location of horizontal well.

Figure 3 shows the corresponding grids used in the numerical models. Previous studies had indicated that the critical processes occur within a limited radius around the horizontal well [1, 4, 32]. Therefore, the grids are refined surrounding the horizontal well with the minimum interval of 0.2 m. The grid size increases with the distance to the well, reaching a size of 2 m at the lateral boundary. Vertical grid size in the HBS is 0.5 m, which gradually increases in both overlying and underlying layers and reaches the maximum size of 5 m.

2.2.2. Reservoir Properties and Parameters. Table 1 presents the main modeling parameters and physical properties for the Shenhu area deposits. These were derived using information gleaned from geophysical well logs and core samples analyses [18, 19, 43, 46]. The initial hydrate saturation is 0.4, which is estimated according to the decrease of chlorinity due to the mixture of fresh water generated by gas hydrate dissociation [46]. The boundary layers of the HBS are saturated by water with a full aqueous saturation of 1.0. The sediment porosity and intrinsic permeability are 0.38 and $1.0 \times 10^{-14} \text{ m}^2$, respectively [10, 26]. To avoid a theoretically correct but computationally intensive solution of the Navier–Stokes equation, the wellbore is simulated as a pseudoporous medium with porosity, permeability, capillary pressure, and low irreducible gas saturation of 1.0, $1.0 \times 10^{-8} \text{ m}^2$, 0 MPa, and 0.005, respectively [4, 5, 48]. Earlier studies had shown the validity of this approximation [8, 49]. The composite thermal conductivity, relative permeability, and capillary pressure models are employed commonly in numerical simulations on gas production from HBS [1, 4, 30–32, 50]. The corresponding parameters for relative permeability and capillary pressure were determined from the field test data by Moridis and Reagan [51]. The changes of effective permeability and capillary pressure are consistent with the porosity and phase saturation during the simulation. With referral to the offshore production test from marine hydrate deposits in the Eastern Nankai Trough of Japan [52], the constant bottom-hole pressure (BHP) P_b is 4 MPa. Consequently, the driving force of the depressurization ΔP is 12 MPa ($\Delta P = P_m - P_b$); P_m is the initial pressure in the HBS at the elevation of the horizontal well (Figure 2).

TABLE 1: Main model parameters of the HBS in Shenhu area of the SCS.

Parameter	Value
HBS thickness, H	40 m
Porosity, ϕ	0.38
Intrinsic permeability, k	$1.0 \times 10^{-14} \text{ m}^2$ (1 mD = $1.0 \times 10^{-15} \text{ m}^2$)
Gas composition	100% CH ₄
Hydrate saturation in the HBS, S_h	0.40
Water salinity, X_i	3.30%
Pressure at the middle of the HBS, P_m	16.0 MPa
Temperature at the middle of the HBS, T_m	13.95°C
Critical mobile porosity, ϕ_{cri}	0.05
Rock grain density, ρ_R	2600 kg/m ³
Wet thermal conductivity, λ_W	3.1 W/m/K
Dry thermal conductivity, λ_D	1.0 W/m/K
Pore compressibility, α_p	$1.0 \times 10^{-8} \text{ Pa}^{-1}$
Bottom-hole pressure, P_b	4 MPa
Composite thermal conductivity model [8]	$\lambda = \lambda_D + (S_A^{1/2} + S_h^{1/2})(\lambda_W - \lambda_D) + \phi S_I \lambda_I$
Capillary pressure model [53]	$P_{\text{cap}} = -P_0([S_A^*]^{-1/m} - 1)^{1/m}$ $S_A^* = \frac{(S_A - S_{\text{ir}A})}{(S_{\text{mx}A} - S_{\text{ir}A})}$
$S_{\text{mx}A}$	1.0
m	0.45
P_0	$1.0 \times 10^5 \text{ Pa}$
Relative permeability model [1]	$k_{rA} = (S_A^*)^{n_A}$ $k_{rG} = (S_G^*)^{n_G}$ $S_G^* = \frac{(S_G - S_{\text{ir}G})}{(1 - S_{\text{ir}A})}$
n_A	3.572
n_G	3.572
$S_{\text{ir}A}$	0.30
$S_{\text{ir}G}$	0.02

2.2.3. Initial and Boundary Conditions. The initial formation pressure was specified in accordance with the hydrostatic pressure, which was computed according to the water depth and a pressure-adjusted saline water density [50]. Figure 4 shows the resultant initial pressure distribution of different dip angles. To the sloping formations, there will be an angle (e.g., equal to the formation dip) between the initial pressure contour lines and the strata lines. The initial temperature was specified to be 3.5°C at the seafloor [5, 46]. The temperature

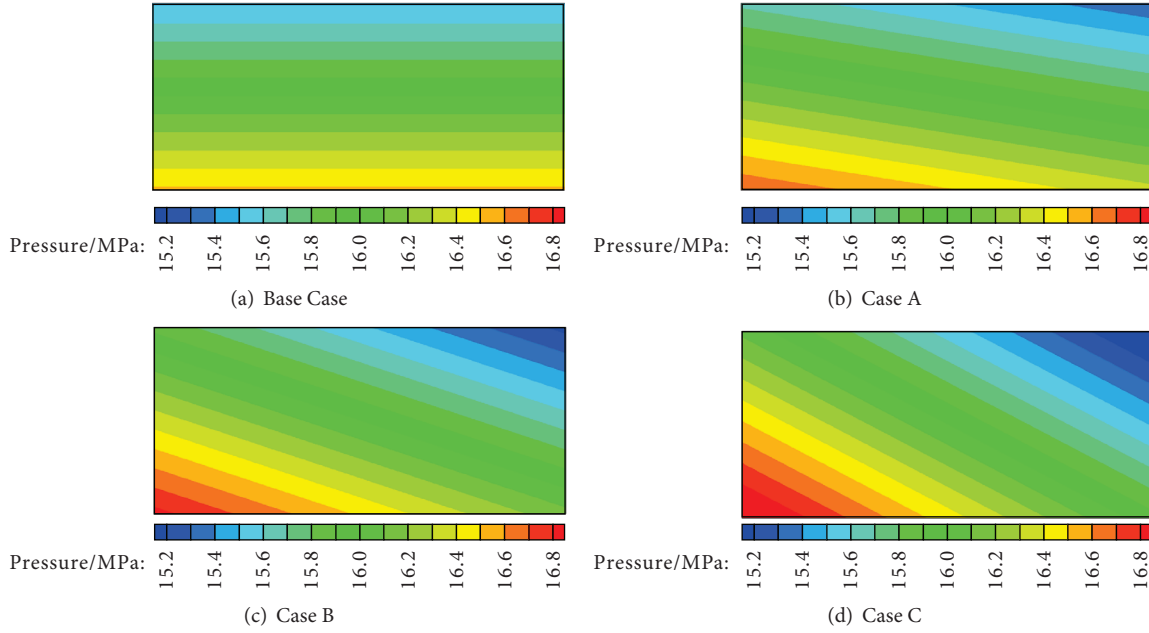


FIGURE 4: Cross section showing the initial pressure distribution: (a) Base Case with dip angle of 0°, (b) Case A with dip angle of 10°, (c) Case B with dip angle of 20°, and (d) Case C with dip angle of 30°.

profile was assigned to vary linearly as a function of depth with a geothermal gradient of 47°C/km [10, 18, 26, 46].

Because of symmetry of the horizontal strata, there is no flow of fluids and heat through the lateral boundaries. For the inclined formation, there exists the lateral boundary fluid and heat flow due to the acceleration of gravity. However, the hydrate dissociation zone is limited around the production well for the specified unconfined Class 2 HBS (e.g., the dissociation radius is no more than 30 m); thus, the lateral boundary flow has insignificant influence on gas production from hydrate reservoir (e.g., verified by the sensitivity study). Consequently, for both the horizontal strata and inclined formation, no flow of fluids and heat are specified for the lateral boundaries [32]. Because the boundary layers have similar lithology to that in HBS, the top and bottom boundaries are designed as constant temperature and pressure boundaries [50].

2.2.4. *The Numerical Simulation Code.* In this numerical study, we use TOUGH + HYDRATE to investigate the effects of formation dip on gas production performance from the marine HBS. This code can model the nonisothermal hydration reaction, multiphase behavior, and flow of fluids and heat under conditions typical in geological media containing gas hydrates [4, 6]. It includes both an equilibrium and a kinetic model of hydrate formation and dissociation. These models cover four phases (i.e., gas, aqueous, ice, and hydrate) and four mass components (i.e., H₂O, CH₄, hydrate, and water-soluble inhibitors such as salts or alcohols) with each component existing in each phase [6].

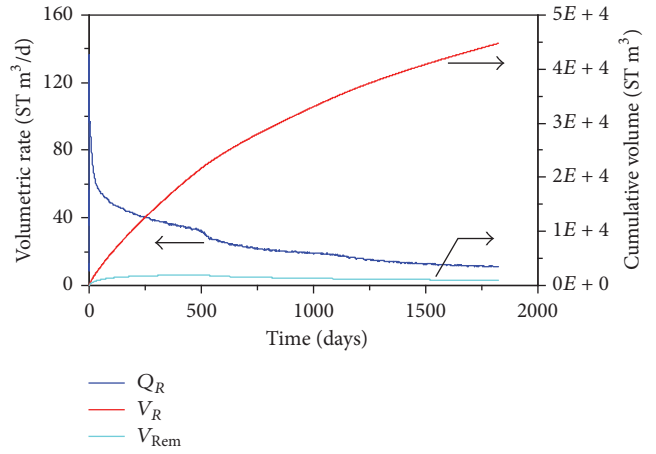


FIGURE 5: Evaluation of methane release rate (Q_R), the cumulative volume of methane released in the reservoir (V_R), and the cumulative volume of methane remaining in the reservoir (V_{Rem}) during gas production from horizontal strata.

3. Simulation Results and Discussions

3.1. *Production Behaviors of Horizontal Strata.* The extraction of fluid (e.g., gas and water) from the horizontal well leads to depressurization-induced hydrate dissociation in the HBS. Figure 5 shows the evolution of methane release rate (Q_R), the cumulative volume of methane released from hydrate dissociation (V_R), and the cumulative volume of methane remaining in the reservoir (V_{Rem}) over 5-year period. In this section, all of the following plotted results reveal the unit section (1 m) of horizontal well.

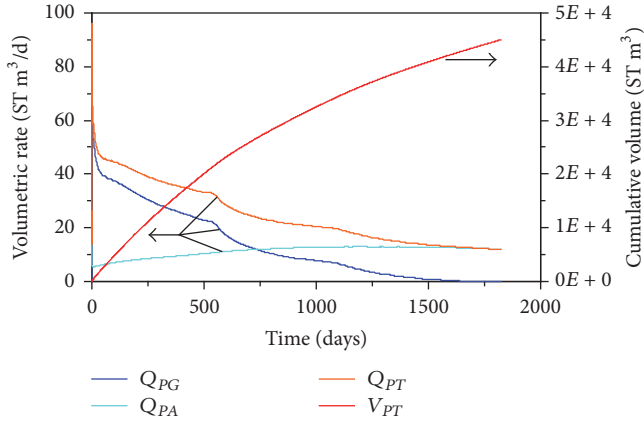


FIGURE 6: Evaluation of methane gas production rate (Q_{PG}), the dissolved methane production rate (Q_{PA}), the total methane production rate (Q_{PT}), and the cumulative methane volume produced at the well (V_{PT}) during gas production from horizontal strata.

As shown in Figure 5, the constant depressurization at the well results in an initial burst of gas release in the vicinity of the horizontal well. Consequently, the maximum Q_R occurs at the initial point with the value of approximately $136 \text{ ST m}^3/\text{d}$. This phenomenon is usually called “gas cavity” [23, 54]. This is because the drastic decrease of fluid pressure in hydrate reservoir causes the significant hydrate dissociation, resulting in an immediate increase of Q_R . Meanwhile, the massive gas released from hydrate dissociation results in reservoir pressure increase abruptly, which limits the hydrate dissociation rate significantly. After the incident of “gas cavity,” Q_R rapidly drops at the early stage and gradually decreases with a slowing decline rate. This is mainly because (1) the low effective permeability of hydrate reservoir results in the fact that free gas could not be yielded from the HBS timely and, as a consequence, the dissociation front with a high pressure level; (2) the endothermic nature of hydrate dissociation results in a low temperature region around the horizontal well; (3) the function of self-sealing gradually disappears with hydrate dissociation above and below the horizontal well, resulting in the fact that water seepage from boundary layers catches up with the water discharge from the HBS to the borehole. All of these reasons impede the rapid hydrate dissociation in the HBS. At the end of 5-year production period, a total of $V_R = 4.48 \times 10^4 \text{ m}^3$ have been produced from the methane hydrate dissociation.

Figure 6 shows the evolution of methane gas production rate (Q_{PG}), the dissolved methane production rate (Q_{PA}), the total methane production rate ($Q_{PT} = Q_{PG} + Q_{PA}$), and the cumulative methane volume produced at the well (V_{PT}) over 5-year period. Due to the produced methane mainly from the hydrate dissociation, Q_{PT} changes following the trend of Q_R (Figure 5). As shown in Figure 6, the maximum Q_{PT} occurs at the initial point with the value of approximately $96 \text{ ST m}^3/\text{d}$. As expected, Q_{PG} is consistently lower than Q_R because of dissolving in formation water and the need for gas accumulation in the reservoir until the gas saturation overcomes its irreducible level of S_{irG} . Q_{PG} decreases in the

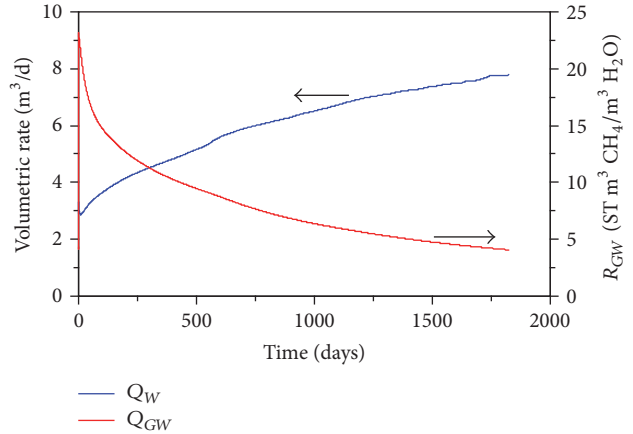


FIGURE 7: Evaluation of water volumetric production rate (Q_W) and the gas-to-water ratio (R_{GW}) during gas production from horizontal strata.

whole production stage until no free methane gas is produced from the hydrate reservoir (e.g., $Q_{PG} = 0$). This is because Q_R decreases with time (Figure 5), which results in low gas saturation in the reservoir at the late stage. Meanwhile, the total methane production rate Q_{PT} is low and almost constant at the late stage, because the methane is produced mainly by the dissolved methane (Q_{PA}) exsolution from the formation water. At the end of 5-year production period, a total of $V_{PT} = 4.51 \times 10^4 \text{ ST m}^3$ have been produced at the unit section (1 m) of horizontal well. Comparing V_{PT} and V_R (Figure 5) indicates that the majority of the produced methane originated from the hydrate dissociation and the additional methane comes from original dissolved methane in the formation water.

Figure 7 shows the evolution of water volumetric production rate (Q_W) and the gas-to-water ratio (R_{GW}) over 5-year period. R_{GW} is a relative criterion for evaluating the methane production efficiency, which is defined as

$$R_{GW} = \frac{\int Q_{PT} dt}{\int Q_W dt}. \quad (1)$$

As shown in Figure 7, Q_W increases at a decreasing rate and reaches the maximum value of $7.78 \text{ m}^3/\text{d}$. This pattern follows a typical water discharge curve in the unconfined aquifer discharged by the well under a constant pressure [10]. The pseudo-steady state at the late stage indicates that the water recharge by the seepage from boundary layers catches up with the water discharge from the HBS to the borehole (Figure 8(b)). Meanwhile, R_{GW} decreases at a decreasing rate which is affected by Q_{PT} and Q_W simultaneously (see (1)). This indicates that the major products output from borehole are methane in the early stage, while water only accounts for a small part. However, as mining continues, water becomes the major product at the late stage, and the methane output decreases to a significant low level (Figure 6). This is mainly because the solid hydrates above and below the horizontal well can temporarily act as sealing layers to prevent water production and free gas escaping from hydrate reservoir into surrounding formations (Figure 8(a)).

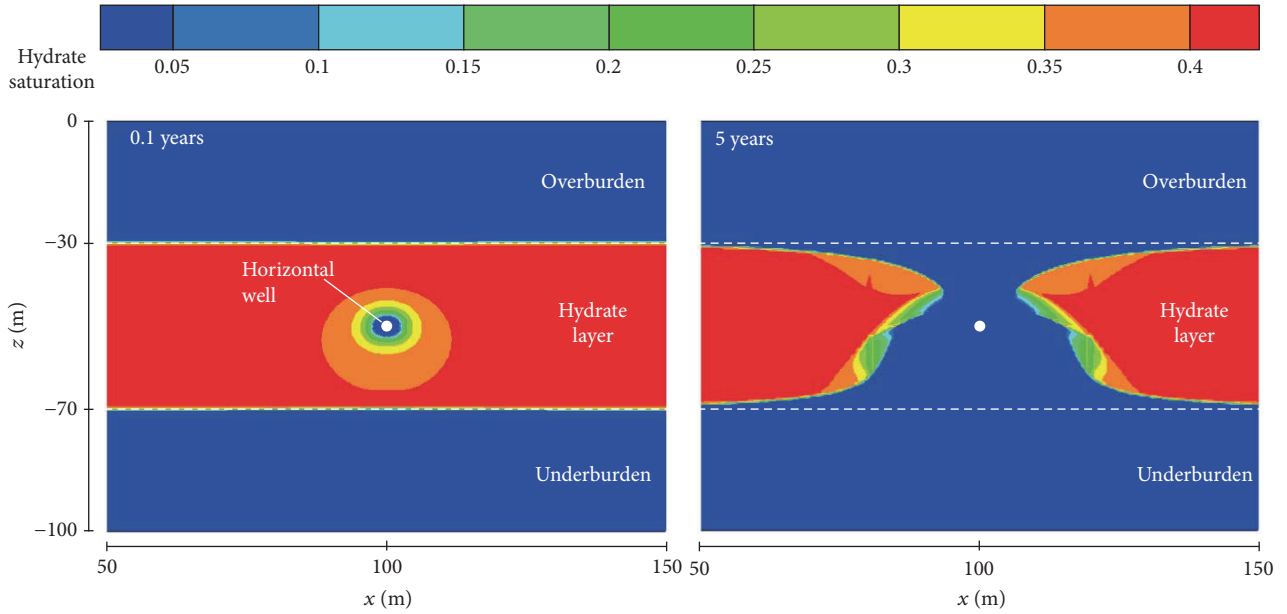


FIGURE 8: Spatial distribution of hydrate saturation in the reservoir during gas production from the unconfined Class 2 HBS.

However, once the hydrate above and below the horizontal well dissociates completely, the self-sealing function will disappear (Figure 8(b)); as a result, the methane production efficiency (R_{GW}) decreases significantly.

Moridis and Kowalsky [47] had evaluated the gas production potential of such deposits (e.g., unconfined Class 2 HBS) using both single-well and five-spot well configurations. Their results indicated that unconfined Class 2 HBS are among the most challenging targets for methane production because (1) the absence of confining boundaries limits the effectiveness of depressurization, (2) the rate of methane production at the well is much lower (e.g., less than $200 \text{ m}^3/\text{d}$), and (3) methane production is accompanied by the production of very large volumes of water. However, the modeling results of this work indicate that the strategy of horizontal well through depressurization is an effective method to exploit the gas hydrate in this unconfined Class 2 HBS. Review of Figure 6 shows that the average methane production rates and the cumulative methane volume produced at the well over 5-year period reach $2.47 \times 10^4 \text{ ST m}^3/\text{d}$ and $4.51 \times 10^7 \text{ ST m}^3$ over the length of 1000 m horizontal well, respectively. However, the obvious issue is relatively low exploitation efficiency of methane (e.g., R_{GW} shown in Figure 7) because gas production is accompanied by the recovery of very large volumes of water. Consequently, the development of the favorable well completion method to prevent water production is significantly important to realize large scale hydrate exploitation in the future.

3.2. Impact of Formation Dip on Hydrate

Production Performance

3.2.1. Gas Release from Hydrate Dissociation. Figure 9 shows the difference of V_R and V_{Rem} between horizontal strata and

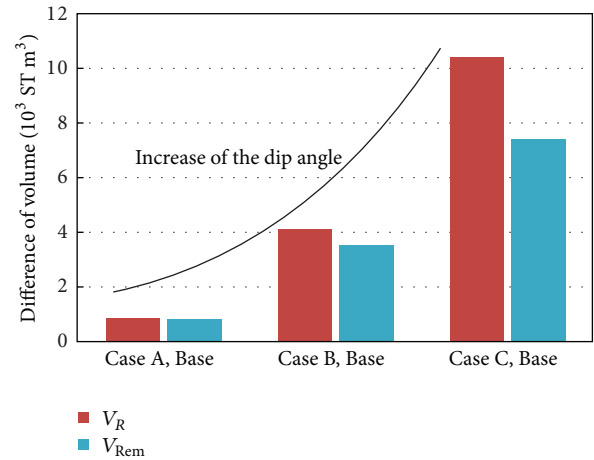


FIGURE 9: The difference of the cumulative volume of methane released from hydrate dissociation (V_R) and methane remaining in the reservoir (V_{Rem}) between horizontal strata and those sloping formations at the end of 5-year production period.

those sloping formations over the length of 1000 m horizontal well. As shown in this figure, the sloping formation has a higher V_R than that of horizontal strata. When the dip angles change from 0° , to 10° , 20° , and 30° , the cumulative volume of methane released from hydrate dissociation (V_R) increased by 881 ST m^3 , 4098 ST m^3 , and 10490 ST m^3 , respectively. This indicates that the sloping formation causes the gas hydrate in the HBS to be unstable, because the lower half portion of the hydrate reservoir is closer to the bottom of hydrate stability zone (BHSZ). This means that hydrate dissociation behavior of sloping formation is sensitive to changes in the reservoir pressure, which can be used to explain the phenomenon that a

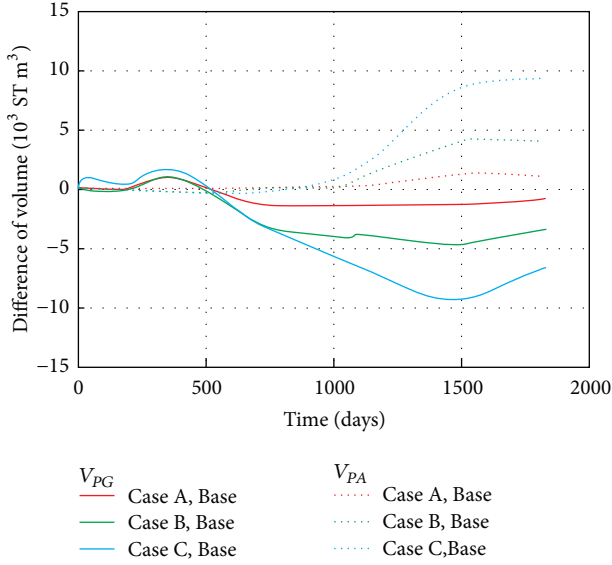


FIGURE 10: The difference of the cumulative volume of methane gas produced at the well (V_{PG}) and the dissolved methane produced at the well (V_{PA}) between horizontal strata and those sloping formations over 5-year production period.

large number of marine gases release during geologic activity. In the actual situation, this process is more obvious because of the upper half portion of the hydrate reservoir with rapid decline of pressure, but slightly temperature decreases in a short period of time. On the other hand, the difference of V_{Rem} between horizontal strata and those sloping formations (Figure 9) indicates that the dip angle is not conducive to gas recovery during gas production from the hydrate reservoir. This is because free gas far from the production well is hard to yield from the hydrate reservoir.

3.2.2. Gas Production at the Well. Figure 10 shows the difference of V_{PG} and V_{PA} between horizontal strata and those sloping formations over the length of 1000 m horizontal well. As shown in this figure, the influence of the formation dip on V_{PG} and V_{PA} is quite different, both of which have two stages.

In the first 500 days, the dip angle has very slight effect on V_{PG} , because the available hydrate in the vicinity of the horizontal well has not been exhausted. However, the sloping formation has a lower V_{PG} than that of horizontal strata at the late stage. This further proves that the inclined formation is not conducive to free gas recovery from the unconfined Class 2 HBS. On the other hand, the difference of V_{PA} shows that the dip angle has very slight effect on V_{PA} in the first 1000 days. However, the sloping formation has a higher V_{PA} than that of horizontal strata at the late stage. When the dip angles change from 0° , to 10° , 20° , and 30° , the cumulative volume of V_{PA} increased by 1034 ST m^3 , 3988 ST m^3 , and 9306 ST m^3 , respectively. This is because the methane is produced mainly by the free gas from the hydrate reservoir in the early stage, while, at the late stage, the methane is produced mainly by the dissolved methane exsolution from the formation water (Figure 6).

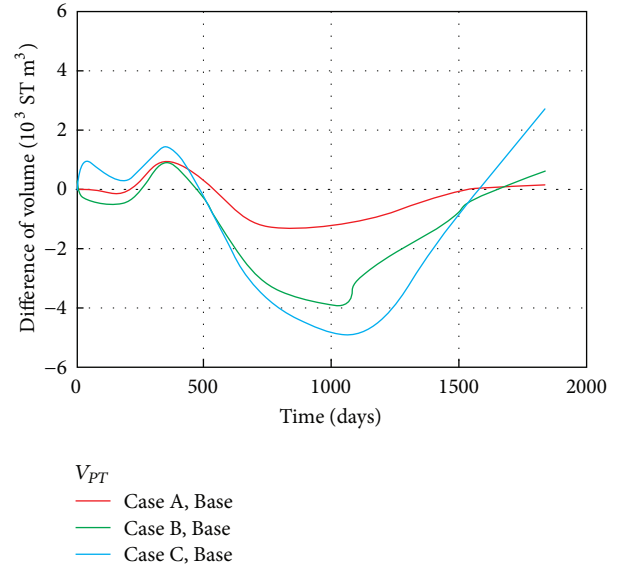


FIGURE 11: The difference of the cumulative volume of total methane gas produced at the well (V_{PT}) between horizontal strata and those sloping formations over 5-year production period.

Figure 11 shows the difference of total methane produced at the well between horizontal strata and those sloping formations over the length of 1000 m horizontal well. The initial oscillation illustrates that the hydrate dissociation behavior of sloping formation is sensitive to changes in the reservoir pressure. With the stability of reservoir pressure, the sloping formation results in a lower V_{PT} than that of horizontal strata. The greater the dip angle, the more significant the maximal difference of V_{PT} . This is because the methane is produced mainly by the free gas (V_{PG}) during this stage and the inclined formation is not conducive to gas recovery from the unconfined Class 2 HBS (Figure 9). However, this situation is reversed at the late stage because the available hydrate in the vicinity of horizontal well is exhausted and the methane is produced mainly by the dissolved gas.

3.2.3. Water Production at the Well. Figure 12 shows the difference of V_W and R_{GW} between horizontal strata and those sloping formations over the length of 1000 m horizontal well. As shown in this figure, the sloping formations yield lower water production compared with the horizontal strata. When the dip angles change from 0° , to 10° , 20° , and 30° , the cumulative volume of V_W decreased by 97 m^3 , 777 m^3 , and 1554 m^3 , respectively. This means that the inclined formation can restrict water from the boundary layers to the production well to some extent. Meanwhile, the sloping formation has a neglected influence on R_{GW} as shown in Figure 12. This is because sloping formation has a slight influence on both V_{PT} and V_W for the unit section (1 m) of horizontal well.

4. Conclusions

In this study, we numerically investigated the effects of the formation dip on gas production from the unconfined marine

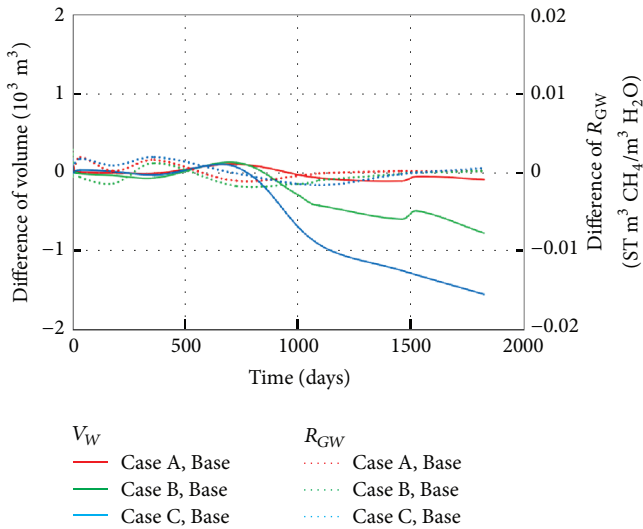


FIGURE 12: The difference of the cumulative volume of water produced at the well (V_W) and gas-to-water ratio (R_{GW}) between horizontal strata and those sloping formations over 5-year production period.

hydrate-bearing sediments (HBS) in Shenhu area of the South China Sea. The present modeling and analysis results are specific to the conditions and parameters considered. Based on the numerical simulations, the following conclusions can be drawn:

- (1) The horizontal well configuration through depressurization is an effective production method related to the challenging unconfined Class 2 HBS. The model predicted that the average methane production rates and the cumulative volume produced at the 1000 m horizontal well reach 2.47×10^4 ST m³/d and 4.51×10^7 ST m³ over 5-year period, respectively.
- (2) The methane is produced mainly by the free gas from the hydrate reservoir in the early stage, while the methane is produced mainly by the dissolved methane exsolution from the formation water at the late stage.
- (3) The hydrate dissociation behavior of sloping formation is sensitive to changes in the reservoir pressure. When the dip angles change from 0°, to 10°, 20°, and 30°, the cumulative volume of methane released from hydrate dissociation increased by 881 ST m³, 4098 ST m³, and 10490 ST m³, respectively.
- (4) The sloping formation is not conducive to free methane gas recovery from the unconfined Class 2 HBS, which results in more dissolved methane produced at the horizontal well. Consequently, the dip angle is not one of the main parameters that greatly affect the total methane production performance from the unconfined marine hydrate reservoir.
- (5) The sloping formation yields lower water production which can restrict water from the boundary layers to the production well to some extent.

- (6) As in unconfined Class 2 HBS, the obvious issue is relatively low exploitation efficiency of methane because gas production is accompanied by the recovery of very large volumes of water. Consequently, the development of the favorable well completion method to prevent water production is significantly important to realize large scale hydrate exploitation in the future.

Conflicts of Interest

There are no conflicts of interest of other works related to this paper.

Acknowledgments

This work was supported by the National Program on Key Research and Development Project (no. 2017YFC0307304) and the Graduate Innovation Found of Jilin University (no. 2017018).

References

- [1] J. Rutqvist and G. J. Moridis, "Numerical studies on the geomechanical stability of hydrate-bearing sediments," *SPE Journal*, vol. 14, no. 2, pp. 267–282, 2009.
- [2] Y. Konno, T. Fujii, A. Sato et al., "Key findings of the world's first offshore methane hydrate production test off the coast of Japan: toward future commercial production," *Energy & Fuels*, vol. 31, no. 3, pp. 2607–2616, 2017.
- [3] M. Kurihara, A. Sato, H. Ouchi et al., "Prediction of gas productivity from eastern Nankai trough methane-hydrate reservoirs," *SPE Reservoir Evaluation and Engineering*, vol. 12, no. 3, pp. 477–499, 2009.
- [4] G. J. Moridis and M. T. Reagan, "Estimating the upper limit of gas production from Class 2 hydrate accumulations in the permafrost: 2. Alternative well designs and sensitivity analysis," *Journal of Petroleum Science and Engineering*, vol. 76, no. 3–4, pp. 124–137, 2011.
- [5] G. Li, X.-S. Li, K. Zhang, B. Li, and Y. Zhang, "Effects of impermeable boundaries on gas production from hydrate accumulations in the shenhu area of the South China sea," *Energies*, vol. 6, no. 8, pp. 4078–4096, 2013.
- [6] G. J. Moridis and K. Pruess, *User's manual for the hydrate v1.5 option of TOUGH+ v1.5: a code for the simulation of system behavior in hydrate-bearing geologic media*, LBNL, Berkeley, Calif, USA, 2014.
- [7] X. S. Li, C. G. Xu, Y. Zhang, X. K. Ruan, G. Li, and Y. Wang, "Investigation into gas production from natural gas hydrate: a review," *Applied Energy*, vol. 172, pp. 286–322, 2016.
- [8] G. J. Moridis, M. B. Kowalsky, and K. Pruess, "Depressurization-induced gas production from class 1 hydrate deposits," *SPE Reservoir Evaluation and Engineering*, vol. 10, no. 5, pp. 458–481, 2007.
- [9] L. Huang, Z. Su, N. Wu, and J. Cheng, "Analysis on geologic conditions affecting the performance of gas production from hydrate deposits," *Marine and Petroleum Geology*, vol. 77, pp. 19–29, 2016.
- [10] G. Jin, T. Xu, X. Xin, M. Wei, and C. Liu, "Numerical evaluation of the methane production from unconfined gas hydrate-bearing sediment by thermal stimulation and depressurization

- in Shenhu area, South China Sea,” *Journal of Natural Gas Science and Engineering*, vol. 33, pp. 497–508, 2016.
- [11] V. Kamath and S. P. Godbole, “Evaluation of hot-brine stimulation technique for gas production from natural gas hydrates,” *Journal of Petroleum Technology*, vol. 39, no. 11, pp. 1379–1388, 1985.
- [12] X. S. Li, L. H. Wan, G. Li, Q. P. Li, Z. Y. Chen, and K. F. Yan, “Experimental investigation into the production behavior of methane hydrate in porous sediment with hot brine stimulation,” *Industrial & Engineering Chemistry Research*, vol. 47, pp. 9–11, 2008.
- [13] G. Li, G. J. Moridis, K. Zhang, and X.-S. Li, “The use of huff and puff method in a single horizontal well in gas production from marine gas hydrate deposits in the Shenhu Area of South China Sea,” *Journal of Petroleum Science and Engineering*, vol. 77, no. 1, pp. 49–68, 2011.
- [14] G. Li, X. S. Li, L. G. Tang, and Y. Zhang, “Experimental investigation of production behavior of methane hydrate under ethylene glycol injection in unconsolidated sediment,” *Energy & Fuels*, vol. 21, pp. 180–186, 2007.
- [15] M. Kurihara, H. Ouchi, A. Sato et al., “Prediction of performances of methane hydrate production tests in the eastern Nankai Trough,” in *Proceedings of the 7th International Conference on Gas Hydrates*, 2011.
- [16] T. S. Collett, A. H. Johnson, C. C. Knapp, and R. Boswell, “Natural gas hydrates—a review,” *Browse Collections*, vol. 89, pp. 146–219, 2009.
- [17] G. J. Moridis, T. S. Collett, M. Pooladi-Darvish et al., “Challenges, uncertainties, and issues facing gas production from gas-hydrate deposits,” *SPE Reservoir Evaluation and Engineering*, vol. 14, no. 1, pp. 76–112, 2011.
- [18] N. Wu, H. Zhang, S. Yang et al., “Gas hydrate system of Shenhu area, Northern South China sea: geochemical results,” *Journal of Geological Research*, 2011.
- [19] X. Wang, T. S. Collett, M. W. Lee, S. Yang, Y. Guo, and S. Wu, “Geological controls on the occurrence of gas hydrate from core, downhole log, and seismic data in the Shenhu area, South China Sea,” *Marine Geology*, vol. 357, pp. 272–292, 2014.
- [20] S. Yang, M. Zhang, J. Liang et al., “Preliminary results of China’s third gas hydrate drilling expedition: a critical step from discovery to development in the South China Sea,” *Fire in the Ice*, vol. 15, pp. 1–5, 2015.
- [21] X. Wang and D. Pan, “Application of AVO attribute inversion technology to gas hydrate identification in the Shenhu Area, South China Sea,” *Marine and Petroleum Geology*, vol. 80, pp. 23–31, 2017.
- [22] K. Zhang, G. J. Moridis, N. Wu, X. Li, and M. T. Reagan, “Evaluation of alternative horizontal well designs for gas production from hydrate deposits in the Shenhu area, South China Sea,” in *Proceedings of the International Oil and Gas Conference and Exhibition in China 2010: Opportunities and Challenges in a Volatile Environment (IOGCEC ’10)*, pp. 1417–1434, Society of Petroleum Engineers, June 2010.
- [23] G. Li, G. J. Moridis, K. Zhang, and X.-S. Li, “Evaluation of gas production potential from marine gas hydrate deposits in Shenhu area of South China sea,” *Energy & Fuels*, vol. 24, no. 11, pp. 6018–6033, 2010.
- [24] Z. Su, Y. Cao, N. Wu, and Y. He, “Numerical analysis on gas production efficiency from hydrate deposits by thermal stimulation: application to the Shenhu Area, South China Sea,” *Energies*, vol. 4, no. 2, pp. 294–313, 2011.
- [25] Z. Su, Y. He, N. Wu, K. Zhang, and G. J. Moridis, “Evaluation on gas production potential from laminar hydrate deposits in Shenhu Area of South China Sea through depressurization using vertical wells,” *Journal of Petroleum Science and Engineering*, vol. 86–87, pp. 87–98, 2012.
- [26] Z. Su, G. J. Moridis, K. Zhang, and N. Wu, “A huff-and-puff production of gas hydrate deposits in Shenhu area of South China Sea through a vertical well,” *Journal of Petroleum Science and Engineering*, vol. 86–87, pp. 54–61, 2012.
- [27] J. Sun, F. Ning, S. Li et al., “Numerical simulation of gas production from hydrate-bearing sediments in the Shenhu area by depressurising: the effect of burden permeability,” *Journal of Unconventional Oil & Gas Resources*, vol. 12, pp. 23–33, 2015.
- [28] L. Huang, Z. Su, and N.-Y. Wu, “Evaluation on the gas production potential of different lithological hydrate accumulations in marine environment,” *Energy*, vol. 91, pp. 782–798, 2015.
- [29] Y. Yuan, T. Xu, X. Xin, and Y. Xia, “Multiphase flow behavior of layered methane hydrate reservoir induced by gas production,” *Geofluids*, vol. 2017, Article ID 7851031, 15 pages, 2017.
- [30] J. Sun, L. Zhang, F. Ning et al., “Production potential and stability of hydrate-bearing sediments at the site GMGS3-W19 in the South China Sea: a preliminary feasibility study,” *Marine and Petroleum Geology*, vol. 86, pp. 447–473, 2017.
- [31] J. Rutqvist and G. J. Moridis, “Coupled hydrologic, thermal and geomechanical analysis of well bore stability in hydrate-bearing sediments,” in *Proceedings of the Offshore Technology Conference*, 2008.
- [32] J. Rutqvist, G. J. Moridis, T. Grover, and T. Collett, “Geomechanical response of permafrost-associated hydrate deposits to depressurization-induced gas production,” *Journal of Petroleum Science and Engineering*, vol. 67, no. 1–2, pp. 1–12, 2009.
- [33] S. Uchida, K. Soga, A. Klar, and K. Yamamoto, “Geomechanical study of the Mallik gas hydrate production field trials,” *Bulletin of the Geological Survey Canada*, vol. 601, pp. 191–204, 2012.
- [34] M. Jiang, H. Chen, M. Tapias, M. Arroyo, and R. Fang, “Study of mechanical behavior and strain localization of methane hydrate bearing sediments with different saturations by a new DEM model,” *Computers & Geosciences*, vol. 57, pp. 122–138, 2014.
- [35] S. Uchida, A. Klar, and K. Yamamoto, “Sand production model in gas hydrate-bearing sediments,” *International Journal of Rock Mechanics and Mining Sciences*, vol. 86, pp. 303–316, 2016.
- [36] F. Wang, J. Jing, T. Xu, Y. Yang, and G. Jin, “Impacts of stratum dip angle on CO₂ geological storage amount and security,” *Greenhouse Gases: Science and Technology*, vol. 6, no. 5, pp. 682–694, 2016.
- [37] F. Wang, J. Jing, Y. Yang et al., “Impacts of injection pressure of a dip-angle sloping strata reservoir with low porosity and permeability on CO₂ injection amount,” *Greenhouse Gases: Science and Technology*, vol. 7, no. 1, pp. 92–105, 2017.
- [38] T. Fujii, K. Suzuki, T. Takayama et al., “Geological setting and characterization of a methane hydrate reservoir distributed at the first offshore production test site on the Daini-Atsumi Knoll in the eastern Nankai Trough, Japan,” *Marine and Petroleum Geology*, vol. 66, pp. 310–322, 2015.
- [39] K. Yamamoto, T. Kanno, X.-X. Wang et al., “Thermal responses of a gas hydrate-bearing sediment to a depressurization operation,” *RSC Advances*, vol. 7, no. 10, pp. 5554–5577, 2017.
- [40] X. Wang, M. Lee, T. Collett, S. Yang, Y. Guo, and S. Wu, “Gas hydrate identified in sand-rich inferred sedimentary section using downhole logging and seismic data in Shenhu area, South China Sea,” *Marine and Petroleum Geology*, vol. 51, pp. 298–306, 2014.

- [41] H. Wang, S. Yang, N. Wu, G. Zhang, J. Liang, and D. Chen, "Controlling factors for gas hydrate occurrence in Shenhu area on the northern slope of the South China Sea," *Science China Earth Sciences*, vol. 56, no. 4, pp. 513–520, 2013.
- [42] R. Yang, P. Yan, N. Wu, Z. Sha, and J. Liang, "Application of AVO analysis to gas hydrates identification in the northern slope of the South China Sea," *Acta Geophysica*, vol. 62, no. 4, pp. 802–817, 2014.
- [43] M. Su, R. Yang, H. Wang et al., "Gas hydrates distribution in the Shenhu area, Northern South China sea: comparisons between the eight drilling sites with gashydrate petroleum system," *Geologica Acta*, vol. 14, no. 2, pp. 79–100, 2016.
- [44] M. Reagan, G. J. Moridis, T. Collett et al., "Toward production from gas hydrates: current status, assessment of resources, and simulation-based evaluation of technology and potential," *Spe Reservoir Evaluation & Engineering*, vol. 12, pp. 745–771, 2008.
- [45] N.-Y. Wu, H.-Q. Zhang, S.-X. Yang, J. Liang, and H.-B. Wang, "Preliminary discussion on natural gas hydrate (NGH) reservoir system of Shenhu Area, north slope of South China Sea," *Natural Gas Industry*, vol. 27, pp. 1–6, 2007.
- [46] X. Wang, D. R. Hutchinson, S. Wu, S. Yang, and Y. Guo, "Elevated gas hydrate saturation within silt and silty clay sediments in the Shenhu area, South China Sea," *Journal of Geophysical Research: Solid Earth*, vol. 116, no. 5, Article ID B05102, 2011.
- [47] G. J. Moridis and M. Kowalsky, "Gas production from unconfined class 2 hydrate accumulations in the oceanic subsurface," *Economic Geology of Natural Gas Hydrate*, vol. 7, pp. 249–266, 2006.
- [48] G. J. Moridis, S. Silpngarmert, M. T. Reagan, T. Collett, and K. Zhang, "Gas production from a cold, stratigraphically-bounded gas hydrate deposit at the Mount Elbert Gas Hydrate Stratigraphic Test Well, Alaska North Slope: implications of uncertainties," *Marine and Petroleum Geology*, vol. 28, no. 2, pp. 517–534, 2011.
- [49] G. J. Moridis and M. T. Reagan, "Gas production from class 2 hydrate accumulations in the permafrost," in *Proceedings of the SPE Annual Technical Conference and Exhibition 2007 (ATCE '07)*, pp. 3950–3976, Society of Petroleum Engineers, November 2007.
- [50] J. Sun, F. Ning, L. Zhang et al., "Numerical simulation on gas production from hydrate reservoir at the 1st offshore test site in the eastern Nankai Trough," *Journal of Natural Gas Science and Engineering*, vol. 30, pp. 64–76, 2016.
- [51] G. J. Moridis and M. T. Reagan, "Estimating the upper limit of gas production from Class 2 hydrate accumulations in the permafrost: 1. Concepts, system description, and the production base case," *Journal of Petroleum Science and Engineering*, vol. 76, no. 3-4, pp. 194–204, 2011.
- [52] K. Yamamoto, Y. Terao, T. Fujii et al., "Operational overview of the first offshore production test of methane hydrates in the Eastern Nankai Trough," in *Proceedings of the Offshore Technology Conference 2014 (OTC '14)*, pp. 1802–1812, May 2014.
- [53] M. T. van Genuchten, "A closed-form equation for predicting the hydraulic conductivity of unsaturated soils," *Soil Science Society of America Journal*, vol. 44, no. 5, pp. 892–898, 1980.
- [54] J. Zhao, T. Yu, Y. Song et al., "Numerical simulation of gas production from hydrate deposits using a single vertical well by depressurization in the Qilian Mountain permafrost, Qinghai-Tibet Plateau, China," *Energy*, vol. 52, pp. 308–319, 2013.

Research Article

Effects of Maceral Compositions of Coal on Methane Adsorption Heat

Yingke Liu,^{1,2} Jianhong Kang ,^{1,2} Fubao Zhou ,^{1,2} Yanming Fan,¹ and Haijian Li¹

¹Faculty of Safety Engineering, China University of Mining & Technology, Xuzhou, Jiangsu 221116, China

²Key Laboratory of Gas and Fire Control for Coal Mines (Ministry of Education), China University of Mining & Technology, Xuzhou, Jiangsu 221116, China

Correspondence should be addressed to Fubao Zhou; zfbcumt@gmail.com

Received 17 October 2017; Revised 6 February 2018; Accepted 30 April 2018; Published 5 June 2018

Academic Editor: Egor Dontsov

Copyright © 2018 Yingke Liu et al. This is an open access article distributed under the Creative Commons Attribution License, which permits unrestricted use, distribution, and reproduction in any medium, provided the original work is properly cited.

The role of maceral compositions (vitrinite and inertinite) in the adsorption characteristics of coal has not been fully understood in terms of energy. In this study, using a microcalorimeter, the adsorption heat of maceral compositions for methane is directly measured for five groups of Chinese coal samples with different coal ranks. The results show that the adsorption heat of the maceral concentrates varies with increasing coal rank, but for the same coal sample, the vitrinite concentrates have a higher adsorption heat than the inertinite concentrates. Furthermore, the adsorption heat of both vitrinite and inertinite concentrates is highest at the long-flame coal stage. This finding indicates that the coalification and maceral compositions have significant effects on the adsorption heat of coal for methane. It is observed that although the inertinite concentrates have a larger pore volume, they are less microporous than their rank equivalent vitrinite concentrates, resulting in lower adsorption heat. Furthermore, it is revealed that the adsorption heat of both vitrinite and inertinite concentrates is primarily correlated to the content of oxygen-containing functional groups and aliphatic hydrocarbons.

1. Introduction

Coalbed methane (CBM, also known as gas in coal mines) is a type of unconventional gas resource but is also a hazardous gas in underground coal mining and a greenhouse gas. CBM has a greenhouse effect that is 20 times that of carbon dioxide. Motivated by the coalbed methane exploitation, as well as the need to improve the environment, gas storage and transport in coal seams have received considerable attention and continue to be an intense research topic [1, 2]. Unlike a conventional gas reservoir, most gas in coal seams is originally adsorbed on the porous coal matrix, rather than being stored as a free gas. The gas adsorption capacity of coal is one critical issue for the estimation of a coalbed methane reservoir, coalbed methane production, and carbon dioxide sequestration with enhanced CBM recovery [3]. As a result, the study of adsorption characteristics of coal has been an ongoing and important research area in this field [4, 5].

Over recent decades, extensive theoretical and experimental research has been performed on gas adsorption by

coal, most of which focused on the effects of physical and chemical properties of coal (such as maceral and mineral composition [6], pore structure [7], and functional group content [8]) and experimental conditions (such as temperature [9], pressure [10], adsorbates [11], and moisture [12]). For example, Jian et al. [13] investigated the coal samples at the vitrinite reflectance of 0.24~0.65% using mercury porosimetry and isothermal adsorption. It was observed that the coal rank was not the main factor affecting the adsorption capacity of coal, while the change of the micropore volume had a significant influence on the adsorption capacity. In addition, coal that has a large specific surface area and is rich in aromatic structure has a high adsorption capacity with methane. Wang et al. [14] studied the adsorption isotherms under low temperature conditions. These researchers' results indicated that the low temperature inhibited the migration of methane in coal seams but could improve the adsorption capacity of coal for methane. With a method combining SEM-EDS and infrared thermal imaging, Feng et al. observed the meso structures with different maceral compositions and

the methane distribution and evolution characteristics in coal [15, 16]. Pini et al. [17] conducted theoretical and experimental investigations on the adsorption isotherms for carbon dioxide, methane, and nitrogen and observed that the adsorption capacity of coal decreased with the increase of vitrinite reflectance. Based on an overview of these references, it was observed that the adsorption volume is usually used to describe the adsorption characteristics of coal for methane. However, the experimentally measured adsorption volume is actually the total volume of gas adsorbed into the pore structure, which includes the adsorbed gas, as well as the free gas, while the theoretically calculated adsorption volume largely depends on the choice of adsorption models and corresponding assumptions [17, 18]. It has been reported that the Langmuir model underestimates the sorption capacity in coal by approximately 30% at 15 MPa [19]. As a result, the adsorption volume has certain limitations for characterizing the adsorption capacity of coal for methane.

Conversely, gas adsorption by coal is essentially the interaction between the molecular structure of coal and gas molecules, which is normally an exothermal process. The heat of adsorption is an inherent property of the adsorption process, reflecting the energy state of gas molecules on the surface adsorption field of coal. Thus, adsorption heat can be used to characterize the adsorbent material energetically and is needed to provide basic data for developing new theories of adsorption equilibria and kinetics [20]. In the literature, there have been several studies examining the adsorption heat accompanying adsorption process. Nodzeński [21] calculated the isosteric heats of sorption methane and carbon dioxide on hard coal using the thermal sorption equation of the virial form. Bülow et al. [22] introduced the method for calculating the isosteric adsorption heat using the Clausius-Clapeyron equation. Chikatamarla and Crosdale [23] calculated the isosteric heats of methane on dry Australian coals based on the Langmuir and BET isotherm models. From a modified Dubinin-Radushkevich model, Day et al. [4, 24] estimated the adsorption heat of carbon dioxide on coal under supercritical conditions. In addition, using the molecular simulation method of quantum chemistry, Jiang et al. [25] and Chen et al. [26] calculated the adsorption heat of methane on coal. Tang et al. calculated the heat of adsorption of methane in such geomaterials as coal and shale by considering the contribution of the adsorbed volume and real gas behavior [27, 28]. In conclusion, the adsorption heat in these studies was calculated by modeling the adsorption isotherms on the basis of molecular simulation. However, the accuracy of molecular simulation is significantly influenced by the selection of the chemical structure model of coal and potential function of the force field [29]. In addition, most estimates of the adsorption heat made from adsorption equilibrium data are subject to potential uncertainty due to the widely varying estimates of model parameters [4]. For example, determining the adsorption heat from the BET isotherms has been criticized because this model assumes that the adsorption heat is constant during the monolayer adsorption but drops to zero after the monolayer is completed [24]. The calculation of mixture heats from extension of the Clapeyron equation is impractical [30].

Compared with the calculation method of adsorption heat as mentioned above, the method of calorimetric measurement for determining adsorption heat of coal for methane has received little attention. However, it is very necessary to perform calorimetric adsorption experiments because the calculation method of adsorption heat hardly takes into account the energetic heterogeneity of coal [20]. To date, there have been few studies on this subject. Glass and Larsen [31] directly measured the isosteric heat of adsorption of various sorbates onto coal using an inverse chromatographic method. Taraba [32] measured the adsorption heat of gas onto coal when studying the competitive adsorption of methane and carbon dioxide. More recently, Zhou et al. [33] studied the effects of coal functional groups on the adsorption microheat of coalbed methane using a C80 microcalorimeter.

Despite the significant effects of the coal type on gas adsorption by coal, no agreement has been reached on how the maceral compositions are correlated to the adsorption capacity of coal for methane [34]. Most studies agree that vitrinite-rich coals have a greater methane adsorption capacity than inertinite-rich coals at the same rank [35]. However, others have found poor or no correlation between adsorption capacity and maceral compositions [4, 36, 37]. To better clarify this confusion on the possible correlation between maceral compositions and methane adsorption capacity, in this study, the effects of maceral compositions on the adsorption characteristics of coal for methane are investigated in terms of adsorption heat by use of the calorimetric measurement method. The maceral concentrates with different coal ranks are prepared by the hand picking and density fraction methods and then are characterized by multipoint Brunauer-Emmett-Teller (BET) measurement and Fourier-transform infrared spectroscopy (FTIR spectroscopy). The correlations between the adsorption heat of maceral concentrates and corresponding pore structure and coal functional groups are discussed in detail.

2. Materials and Methods

2.1. Collection of Coal Samples. Six groups of coal samples were collected from Chinese coal mines. The geological information of coal seams from which the samples were collected is shown in Table 1, and the physical parameters of the collected coal samples are listed in Table 2. Coal sample numbers 1 to 5 were used to investigate the effects of maceral compositions of coal on methane adsorption heat, while number 6 sample was used to compare the isosteric heat of adsorption calculated from adsorption isotherms with that obtained from calorimetric heat. According to the National Standard GB/T 5751-2009 [38], the coal ranks of coal sample numbers 1 to 5 are long-flame coal, fat coal, coking coal, lean coal, and anthracite, respectively. Coal samples were hermetically sealed in bags at 5°C.

2.2. Separation and Preparation of Maceral Concentrates. Coal macerals refer to the basic compositions identified by optical microscopy, primarily including organic macerals and inorganic macerals. According to the genetic type,

TABLE 1: Geological information of coal seams where the samples were collected.

Coal number	Sampling position	Coal field	Geological formation
Number 1	Coal seam numbers 2-3 in Yuejin Coal Mine	Yima	Yima formation of the middle Jurassic system
Number 2	Coal seam number 24 in Shanjiaoshu Coal Mine	Panxian	Longtan formation of the upper Permian system
Number 3	Coal seam number 3 in Renjiashuang Coal Mine	Ningdong	Shanxi formation of the lower Permian system
Number 4	Coal seam number 9 in Jinjia Coal Mine	Panxian	Longtan formation of the upper Permian system
Number 5	Coal seam number 2 in Baijigou Coal Mine	Helanshan	Yanan formation of lower Jurassic system
Number 6	Coal seam number 3 in Chengzhuang Coal Mine	Qinshui	Shanxi formation of the lower Permian system

TABLE 2: Physical parameters of the collected coal samples.

Coal number	Mass (kg)	$R_{o,max}$ (%)	M_{ad}	Proximate (%)			Coal quality indices			Coal rank
				A_{ad}	V_{ad}	FC_{ad}	V_{daf} (%)	G (%)	Y (mm)	
Number 1	3.6	0.59	7.82	25.12	27.85	39.21	41.53	27.6	—	Long-flame coal
Number 2	2.9	1.12	1.01	8.3	31.57	59.12	34.81	92.1	29.8	Fat coal
Number 3	3.1	1.46	6.03	9.13	29.58	55.26	34.87	84.47	13.7	Coking coal
Number 4	4.2	2.11	0.91	13.42	8.66	77.01	10.11	3.2	—	Lean coal
Number 5	3.8	2.86	1.27	5.67	8.9	84.16	9.56	—	—	Anthracite
Number 6	3.4	2.37	0.72	13.88	7.54	77.86	8.83	—	—	Anthracite

organic macerals can be further divided into vitrinite, inertinite, and exinite, among which certain physical differences can be observed. The first difference is their densities. In general, the density of inertinite is the largest, while the density of exinite is the smallest. The second difference is their morphology under the microscope. The morphologies of vitrinite, inertinite, and exinite under the immersion reflection microscope are shown in Figure 1. Since the adsorption capacity of vitrinite and inertinite is much greater than that of exinite [35, 36], this paper only focuses on vitrinite and inertinite.

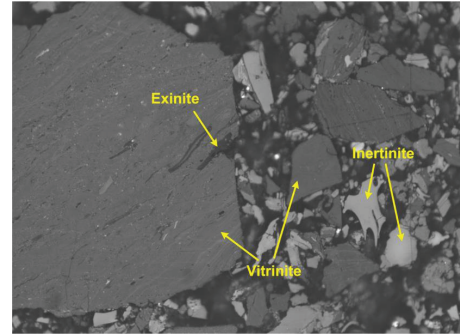


FIGURE 1: Coal maceral compositions of coal.

2.2.1. Method of Separation and Enrichment. The separation and enrichment methods of coal macerals is based on the physical differences of macerals, such as hand picking and density fractionation. In this study, the hand picking and sieving are used for the preliminary separation of coal macerals, and the method of density fractionation is applied for further enrichment.

- Hand picking. Macroscopic compositions of coal refer to the basic unit of coal that can be distinguished by the naked eye, which can be divided into vitrain, clarain, durain, and fusain. The gloss of four macroscopic compositions is gradually weakened. After the coal sample was cracked by a hammer, macroscopic compositions were separated and collected on the basis of the differences of coal color and gloss. In general, vitrain and clarain are rich in vitrinite, while durain and fusain are rich in inertinite.
- Sieving. Since the brittleness and the Hardgrove Grindability Index (HGI) of vitrain are lower than those of fusain [39], the vitrinite gathers in large coal particles and can be easily broken into pieces, while

the inertinite gathers in small coal particles and can be easily broken into powder. Thus, the larger particle size helps to obtain vitrinite concentrates of higher purity. Otherwise, the particle size should be as small as possible in order to obtain inertinite concentrates of higher purity. Considering that too-small particles will affect the subsequent experiments, a mesh of 60~80 (0.2~0.25 mm) particle size of the coal samples was used in this study.

- Density fractionation. The principle of density fractionation is based on the density differences of vitrinite and inertinite. Coal samples of certain particle size were added into the heavy liquid of different densities and were separated by the centrifugal method. The main apparatus for density fractionation consists of an electronic balance, KJLXCD-4004L centrifugal precipitation machine, drying oven, and liquid densimeter. Carbon tetrachloride and benzene were used as the heavy liquid. Finally, the vitrinite and inertinite

concentrates were obtained through the processes of sampling, centrifugation, filtration, and drying.

2.2.2. Method of Detection and Analysis. After the maceral concentrates were prepared by the separation and enrichment as described above, the method of counting pixels was used to quantitatively determine the content of each maceral composition. First, the sample was labeled with a plurality of grids. While moving the microscope lens to the grid nodes, the cross-center of the lens was observed. If the cross-center was located on certain coal particle, this grid was assumed to be an available point. Furthermore, the maceral composition of this coal particle represented the maceral composition of the current grid. According to the National Standard GB/T 8899-2013 [40], more than 500 available points should be recorded in order to accurately measure the content of maceral compositions. The main procedure of this method is described as follows:

- (a) Preparing the slice of maceral concentrates: Unsaturated polyester resin, curing agent, and promoter were mixed in the volume ratio of 100:4:4. Maceral concentrates and binder were mixed in the mass ratio of 10:7. The two mixtures were blended and poured into a cold plastic mold.
- (b) Polishing the slice: An automatic polishing-grinding machine was used to polish the slice. After being polished, the slice was washed by water and then cleaned by an ultrasonic cleaner.
- (c) Counting pixels under a microscope: The polished slice was placed on the microscope stage, and a drop of oil was dripped on the surface of the polished slice such that the slice object was immersed in oil. The focal length was adjusted so that the coal macerals could be clearly observed. After that step, more than 500 available points were measured according to the method of counting pixel, and the data were automatically recorded by a VB computer program.

2.3. Experimental Method

2.3.1. Determination of Adsorption Heat of Coal for Methane.

The adsorption heat of methane on maceral concentrates was directly measured using a C80 microcalorimeter produced by Setaram Company in France. The microcalorimeter consists of a host and a gas-circulating pool that has an inlet for gas intake and an outlet for gas discharge. The testing temperature ranges from room temperature to 300°C, and its control accuracy is $\pm 0.001^\circ\text{C}$ with a resolution of $0.1\ \mu\text{w}$. Furthermore, the gas-circulating pool is surrounded inside by more than 400 pairs of thermocouples to measure the heat flux from the circumferential direction.

The experimental temperature and ambient pressure in both sample and reference vessels were set to 15°C and 0.101 MPa, respectively. The effects of the particle size, quantity of coal samples, and the gas flow rate

were taken into account to measure the adsorption heat more accurately.

- (a) Size of coal samples: By repeated tests, a particle size of 60~80 mesh was used in this study.
- (b) Quantity of coal samples: If the quantity is too small, the gas cannot fully adsorb onto the coal. If the quantity is too large, the programmed sample temperature may deviate from the environmental temperature, resulting in large experimental errors. Considering the capacity of the sample cell and the above factors, 2.5 g of coal samples was used in the current experiment.
- (c) Gas flow: To guarantee sufficient methane adsorption, the gas flow was set to $30\ \text{mL}\cdot\text{min}^{-1}$ in consideration of the experimental accuracy and efficiency.

Furthermore, coal samples may adsorb other gases when they are exposed to air, which affects the accuracy of methane adsorption experiment. Thus, the vacuum-pumping system was used to extract these other gases from the vessels and coal matrix before the test. The vacuum pumping took one hour off after eight hours extracting and this working pattern repeated three times, and, namely, the total time of vacuum pumping was approximately 24 hours. Next, methane was injected into the gas circulating pool.

2.3.2. Determination of Coal Functional Group Types and Contents

- (a) Fourier-Transform infrared spectroscopy: The infrared spectroscopy experiments were carried out on a VERTEX 80v Fourier-transform infrared spectrometer which was produced by Bruker Corporation in Germany. The scanned area was $400\text{--}4000\ \text{cm}^{-1}$ with a resolution of $4\ \text{cm}^{-1}$. To obtain accurate infrared spectrograms, coal samples used in the experiment were smaller than 200 mesh ($<76\ \mu\text{m}$) and were dehydrated for 24 hours. The coal samples were prepared by the KBr disc technique. Pulverized coal was mixed with KBr in the ratio of 1:180 (the total weight is 0.1 g). A KBr disc (0.1 g) was used as a blank background.
- (b) Types and contents of surface functional groups: The type and content of functional groups on maceral concentrates were obtained by the qualitative and semiquantitative analysis of the infrared spectrograms. First, according to the peaks on the infrared spectrograms, the major functional groups was determined by comparing the attribution of absorption frequency of the coal molecules with the coal molecular structure. The overlapped peaks could be separated by the peak resolution function, such as the OMNIC software. Then, the content of functional groups was analyzed qualitatively by calculating the peak areas for the functional groups. The semiquantitative analysis of the infrared

spectrograms is based on the Lambert-Beer law, which is given as [41]

$$A(\nu) = \lg \frac{1}{T(\nu)} = K(\nu)bc, \quad (1)$$

where $A(\nu)$ is the absorbance, $K(\nu)$ is the absorbance coefficient, b is the thickness of coal sample, c is the concentration of coal sample, and $T(\nu)$ is the percent transmittance.

2.3.3. Aided Tests

- Pore characteristics of maceral concentrates: The pore structure of coal samples was characterized by the method of low temperature liquid nitrogen adsorption, which was carried out on a nitrogen adsorption-desorption spectrometer (BET) produced by Japanese BEL Company. The pressure range is 0~133 KPa with a resolution of 1.6×10^{-5} Pa.
- Proximate analysis: The proximate analysis including water (M_{ad}), ash (A_{ad}), volatile (V_{ad}), and fixed carbon (FC_{ad}) was carried out on an SDTGA5000 automatic analyzer produced by the Chinese Sande Company. According to the National Standard GB/T 5751-2009 [38], the type of coal can be determined by the dry ash-free basis volatile (V_{daf}), caking index (G), and maximal thickness of the plastic layer (Y).
- Mean maximum reflectance of vitrinite: The determination of the mean maximum reflectance of vitrinite ($R_{o,max}$, %) in the coal samples was performed in compliance with the National Standard GB/T 6948-2008 [42] and was recorded by an Axio Imager microscope produced by the Carl Zeiss Foundation Group.

3. Results and Discussion

The adsorption of gas molecules on coal surface is definitely accompanied by the changes of energy. Compared with the adsorption capacity characterized by the adsorption isotherms, the adsorption heat of gas on coal can reflect the adsorption capacity in terms of energy. In this section, based on a comparison between isosteric heat of adsorption calculated from adsorption isotherms and that obtained from calorimetric heat, we mainly focus on how the coalification and maceral compositions of coal affect the adsorption heat of coal for methane.

3.1. Isosteric Heat of Adsorption and Calorimetric Heat of Adsorption of Methane. The isosteric heat of adsorption is defined as the difference of partial molar enthalpy in the gas phase and the excess partial molar enthalpy in the adsorbed phase [43]. The isosteric heat of adsorption can be derived from the Clausius-Clayperon equation as follows [43, 44]:

$$\frac{d \ln P}{dT} = \frac{q_{st}}{RT^2}, \quad (2)$$

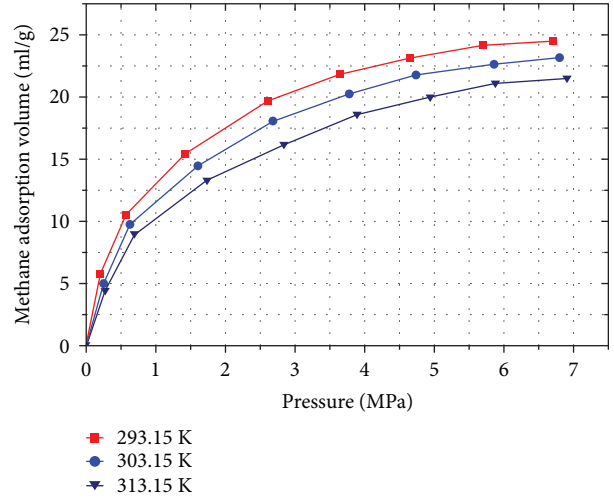


FIGURE 2: Adsorption isotherms of methane at different temperatures.

where q_{st} is the isosteric heat of adsorption, R is the gas constant, T is the absolute temperature, and P is the pressure.

Integrating both sides of (2), (2) can be expressed as

$$\ln P = \frac{k}{T} + c, \quad (3)$$

where k is the slope of the straight line for $\ln P-1/T$, and it can be calculated as follows:

$$k = \frac{-q_{st}}{R}. \quad (4)$$

According to (4), q_{st} can be obtained as follows:

$$q_{st} = -kR. \quad (5)$$

Taking number 6 coal sample as an example (Table 1), the adsorption isotherms for methane at different temperatures are shown in Figure 2. Based on Figure 2, the relationship between pressures (logarithms) and molar adsorption amounts in adsorption process and the corresponding fitting equations of $\ln P-n$ are shown in Figure 3, where n is the molar adsorption amount, in mmol/g. According to Figure 3 and those fitting equations of $\ln P-n$, the relationship between $\ln P$ and $1/T$ under the conditions with different n can be obtained, as shown in Figure 4. The slope of each fitting line of $\ln P-1/T$ for different molar adsorption amounts and corresponding isosteric heat of adsorption based on (5) are shown in Table 3.

On the other hand, the adsorption heat of coal for methane measured by C80 microcalorimeter is integral adsorption heat. According to the definitions of isosteric heat of adsorption and integral adsorption heat, the relationship of them can be expressed using the following [45]:

$$q_{st} = \frac{dQ}{dn}, \quad (6)$$

where Q is the calorimetric heat of adsorption, in J/g.

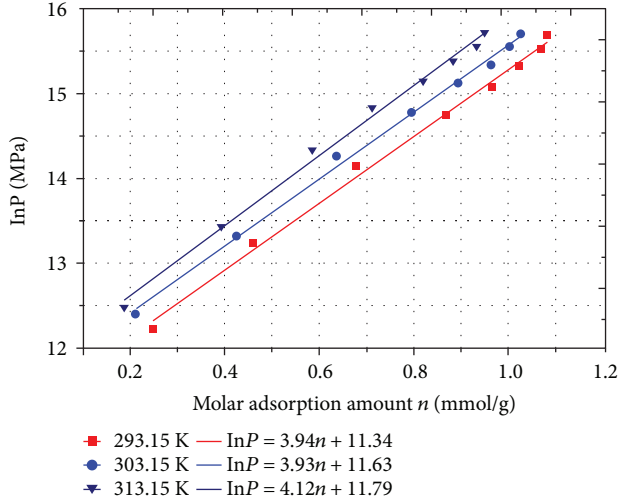


FIGURE 3: Relationship between pressures (logarithms) and molar adsorption amount.

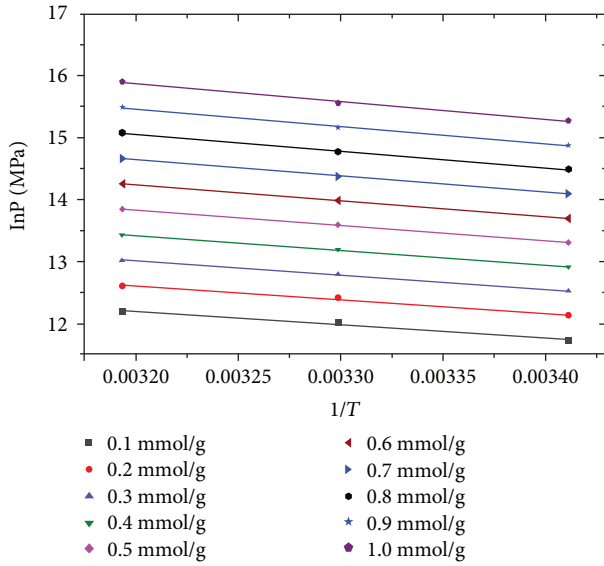


FIGURE 4: Relationship between $\ln P$ and $1/T$ under the conditions with different molar adsorption amount.

According to (6) and the calorimetric heat of adsorption in the adsorption process, the isosteric heat of adsorption can be calculated using the following:

$$q_{st-i} = 0.5 \times \left(\frac{Q_i - Q_{i-1}}{n_i - n_{i-1}} + \frac{Q_{i+1} - Q_i}{n_{i+1} - n_i} \right). \quad (7)$$

For the number 6 coal sample, the calorimetric heat of adsorption for methane measured by C80 microcalorimeter in the adsorption process is shown in Figure 5. According to Figure 5 and (7), the isosteric heat of adsorption obtained from measurement using C80 microcalorimeter is shown in Table 4.

TABLE 3: Slope of each fitting line of $\ln P-1/T$ and corresponding isosteric heat of adsorption obtained from adsorption isotherms.

Molar adsorption amount (mmol/g)	Slope	Isosteric heat of adsorption (kJ/mol)
0.1	-2138.6	17.78
0.2	-2221.1	18.47
0.3	-2303.5	19.15
0.4	-2385.9	19.84
0.5	-2468.4	20.52
0.6	-2550.8	21.21
0.7	-2633.3	21.89
0.8	-2715.7	22.58
0.9	-2798.1	23.26
1	-2880.6	23.95

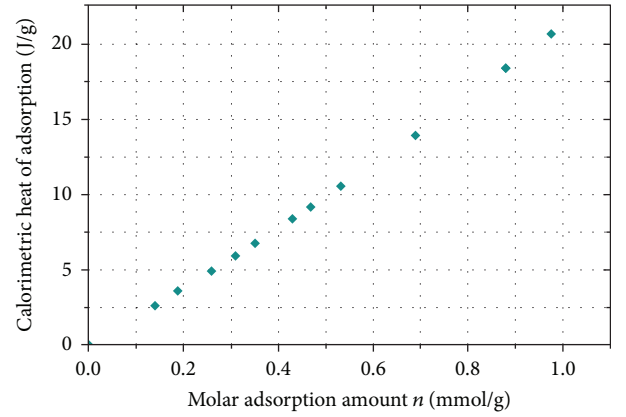


FIGURE 5: Calorimetric heat of adsorption for methane measured by C80 microcalorimeter.

TABLE 4: Isosteric heat of adsorption obtained from measurement using C80 microcalorimeter.

Molar adsorption amount (mmol/g)	Isosteric heat of adsorption (kJ/mol)
0.139	19.01
0.188	19.25
0.258	19.66
0.310	19.96
0.350	20.27
0.430	20.72
0.468	21.09
0.532	21.35
0.689	22.46
0.880	23.68

According to Tables 3 and 4, a comparison between isosteric heat of adsorption calculated from adsorption isotherms and that obtained from measurement using C80 microcalorimeter is shown in Figure 6. It is found that there

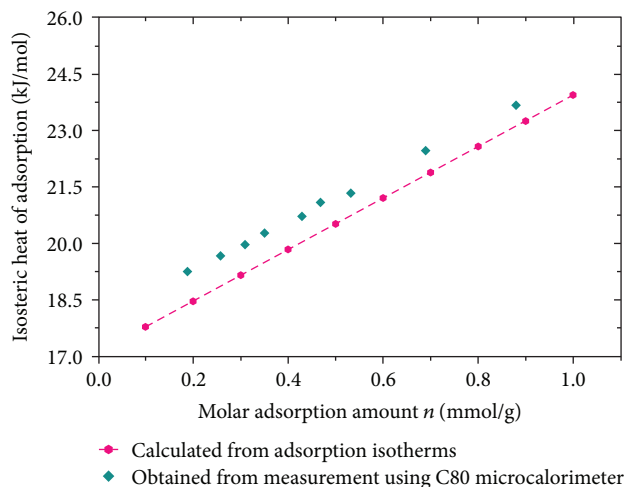


FIGURE 6: Comparison between isosteric heat of adsorption obtained from adsorption isotherms and that obtained from calorimetric heat.

is just a little difference between them, and they have a same change trend. So the adsorption heat measured using C80 microcalorimeter is reliable and can be used to make more analysis.

3.2. Purity of Maceral Concentrates for Different Coal Ranks.

In general, the densities of vitrinite, inertinite, and exinite change with the rank of coal. Even though the degree of metamorphism is the same, the densities of coal samples from different regions may be different from each other. Therefore, when the maceral concentrates were prepared, we needed to determine whether the purity met the experimental requirements. If the experimental requirements are satisfied, the heavy liquid of this density is used for further separation and enrichment. Otherwise, the density of heavy liquid is adjusted, and the following steps are repeated until the desirable purity of maceral concentrates is obtained: separation and enrichment, preparation of powder coal slice, polishing, and microscope observation.

Using the heavy liquid of different density intervals, the purity of vitrinite and inertinite concentrates for five coal samples is shown in Table 5, where VC represents vitrinite concentrates and IC represents inertinite concentrates. For the number 1 coal sample, the VC with a purity of 90% and IC with a purity of 93% were obtained after using two density intervals, respectively. The heavy liquids with three different density intervals were used to concentrate the number 2 coal sample. The purity of number 2 VC in the density interval of 1.26~1.28 g/cm³ is the highest (86.9%), while the purity of number 2 IC in the density interval of 1.45~1.50 g/cm³ is the highest (82.4%). For the number 3 coal sample, the purity of VC reached 91.4% in the density interval of 1.28~1.30 g/cm³, while the highest purity of IC is 87.8% in the density interval of 1.45~1.55 g/cm³ which is slightly higher than that in the density intervals of 1.40~1.45 g/cm³ and 1.55~1.65 g/cm³. For the number 4 coal sample, the VC with a purity of 95.2% was obtained

in the density interval of 1.28~1.30 g/cm³, and the IC with a purity of 97.4% was obtained in the density interval of 1.45~1.55 g/cm³. Such high-purity samples satisfied the experimental requirements, and no further separation and enrichment continued. For the number 5 coal sample, the purity of VC reached a higher value in both the density intervals of 1.26~1.28 g/cm³ and 1.28~1.30 g/cm³. The purity of IC is only 79.3% in the density interval of 1.40~1.45 g/cm³. After the density of heavy liquid increased to the interval of 1.45~1.50 g/cm³, its purity increased to 84% accordingly. However, when the density of heavy liquid further increased to the interval of 1.50~1.60 g/cm³, the purity of IC decreased to 63.6%, and the percentage of minerals increased from 3.2% to 30%. This finding is observed because when the density of heavy liquid is too large, many coal gangue and other minerals are also concentrated in the product.

3.3. Adsorption Heat of Different Maceral Concentrates for Methane.

Figure 7 shows the flux of methane adsorption heat released from the VC and IC of different coals. As shown in Figure 7, the heat flux goes up quickly at the beginning of the methane adsorption and later decreases gradually until the equilibrium of adsorption. Additionally, Figure 8 shows the adsorption heat of VC and IC for methane in terms of energy per unit mass of coal. As shown in Figure 8, the adsorption heat of vitrinite concentrate for methane is always greater than that of the inertinite concentrate for all five coal samples, indicating that the adsorption capacity of vitrinite concentrate is larger than that of the inertinite concentrate. This result agrees well with that of Li et al. [46], who observed that the coal surface with a higher content of vitrinite seems to have a faster adsorption rate and higher affinity with methane. This finding also agrees with that of Crosdale et al. [35], who found that in most cases, vitrinite-rich coals have a greater adsorption capacity than their inertinite-rich equivalents. Furthermore, the adsorption heat of maceral concentrates for methane varies with the increasing coal rank. The maximum values of adsorption heat of vitrinite and inertinite concentrates for methane were reached at the long-flame coal stage (number 1 coal sample, $R_{o,max} = 0.59\%$), which were determined to be 6.19 J/g and 4.76 J/g, respectively. The minimum values of 0.19 J/g and 0.05 J/g were reached at the lean-coal stage (number 4 coal sample, $R_{o,max} = 2.11\%$) for the adsorption heat of vitrinite and inertinite concentrates, respectively.

It can also be seen from Figure 8 that in the bituminous coal stage (i.e., $0.59\% < R_{o,max} < 2.11\%$), the adsorption heat of inertinite concentrates for methane decreased monotonically and reached a minimum at the lean-coal stage, while the adsorption heat of vitrinite concentrates for methane fluctuated with the increase of coal rank. In contrast, from the bituminous coal stage to the anthracite stage (i.e., $2.11\% < R_{o,max} < 2.86\%$), the adsorption heat of inertinite concentrates for methane monotonically increased, and the adsorption heat of vitrinite concentrates has a similar trend. Overall, the adsorption heat of maceral concentrates for methane first decreases with the increasing coal rank, reaching the lowest value at the lean-coal stage, and then increases at the anthracite stage. This indicates that the

TABLE 5: The purity of maceral concentrates by using heavy liquid of different density intervals.

Sample name	Density interval (g/cm ³)	Vitrinite (%)	Percentage of macerals		
			Inertinite (%)	Exinite (%)	Minerals (%)
Number 1 VC	1.26~1.28	89.6	6.6	3.2	0.6
	1.28~1.32	90	4.1	1.7	4.2
Number 1 IC	1.40~1.45	8	87.4	0.7	3.9
	1.45~1.55	2.5	93	0	4.5
Number 2 VC	1.24~1.26	83.1	11.3	4.7	0.9
	1.26~1.28	86.9	8.7	3.5	0.9
	1.28~1.32	81.7	13.3	3	2
Number 2 IC	1.40~1.45	17.6	78	0.6	3.8
	1.45~1.50	13.5	82.4	1.8	2.3
	1.50~1.55	11.4	78.9	2.1	7.6
Number 3 VC	1.26~1.28	87	9.2	3.8	0
	1.28~1.30	91.4	6.7	1.7	0.2
Number 3 IC	1.40~1.45	11.7	86.8	1.6	0.8
	1.45~1.55	8.6	87.8	2.1	1.5
	1.55~1.65	9.3	82.3	1.5	7.9
Number 4 VC	1.28~1.30	95.2	1.4	3.4	0
Number 4 IC	1.40~1.45	7.9	89.5	1.8	0.8
	1.45~1.55	1.3	97.4	0	1.3
Number 5 VC	1.26~1.28	92.3	5.6	2.1	0
	1.28~1.30	94.7	4.5	0.8	0
Number 5 IC	1.40~1.45	18.7	79.3	1.4	0.6
	1.45~1.50	11.2	84	1.6	3.2
	1.50~1.60	5.5	63.6	0.9	30

coalification has significant effects on the adsorption heat of maceral concentrates for methane.

3.4. Correlation between the Adsorption Heat and the Pore Structure of Coal. It is generally understood that high porosity provides great access into the internal microporosity where most of the gas adsorption occurs [4]. Thus, the pore structure of the coal matrix is closely related with the adsorption capacity of coal for methane and is expected to partly account for the variations of the adsorption heat of different maceral concentrates.

The changes of the average pore size and total pore volume are shown in Figure 9. From Figure 9(a), it can be seen that the minimum and maximum average pore sizes of vitrinite and inertinite concentrates for five coal samples are 1.26 nm and 9.69 nm, respectively. According to the pore size classification by Cai et al. [7], pores whose size is less than 10 nm belong to micropores. Therefore, the micropores account for the largest percentage of pore size for the maceral concentrates. In addition, with the increase of $R_{o,max}$, the variations of average pore size for the inertinite concentrates and vitrinite concentrates have the same trends. In contrast, the variation of total pore volume of vitrinite concentrates does not coincide with that of inertinite concentrates, as shown in Figure 9(b). In particular, the total pore volume of inertinite concentrate for the number 1 coal sample

reaches 0.0152 mL/g, which is almost 15 times the total pore volume of its rank equivalent vitrinite concentrates.

According to the geological genesis of coal macerals, the vitrinite is mainly formed by the gelatification of wood fiber, while the inertinite is primarily formed by the fusinization of fibrous tissue of plants. The fusinite contains a large number of pores as shown in Figure 10, which explains why the total pore volume and average pore size of inertinite concentrates are greater than those of vitrinite concentrate. As illustrated in Table 5, the purity of inertinite concentrates for five coal sample has little difference, but their pore parameters shown in Figure 9 make a great difference, indicating that although the inertinite concentrates contain abundant fusinite, there are great differences in the pore structure of fusinite for different coal ranks.

An interesting paradox can be found by comparing the results obtained from Figures 8 and 9(b). It has been understood that the larger pore volume corresponds to a stronger adsorption capability of coal for methane [4, 46]. From Figure 9(b), it is clearly observed that the total pore volume of inertinite concentrates is larger than that of vitrinite concentrates, indicating that the inertinite concentrates should adsorb more methane than their rank equivalent vitrinite concentrates. As a result, the adsorption heat of inertinite concentrates for methane should be higher than that of vitrinite concentrates. However, the opposite conclusion is

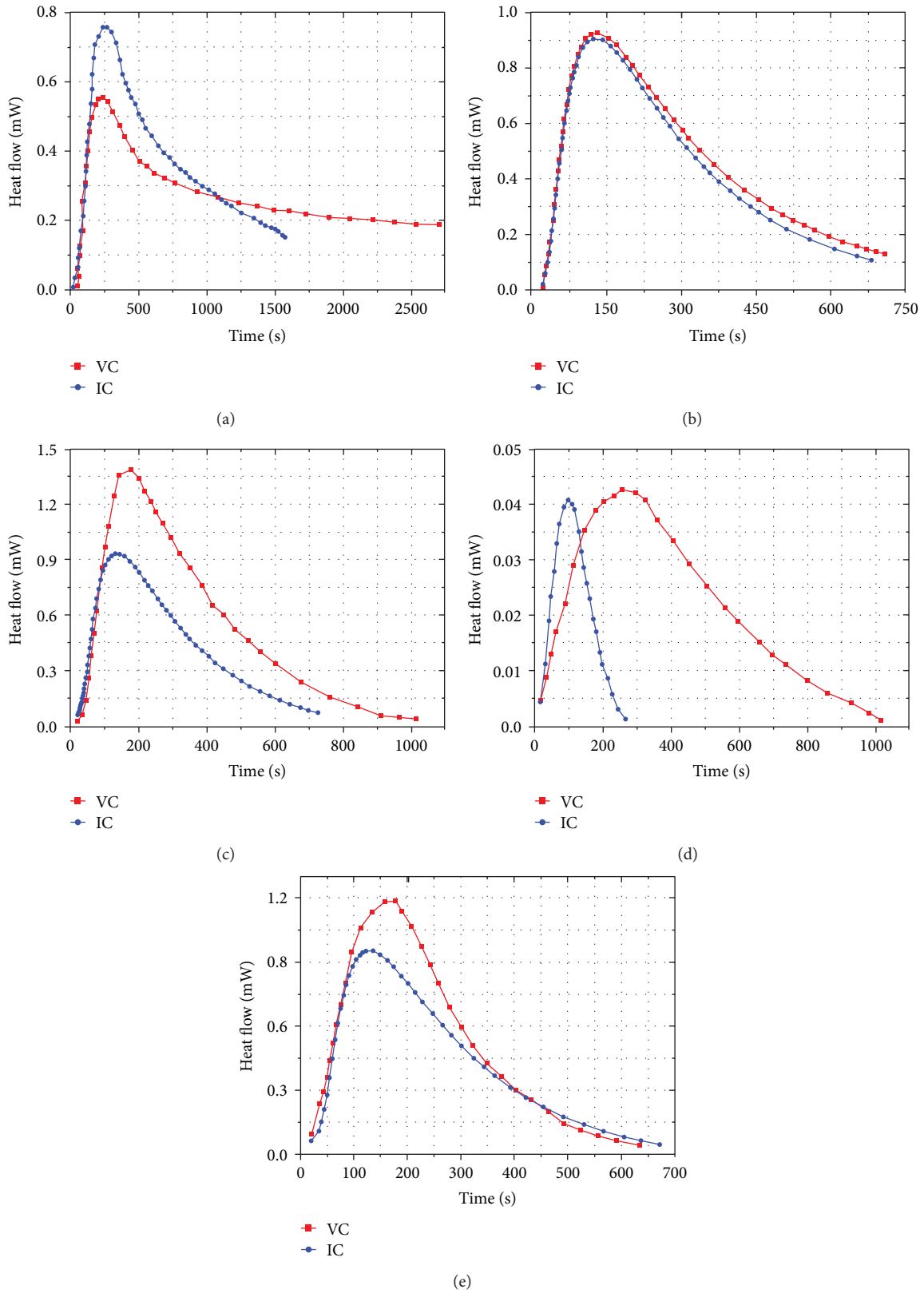


FIGURE 7: Curves of flux of methane adsorption heat released from maceral concentrates of coal sample numbers 1 (a), 2 (b), 3 (c), 4 (d), and 5 (e).

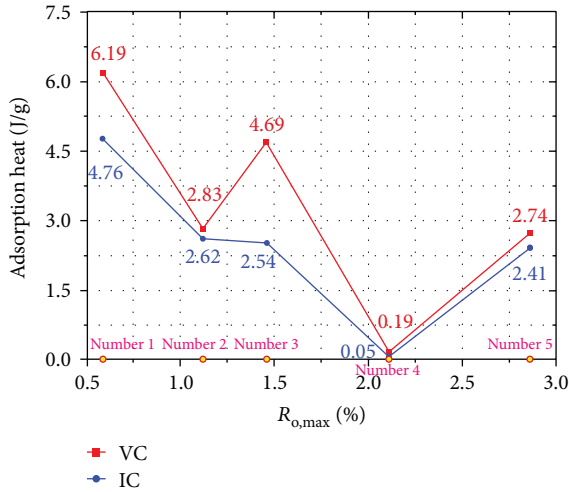
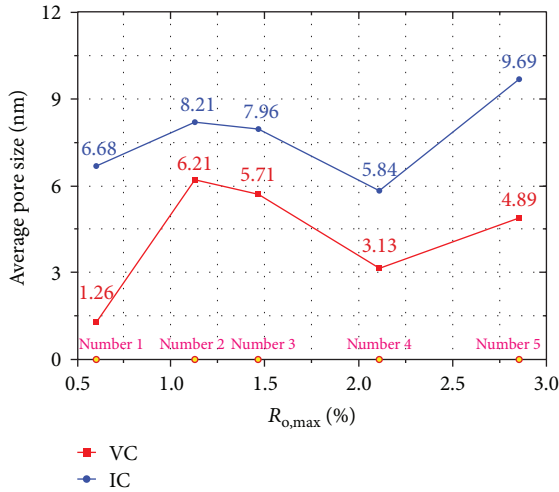
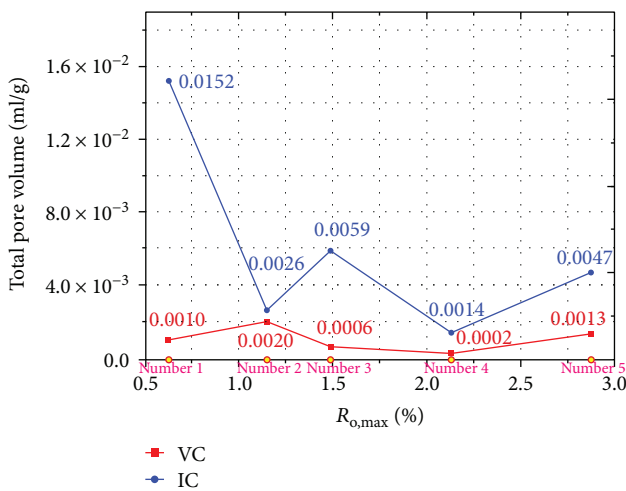


FIGURE 8: Curves of adsorption heat for maceral concentrates of different coals.



(a)



(b)

FIGURE 9: Curves of average pore size (a) and total pore volume (b) for maceral concentrates.

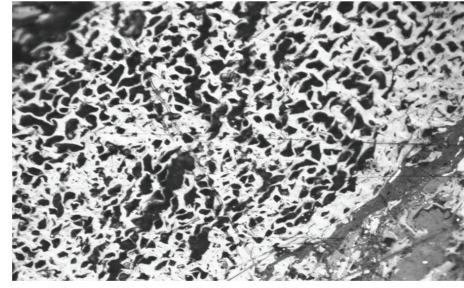


FIGURE 10: Morphology of fusinite under a microscope.

drawn from Figure 8, where the adsorption heat of the vitrinite concentrates is higher than that of the inertinite concentrates. This abnormal phenomenon may be caused by the following two factors. (1) At low pressures, gas adsorption by coal has traditionally been assumed as a surface monolayer coverage with the Langmuir adsorption model [24, 47]. Although the total pore volume of inertinite concentrates is larger than that of vitrinite concentrates, the inertinite concentrates are more macroporous and less microporous than their rank equivalent vitrinite concentrates, which results in smaller specific surface area and less adsorption heat of inertinite concentrates accordingly. (2) The type and content of surface functional groups of vitrinite and inertinite concentrates are quite different, which could lead to the differences of adsorption heat between vitrinite and inertinite concentrates, as is discussed in the next subsection.

Furthermore, to investigate the correlation between the adsorption heat of maceral concentrates and corresponding pore parameters, the comparison of the maximum heat flow, adsorption heat, and the pore parameters are illustrated in Figure 11. It is shown that with the increase of $R_{o,max}$, the variation of adsorption heat with pore parameters of vitrinite concentrates is notably different from that of inertinite concentrates. For the case of vitrinite concentrates, from the long-flame coal (number 1 coal sample, $R_{o,max} = 0.59\%$) to coking coal stage (number 3 coal sample, $R_{o,max} = 1.46\%$) (i.e., the low- and medium-coal rank), the adsorption heat decreases with the increase of total pore volume and average pore diameter. In other words, the pore parameters are negatively correlated with the adsorption heat. However, from the coking coal (number 3 coal sample) to anthracite stage (number 5 coal sample, $R_{o,max} = 2.86\%$) (i.e., the medium- and high-coal rank), the pore parameters show a positive correlation with the adsorption heat. For the case of inertinite concentrates, the pore parameters are positively correlated with the adsorption heat on the whole.

Additionally, there are regional influences on the porosity of coals [48]. Both coal sample numbers 2 and 4 were collected from Panxian Coal Field, so VC and IC of these two samples have very similar value of the total pore volume (Figure 9), which leads to very small differences between the adsorption heat of vitrinite and inertinite concentrates of sample numbers 2 and 4 (Figure 8). Moreover, the flow rate of methane gas in coal samples is controlled by the porosity of coal, so Figure 11 also shows that with

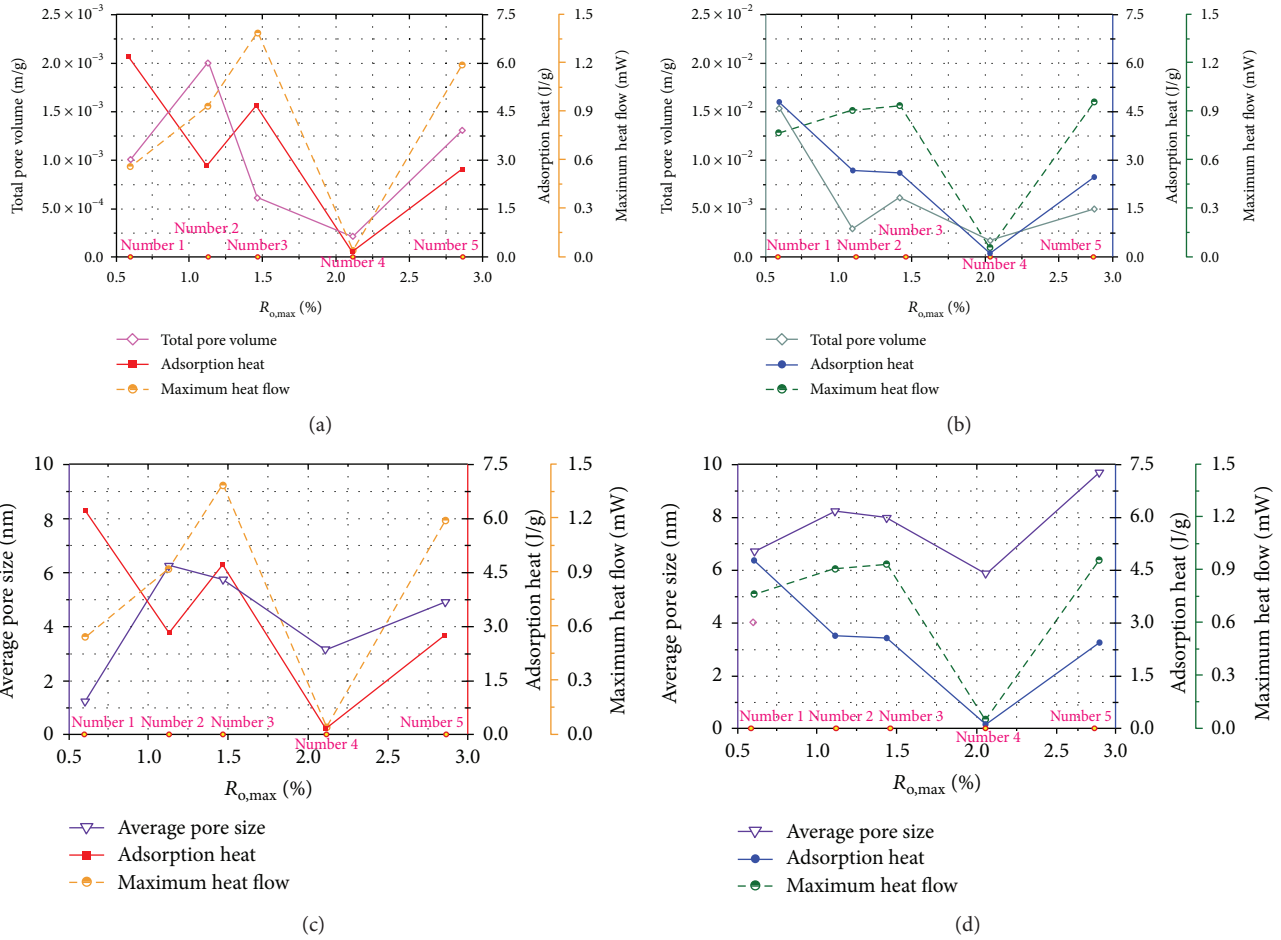


FIGURE 11: Correlation between the adsorption heat and the total pore volume of VC (a) and IC (b) and the average pore diameter of VC (c) and IC (d), respectively.

the increase of the pore parameters, the maximum heat flow during adsorption goes up.

3.5. Correlation between the Adsorption Heat and the Surface Functional Groups. For a further understanding of the factors influencing methane adsorption and the differences between the adsorption heat of vitrinite and inertinite concentrates, the type and content of chemical functional groups on the surface of maceral concentrates were determined by infrared spectroscopy, which directly affects the adsorption heat of maceral concentrates for methane via the adsorption potential of methane molecules on the coal surface.

Figure 12 shows the peak areas for the surface functional groups together with the adsorption heat of vitrinite and inertinite concentrates. Typical functional groups mainly include the aliphatic hydrocarbons ($-\text{CH}_3/-\text{CH}_2/-\equiv\text{CH}$) and aromatic structures ($\text{C}=\text{C}$) and oxygen-containing functional groups ($-\text{OH}$, $-\text{COOH}$, $-\text{COO}-$, $-\text{C}-\text{O}-$, and $\text{C}=\text{O}$). The content and distribution of surface functional groups for vitrinite and inertinite concentrates of the same coal sample differ greatly from each other. For the vitrinite concentrates, as shown in Figure 12(a), the oxygen-containing functional groups and aromatic structures dominate the content and distribution of functional groups. With

the increase of $R_{o,max}$, the total content of various functional groups in vitrinite concentrates exhibits a downward trend, reaching the minimum value at the lean coal stage (number 4 coal sample, $R_{o,max} = 2.11\%$), and then an upward trend for aromatic structures at the anthracite stage (number 5 coal sample, $R_{o,max} = 2.86\%$). The number 1 coal sample has the highest and balanced distribution of different functional groups. Particularly, the number 4 coal sample has the lowest aliphatic hydrocarbons and aromatic structures, while the number 5 coal sample has the lowest oxygen-containing functional groups. On the other hand, for the inertinite concentrates, as shown in Figure 12(b), the oxygen-containing functional groups are predominant for most coal samples (number 1, number 3, and number 5). The oxygen-containing functional groups in the low-rank coal is the highest (number 1 coal sample, $R_{o,max} = 0.59\%$), but it decreases with the increase of $R_{o,max}$. The content of aliphatic hydrocarbons in the medium-rank coal is the highest (number 2 coal sample, $R_{o,max} = 1.12\%$), but it is lower in the other coal samples. Overall, for five different coal samples, the content of oxygen-containing functional groups in the vitrinite concentrates has few differences from that in the inertinite concentrates, but the content of aliphatic hydrocarbons and aromatic structures in the

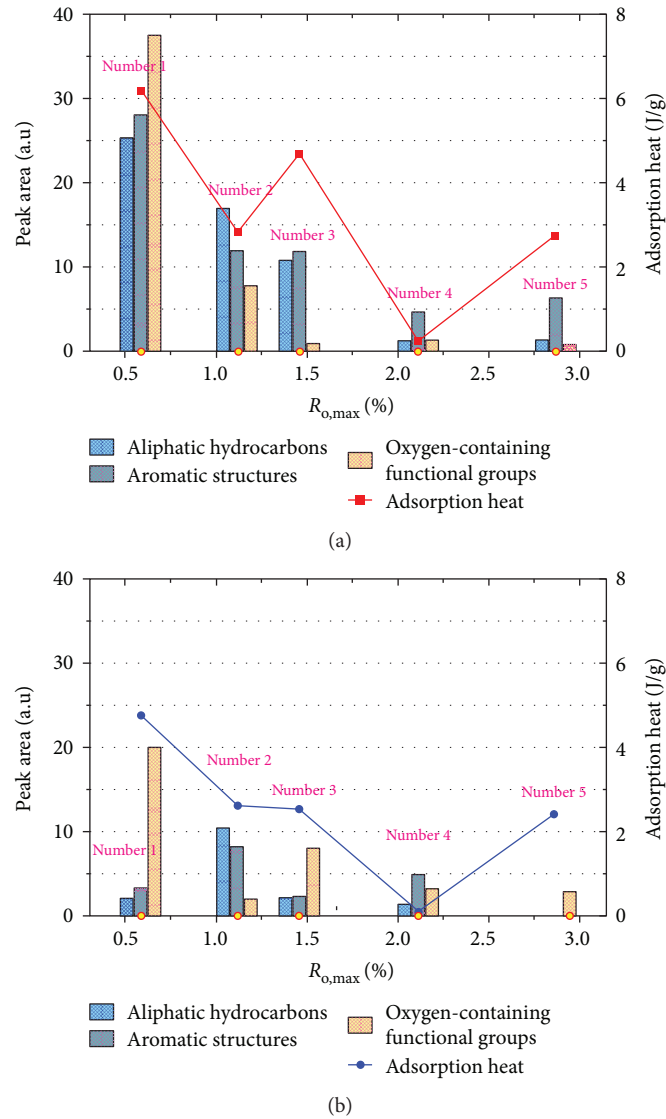


FIGURE 12: Correlation between the adsorption heat and the surface functional groups of vitrinite (a) and inertinite (b) concentrates.

vitrinite concentrates is significantly higher than that in the inertinite concentrates.

The adsorption of methane by coal is physical absorption and depends on an intermolecular force. Larger intermolecular forces and larger molecular polarity of the functional groups of coal are associated with a greater adsorption potential, stability of adsorption, and adsorption heat [49, 50]. In general, oxygen-containing functional groups influence the adsorption heat via the adsorption potential of methane molecules, and the adsorption heat of oxygen-containing functional groups which have stronger polarity is greater than that of other functional groups [33]. Aromatic nuclei and methane molecules are both nonpolar molecules with polar bonds, so the adsorption heat of aromatic structures is very small. While the aliphatic hydrocarbons are polar molecules, their intermolecular forces associated with methane are larger than those of aromatic nuclei [33]. Accordingly, the adsorption heat of aliphatic hydrocarbons for methane is greater than that of aromatic nuclei. However, if

the aromatic condensed nuclei have side chains with other types of functional groups, the adsorption heat of aromatic structures increases accordingly.

The variations of adsorption heat of maceral concentrates for different coal samples are closely related with the type and content of typical functional groups. As shown in Figure 12, it is shown that the variation tendency of adsorption heat of both vitrinite and inertinite concentrates for methane is positively correlated to the content and distribution of oxygen-containing functional groups and aliphatic hydrocarbons. The long-flame coal (number 1 coal sample, $R_{o,max} = 0.59\%$) has the highest content of oxygen-containing functional groups; thus, the value of adsorption heat is maximum. With the increase of $R_{o,max}$, the content of oxygen-containing functional groups and aliphatic hydrocarbons decreases, which results in a decline of adsorption heat of both vitrinite and inertinite concentrates for methane. For the lean coal (number 4 coal sample, $R_{o,max} = 2.11\%$), the adsorption heat is minimum with the lower content of total functional

groups. From the lean-coal stage (number 4 coal sample) to the anthracite stage (number 5 coal sample, $R_{o,max} = 2.86\%$), the adsorption heat of maceral compositions of coal has an obvious increase with few changes of the content of oxygen-containing functional groups and aliphatic hydrocarbons. This is because both the total pore volume and the average pore size increase significantly (Figure 11). Additionally, for the same coal sample, the peak areas of oxygen-containing functional groups and aliphatic hydrocarbons for vitrinite concentrates are larger than those for inertinite concentrates. This result suggests that the contents of oxygen-containing functional groups and aliphatic hydrocarbons in the vitrinites may dominate the adsorption heat of coal for methane.

4. Conclusions

The objective of this study is to investigate the effects of maceral composition of coal on the adsorption heat of methane on coal and further deepen our understanding of the adsorption theory of coalbed methane. To this end, five groups of Chinese coal samples with different coal ranks were collected to prepare the vitrinite and inertinite concentrates. The adsorption heat of maceral concentrates for methane was directly measured by the method of calorimetric measurement. The main findings of this study are summarized as follows.

- (1) For all coal samples, the adsorption heat of vitrinite concentrates for methane is higher than their rank equivalent inertinite concentrates. Furthermore, the adsorption heat varies with the increasing coal rank. The highest adsorption heats of vitrinite and inertinite concentrates are achieved at the long-flame coal stage, which are approximately 6.19 J/g and 4.76 J/g, respectively. The lowest adsorption heats of vitrinite and inertinite concentrates are achieved at the lean coal stage, which are 0.19 J/g and 0.05 J/g, respectively.
- (2) For the vitrinite concentrates, the total pore volume and average pore size are negatively correlated with the adsorption heat at the low- and medium-coal ranks, but a positive correlation is observed at the medium- and high-coal ranks. For the inertinite concentrates, the total pore volume and average pore size are positively correlated with the adsorption heat as a whole.
- (3) The type and content of surface functional groups for vitrinite and inertinite concentrates are quite different. Overall, the adsorption heat of both vitrinite and inertinite concentrates is primarily correlated to the content of oxygen-containing functional groups and aliphatic hydrocarbons.
- (4) For the same coal sample, the peak areas of oxygen-containing functional groups and aliphatic hydrocarbons for vitrinite concentrates are larger than those for inertinite concentrates. That is, the fundamental

reason of the fact that the adsorption heat of vitrinite concentrates for methane is higher than their rank equivalent inertinite concentrates.

Conflicts of Interest

The authors declare that there are no conflicts of interest regarding the publication of this paper.

Acknowledgments

This work was supported by the National Key R&D Program of China (2016YFC0802900), the National Natural Science Foundation of China (51774277), and the Fundamental Research Funds for the Central Universities (2013QNA02).

References

- [1] T. A. Moore, "Coalbed methane: a review," *International Journal of Coal Geology*, vol. 101, pp. 36–81, 2012.
- [2] A. Busch and Y. Gensterblum, "CBM and CO₂-ECBM related sorption processes in coal: a review," *International Journal of Coal Geology*, vol. 87, no. 2, pp. 49–71, 2011.
- [3] C. M. White, D. H. Smith, K. L. Jones et al., "Sequestration of carbon dioxide in coal with enhanced coalbed methane recovery – a review," *Energy & Fuels*, vol. 19, no. 3, pp. 659–724, 2005.
- [4] S. Day, G. Duffy, R. Sakurovs, and S. Weir, "Effect of coal properties on CO₂ sorption capacity under supercritical conditions," *International Journal of Greenhouse Gas Control*, vol. 2, no. 3, pp. 342–352, 2008.
- [5] J. Kang, F. Zhou, G. Ye, and Y. Liu, "An anomalous subdiffusion model with fractional derivatives for methane desorption in heterogeneous coal matrix," *AIP Advances*, vol. 5, no. 12, article 127119, 2015.
- [6] M. J. Kotarba and D. D. Rice, "Composition and origin of coalbed gases in the lower Silesian basin, Southwest Poland," *Applied Geochemistry*, vol. 16, no. 7–8, pp. 895–910, 2001.
- [7] Y. Cai, D. Liu, Z. Pan, Y. Yao, J. Li, and Y. Qiu, "Pore structure and its impact on CH₄ adsorption capacity and flow capability of bituminous and subbituminous coals from Northeast China," *Fuel*, vol. 103, pp. 258–268, 2013.
- [8] S. Hao, J. Wen, X. Yu, and W. Chu, "Effect of the surface oxygen groups on methane adsorption on coals," *Applied Surface Science*, vol. 264, pp. 433–442, 2013.
- [9] G. Yue, Z. Wang, X. Tang, H. Li, and C. Xie, "Physical simulation of temperature influence on methane sorption and kinetics in coal (II): temperature evolution during methane adsorption in coal measurement and modeling," *Energy & Fuels*, vol. 29, no. 10, pp. 6355–6362, 2015.
- [10] H. J. Kim, Y. Shi, J. He, H.-H. Lee, and C.-H. Lee, "Adsorption characteristics of CO₂ and CH₄ on dry and wet coal from subcritical to supercritical conditions," *Chemical Engineering Journal*, vol. 171, no. 1, pp. 45–53, 2011.
- [11] J. E. Fitzgerald, Z. Pan, M. Sudibandriyo, R. L. Robinson Jr., K. A. M. Gasem, and S. Reeves, "Adsorption of methane, nitrogen, carbon dioxide and their mixtures on wet Tiffany coal," *Fuel*, vol. 84, no. 18, pp. 2351–2363, 2005.
- [12] M. Švabová, Z. Weishauptová, and O. Přibyl, "The effect of moisture on the sorption process of CO₂ on coal," *Fuel*, vol. 92, no. 1, pp. 187–196, 2012.

- [13] K. Jian, X. Fu, Y. Ding, H. Wang, and T. Li, "Characteristics of pores and methane adsorption of low-rank coal in China," *Journal of Natural Gas Science and Engineering*, vol. 27, Part 1, pp. 207–218, 2015.
- [14] Z. Wang, X. Tang, G. Yue, B. Kang, C. Xie, and X. Li, "Physical simulation of temperature influence on methane sorption and kinetics in coal: benefits of temperature under 273.15 K," *Fuel*, vol. 158, pp. 207–216, 2015.
- [15] Z. Feng, T. Cai, D. Zhou, D. Zhao, Y. Zhao, and C. Wang, "Temperature and deformation changes in anthracite coal after methane adsorption," *Fuel*, vol. 192, pp. 27–34, 2017.
- [16] D. Zhou, Z. Feng, D. Zhao, Y. Zhao, and T. Cai, "Experimental meso scale study on the distribution and evolution of methane adsorption in coal," *Applied Thermal Engineering*, vol. 112, pp. 942–951, 2017.
- [17] R. Pini, S. Ottiger, L. Burlini, G. Storti, and M. Mazzotti, "Sorption of carbon dioxide, methane and nitrogen in dry coals at high pressure and moderate temperature," *International Journal of Greenhouse Gas Control*, vol. 4, no. 1, pp. 90–101, 2010.
- [18] S. Harpalani, B. K. Prusty, and P. Dutta, "Methane/CO₂ sorption modeling for coalbed methane production and CO₂ sequestration," *Energy & Fuels*, vol. 20, no. 4, pp. 1591–1599, 2006.
- [19] R. Sakurovs, S. Day, S. Weir, and G. Duffy, "Temperature dependence of sorption of gases by coals and charcoals," *International Journal of Coal Geology*, vol. 73, no. 3–4, pp. 250–258, 2008.
- [20] W. Zimmermann and J. U. Keller, "A new calorimeter for simultaneous measurement of isotherms and heats of adsorption," *Thermochimica Acta*, vol. 405, no. 1, pp. 31–41, 2003.
- [21] A. Nodzeński, "Sorption and desorption of gases (CH₄, CO₂) on hard coal and active carbon at elevated pressures," *Fuel*, vol. 77, no. 11, pp. 1243–1246, 1998.
- [22] M. Bülow, D. Shen, and S. Jale, "Measurement of sorption equilibria under isosteric conditions: the principles, advantages and limitations," *Applied Surface Science*, vol. 196, no. 1–4, pp. 157–172, 2002.
- [23] L. Chikatamarla and P. J. Crosdale, "Heat of methane adsorption of coal: implications for pore structure development," in *Proceedings of the International Coalbed Methane Symposium*, pp. 151–162, Tuscaloosa, AL, USA, 2001, University of Alabama.
- [24] S. Day, R. Sakurovs, and S. Weir, "Supercritical gas sorption on moist coals," *International Journal of Coal Geology*, vol. 74, no. 3–4, pp. 203–214, 2008.
- [25] W. Jiang, Y. Cui, Q. Zhang, L. Zhong, and Y. Li, "The quantum chemical study on different rank coals surface interacting with methane," *Journal of China Coal Society*, vol. 32, no. 3, pp. 292–295, 2007.
- [26] C. G. Chen, X. W. Wei, and X. F. Xian, "AB initio study on the interaction between CH₄ and the coal surface," *Journal of Chongqing University*, vol. 23, no. 3, pp. 77–82, 2000.
- [27] X. Tang, Z. Wang, N. Ripepi, B. Kang, and G. Yue, "Adsorption affinity of different types of coal: mean isosteric heat of adsorption," *Energy & Fuels*, vol. 29, no. 6, pp. 3609–3615, 2015.
- [28] X. Tang, N. Ripepi, N. P. Stadie, and L. Yu, "Thermodynamic analysis of high pressure methane adsorption in Longmaxi shale," *Fuel*, vol. 193, pp. 411–418, 2017.
- [29] H. Hu, X. Li, Z. Fang, N. Wei, and Q. Li, "Small-molecule gas sorption and diffusion in coal: molecular simulation," *Energy*, vol. 35, no. 7, pp. 2939–2944, 2010.
- [30] F. Siperstein, R. J. Gorte, and A. L. Myers, "A new calorimeter for simultaneous measurements of loading and heats of adsorption from gaseous mixtures," *Langmuir*, vol. 15, no. 4, pp. 1570–1576, 1999.
- [31] A. S. Glass and J. W. Larsen, "Coal surface properties. Specific and nonspecific interactions for polar molecules and surface tensions for hydrocarbons at the surface of Illinois no. 6 coal," *Energy & Fuels*, vol. 8, no. 3, pp. 629–636, 1994.
- [32] B. Taraba, "Flow calorimetric insight to competitive sorption of carbon dioxide and methane on coal," *Thermochimica Acta*, vol. 523, no. 1–2, pp. 250–252, 2011.
- [33] F. Zhou, S. Liu, Y. Pang, J. Li, and H. Xin, "Effects of coal functional groups on adsorption microheat of coal bed methane," *Energy & Fuels*, vol. 29, no. 3, pp. 1550–1557, 2015.
- [34] G. R. L. Chalmers and R. Marc Bustin, "On the effects of petrographic composition on coalbed methane sorption," *International Journal of Coal Geology*, vol. 69, no. 4, pp. 288–304, 2007.
- [35] P. J. Crosdale, B. B. Beamish, and M. Valix, "Coalbed methane sorption related to coal composition," *International Journal of Coal Geology*, vol. 35, no. 1–4, pp. 147–158, 1998.
- [36] I. Ettinger, I. Eremin, B. Zimakov, and M. Yanovskaya, "Natural factors influencing coal sorption properties: I. Petrography and the sorption properties of coals," *Fuel*, vol. 45, pp. 267–275, 1966.
- [37] M. M. Faiz, N. I. Aziz, A. C. Hutton, and B. G. Jones, "Porosity and gas sorption capacity of some eastern Australian coals in relation to coal rank and composition," in *Coalbed Methane Symposium*, pp. 19–21, Townsville, QLD, Australia, 1992.
- [38] The National Standards Compilation Group of Peoples Republic of China, *GB/T 5751–2009 Chinese Classification of Coals*, Standards Press of China, Beijing, China, 2009.
- [39] A. S. Trimble and J. C. Hower, "Studies of the relationship between coal petrology and grinding properties," *International Journal of Coal Geology*, vol. 54, no. 3–4, pp. 253–260, 2003.
- [40] The National Standards Compilation Group of Peoples Republic of China, *GB/T 8899–2013 Determination of Maceral Composition and Minerals in Coal*, Standards Press of China, Beijing, China, 2013.
- [41] S. Ye, C. Liu, S. Chen, F. Wang, Y. Jia, and Z. Li, "A judgement method of matrix resin based on infrared spectra of low emissivity coatings," *Infrared Technology*, vol. 38, no. 6, pp. 524–528, 2016.
- [42] The National Standards Compilation Group of Peoples Republic of China, *GB/T 6948–2008 Method of Determining Microscopically the Reflectance of Vitrinite in Coal*, Standards Press of China, Beijing, China, 2008.
- [43] A. J. Ramirez-Pastor and F. Bulnes, "Differential heat of adsorption in the presence of an order–disorder phase transition," *Physica A: Statistical Mechanics and Its Applications*, vol. 283, no. 1–2, pp. 198–203, 2000.
- [44] S. Chattaraj, D. Mohanty, T. Kumar, and G. Halder, "Thermodynamics, kinetics and modeling of sorption behaviour of coalbed methane – a review," *Journal of Unconventional Oil and Gas Resources*, vol. 16, pp. 14–33, 2016.
- [45] A. Auroux, *Calorimetry and Thermal Methods in Catalysis*, Springer-Verlag, Berlin, Heidelberg, 2013.
- [46] Q. Li, B. Lin, K. Wang, M. Zhao, and M. Ruan, "Surface properties of pulverized coal and its effects on coal mine methane adsorption behaviors under ambient conditions," *Powder Technology*, vol. 270, Part A, pp. 278–286, 2015.

- [47] G. F. Cerofolini and L. Meda, "Clustering and melting in multilayer equilibrium adsorption," *Journal of Colloid and Interface Science*, vol. 202, no. 1, pp. 104–123, 1998.
- [48] R. Sakurovs, L. Koval, M. Grigore, A. Sokolova, L. F. ruppert, and Y. B. Melnichenko, "Nanometre-sized pores in coal: variations between coal basins and coal origin," *International Journal of Coal Geology*, vol. 186, pp. 126–134, 2018.
- [49] J. N. Israelachvili, *Intermolecular and Surface Forces*, Academic Press, Pittsburgh, USA, 2011.
- [50] A. Stone, *The Theory of Intermolecular Forces*, Oxford University Press, New York, NY, USA, 2013.

Research Article

Triple-Porosity Modelling for the Simulation of Multiscale Flow Mechanisms in Shale Reservoirs

Mingyao Wei ¹, Jishan Liu ², Derek Elsworth,³ and Enyuan Wang⁴

¹State Key Laboratory of Geomechanics and Geotechnical Engineering, Institute of Rock and Soil Mechanics, Chinese Academy of Sciences, Wuhan 430071, China

²School of Mechanical and Chemical Engineering, The University of Western Australia, 35 Stirling Highway, Perth, WA 6009, Australia

³Department of Energy and Mineral Engineering, G3 Center and Energy Institute, The Pennsylvania State University, University Park, PA 16802, USA

⁴State Key Laboratory of Coal Resources and Safe Mining, School of Safety Engineering, China University of Mining and Technology, Xuzhou 221116, China

Correspondence should be addressed to Mingyao Wei; cumtwmy@sina.com

Received 21 September 2017; Revised 11 January 2018; Accepted 16 January 2018; Published 28 May 2018

Academic Editor: Paolo Fulignati

Copyright © 2018 Mingyao Wei et al. This is an open access article distributed under the Creative Commons Attribution License, which permits unrestricted use, distribution, and reproduction in any medium, provided the original work is properly cited.

Shale gas reservoir is a typical type of unconventional gas reservoir, primarily because of the complex flow mechanism from nanoscale to macroscale. A triple-porosity model (M3 model) comprising kerogen system, matrix system, and natural fracture system was presented to describe the multispace scale, multitime scale, and multiphysics characteristic of gas flows in shale reservoir. Apparent permeability model for real gas transport in nanopores, which covers flow regime effect and geomechanical effect, was used to address multiscale flow in shale matrix. This paper aims at quantifying the shale gas in different scales and its sequence in the process of gas production. The model results used for history matching also showed consistency against gas production data from the Barnett Shale. It also revealed the multispace scale process of gas production from a single well, which is supplied by gas transport from natural fracture, matrix, and kerogen sequentially. Sensitivity analysis on the contributions of shale reservoir permeability in different scales gives some insight as to their importance. Simulated results showed that free gas in matrix contributes to the main source of gas production, while the performance of a gas shale well is strongly determined by the natural fracture permeability.

1. Introduction

The organic-rich shales provide the basis of unconventional energy production that has recently come to the forefront of the world's energy discussion. A current area of research is the impact of multiscale pore structure on shale gas transport mechanisms and ultimate gas recovery. Many investigators have been inspired to establish suitable models to characterize gas flow in shale encountering great challenges along the way.

Traditionally, dual-porosity models have been used to model naturally fractured reservoirs, which are composed of a porous matrix surrounded by a larger-scale fracture system. The dual-porosity models assume uniform matrix

properties throughout the reservoir which may not capture the relevant physics accurately in shale reservoirs, because the shale matrix is comprised of predominantly clay minerals, quartz, pyrite, and organic matter. Studies of porosity and microstructure on high-quality flat surfaces using SEM indicate that shale exhibits a high degree of microstructure, causing low permeability and low porosity [1, 2]. These pores ranging from nanometer to micrometer size in shales can be attributed with at least four distinct types: inorganic bulk, organic matter, natural microfractures, and hydraulic fractures [3]. Kerogen (organic matter) is finely dispersed within the inorganic matrix, which can adsorb and store free gas simultaneously. In order to describe those complex physics, the triple-porosity model has been used to improve dual-

porosity models. Ci-qun [4, 5] firstly developed a triple-porosity model for radial flow of slightly compressible fluids through a triple-porosity reservoir under pseudo-steady state interporosity flow. Abdassah and Ershaghi [6] built on this model to consider dual matrix systems with different properties. Wang et al. [3] introduced four types of porous media in productive gas-shale systems. Dehghanpour and Shirdel [7] proposed a triple-porosity model composed of two fracture systems and matrix system without considering desorption, diffusion, and slip flow. Alharthy et al. [8] developed a triple-porosity finite-difference (FD) model which combines a several flow mechanisms in nanopores. Huang et al. [9] presented a new triporosity model for shale gas reservoir with consideration of flow mechanisms from nanoscale to macroscale. Peng et al. [10] investigated the effect of deformation and natural fracture on shale gas recovery rate. Cao et al. [11] developed a coupled multiscale model to analyze the impacts of flow regimes, effective stress, and adsorption on the production rate. However, the geomechanical effects on the gas flow are neglected in all these models which are important to determine shale permeability.

Although many previous studies have contributed to better understanding of the complex flow mechanism from nanoscale to macroscale in shale, little work has been done to simultaneously combine the multiscale flow and coupling effect with geomechanics. For example, permeability evolution in shale under the influence of effective stress is not fully addressed. The flow mechanism of these models also is not able to cover the whole range of shale pore scale. In this work, a triple-porosity model comprising kerogen system, matrix system, and natural fracture system was established. This model was valid over the entire range of flow regimes in shale. The permeability evolution fully coupled with effective stress for matrix and fracture was considered simultaneously. To evaluate the impact of shale deposits and reservoir permeability on the production of shale gas, several case studies will be introduced.

2. Triple-Porosity Systems

2.1. Reservoir Characterization. Understanding the physical multiscale process of gas production from shale reservoirs is important for reservoir evaluation and production optimization. With the scanning electron microscope (SEM) and backscattered electron (BSE) images, many researchers indicate that shales exhibit compositional heterogeneity and variations in pore structures and composition existing on many scales, from the nanoscale to the macroscale [1]. Shale gas flows through a network of pores with different diameters ranging from nanometers to micrometers [12]. In addition, microstructural features within shales ultimately affect shale's ability to generate, store, and produce gas.

Figure 1 shows a view of shale gas reservoirs in different scales. In the macroscale view, the shale reservoir contains a connected network of large fractures surrounding the large matrix blocks after hydraulic fracturing. The horizontal well is connected to a complex macrofracture network. The shale gas production rate strongly depends on the hydraulic fractures which are highways for gas transfer

from shale matrix blocks to the horizontal well. There are also numerous natural fractures existing in the shale matrix in the microscale view. These natural fractures are generally narrow and may enhance permeability locally. These fracture and matrix systems can compose the usual dual-porosity system similar to the conventional natural fracture reservoirs. However, unconventional resources such as shale gas have a complicated pore distribution. The significant difference between pores in conventional and unconventional gas reservoirs is that the number of nanopores is much higher in unconventional shale gas sediments [15] as shown in Figure 1. The SEM image shows that the reservoir matrix is commonly/primarily composed of clay/silica, organic matter/kerogen, and some minerals primarily. Kerogen bulks have a disorderly distribution in matrix and surrounded by inorganic matters. Free gas in shale is stored in the natural fractures and micropores of the matrix system. Moreover, the massive adsorbed gas, which might account for a part of gas storage in gas shale, is stored in the organic nanopores which have a large surface area with strong affinity. Note that the amount of adsorbed gas by the inorganic walls is considered negligible compared to adsorbed gas in kerogen.

Based on the multispace scale of pore distribution, we proposed a triple-porosity system that comprises three contiguous porous media: the kerogen, inorganic matrix, and natural fractures. The organic material in kerogen system mainly consists of micropores (pore lengths less than 2.0 nm) and mesopores (pore lengths between 2 and 50 nm), with an average pore size below 4-5 nm [16]. The kerogen system includes organic material and also large interconnected nanopores that provide active sites for gas adsorption. Furthermore, pores in kerogen are on the order of nanometers in size, which is gas transfer channel for the higher mass of gas molecules. Since most kerogen is scattered within inorganic minerals, any other porosity systems in shale should communicate with the kerogen through a few nanopores in the inorganic matrix system. Inorganic slit-shaped pore in the matrix is stress sensitive. However, the round-shaped pores in kerogen system can be neglected [14]. For the sake of simplicity, we assumed all pores in the matrix are rounded shape. Shale matrix is surrounded by natural fractures which are pathways to connect with hydraulic fractures or the wellbore. The width of natural fracture systems generally is less than 0.05 mm [17]. Based on the scale of pores, we assume that mass transferring from kerogen to matrix can be considered as diffusion process and define the gas flow mechanism in the nanopore of the matrix with apparent permeability and viscous flow as the transport mechanism within natural fractures.

The process of gas production in shale gas reservoirs is a combined sequence of gas flow at different length scales. The main gas flows through the natural fractures which feed the hydraulic fractures while they receive flow from the matrix system only. During reservoir depletion, the thermodynamic equilibrium between gas in kerogen and matrix spaces changes. Hence, gas desorbs from the surface of the organic matters and nanopores in the kerogen system. This nonequilibrium process further drives the gas

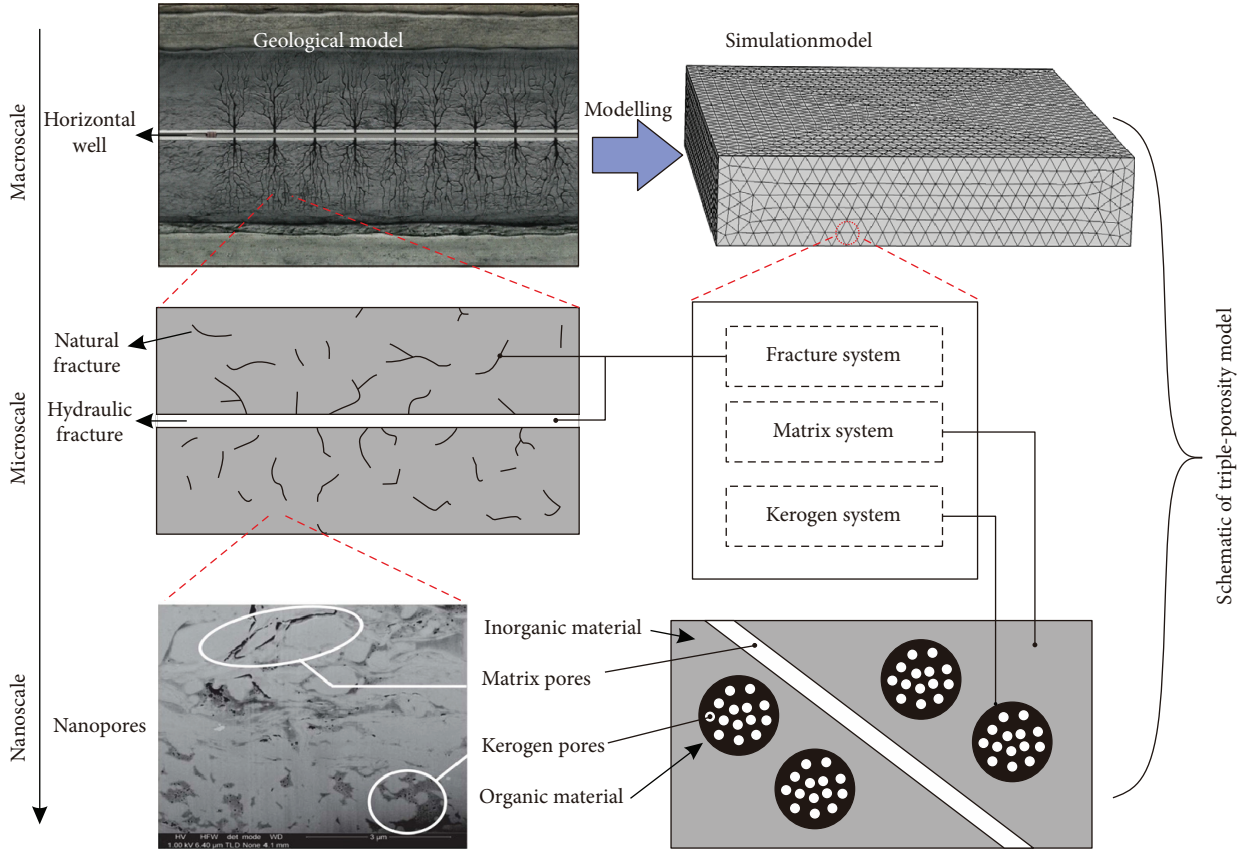


FIGURE 1: Conceptual triple-porosity model for shale gas reservoir at various scales (SEM image is from Ambrose et al. [13], figure in lower right is from Wasaki and Akkutlu [14]).

molecules to diffuse from the bulk of the organic matters to the surface of the kerogen exposed to the nanopore network [15]. The kerogen pore network hydraulically communicates with the inorganic matrix such that mass transport takes place in the one-way sequence during the gas release. Therefore, the gas flow is sequential from one medium to the other in different space scales. In shale gas systems, these multiscale pores form the flow-path network that allows the flow of gas from the kerogen to the wellbore during shale gas production. Each process of gas flow follows its own path and obeys different transport mechanisms at different length scales. The application of the triple-porosity model requires that each porous medium is distributed continuously in space and holds the porous media conditions.

2.2. Governing Equations of Gas Flow in Kerogen. Microscale flow of hydrocarbons through porous media involves various distinct transport mechanisms. The conventional Darcy’s law cannot be in general applicable to describe the variety of the relevant flow regimes other than the viscous flow regime. For Knudsen numbers less than 0.01, the use of ideal gas constant in Darcy’s law and the assumption of continuum flow remain valid. For Knudsen numbers greater than 0.01, an effective permeability must be computed to compensate for the Knudsen diffusion and/or the slippage flow. As for the pore diameter in kerogen on the scale of a nanometer, gas

transport is dominated by collisions between gas molecules and the walls, which is called the Knudsen diffusion. Thus, the gas mass flux in kerogen can be expressed by the Knudsen diffusion equation [18, 19]:

$$J_k = -D_K \frac{M}{RT} \nabla P_k, \tag{1}$$

$$D_K = \frac{2r_k}{3} \sqrt{\frac{8RT}{\pi M}}, \tag{2}$$

where D_K is the Knudsen diffusion constant, M is the molar mass, R ($=8.314$ J/mol/K) is the gas constant, r_k is the pore radius in kerogen, T is the absolute temperature in Kelvin, and P_k is the gas pressure in kerogen. Throughout this paper, kerogen, matrix, and fractures are identified with subscripts k , m , and f , respectively.

Under the initial condition of shale gas reservoirs, an equilibrium exists between adsorbed gas and bulk gas in nanopores. Langmuir adsorption can be used to calculate the adsorbed gas amount [20]. For the sake of simplicity, the basic premise of this work is that kerogen bulk has to be saturated with gas at a particular pressure before it can liberate gas into the pores. During depressurization development of shale gas reservoirs, compared with surface diffusion, adsorption/desorption is a very quick

physical process. Hence, the adsorbed gas amount can still be calculated using Langmuir adsorption [21]:

$$m_a = (1 - \phi_k) \rho_s \rho_{ka} \frac{L_a P_k}{P_k + L_b}, \quad (3)$$

where ϕ_k is porosity of kerogen in shale, ρ_s is shale density, ρ_{ka} is gas density at atmospheric pressure in kerogen system, L_a represents the Langmuir volume constant, and L_b represents the Langmuir pressure.

The mass transfer from kerogen to matrix can be considered as diffusion through nanopores connecting these two systems. Once the gas molecules from the kerogen desorb to the matrix, the difference of gas concentration between two continua at the interface controls gas diffusion behavior. Thus, the mass transfer rate of gas desorption from kerogen into matrix can be described as [22]

$$Q_{km} = a_{km} D_{km} (\rho_m - \rho_k), \quad (4)$$

where a_{km} is the shape factor, ρ_m is the gas density in the matrix system, ρ_k is the gas density in the kerogen system, and D_{km} is the diffusion coefficient.

Based on the discussions on pore characteristic of kerogen, we assume Knudsen diffusion as the transport mechanism within the kerogen system. Combining (1) and (4), the mass balance equation of the kerogen system was obtained:

$$\frac{\partial}{\partial t} \left((1 - \phi_k) \rho_s \rho_{ka} \frac{L_a P_k}{P_k + L_b} \right) + \left(-D_k \frac{M}{RT} \nabla P_k \right) = a_{km} D_{km} (\rho_m - \rho_k). \quad (5)$$

2.3. Governing Equations of Gas Flow in Matrix. The conventional Darcy equation fails to fully capture the physics of flow in the nanopore structure of shale matrix. To describe gas flow in ultratight natural porous media, apparent permeability function is adopted which accounts for some complexities in the gas flow. Beskok and Karniadakis [23] developed a unified model for gas flow through microtubes that are valid over the entire range of flow regimes. It is a general expression to capture continuum, transition, and Knudsen flow for the apparent gas permeability of tight porous media. Florence et al. [24] derived the following model, which relates the apparent permeability k_a and intrinsic permeability k_∞ :

$$k_a = k_\infty f(K_n) = k_\infty (1 + \gamma K_n) \left(1 + \frac{4K_n}{1 + K_n} \right), \quad (6)$$

where $f(K_n)$ is correction parameter for non-Darcy flow in nanopores.

Knudsen number is defined as the ratio of the gas mean free path (λ) and the pore diameter ($2r_m$):

$$\begin{aligned} K_n &= \frac{\lambda}{2r_m}, \\ \lambda &= \frac{B_k T}{\sqrt{2} \pi d_g^2 P_m}, \\ \gamma &= \frac{128}{15\pi^2} \tan^{-1}(4K_n^{0.4}), \end{aligned} \quad (7)$$

in which B_k is the Boltzmann constant, d_g is the effective molecular diameter, and P_m is gas pressure in matrix.

It is noted that the Knudsen flow relies only on the Knudsen number and the intrinsic permeability of the porous medium. With regard to the permeability, there are many experimental observations suggesting that the change in effective stress varies the intrinsic permeability of the shale matrix [25, 26]. Therefore, the intrinsic permeability does not remain constant during shale gas extraction. To investigate the effective stress effect, we consider the intrinsic permeability as absolute permeability instead which is an effective strain-based model. According to our previous work on the effective strain-based absolute permeability model [27, 28], the multiscale permeability model for shale matrix is described as

$$\begin{aligned} k_\infty &= k_{m0} \left(1 + \frac{\alpha}{\phi_{m0}} \Delta \varepsilon_e \right)^3, \\ k_a &= k_\infty f(K_n) = k_{m0} \left(1 + \frac{\alpha}{\phi_{m0}} \Delta \varepsilon_e \right)^3 (1 + \beta K_n) \left(1 + \frac{4K_n}{1 + K_n} \right), \end{aligned} \quad (8)$$

where the effective strain increment is calculated by

$$\Delta \varepsilon_e = \Delta \varepsilon_v - \frac{\Delta P_m}{K_s} + \Delta \varepsilon_s, \quad (9)$$

$$\varepsilon_s = \varepsilon_L \frac{P_k}{P_k + L_b}, \quad (10)$$

where ϕ_{m0} and k_{m0} are the initial porosity and permeability of matrix, $\Delta \varepsilon_v$ is total volumetric strain increment, $\Delta P_m / K_s$ is the changing in compressive strain, K_s is the bulk modulus of the shale grains, α is the Biot coefficient, $\Delta \varepsilon_s$ is the gas sorption-induced volumetric strain increment, and ε_L the Langmuir volumetric strain constant representing the volumetric strain at infinite pore pressure. For the sake of simplification, we assume that gas sorption-induced strain in the kerogen system results in the volumetric strain of the matrix system. This permeability model considers the principal controlling factors, including the mechanical deformation-induced pore volume change (first term in the right-hand side of 8), the gas pressure-induced pore volume change (second term), and the sorption-induced pore volume change (third term).

The gas mass in the inorganic matrix exists in free phase. The gas mass balance equation in the matrix can be expressed as

$$\frac{\partial}{\partial t} \left(\phi_m P_m \frac{M}{RT} \right) + \nabla \left(-\frac{k_a}{u} \frac{M}{RT} P_m \nabla P_m \right) = -Q_{km} - Q_{mf}, \quad (11)$$

where u is the gas viscosity.

The mass exchange between the matrix and fracture is captured by a coupling term Q_{mf} which is similar to (4):

$$Q_{mf} = a_{mf} D_{mf} (\rho_m - \rho_f), \quad (12)$$

where a_{mf} is the shape factor and D_{mf} is the diffusion coefficient.

2.4. Governing Equations of Gas Flow in Natural Fracture. Based on the two-part Hooke model (TPHM) proposed by Liu et al. [29], the fracture aperture b under the condition of compression is defined as

$$b = b_r + b_f \exp(-C_f \sigma_n), \quad (13)$$

where b_r is the “hard” part of the fracture aperture or the residual fracture aperture that does not change with stress, b_f is the stress-sensitive part, and C_f is the fracture compressibility. Then, the porosity and permeability of the fracture system are defined as [30]

$$\begin{aligned} \frac{\phi_f}{\phi_{f0}} &= \frac{b}{b_0} = \frac{b_r + b_f \exp(-C_f \sigma_n)}{b_0}, \\ \frac{k_f}{k_{f0}} &= \left(\frac{b_r + b_f \exp(-C_f \sigma_n)}{b_0} \right)^3, \end{aligned} \quad (14)$$

Because the most efficient transport mechanism is pressure-driven volume flow, Darcy flow is dominant in fracture networks. The gas mass balance equation in the fracture is given as

$$\frac{\partial}{\partial t} \left(\phi_f P_f \frac{M}{ZRT} \right) - \frac{\rho_f k_f}{u} \nabla P_f = Q_{mf}, \quad (15)$$

where ϕ_f is the porosity of natural fracture, k_f is the permeability of fracture, ϕ_{f0} is the initial porosity of natural fracture, k_{f0} is the initial permeability of natural fracture, P_f is the gas pressure in the fracture, ρ_f is the gas density in the fracture system.

2.5. Governing Equations of Mechanics. In porous elastic media, such as coal, exists the interaction between the interstitial fluid and coal deformation. The effective stress concept introduced by Terzaghi [31] and refined by Biot [32] points out that the pore pressure helps counteract the mechanical stress carried through grain-to-grain contact. Considering the coal swelling/shrinkage stress σ_s induced by gas absorption/adsorption [33], the effective stress equation can be expressed as

$$\sigma_{ij} = \sigma'_{ij} + \alpha p \delta_{ij} + \sigma_s, \quad (16)$$

where σ_{ij} is the total stress (positive in compression), σ'_{ij} the effective stress, p the pore pressure, δ_{ij} the Kronecker delta ($\delta_{ij} = 1$ as $i = j$ and 0 in other cases), and σ_s the adsorption swelling stress. The parameter α is called the Biot coefficient; it relates the volume of fluid added (or lost) in a porous material element to the volumetric change of the same element.

According to the theory of continuum mechanics, the combination of equilibrium equation with the constitutive equations for the homogeneous, isotropic, and elastic media finds the Navier-type equation [33],

$$G u_{i,kk} + \frac{G}{1-2\nu} u_{k,ik} - \delta P_{m,i} - \beta P_{f,i} - K \varepsilon_L \frac{P_L}{(P_k + P_L)^2} P_{k,i} + f_i = 0, \quad (17)$$

where u_i is the component of displacement in the i direction, G the shear modulus, ν the Poisson ratio, and f_i the

component of body force in the i direction. Here, the pore pressure is the gas pressure in the fracture system and δ and β are the Biot coefficient. The Biot coefficient can be written as

$$\begin{aligned} \delta &= 1 - \frac{K}{K_s}, \\ \beta &= 1 - \frac{K}{a} C_f, \end{aligned} \quad (18)$$

where K is the bulk modulus, K_s is the grain elastic modulus, and a is the uniform spacing between fractures defining the edge dimension of the REV cubic matrix.

The coupling relationship between fluid flow and deformation in shale was built based on the equilibrium equation that describes an equilibrium state among deformation, gas flow-induced friction force, and swelling-induced body force.

3. Model Validation

This paper validates the numerical model in the context of the process of performing a simulation study. History matching between simulated results and field data for a horizontal well in Barnett Shale is discussed [34]. In this case, the well was stimulated by a multistage fracturing with a single, perforated interval for each stage. The derived governing equations for the gas flow in kerogen, matrix, and fracture system are a set of nonlinear partial differential equations (PDE) with the second order in space and the first order in time. Such a complete set of coupled equations is coupled into the interfaces of COMSOL Multiphysics and solved using the powerful desktop computer. The reservoir is assumed to be homogeneous with a volume of $1000 \times 500 \times 91.4$ m. The model contains 28 hydraulic fractures with 30.5 m spacing evenly. The half-length of all fractures is 47.2 m. Detailed reservoir information of the Barnett Shale and parameters used in simulations are all listed in Table 1 [9, 22, 35–37].

The history matching of field data with the M3 model is presented in Figure 2. It shows a reasonable match between the numerical simulation results and the actual field gas flow data. Compared to the simulated result with single porosity model from Yu and Sepehrnoori [37], the M3 model gives a better agreement with field data over the first 1 year. The simulated result of the well production for 30 years is also shown in Figure 2. It shows a typical production decline curve that production in the initial several years declines hyperbolically and the production decline levels off reflecting an exponential decline rate at some point.

Simulations are performed with the M3 model in which all fractures, inorganic, and organic porosity systems are allowed to flow among themselves and between different porosity types. This is different from conventional single or dual porosity/permeability models which are not sufficient to describe the complex physics of shale gas. A comparison between M3 model and conventional models is shown in Figure 3. The single-porosity model consists of matrix system only, while the dual-porosity model consists of matrix and fracture systems. As can be seen, evidence gap exists between the M3 model and conventional models in the first 1 year and

TABLE 1: Values of variables used for the simulation.

Parameter	Value
Model dimension (length \times width \times height)	1000 \times 1000 \times 91.4 m
Pore radius, r_k	10 nm
Pore radius, r_m	100 nm
Langmuir volume constant, L_a	0.00272 m ³ /kg
Langmuir pressure, L_b	4.48 MPa
Shale density, ρ_s	2580 kg/m ³
Gas viscosity, u	1.84×10^{-5} Pa·s
Shape factor, a_{km}	1
Shape factor, a_{mf}	1
Diffusion coefficient, D_{km}	2×10^{-10} m ² /s
Diffusion coefficient, D_{mf}	1×10^{-9} m ² /s
Porosity of kerogen, ϕ_k	0.00532
Initial porosity of matrix ϕ_{m0}	3%
Initial fracture porosity, ϕ_{f0}	0.5%
Initial permeability of matrix, k_{m0}	1.5×10^{-19} m ²
Initial fracture permeability, k_{f0}	3×10^{-18} m ²
Fracture aperture, b_r	0.0001 m
Fracture aperture, b_f	0.0001 m
Fracture compressibility, C_f	0.363 GPa ⁻¹
Biot coefficient, δ	0.5
Biot coefficient, β	0.5
Bulk modulus, K	20 GPa
Poisson's ratio, ν	0.272
Langmuir volumetric strain constant, ϵ_L	0.002295
Initial reservoir pressure	20.3 MPa
Reservoir depth	1665.1 m
Reservoir stress	26.7 MPa
Reservoir temperature, T	338 K
Wellbore pressure	3.45 MPa
Half of hydraulic fracture length	47.2 m
Hydraulic fracture spacing	30.5 m
Formation thickness	91.4 m
Hydraulic fracture permeability	3×10^{-16} m ²
Horizontal well length	904.6 m
Number of hydraulic fractures	28
Permeability of hydraulic fractures	1×10^{-14} m ²
Hydraulic fracture thickness	0.003 m

late period process of gas production markedly. Again, it supports that the simulated result with the M3 model is in better agreement than conventional models that could account for the multispace and multitime process of shale gas flow.

4. Application Study

For the results of evaluation of the M3 model, we perform sensitivity study of multispace and multitime process and

permeability evolution of the gas flow in shale. This paper focuses on contributions of permeability in different scales which are important factors for shale gas production.

4.1. Multispace and Multitime Process of Gas Flow in Shale. As discussed above, gas production from shale reservoir is a physical multiscale process from nanoscale to macroscale. Figure 4 shows the curves of the gas flow rate in kerogen, matrix and fracture, respectively. The transporting behaviors for shale gas are desorption and diffusion in nanoscale pores, flow and diffusion in the matrix, and flow in fractures. As the fractures exhibit very high permeability but very low porosity, a rapid initial outflow of gas appears in fractures. After a short term, the gas flow rate drops rapidly in the fracture and then keeps at a lower level relatively (stage I). Just when fractures are depleted mostly, the gas in the matrix starts feeding the fractures and then flows into the well through fractures (stage II). The gas flow from matrix-dominated total flow lasts until about 10 days before a dramatical decline of gas flow rate occurs. As the gas pressure drops in the matrix, gas starts desorbing from the kerogen pore walls into the nanopores and feeding the matrix then (stage III). This stage is the major recovery stage, contributing 96.8% of cumulative production. It should be noted that free gas in the matrix system is the main source of the gas flow in the period process of gas production. This phenomenon is more evidence for stack column chart as shown in Figure 5. The contribution of gas in matrix systems to cumulative production is nearly 79%. The gas production from the kerogen system keeps increasing throughout the production time that accounts for the 15% of total gas production.

4.2. Permeability Evolution in the Process of Gas Production. Reservoir permeability is a crucial parameter for shale gas production. The evolution permeability in shale is strongly related to complex geomechanical processes such as the transport of gas, adsorption, desorption, changing horizontal stress, and vertical strain. This study investigated the evolution of matrix and fracture permeabilities. Then, the effect of matrix permeability and fracture permeability on shale gas production was investigated.

During the period of gas production, the evolution of matrix permeability is attributable to a number of mechanisms. The intrinsic permeability decreases slightly with the decrease of gas pressure due to the increasing effective stress. However, the permeability increases with the decrease of reservoir pressure under the influence of slippage effect. Considering both the effects of flow regimes acting and effective stress, the apparent permeability of matrix increases rapidly at the primary stage of gas production, as shown in Figure 6. After then, it increases slightly with the decrease of reservoir pressure. The fracture permeability decreases severely under the effect of effective stress, suggesting that fracture permeability is more sensitive to effective stress than the matrix. The impact of permeability evolution on gas production was studied by carrying out three comparative cases. Although the matrix permeability increases 1.94 times after twelve years of production, it results into an increase by 0.002% in cumulative gas production compared to the

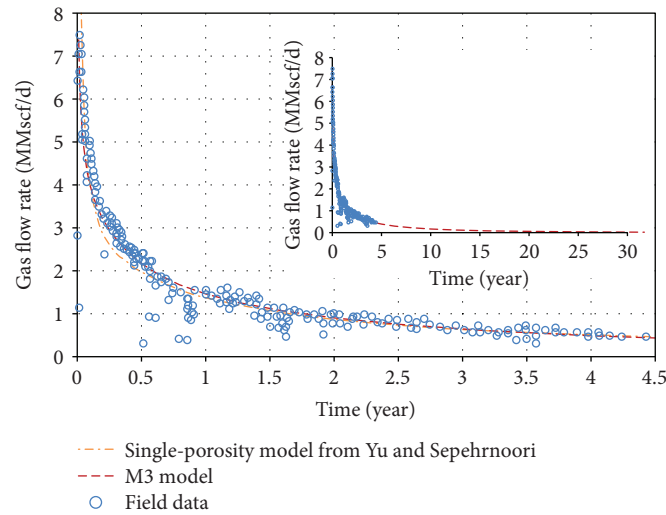


FIGURE 2: History matching of Barnett Shale with simulation result.

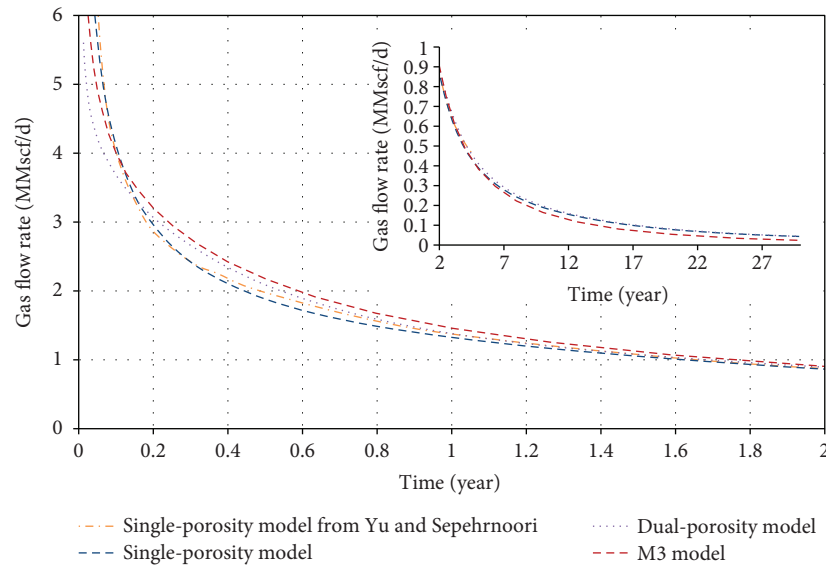


FIGURE 3: Gas flow rate curves to compare the M3 model with conventional models.

standard case. It indicates that gas production is not sensitive to matrix permeability. Another case shows that cumulative gas production drops to 71.92% with decreasing fracture permeability. It suggests that fracture permeability has a strong influence on gas production.

The shale permeability varies over several orders of magnitude in the different reservoir. Several cases were further studied to determine the controlling effects of permeability on gas well performance.

4.3. The Impact of Different Permeability on Production Rate Curves. Figure 7 compares the gas production for shales with constant initial fracture permeability, but with initial matrix permeability at 10 nD, 100 nD, 1000 nD and 10000 nD. The cumulative production only increases by 1.05 times as matrix permeability is 1000 times greater. Further increasing

the matrix permeability will not result in increased production. This result indicates that matrix permeability has a minor effect on gas production. However, if the natural fracture permeability is much greater than the matrix, then gas is being transported through the natural fracture network at a higher rate than gas flowing through the matrix into the fractures. In this case, the gas production is dependent on the matrix permeability.

The fractures, on the other hand, are the discontinuous natural microfractures with high permeability, which are surrounding shale matrix to communicate with hydraulic fractures and the wellbore. Simulations were conducted for a series of shales with initial fracture permeability varying between 500 nD and 10000 nD. It is apparent in Figure 8 that significantly higher production are achieved for wells producing from shales with higher fracture permeabilities. The

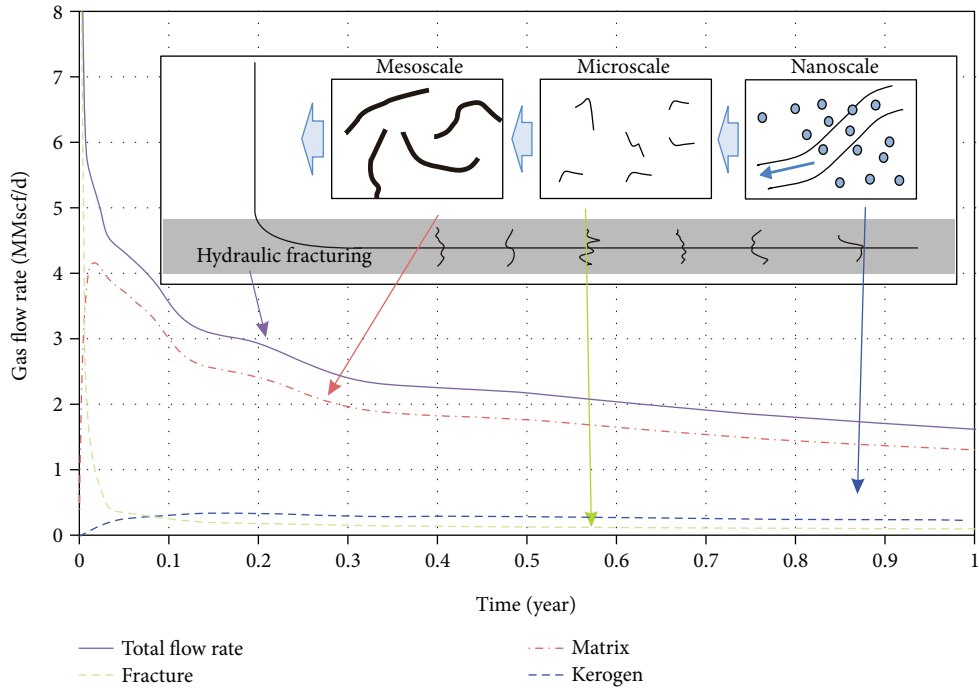


FIGURE 4: Gas flow rate curves in different systems.

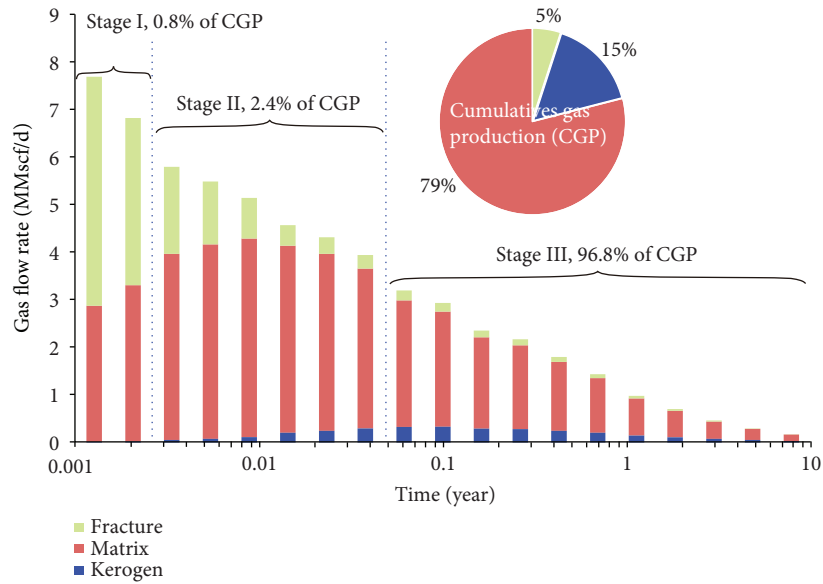


FIGURE 5: Cumulative production curves in different systems.

final cumulative production increases by 1.2, 1.8 and 2.1 times for fracture permeability varying from 500 nD to 1000 nD, 5000 nD and 10000 nD, respectively. Fracture permeability controls the pressure drawn down in the natural fractures, which in turn drives the rate of gas transfer from the matrix. Although free gas in matrix contributes to the main source of gas production, fracture permeability determines the gas production behavior. It indicates that high permeability fracture networks in matrix system accelerate production by providing high conductivity channels for the

flow through a reservoir. For unconventional and tight reservoirs with extreme low-matrix permeability, natural fractures have the potential to play a crucial role in the gas production.

5. Conclusion

The gas production in shale reservoirs is a combined sequence of gas flow mechanisms at different length scales. Therefore, a triple-porosity model (M3 model) was proposed for understanding the complex flow mechanisms occurring

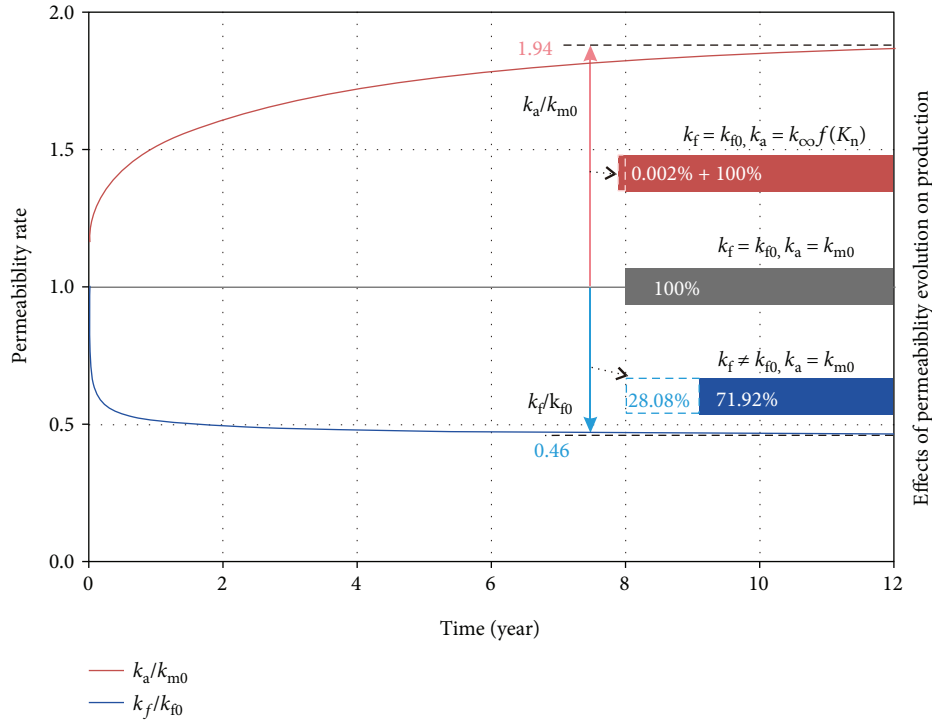


FIGURE 6: Evolution of matrix and fracture permeability.

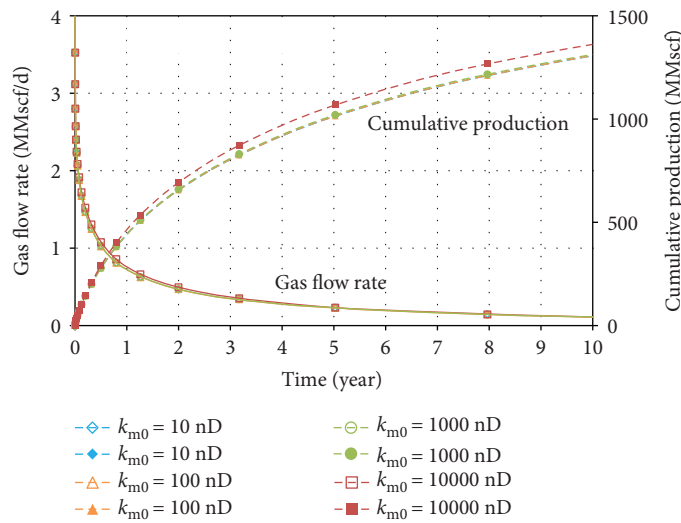


FIGURE 7: Impact of matrix permeability on gas production.

in these reservoirs. The M3 model capturing multiple pore scales and flow consists of three contiguous porous media: the kerogen, inorganic matrix, and natural fractures. In shale gas systems, these multiscale pores form the flow-path network that allows the flow of gas from the kerogen to wellbore during shale gas production. Each process of gas flow follows its own path and obeys different transport mechanisms at different length scales. We performed history matching of field production data from Barnett Shale. The results indicate that the M3 model produces better performance than the conventional dual porosity/permeability

models. Based on the application study, the following conclusions can be drawn:

- (1) At an early stage of gas production, free gas in the fracture system contributes to the main source of gas flow. Next, gas in the matrix starts feeding the fractures and flows into the well through fractures. Finally, gas starts desorbing from the pore walls into the nanopores and feeding the matrix. The contribution of gas in matrix systems to cumulative production is nearly 80%. Both gas in kerogen and fracture

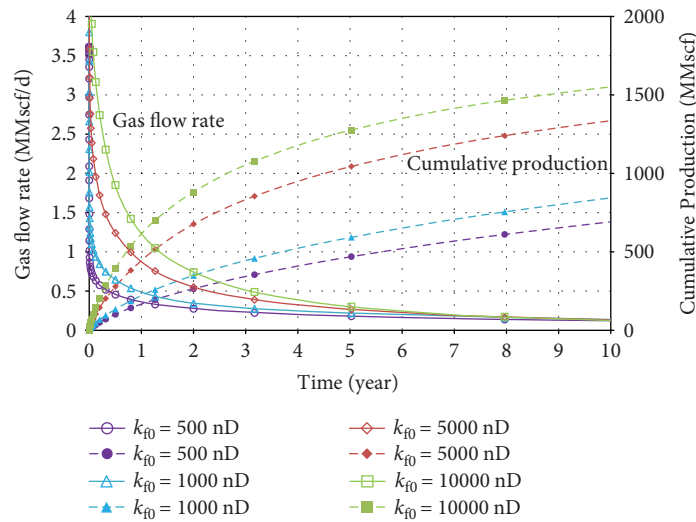


FIGURE 8: Impact of natural fracture permeability on gas production.

systems account for a much smaller portion. It is important to point out that the M3 model is able to capture the onset of different contributing storage and transport mechanisms.

- (2) Reservoir permeability is another crucial parameter influencing shale gas production. The results show that apparent permeability of the matrix system increases with the decreasing reservoir pressure, by considering both effects of flow regimes acting and effective stress. The fracture permeability decreases severely under the effect of effective stress, suggesting that fracture system is more sensitive to effective stress. Gas production has a strong relationship with natural fracture permeability than matrix permeability, which controls the pressure drawn down in the natural fractures which in turn drives the rate of gas transfer from the matrix. This phenomenon suggests that free gas in the matrix contributes to the main source of gas production, while natural fracture permeability determines the gas production behavior.

Conflicts of Interest

The authors declare that they have no conflicts of interest.

Acknowledgments

This work is a partial result of funding by the National Key R&D Program of China (Grant no. 2017YFC0804203) and the Natural Science Foundation of China (51504235, 51474204). These supports are gratefully acknowledged. The authors would like to thank Dr. Liu Liu and Professor Pengzhi Pan for their immense polishing skills and contribution to this paper.

References

- [1] M. E. Curtis, B. J. Cardott, C. H. Sondergeld, and C. S. Rai, "Development of organic porosity in the Woodford Shale with increasing thermal maturity," *International Journal of Coal Geology*, vol. 103, pp. 26–31, 2012.
- [2] C. H. Sondergeld, R. J. Ambrose, C. S. Rai, and J. Moncrieff, "Micro-structural studies of gas shales," in *SPE Unconventional Gas Conference*, p. 17, Society of Petroleum Engineers, Pittsburgh, PA, USA, February 2010.
- [3] F. P. Wang, R. M. Reed, A. John, and G. Katherine, "Pore networks and fluid flow in gas shales," in *SPE Annual Technical Conference and Exhibition*, New Orleans, LA, USA, October 2009.
- [4] L. Ci-qun, "Exact solution for the compressible flow equations through a medium with triple-porosity," *Applied Mathematics and Mechanics*, vol. 2, no. 4, pp. 457–462, 1981.
- [5] L. Ci-qun, "Exact solution of unsteady axisymmetrical two-dimensional flow through triple porous media," *Applied Mathematics and Mechanics*, vol. 4, no. 5, pp. 717–724, 1983.
- [6] D. Abdassah and I. Ershaghi, "Triple-porosity systems for representing naturally fractured reservoirs," *SPE Formation Evaluation*, vol. 1, no. 2, pp. 113–127, 1986.
- [7] H. Dehghanpour and M. Shirdel, "A triple porosity model for shale gas reservoirs," in *Canadian Unconventional Resources Conference*, Calgary, Alberta, Canada, November 2011.
- [8] N. Alharthy, M. Al Kobaisi, M. A. Torcuk, H. Kazemi, and R. Graves, "Physics and modeling of gas flow in shale reservoirs," in *SPE 161893, Presented at the Abu Dhabi International Petroleum Exhibition & Conference*, Abu Dhabi, UAE, November 2012.
- [9] T. Huang, X. Guo, and F. F. Chen, "Modeling transient flow behavior of a multiscale triple porosity model for shale gas reservoirs," *Journal of Natural Gas Science and Engineering*, vol. 23, pp. 33–46, 2015.
- [10] Y. Peng, J. S. Liu, Z. J. Pan, and L. D. Connell, "A sequential model of shale gas transport under the influence of fully coupled multiple processes," *Journal of Natural Gas Science and Engineering*, vol. 27, pp. 808–821, 2015.
- [11] P. Cao, J. S. Liu, and Y. K. Leong, "A fully coupled multi-scale shale deformation-gas transport model for the evaluation of shale gas extraction," *Fuel*, vol. 178, pp. 103–117, 2016.

- [12] T. J. Katsube, "Shale permeability and pore-structure evolution characteristics," in *Geological Survey of Canada, Current Research 2000-E15*, p. 9, Government of Canada publications, Ottawa, Canada, 2000.
- [13] R. J. Ambrose, R. C. Hartman, M. Diaz-Campos, I. Y. Akkutlu, and C. H. Sondergeld, "Shale gas-in-place calculations part I - new pore-scale considerations," *SPE Journal*, vol. 17, no. 01, pp. 219–229, 2012.
- [14] A. Wasaki and I. Y. Akkutlu, "Permeability of organic-rich shale," *SPE Journal*, vol. 20, no. 6, pp. 1384–1396, 2015.
- [15] F. Javadpour, D. Fisher, and M. Unsworth, "Nanoscale gas flow in shale gas sediments," *Journal of Canadian Petroleum Technology*, vol. 46, no. 10, pp. 55–61, 2007.
- [16] S. M. Kang, E. Fathi, R. J. Ambrose, I. Y. Akkutlu, and R. F. Sigal, "Carbon dioxide storage capacity of organic-rich shales," *SPE Journal*, vol. 16, no. 04, pp. 842–855, 2011.
- [17] G. E. King, "Thirty years of gas shale fracturing: what have we learned?," in *SPE Annual Technical Conference and Exhibition*, Florence, Italy, September 2010.
- [18] W. Kast and C. R. Hohenthanner, "Mass transfer within the gas-phase of porous media," *International Journal of Heat and Mass Transfer*, vol. 43, no. 5, pp. 807–823, 2000.
- [19] S. Roy, R. Raju, H. F. Chuang, B. A. Cruden, and M. Meyyappan, "Modeling gas flow through microchannels and nanopores," *Journal of Applied Physics*, vol. 93, no. 8, pp. 4870–4879, 2003.
- [20] X. Cui, A. M. M. Bustin, and R. M. Bustin, "Measurements of gas permeability and diffusivity of tight reservoir rocks: different approaches and their applications," *Geofluids*, vol. 9, no. 3, pp. 223 pages, 2009.
- [21] X. Xiong, D. Devegowda, G. G. Michel Villazon, R. F. Sigal, and F. Civan, "A fully-coupled free and adsorptive phase transport model for shale gas reservoirs including non-Darcy flow effects," in *SPE Annual Technical Conference and Exhibition*, San Antonio, TX, USA, October 2012.
- [22] E. Fathi and I. Y. Akkutlu, "Multi-component gas transport and adsorption effects during CO₂ injection and enhanced shale gas recovery," *International Journal of Coal Geology*, vol. 123, pp. 52–61, 2014.
- [23] A. Beskok and G. E. Karniadakis, "Report: a model for flows in channels, pipes, and ducts at micro and nano scales," *Micro-scale Thermophysical Engineering*, vol. 3, no. 1, pp. 43–77, 1999.
- [24] F. A. Florence, J. A. Rushing, K. E. Newsham, and T. A. Blasingame, "Improved permeability prediction relations for low permeability sands," in *Rocky Mountain Oil & Gas Technology Symposium*, Denver, CO, USA, April 2007.
- [25] R. Heller and M. Zoback, "Laboratory measurements of matrix permeability and slippage enhanced permeability in gas shales," in *Unconventional Resources Technology Conference*, Denver, CO, USA, August 2013.
- [26] O. Kwon, A. K. Kronenberg, A. F. Gangi, B. Johnson, and B. E. Herbert, "Permeability of illite-bearing shale: 1. Anisotropy and effects of clay content and loading," *Journal of Geophysical Research-Solid Earth*, vol. 109, no. B10, pp. 1–19, 2004.
- [27] J. S. Liu, Z. W. Chen, D. Elsworth, H. Y. Qu, and D. Chen, "Interactions of multiple processes during CBM extraction: a critical review," *International Journal of Coal Geology*, vol. 87, no. 3-4, pp. 175–189, 2011.
- [28] M. Y. Wei, J. S. Liu, X. T. Feng, C. G. Wang, and F. B. Zhou, "Evolution of shale apparent permeability from stress-controlled to displacement-controlled conditions," *Journal of Natural Gas Science and Engineering*, vol. 34, pp. 1453–1460, 2016.
- [29] H.-H. Liu, M.-Y. Wei, and J. Rutqvist, "Normal-stress dependence of fracture hydraulic properties including two-phase flow properties," *Hydrogeology Journal*, vol. 21, no. 2, pp. 371–382, 2013.
- [30] M. Wei, J. Liu, X. Feng et al., "Quantitative study on coal permeability evolution with consideration of shear dilation," *Journal of Natural Gas Science and Engineering*, vol. 36, pp. 1199–1207, 2016.
- [31] K. Terzaghi, *Theoretical Soil Mechanics*, Wiley, New York, NY, USA, 1932.
- [32] M. A. Biot, "Generalized theory of acoustic propagation in porous dissipative media," *The Journal of the Acoustical Society of America*, vol. 34, no. 9A, pp. 1254–1264, 1962.
- [33] Y. Wu, J. S. Liu, D. Elsworth, Z. W. Chen, L. Connell, and Z. J. Pan, "Dual poroelastic response of a coal seam to CO₂ injection," *International Journal of Greenhouse Gas Control*, vol. 4, no. 4, pp. 668–678, 2010.
- [34] H. A. Al-Ahmadi, S. Aramco, and R. A. Wattenbarger, "Triple-porosity models: one further step towards capturing fractured reservoirs heterogeneity," in *SPE/DGS Saudi Arabia Section Technical Symposium and Exhibition*, Al-Khobar, Saudi Arabia, May 2011.
- [35] V. Swami, *Development of a 'Quad Porosity' Numerical Flow Model for Shale Gas Reservoirs*, M.S. Thesis, Schulich School of Engineering, University of Calgary, Calgary, Canada, 2013.
- [36] C. Wang and Y. Wu, "Characterizing hydraulic fractures in shale gas reservoirs using transient pressure tests," *Petroleum*, vol. 1, no. 2, pp. 133–138, 2015.
- [37] W. Yu and K. Sepehrnoori, "Simulation of gas desorption and geomechanics effects for unconventional gas reservoirs," *Fuel*, vol. 116, pp. 455–464, 2014.

Research Article

A Two-Phase Flowback Model for Multiscale Diffusion and Flow in Fractured Shale Gas Reservoirs

Huimin Wang,¹ J. G. Wang ,^{1,2} Feng Gao ,¹ and Xiaolin Wang ³

¹State Key Laboratory for Geomechanics and Deep Underground Engineering, China University of Mining and Technology, Xuzhou 221116, China

²School of Mechanics and Civil Engineering, China University of Mining and Technology, Xuzhou 221116, China

³School of Engineering, University of Tasmania, Hobart, TAS 7001, Australia

Correspondence should be addressed to J. G. Wang; nuswjg@yahoo.com

Received 24 October 2017; Revised 11 January 2018; Accepted 29 January 2018; Published 16 May 2018

Academic Editor: Xiangzhao Kong

Copyright © 2018 Huimin Wang et al. This is an open access article distributed under the Creative Commons Attribution License, which permits unrestricted use, distribution, and reproduction in any medium, provided the original work is properly cited.

A shale gas reservoir is usually hydraulically fractured to enhance its gas production. When the injection of water-based fracturing fluid is stopped, a two-phase flowback is observed at the wellbore of the shale gas reservoir. So far, how this water production affects the long-term gas recovery of this fractured shale gas reservoir has not been clear. In this paper, a two-phase flowback model is developed with multiscale diffusion mechanisms. First, a fractured gas reservoir is divided into three zones: naturally fractured zone or matrix (zone 1), stimulated reservoir volume (SRV) or fractured zone (zone 2), and hydraulic fractures (zone 3). Second, a dual-porosity model is applied to zones 1 and 2, and the macroscale two-phase flow flowback is formulated in the fracture network in zones 2 and 3. Third, the gas exchange between fractures (fracture network) and matrix in zones 1 and 2 is described by a diffusion process. The interactions between microscale gas diffusion in matrix and macroscale flow in fracture network are incorporated in zones 1 and 2. This model is validated by two sets of field data. Finally, parametric study is conducted to explore key parameters which affect the short-term and long-term gas productions. It is found that the two-phase flowback and the flow consistency between matrix and fracture network have significant influences on cumulative gas production. The multiscale diffusion mechanisms in different zones should be carefully considered in the flowback model.

1. Introduction

Shale gas reservoirs have gradually become a major source of hydrocarbon fuel in the global energy market [1–3]. However, the extraction of shale gas confronts difficulty because shale gas reservoirs have extremely low permeability and high formation pressure [4, 5]. Horizontal drilling and multistaged hydraulic fracturing techniques have made shale gas production economically feasible [6, 7]. A horizontal well is hydraulically fractured through the injection of fracturing fluids. Generally, multistaged hydraulic fracturing techniques are used to fracture the shale gas reservoirs, forming a stimulated reservoir volume or fractured zone (SRV). The permeability of this zone is largely enhanced due to the hydraulic fractures and the microfractures in the SRV zone. The shale gas diffuses from matrix into the fractured zone

and finally flows into the production well along hydraulic fractures. When the bottomhole pressure is drawn down or injection is shut in for gas production, the injected fracturing fluid (assumed water) in the hydraulic fractures and the fractured zone will flow back. This poststimulation flow period is called “flowback” [8]. Usually, higher total injected-water volume leads to larger effective fracture pore volume [9]. In most cases, these flowback data are ignored if single-phase flow is used for the prediction of shale gas production [10–12]. This ignorance of two-phase flowback makes the predicted gas production curve inconsistent with the actual field observation in the early period [13]. In this paper, the two-phase flow in the fractured zone and hydraulic fractures is studied through our fully coupled model. The relationship between shale gas production rate and water flowback rate is explored. It is found that the two-phase flowback has

significant impacts on the gas production rate, thus being not ignorable.

The fracture properties of fractured shale gas reservoirs have been characterized by many methods. For example, Crafton and Gunderson [14] used the high frequency single-phase flowback data to characterize fracture properties. Further, Williams-Kovacs et al. [15] developed a flowing material balance equation with single-phase flow. However, these single-phase flow models ignore the analysis for water flowback data. Their prediction accuracy thus was not well evaluated in the two-phase flow period and later stages. The immediate two-phase flow after the shut-in period was observed in the Barnett shale and the Marcellus shale [16]. A transient flowing model considering the effect of two-phase flow after the hydraulic fracturing was also developed for gas production [13]. This model further analyzes the response of transient pressure. Yang et al. [17] developed a semianalytical model to simulate the two-phase flow during the flowback period with complex fracture networks. They found that increasing the fracture network complexity is favorable to gas production enhancement. Ezulike and Dehghanpour [6] applied a dynamic relative permeability on the two-phase flow in the hydraulic fractures. Their results showed that the relative permeability varies with reservoir parameters in the early flowback period. Xu et al. [18] analyzed the mechanisms for flowback behaviors and put forward a material balance approach to estimate the effective fracture volume in the Horn River Basin. Ezulike et al. [19] developed a two-phase flowback tank model for estimating fracture pore volume independent of fracture geometry. Their results indicated that the effective fracture pore volume is the most sensitive to fracture pore volume compressibility. Alkough et al. [20] provided an effective method to estimate fracture volume through the water flowback and gas production data. Therefore, different methods have been used to characterize the fracture properties but the interaction between fracture flow and shale gas diffusion has not been considered in the two-phase flowback stage.

The above-mentioned two-phase flowback or single-phase gas models have an obvious limitation: the microdiffusion and macroflow mechanisms are not consistently described by a fully coupled model for the prediction of gas production rate. This inconsistency may affect the prediction of gas production rate in the two-phase flowback period and even the full gas production period. Therefore, it is necessary to analyze the two-phase flow of the fractured shale reservoir after hydrofracturing treatment. In this paper, the full interaction between the microscale gas diffusion in matrix and the macroscale two-phase flow in fractures is considered through our fully coupled model.

2. A Conceptual Model

In order to enhance the permeability of shale matrix, a big amount of water-based fracturing fluid is injected through the horizontal well, forming a fractured zone or SRV [21]. The water is retained in the fractures and increases the water

saturation. With gas production, 10–40% of the water can be recovered along the hydraulic fractures [22]. In this period, the capillary pressure is directly linked with the process of two-phase flowback, which is necessary to be discussed. Hydraulic fractures are the main channels for the flow from the fractured zone to the well, whose properties are important to gas production. In the fractured zone, macroscale water-gas two-phase flow in the fractures and microscale diffusion in the shale matrix occur simultaneously. With the process of flowback or continuous gas extraction, the gas pressure in the matrix began to decline and gas desorbs from the surface of matrix. This free gas diffuses from the matrix to the fractured zone and further flows into the wellbore along the hydraulic fractures. Therefore, the flow consistency in the matrix, fractured zone, and hydraulic fractures should be the focus.

Based on different flow regimes, a given computational domain is roughly divided into three zones as shown in Figure 1: shale matrix or naturally fractured zone (zone 1), (artificially and naturally) fractured zone (zone 2), and hydraulic fractures (zone 3). In zone 1, shale matrix is usually regarded as a single-porosity model in the traditional models. However, experimental measurements (such as SEM and CT) have observed a mass of micropores even microfractures in the shale [23]. The gas diffusion and flow in the microfractures of shale matrix are considerably complicated [24, 25]. Thus, the traditional models neglecting the microdiffusion in the matrix block are not applicable. In this study, a dual-porosity model is proposed to describe the gas diffusion and flow mechanisms in the zone 1. A new apparent permeability model for matrix is introduced into the dual-porosity model to consider three important physical processes: viscous flow, free molecular diffusion, and surface diffusion. In zone 2, the fractured zone is also defined as a dual-porosity model, but they have different properties. The two-phase flow is considered in the fracture and relative permeability varies with water saturation. The microfractures in this zone are different from those in zone 1, which are also induced by water fracturing. It is noted that the effective connectivity of different kinds of microfractures (in zones 1 and 2) is not described in this paper. In zone 3, the two-phase flow is still considered along the hydraulic fractures. The capillary pressure and relative permeability models are same with the fractured zone.

Overall, a series of interactions are included in the shale gas production within the reservoir. The three zones interact with each other and have a consistency impact of flow and pressure on short-term and long-term shale gas productions. In the following section, we will formulate this conceptual model by a set of governing equations in the three zones.

3. Governing Equations for Gas and Water Flows in Multiscale Porous Media

The three-zone model is shown in Figure 1. The flows in each zone have different diffusion and flow mechanisms. Figure 2 presents the details of the diffusion and flow in each zone. Their governing equations are stated below.

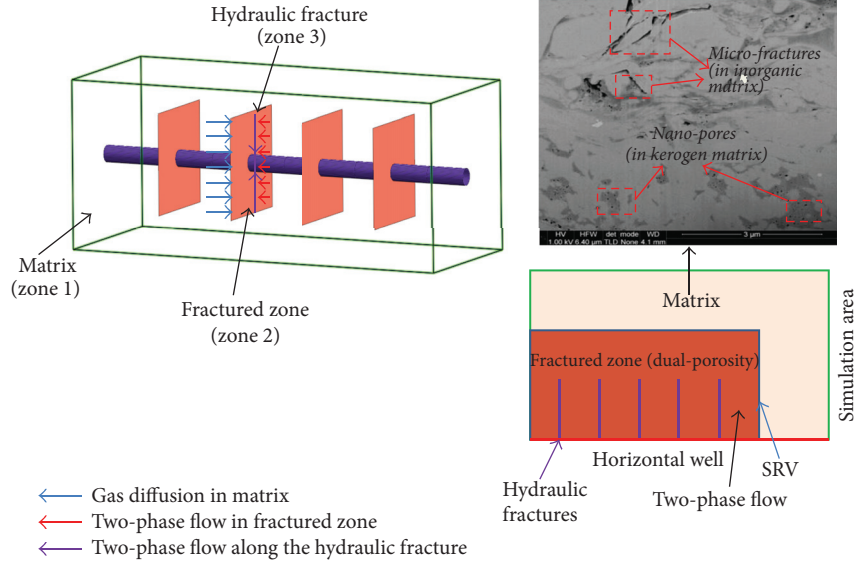


FIGURE 1: Snapshot of shale gas recovery in typical three zones (SEM from [23]).

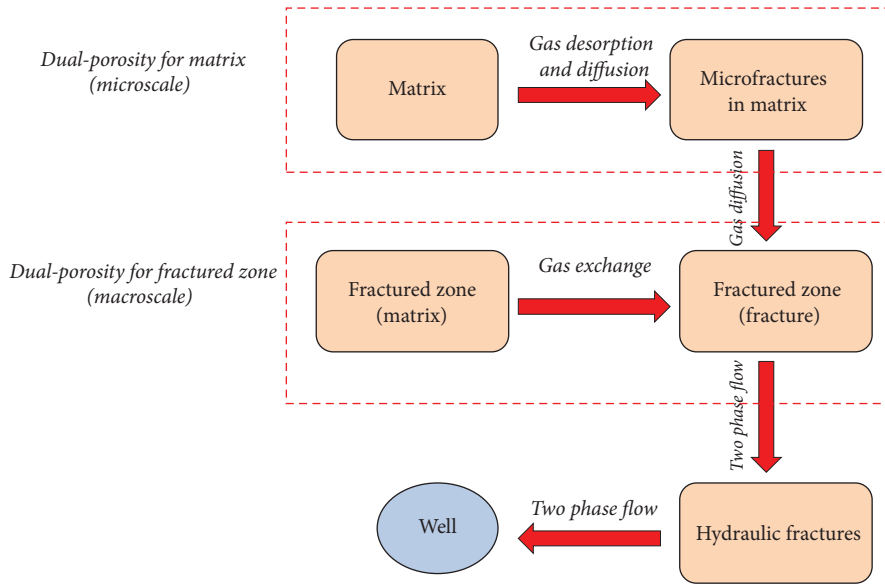


FIGURE 2: Flow and diffusion processes in multiscale zones.

3.1. Shale Gas Flow in the Microfractures of Matrix (Zone 1). The mass conservation law for the gas flow in the microfractures of matrix (zone 1) is governed by

$$\frac{\partial (\rho_{gf} \phi_f)}{\partial t} - \nabla \cdot \left(\frac{k_{mapp}}{\mu_{nw}} \rho_{gf} \nabla p_f \right) = Q_{mf}, \quad (1)$$

where ρ_{gf} is the gas density in the microfractures and ϕ_f is the porosity of microfractures. It is noted that only free gas is taken into consideration in microfractures of this matrix (zone 1). μ_{nw} and p_f represent the gas viscosity and pressure, respectively. k_{mapp} is the apparent permeability for microfractures in the matrix (zone

1). This apparent permeability is directly expressed as [26]

$$k_{mapp} = \frac{\phi_f d_f^2}{32 \tau_h} \left(1 + \frac{b}{p_f} \right). \quad (2)$$

Here d_f is the aperture of microfractures in this zone and can be measured by many experiments such as SEM, AFM, and CT tests. τ_h reflects the degree of tortuosity in porous medium. b is a Klinkenberg factor determined by the pore structure of the matrix and the reservoir temperature.

$$b = \frac{64 \mu_{nw}}{3 \pi d_f M} \sqrt{2 \pi MRT}, \quad (3)$$

where M is the gas molecular weight. R represents the universal gas constant. T is the reservoir temperature. The right-hand term of (1), the Q_{mf} , is the source of gas. It expresses the gas exchange between micropores and microfractures in the matrix.

$$Q_{mf} = \frac{\rho_{gm} k_k a}{\mu_{nw}} (p_m - p_f), \quad (4)$$

where p_m is the gas pressure in the matrix. k_k is the apparent permeability of the matrix which will be described in the next section. ρ_{gm} is the gas density in the shale matrix. a is a shape factor of matrix block. For isotropic matrix, the shape factor is [27]

$$a = \pi^2 \left(\frac{1}{L_x^2} + \frac{1}{L_y^2} \right), \quad (5)$$

where L_x and L_y are the fracture spacing in the x -direction and the y -direction, respectively.

3.2. Gas Diffusion in Shale Matrix

3.2.1. Knudsen Number. In molecular dynamics of gas, the probability of gas collisions or diffusion is directly related to an important index, the molecular mean free path. This free path is the mean path for a molecular free motion in an interval of two consecutive collisions [28]:

$$\lambda = \frac{\mu_{nw}}{p_m} \sqrt{\frac{\pi RT}{2M}}. \quad (6)$$

The gas molecular flow usually obeys different mechanisms, depending on the scale of flow channel. Knudsen number is defined as the ratio of the mean free path of gas flow to the characteristic size of gas flow channel:

$$K_n = \frac{\lambda}{d_f}. \quad (7)$$

3.2.2. Diffusion in Matrix. The mass conservation law for the gas diffusion in matrix can be given as

$$\frac{\partial(m_m)}{\partial t} - \nabla \cdot \left(\frac{k_k}{\mu_{nw}} \rho_{gk} \nabla p_k \right) = -Q_{mf} \quad (8)$$

$$m_m = \rho_{gk} \phi_m + \rho_{ga} \rho_s \frac{V_L p_m}{p_m + V_L}.$$

The gas mass (m_m) in the matrix consists of both free phase and adsorbed phase gases. ρ_{gk} is the gas density in the matrix. $-Q_{mf}$ means the gas exchange between matrix and microfractures of the matrix. k_k is the permeability of matrix which is obtained by

$$k_k = \frac{D \mu_{nw}}{p_m}, \quad (9)$$

where D is the effective diffusion coefficient of the matrix and has three components:

$$D = D_c + D_e + D_{es}. \quad (10)$$

The diffusion coefficients of D_c , D_e , D_{es} are determined as follows.

For a given temperature, the gas mass in matrix transports mainly in three forms: (1) viscous flow; (2) molecular and Knudsen diffusion; (3) surface diffusion in the adsorbed layer.

The viscous flow induced diffusion coefficient is [24]

$$D_c = \frac{\phi_m}{\tau_h} (1 + 8K_n) \frac{d_m^2 p_m}{32 \mu_{nw}}, \quad (11)$$

where ϕ_m is the porosity of matrix. d_m is the diameter of pores in matrix.

Further, the effective diffusion coefficient varies from the limit of molecular diffusion ($K_n \rightarrow 0$) to fully developed Knudsen diffusion ($K_n \rightarrow \infty$) [29]. Therefore, the effective molecular-Knudsen diffusion coefficient is

$$D_e = \frac{\phi_m}{\tau_h} D_k (\zeta^{-(D_f-2)} + K_n^{-1})^{-1}, \quad (12)$$

where ζ is the ratio of molecular size to average pore diameter. D_f means the fractal dimension of the pores surface and is assumed to be 2.5 in this study. D_k represents the Knudsen diffusion coefficient which is obtained as

$$D_k = \frac{1}{3} d_m \sqrt{\frac{8RT}{\pi M}}. \quad (13)$$

In addition to the gas desorption from the surface of matrix pores, gas can migrate within the adsorbed layer [30, 31], forming a surface diffusion. This diffusion is usually significant when the temperature is high relative to the normal boiling point of the adsorbed gas [32]. Its effective surface diffusion coefficient is given as

$$D_{es} = \frac{1 + \phi_m}{\phi_m} \rho_s \rho_{ga} \frac{V_L P_L}{(P_L + p_m)^2} D_s, \quad (14)$$

where ρ_s and ρ_{ga} are the matrix density and the gas density under standard conditions, respectively. V_L is the Langmuir volume constant and P_L the Langmuir pressure. D_s is the surface diffusion coefficient which is expressed as [33]

$$D_s = 8.29 \times 10^{-7} \times T^{0.5} \exp\left(-\frac{20}{RT}\right). \quad (15)$$

Combining (11), (12), and (14), the final effective diffusion coefficient for the whole matrix is given as

$$\begin{aligned} D = & \frac{\phi_m}{\tau_h} (1 + 8K_n) \frac{d_m^2 p_m}{32 \mu_{nw}} \\ & + \frac{\phi_m}{\tau_h} D_k (\zeta^{-(D_f-2)} + K_n^{-1})^{-1} \\ & + \frac{1 + \phi_m}{\phi_m} \rho_s \rho_{ga} \frac{V_L P_L}{(P_L + p_m)^2} D_s. \end{aligned} \quad (16)$$

3.3. Two-Phase Flow in the Fractured Zone. The two-phase flow of gas and water occurs in the microfractures of the fractured zone, where the wetting phase is water and the nonwetting phase is gas. Their governing equations are obtained from the mass conservation laws of water and gas, respectively [34].

For the water phase:

$$\frac{\partial(\phi\rho_w s_w)}{\partial t} + \nabla \left(-\frac{k k_{rw}}{\mu_w} \rho_w \nabla p_w \right) = f_w, \quad (17)$$

For the gas phase:

$$\frac{\partial(\phi\rho_{nw} s_{nw})}{\partial t} + \nabla \left(-\frac{k k_{rnw}}{\mu_{nw}} \rho_{nw} \nabla p_{nw} \right) = f_{nw}, \quad (18)$$

where k is the absolute permeability of the fractured zone. ϕ is the porosity of the fractured zone. μ_w and μ_{nw} are the viscosities of water and gas under in situ conditions, respectively. p_w is the pore pressure of water in the fractures and p_{nw} is the pore pressure of gas in the fractures. s_w denotes the saturation of water and s_{nw} denotes the saturation of gas. k_{rw} and k_{rnw} are the relative permeabilities of water and gas, respectively. Saturation, capillary pressure and relative permeability satisfy capillary pressure model and relative permeability model as given in the appendix. At the right term, f_w and f_{nw} are the sources of water and gas, respectively. f_{nw} has two sources: one is the gas exchange between fractures and matrix in the fractured zone (zone 2); the other is the generated gas source at site. The gas from zone 1 is input into zone 2 as a boundary source.

3.4. Two-Phase Flow in Hydraulic Fractures. In the two-dimensional computational model of this study, the hydraulic fractures are expressed by one-dimensional lines. The two-phase flow in hydraulic fractures still follows the Darcy law. The porosity of hydraulic fractures is usually enhanced or limited by the effects of pressure, swelling, and geochemical reaction [35]. Xu et al. [36] indicated that 30% of the effective fracture volume is lost due to pressure depletion during early-time water flowback. In this study, these effects are not considered for hydraulic fractures and thus the porosity of each hydraulic fracture is constant. Therefore, the mass conservation equations along a hydraulic fracture are as follows.

For water

$$d_{hf} \frac{\partial}{\partial t} (\rho_w \phi_{hf} S_w) + \nabla_T \left(-d_{hf} \rho_w \frac{k_{hf} k_{rw}}{\mu_w} \right) = d_{hf} Q_w, \quad (19)$$

For gas

$$\begin{aligned} d_{hf} \frac{\partial}{\partial t} (\rho_{nw} \phi_{hf} S_{nw}) + \nabla_T \left(-d_{hf} \rho_{nw} \frac{k_{hf} k_{rnw}}{\mu_{nw}} \right) \\ = d_{hf} Q_{nw}, \end{aligned} \quad (20)$$

where d_{hf} is the average width of a hydraulic fracture. ϕ_{hf} and k_{hf} are the porosity and permeability of the hydraulic fracture, respectively. Q_w represents the source or sink of water and Q_{nw} represents the source or sink of gas.

4. Model Validations

The above fully coupled model describes the multiphysical processes and interactions in different scales, including two-phase flow, capillary pressure, relative permeability, and multiscale diffusion. This formulates a fully coupled flowback model for the two-phase flow simulations of the shale gas

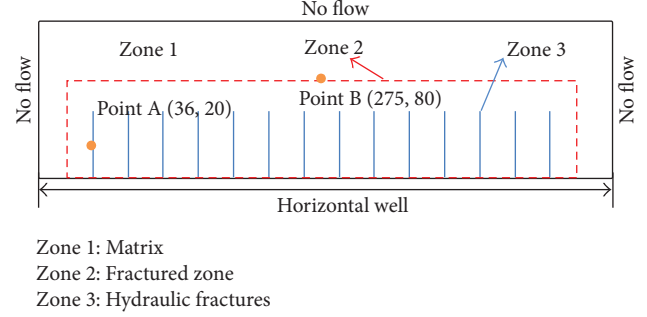


FIGURE 3: Computational model for fractured shale reservoirs.

production in a fractured shale reservoir. COMSOL Multiphysics, a commercial partial differential equation solver, is used for its implementation. This fully coupled model is validated through following two examples.

4.1. Example 1: Comparison of Single-Phase and Two-Phase Flows. The gas production is predicted and compared with single-phase flow and two-phase flow models. Yu and Sepehrnoori [16] performed the history matching with two sets of field gas production data from the Barnett shale and the Marcellus shale. They analyzed the contribution of gas desorption and geomechanics on gas production through single-phase flow. The immediate two-phase flow was also observed in the Barnett shale [37]. Therefore, our fully coupled model is applied to the Barnett shale. A typical computational model is set up in Figure 3. This model is 550 m long and 145 m high, and the initial reservoir pressure is 20.34 MPa. This horizontal well is located at the bottom boundary with a fixed pressure (3.45 MPa), and no-flow is assumed at its left and right boundaries. The simulation parameters and hydraulic fractures for the Barnett shale are listed in Table 1. The parameters used in this simulation are taken from the paper of Yu and Sepehrnoori [16]. Most of the parameters are the same as those they used. This example has no water flowback data available, thus we take longer gas production time than two-phase flowback period for comparison. The numerical results are used to validate the prediction accuracy of long-term gas production with two-phase flowback model. The comparison of the simulation results and field data is presented in Figure 4. This figure observes that the two-phase flowback model better matches with actual gas production data than single gas flow model. After 200 days, the gas production rate declines by 80%, reaching the value of 5×10^4 m³/d. The flow rate of simulation is little lower than that from the field data during the later production. That is because the permeability in the actual condition would be higher than the uniform hydraulic fracture in the simulation model. The hydraulic fractures are usually multiscale and contact with natural fractures to form a complicated fracture network. Thus, uniform fractures are not sufficient to describe this problem. The effects of fracture properties should be further discussed in four aspects: fracture spacing, fracture width, fracture uniformity, and fracture geometry. This will be done in Section 5.2.

TABLE 1: Model parameters for Barnett shales.

Parameter	Unit	Value	Physical meanings
S_{rmw}		0.15	Residual saturation of gas
S_{rw}		0.6	Residual saturation of water
μ_w	Pa*s	3.6×10^{-4}	Water viscosity
λ_w		2	Pore size distribution index
N_w		2	Corey parameter for water
N_{nw}		2	Corey parameter for gas
P_i	MPa	20.34	Initial reservoir pressure
h_f	m	47.2	Fracture half-length
P_b	MPa	3.45	Well pressure
k_0	mD	0.7	Initial permeability in fractured zone
ϕ_0		0.2	Initial porosity in fractured zone
k_{hf}	mD	50	Permeability in hydraulic fracture
ϕ_{hf}		0.25	Porosity in hydraulic fracture
ϕ_f		0.03	Initial porosity in microfracture of matrix
ϕ_m		0.01	Initial porosity in matrix
N_f		14	Number of hydraulic fractures
p_e	MPa	2	Entry capillary pressure
ν		0.3	Poisson's ratio of shale
ρ_s	kg/m ³	2300	Shale density
P_L	MPa	6	Langmuir pressure of gas in shale
V_L	m ³ /kg	0.03	Langmuir sorption capacity of shale for gas
k_{rw}^{max}		0.9	End-point relative permeability for water phase
k_{rnw}^{max}		1	End-point relative permeability for gas phase
T	K	352	Reservoir temperature
d_f	m	1×10^{-7}	Aperture of microfracture in matrix
d_m	m	1×10^{-9}	Diameter of pore in matrix
d_{hf}	m	0.003	Hydraulic fracture width

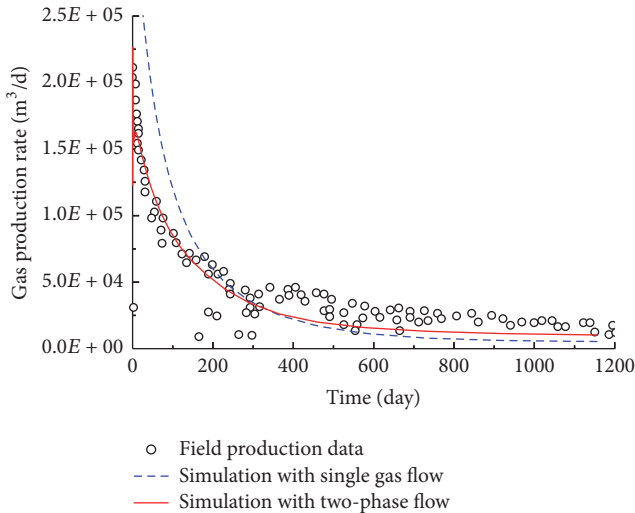


FIGURE 4: Comparison of numerical simulation and site production in Barnett shale reservoir.

4.2. *Example 2: Two-Phase Flowback Data of a China Shale Gas Well.* Further, both gas and water productions from an actual shale gas well [17] are used to verify this model.

This computational model is 1380 m long and 250 m high and has 11 hydraulic fractures. The initial reservoir pressure is 27.4 MPa and the bottomhole pressure is 19.67 MPa. Its left and right boundaries are assumed to be no-flow. The parameters in simulations are taken from Yang et al. [17] and listed in Table 2. The gas production rate is presented in Figure 5(a) and the water flow rate is compared in Figure 5(b). It is noted that gas flow rate rapidly increases and reaches the maximum of 2×10^5 m³/d at the 10th day and then follows a slight decline. The water flowback rate has a rapid decrease from 22 m³/d to 2.8 m³/d after the first 50 days and then keeps stable during the flowback period up to 200 days. Our simulations are in a good match with both production rates of gas and water.

These two examples verify the applicability of this fully coupled model to different time periods. Example 1 focuses on the prediction accuracy of long-term gas production when the two-phase flowback is considered. Example 2 compares the production data of both water and gas in the early production period. These two examples suggest that this fully coupled model is feasible to evaluate the gas production in short-term and long-term period.

TABLE 2: Simulation parameters for field data.

Parameter	Unit	Value	Physical meanings
S_{rmw}		0.15	Residual saturation of gas
S_{rw}		0.2	Residual saturation of water
λ_w		2	Pore size distribution index
N_w		2	Corey parameter for water
N_{nw}		2	Corey parameter for gas
P_i	MPa	27.4	Initial reservoir pressure
h_f	m	143	Fracture half-length
P_b	MPa	19.67	Well pressure
k_0	mD	0.0008	Initial permeability in fractured zone
ϕ_0		0.08	Initial porosity in fractured zone
k_{hf}	mD	0.1	Permeability in hydraulic fracture
ϕ_{hf}		0.25	Porosity in hydraulic fracture
ϕ_f		0.03	Initial porosity in microfracture of matrix
ϕ_m		0.01	Initial porosity in matrix
N_f		11	Number of hydraulic fractures
p_e	MPa	2	Entry capillary pressure
ν		0.3	Poisson's ratio of shale
ρ_c	kg/m ³	2630	Shale density
P_L	MPa	6	Langmuir pressure of gas in shale
V_L	m ³ /kg	0.03	Langmuir sorption capacity of shale for gas
T	K	327.6	Reservoir temperature

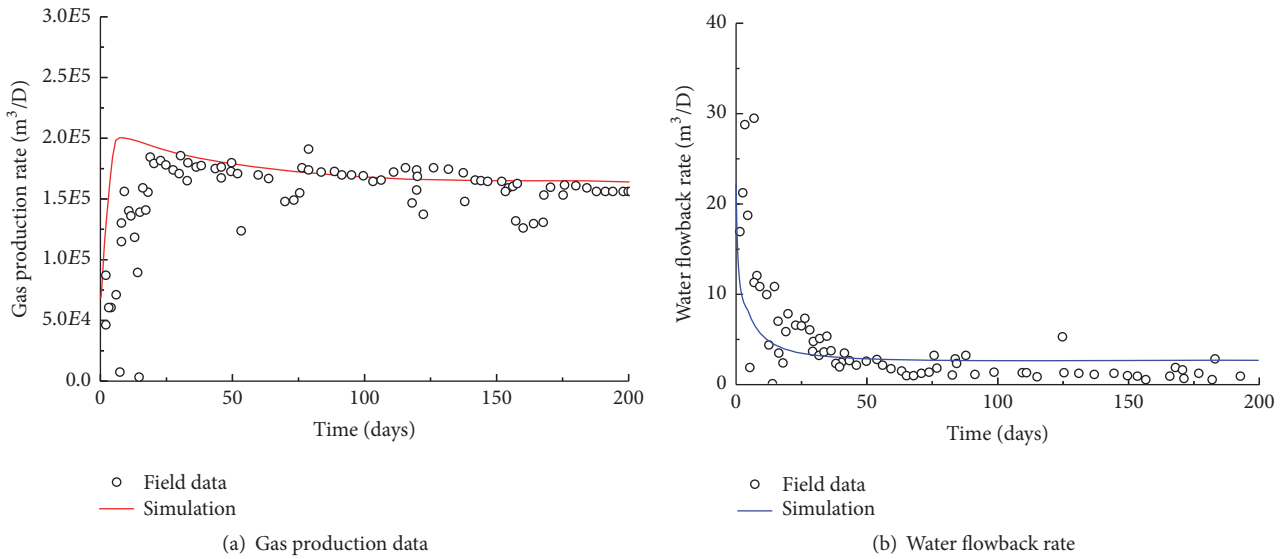


FIGURE 5: Comparison of numerical simulation with field production data at some China shale gas well.

5. Parametric Study and Discussions

5.1. Impact of Two-Phase Flowback on Gas Production in the Early Period. The impact of two-phase flowback on gas production in the early period is investigated here. The two-phase flowback usually occurs in zones 2 and 3, because the water-based fracturing fluid can only penetrate into such a range [38]. Figure 6 compares the cumulative gas productions with and without the consideration of two-phase flowback.

Generally, the cumulative gas production increases rapidly in the early 100 days. This increase then starts to slow down until 230 days. At this time, the cumulative gas production reaches 1.3×10^7 m³ for the case of two-phase flowback and is 2.07×10^7 m³ for the case of single-phase gas flow. Obviously, the cumulative gas production is much lower if the two-phase flowback is considered. On the other hand, the two-phase flowback would affect the gas production in the early period. This may be the reason why the previous models based on

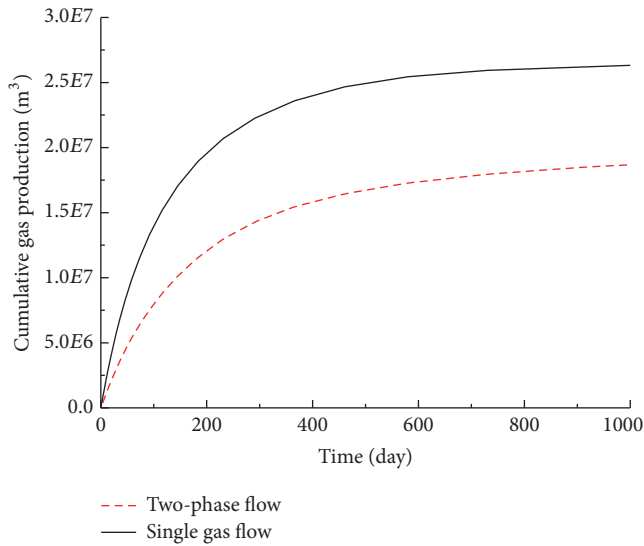


FIGURE 6: Comparisons of cumulative gas production for single-phase gas flow and two-phase flow.

single-phase gas flow usually have a higher production rate than actual field data.

5.2. Impacts of Fracture Properties on Gas Production. As a fine tune, the impacts of fracture properties on the long-term gas production are investigated. The following four parameters are chosen: the fracture spacing, the fracture width, the fracture uniformity, and the fracture geometry. They describe the fracture properties in the two-phase flow process. This parametric study is to explore the favorable fracture properties for the enhancement of long-term gas production.

5.2.1. Effect of Fracture Spacing. The fracture spacing is an index to express the density of fractures generated in a fixed domain which has a definite volume. In this computation, each fracture has the same properties, but 14 hydraulic fractures are distributed in the hydraulic fractured zone with different spacings. Two fracture spacings of 36.2 m and 25 m are assumed. Figure 7 compares the gas production rate under these two spacings. In the same region, more sparse distribution of hydraulic fractures means larger stimulated reservoir volume (zone 2) and less matrix volume (zone 1). Thus, the pressure nearby hydraulic fracturing zone decreases more quickly and the gas in the fractured zone can flow into the well more easily. With the process of gas production, the difference of gas production rate under different fracture spacings gradually vanishes due to the completion of pressure. The gas production rate with fracture spacing of 25 m is higher than that of the original model at later production time because the gas in the zone 1 begins to flow into the well.

5.2.2. Effect of Fracture Width. The fracture properties such as fracture conductivity heavily change with fracture width. In this subsection, the effect of fracture width on gas production

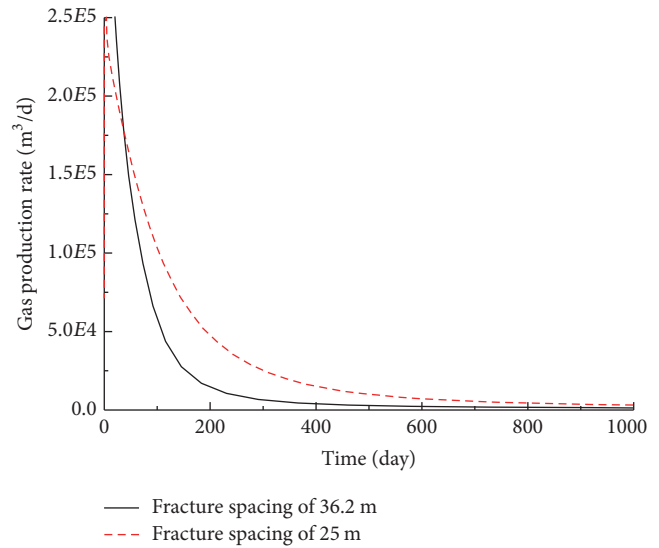


FIGURE 7: Effect of fracture density on gas production rate.

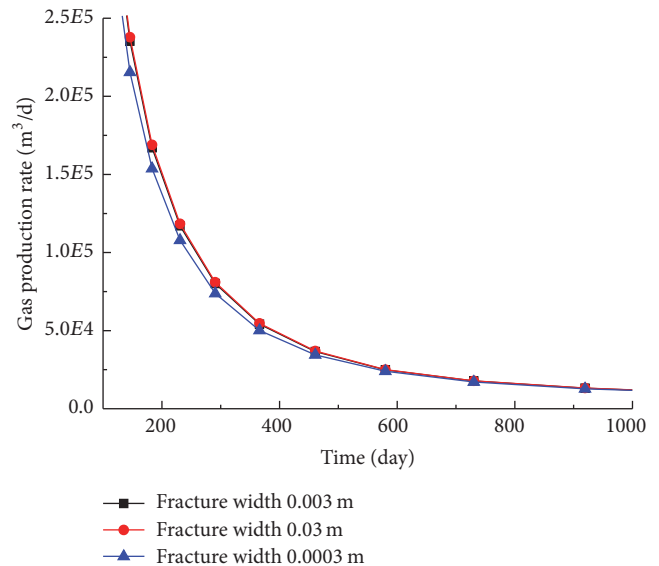


FIGURE 8: Effect of fracture width on gas production rate.

is examined. The fracture width is taken as 0.03, 0.003, and 0.0003 m, respectively. As shown in Figure 8, the gas production rate declines rapidly. However, the history curves are almost identical regardless of fracture width. This implies that the gas production rate is not controlled by the conductivity of fracture. This is reasonable because fracture only provides a channel for gas flow. When its capacity is larger than the demand for gas flow, the fracture does not affect the gas flow any more.

5.2.3. Effect of Fracture Uneven Length. After the treatment of hydraulic fracturing in shale gas reservoirs, a complex fracture network can be generated in the fractured zone. In the previous discussion, the hydraulic fractures are assumed to have equal length, called uniform fracture length. The

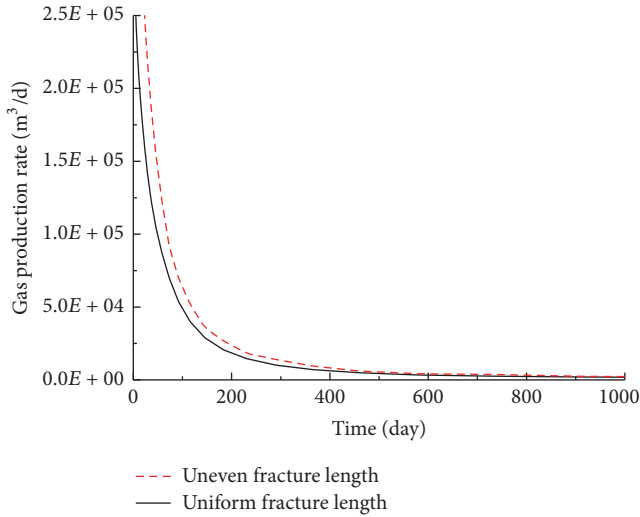


FIGURE 9: Effect of fracture uniformity on gas production rate.

fracture length may vary in the actual field. In order to evaluate the impact of fracture length on gas production rate, the total length of fractures is kept constant but each fracture has different length. This case is called uneven fracture length. The gas production rates of these two cases are compared in Figure 9. The gas production rate with the uniform fracture length decreases quickly and soon falls to a low point. After the production of 230 days, the gas production rate decreases to approximate $1.06 \times 10^4 \text{ m}^3/\text{d}$. The gas production rate with the uneven fracture length only declines to about $7 \times 10^3 \text{ m}^3/\text{d}$ at 230 days. This may be a good explanation why the simulated gas production rate with uniform fracture length is lower than the actual filed data.

5.2.4. Effect of Fracture Geometry. In the simulation model, the hydraulic fracture is usually assumed to be a straight line. This may deviate from the real case where the complicated fracture network is formed. The assumption of straight line may affect the distributions of gas and water pressure, further changing the gas production rate. In order to reveal the effect of fracture geometry on gas and water production, the gas drainage maps are presented in Figure 10. After the 36.5 days, the fractures in both geometry 1 and geometry 2 have their own drainage area. The hydraulic fractures would have an interference with neighboring fracture network to form an integrated drainage area. The drainage area varies with the geometric shape of fractures. If the height of fracture is the same, the length of fracture in geometry 2 is longer because of tortuosity. This means that the hydraulic fracture has a larger contact area with the surrounding fractured zone. Figure 11 compares the gas production rates in geometries 1 and 2. Because geometry 2 adds the contact area, its gas production rate is always higher. This effect is similar to that of fracture uniformity.

As a summary, both fracture uniformity and geometry shape add the complexity of fracture network. Their effects on gas production rate are similar. Denser distribution of

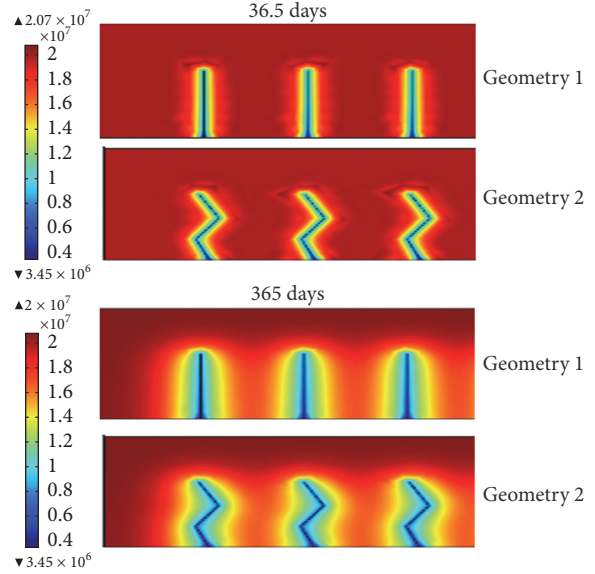


FIGURE 10: Effect of fracture geometry on gas pressure at the early and late production periods.

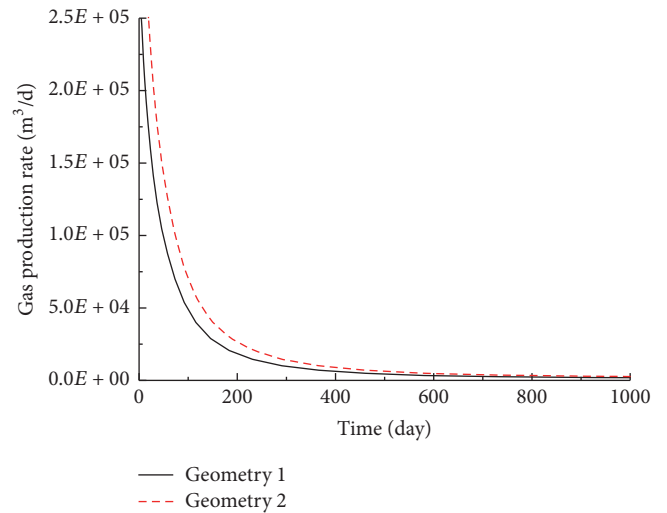


FIGURE 11: Effect of fracture geometry on gas production rate.

hydraulic fractures means higher level of hydraulic fracturing and can enhance the gas production. However, the increase of hydraulic fracture width has less influence on gas production, if the hydraulic fracture width is larger than some value.

5.3. Evolution of Capillary Pressure. Capillary pressure ($p_c = p_{nw} - p_w$) is the difference between gas pressure p_{nw} (the nonwetting phase) and water pressure p_w (the wetting phase). It is an important parameter in two-phase flow and is affected by many factors like wettability, contact angle, pore size distribution, and permeability. When the capillary pressure is higher, the gas production rate is greater at the beginning

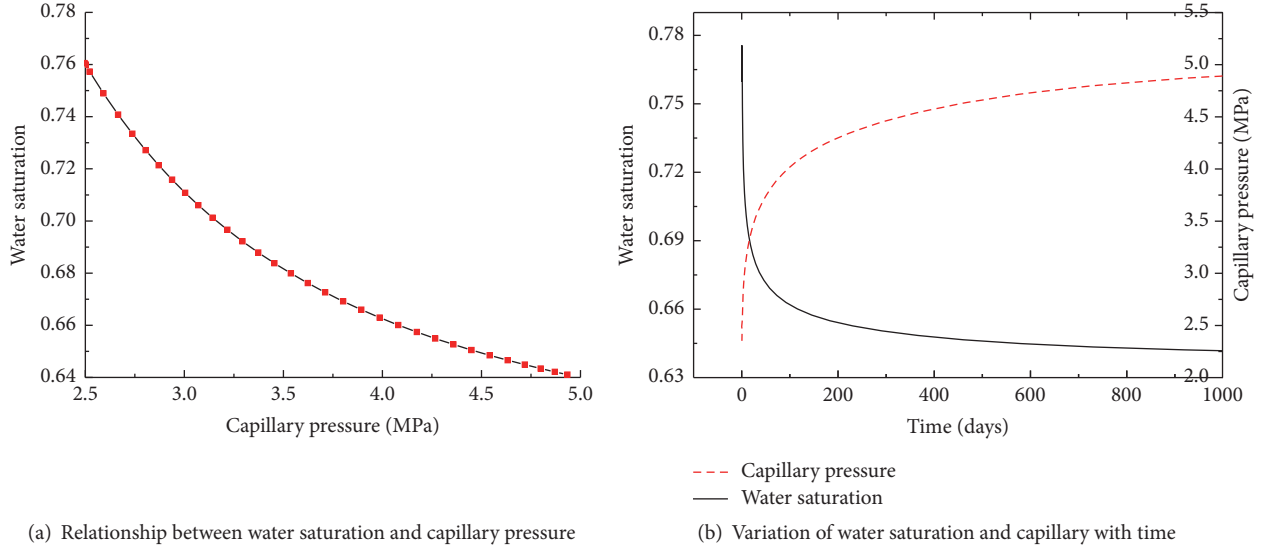


FIGURE 12: Change of water saturation and capillary with time at point A (36, 20) near the hydraulic fracture.

of flowback but declines later [39]. The water saturation is a function of capillary pressure as

$$s_w = \left(\frac{p_e}{p_c} \right)^{\lambda_w} (1 - s_{rnw} - s_{rw}) + s_{rw}. \quad (21)$$

This equation shows that the capillary pressure is directly related to water saturation. The point A (36, 20) near the hydraulic fracture is selected for observation. The evolution of water saturation with capillary pressure is plotted in Figure 12(a). The changes of water saturation and capillary pressure with time at this point A are plotted in Figure 12(b). During the gas production, the water originally in the fracture is extracted with the two-phase flowback. The capillary pressure changes from 2.4 MPa to 5 MPa. This reflects the process of gas-water displacement. As a sequence, the water saturation declines from 0.78 to 0.66 after almost 100 days. In computation, the irreducible water saturation is specified as 0.6. The free water in the fractured zone is too little to form water flow when the water saturation at point A decreases to 0.66. The remaining water adsorbs on the surface of matrix and may form a thin film of water [40]. As the gas production continues, the water would be extracted with gas flow.

5.4. Impact of Entry Capillary Pressure. Entry capillary pressure describes the occurrence of gas-water displacement and directly depends on the aperture of fracture [35]. This entry capillary pressure varies with rock type and a typical range of 0.1–48.3 MPa was observed [41]. In this study, the effect of entry capillary pressure on gas production is investigated when entry capillary pressure is taken as 2, 4, and 6 MPa, respectively. The effect is presented in Figure 13(a) on gas production rate and in Figure 13(b) on water production rate. Both gas and water production rates decrease with the increase of entry capillary pressure. At production of 100 days, the water flowback rate declines to almost $98.8 \text{ m}^3/\text{d}$ for $P_e = 2 \text{ MPa}$, which is higher 35.5% than that at $P_e = 6 \text{ MPa}$.

This difference of gas production rate due to entry capillary pressure is larger at 100 days. These results show that the increase of entry capillary pressure has much more increasing impacts on gas production rate than on water flowback rate.

5.5. Contribution of Multiscale Diffusion Mechanism to Gas Production. The shale gas production rate has been investigated by single-scale models, in which the fractured zone has hydraulic fractures with high permeability and matrix with low permeability. Such models ignore the microfractures in matrix. This may lose the prediction accuracy of gas production rate. If the matrix is only treated as a porous medium with extremely low permeability, the microscale gas diffusion cannot be described. This produces lower gas production than the actual field data. This section will use our fully coupled model (called multiscale model) to discuss the evolution of permeability in the fractured zone and the apparent permeability in microfractures of matrix. The gas pressure in matrix and the gas exchange rate as the gas source between microfractures and matrix are also discussed in a long-term gas production.

5.5.1. Fracture Permeability. When a large amount of water-based fracturing fluid is extracted with two-phase flow, the gas pressure in the fractured zone is lower than its initial value. At this time, the gas absorbed on the surface of matrix begins to flow into the fractured zone through the microscale diffusion and flow mechanism. Figure 14(a) gives the comparison of gas production rates in single-scale and multiscale models. The gas production rate with multiscale diffusion is always higher than that with single-scale diffusion. Because of microscale diffusion, the gas in microfractures would offer a stable source to gas production. The cumulative gas production is shown in Figure 14(b). Before the production of 100 days, the cumulative gas productions in single-scale and multiscale models are almost the same. The gap between

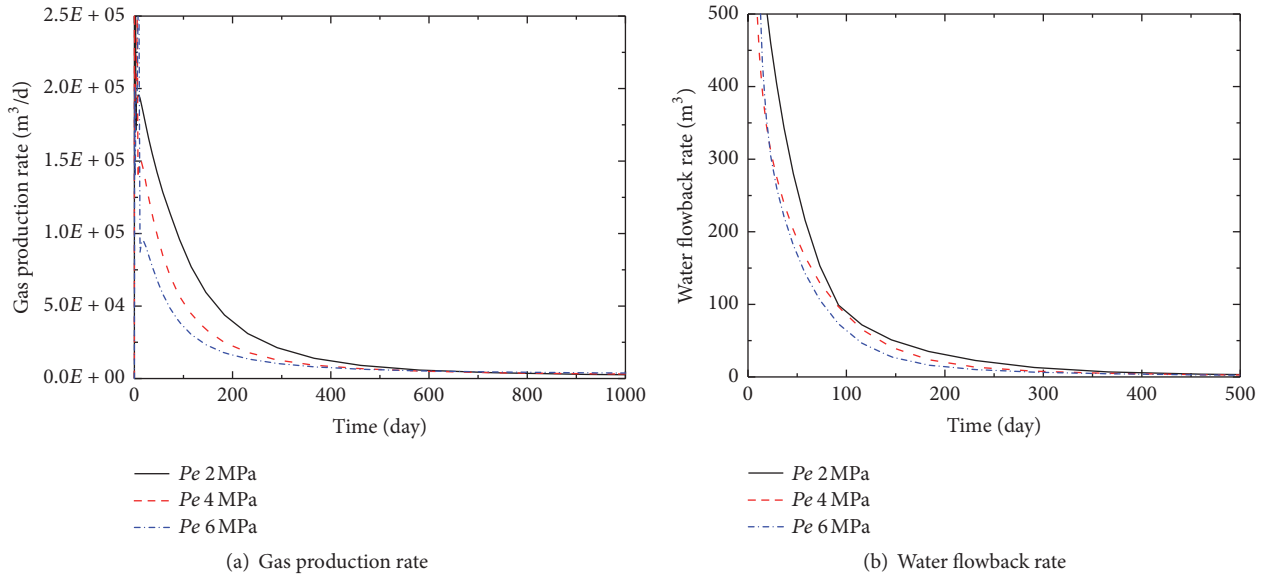


FIGURE 13: Impact of entry capillary pressure on gas and water flowback rates.

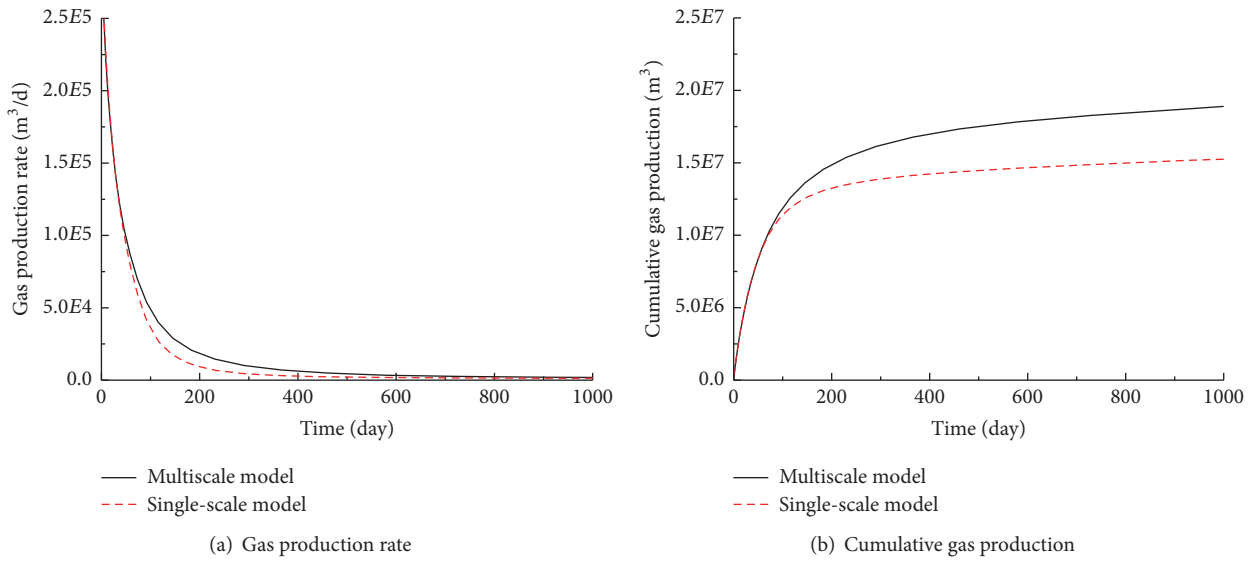


FIGURE 14: Comparison of gas production prediction by multiscale and single-scale models.

single-scale model and multiscale model is 21.9% after 580 days. These results indicate that gas flows in zones 2 and 3 dominate the early gas production. During this period, the contribution of microscale gas diffusion in the matrix can be ignored. As the gas production continues, most of gas in the fractures is extracted and the gas pressure begins to decline. Due to the pressure difference, the gas in matrix flows into the fractured zone. This process becomes significant in gas production and the effect of microscale diffusion and flow on gas production is presented. Therefore, the microscale diffusion and flow mechanism in matrix should be carefully considered, especially for the gas production in the later period.

The permeabilities of microfractures in matrix and fractured zone are in different orders of magnitude. The evolution of permeabilities in matrix and fractured zone at point B (275, 80) are presented in Figure 15. Due to the decline of pore pressure induced by gas extraction, the pore volume in the fractured zone would decrease accordingly. Therefore, this permeability declines with production time. Such a decline is consistent with the curve of gas production rate. Finally, a 0.7% decrease of permeability in the fractured zone is observed. However, the apparent permeability of microfractures in matrix has the opposite variation. Because of the gas desorption, the matrix shrinks and the permeability of microfractures in matrix gradually increases, approaching

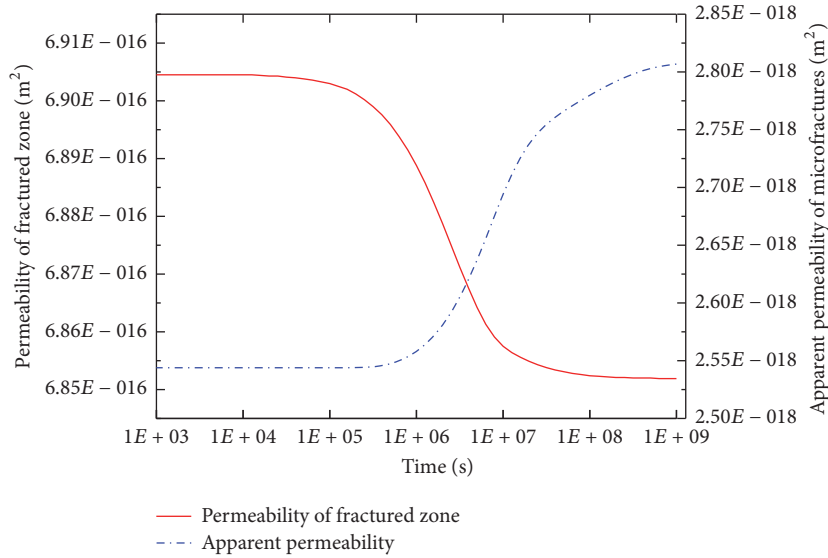


FIGURE 15: Evolution of permeabilities in fractured zone and microfractures of matrix.

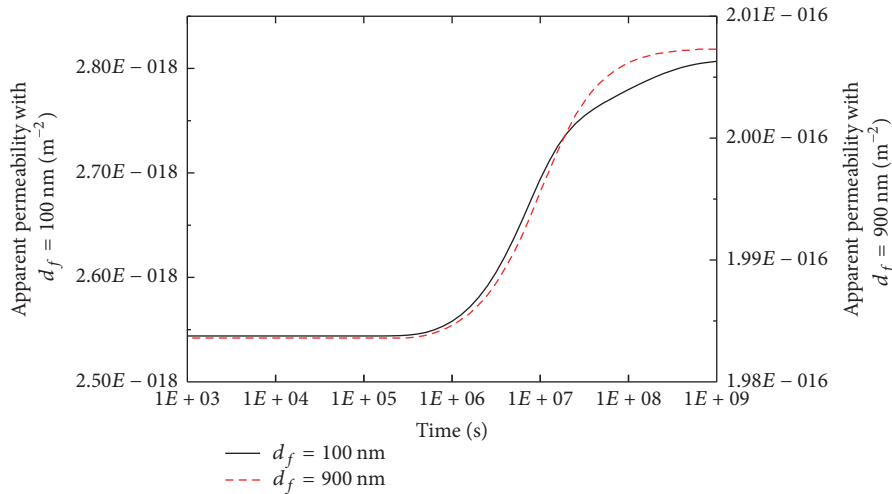


FIGURE 16: Evolution of apparent permeability with time under different aperture.

to the permeability in the fractured zone. Though the permeability of microfractures in matrix is a few orders of magnitude lower than that in the fractured zone, it increases by 10.4% compared to its initial value. If the microfracture size is bigger, the contribution of microscale diffusion and flow to gas production is greater.

5.5.2. Apparent Permeability. The above results indicate that the aperture of microfractures in matrix becomes a critical parameter to the gas exchange between fractured zone (zone 2) and matrix (zone 1). The aperture was observed to vary from 10 nm to 50 μm [42]. The value of aperture is used to divide the matrix system into microfractures and micropores in this paper. Here, the apertures of microfractures are assumed to be 100 nm and 900 nm, respectively. Figure 16 presents the variation of apparent permeability with aperture at point B. The black line represents the base case that was

presented in Figure 15. The red dashed line represents the apparent permeability when the microfracture aperture is 900 nm. This figure shows that the aperture of microfracture has important impacts on apparent permeability. When the aperture is 900 nm, the apparent permeability is nearly two orders of magnitude higher than the base case. This value would get closer to the permeability of fractures (zone 2) as the aperture increases. Previous study shows that with the pressure decline in the fractured zone, the gas in matrix flows into the fractured zone and dominates the gas production. The aperture of microfractures has a salient influence on the apparent permeability. Therefore, the gas in matrix through the microscale diffusion and flow is the key contribution to gas production, especially in the later production period.

5.5.3. Gas Exchange between Microfractures and Matrix. Pore size is an important parameter to gas production because

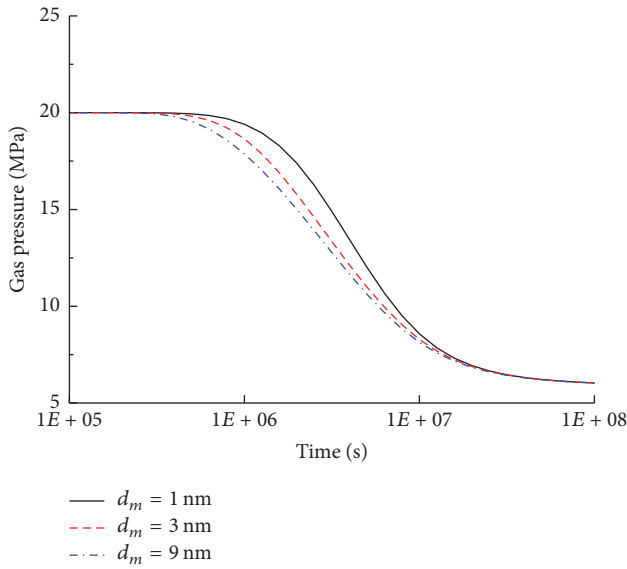


FIGURE 17: Gas pressures in matrix at different pore sizes.

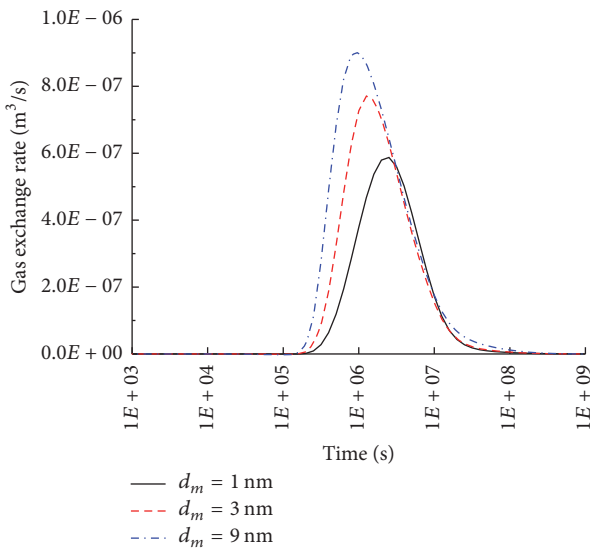


FIGURE 18: Variation of gas exchange rate with time at different pore sizes.

it is the channel of gas diffusion from the matrix into the microfractures. When the diameters of pores in matrix are assumed to be 1, 3, and 9 nm, respectively, Figure 17 presents the variation of gas pressure with diameter. It is found that the pore size is greater and the pressure drops faster. More gas desorbs from the surface of matrix when the diameter of pore in matrix is 9 nm. The impact of pore diameter on the gas exchange rate between matrix and microfractures is presented. These variation curves all present the shapes of mountain in Figure 18. Due to faster gas pressure drop, the gas exchange rate firstly increases when the diameter of pore is 9 nm. With the decrease of pore diameter, this increase of gas exchange rate would delay correspondingly. Further, the diameter of pore is bigger, the diffusion coefficient is

bigger, and the gas exchange rate reaches higher peak. That is because bigger diameter of pore is directly linked to higher matrix permeability. Finally, the gas exchange rate becomes zero. It means that the pressure in matrix and the pressure in microfractures reach a balance. More gas desorbs from the surface of matrix when the diameter of pore is bigger. This is the gas supply to gas production after the gas in the fractured zone is extracted.

6. Conclusions

This study numerically investigated the impact of water flowback in the water-based fracturing fluid on the short-term and long-term shale gas production. A fully coupled multiscale two-phase flowback model was proposed for the three zones model and the multiscale diffusion mechanisms were incorporated. Both water and gas production rates in the early period and the gas production rate in the later production period were studied under different fracture properties like fracture spacing, fracture width, fracture uniformity, and fracture geometry. The evolution curves of capillary pressure and water saturation, the contribution of multiscale diffusion to gas production, and the gas exchange between microfractures and matrix in different zones were explored. From these studies, the following conclusions can be made.

First, this fully coupled multiscale two-phase flowback model can not only describe the process of two-phase flowback in the early production period, but also well describe the impacts of fracture properties and multiscale gas diffusion in the later production period. It thus provides a useful tool for the assessment of gas production in the water-based fracturing process. The two-phase flow affects the gas production in the early and long-term periods. Our example shows that the cumulative gas production at 230 days has a 58.2% decline after considering the effect of two-phase flowback. Thus, the two-phase flowback should be carefully included when the gas production in fractured shale reservoirs is evaluated.

Second, the hydraulic fracture properties of fracture spacing, fracture width, fracture uniformity, and fracture geometry have variable influences on gas production rate. The increase of fracture density has an obvious positive enhancement on gas production rate. The uniformity and geometry of fractures have similar effects on gas production rate, particularly at the early production period. The fracture width may have no effect when it is larger than some value. The hydraulic fracture network in the actual field is interconnected and not uniform. Their impacts on gas production rate should be further studied.

Finally, the gas production rate with multiscale two-phase flow model is always higher than that with single-scale model. In microscale diffusion and flow mechanism, the gas in microfractures of matrix is a stable source to gas production. With gas extraction, the permeability of microfractures in matrix gradually increases and approaches to the permeability in the fractured zone. This phenomenon reflects the flow consistency in the macroscale flow and the microscale diffusion. The contribution from microfractures is

obvious when the aperture of microfractures increases, thus being not ignorable.

Appendix

The Evolution of Relative Permeability with Water Saturation

Altundas et al. [43] developed a normalized saturation s_w^* of wetting phase as

$$s_w^* = \left(\frac{p_e}{p_c} \right)^{\lambda_w} \quad (\text{A.1})$$

$$s_w = s_w^* (1 - s_{rnw} - s_{rw}) + s_{rw},$$

where $p_c = p_{nw} - p_w$ is the capillary pressure which is the difference between water pressure p_w (the wetting phase) and gas pressure p_{nw} (the nonwetting phase). λ_w is the pore size distribution index. s_{rw} and s_{rnw} are the irreducible saturations of wetting and nonwetting phases, respectively. p_e is the entry capillary pressure. Therefore, the compressibility with respect to capillary pressure is [34]

$$\begin{aligned} C_s &= \frac{\partial s_w}{\partial p_c} = \frac{\partial s_w}{\partial s_w^*} \cdot \frac{\partial s_w^*}{\partial p_c} \\ &= (1 - s_{rnw} - s_{rw}) \cdot \left[-\frac{\lambda_w}{p_e} (s_w^*)^{1+1/\lambda_w} \right]. \end{aligned} \quad (\text{A.2})$$

Various relative permeability models have been proposed for different gases and rock samples. The water saturation in matrix is assumed to be constant in the early flowback period [44]. Thus, matrix has only gas without water. Bachu and Benion [45] measured the relation of relative permeability and saturation for sandstone, carbonate, and shale formations. Under the in situ conditions of temperature, water salinity, and pore pressure, they directly linked relative permeability with saturation as

$$\begin{aligned} k_{rw} &= k_{rw}^{\max} (s_w^*)^{N_w} \\ k_{rnw} &= k_{rnw}^{\max} (s_{nw}^*)^{N_{nw}} \\ s_w^* &= 1 - s_{nw}^* \\ s_{nw}^* &= \frac{s_{nw} - s_{rnw}}{1 - s_{rw} - s_{rnw}}, \end{aligned} \quad (\text{A.3})$$

where k_{rw} and k_{rnw} are the relative permeabilities of water and gas, respectively. k_{rw}^{\max} and k_{rnw}^{\max} represent the endpoint relative permeabilities for water and gas, respectively. N_w and N_{nw} are the reference parameters. s_{nw} is the saturation of gas. s_{rw} is the water irreducible saturation, and s_{rnw} is the gas irreducible saturation.

Conflicts of Interest

The authors declare that they have no conflicts of interest.

Acknowledgments

The authors are grateful for the financial support from the National Natural Science Foundation of China (Grant nos. 51674246, 51674250) and Creative Research and Development Group Program of Jiangsu Province (2014-27).

References

- [1] S. Zahid, A. Bhatti, H. A. Khan, and T. Ahmad, "Development of unconventional gas resources: stimulation perspective," in *Proceedings of the Production Operations Symposium*, 2007.
- [2] A. Khlaifat, H. Qutob, and N. Barakat, "Tight gas sands development is critical to future world energy resources," *Society of Petroleum Engineers*, Article ID 142049, 2011.
- [3] A. Sharma, S. Namsani, and J. K. Singh, "Molecular simulation of shale gas adsorption and diffusion in inorganic nanopores," *Molecular Simulation*, vol. 41, pp. 414–422, 2015.
- [4] O. O. Owolabi, R. F. Volz, and P. S. Smith, "Can Shale-Like Stimulations Unlock the Potential of Extremely Low Permeability Tight Gas Reservoirs?" in *Proceedings of the Society of Petroleum Engineers*, 2013.
- [5] B. Yang, D. Luo, X. Zhang, D. Wu, and S. Shang, "A study of stress sensitivity of abnormal high pressure shale gas reservoir and reasonable productivity allocation," *Journal of Southwest Petroleum University*, vol. 38, no. 2, pp. 115–121, 2016.
- [6] O. D. Ezulike and H. Dehghanpour, "Modelling flowback as a transient two-phase depletion process," *Journal of Natural Gas Science and Engineering*, vol. 19, pp. 258–278, 2014.
- [7] M. A. Abbasi, D. O. Ezulike, H. Dehghanpour, and R. V. Hawkes, "A comparative study of flowback rate and pressure transient behavior in multifractured horizontal wells completed in tight gas and oil reservoirs," *Journal of Natural Gas Science and Engineering*, vol. 17, pp. 82–93, 2014.
- [8] P. Jia, L. Cheng, C. R. Clarkson, and J. D. Williams-Kovacs, "Flow behavior analysis of two-phase (gas/water) flowback and early-time production from hydraulically-fractured shale gas wells using a hybrid numerical/analytical model," *International Journal of Coal Geology*, vol. 182, pp. 14–31, 2017.
- [9] Y. Fu, H. Dehghanpour, D. O. Ezulike, and R. S. Jones, "Estimating effective fracture pore volume from flowback data and evaluating its relationship to design parameters of multistage-fracture completion," in *Proceedings of the SPE Production & Operations*.
- [10] W. Zhou, R. Banerjee, B. Poe, J. Spath, and M. Thambayagam, "Semianalytical production simulation of complex hydraulic-fracture networks," *SPE Journal*, vol. 19, no. 1, pp. 6–18, 2014.
- [11] J. Deng, W. Zhu, and Q. Ma, "A new seepage model for shale gas reservoir and productivity analysis of fractured well," *Fuel*, vol. 124, pp. 232–240, 2014.
- [12] J. Liu, J. G. Wang, F. Gao, Y. Ju, and F. Tang, "Impact of micro- and macro-scale consistent flows on well performance in fractured shale gas reservoirs," *Journal of Natural Gas Science Engineering*, vol. 36, pp. 1239–1252, 2016.
- [13] W. Y. Xie, X. P. Li, H. L. Zhang, X. H. Tan, J. C. Wang, and H. T. Wang, "Production decline analysis for two-phase flow in multifractured horizontal well in shale gas reservoirs," *Journal of Chemistry*, vol. 2015, no. 2, pp. 1–10, 2015.
- [14] J. W. Crafton and D. W. Gunderson, "Use of extremely high time-resolution production data to characterize hydraulic fracture properties," in *Proceedings of the SPE Annual Technical*

- Conference and Exhibition*, pp. 24–27, San Antonio, Tex, USA, 2006.
- [15] J. D. Williams-Kovacs, C. R. Clarkson, and B. Zanganeh, “Case studies in quantitative flowback analysis,” in *Proceedings of the SPE/CSUR Unconventional Resources Conference*, can, October 2015.
- [16] W. Yu and K. Sepehrnoori, “Simulation of gas desorption and geomechanics effects for unconventional gas reservoirs,” *Fuel*, vol. 116, pp. 455–464, 2014.
- [17] R. Yang, Z. Huang, G. Li et al., “An innovative approach to model two-phase flowback of shale gas wells with complex fracture networks,” in *Proceedings of the SPE Technical Conference and Exhibition*, 2016.
- [18] Y. Xu, O. A. Adefidipe, and H. Dehghanpour, “Estimating fracture volume using flowback data from the Horn River Basin: A material balance approach,” *Journal of Natural Gas Science and Engineering*, vol. 25, pp. 253–270, 2015.
- [19] D. O. Ezulike, H. Dehghanpour, C. J. Virues, R. V. Hawkes, and R. S. Jones, “Flowback fracture closure: A key factor for estimating effective pore volume,” in *Proceedings of the SPE Reservoir Evaluation & Engineering*, vol. 19, pp. 567–582, 2016.
- [20] A. Alkough, S. McKetta, and R. A. Wattenbarger, “Estimation of effective-fracture volume using water-flowback and production data for shale-gas wells,” *Journal of Canadian Petroleum Technology*, vol. 53, no. 5, pp. 290–303, 2014.
- [21] C. Li, R. Lafollette, A. Sookprasong, and S. Wang, “Characterization of hydraulic fracture geometry in shale gas reservoirs using early production data,” in *Proceedings of the International Petroleum Technology Conference*, 2013, <https://doi.org/10.2523/16896-MS>.
- [22] A. Alkough and R. A. Wattenbarger, “New advances in shale reservoir analysis using flowback data,” in *Proceedings of the Society of Petroleum Engineers Eastern Regional Meeting 2013: Bridging Experience and Technology*, pp. 555–570, usa, August 2013.
- [23] R. J. Ambrose, R. C. Hartman, M. Diaz-Campos, I. Y. Akkutlu, and C. H. Sondergeld, “Shale gas-in-place calculations Part I: New pore-scale considerations,” *SPE Journal*, vol. 17, no. 1, pp. 219–229, 2012.
- [24] H. Singh and F. Javadpour, “A new non-empirical approach to model transport of fluids in shale gas reservoirs,” in *Proceedings of the Unconventional Resources Technology Conference*, vol. 13, pp. 1258–1273, 2013.
- [25] F. Gao, J. Liu, J. G. Wang, Y. Ju, and C. F. Leung, “Impact of micro-scale heterogeneity on gas diffusivity of organic-rich shale matrix,” *Journal of Natural Gas Science Engineering*, vol. 45, pp. 75–87, 2017.
- [26] L. Zhang, C. Zhang, S. Tu, H. Tu, and C. Wang, “A study of directional permeability and gas injection to flush coal seam gas testing apparatus and method,” *Transport in Porous Media*, vol. 111, no. 3, pp. 573–589, 2016.
- [27] K. Lim and K. Aziz, “Matrix-fracture transfer shape factors for dual-porosity simulators,” *Journal of Petroleum Science Engineering*, vol. 13, no. 3–4, pp. 169–178, 1995.
- [28] F. Civan, “Effective correlation of apparent gas permeability in tight porous media,” *Transport in Porous Media*, vol. 82, no. 2, pp. 375–384, 2010.
- [29] I. Lunati and S. H. Lee, “A dual-tube model for gas dynamics in fractured nanoporous shale formations,” *Journal of Fluid Mechanics*, vol. 757, pp. 943–971, 2014.
- [30] X. Xiong, D. Devegowda, G. G. Michel Villazon, R. F. Sigal, and F. Civan, “A Fully-Coupled Free and Adsorptive Phase Transport Model for Shale Gas Reservoirs Including Non-Darcy Flow Effects,” in *Proceedings of the SPE Annual Technical Conference and Exhibition*, San Antonio, Tex, USA, 2012.
- [31] I. Yucel Akkutlu and E. Fathi, “Multiscale gas transport in shales with local kerogen heterogeneities,” *SPE Journal*, vol. 17, no. 4, pp. 1002–1011, 2012.
- [32] S. A. Hashemifard, A. F. Ismail, and T. Matsuura, “To what extent the conventional gas permeation testing method is reliable for membrane systems?” *Separation and Purification Technology*, vol. 114, no. 32, pp. 90–98, 2013.
- [33] K. Wu, X. Li, C. Wang, W. Yu, and Z. Chen, “Model for surface diffusion of adsorbed gas in nanopores of shale gas reservoirs,” *Industrial & Engineering Chemistry Research*, vol. 54, no. 12, pp. 3225–3236, 2015.
- [34] J. G. Wang and Y. Peng, “Numerical modeling for the combined effects of two-phase flow, deformation, gas diffusion and CO₂ sorption on caprock sealing efficiency,” *Journal of Geochemical Exploration*, vol. 144, pp. 154–167, 2014.
- [35] J. G. Wang, Y. Ju, F. Gao, Y. Peng, and Y. Gao, “Effect of CO₂ sorption-induced anisotropic swelling on caprock sealing efficiency,” *Journal of Cleaner Production*, vol. 103, pp. 685–695, 2015.
- [36] Y. Xu, H. Dehghanpour, O. Ezulike, and C. Virues, “Effectiveness and time variation of induced fracture volume: Lessons from water flowback analysis,” *Fuel*, vol. 210, pp. 844–858, 2017.
- [37] Y. Zhang and C. Ehlig-Economides, “Accounting for remaining injected fracturing fluid in shale gas wells,” in *Proceedings of the Unconventional Resources Technology Conference*, 2014.
- [38] X. Zhang, J. G. Wang, F. Gao, Y. Ju, and J. Liu, “Impact of water and nitrogen fracturing fluids on fracturing initiation pressure and flow pattern in anisotropic shale reservoirs,” *Computers Geotechnics*, vol. 81, pp. 59–76, 2017.
- [39] E. Ghanbari and H. Dehghanpour, “The fate of fracturing water: A field and simulation study,” *Fuel*, vol. 163, pp. 282–294, 2016.
- [40] T. Teng, J. G. Wang, F. Gao, Y. Ju, and C. Jiang, “A thermally sensitive permeability model for coal-gas interactions including thermal fracturing and volatilization,” *Journal of Natural Gas Science Engineering*, vol. 32, pp. 319–333, 2016.
- [41] N. Tonnet, G. Mouronval, P. Chiquet, and D. Broseta, “Petrophysical assessment of a carbonate-rich caprock for CO₂ geological storage purposes,” *Energy Procedia*, vol. 4, no. 4, pp. 5422–5429, 2011.
- [42] F. Javadpour, D. Fisher, and M. Unsworth, “Nanoscale gas flow in shale gas sediments,” *Journal of Canadian Petroleum Technology*, vol. 46, no. 10, pp. 55–61, 2007.
- [43] Y. B. Altundas, T. S. Ramakrishnan, N. Chugunov, and R. De Loubens, “Retardation of CO₂ caused by capillary pressure hysteresis: A new CO₂ trapping mechanism,” *SPE Journal*, vol. 16, no. 4, pp. 784–794, 2011.
- [44] J. D. Williams-Kovacs and C. R. Clarkson, “A modified approach for modeling two-phase flowback from multi-fractured horizontal shale gas wells,” *Journal of Natural Gas Science and Engineering*, vol. 30, pp. 127–147, 2016.
- [45] S. Bachu and B. Bennion, “Effects of in-situ conditions on relative permeability characteristics of CO₂-brine systems,” *Environmental Geology*, vol. 54, no. 8, pp. 1707–1722, 2008.

Research Article

Brittleness Evaluation of Shale Based on the Brazilian Splitting Test

Bing Hou,^{1,2} Yijin Zeng ,^{1,3} Meng Fan,² and Dandan Li^{1,3}

¹State Key Laboratory of Shale Oil and Gas Enrichment Mechanisms and Effective Development, Beijing 100101, China

²State Key Laboratory of Petroleum Resources and Engineering, China University of Petroleum-Beijing, Beijing 102249, China

³Sinopec Research Institute of Petroleum Engineering, Beijing 100101, China

Correspondence should be addressed to Yijin Zeng; yijinzen@163.com

Received 15 December 2017; Accepted 28 February 2018; Published 16 April 2018

Academic Editor: Xiangzhao Kong

Copyright © 2018 Bing Hou et al. This is an open access article distributed under the Creative Commons Attribution License, which permits unrestricted use, distribution, and reproduction in any medium, provided the original work is properly cited.

Brittleness is an important mechanical parameter of shale reservoirs and has a significant effect on hydraulic fracturing. Traditional evaluation methods of shale brittleness are mainly based on complete stress-strain curves under compressive loading, which can barely describe the fracture characteristics of shale during hydraulic fracturing. This paper proposes to define the brittleness index based on the Brazilian splitting test and establishes a corresponding evaluation method, forming a tensile brittleness evaluation system for noncontinuous shale. The Brazilian splitting test and discrete element numerical simulation are carried out to study the crack distribution characteristics after tensile failure as well as the influence of anisotropy and scale effect on the brittleness of shale. The results show that the tensile brittleness index is more accurate and sensitive to condition changes than the compressive brittleness index. The experimental shale cores are from the Longmaxi formation, Silurian system, Sichuan basin.

1. Introduction

Rock brittleness is the key index for evaluating reservoir geomechanical properties. It has a significant impact on hydraulic fracturing results. Scholars have different opinions on the definition of rock brittleness. Ramsay [1] defined brittleness as the ability to overcome intrinsic cohesion forces when brittle failure occurs in a material. Morley and Heteny [2, 3] proposed that brittleness is a deficiency of plasticity during material failure. Obert and Duvall [4] conducted experiments using rocks and suggested that the material slightly reaches or exceeds its yield strength during loading. The industry also put forward specific evaluation methods for calculating the brittleness index [5]. Rickman et al. [6] showed that rock brittleness is mainly influenced by the elastic modulus and Poisson ratio. They summarized their results from Barnett shale and proposed that the lower the Poisson ratio and the higher the elastic modulus are, the more brittle the rocks would be. Li et al. [7] considered the entire rock failure process based on the complete stress-strain curve,

evaluated brittleness using mechanical properties before and after the curve peak, and calculated the comprehensive brittleness index by combining the empirical formulas. Jarvie et al. [8] proposed a method to calculate brittleness index based on the brittle mineral content. In 2009, Wang and Gale [9] improved Jarvie et al.'s definition of brittleness by classifying dolomite as brittle mineral and organic matter as ductile mineral. In 2010, Chong et al. [10] used the brittle mineral content in shale combined with geomechanical parameters to represent the shale brittleness, which provides a quantitative basis for evaluating shale brittleness.

Jin et al. [11] defined the brittleness from the energy point of view. They suggested that rock is ductile if it absorbs a great deal of energy before failure; otherwise, the rock is brittle. The energy method in fracture mechanics can be used to reliably and quantitatively evaluate rock brittleness. The increase of rock ductility can be viewed as an increase of energy dissipation [12]. Chen et al. [13] put forward a brittleness evaluation method based on energy dissipation mechanism. They indicated that the larger the energy



FIGURE 1: Shale outcrops in Longmaxi formation.



FIGURE 2: Cores from the Longmaxi shale gas reservoir.

dissipation, the lower the brittleness index. Cai et al. [14] conducted tensile experiments to study fracture initiation and propagation behavior in brittle rocks. They believed that there is a correlation between the brittleness index and fracture initiation stress. During the process of tensile failure in rocks, microfractures initiate and extend until the sample is broken. The corresponding strength is almost equal to the rock tensile strength [15]. Once a microcrack occurs in tensile experiments in brittle rocks, the crack will propagate unstably [16], which shows that the rock tensile testing results agree with the fracture characteristics in shale hydraulic fracturing. Therefore, this paper overcomes the limitation of using the prepeak mechanical parameters and postpeak stress attenuation degree to represent rock brittleness, proposes the definition of the brittleness index based on tensile failure, presents a comprehensive evaluation method and prediction model, and forms a theoretical system for evaluating shale brittleness under tensile conditions.

2. Experimental Study of Shale Brittleness under Brazilian Splitting Testing

2.1. Shale Sampling and Processing. Shale cores are drilled from the 2400 m deep shale reservoir in the Longmaxi formation, Silurian system, Sichuan Basin. The shale outcrops of the Longmaxi formation have well-developed beddings and cracks, and most joints are beddings or cracks perpendicular to the bedding planes (Figure 1). By contrast, the downhole cores from the Longmaxi formation have high-density thin bedding lines on the sample surface (Figure 2).

Brazilian splitting tests are conducted on outcrops and downhole cores from the Longmaxi formation to evaluate the brittleness characteristics of shale.

Cylinder samples with a diameter of 25 mm and a height of 50 mm are drilled parallel to the bedding planes. Then, they are cut into disk samples with a diameter of 25 mm and thickness of 5 mm (Figure 3). The test angle is defined as the angle between the loading direction and the normal direction of the bedding planes. To study the brittle characteristics of shale under different test angles, a loading line parallel to the loading direction is drawn on each sample before the test.

2.2. Brazilian Splitting Test. The apparatus used to conduct the Brazilian splitting test is the RTR-1500 HTHP triaxial rock testing system produced by GCTS located in Tempe, Arizona, USA, as shown in Figure 4. The system is capable of testing and analyzing the acoustic velocity, permeability, in situ stress, and mechanical strength of cores in a high-temperature and high-pressure environment.

At the beginning of the test, samples are placed into an arc-shaped fixture, ensuring that the loading line is aligned with the loading direction (Figure 5). The test rack is then placed on the compression machine, which exerts small radial loading on samples through a pressure servo. During the tests, the loading stress increases slowly and steadily and the pressure head goes down constantly at a predefined speed until the sample fails.

2.3. Experimental Scheme and Results. Factors such as the buried depth, mineral content, coring angle, and test condition have a large impact on the mechanical characteristics of shale [17]. Therefore, core samples are divided into 4 groups according to their buried depth. In the second group, the test angles are set at 0° , 45° , and 90° . Since the loading rate has an impact on the mechanical behavior of rocks [18], different loading rates are used to analyze the sensitivity of shale brittleness to the loading rate. The experimental scheme is shown in Table 1.

Strain-stress curves are recorded during the experiments. By comparing the results under different test conditions (Figure 6), it can be found that shale outcrops have the lowest tensile strength. As the buried depth increases, the tensile strength of cores increases gradually. The mechanical parameters of shale are highly sensitive to the loading rate. The tensile strength of shale outcrops decreases gradually as the loading rate increases. The loading rate has an even larger impact on downhole cores, and the effect is also highly related to the bedding plane direction. Specifically, when the test angle is 45° , the tensile strength of downhole shale samples increases as the loading rate increases. Under high loading rates, shale tends to fail and forms multiple splitting planes; however, under low loading rates, tensile cracks are difficult to develop. Hence, the loading rate is set between 0.01 and 0.02 mm/min to guarantee the accuracy of the test results.

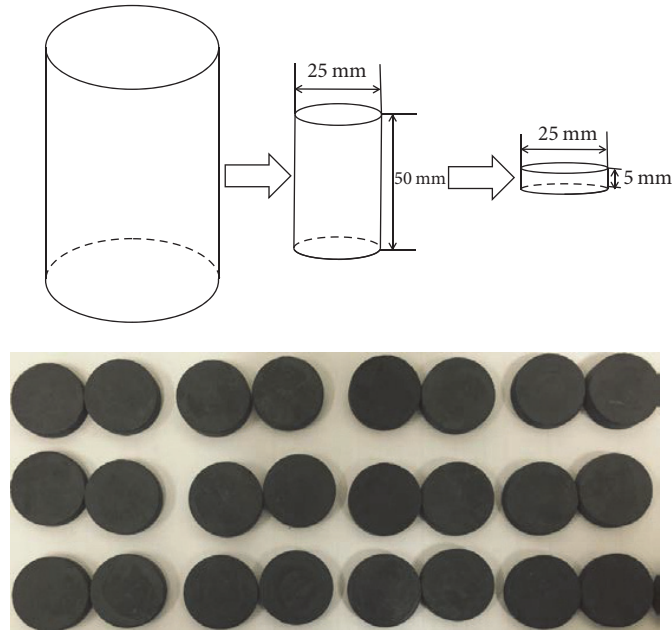


FIGURE 3: Schematic diagram of cores and disks used for Brazilian splitting testing.



FIGURE 4: RTR-1500 HTHP triaxial rock testing system.

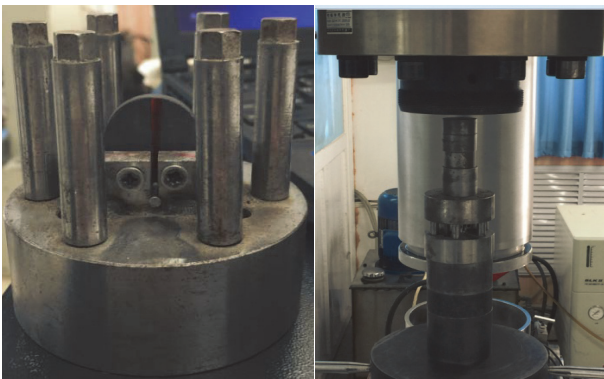


FIGURE 5: Brazilian splitting test rack.

3. Tensile Brittleness Evaluation Model Based on the Brazilian Splitting Test

3.1. Mechanism of Shale Brittleness Evaluation under Tensile Loading. Shale with developed cracks has high brittleness

[19]. However, when a triaxial compression test is conducted to evaluate brittleness, the fracture closure behavior strongly affects the experiment results (as shown in Figure 7(a)). On the contrary, when shale is under tensile loading, the bonding strength of the bedding planes decreases, forming a large number of microcracks, which then propagate and intersect each other. Hence, the prepeak part of the stress-strain curve of shale under tensile loading exhibits an obvious fluctuation behavior, reflecting the brittle characteristics of shale (as shown in Figure 7(b)).

SEM is utilized to scan the failed shale samples (as shown in Figure 8). At the initial phase of brittle failure, the cohesion and bonding forces between mineral grains decrease as the loading stress increases, causing the initiation of cracks in samples. As loading stress continues to increase, microcracks start to propagate and intersect with each other, forming macroscale cracks. When the brittle failure enters the stable phase, the friction force between fracture surfaces increases as the loading stress increases. During the stable phase, macroscale cracks bear most of the loading. The friction force vanishes the instant it reaches the maximum bearing capacity of the fracture surfaces, causing brittle failure of the rocks.

Three types of failure characteristics can be observed after Brazilian splitting testing (Figure 9).

(1) *Tensile Splitting*. The fracture plane has a linear shape, and its direction is parallel to the loading direction and perpendicular to the tensile stress direction. Under this circumstance, the surface profile is rough and the sample has the highest brittleness.

(2) *Tensile-Shear Failure*. The fracture plane has a half-moon shape. Due to the increase of the bonding strength between bedding surfaces, rock failure is suppressed and fractures

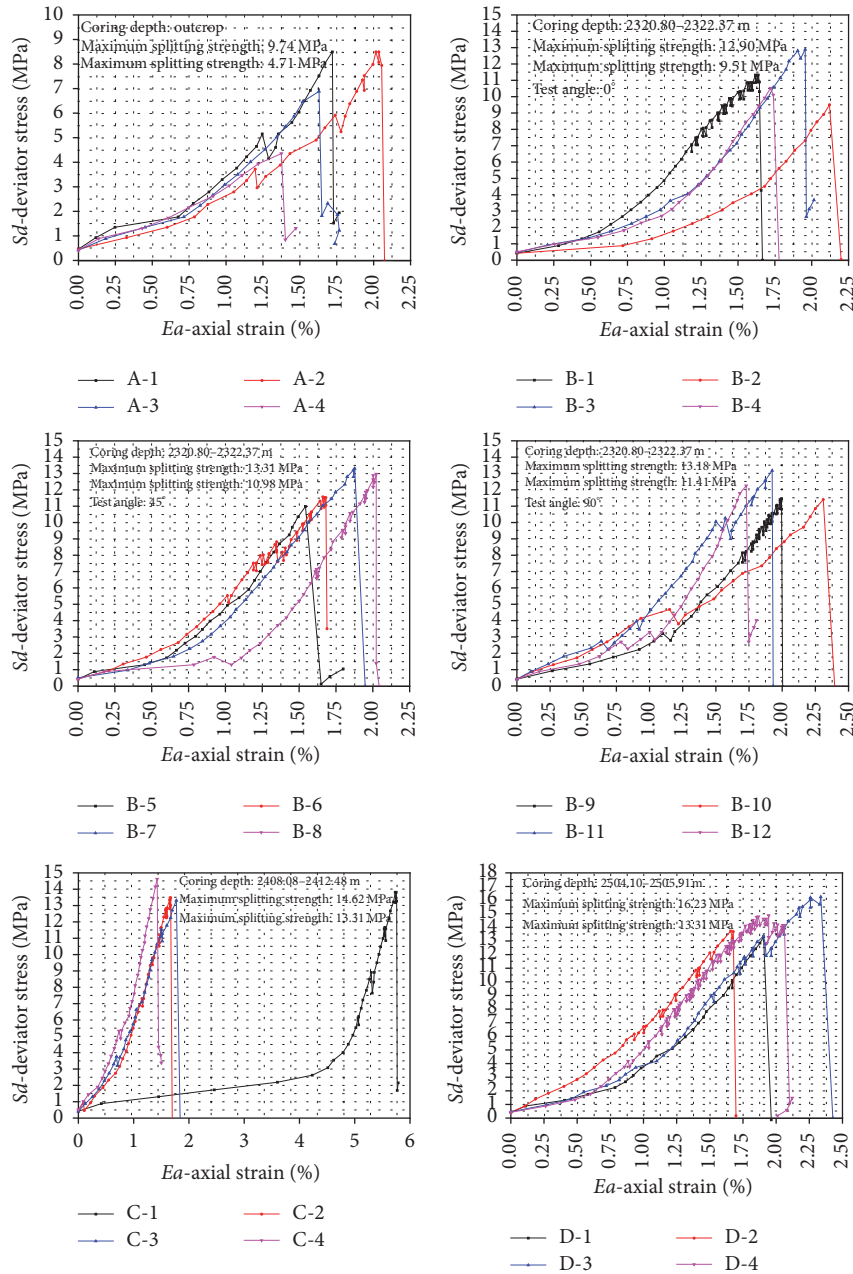


FIGURE 6: Stress-strain curves of the Brazilian splitting test.

propagate along the bedding planes and surrounding microcracks, causing tensile-shear failure. The shale brittleness under this condition is lower than the brittleness of shale which exhibits tensile splitting characteristics.

(3) *Shear Failure*. The fracture plane has a short curve shape. The fracture surfaces slip along the bedding planes, during which the shear force plays a leading role in rock failure. The shale brittleness is the lowest under this circumstance.

In the field fracturing operation process, when the wellbore internal pressure increases instantly, many microcracks form around natural weak planes under tensile loading before

formation fracture. Hence, the results are more consistent with the field condition when the brittle rock characteristics are evaluated under tensile loading.

3.2. Evaluation Model of Shale Brittleness under Tensile Loading

3.2.1. *Brittleness Index BI_E Based on Elastic Parameters*. Referring to the model proposed by Rickman et al. [6] that evaluates rock brittleness under compressive loading based on Young's modulus and Poisson's ratio, the elastic parameters of rock under tensile loading are used to evaluate shale

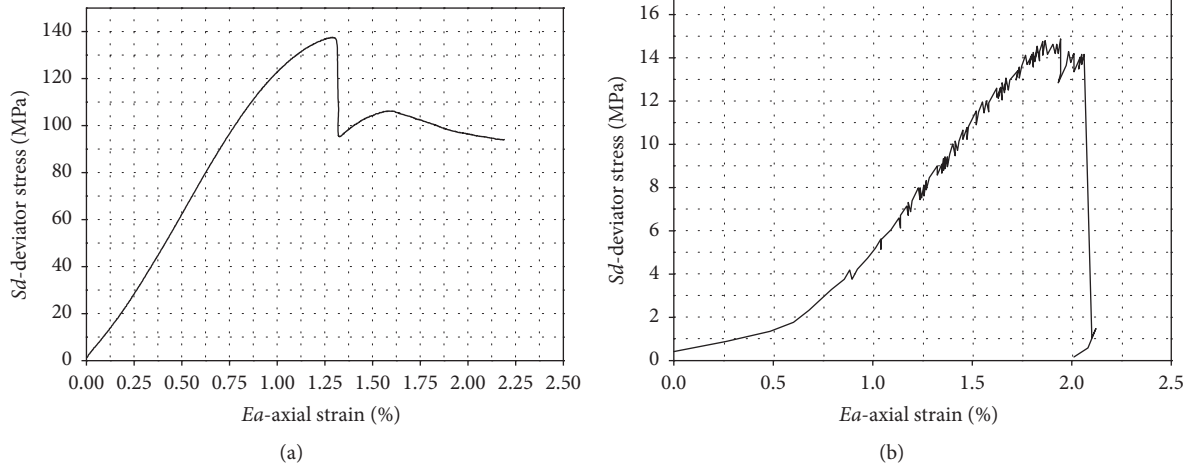


FIGURE 7: Stress-strain curves of shale under compressive and tensile loading.

TABLE 1: Experimental scheme.

Coring depth	Group	Sample number	Test angle ($^{\circ}$)	Loading rate (mm/min)
Outcrop	1	A-1	/	0.01
		A-2		0.02
		A-3		0.04
		A-4		0.05
2320.80 m–2322.37 m	2(1)	B-1	0°	0.01
		B-2		0.02
		B-3		0.04
		B-4		0.05
2320.80 m–2322.37 m	2(2)	B-5	45°	0.01
		B-6		0.02
		B-7		0.04
		B-8		0.05
2320.80 m–2322.37 m	2(3)	B-9	90°	0.01
		B-10		0.02
		B-11		0.04
		B-12		0.05
2408.08 m–2412.48 m	3	C-1	/	0.01
		C-2		0.02
		C-3		0.04
		C-4		0.05
2504.10 m–2505.91 m	4	D-1	/	0.01
		D-2		0.02
		D-3		0.04
		D-4		0.05

brittleness. Brazilian splitting tests are conducted to obtain Young's modulus and Poisson's ratio of shale under tensile loading. The elastic parameters are normalized to calculate the shale brittleness index BI_E under tensile loading:

$$BI_E = \alpha \bar{E} + \beta \bar{\nu}, \quad (1)$$

where \bar{E} is the normalized Young's modulus (GPa), $\bar{\nu}$ is the normalized Poisson's ratio, and α and β are correction factors. The value range of BI_E is 0~1. The more brittle the rock is, the closer BI_E is to 1.

3.2.2. Brittleness Index BI_{Pt} Based on the Curve Peak Characteristics. Smaller rock deformation before reaching peak

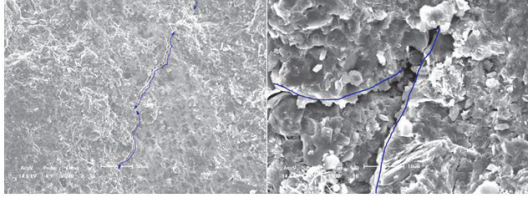


FIGURE 8: Intersection mode of microcracks of shale under tensile failure.



--> Loading direction
— Crack propagation direction

FIGURE 9: Three failure modes of shale in the Brazilian splitting test.

strength indicates a lower ductile deformation degree and higher brittleness [7]. The peak point in the stress-strain curve of rocks under tensile loading is chosen as the feature point of rock failure. Tensile strength characterizes the ability of rocks to resist damage, and the deformation at the peak point characterizes the deformation degree of rocks when they fail. Hence, the brittleness index BI_{Pt} based on the peak characteristics of the stress-strain curve can be calculated as follows:

$$BI_{Pt} = \left(\frac{P_t}{\varepsilon_t} \right), \quad (2)$$

in which P_t is the tensile strength (MPa) and ε_t is the deformation at peak point (%).

3.2.3. Brittleness Index BI_R Based on Energy Dissipation. From the perspective of energy dissipation, rock brittleness can be evaluated by the magnitude of the rock intrinsic cohesion and crack propagation resistance, and the latter reflects the unrecoverable nature of rock ductile failure [13]. The ratio of the rock intrinsic cohesion to the crack propagation resistance under tensile loading can be used to quantify the brittleness of rocks; thus, the brittleness index BI_R under tensile loading can be calculated as follows:

$$BI_R = \left(\frac{R_0}{R_\mu^\infty} \right), \quad (3)$$

where R_0 is the intrinsic cohesion of rocks and R_μ^∞ is the total fracture propagation resistance exerted by the frontal zone when stress reaches the peak value.

Three types of brittleness are obtained via the above three methods. Cores with brittleness indexes of a higher

TABLE 2: Brittleness indexes with large dispersion degree.

Sample number	BI_E	BI_{Pt}	BI_R	Standard deviation
B-1	0.62	0.80	0.11	0.3579
B-6	0.51	0.76	0.15	0.3066
B-10	0.67	0.27	0.18	0.2608
B-12	0.19	0.70	0.88	0.3579
C-1	0.16	0.02	0.74	0.3817
C-2	0.54	0.96	0.10	0.4300
D-2	0.50	1.00	0.17	0.4178
D-3	0.35	0.70	0.08	0.3108

dispersion degree are chosen as objects to compare the brittleness indexes obtained by different methods, as shown in Table 2.

It can be seen from the results that the three types of brittleness indexes are inconsistent with each other when they are used to evaluate rock brittleness. If only one of the three methods is used for evaluation, other factors affecting rock brittleness will be neglected, leading to uncertainties in the brittleness evaluation. Hence, a multiple regression method is utilized to calculate the comprehensive brittleness index of rock under tensile loading:

$$I_{BT} = m_1 BI_E + m_2 BI_{Pt} + m_3 BI_R + C, \quad (4)$$

where m_1 , m_2 , and m_3 are weight coefficients and C is the regression correction coefficient.

Calculation results with errors less than 0.1 are chosen to obtain the unknown coefficients in (4). The resulting equation is as follows:

$$I_{BT} = 0.3825 BI_E + 0.6218 BI_{Pt} + 0.1591 BI_R - 0.0376, \quad (5)$$

where the regression coefficients for BI_E , BI_{Pt} , and BI_R are 0.8075, 0.4271, and 0.6615, respectively.

The comprehensive brittleness index is used to evaluate the shale core brittleness, the results of which are shown in Table 3.

Compared with the brittleness index calculated under compressive loading, the brittleness index calculated under tensile loading is more sensitive and accurate.

4. Tensile Brittleness Evaluation Model Based on the Discrete Element Method

To simulate the failure and crack propagation process of shale during Brazilian splitting testing and verify the accuracy of the established brittleness evaluation model, the discrete element method is utilized to establish the Brazilian splitting test model for layered shale and conduct a numerical simulation on the tensile brittle failure of shale. The influence of factors such as the bedding plane angle and core scale effect on the tensile brittleness is analyzed based on the simulation results.

4.1. Discrete Element Model for the Tensile Brittleness Evaluation. A uniaxial compression simulation model is first

TABLE 3: Comprehensive brittleness index of shale.

Coring depth	Sample number	Comprehensive brittleness index I_{BT}
Outcrop	A-1	0.32
	A-2	0.5
2320.80 m–2322.37 m	B-1	0.71
	B-3	0.59
	B-4	0.43
	B-7	0.68
	B-8	0.62
	B-9	0.58
	B-10	0.42
2320.80 m–2322.37 m	B-12	0.61
	C-2	0.75
2408.08 m–2412.48 m	C-4	0.87
	D-1	0.56
2504.10 m–2505.91 m	D-2	0.80
	D-3	0.54
	D-4	0.63

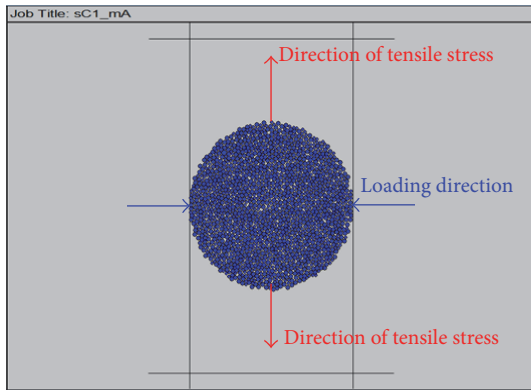


FIGURE 10: Schematic diagram of the loading direction.

established by PFC to help adjust the microscopic physical parameters by making the macroscopic physical parameters of the simulation model identical to those of the core samples used for laboratory uniaxial compression test. The detailed parameters of PFC model and the comparison between simulation model and rock sample are listed separately in Tables 4 and 5. The loading direction in the simulation is shown in Figure 10.

Cracks initiate from the center of the disk. As loading increases, cracks propagate along the diameter whose direction is perpendicular to the tensile stress. The propagation rate continues to increase until the loading stress reaches the failure strength and the crack penetrates through the entire disk (Figure 11). The number of cracks is related to the mechanical parameters of the samples. The more brittle

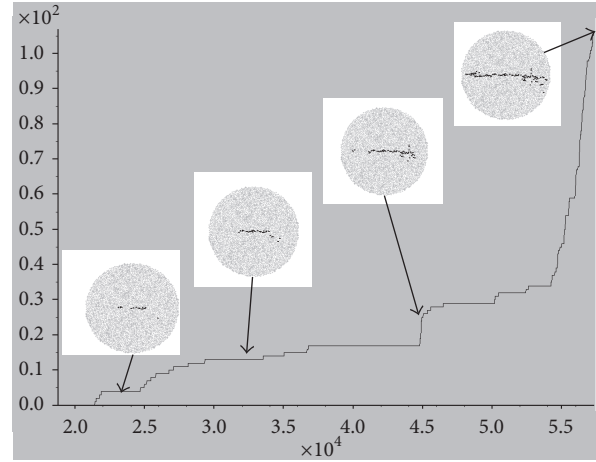


FIGURE 11: Crack propagation process.

the rock is, the more cracks would form. By recording the crack number of each simulation, a relationship between the tensile brittleness index and the crack number is established to evaluate the reliability of the proposed method.

Numerical simulations of shale tensile testing under different conditions are conducted to obtain the crack distribution characteristics of samples with different tensile brittleness indexes. The simulation results show that the higher the brittleness index is, the more cracks would form and the more complex the failure mode is (Table 6). Hence, the accuracy of the tensile brittleness index evaluation method is verified by the crack propagation behavior in numerical simulations.

4.2. Factors Affecting the Evaluation of Tensile Brittleness

4.2.1. Influence of Anisotropy on Shale Brittleness. By changing the tensile strength and shear strength between different particles layers (i.e., adding weak bedding planes to the model), 5 different models with different angles between the tensile stress and bedding planes, namely, 0°, 30°, 45°, 60°, and 90°, are established to simulate the different brittle characteristics of shale with different bedding plane angles (Figure 12).

Changing the bedding plane angles has a large impact on crack initiation and propagation. Many microcracks develop around weak bedding planes, but a large difference exists in the number of cracks when the angles between the tensile stress and bedding planes are different. Cracks may also reorient themselves when the direction of the bedding planes is not consistent with that of the tensile stress. By combining the results of the numerical simulation and laboratory Brazilian splitting tests, it can be seen that as the angle between the bedding planes and tensile stress increases, the brittle characteristics of shale first increase and then decrease. When the angle is between 30 and 60°, shale with weak bedding planes has the highest brittleness index under tensile stress (Figure 13).

In the numerical simulation, the number of microcracks is the highest when the bedding plane angle is at 45 degrees

TABLE 4: Values of PFC simulation parameters.

Model diameter W (mm)	Minimum particle radius R_{\min} (mm)	Ratio between the maximum and minimum particle radius R_{\max}/R_{\min}	Normal stiffness coefficient β	Internal stress σ_o (MPa)	Minimum number of free particles N_f	Percentage of free particles N_f/N	Particle density ρ (kg/m^3)	Connection modulus between particles E_c (GPa)	Ratio between normal and tangential stiffness k_n/k_s	Friction factor between particles μ	Average of normal connection strength σ_c (MPa)	Standard deviation of normal connection strength σ_c (MPa)	Average of tangential connection strength τ_c (MPa)	Standard deviation of tangential connection strength τ_c (MPa)
25	0.45	5.78	1.1	-1.0	3	0	1920	8.24	2.5	0.8	15	0.5	1	0.5

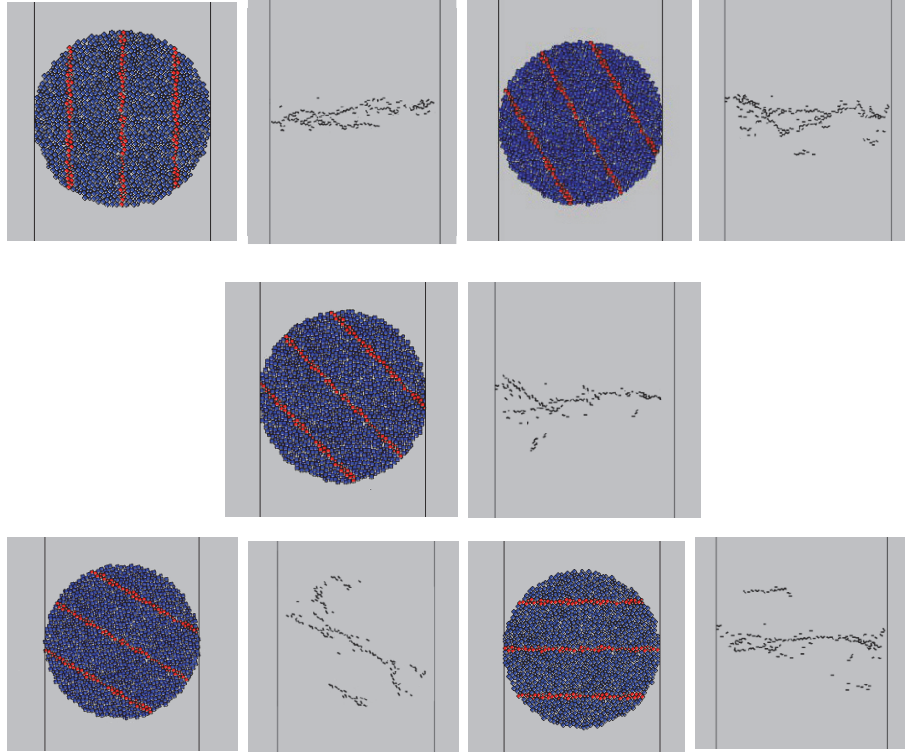


FIGURE 12: Different crack propagation characteristics of shale with different bedding plane angles (the loading direction is vertical).

TABLE 5: Comparison between the mechanical parameters of indoor experiment and PFC model.

	Poisson's ratio	Elastic modulus (GPa)	Failure load (kN)	Peak strain (%)	Tensile strength (MPa)
Indoor experiment	0.1	11.14	3.2	1.728	13.48
PFC model	0.103	11.251	3.225	1.780	13.785
Numerical simulation error	3%	1%	0.8%	3%	0.8%

due to the setting cohesive force between particle balls and the friction factor between bedding plane surfaces.

4.2.2. *Influence of the Scale Effect on the Brittleness of Shale.* By simulating Brazilian splitting tests with different disk sizes, the scale effect influence on shale brittleness is studied by combining the comprehensive brittleness index model with the simulation results (Table 7).

The relationship between the comprehensive tensile brittleness index and disk diameter is drawn based on the simulation results, as shown in Figure 14.

There is a linear relationship between the number of microcracks and the diameter of the disk, but the variation is small. Similarly, the change in disk diameter has little influence on the comprehensive tensile brittleness index.

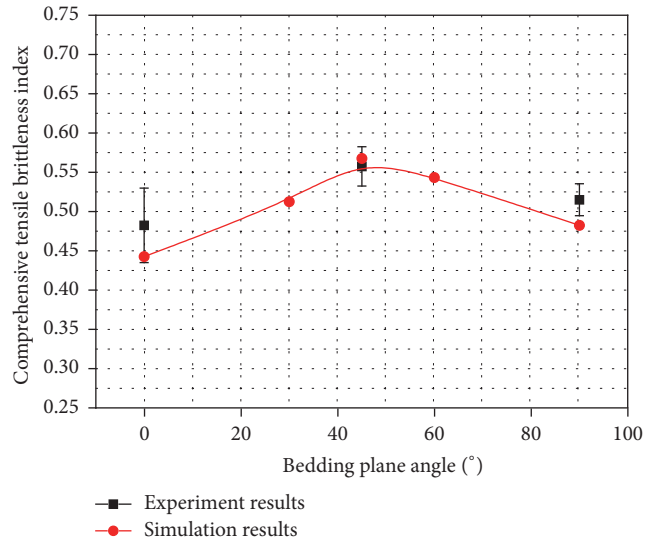


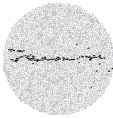
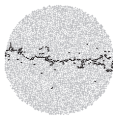
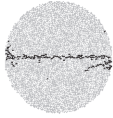
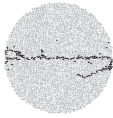
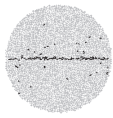
FIGURE 13: Influence of anisotropy on shale brittleness.

Hence, the scale effect of the core has very little influence on shale brittleness in laboratory experiments.

5. Conclusions

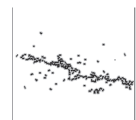
(1) Microcracks around shale bedding planes easily intersect with each other under tensile loading, causing cracks to

TABLE 6: Crack distribution characteristics of samples in numerical Brazilian splitting tests.

Sample number	Brittleness index	Number of cracks
A-1	0.32	102
		
B-1	0.71	163
		
B-7	0.68	161
		
B-8	0.62	142
		
B-10	0.43	114
		
B-12	0.58	137
		
C-2	0.75	175
		
C-4	0.87	206
		
D-1	0.56	126
		

propagate rapidly, leading to the brittle fracture of shale. Based on Brazilian splitting tests, a brittleness evaluation method of shale under tensile loading is proposed. Compared with compressive brittleness index which has a large

TABLE 7: Crack propagation characteristics of disk samples with different sizes.

Sample diameter	Number of cracks
20 mm	60
	
25 mm	79
	
30 mm	87
	
40 mm	153
	
50 mm	218
	

discreteness, the brittleness index calculated by the proposed method has a stronger sensitivity to environment change, thus giving a more accurate evaluation of shale brittleness during hydraulic fracturing.

(2) The results of the numerical Brazilian splitting tests show that samples with larger calculated tensile brittleness index have more microcracks after failure, verifying the reliability of the brittleness evaluation method based on Brazilian splitting tests.

(3) When the angle between the tensile stress and bedding planes is between 30 and 60°, shale has the highest tensile brittleness index. As the loading rate increases, the brittle characteristics of shale become more obvious, but the sample sizes used for the Brazilian splitting tests have little effect on the brittle characteristics of shale.

Conflicts of Interest

The authors declare that there are no conflicts of interest regarding the publication of this paper.

Acknowledgments

The authors are grateful for the support of NSFC (no. 51574260, no. 51490651, and no. 51521063) and Foundation of State Key Laboratory of Shale Oil and Gas Enrichment

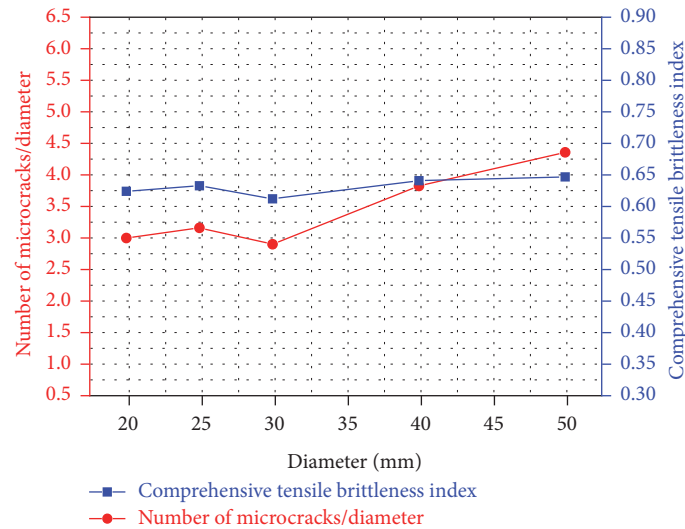


FIGURE 14: Influence of scale effect on shale brittleness.

Mechanisms and Effective Development (no. 10010099-16-ZC0607-0019).

References

- [1] J. G. Ramsay, *Folding and Fracturing of Rocks*, McGraw-Hill, London, UK, 1967.
- [2] A. Morley, *Strength of Materials*, Longman Green, London, UK, 1944.
- [3] M. Heteny, *Handbook of Experimental Stress Analysis*, John Wiley, New York, NY, USA, 1966.
- [4] L. Obert and W. I. Duvall, *Rock Mechanics and the Design of Structures in Rock*, John Wiley, New York, NY, USA, 1967.
- [5] V. Hucka and B. Das, "Brittleness determination of rocks by different methods," *International Journal of Rock Mechanics and Mining Sciences & Geomechanics Abstracts*, vol. 11, no. 10, pp. 389–392, 1974.
- [6] R. Rickman, M. Mullen, E. Petre, B. Grieser, and D. Kundert, "A practical use of shale petrophysics for stimulation design optimization: All shale plays are not clones of the Barnett Shale," in *Proceedings of the SPE Annual Technical Conference and Exhibition, ATCE 2008*, pp. 840–850, USA, September 2008.
- [7] Q. Li, M. Chen, Y. Jin, F. P. Wang, B. Hou, and B. Zhang, "Indoor evaluation method for shale brittleness and improvement," *Chinese Journal of Rock Mechanics and Engineering*, vol. 31, no. 8, pp. 1680–1685, 2012.
- [8] D. M. Jarvie, R. J. Hill, T. E. Ruble, and R. M. Pollastro, "Unconventional shale-gas systems: the Mississippian Barnett Shale of north-central Texas as one model for thermogenic shale-gas assessment," *AAPG Bulletin*, vol. 91, no. 4, pp. 475–499, 2007.
- [9] F. P. Wang and J. W. Gale, "Screening criteria for shale-gas systems. Gulf Coast Association of Geological Societies Transactions," *Journal of Petroleum Science and Engineering*, vol. 59, no. 3, pp. 779–793, 2009.
- [10] K. K. Chong, W. V. Grieser, A. Passman, H. C. Tamayo, N. Modeland, and B. E. Burke, "A completions guide book to shale-play development: a review of successful approaches toward shale-play stimulation in the last two decades," in *Proceedings of the Canadian Unconventional Resources and International Petroleum Conference*, Calgary, Alberta, Canada.
- [11] X. Jin, S. N. Shah, J.-C. Roegiers, and B. Zhang, "Fracability evaluation in shale reservoirs - An integrated petrophysics and geomechanics approach," in *Proceedings of the SPE Hydraulic Fracturing Technology Conference 2014*, pp. 153–166, February 2014.
- [12] B. Lawn, *Fracture of Brittle Solids*, Cambridge University Press, New York, NY, USA, 1993.
- [13] Y. Chen, Y. Jin, and M. Chen, "A rock brittleness evaluation method based on energy dissipation," *Lixue Xuebao/Chinese Journal of Theoretical and Applied Mechanics*, vol. 47, no. 6, pp. 984–993, 2015.
- [14] M. Cai, P. K. Kaiser, Y. Tasaka, T. Maejima, H. Morioka, and M. Minami, "Generalized crack initiation and crack damage stress thresholds of brittle rock masses near underground excavations," *International Journal of Rock Mechanics and Mining Sciences*, vol. 41, no. 5, pp. 833–847, 2004.
- [15] R. Altindag, "Correlation of specific energy with rock brittleness concepts on rock cutting," *Journal of The South African Institute of Mining and Metallurgy*, vol. 103, no. 3, pp. 163–171, 2003.
- [16] L. G. Tham, H. Liu, C. A. Tang, P. K. K. Lee, and Y. Tsui, "On tension failure of 2-D rock specimens and associated acoustic emission," *Rock Mechanics and Rock Engineering*, vol. 38, no. 1, pp. 1–19, 2005.
- [17] D. Zhang, P. G. Ranjith, and M. S. A. Perera, "The brittleness indices used in rock mechanics and their application in shale hydraulic fracturing: A review," *Journal of Petroleum Science and Engineering*, vol. 143, pp. 158–170, 2016.
- [18] Q. B. Zhang and J. Zhao, "Effect of loading rate on fracture toughness and failure micromechanisms in marble," *Engineering Fracture Mechanics*, vol. 102, pp. 288–309, 2013.
- [19] B. Hou, M. Chen, W. Cheng, and C. Diao, "Investigation of Hydraulic Fracture Networks in Shale Gas Reservoirs with Random Fractures," *Arabian Journal for Science and Engineering*, vol. 41, no. 7, pp. 2681–2691, 2016.

Research Article

Visualized Experimental Investigation on the Gas-Water Distribution Characteristics in Intersecting Fractures

Chen Wang ¹, Yujing Jiang ¹, Richeng Liu ², and Changsheng Wang ¹

¹Graduate School of Engineering, Nagasaki University, Nagasaki 8528521, Japan

²State Key Laboratory for Geomechanics and Deep Underground Engineering, China University of Mining and Technology, Xuzhou 221116, China

Correspondence should be addressed to Yujing Jiang; jiang@nagasaki-u.ac.jp

Received 17 December 2017; Revised 9 February 2018; Accepted 15 February 2018; Published 26 March 2018

Academic Editor: Fengshou Zhang

Copyright © 2018 Chen Wang et al. This is an open access article distributed under the Creative Commons Attribution License, which permits unrestricted use, distribution, and reproduction in any medium, provided the original work is properly cited.

In coal-bed methane recovery, water is generally drained out along with gas. In order to address the influence of different gas-water ratios, fracture intersecting angles, and gas desorption positions on gas and water distributions along fractures and hence understand the two-phase flow behavior in fracture network, an experimental study was conducted on three artificial models with intersecting fractures. The results show that (1) with gas and water injected at different rates, the flow of water and gas is divided into three stages. In the first stage, gas flowed as small bubbles. The transport of gas was stable, which was similar to single-phase laminar flow. The difference in gas injection positions led to totally contrary flow results of water and gas. (2) In the second stage, larger gas bubbles were formed and the interactions between water and gas became serious. The gas-water distribution was dominated by different inertias between water and gas. The difference in gas injection positions did not take much effect on the gas-water distribution. (3) In the third stage, the influence of the inertia difference was still important, but some other factors also influenced the gas-water distribution. The difference in gas injection positions led to different distribution results. (4) The water injection rate has impact on the distribution of the water flow rate in each outlet. In the second stage, when water was injected at small rates, the difference between the cases in which gas was injected from different positions can be neglected. When water injection rates became larger, this difference became obvious. (5) The intersecting angle of the fractures influences the distribution of water and gas. The larger the intersecting angle is, the larger the inertial effect will be. Consequently, the intersecting angle influences the length of the second stage, which is dominated by the inertial effect.

1. Introduction

The gas-water two-phase flow exists in many engineering applications, including coal-bed methane recovery, CO₂ sequestration, geothermal energy development, and contaminant transport in geological rock strata [1–5]. Generally, the coal seams are abounded with water, and the recovery of coal-bed methane experiences a two-phase flow process at the initial stage of exploitation. In the first stage of coal-bed methane drainage, water is drained out from the coal seams, which is a single-phase flow process. With the depletion of pressure of the seam, gas in the absorbed phase begins to desorb from the coal matrix. Due to its small quantity, in the second stage, the gas phase is discontinuous and bubbly flow is formed. In the above-mentioned process, there is

a transition from single-phase flow to two-phase flow in the fracture network, and the gas desorption rate varies with respect to time. Consequently, a two-phase flow with different gas-water ratios will be formed. This is why the flow behavior with different gas-water ratios requires to be well understood. By the way, the parameters of the fracture network such as the fracture intersecting angle also have an impact on the flow behavior. As a basis, a study on the fracture intersections is needed to seek understanding the influence of parameters such as the intersecting angle on the flow behavior. In applications of coal-bed methane recovery, by investigating the statistical parameters in the coal seam fracture network and based on the field data such as the water or gas percentage and the pressure depletion curve, the

flowing state can be estimated and the optimal exploitation scheme can be determined.

Existing studies on two-phase flow can be divided into two broad categories, namely, the displacement mechanisms [6] and simultaneous flow of two phases in the fractures or porous media [7, 8]. Conventional theories on the two-phase flow originate from the aspection of porous media based on the concept of relative permeability. Commonly used models of relative permeability of two-phase flow in porous media include the X-model [9], the viscous-coupling model [10], and the Brooks-Corey model [11]. The X-model has been used to simulate reservoir behaviors for its priority in simplicity [12, 13], but its application is limited because it neglects the interaction between different phases. In the viscous-coupling model, the interaction between different phases due to the viscosity difference is included [14]. The Corey model is one of the most commonly used models in porous media [15], in which capillary pressure plays a dominant role.

Even though distinct differences exist between rock pores and rock fractures, such as geometry and connectivity, it has been found that the flow behavior of two-phase fluid through a single fracture can be described by models proposed for porous media. In the gas-water flow experiment in smooth fractures by Diomampo, the results followed the Corey model [16], which indicates that in some cases the two-phase flow behavior in fractures is a limiting case of that in porous media. Romm conducted the kerosene-water two-phase flow tests in parallel artificial fractures, which confirmed to the X-model. Fourar and Bories investigated the air-water flow in parallel artificial fractures, and the relative permeability complies with viscous-coupling model [17]. Watanabe et al. conducted a series of experiments with decane-water and nitrogen-water in real fractures with different wettability values, in which a new v-type relative permeability was indicated [18]. Conventional models for relative permeability are mainly expressed as the function of saturations, which neglects the contributions of fracture roughness. In consideration of this deficiency, Chen established the correlation between the flow structures and the relative permeability in single fractures through visualization experiment [19], in which the flow structures are the indications of fracture roughness and capillary pressure. In addition, the gas-water ratio is a critical and fundamental parameter. Different gas-water ratios will lead to different structures such as bubble flow, slug flow, or stratified flow and correspondingly lead to different influences of viscosity and capillary pressure. Therefore, there will be different pressure drop characteristics [20, 21]. However, the diversity of two-phase models and experimental results in fractures indicates that a more generalized model to describe the multiphase behavior is still absent. Fundamental problems, such as whether the contributions of viscous force or capillary pressure dominate the flow in different kinds of fractures, still require to be investigated.

In addition, most present studies on the two-phase flow in fractures were carried out in a single fracture to achieve their conductivity, while the two-phase flow behavior in combined fractures or fracture network still require to be further investigated. On the distribution characteristics of gas-water two-phase flow, many studies have been conducted

in T-junctions [22–25], and the distribution of water and gas is influenced by the effect of inertial effect and gravity [26, 27]. It is reported that gas and water can be separated due to the difference of inertial effects [26, 28–30]. Small bubbles or solid particles are more likely to be carried by the fluid flow, while large bubbles or solid particles are likely to deviate from the streamline of the fluid, and small bubbles or slug bubbles show different inertial effects [31–34]. In a flow channel junction (intersection), different gas-water ratios will lead to different separation results [29] since the influence of the inertial effect is different. Therefore, the gas-water ratio plays a role in two-phase flow behavior which requires to be investigated. Inertia separator is developed based on this mechanism, and, in fractures, it is indicated that the inertial effect cannot be neglected in many conditions [21, 35, 36], so such effects still require to be further studied, especially quantitative investigations are expected. In addition, the flow characteristics in single fractures and fracture intersections provide basis for deeply understanding the fluid flow behavior in the fracture networks. The fractures can intersect at different angles. The intersecting angle is a critical parameter that influences the flow characteristics because the fluid is redistributed at the intersection. Li et al. studied the influence of the intersecting angle on nonlinear flow at fracture intersections. They reported that the larger intersecting angle results in the stronger nonlinearity of flow regimes [37]. In two-phase flow, the phase separation is influenced by the intersecting angle between the two outlets due to the different inertias of the phases [29]. Therefore, the influence of intersecting angle should be investigated.

In the present study, a series of two-phase flow tests were conducted in artificial smooth intersecting fractures with the developed experimental system. Then, the influence of different gas-water ratios, fracture intersecting angles, and gas injection positions on the gas and water distributions was analyzed. This experiment simulates the evolution of water flow rate with respect to different gas desorption rates in coal seams, with the expectation that by evaluating the water flow rate the gas desorption state can also be forecasted. This experiment provides a basis for further studies to understand the distribution of gas and water in the two-phase flow in fracture networks.

2. Experiment

2.1. Experimental Setup. In order to investigate two-phase fluid flow behavior through intersecting fractures, an experimental system was developed. It consists of three main units: the fluids supply unit, the fracture model, and the data measurement unit. The detailed schematic of the experiment system is shown in Figure 1. Gas (Nitrogen) is supplied from the gas cylinder, in which the initial gas pressure is 15 MPa. Since the mass flow controller which was connected to the cylinder cannot bear the pressure over 1 MPa, the pressure is decreased to the range of 0.1–0.3 MPa with a pressure regulator. With the mass flow controller, gas was injected into the testing model with a constant flow rate in a range of 0–2000 mL/min. Gas injection rate can be visually displayed on the digital screen of mass flow controller. Water was

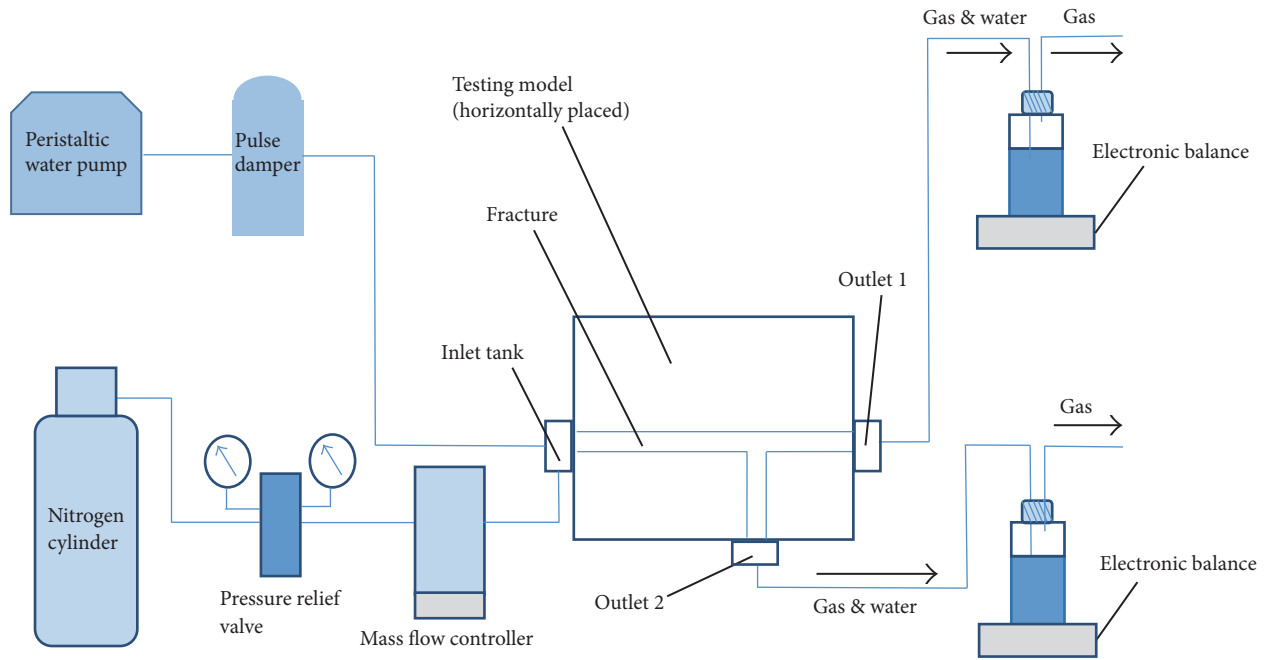


FIGURE 1: The schematic of the experiment system.

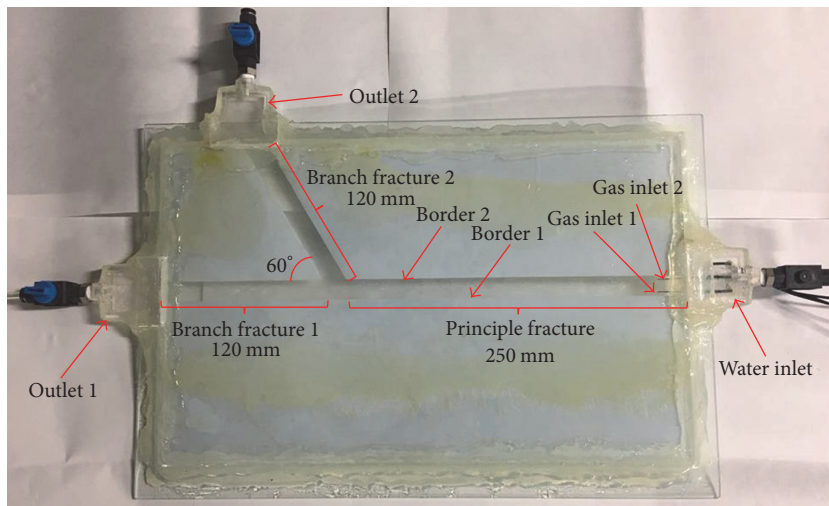


FIGURE 2: The testing model with fractures intersecting at 60°.

injected with the peristaltic pump with a constant flow rate. In this experiment, water was injected with 500 mL/min, 700 mL/min, 900 mL/min, and 1100 mL/min. Gas and water were injected into the inlet tank of the fracture model simultaneously and flowed out from the two outlet tanks, which are named as Outlet 1 and Outlet 2, respectively. At the two outlets, gas was released to the atmosphere while water was collected in a bottle and weighed by a precise electronic balance. The data of water mass in each bottle was transmitted into the computer in real time. Consequently, the water flow rate was obtained.

Three testing models were manufactured with toughened glasses and resin plates. In each model, two fractures intersect

at a certain angle (30°, 60°, or 90°). Figure 2 shows the testing model in which fractures intersect at 60°. Each testing model consists of three layers. Two toughened glasses were used as upper and lower layers, respectively, for purpose of visual observation. Resin plates with a thickness of 1 mm were set as the middle layer. The resin plates have three separate parts to form an artificial fracture with a thickness of 1 mm. The aperture of the fractures is 15 mm. Compared with the aperture of natural fractures, the adopted aperture in the experiment is much larger because we want to visually observe the two-phase flow phenomenon within the void spaces of a fracture. If the fracture aperture is in the natural scale, that is, 0.01~1 mm, it is quite difficult to capture

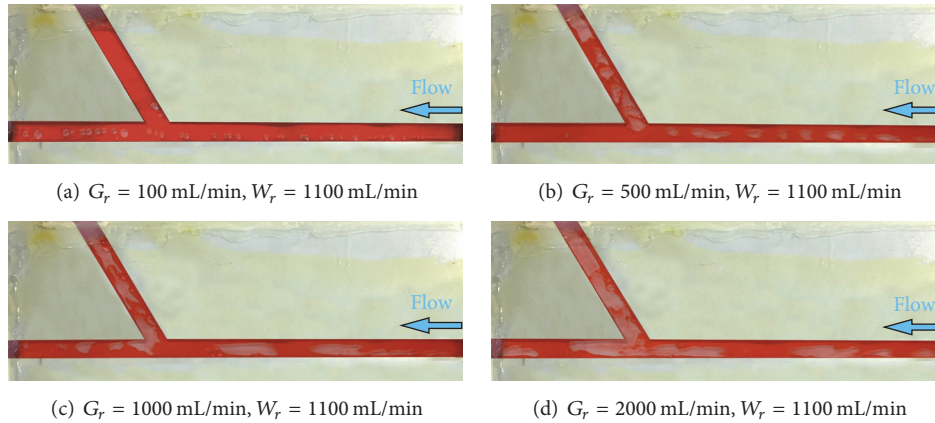


FIGURE 3: The flow structures at the water injection rate of 1100 mL/min with gas injected from Gas Inlet 1.

images of fluid flow and bubble distributions using the current visualization techniques. However, we accept that, to simulate the real two-phase flow at the fracture intersection, the fracture that has a real-scale aperture should be used. Therefore, in the following future works, we will investigate the influence of fracture aperture size on the two-phase flow behaviors.

Here we define the principle fracture, Branch Fracture 1, and Branch Fracture 2, as indicated in Figure 2. In each model, both Branch Fracture 1 and Branch Fracture 2 have a length of 120 mm to achieve identical conductivity in two branch fractures. The principle fracture has a length of 250 mm. The only difference between these testing models is the intersecting angle, while all the other sizes are identical. Grease was coated on the resin to restrain the water and gas from flowing into the areas beyond the fractures. At the boundaries of the testing model, silicone sealant was used to fix the glasses and the plate and also for sealing up. Near the water inlet tank, there were two needles with an inner diameter of 0.8 mm acting as gas inlets, as shown in Figure 2. This is designed to estimate the influence of gas injection positions on the water and gas distribution. The two boundaries of the principle fracture are designated as Border 1 and Border 2, respectively.

2.2. The Testing Procedures. If the testing model was not horizontally placed in the test, the two outlets will be of different elevations, and the flow rates of liquids can be seriously influenced. Consequently, prior to the flow test, the testing model was horizontally laid, and the horizontality was checked with a level gauge. In each testing model, Branch Fracture 1 and Branch Fracture 2 have the same fracture thicknesses and widths. Therefore, theoretically they should have identical permeability values when the inertial effects are not strong when fluids transport at small velocity. To further test the horizontality, water was injected to the specimen at very small flow rates. It shows that the flow rates of water from 2 outlets were approximately identical at a flow rate of 30 mm/min, indicating that the specimen was laid flat. Then water was injected to the specimen at a constant flow rate of 500, 700, 900, and 1100 mL/min, and nitrogen was injected

with a constant flow rate in the range of 0–2000 mL/min. The gas flow rate of 0–2000 mL/min in this study corresponds to a superficial velocity of 0–2 m/s, and the water flow rate of 500–1100 mL/min corresponds to a superficial velocity of 0.55–1.2 m/s. The gas velocity and flow velocity are in the same order of magnitude as those reported in the literature. For example, to investigate the two-phase flow pressure drop characteristics in fractures, a gas superficial velocity of 0–5 m/s and a water superficial velocity of 0–0.41 m/s were adopted in Fourar and Bories [17]. In each test round, the flow of two different phases of fluid was kept for 1–2 min to achieve a stable flow state prior to the measurement of flow rates in each outlet.

2.3. Results and Discussion. According to the testing results, the distribution of water in the two outlets was seriously influenced when gas was injected at different rates. On the other hand, the water injection rate also had an impact on the distribution of gas in the two outlets. In this study, the evolution of water flow rates in the two outlets was quantitatively measured and analyzed along with the gas flow structures which were qualitatively measured with the visualization photos. The 60° model is firstly selected as an example for analyzing the effect of the gas injection rate.

(1) The Effect of Gas Injection Rate. Figure 3 shows the cases in which water was injected at 1100 mL/min and gas was injected from Gas Inlet 1. The gas injection rate was increased step by step. The evolution of the flow characteristics can be divided into 3 stages.

In the first stage, when gas was injected at a small rate, as shown in Figure 3(a). In this stage, gas bubbles transported in a stable state, and the morphology of gas bubbles was regular. This indicates that the turbulence was not serious, which is similar to the single-phase laminar flow. Since gas was injected from Gas Inlet 1 which is close to Border 1, the gas bubbles flowed along Border 1 of the principle fracture, and consequently almost all the gas transported to Branch Fracture 1. Therefore, more gas was driven to Branch Fracture 2. Corresponding to the transport of gas in this stage, the transport characteristics of water can be indicated in Figure 8.

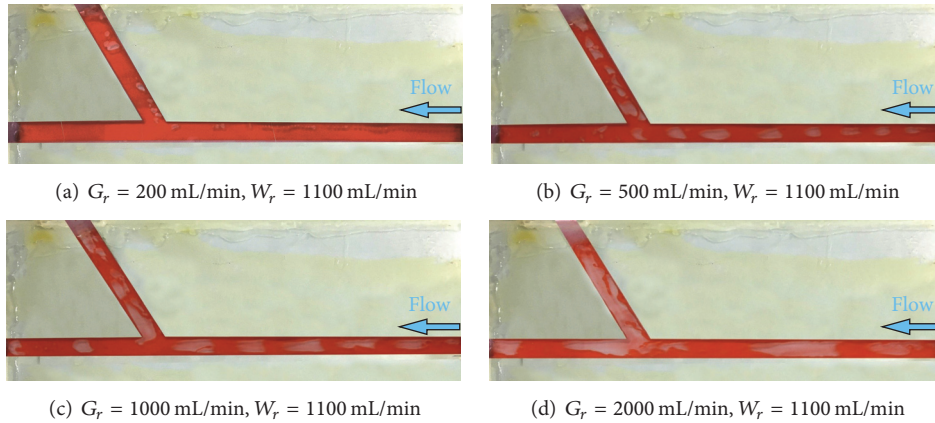


FIGURE 4: The flow structures at the water injection rate of 1100 mL/min with gas injected from Gas Inlet 2.

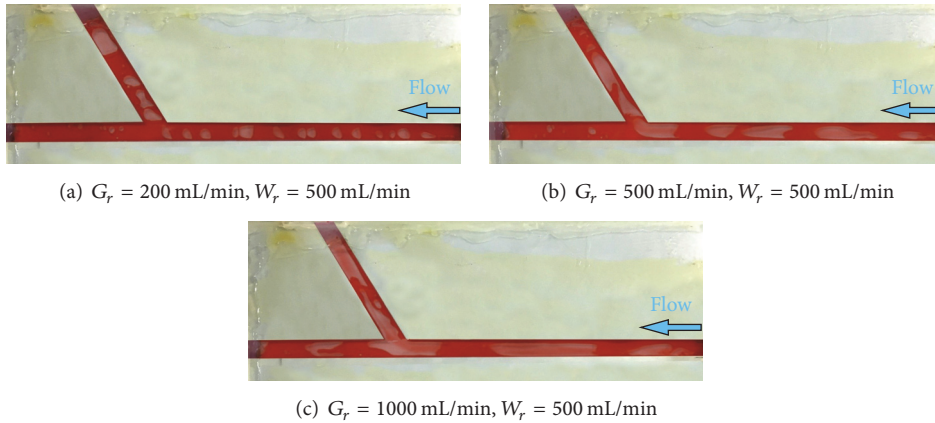


FIGURE 5: The flow structures at the water injection rate of 500 mL/min with gas injected from Gas Inlet 1.

As shown in Figure 8(a) in which gas was injected from Inlet 1, when water was injected at 500 mL/min ($W_r = 500$), the water flow rate in Outlet 1 decreased when gas injection rate increased from 0 to 100 mL/min. This is because all the gas bubble transported into Branch Fracture 1 and more water was driven into Branch Fracture 2. This is why the water flow rate in Outlet 2 increased as indicated in Figure 8(b), while the water flow rate in Outlet 1 decreased as indicated in Figure 8(a). When gas was injected from Gas Inlet 2, gas totally flow into Outlet 2, as shown in Figure 4(a); water flow rate in the Outlet 1 increased with respect to the increase of gas injection rate, as shown in Figure 8(a). This is totally contrary to the case when gas was injected from Gas Inlet 1.

To summarize, gas transported stably as small bubbles in this stage. The turbulence was not serious, which was similar to the laminar flow. The difference in gas injection positions would lead to totally contrary flow conditions of both water and gas: when gas was injected from different positions, the gas bubbles flowed into different branch outlets (Figures 3(a) and 4(a)), and the water flow rates in Outlet 1 (Figure 7(a)) would also evolve in opposite trends, as well as that in Outlet 2 (Figure 7(a)).

In the second stage, because gas was injected with a larger rate, larger bubbles were formed, as shown in Figures 3(b) and 4(b). By comparing Figures 3(b) and 4(b), it can be indicated that no matter gas was injected from Gas Inlet 1 or Gas Inlet 2, almost all gas bubbles transported into Branch Outlet 2, which is quite different from the first stage. Comparisons between Figure 5(a) and Figure 6(a) or Figure 5(b) and Figure 6(b) show the same phenomena. Correspondingly, as shown in Figure 8(a), when water flow rate was 500 mL/min, when the gas injection rate was increased 300–900 mL/min, the evolution of water flow rate (with gas injected from Gas Inlet 1) was identical to the evolution of water flow rate (with gas injected from Gas Inlet 2). In Figure 8(b), the same phenomenon is indicated. In this stage larger bubbles were formed, and the morphology of gas bubbles was no longer regular. The turbulence became significant due to the drastic interactions between water and gas, and consequently the gas bubbles no longer remained close to the border. The distribution of water and gas was dominated by the different inertias of water and gas. Both Figures 3(b) and 4(b) show that almost all the gas transported to Branch Fracture 2. In such conditions, the reason why most gas bubbles moved into

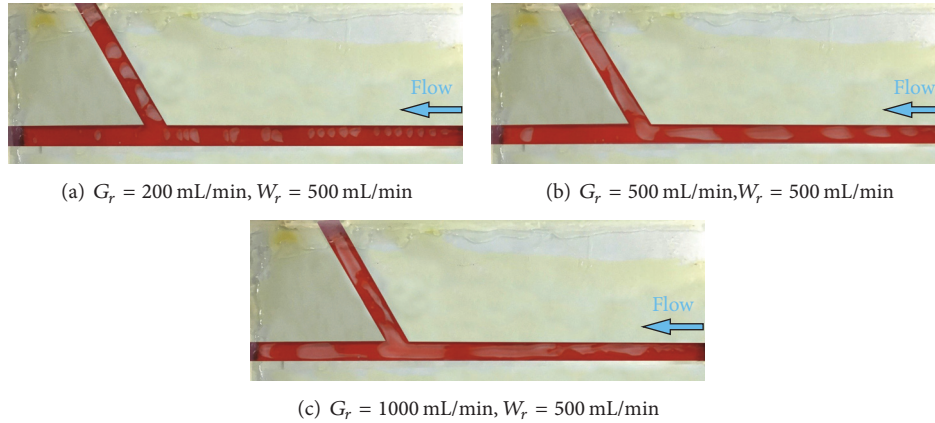


FIGURE 6: The flow structures at the water injection rate of 500 mL/min with gas injected from Gas Inlet 2.

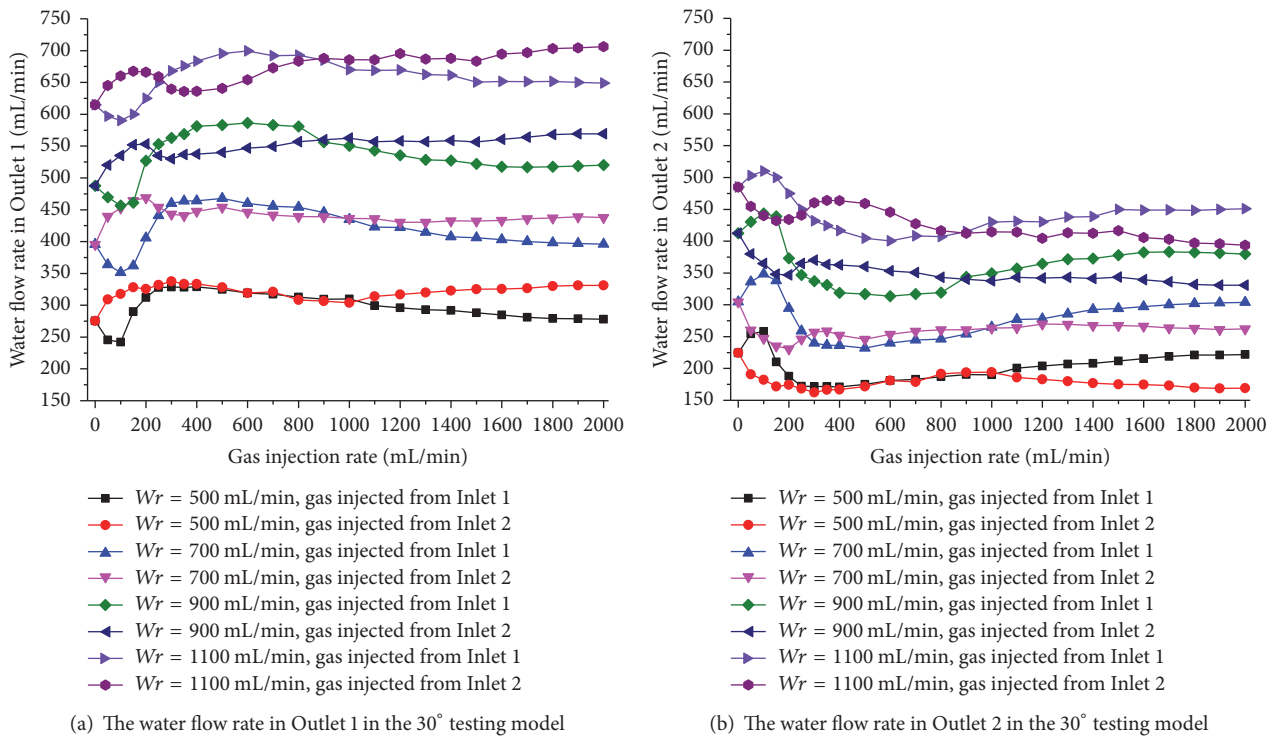


FIGURE 7

Branch Outlet 2 is that the density of water is about 800 times as that of gas, and thus there is a difference in the inertial effects. In such conditions, water, the liquid with a larger inertial effect, would be more likely to transport into Branch Outlet 1, which is connected to the principle fracture without diversion angle, and drove gas into Branch Outlet 2.

To summarize, in this stage, the transport of water and gas was quite turbulent with serious interactions between water and gas. The distribution of water and gas was dominated by the different inertias between water and gas, and the gas injection positions did not take much effect on the water and gas distribution when the water flow rate was small.

In the third stage, because gas injection rate was further increased, slug bubbles were formed, as shown in Figures 3(c),

3(d), 4(c), and 4(d). The gas injection rate was larger, and the flow of both water and gas was more turbulent, and there are many factors that influence the distribution of water and gas. The distribution of gas into two outlets became more even, but it is still that more gas transported to Branch Fracture 2, indicating that the effect of different inertias on distribution was still important. Figures 5(c) and 6(c) show the same phenomena. By comparing Figures 3(b), 3(c), and 3(d), it can be noticed that the flow structures evolved from bubble flow to slug flow, and the percentage of gas that transported into Branch Fracture 1 also increased, meaning that the distribution behavior was also influenced by the flow structures. The evolution of the water flow rates in two outlets went into a stable state when gas injection rate

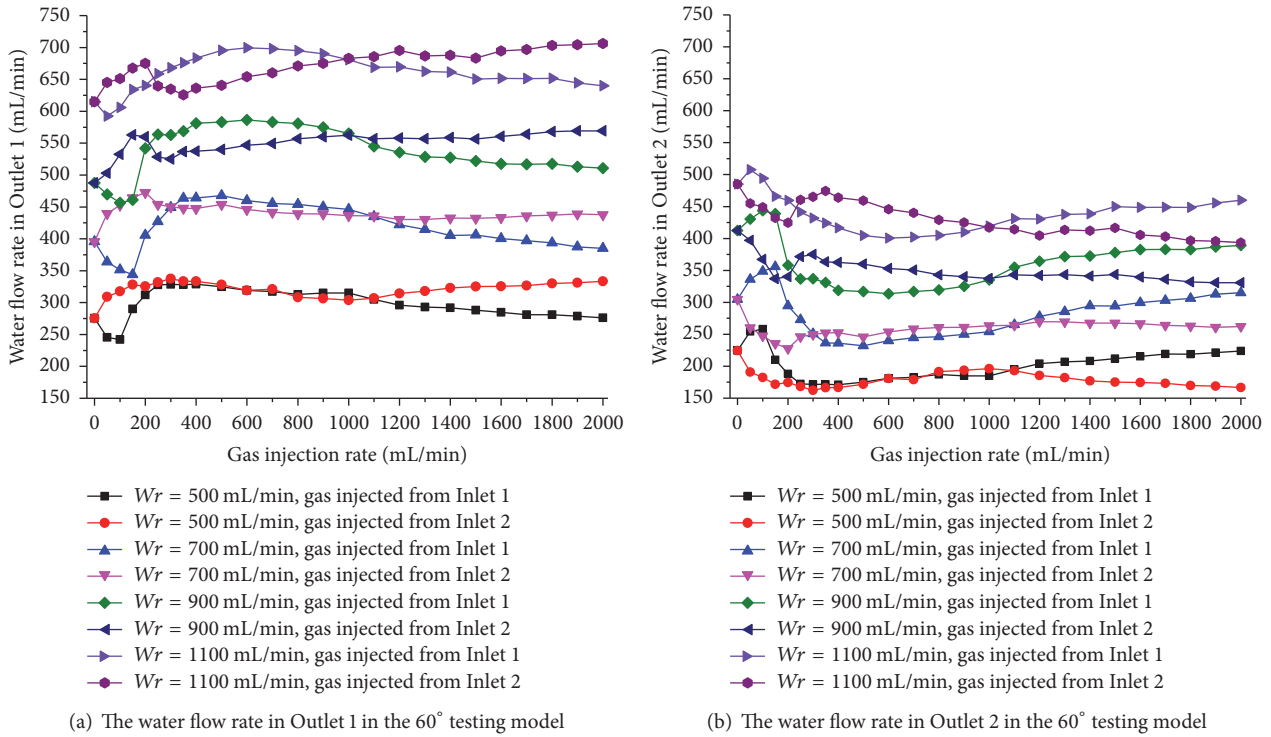


FIGURE 8

increased from 1000 to 2000 mL/min, as shown in Figures 8(a) and 8(b). Different from that in the second stage, the difference between the cases in which gas was injected from different positions became obvious. This means that, in this stage, though the effect of different inertias was still important, some other factors also had influence and lead to this difference if gas was injected from different gas injection inlets.

The results of 30° model and 90° model also show the same evolution process, as shown in Figures 7 and 9.

(2) *The Effect of Water Injection Rate and Fracture Intersecting Angle.* The 90° model is selected as an example for analyzing the effect of water injection rate. Figure 9(a) shows the evolution of water flow rate in Outlet 1 when water was injected with different injection rates at the water inlet, and Figure 9(b) shows that in Outlet 2. As mentioned above, the evolution of gas and water in each outlet can be divided into three stages. It can be indicated in Figures 9(a) and 9(b) that no matter water was injected at which rate (500 mL/min, 700 mL/min, 900 mL/min, and 1100 mL/min), the evolution of the water flow rate in Outlet 1 or Outlet 2 always has these three stages. But at different water injection values, some differences can be noticed. In the second stage, as shown in Figure 9(a), when water was injected at 500 mL/min, the difference between the cases when gas was injected from different positions can be neglected. When water was injected at 700 mL/min, this difference became larger but still not significant. When water was injected at 900 mL and 1100 mL, this difference became obvious. This is because, in

the second stage, when water was injected at small rates, such as 500 mL/min, the distribution of water and gas is dominated by the different inertias between water and gas, as mentioned previously. When the water injection rate went higher, the flow became more turbulent and some other factors took more effect which would lead to such a difference. In the third stage, despite the fact that water was injected at different rates, the difference between each case in which gas was injected from different positions was similar.

By comparing Figures 7–9, it can be noticed that, with the increase of intersecting angle, there is some difference in the evolution of water flow rates in the outlets. As mentioned above, the evolution of water flow rates in the two outlets can be divided into three stages. As indicated by Figure 7, for the 30° model, in the cases of $W_r = 500$ mL/min and $W_r = 700$ mL/min, when the gas injection rate passed 900 mL/min, the flow of water transferred from the second stage to the third stage. For $W_r = 900$ mL/min and $W_r = 1100$ mL/min, this transferring point is 1000 mL/min. For the 60° model, in the cases of $W_r = 500$ mL/min and $W_r = 700$ mL/min, this transferring point is 1000 mL/min. For $W_r = 900$ mL/min and $W_r = 1100$ mL/min, this transferring point is 1100 mL/min. For the 90° model, in the cases of $W_r = 500$ mL/min and $W_r = 700$ mL/min, $W_r = 900$ mL/min, and $W_r = 1100$ mL/min, this transferring point is 1200 mL/min. This indicates that, with the increase of the intersecting angle of fractures, the transferring point of the gas injection rate, which indicates the transfer from the second stage to the third stage, would increase. This is because the second stage is dominated by the inertial effect of water and gas. With a

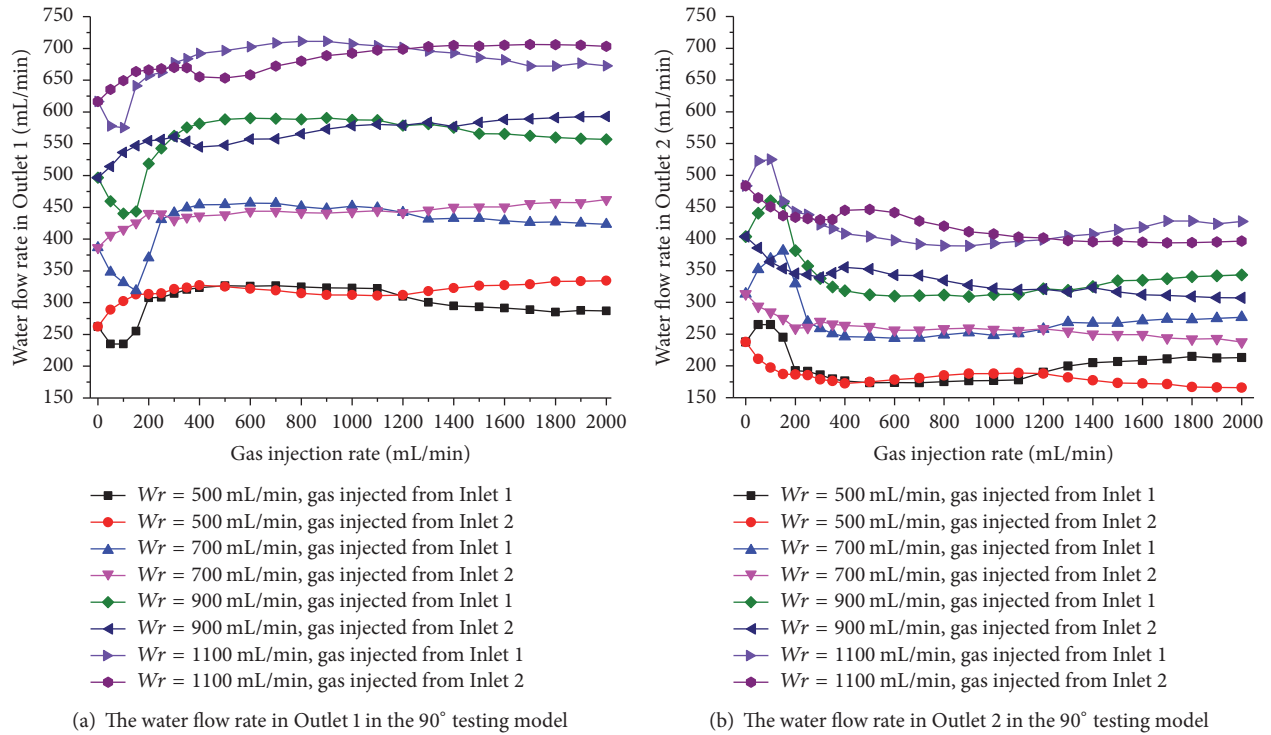


FIGURE 9

larger intersecting angle of the two fractures, the difference of the inertial effects between phases will play a more significant role. Consequently, the second stage would be extended in the model with a larger fracture intersecting angle since the second stage is inertial effect dominated.

Actually, the mentioned factors which would influence the distribution of water and gas into two outlets, including the gas injection rate, water injection rate, gas injection positions, and fracture intersecting angle, are coupled with each other, meaning that any variation in one factor will contribute to changes in the magnitudes of the influence by the other factors. It has to be addressed that this study is a preliminary study for the distribution of two flowing phases through two intersecting fractures using the newly developed visualization testing system of two-phase flow. In the present study, the reason why the flow has three stages is that different physical effects take turns to be the dominate factors, so in future studies we will focus on the quantitative analysis of different physical factors including the inertial effect, the viscous effect, the capillary pressure, and so forth to seek more accurate quantitative description methods for describing such flow phenomenon.

3. Conclusions

With the developed visual experimental system, the two-phase flow through different intersecting fractures at different water and gas injection rates is investigated. The results can be concluded as follows.

With gas and water injected at different rates, the flow of both water and gas can be divided into three stages. In the first

stage, gas flowed as small bubbles, and the transport of gas and water was stable. The turbulence was not serious, which is similar to the single-phase laminar flow. The difference in gas injection positions would lead to totally contrary flow conditions of both water and gas: when gas was injected from different positions, the gas bubbles flowed into different branch outlets, and the water flow rate in Outlet 1 or Outlet 2 would also evolve in opposite trends.

In the second stage, because larger bubbles were formed, the turbulence became significant due to the drastic interactions between water and gas. The difference of the inertial effects between water and gas dominates the distribution of water and gas. In such conditions, most gas bubbles transported into Branch Outlet 2 and drove more water into Branch Outlet 1. In this stage, the difference in the gas injection positions did not take much effect on the water and gas distribution.

In the third stage, the turbulence became more significant and the interactions between water and gas were more serious. Though the effect of different inertias was still important, some other factors also became to take more effect. The difference of the gas injection positions would lead to different evolution curves of water flow rates in each outlet.

The water injection rate also has impact on the distribution of the water flow rate in each outlet, particularly in the second stage. In the second stage (gas injection rate between 200 and 1000 mL/min), when water was injected in small flow rates (500 mL/min and 700 mL/min), the difference between the cases in which gas was injected from different positions can be neglected. When the water was injected in larger flow rates (900 mL/min and 1100 mL/min), this difference became

obvious. This indicates the transformation from an inertial effect dominated process to a multieffect influenced process. The intersecting angle of the fractures also influences the distribution of water and gas. The larger the intersecting angle is, the larger the inertial effect will be. Consequently, the intersecting angle influences the range of the second stage, which is dominated by the inertial effect.

The factors which influence the distribution of water and gas into two outlets, including the gas injection rate, water injection rate, gas injection positions, and fracture intersecting angle, are coupled with each other, meaning that any variation in one factor will contribute to changes in the influence magnitudes of the other factors, so in future studies more accurate quantitative description methods for such flow phenomenon are supposed to be developed.

Conflicts of Interest

The authors declare that they have no conflicts of interest.

Acknowledgments

This study has been partially funded by JSPS-NSFC Bilateral Joint Research Project, Japan (Grant nos. 17H03506 and 51611140122), the National Natural Science Foundation of China, China (Grant no. 51709260), the Natural Science Foundation of Jiangsu Province, China (no. BK20170276), and China Scholarship Council (CSC). These supports are gratefully acknowledged.

References

- [1] S. Kimura, "Geothermal energy development and multiphase flows," *Japanese Journal of Multiphase Flow*, vol. 11, no. 1, pp. 11–14, 1997.
- [2] R. L. Detwiler, H. Rajaram, and R. J. Glass, "Interphase mass transfer in variable aperture fractures: Controlling parameters and proposed constitutive relationships," *Water Resources Research*, vol. 45, no. 8, Article ID W08436, 2009.
- [3] P. Persoff and K. Pruess, "Two-phase flow visualization and relative permeability measurement in natural rough-walled rock fractures," *Water Resources Research*, vol. 31, no. 5, pp. 1175–1186, 1995.
- [4] E. A. Sudicky and E. O. Frind, "Contaminant transport in fractured porous media: Analytical solutions for a system of parallel fractures," *Water Resources Research*, vol. 18, no. 6, pp. 1634–1642, 1982.
- [5] P. Nuske, B. Faigle, R. Helmig, J. Niessner, and I. Neuweiler, "Modeling gas-water processes in fractures with fracture flow properties obtained through upscaling," *Water Resources Research*, vol. 46, no. 9, Article ID W09528, pp. 201–210, 2010.
- [6] T. Babadagli, X. Ren, and K. Develi, "Effects of fractal surface roughness and lithology on single and multiphase flow in a single fracture: an experimental investigation," *International Journal of Multiphase Flow*, vol. 68, pp. 40–58, 2015.
- [7] A. Fumagalli and A. Scotti, "A numerical method for two-phase flow in fractured porous media with non-matching grids," *Advances in Water Resources*, vol. 62, pp. 454–464, 2013.
- [8] V. L. Hauge and J. E. Aarnes, "Modeling of two-phase flow in fractured porous media on unstructured non-uniformly coarsened grids," *Transport in Porous Media*, vol. 77, no. 3, pp. 373–398, 2009.
- [9] E. S. Romm, *Fluid Flow in fractured rocks*, Nebra Publishing House, Moscow, Russia, 1966.
- [10] M. Fourar and R. Lenormand, "A viscous coupling model for relative permeabilities in a fracture," *Society of Petroleum Engineers Journal*, 1998.
- [11] R. Brooks and A. Corey, *Hydraulic properties of porous media*, Colorado State University, 1964.
- [12] J. R. Gilman and H. Kazemi, "Improvements in simulation of naturally fractured reservoirs," *Society of petroleum engineers Journal*, vol. 23, no. 4, pp. 695–707, 1983.
- [13] L. K. Thomas, T. N. Dixon, and R. G. Pierson, "Fractured reservoir simulation," *Society of Petroleum Engineers Journal*, vol. 23, no. 1, pp. 42–54, 1983.
- [14] S. Whitaker, "Flow in porous media II: The governing equations for immiscible, two-phase flow," *Transport in Porous Media*, vol. 1, no. 2, pp. 105–125, 1986.
- [15] A. T. Corey, "The Interrelation between gas and oil relative permeabilities," *Producers Monthly*, vol. 19, p. 38, 1954.
- [16] G. P. Diomampo, "Viscous Coupling in Two-phase flow in porous media and its effect on relative permeabilities," *Transport in Porous Media*, vol. 11, no. 3, pp. 201–218, 1993.
- [17] M. Fourar and S. Bories, "Experimental study of air-water two-phase flow through a fracture (narrow channel)," *International Journal of Multiphase Flow*, vol. 21, no. 4, pp. 621–637, 1995.
- [18] N. Watanabe, K. Sakurai, T. Ishibashi et al., "New v-type relative permeability curves for two-phase flows through subsurface fractures," *Water Resources Research*, vol. 51, no. 4, pp. 2807–2824, 2014.
- [19] C.-Y. Chen, *Liquid-Gas Relative Permeabilities in Fractures: Effects of Flow Structures, Phase Transformation and Surface Roughness*, Stanford University, 2005.
- [20] J. Reimann and W. Seeger, "Two-phase flow in a T-junction with a horizontal inlet. Part II: Pressure differences," *International Journal of Multiphase Flow*, vol. 12, no. 4, pp. 587–608, 1986.
- [21] M. Fourar, S. Bories, R. Lenormand, and P. Persoff, "Two-phase flow in smooth and rough fractures: Measurement and correlation by porous-medium and pipe flow models," *Water Resources Research*, vol. 29, no. 11, pp. 3699–3708, 1993.
- [22] A. Azzi, A. Al-Attiyah, Q. Liu, W. Cheema, and B. J. Azzopardi, "Gasliquid two-phase flow division at a micro-T-junction," *Chemical Engineering Science*, vol. 65, no. 13, pp. 3986–3993, 2010.
- [23] S. Wang, K. He, and J. Huang, "Phase splitting of a slug-annular flow at a horizontal micro-T-junction," *International Journal of Heat and Mass Transfer*, vol. 54, no. 1-3, pp. 589–596, 2011.
- [24] K. He, S. Wang, and J. Huang, "The effect of flow pattern on split of two-phase flow through a micro-T-junction," *International Journal of Heat and Mass Transfer*, vol. 54, no. 15-16, pp. 3587–3593, 2011.
- [25] J. Chen, S. Wang, and S. Cheng, "Experimental investigation of two-phase distribution in parallel micro-T channels under adiabatic condition," *Chemical Engineering Science*, vol. 84, pp. 706–717, 2012.
- [26] S. M. Bhagwat and A. J. Ghajar, "Experimental investigation of non-boiling gas-liquid two phase flow in downward inclined pipes," *Experimental Thermal and Fluid Science*, vol. 89, pp. 219–237, 2017.

- [27] Y. Liu, W. Sun, W. Wu, and S. Wang, "Gas-liquid two-phase flow distribution in parallel micro-channels with different header and channels' orientations," *International Journal of Heat and Mass Transfer*, vol. 112, pp. 767–778, 2017.
- [28] Y. Tabe, Y. Lee, T. Chikahisa, and M. Kozakai, "Numerical simulation of liquid water and gas flow in a channel and a simplified gas diffusion layer model of polymer electrolyte membrane fuel cells using the lattice Boltzmann method," *Journal of Power Sources*, vol. 193, no. 1, pp. 24–31, 2009.
- [29] W. Seeger, J. Reimann, and U. Müller, "Two-phase flow in a T-junction with a horizontal inlet. Part I: Phase separation," *International Journal of Multiphase Flow*, vol. 12, no. 4, pp. 575–585, 1986.
- [30] M. A. Mohamed, H. M. Soliman, and G. E. Sims, "Experimental investigation of two-phase flow splitting in an equal-sided impacting tee junction with inclined outlets," *Experimental Thermal and Fluid Science*, vol. 35, no. 6, pp. 1193–1201, 2011.
- [31] H.-W. Li, J.-W. Li, Y.-L. Zhou et al., "Phase split characteristics of slug and annular flow in a dividing micro-T-junction," *Experimental Thermal and Fluid Science*, vol. 80, pp. 244–258, 2017.
- [32] S. Kim and S. Y. Lee, "Split of two-phase plug flow with elongated bubbles at a microscale branching T-junction," *Chemical Engineering Science*, vol. 134, pp. 119–128, 2015.
- [33] J. Chen, S. Wang, H. Ke, S. Cai, and Y. Zhao, "Gas-liquid two-phase flow splitting at microchannel junctions with different branch angles," *Chemical Engineering Science*, vol. 104, pp. 881–890, 2013.
- [34] W. Sun, Y. Liu, K. He, and S. Wang, "The phase distribution of gas-liquid two-phase flow in microimpacting T-junctions with different branch channel diameters," *Chemical Engineering Journal*, vol. 333, pp. 34–42, 2018.
- [35] G. Radilla, A. Nowamooz, and M. Fourar, "Modeling non-Darcian single- and two-phase flow in transparent replicas of rough-walled rock fractures," *Transport in Porous Media*, vol. 98, no. 2, pp. 401–426, 2013.
- [36] M. Fourar and R. Lenormand, "Inertial effects in two-phase flow through fractures," *Oil & Gas Science and Technology*, vol. 55, no. 3, pp. 259–268, 2000.
- [37] B. Li, R. Liu, and Y. Jiang, "Influences of hydraulic gradient, surface roughness, intersecting angle, and scale effect on non-linear flow behavior at single fracture intersections," *Journal of Hydrology*, vol. 538, pp. 440–453, 2016.

Research Article

Study on Pulse Characteristic of Produced Crude Composition in CO₂ Flooding Pilot Test

Pengxiang Diwu,¹ Tongjing Liu ,¹ Zhenjiang You ,² Ganggang Hou,¹ Runwei Qiao,¹ and Lekun Zhao¹

¹Enhanced Oil Recovery Institute, China University of Petroleum, Beijing 102249, China

²Australian School of Petroleum, The University of Adelaide, Adelaide, SA 5005, Australia

Correspondence should be addressed to Tongjing Liu; ltjcup@cup.edu.cn

Received 27 October 2017; Revised 6 February 2018; Accepted 12 February 2018; Published 13 March 2018

Academic Editor: Zhongwei Chen

Copyright © 2018 Pengxiang Diwu et al. This is an open access article distributed under the Creative Commons Attribution License, which permits unrestricted use, distribution, and reproduction in any medium, provided the original work is properly cited.

It has been observed in many laboratory tests that the carbon number of the maximum concentration components (CNMCC) of produced oil varies monotonically with CO₂ injection volume at the core scale. However, in CO₂ flooding pilot test at the field scale, we find that the CNMCC is usually nonmonotonic function of CO₂ injection volume, which is called “pulse characteristic” of CNMCC. To investigate the mechanism of this phenomenon, we analyze the physical process of CO₂ flooding in heterogeneous reservoir and explain the reason of the pulse characteristic of CNMCC. Moreover, two 3D reservoir models with 35 nonaqueous components are proposed for numerical simulation to validate the conjecture. The simulation results show that pulse characteristic of CNMCC only occurs in the heterogeneous model, confirming that the pulse characteristic results from the channeling path between wells, which yields nonmonotonic variation of oil-CO₂ mixing degree. Based on it, a new method can be developed to identify and quantify the reservoir heterogeneity.

1. Introduction

In recent years, the gas drive technology has been rapidly developed and widely applied. It has become another important way to improve oil recovery, besides thermal recovery and chemical flooding [1, 2]. CO₂ has several advantages on enhancing oil recovery, such as being easily soluble in oil, reducing oil viscosity [3], and reducing residual oil saturation [4]. Therefore, CO₂ drive is widely used in different types of oilfield, including sand and carbonate reservoirs [5–8].

The process of CO₂ displacement differentiates different components in oil [9]. This differentiation results in different flow rates among the compositions with different viscosities: light compositions are quickly carried away by CO₂, while heavy compositions move significantly slower. Consequently, produced oil composition will change along with the increase of displacement time.

It is widely known that the carbon number of maximum concentration components (CNMCC) increases monotonically with CO₂ injection volume, which has been confirmed by the experimental results [10, 11]. In 2011, Yang et al.

[10] analyzed the produced oil components in a CO₂ slime tube tests under conditions of immiscible and miscible flooding, respectively. The chromatograph analysis results of the two tests both show that the CNMCC of the produced oil increases monotonically with CO₂ injection volume. In 2015, Zhou et al. [11] analyzed the contents of the fluid compositions under different pressures by an 18-meter slime tube made of quartz. The results show that, at 18.1 MPa, the CNMCC of produced oil increases from C9 to C14 monotonically and gradually with the increase of CO₂ injection volume. At 25.2 MPa, the CNMCC of produced oil increases from C10 to C20 monotonically and quickly with the increase of CO₂ injection volume.

Despite several laboratory studies on CNMCC variation at core scale, the researchers tend to pay more attention to asphalt deposition, rather than the CNMCC variation at reservoir scale [12–15]. In fact, the latter is still not well understood during CO₂ flooding process in oil reservoirs. Generally, the differences in length and thickness between core and reservoir scales can result in different heterogeneity in horizontal and vertical directions. CO₂ channeling in flow

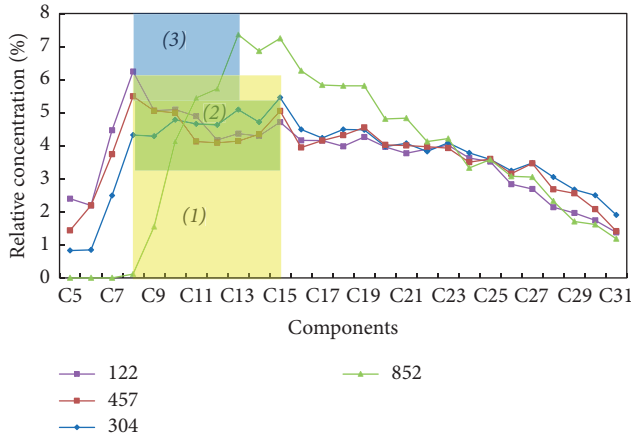


FIGURE 1: Relative concentration of produced oil compositions of production well W1 at different injection time.

direction at core scale is weaker than that at reservoir scale. Meanwhile, in vertical direction, CO_2 and oil at reservoir scale are mixed more thoroughly than at core scale. Based on these two main differences, it is reasonable to believe that the variation mechanism of CNMCC at reservoir scale would be quite different from that at core scale.

To investigate the CNMCC variation mechanism in CO_2 field flooding, this paper introduces a new concept “pulse characteristic” to characterize the CNMCC change law in produced oil, based on the field data. The physical process of displacement in heterogeneous formation is analyzed, and a scientific conjecture on the reason of the pulse characteristic of CNMCC at reservoir scale is proposed. Moreover, two numerical components models are established to validate the conjecture successfully. The pulse characteristic of CNMCC may provide a new way to identify and quantify the heterogeneity of CO_2 flooding reservoirs.

2. CNMCC Variation at Reservoir Scale

Based on the experimental results on CO_2 flooding [10, 11], it is believed that CNMCC should increase monotonically with CO_2 injection volume. However, CO_2 flooding pilot test at reservoir scale give us different results.

Composition analysis of produced oil from production well W1 in oil field H1 (China) has been performed. Figure 1 illustrates the relative component concentrations of produced oil at different time (from 122 to 852 days), in which x -axis shows components in oil phase and y -axis presents relative concentration. The relative component concentrations are calculated as normalized concentrations of components C5 to C31.

There is strong heterogeneity in the oil field H1, resulting from microcracks. The main parameters of the reservoir and fluid are listed in Table 1.

The commissioning date of production well W1 is one month before the commissioning date of corresponding injection well, which has a continuous CO_2 injection rate of 30 t/d. We set the commissioning date of corresponding injection well as the initial time; that is, injection time equals

TABLE 1: Main parameters of the reservoir and fluid.

Parameter	Values
Initial formation pressure	22.5 MPa
Formation temperature	88°C
Porosity	0.12
Permeability	5 mD
Initial oil saturation	0.56
Oil viscosity	0.44 mPa·s
Oil density	0.73
Flash gas oil ratio	34 m ³ /m ³
Bubble point	6.3 MPa
Minimum miscible pressure (MMP)	21.5 MPa

zero. The CNMCC variation of production well W1 can be divided into the following three stages (shown as three highlighted regions in Figure 1).

(1) From 122 to 304 days (pink and blue lines), the relative concentrations of compositions C5–C11 in produced oil decrease, while the relative concentrations of compositions C12–C16 increase. The corresponding CNMCC increases from C8 to C15. In this stage, the CNMCC has positive correlation with CO_2 injection volume, which coincides with the core experiments [10, 11].

(2) From 304 to 457 days (blue and red lines), the relative concentrations of compositions C5–C10 in produced oil increase, while the relative concentrations of compositions C11–C16 decrease. In this stage, the CNMCC has negative correlation with CO_2 injection volume. It indicates the nonmonotonic variation of CNMCC in the reservoir scale.

(3) From 457 to 852 days (red and green lines), while the relative concentrations of compositions C5–C10 in produced oil decrease, the relative concentrations of compositions C11–C23 increase. The corresponding CNMCC of produced oil increases again from C8 to C13.

As shown in Figure 1, the CNMCC of production well W1 changes nonmonotonically with the CO_2 injection volume; that is, it increases at the beginning, then decreases later, and increases again. We propose the concept of “pulse characteristic” to describe the nonmonotonic variation of CNMCC at reservoir scale. To explain the mechanism of this phenomenon, we analyze the entire CO_2 -oil interaction process in heterogeneous reservoir and provide our explanation in the next section.

3. Mechanism of Pulse Characteristic

According to the composition characteristics of produced oil, there are three main stages in the process of CO_2 flooding in homogeneous reservoirs [16–18]. The produced oil in the early stage is not in contact with CO_2 , so its compositions are the same as the original oil compositions. In the middle stage, the produced oil is from the leading displacement edge, where mainly the light oil compositions occupy, because of the oil- CO_2 extraction and dissolution. The produced oil in the late stage mainly consists of the remaining oil and usually has heavy compositions. Since the characteristic of

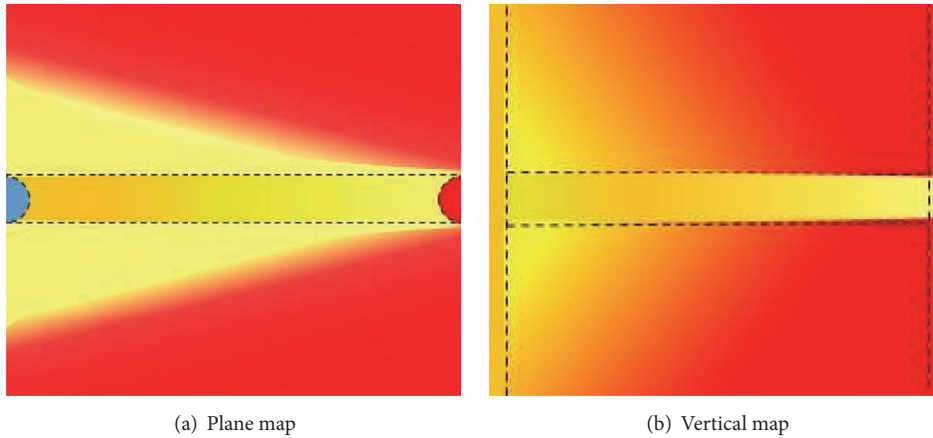


FIGURE 2: CO₂ (yellow) and oil (red) distribution and profile schematic diagram in the late stage.

the middle stage is not significant [11], the CNMCC increases monotonically with CO₂ injection volume at core scale.

However, the core scale usually exhibits lower heterogeneity than the reservoir scale. If there is plane heterogeneity, that is, CO₂ channeling-paths in the formation, the above three stages of CO₂ flooding would be different.

The main difference occurs in the late stage when CO₂ has occupied the whole CO₂ channeling-paths. The produced oil in this stage is mainly from outside of the channeling-paths, since CO₂ has displaced almost all the oil in the channeling-paths, as shown in Figure 2. This “fresh oil” has not been extracted thoroughly and still has quite a few light compositions. Therefore, the light compositions in produced oil will increase, which results in CNMCC decrease in the late stage. To sum up, the interaction degree between oil and injected CO₂ is not monotonic with time anymore under heterogeneous condition.

Based on the above analysis, we propose a conjecture to explain the CNMCC pulse characteristic at reservoir scale: the CNMCC will show back-and-forth pulse characteristic if there is plane heterogeneity in the reservoir, that is, channeling-paths. In the next section, this conjecture will be validated by two fully compositional models numerically.

4. Validation by Numerical Simulation

4.1. Fully Compositional Model Setting. To validate the conjecture in Section 3, we establish two fully compositional numerical models from Eclipse E300 module to simulate homogenous and heterogeneous scenarios, respectively. The heterogeneous model has an interwell channeling path which permeability is 100 mD. The corresponding formation and fluid parameters of the models are the same as those listed in Table 1. To investigate the components variation, we set 35 nonaqueous components in the models, including CO₂, N₂, C1–C32, and C32+. The oil compositions are shown in Table 2. The corresponding relative component concentrations are shown in Figure 3 (blue line), illustrating that initial CNMCC is C9.

According to the field flow regime, the development processes are depletion drive until formation pressure reaches

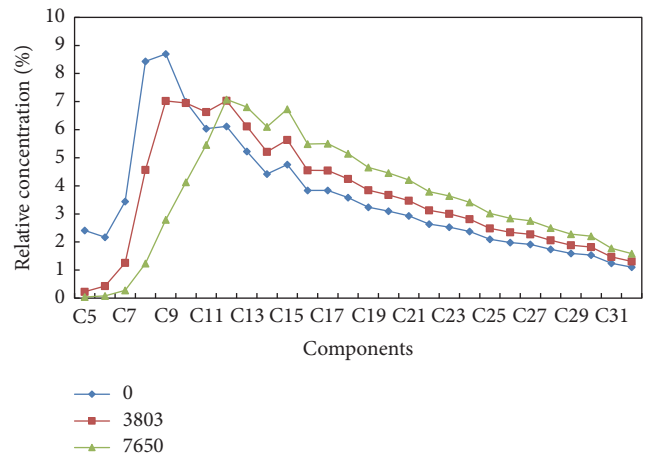


FIGURE 3: Relative concentration of produced oil at different time in the homogeneous model.

12 MPa, then water drive, and finally CO₂ drive development. In CO₂ flooding, the injection and production rates are constant (7500 sm³/day and 2.5 rm³/day, resp.). Based on the MMP in Table 1, it is miscible flooding near injection well and immiscible flooding away from injection well.

4.2. Simulation Results. Figure 3 shows the produced oil composition of the homogeneous model at different time. During CO₂ flooding process, the CNMCC increases monotonically from C9 to C12 with CO₂ injection volume. Although the CNMCC of produced oil are constant at C12 from injection time 3803 to 7650 days, we still observe the increasing relative concentration of heavy compositions and decreasing relative concentration of light compositions.

Figure 4 shows the produced oil composition of the heterogeneous model at different time. The CNMCC of produced oil increases from C9 to C30 during CO₂ injection time 0–210 days. After 210 days, the CNMCC of produced oil decreases from C30 to C12 until 788 days. Then the CNMCC of produced oil remains constant at C12. The nonmonotonic

TABLE 2: Oil component compositions in the models.

Component	Composition
CO ₂	0.0035
N ₂	0.0201
C1	0.1703
C2	0.06
C3	0.0392
C4	0.0173
C5	0.0241
C6	0.016
C7	0.0229
C8	0.0541
C9	0.0544
C10	0.0434
C11	0.0373
C12	0.0377
C13	0.0322
C14	0.0272
C15	0.0293
C16	0.0237
C17	0.0236
C18	0.0221
C19	0.02
C20	0.0191
C21	0.018
C22	0.0163
C23	0.0156
C24	0.0146
C25	0.0129
C26	0.0122
C27	0.0118
C28	0.0107
C29	0.0098
C30	0.0095
C31	0.0076
C32	0.0068
C32+	0.0567

variation of CNMCC only occurs in heterogeneous scenario, which is also observed in the field case shown in Figure 1.

5. Discussion

The CNMCC increases monotonically from C9 to C12 with CO₂ injection volume in the homogenous model, exhibiting the same change law with the experimental results [10, 11]. Based on the analysis in Section 3, it results from the monotonic variation of oil-CO₂ mixing degree in homogenous model.

The variation of CNMCC shows pulse characteristic in the heterogeneous model (Figure 4), which validates the conjecture in Section 3. Figure 5 presents the gas-oil ratio (GOR) and the oil saturation inside and out of the channel at the half of interwell distance.

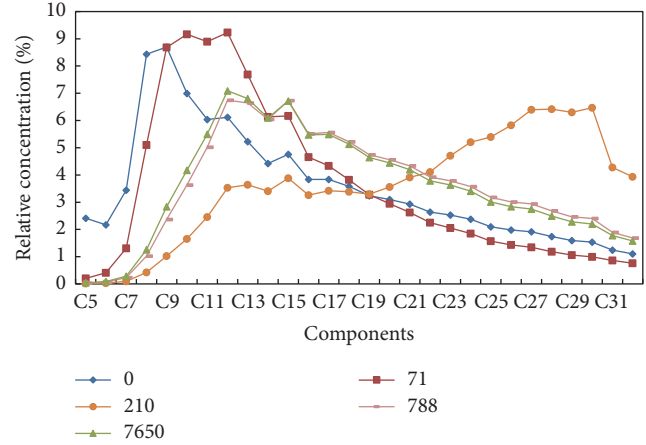


FIGURE 4: Relative concentration of produced oil at different time in the heterogeneous model.

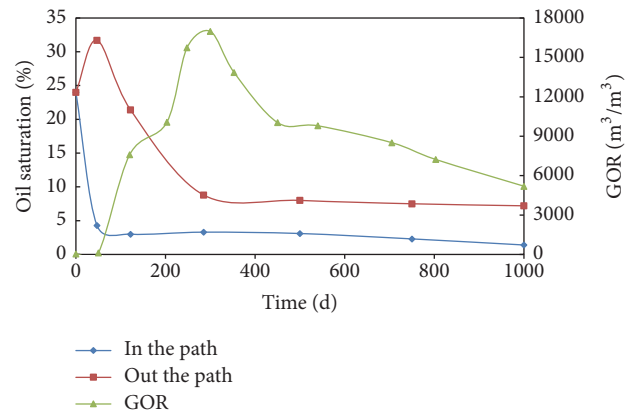


FIGURE 5: The oil saturation and GOR curves versus CO₂ injection time.

Before injection time 210 days, the produced oil is mainly from the channeling path, since the oil saturation in the path decreases rapidly (blue line). The mixing degree between oil and injected CO₂ is increased monotonically. Therefore, the CNMCC increases from C9 to C30 monotonically as well.

In the period of injection time 210–788 days, the produced oil is mainly from outside of the path, since the oil saturation out of the path decreases rapidly (red line). The interaction degree between the oil and injection CO₂ becomes nonmonotonic because the new oil enters and contributes to the produced oil. Therefore, the CNMCC decreases from C30 to C12 in this period.

The current work proposes a sufficient condition for pulse characteristic of CNMCC at reservoir scale. More intensive research needs to be conducted on the effects of other factors, including formation pressure, oil composition, and water saturation.

6. Conclusions

To investigate the CNMCC variation mechanism at reservoir scale, the present paper introduces the concept of pulse

characteristic to describe the CNMCC change law in CO₂ flooding pilot test. Two fully compositional numerical models are established to validate the conjecture on the pulse characteristic. The main conclusions are drawn as follows.

(1) The CO₂ flooding field data exhibits pulse characteristic; that is, the CNMCC of produced oil increases in the early stage, then decreases, and increases again in the late stage. It is different from the monotonic increasing characteristic at core scale.

(2) The pulse characteristic of CNMCC only occurs in heterogeneous formation, resulting from the nonmonotonic change of interaction degree between oil and injected CO₂. It is validated by simulation results of the two fully compositional models.

(3) A new method may be developed to identify and quantify the reservoir heterogeneity, using the idea of pulse characteristic of CNMCC, since it contains the information of CO₂ channeling path.

Conflicts of Interest

The authors declare no conflicts of interest regarding the publication of this paper.

Acknowledgments

This work was supported by the National Science and Technology Major Projects (2017ZX05009004) and Beijing Natural Science Foundation (2173061).

References

- [1] H. Lei, S. Pingping, J. Ying, Y. Jigen, L. Shi, and B. Aifang, "Prediction of asphaltene precipitation during CO₂ injection," *Petroleum Exploration and Development*, vol. 37, no. 3, pp. 349–353, 2010.
- [2] M. Dong, S. S. Huang, and R. Srivastava, "A laboratory study on near-miscible CO₂ injection in Steelman reservoir," *Journal of Canadian Petroleum Technology*, vol. 40, no. 2, pp. 53–61, 2001.
- [3] Y. M. Hao, Q. W. Bo, and Y. M. Chen, "Laboratory investigation of CO₂ flooding," *Petroleum Exploration and Development*, vol. 32, no. 2, pp. 110–112, 2005.
- [4] M. T. Li, W. W. Shan, X. G. Liu et al., "Laboratory study on miscible oil displacement mechanism of supercritical carbon dioxide," *Acta Petrolei Sinica*, vol. 27, no. 3, pp. 80–83, 2006.
- [5] E. H. Luo, Y. L. Hu, and B. Z. Li, "Practices of CO₂ EOR in China," *Special Oil and Gas Reservoirs*, vol. 20, no. 2, pp. 1–7, 2013.
- [6] J. Qin, H. Han, and X. Liu, "Application and enlightenment of carbon dioxide flooding in the United States of America," *Shiyou Kantan Yu Kaiifa/Petroleum Exploration and Development*, vol. 42, no. 2, pp. 209–216, 2015.
- [7] H.-Q. Chen, Y.-L. Hu, and C.-B. Tian, "Advances in CO₂ displacing oil and CO₂, sequestered researches," *Oil-Field Chemistry*, vol. 29, no. 1, pp. 116–127, 2012.
- [8] C. Qiao, L. Li, R. T. Johns, and J. Xu, "Compositional modeling of dissolution-induced injectivity alteration during CO₂ flooding in carbonate reservoirs," *SPE Journal*, vol. 21, no. 3, pp. 809–826, 2016.
- [9] M. A. Kelingsi, *Carbon Dioxide Enhanced Oil Recovery Mechanism and Engineering Design*, Petroleum Industry Press, Beijing, China, 1989, Translated by S. J. Cheng.
- [10] Z. M. Yang, L. G. Tang, and S. Zhang, "Microcosmic mechanisms of CO₂ flooding in low permeability reservoirs," *Intelligent Information Technology Application Association*, vol. 5, 2011.
- [11] T. Zhou, X. Liu, Z. Yang, X. Li, and S. Wang, "Experimental analysis on reservoir blockage mechanism for CO₂ flooding," *Petroleum Exploration and Development*, vol. 42, no. 4, pp. 548–553, 2015.
- [12] R. J. Hwang and J. Ortiz, "Effect of CO₂ flood on geochemistry of McElroy oil," *Organic Geochemistry*, vol. 29, no. 1-3, pp. 485–503, 1998.
- [13] N. A. E. da Silva, V. R. D. R. Oliveira, M. M. S. Souza, Y. Guerrieri, and G. M. N. Costa, "New method to detect asphaltene precipitation onset induced by CO₂ injection," *Fluid Phase Equilibria*, vol. 362, pp. 355–364, 2014.
- [14] J. Vuillaume, I. Akervoll, and P. Bergmo, "CO₂ injection efficiency, synthesis of conceptual chalk model: incremental oil recovery and CO₂ storage potential," in *Proceedings of the Brazil Offshore Conference 2011*, pp. 578–589, June 2011.
- [15] E. Huang, "The effect of oil composition and asphaltene content on CO₂ displacement," in *Proceedings of the SPE/DOE Enhanced Oil Recovery Symposium*, Tulsa, Oklahoma, 1992.
- [16] F. L. Zhao, H. D. Hao, J. R. Hou et al., "CO₂ mobility control and sweep efficiency improvement using starch gel or ethylenediamine in ultra-low permeability oil layers with different types of heterogeneity," *Journal of Petroleum Science and Engineering*, vol. 133, pp. 52–65, 2015.
- [17] A. Alizadeh, M. H. Ghazanfari, V. Taghikhani, and A. Badakhshan, "Experimental investigation of water alternating CH₄-CO₂ mixture gas injection in light oil reservoirs," *International Journal of Oil, Gas and Coal Technology*, vol. 8, no. 1, pp. 31–40, 2014.
- [18] M. Bickle, N. Kampman, H. Chapman et al., "Rapid reactions between CO₂, brine and silicate minerals during geological carbon storage: Modelling based on a field CO₂ injection experiment," *Chemical Geology*, vol. 468, pp. 17–31, 2017.

Research Article

Investigating Multiphase Flow Phenomena in Fine-Grained Reservoir Rocks: Insights from Using Ethane Permeability Measurements over a Range of Pore Pressures

Eric Aidan Letham  and Robert Marc Bustin

Department of Earth, Ocean and Atmospheric Sciences, The University of British Columbia, 2020-2207 Main Mall, Vancouver, BC, Canada V6T 1Z4

Correspondence should be addressed to Eric Aidan Letham; ealetham@gmail.com

Received 19 September 2017; Revised 13 December 2017; Accepted 3 January 2018; Published 7 March 2018

Academic Editor: Tongqiang Xia

Copyright © 2018 Eric Aidan Letham and Robert Marc Bustin. This is an open access article distributed under the Creative Commons Attribution License, which permits unrestricted use, distribution, and reproduction in any medium, provided the original work is properly cited.

The ability to quantify effective permeability at the various fluid saturations and stress states experienced during production from shale oil and shale gas reservoirs is required for efficient exploitation of the resources, but to date experimental challenges prevent measurement of the effective permeability of these materials over a range of fluid saturations. To work towards overcoming these challenges, we measured effective permeability of a suite of gas shales to gaseous ethane over a range of pore pressures up to the saturated vapour pressure. Liquid/semiliquid ethane saturation increases due to adsorption and capillary condensation with increasing pore pressure resulting in decreasing effective permeability to ethane gas. By how much effective permeability to ethane gas decreases with adsorption and capillary condensation depends on the pore size distribution of each sample and the stress state that effective permeability is measured at. Effective permeability decreases more at higher stress states because the pores are smaller at higher stress states. The largest effective permeability drops occur in samples with dominant pore sizes in the mesopore range. These pores are completely blocked due to capillary condensation at pore pressures near the saturated vapour pressure of ethane. Blockage of these pores cuts off the main fluid flow pathways in the rock, thereby drastically decreasing effective permeability to ethane gas.

1. Introduction

Effective matrix permeability is one control on the deliverability of hydrocarbons, and therefore the economics of shale oil and shale gas wells [1]. Being able to quantify effective permeability at initial reservoir saturation and the range of saturations experienced during production from these reservoirs is thus paramount to efficient exploitation of the resource. Hydrocarbons in shale oil and shale gas reservoirs travel in the presence of multiple immiscible fluids through small pores in the fine-grained matrix prior to reaching a fracture network leading to the wellbore. Immiscible phases include one or both of liquid and gaseous hydrocarbons as well as connate water and imbibed hydraulic fracturing fluid. Capillary pressures across the interfaces of these immiscible phases can be enormous due to how small the pores are in shales (nanometer to micrometer length scale (e.g., [2])). The small pore length scale also means that geometrical

constrictions imposed by fluid adsorbed to pore walls can significantly inhibit flow [3]. Effective permeability of hydrocarbon phases will therefore be very sensitive to the presence and saturation of the different fluid phases [3, 4].

To date, researchers have had minimal success investigating multiphase flow characteristics of shale due to challenges associated with characterizing reservoir rocks with small length scale pore systems. These challenges include the difficulty in controlling and monitoring fluid saturations and distributions in intact samples, and, because of their inherently low permeability, difficulty in quantifying the very low flow rates characteristic of shales. Combined, these challenges have prevented measurement of effective permeability over a range of fluid saturations and thus impaired our understanding of shale multiphase flow phenomena.

In this study, we investigate multiphase flow phenomena in fine-grained rocks by measuring effective permeability of a suite of shale samples to gaseous ethane over a range of

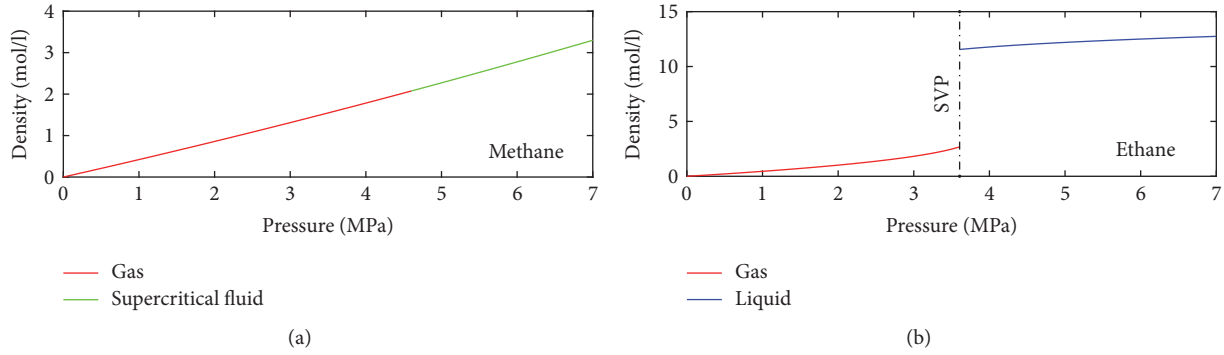


FIGURE 1: Isothermal density-pressure relationships for methane (a) and ethane (b) at laboratory temperature (18°C). SVP is saturated vapour pressure. Data from Lemmon et al., 2017.

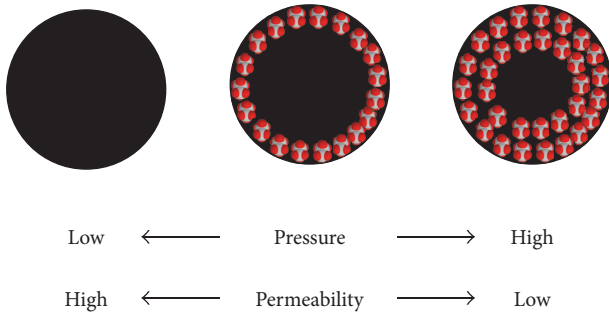


FIGURE 2: Schematic cross sections of pore throats showing adsorbed liquid/semiliquid ethane (red and grey molecules) restricting flow paths for ethane gas at high gas pressure, resulting in decreased effective permeability to ethane gas.

pore pressures up to the saturated vapour pressure (3.59 MPa at 18°C). At laboratory temperature, pure ethane can exist as a liquid or a gas, depending on pressure (Figure 1(b)). In contrast, methane, the dominant component of natural gas, is either a gas or a supercritical fluid (Figure 1(a)). At the range of pressures found in natural gas reservoirs, methane typically adsorbs to the pore walls of organic rich rocks to form a monolayer, resulting in Type I (Langmuir) isotherms [5]. In contrast, multilayer adsorption is expected for ethane at pore pressures approaching the saturated vapour pressure, which is why we chose ethane as a probing gas for this study; a wider range of adsorbed liquid/semiliquid fluid saturations can be achieved using ethane compared to that if methane is used as a probing gas.

Saturation of liquid/semiliquid ethane increases with increasing pore pressure due to adsorption and capillary condensation, resulting in decreased permeability to ethane gas (Figure 2). These permeability decreases vary across a suite of samples with varying pore size. By measuring pore size of the sample suite using gas slippage measurements, we show that the largest drops in ethane relative permeability take place in rocks with the smallest pores. We show that gas slippage measurements can be used to predict relative permeability and therefore aid in predicting the deliverability of hydrocarbons from a shale oil or shale gas reservoir.

2. Methods

2.1. Sample Suite. The sample suite includes two gas shales from the Eagle Ford Formation in Texas, USA (TEFB9 and TEF21), and three gas shales from the Montney Formation in British Columbia, Canada (MONT, B5FD1B6, and B5FD2A2). The Eagle Ford and Montney formations are two very important hydrocarbon producers [7, 8]. The sample suite was chosen so that a wide range of matrix permeabilities and pore sizes were investigated. Sample TEFB9 was subsampled for two 3 cm diameter by ~3 cm length plugs, one oriented for fluid flow parallel to bedding (TEFB9Pll) and one for fluid flow perpendicular to bedding (TEFB9Pd). Subsample TEFB9Pll was evaluated at multiple stress states to understand the impact of the shale's stress sensitive pore structure on its multiphase flow characteristics. For the rest of the samples, a single plug oriented for fluid flow parallel to bedding was evaluated at one stress state to build up a data set large enough that the multiphase flow characteristics of different shales could be compared.

2.2. Permeability Measurements. Permeability measurements to helium and ethane were made on each sample using the pulse decay technique [9] at laboratory temperature (18 degrees Celsius). Helium, an inert gas that does not adsorb to pore walls, was used for petrophysical characterization of pore structures in the absence of adsorbed fluid. Measurements were made at a range of different pore pressures (Figure 3) to vary mean free path of the gas such that Klinkenberg plots could be generated (apparent permeability, K_a , against inverse pore pressure). The difference between pore pressure (P_p) and confining pressure (P_c), referred to herein as "simple effective stress," was kept constant by changing confining pressure by the same amount as pore pressure. Linear fits of the Klinkenberg plot data were extrapolated to infinite pore pressure in order to determine slip-free permeability, K_∞ , and Klinkenberg's slippage factor, b [10]

$$K_a = K_\infty \left(1 + \frac{b}{P_p} \right). \quad (1)$$

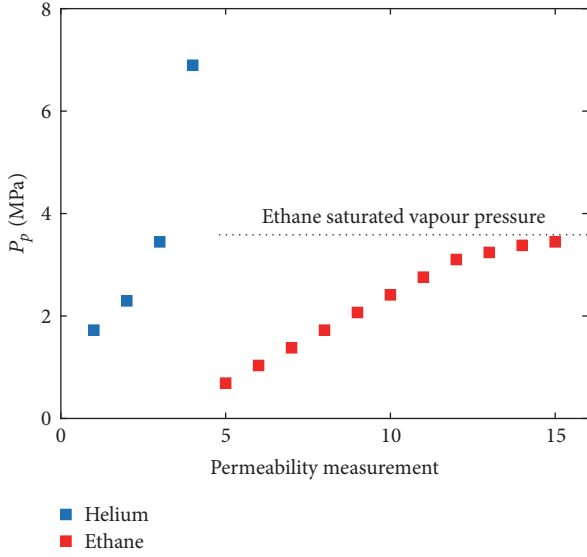


FIGURE 3: Pore pressure schedule for the suite of helium (blue) and ethane (red) permeability measurements made on each sample. The ethane saturated vapour pressure at the temperature of the permeability measurements (18°C) is 3.59 MPa.

Determining b allows calculation of dominant pore size, d [10], which represents an average diameter of the smallest pore throats along those flow paths responsible for the bulk of the fluid flux through the rock, calculated using a simplified model that represents pores as cylindrical capillary tubes [11]

$$d = \frac{8c\lambda P_p}{b}, \quad (2)$$

where c is Adzumi's constant (0.9 [12]), P_p is pore pressure, and λ is mean free path

$$\lambda = \frac{RT}{\sqrt{2}\pi d_{\text{kin}}^2 N_A P}, \quad (3)$$

where R is the gas constant, T is temperature, d_{kin} is kinetic diameter, N_A is Avogadro's constant, and P is pressure [13].

Pore size estimates from gas slippage measurements could also be made assuming pores have slot-shaped cross-sectional geometries [14]. Although some studies argue based on photomicrographs that pores of some gas shales are more slot shaped than circular in cross section (e.g., [15]), recent analysis of a large compiled data set that includes many different gas shales suggests that pores in fine-grained sedimentary rocks are more accurately modelled as circular in cross-sectional geometry [11]. We therefore use the circular model (see (2)) to estimate pore size from gas slippage measurements in this study.

Ethane permeability measurements were made at a range of mean pore pressures increasing from 0.69 to 3.45 MPa (Figure 3). Pressure was allowed to equilibrate for a minimum of 12 hours at each pressure step. Pressure was monitored during the equilibration period and sufficient time was allowed for pressure to stabilize prior to measurement. Pressure pulses of 0.24 MPa were generated by bleeding off pressure from the

downstream reservoir. Pressure pulses need to be small enough that flow is laminar. While early studies of the pulse decay technique suggest a maximum pressure gradient of 0.03 MPa/cm [16], much smaller than the gradients imparted in the present study (0.08 MPa/cm), recent work shows that pressure gradients much greater than 0.03 MPa/cm can be used and flow still be in the laminar flow regime in low permeability samples [17]. Differential pressure was allowed to decay until reaching 0.01 MPa or, for lower permeability samples where differential pressure decays very slowly, until enough data was collected for an accurate permeability measurement.

2.3. Permeability Calculation. Permeability was calculated from the pulse decay data using the equations presented in Cui et al. [18]. An isothermal pressure-viscosity curve [19] was used to determine the correct ethane viscosity for each permeability calculation. Adsorption/desorption was not accounted for in any of the permeability calculations. Ethane is a strongly sorptive gas and therefore adsorption/desorption could impact the accuracy of calculated ethane permeabilities [18]. However, the upstream and downstream reservoirs of the permeameters used in this study are much larger than pore volumes of the samples (~10 times), so error in our permeability measurements resulting from not accounting for adsorption/desorption is less than 10% [18].

Feng et al. [17, 20] presented an experimental setup that would eliminate the need to account for adsorption when calculating permeability from pulse decay data. In their setup, the pressure pulse is generated by both increasing the upstream gas pressure and decreasing the downstream gas pressure by equal amounts from equal volume reservoirs. Pressure would therefore come to equilibrium at the same pressure the sample was soaked at prior to measurement, and the quantity of ethane adsorbed would be the same before and after the pressure decay. We did not adopt the experimental setup of Feng et al. [17, 20] because, in addition to quantifying permeability at each pressure step, we wanted to quantify the rate of change of ethane gas molecules in the adsorbed state with change in pore pressure, herein referred to as the ethane desorption rate. Having an experimental setup where pressure comes to equilibrium after the pressure pulse decay at a different pressure than the initial soak period pressure allowed calculation of the ethane desorption rate.

2.4. Ethane Desorption Rate Calculations. Ethane desorption rates were calculated using the pressure data collected during permeability measurements. The desorption rate is equivalent to the slope of the desorption isotherm at the pore pressure of the permeability measurement. Desorption rate is quantified because it represents how much liquid/semiliquid ethane saturation changes between successive ethane permeability measurements at different mean pore pressures. Because gas pressure is bled from the system when generating differential pressure across the sample, gas pressure in the upstream reservoir, downstream reservoir, and sample pore volume come to equilibrium at a lower pressure than the initial soak period equilibrium pressure. The permeameter is a closed system once the differential pressure is created, so gas

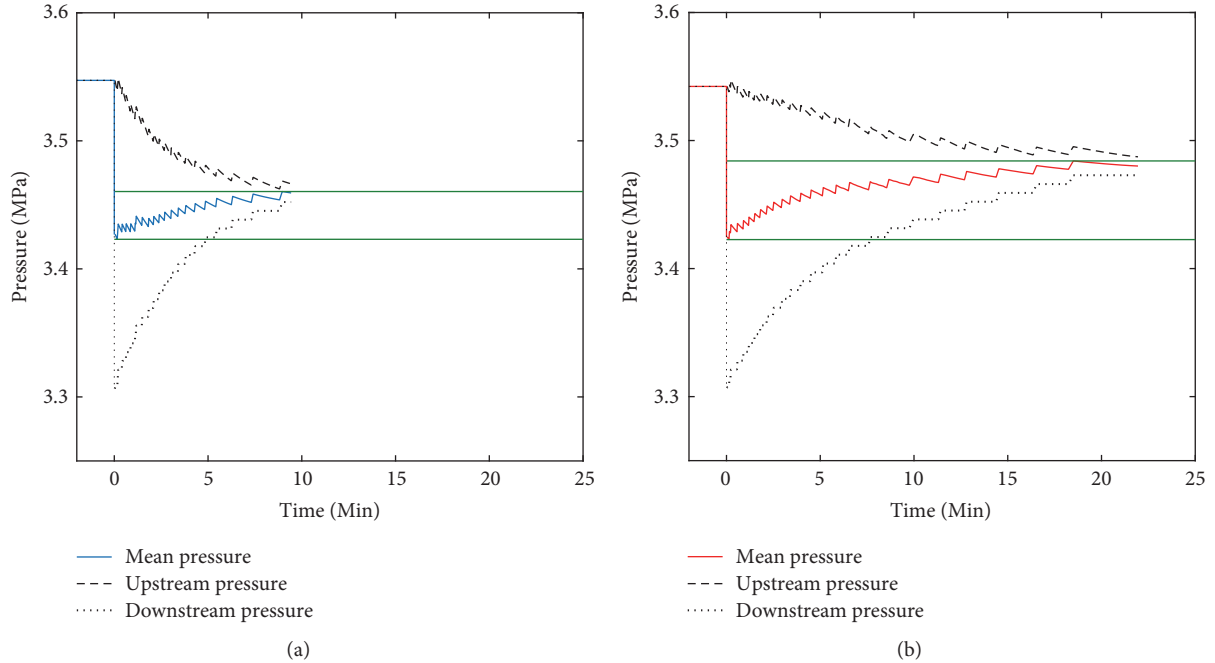


FIGURE 4: Comparison of helium (a) and ethane (b) pulse decay data for sample B5FD2A2. Mean pore pressure increases throughout the helium permeability measurement because the upstream reservoir of the permeameter is larger than the downstream reservoir, and gas was bled from the downstream reservoir to generate the differential pressure. Mean pore pressure increases by more in the ethane measurement than the helium measurement because liquid/semiliquid ethane desorbs to reach equilibrium at the final gas pressure, which is lower than the equilibrium gas pressure during the soak period (time < 0 on graphs). Differential pressure in the ethane permeability measurement takes more than twice as long to decay than the helium differential pressure because adsorbed liquid/semiliquid ethane constricts flow paths resulting in lower ethane gas permeability. Green lines indicate the difference between minimum mean pressure and final equilibrium pressure.

molecules that desorb from the sample due to the drop in pore pressure result in higher post-decay equilibrium gas pressure than if no molecules were to desorb (Figure 4). Using the pressure data, the known reservoir volumes, and estimates of pore volume, Boyle's Law was used to calculate the amount of gas molecules desorbed per MPa drop in total system pressure at the mean pore pressure of each permeability measurement (the ethane desorption rate). Pore volumes were estimated from the dimensions of the samples and porosities determined using a combination of unconfined helium pycnometry and mercury immersion. For the ethane desorption rate calculations, compressibility factors were calculated using the Peng-Robinson equation of state [21].

2.5. Ethane Gas Slippage Estimates. Mean free path decreases with increasing gas pressure resulting in gas slippage being less significant and therefore lower apparent permeability [10]. When ethane is used as a probing gas, effective permeability to ethane gas varies with pore pressure not only due to gas slippage, but also due to changes in liquid/semiliquid ethane saturation resulting from adsorption and capillary condensation. In order to distinguish these two components of permeability variation, Klinkenberg's slippage factor for ethane was calculated by multiplying the slippage factor measured for helium by the ratio of ethane mean free path to helium mean free path at a given pressure and temperature. This ratio is equal to the kinetic diameter of helium (0.26 nm [22]) squared over the kinetic diameter of ethane (0.44 nm

[23]) squared (see (3)). Expected ethane permeability variation due to gas slippage was then calculated using the lowest pressure ethane permeability measurement and the calculated ethane slippage factor.

3. Results

3.1. Helium Klinkenberg Plots. K_{∞} from extrapolation of Klinkenberg plots ranges from 3×10^{-5} to 2×10^{-2} mD (Figure 5). K_{∞} of sample TEFB9 parallel to bedding decreases with increasing simple effective stress from 2×10^{-2} mD at 7 MPa simple effective stress to 8×10^{-4} mD at 48 MPa simple effective stress. K_{∞} of sample TEFB9 perpendicular to bedding at 7 MPa simple effective stress is two orders of magnitude lower than to flow parallel to bedding at the same stress state.

Dominant pore diameter, d , ranges from 42 nm to 473 nm (Figure 6). Rocks with lower permeability have smaller pores (Figure 6). This however is only a general trend with a high degree of scatter. For example, samples MONT and TEF21 have the same dominant pore size but permeabilities that differ by an order of magnitude (yellow triangle and red star in Figure 6).

3.2. Ethane Permeability. Ethane permeability of all samples under all stress states and flow orientations decreases with increasing pore pressure (Figure 7). At mean pore

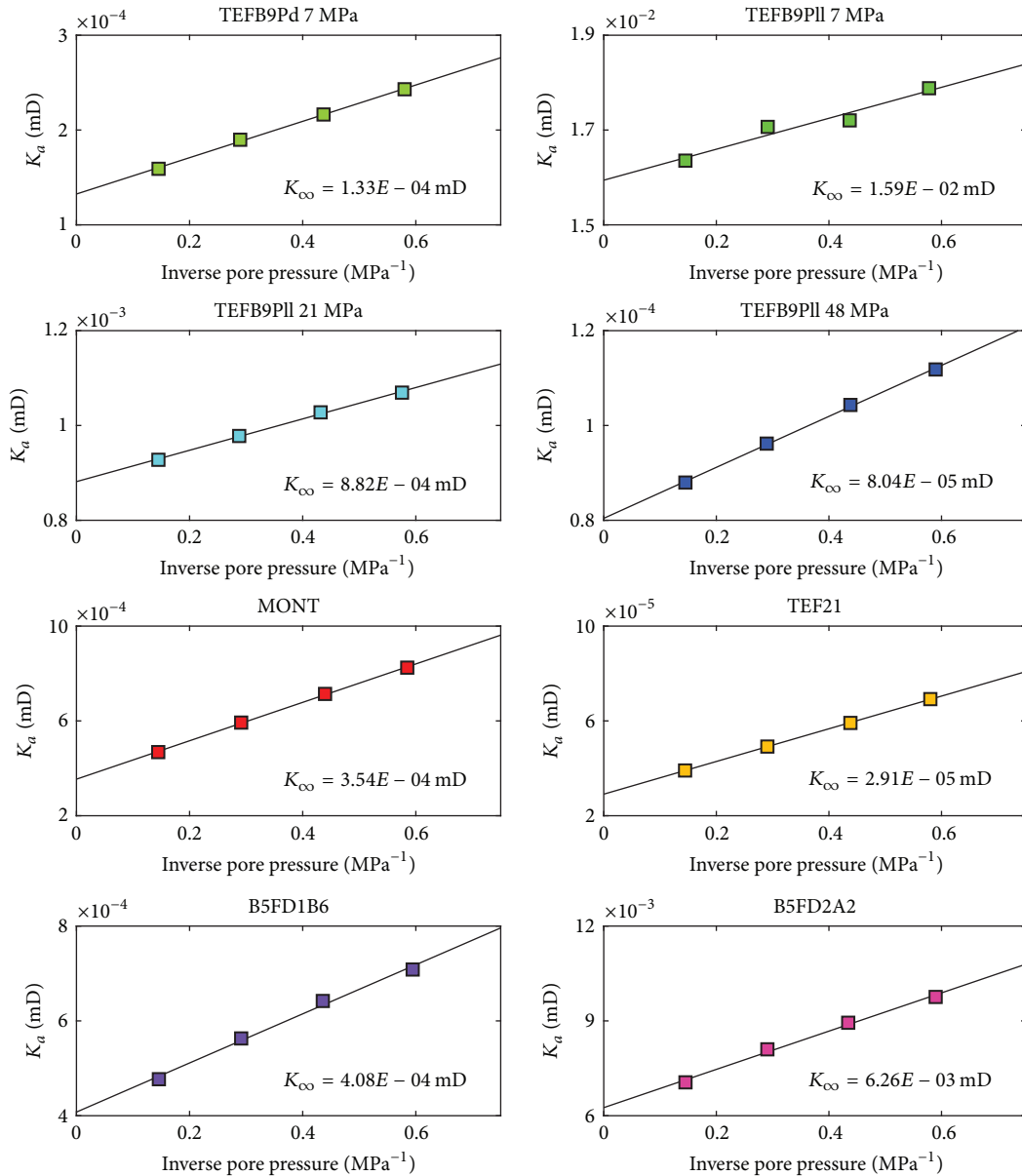


FIGURE 5: Klinkenberg plot for each sample generated using the helium permeability data.

pressures less than 2.3 MPa, the decreases in permeability closely match the predicted permeability decreases due to gas slippage (Figure 7). Ethane permeability deviates from what is predicted due to gas slippage (becoming lower) at higher pore pressures (Figure 7). The pore pressure where deviation takes place varies within the sample suite. The lowest pressure permeability deviation is sample MONT at ~2.3 MPa (Figure 7), whereas for other samples deviation does not occur until pressures are above 3 MPa.

At higher pore pressures, all samples have lower permeability than what is predicted due to gas slippage, but the magnitude of the difference between measured permeability and predicted permeability varies within the sample suite; at 3.45 MPa mean pore pressure (the highest mean pore

pressure measured), the difference between measured permeability and permeability predicted due to gas slippage ranges from 28 to 84 percent (Table 1, column 6).

3.3. Ethane Desorption Rates. Ethane desorption rates over the pressure range of the permeability measurements are only presented for the five highest permeability samples (Figure 8). Desorption rates for the three lowest permeability samples (TEF21, TEFB9Pd at 7 MPa SES, and TEFB9Pll at 48 MPa SES) are not presented because accurate calculations could not be made from the pressure data. Differential pressure was only allowed to partially decay for the low permeability measurements due to the excessive time required for full pressure decay (multiple days to weeks). Pressure data would

TABLE 1: Experimental conditions and tabulated data for each sample.

Sample	Simple effective stress (MPa)	K_{∞} (mD)	b_{helium}	b_{ethane}	% permeability drop at 3.45 MPa*
TEFB9PII	7	$1.59E-02$	0.20	0.07	33
TEFB9PII	21	$8.82E-04$	0.38	0.13	39
TEFB9PII	48	$8.04E-05$	0.67	0.23	45
TEFB9Pd	7	$1.33E-04$	1.45	0.51	28
MONT	21	$3.54E-04$	2.29	0.80	84
TEF21	21	$2.91E-05$	2.37	0.83	76
B5FD1B6	7	$4.08E-04$	1.27	0.44	29
B5FD2A2	21	$6.26E-03$	0.97	0.34	44

* Percent difference between predicted permeability and measured ethane gas permeability at 3.45 MPa mean pore pressure.

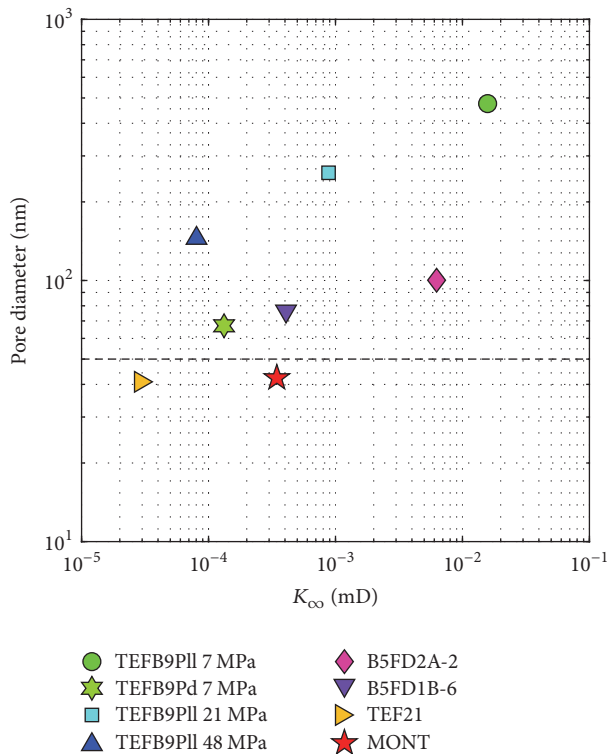


FIGURE 6: Dominant pore size calculated using (2) and the helium Klinkenberg plot data. Pores are generally smaller in samples with lower K_{∞} , but with lots of variability around the trend. Dashed line delineates the macropore-mesopore boundary below which capillary condensation is expected at ethane gas pore pressures close to the saturated vapour pressure [6].

therefore have to be extrapolated to estimate the final equilibrium pressure after decay. Additionally, because pressure data series for the lowest permeability samples are collected over a longer time scale (days) than higher permeability samples (minutes to hours), small temperature fluctuations can significantly influence mean pore pressure (Figure 9). The data were collected in a temperature controlled environment, but at the time scale of days, temperature drifts on the order of a quarter of a degree Celsius take place (e.g., Figure 9(d)).

Sample TEFB9PII at 7 and 21 MPa simple effective stress and sample B5FD2A2 all show measurably elevated ethane

desorption rates at high pore pressure (Figure 8). Samples MONT and B5FD1B6 do not show measurably elevated desorption rates at any mean pore pressure. Calculated desorption rates are slightly negative at some mean pore pressures for samples MONT and B5FD1B6.

4. Discussion

4.1. Desorption Rate Data Quality. Measured desorption rates are valuable data in this study because they represent by how much liquid/semiliquid ethane saturation is changing between successive permeability measurements, and the goal of the study is to make matrix permeability measurements at different fluid saturations. However, the apparatuses used to measure desorption rates in this study (pulse decay permeameters) are not optimized for measuring this rate. A discussion of the resulting data quality is therefore required.

The negative desorption rates calculated at some pore pressures for samples MONT and B5FD1B6 counterintuitively suggest desorption of ethane is occurring when pressure is increasing. These negative rates are not real but are an artifact resulting from the resolution limit of the experimental setup combined with temperature fluctuation (Figure 9). Because the upstream and downstream reservoirs of the permeameters used in this study were chosen to be much larger than the pore volumes of the samples (in order to minimize permeability measurement error due to adsorption), ethane desorbing during permeability measurements only resulted in small mean pore pressure increases (0.06 MPa at most). Small temperature fluctuations therefore result in significant absolute errors in measured desorption rates and large relative errors for small desorption rates. Because of the errors, it is possible that when the calculated desorption rates are near-zero, liquid/semiliquid ethane saturation could be increasing by small amounts between successive permeability measurements.

To illustrate how near-zero desorption rates that cannot be accurately quantified from the pulse decay pressure data could in fact represent small but significant changes in liquid/semiliquid ethane saturation, desorption rate data for sample TEFB9PII at 7 MPa simple effective stress is converted to a liquid/semiliquid ethane saturation curve (Figure 10). This sample is the highest permeability sample of the suite and therefore has the highest quality pressure data for calculating

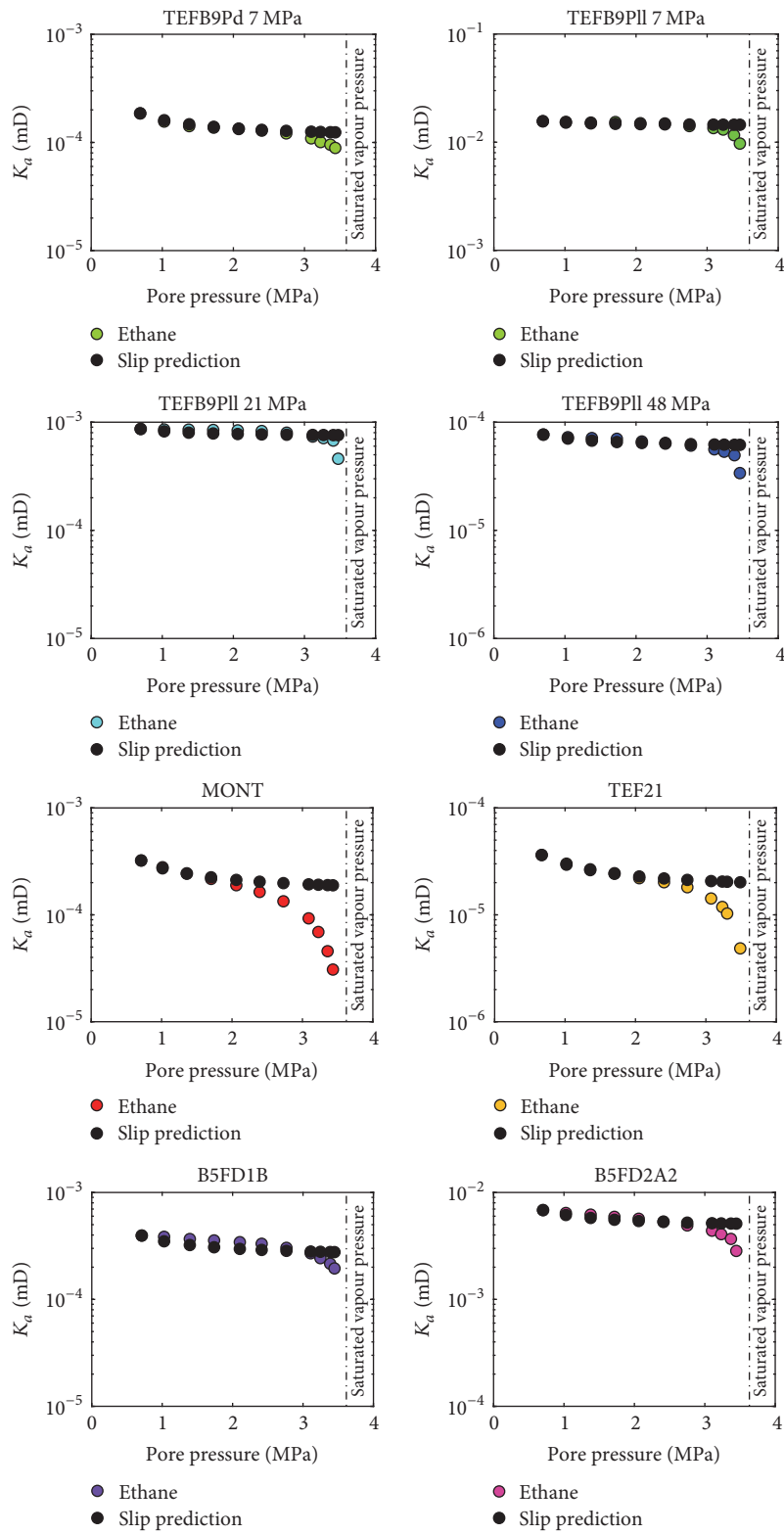


FIGURE 7: Ethane permeability measurements (coloured markers) and predicted permeability variation due to gas slippage (black markers) calculated using the ethane slippage factor, which was derived from the helium permeability data.

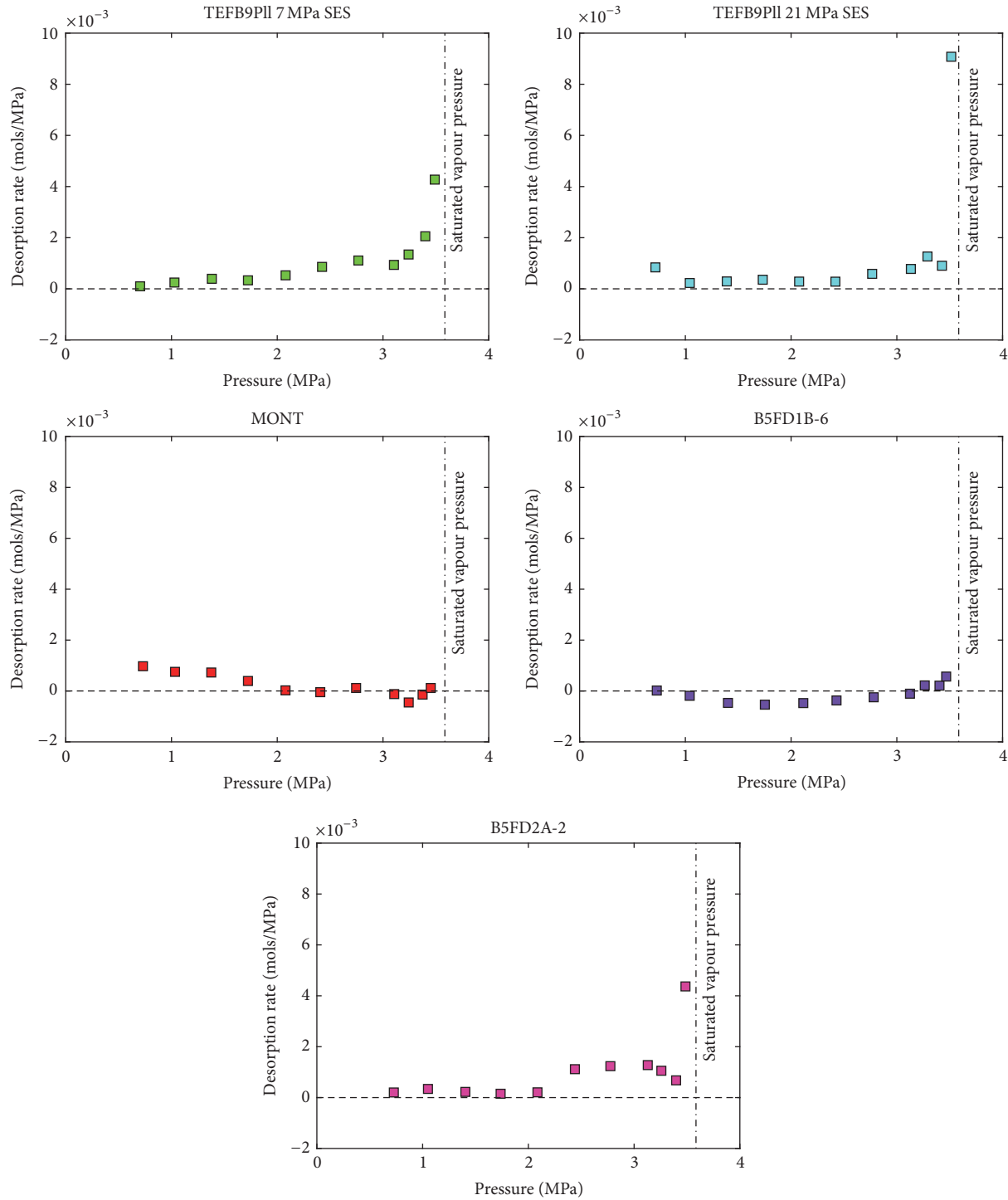


FIGURE 8: Ethane desorption rates calculated from the pulse decay pressure data. Desorption rate is elevated at high pressures for sample TEFB9P11 at 7 and 21 MPa simple effective stress and sample B5FD2A2. Desorption rate is not elevated above resolution limit for samples MONT and B5FD1B6.

desorption rates (it was the least susceptible to temperature fluctuation). An adsorbed liquid/semiliquid fluid density of $11553 \text{ moles per m}^3$, the density of liquid ethane at the ethane saturated vapour pressure at 18°C [19], is assumed for the calculations. Liquid/semiliquid ethane saturation in the sample increases by a small but not insignificant $\sim 5\%$ between

0.7 and 2.2 MPa mean pore pressure (Figure 10) even though desorption rate is only slightly above zero over this pressure range (Figure 8). Due to the resolution limit of the desorption rate measurements, sources of error (temperature fluctuation), and the assumed density, the ethane saturation curve in Figure 10 is a crude estimate and saturation curves for

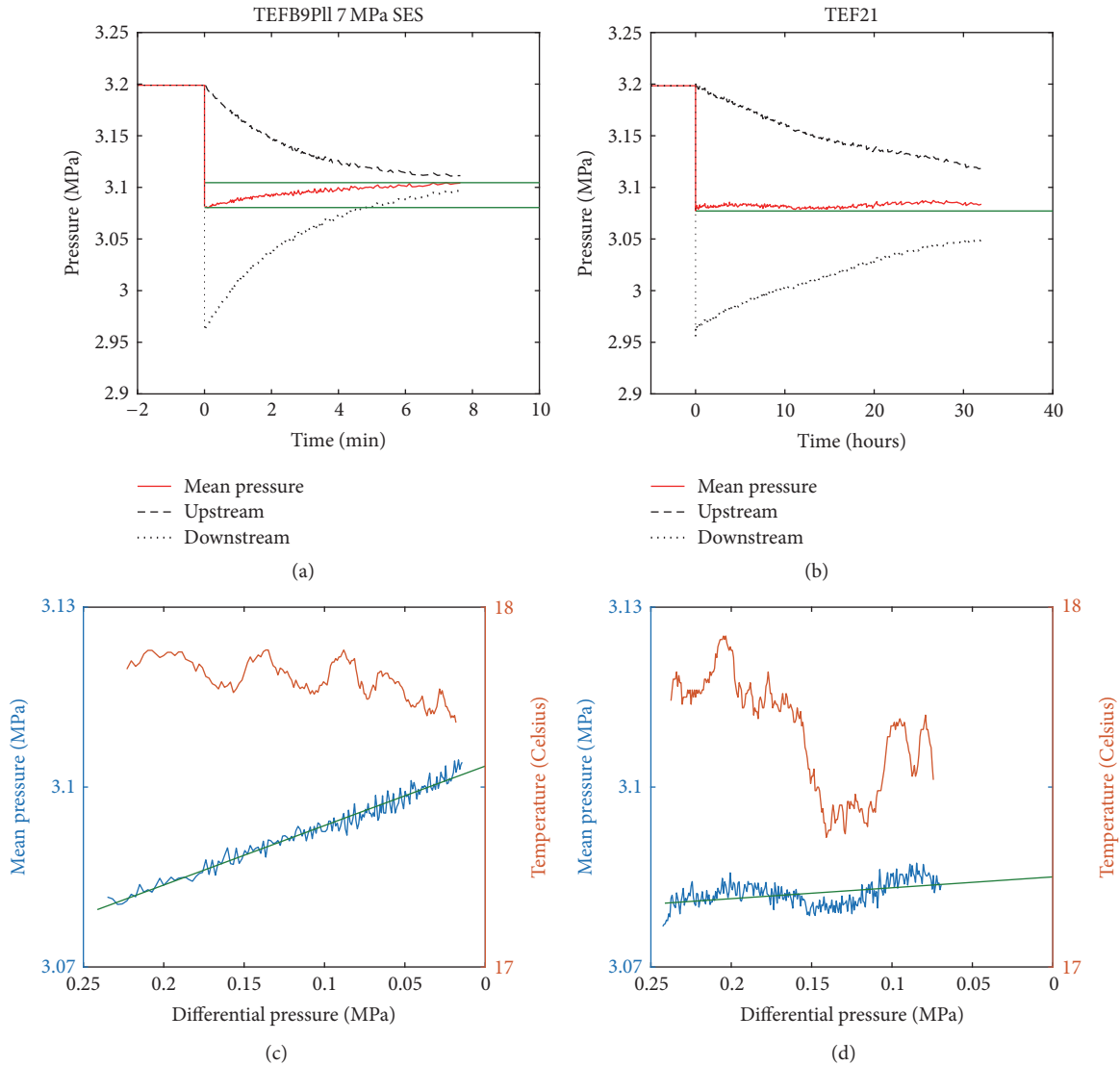


FIGURE 9: Examples of good quality ethane pulse decay pressure data for a high permeability sample from which accurate desorption rates could be calculated ((a) and (c)) and poor quality data for a low permeability sample from which accurate desorption rates could not be calculated ((b) and (d)). Temperature fluctuation over the duration of the measurement has a significant impact on mean pore pressure for the low permeability sample (d). Data collection for the low permeability sample was stopped at ~ 0.07 MPa differential pressure because of the excessive time required for full decay (b). Green lines in (a) and (b) indicate the difference between minimum mean pressure and final equilibrium pressure.

lesser quality data from lower permeability samples are not presented.

4.2. Ethane Permeability at Low Pore Pressures. At low pore pressures (< 2 MPa), the close match between apparent ethane permeability and permeability variation predicted due to gas slippage (Figure 7) indicates that adsorption of liquid/semiliquid ethane is not significantly impacting ethane gas permeability. If liquid/semiliquid ethane was blocking fluid flow, measured apparent permeability would be lower than predicted permeability. Ethane desorption rates for all samples with desorption data are near zero at pore pressures less than 2.2 MPa (Figure 8), indicating no changes in

liquid/semiliquid ethane saturation between successive permeability measurements or changes so small they are not measurable with our experimental setup. No, or very small, liquid/semiliquid ethane saturation increases with increasing pore pressure explains the lack of deviation from permeability variation predicted due to gas slippage.

4.3. Ethane Permeability at High Pore Pressures. At high ethane pore pressures, ethane adsorption \pm capillary condensation results in constrictions \pm restrictions of fluid flow pathways and hence lower ethane gas permeability than is predicted due to gas slippage (Figure 7). Permeability decreases are substantial with up to an 84% difference

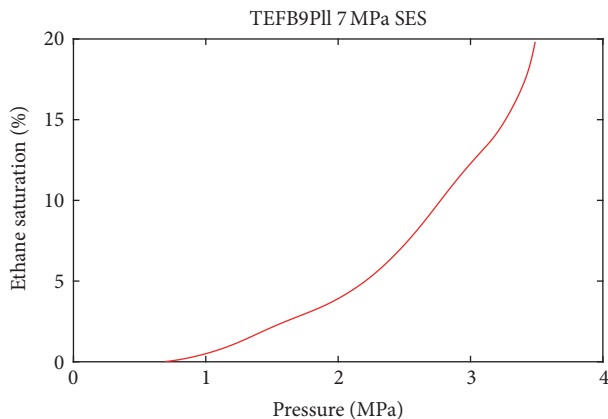


FIGURE 10: Liquid/semiliquid ethane saturation curve for sample TEFB9P11 at 7 MPa simple effective stress.

between measured and predicted apparent ethane permeability (Table 1). The large permeability decreases indicate that permeability of fine-grained rocks with nanometer-scale pore systems can be very sensitive to change in fluid saturation.

Significant increases in liquid/semiliquid ethane saturation with increasing pore pressure are inferred from elevated desorption rates for three of the five samples with desorption data (Figure 8). These desorption rates however do not correlate well with the measured apparent permeability decreases; desorption rates are below measurement resolution over the entire pore pressure range of the ethane permeability measurements for sample MONT (Figure 8) even though that sample has the largest ethane gas permeability decrease relative to predicted permeability (84%).

Difference between predicted ethane gas permeability and measured permeability has a weak negative correlation with K_{∞} (Figure 11(a)). This correlation is expected because lower permeability rocks generally have smaller pores, and the flow capacity of smaller flow conduits should be more sensitive to liquid/semiliquid ethane adsorbed to conduit (pore) walls. A better segregation of the data however is found when difference between predicted ethane gas permeability and measured permeability is plotted against d (Figure 11(b)). The two samples with markedly larger permeability drops (75% and 84%) have dominant pore sizes in the mesopore range compared to all other samples with smaller permeability drops (<45%) and dominant pore sizes in the macropore range. d represents an average size of the smallest pore throats along those flow paths responsible for the bulk of the fluid flux through the rock. If d is in the mesopore range, the main fluid flow conduits can be completely blocked due to capillary condensation at pore pressures near to the saturated vapour pressure [6]. Complete blockage of these conduits explains the very large permeability decreases for the samples with d less than 50 nm (MONT and TEF21, Figures 6 and 7).

Schematic pore network models illustrate the impact of pore structure on the sensitivity of ethane gas permeability to pore pressure (Figure 12). The pore network models are modifications of the network models in Sakhaee-Pour and Bryant [24]. Sakhaee-Pour and Bryant showed that acyclic pore models could reproduce the nonplateau like trends of

capillary pressure versus saturation that are common for gas shales. A key attribute of acyclic pore models is that narrower pore throats do not limit accessibility to the wider pore throats [24]. The pore network model depicted in Figures 12(a) and 12(b) is for a sample with pores in the portion of the pore structure most responsible for limiting fluid flow in the macropore range. This pore network could be used to represent sample TEFB9P11 at 7 MPa simple effective stress. Ethane gas permeability is not very sensitive to pore pressure in this sample (Figure 7), but significant quantities of ethane gas are adsorbed at high pore pressure (Figures 8 and 10). Such data indicate that the main flow conduits have minimum pore throat sizes in the macropore size range that are not completely blocked off at ethane pressures near the saturated vapour pressure (Figure 12(b)). The sample, however, can store significant quantities of ethane in the liquid/semiliquid state in submacropore scale pores whose throats do not limit accessibility to the macropores (Figure 12(b)).

In contrast to TEFB9P11 and the schematic pore network in Figures 12(a) and 12(b), the main flow conduits of the pore network model presented in Figures 12(c) and 12(d) are in the mesopore size range. The mesopores are completely blocked off due to capillary condensation at ethane pressures near the saturated vapour pressure (Figure 12(d)), resulting in ethane gas permeability that is very sensitive to pore pressure. This pore network model would explain the experimental observations of sample MONT; d was 41 nm for MONT and permeability of this sample was most sensitive to pore pressure.

4.4. Stress Sensitivity of Ethane Permeability. Increasing stress narrows the pores and pore throats in sample TEFB9P11 resulting in decreasing K_{∞} (Figure 5). d decreases from 473 to 259 to 145 nm at 7, 21, and 48 MPa simple effective stress, respectively (Table 1). Concomitantly, the difference between predicted permeability and measured ethane gas permeability at 3.45 MPa mean pore pressure increases from 33% to 39% to 45% with increasing stress (Table 1) because liquid/semiliquid ethane adsorbed to pore walls has a greater impact on the flow capacity of smaller flow conduits than larger flow conduits. Stress sensitivity of permeability could only be evaluated for sample TEFB9 for flow parallel to bedding because TEFB9P11 was the only plug in this study measured at multiple stress states.

4.5. Anisotropy of Ethane Permeability. Permeability of sample TEFB9 is highly anisotropic; at 7 MPa simple effective stress K_{∞} to helium parallel to bedding is two orders of magnitude higher than to flow perpendicular to bedding. Calculated d of subsample TEFB9Pd at 7 MPa simple effective stress (67 nm) is seven times smaller than d of sample TEFB9P11 at 7 MPa simple effective stress (473 nm). The large difference in dominant pore size explains the permeability anisotropy. The large difference in pore size however does not explain why ethane permeability is less sensitive to pore pressure at high pore pressures for flow perpendicular to bedding than for flow parallel to bedding; permeability to ethane gas should be more sensitive to adsorption and capillary condensation when flow is in the direction with smaller

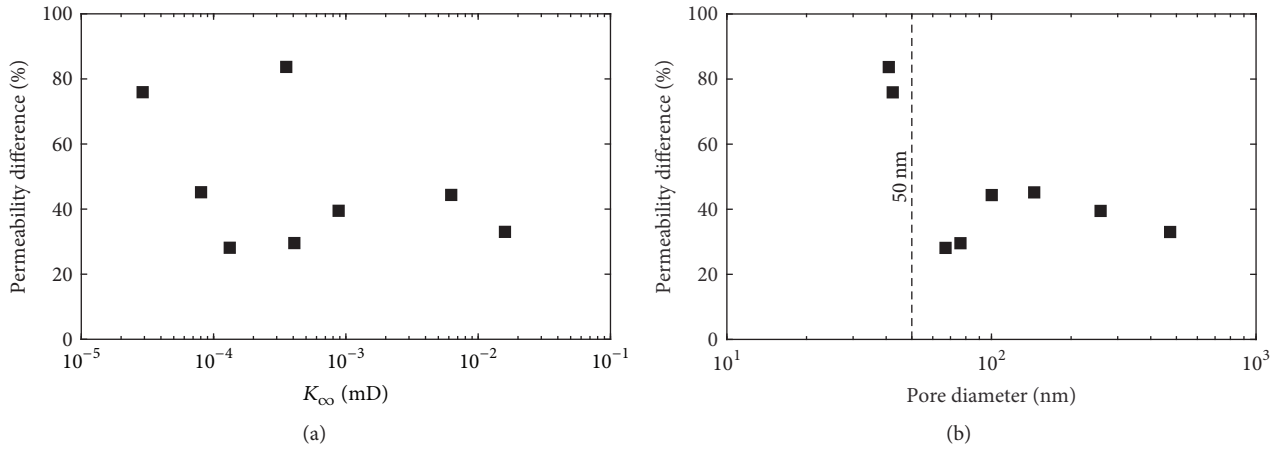


FIGURE 11: Correlation of difference between predicted ethane gas permeability and measured permeability at 3.45 MPa pore pressure (y -axes) and K_{∞} (a) and d (b).

flow paths. The calculated dominant pore sizes, however, only represent an *average* size of the smallest pore throats along those flow paths responsible for the bulk of the fluid flux through the rock. In reality, the pore structure of sample TEFB9 is likely composed of a distribution of different sized pores. It is therefore possible that significant portions of fluid flow parallel to bedding take place along flow paths where the smallest pores are much smaller than the average, as well as in flow paths where the smallest pores are much larger than the average. For example, a continuous network of organic matter with connected, small pores (micro- to mesopores) could contribute significant flow parallel to bedding. This flow would be sensitive to adsorption and capillary condensation at high ethane gas pressures. Perpendicular to bedding, the organic matter might not be continuous and therefore would not contribute to flow. Perpendicular to bedding, the pores most responsible for limiting fluid flow could be on average smaller than parallel to bedding but have a narrower distribution of pore sizes that excludes the very small pores in the organic matter. Ethane permeability perpendicular to bedding could therefore be less sensitive than ethane permeability parallel to bedding to adsorption and capillary condensation at high ethane gas pressure.

4.6. Permeability Hysteresis. The measurements of effective permeability to ethane gas in this study were made over a range of increasing pore pressures. Permeability measurements over a range of decreasing pore pressures could also have been made to investigate the path dependence of permeability but were not made in this study due to time constraints. Capillary condensation is hysteretic [6]. In fine-grained reservoir rocks with mesopores, it is therefore expected that liquid/semiliquid ethane saturation would be path dependent. Path dependent saturation should result in permeability hysteresis. Future studies should measure effective permeability to ethane gas over a range of both increasing and decreasing pore pressures to investigate permeability hysteresis. Valuable insights about pore structure could

potentially be derived from analysis of permeability hysteresis loops.

5. Conclusion

Ethane gas permeability measurements on stressed samples can be used as a tool to explore multiphase flow phenomena in fine-grained sedimentary rocks at in situ reservoir stress conditions. Because pores in fine-grained sedimentary rocks are generally of submicrometer length scale, significant liquid/semiliquid ethane saturation exists due to adsorption and capillary condensation at ethane gas pressures near the saturated vapour pressure. The liquid/semiliquid ethane causes restrictions and blockages of flow pathways and therefore reductions to the flow capacity of fine-grained sedimentary rocks.

The sensitivity of ethane gas permeability to adsorption and capillary condensation at high pore pressures varies within the suite of stressed samples analyzed in this study. The variability is controlled by the size of the pores most responsible for limiting fluid flow, which can be determined using gas slippage measurements. Dominant pore size ranges from tens to hundreds of nanometers. Samples with dominant pore sizes in the mesopore range are far more sensitive to ethane gas pore pressure because capillary condensation causes complete blockage of the main flow conduits at pore pressures near the saturated vapour pressure.

The multiphase flow characteristics of sample TEFB9P11 vary with stress state; ethane permeability of sample TEFB9P11 is more sensitive to pore pressure at higher stress states. At higher stress states, the pores are smaller and therefore the presence of liquid/semiliquid ethane has a larger impact on flow capacity. The stress sensitivity of multiphase flow characteristics revealed here highlights the importance of measuring effective permeability at in situ reservoir stress conditions in order to obtain accurate reservoir simulation inputs.

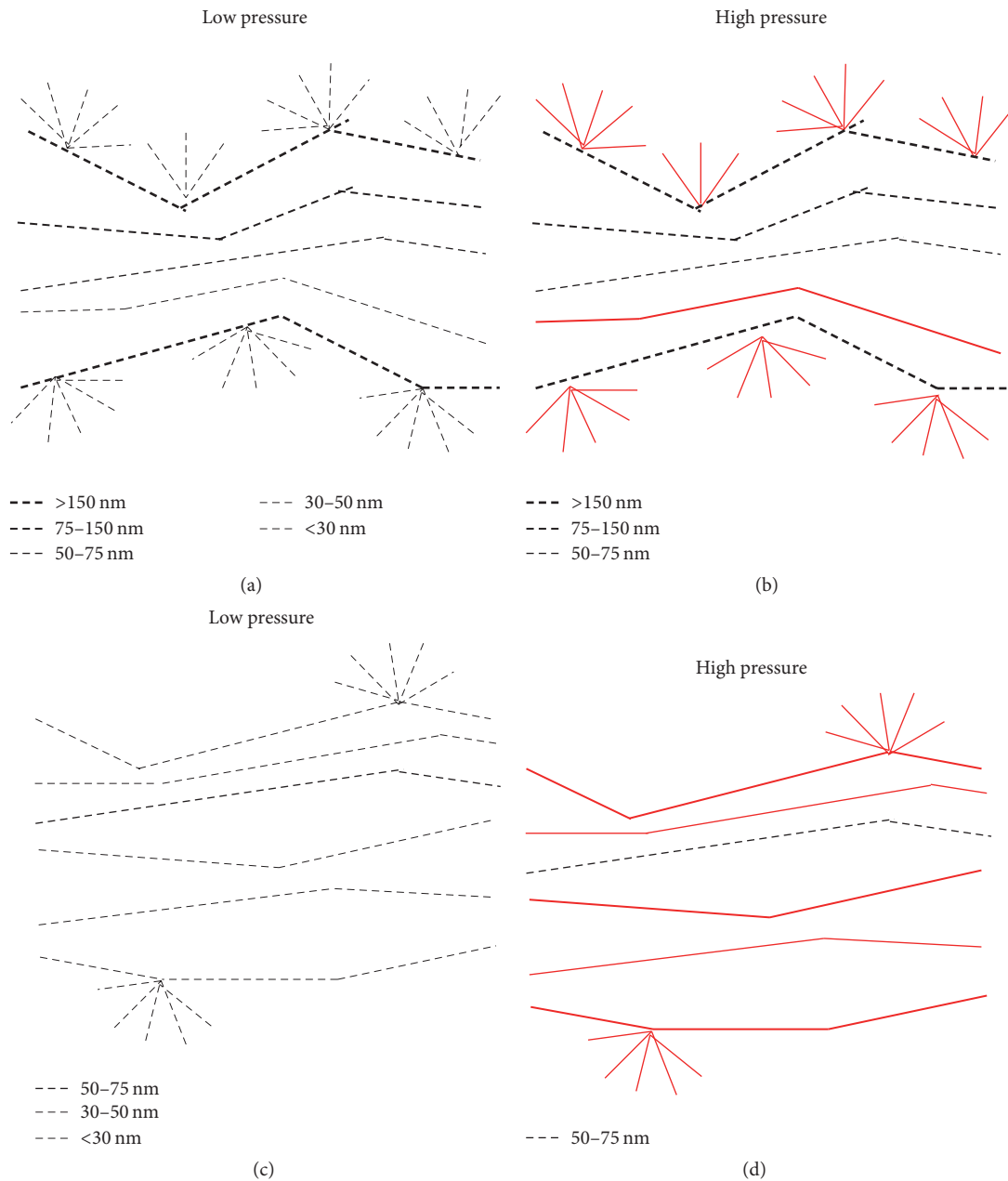


FIGURE 12: Acyclic pore network model for a pore structure where the pores most responsible for limiting fluid flow are in the macropore range ((a) and (b)) and mesopore range ((c) and (d)). Solid red lines indicate pores filled with liquid/semiliquid ethane. Ethane capillary condensation at high pore pressures completely blocks off the highest flow capacity flow paths in the mesoporous pore network (d) but has a limited impact on flow capacity in the macroporous pore network (b). Pore network models are modified from Sakhaee-Pour and Bryant, 2015.

Conflicts of Interest

The authors declare that there are no conflicts of interest regarding the publication of this paper.

References

- [1] A. M. M. Bustin and R. M. Bustin, "Importance of rock properties on the producibility of gas shales," *International Journal of Coal Geology*, vol. 103, pp. 132–147, 2012.
- [2] C. R. Clarkson, N. Solano, R. M. Bustin et al., "Pore structure characterization of North American shale gas reservoirs using USANS/SANS, gas adsorption, and mercury intrusion," *Fuel*, vol. 103, pp. 606–616, 2013.
- [3] H. Aljamaan, M. Al Ismail, and A. R. Kavscek, "Experimental investigation and Grand Canonical Monte Carlo simulation of gas shale adsorption from the macro to the nano scale. Journal of Natural Gas Science and Engineering," *Journal of Natural Gas Science and Engineering*, vol. 48, pp. 119–137, 2016.

- [4] D. B. Bennion and S. Bachu, "Drainage and imbibition relative permeability relationships for supercritical CO₂/brine and H₂S/brine systems in intergranular sandstone, carbonate, shale, and anhydrite rocks," *SPE Reservoir Evaluation and Engineering*, vol. 11, no. 3, pp. 487–496, 2008.
- [5] D. J. K. Ross and R. M. Bustin, "Impact of mass balance calculations on adsorption capacities in microporous shale gas reservoirs," *Fuel*, vol. 86, no. 17–18, pp. 2696–2706, 2007.
- [6] S. J. Gregg, *Adsorption, Surface Area, And Porosity*, Academic Press, 1982.
- [7] T. Tunstall, "Economic impact of the Eagle Ford Shale," in *Petroleum Accounting and Financial Management Journal*, vol. 33, no. 2, pp. 11–22, Denton, Tex, USA, 2014.
- [8] C. Rivard, D. Lavoie, R. Lefebvre, S. Séjourné, C. Lamontagne, and M. Duchesne, "An overview of Canadian shale gas production and environmental concerns," *International Journal of Coal Geology*, vol. 126, pp. 64–76, 2014.
- [9] W. F. Brace, J. B. Walsh, and W. T. Frangos, "Permeability of granite under high pressure," *Journal of Geophysical Research: Atmospheres*, vol. 73, no. 6, pp. 2225–2236, 1968.
- [10] L. J. Klinkenberg, "The permeability of porous media to liquids and gases," in *Drilling and Production Practice*, American Petroleum Institute, New York, NY, USA, 1941.
- [11] E. A. Letham, *New insights into pore structure characterization and permeability measurement of fine-grained sedimentary reservoir rocks in the laboratory at reservoir stress states [doctoral thesis]*, The University of British Columbia, Vancouver, Canada, 2018.
- [12] H. Adzumi, "Studies on the flow of gaseous mixtures through capillaries. III. The flow of gaseous mixtures at medium pressures," *Bulletin of the Chemical Society of Japan*, vol. 12, no. 6, pp. 292–303, 1937.
- [13] L. B. Loeb, *The Kinetic Theory of Gases*, Dover Publications, 2004.
- [14] P. L. Randolph, D. J. Soeder, and P. Chowdiah, "Porosity and permeability of tight sands," in *Proceedings of the SPE Unconventional Gas Recovery Symposium*, Pittsburgh, Pa, USA, 1984.
- [15] D. J. Soeder, "Porosity and permeability of eastern devonian gas shale," *SPE Formation Evaluation*, vol. 3, no. 1, pp. 116–124, 1988.
- [16] S. C. Jones, "A technique for faster pulse-decay permeability measurements in tight rocks," *SPE Formation Evaluation*, vol. 12, no. 1, pp. 19–24, 1997.
- [17] R. Feng, J. Liu, and S. Harpalani, "Optimized pressure pulse-decay method for laboratory estimation of gas permeability of sorptive reservoirs: Part 1—Background and numerical analysis," *Fuel*, vol. 191, pp. 555–564, 2017.
- [18] X. Cui, A. M. M. Bustin, and R. M. Bustin, "Measurements of gas permeability and diffusivity of tight reservoir rocks: different approaches and their applications," *Geofluids*, vol. 9, no. 3, pp. 208–223, 2009.
- [19] E. W. Lemmon, M. O. McLinden, and D. G. Friend, "Thermophysical Properties of Fluid Systems" in NIST Chemistry WebBook, NIST Standard Reference Database Number 69," in *National Institute of Standards and Technology*, P. J. Linstrom and W. G. Mallard, Eds., Gaithersburg, Md, USA, 2017.
- [20] R. Feng, S. Harpalani, and J. Liu, "Optimized pressure pulse-decay method for laboratory estimation of gas permeability of sorptive reservoirs: Part 2-experimental study," *Fuel*, vol. 191, pp. 565–573, 2017.
- [21] D. Y. Peng and D. B. Robinson, "A new two-constant equation of state," *Industrial & Engineering Chemistry Fundamentals*, vol. 15, no. 1, pp. 59–64, 1976.
- [22] D. W. Breck, *Zeolite Molecular Sieves—Structure, Chemistry, and Use*, John Wiley & Sons, 1974.
- [23] S. Aguado, G. Bergeret, C. Daniel, and D. Farrusseng, "Absolute molecular sieve separation of ethylene/ethane mixtures with silver zeolite A," *Journal of the American Chemical Society*, vol. 134, no. 36, pp. 14635–14637, 2012.
- [24] A. Sakhaee-Pour and S. L. Bryant, "Pore structure of shale," *Fuel*, vol. 143, pp. 467–475, 2015, <https://doi.org/10.1016/j.fuel.2014.11.053>.

Research Article

Methane Extraction from Abandoned Mines by Surface Vertical Wells: A Case Study in China

Shengyong Hu ^{1,2}, Ao Zhang,¹ Guorui Feng ^{1,2}, Xiangqian Guo,³ Xuyang Miu,¹ Chao Li,³ Dandan Han,¹ Jin Wang,¹ and Lixun Kang^{1,2}

¹College of Mining Engineering, Taiyuan University of Technology, Taiyuan 030024, China

²Green Mining Engineering Technology Research Center of Shanxi Province, Taiyuan 030024, China

³State Key Laboratory of Coal and CBM Co-Mining, Jincheng 048006, China

Correspondence should be addressed to Guorui Feng; fgrhsy@163.com

Received 25 October 2017; Revised 27 December 2017; Accepted 5 February 2018; Published 1 March 2018

Academic Editor: Egor Dontsov

Copyright © 2018 Shengyong Hu et al. This is an open access article distributed under the Creative Commons Attribution License, which permits unrestricted use, distribution, and reproduction in any medium, provided the original work is properly cited.

Considerable methane resources exist in abandoned coal mines. However, methane extraction from abandoned mines in China is still in the exploratory stage. This study presents technologies and engineering practices suitable for the extraction of gob methane from abandoned mines using surface vertical wells, including methane drainage systems, well bottom locations, and an intermittent drainage method. Seven surface wells in the Yongan abandoned mine in China were selected for gob methane extraction. Field results showed that the methane volumetric flow rate of a well whose bottom was close to the gob bottom was 2.5 times greater than that of a well with a bottom located in the gob fractured zone. Moreover, intermittent extraction can enable a well to extract methane cyclically at a high volumetric flow rate. A well drilled mistakenly into a coal pillar can be reused through hydraulic fracturing. The overall maximum methane volumetric flow rate, average concentration, and extraction span were 210 m³/h, 83%, and 1100 days, respectively.

1. Introduction

Coal mines are abandoned when they complete their useful economic life, and abandoned underground mines can be found in every country that has coal resources [1]. The UK has 900 abandoned mines, of which approximately 400 leak methane into the atmosphere [2]. Europe, Ukraine, and Russia also have many abandoned mines [1]. In China, Shanxi Province alone has more than 4700 abandoned mines, with methane reserves of approximately 3 billion m³ [3]. Methane in abandoned mines can create various environmental, health, safety, and economic concerns. For example, methane accumulated in abandoned mine gobs can leak out to the surface through cracks [4]. Therefore, it is necessary to extract abandoned mine methane, and this has been successfully done in the UK, Czech Republic, USA, Germany, France, and China [5].

Many studies have focused on using surface wells for stress-relief methane drainage to release the methane pressure that accumulates in gobs or coal seams during

mining. Sang et al. [6] summarized current engineering practice and technology for stress-relief methane drainage with surface vertical wells in China. Sun et al. [7] studied deformation of surface well casings. Sun et al. [8] developed a shear deformation fracture model to study the well casing displacement that occurs as the working face advances. Schatzel et al. [9] investigated the effects of reservoir conditions and longwall panel response during mining on gob gas well performance. Guo et al. [10] developed a conceptual model to provide simple practical guidance for horizontal methane drainage design. Karacan [11] assessed the production performance of gob gas ventholes drilled along wall panels. Zhang et al. [12] analyzed the total gas flow rates from 29 surface gas ventholes located on four longwall faces for stress-relief methane drainage. Qin et al. [13] studied the optimal placement of abandoned gob wells. Qu et al. [14] conducted field trials at two Australian coal mines to evaluate the performance and effectiveness of surface directional boreholes. Liu et al. [15] investigated the impact of gob gas venthole drainage on gob gas flow. An et al. [16] applied

TABLE 1: Coal seam occurrence in the Yongan mine.

Coal seam number (#)	Coal seam thickness (m)	Coal seam distance (m)		Roof lithology	Floor lithology	Workability
	Minimum–maximum Average	Minimum–maximum Average				
3	6.1–6.8 6.3			Mudstone Siltstone	Mudstone Siltstone	Completely minable
9	0.3–1.0 0.6	42.6–63.2 53.2	21.0–34.1 28.1	Mudstone Siltstone	Mudstone Siltstone	Partially minable
15	2.4–4.0 3.0			Limestone	Mudstone Siltstone	Partially minable

directional boreholes for methane drainage in adjacent seams during mining. These studies have all focused primarily on the efficient extraction of stress-relief methane with surface wells. Currently, the studies of methane extraction from abandoned mines in China are still at an exploratory stage [3].

Some studies about methane emissions and extraction of abandoned mines have also been conducted. The EPA [17] proposed a formula to calculate the methane emission rate from abandoned coal mines in the United States. Leifer and Wilson [18] measured the gas seepage at a repeatedly abandoned well in Nearshore Summerland, California. Palchik [19] analyzed the data of time-dependent methane emission and estimated the gas flow rate parameters and cumulative production of the wells drilled to partly flooded abandoned workings at shallow depth by exponential decline analysis. Karacan [1] studied methane extraction characteristics of abandoned mines by modeling study and data analysis. All of these studies can provide theoretical guidance for methane extraction from abandoned mines. However, existing studies did not consider some unique characteristics of abandoned mines in China, such as residual methane pressure, overlying strata development, and aquifers. These characteristics will directly affect the arrangements of the methane drainage system, the well bottom location, and the methane drainage adjustment used for the methane drainage of abandoned mines [5, 20]. It is essential to propose some technologies, especially considering these unique characteristics.

This paper presents and describes in detail the technologies of the methane extraction of abandoned mines using surface wells, especially considering those unique characteristics of abandoned mines in China. These technologies were then verified with a field engineering trial at the Yongan abandoned mine in China.

2. Description of the Yongan Abandoned Mine

The Yongan abandoned mine is a gassy coal mine in China that has been completely closed since November 2011. It stretches from south to north and has a length of 5.2 km and width of 2.8 km, covering a total area of 6.5101 km². Before its closure, the mine produced 0.9 million tons of anthracite coal annually. The average original methane pressure and total methane content were 1.08 MPa and 18 m³/t, respectively.

The Yongan mine is located in the southern part of the Qinshui Coalfield, which is in an area with low mountains and hills; the maximum relative elevation difference of the terrain is approximately 283 m. The mine has a moderate hydrogeological type, and the groundwater storage is dominated by diving. The aquifer thickness is small and has a shallow water table depth.

The minable coal seams in the Yongan mine were coal seam #3 in the lower group of the Shanxi Formation and coal seams #9 and #15 in the Upper Carboniferous Taiyuan Formation. As summarized in Table 1, coal seam #3 is nearly horizontal and is stable in the mine area. This coal seam is 6.1–6.8 m thick, with an average thickness of 6.3 m. The immediate roof of coal seam #3 is approximately 5.3 m thick and is composed primarily of mudstone and siltstone. The floor is mudstone and siltstone and has a thickness of approximately 1.8 m. Coal seam #9 is unstable, while coal seam #15 is stable and minable in the entire mine area.

Historically, coal seam #3 of the Yongan mine was mined using the longwall mining method at a mining depth of between 320 m and 360 m. The distribution of coal mine gobs formed within the Yongan mine range is shown in Figure 1. Six surface wells have been drilled to extract the methane in these abandoned gobs, and their locations are also shown in Figure 1.

3. Methane Drainage Trials at the Abandoned Mine

3.1. Methane Drainage System. The methane drainage system consists of the borehole camera detection method (Figure 2), a configuration of wellbore (Figure 3), and a surface methane drainage system (Figure 4). During the dynamic and continuous mining process, the stresses in the overlying strata vary continuously, which can significantly affect the stability of the surface vertical wells located in the overlying strata [6]. Therefore, structural designs for these surface wells mainly consider the effects of mining stress [7, 8, 21, 22]. However, in an abandoned mine, the mining stress has stabilized, and thus water influx from aquifers into the abandoned gobs is the most significant problem. The drilled wells pass through aquifers to reach the gobs, which can allow underground water to flow into the gobs, significantly affecting the gob methane flow to the wells.



FIGURE 1: Abandoned gob distribution within the Yongan mine range.



FIGURE 2: Borehole camera images along the drilled wells.

A borehole camera detection method [23] was used to detect aquifers above the abandoned gobs in the Yongan mine. Figure 2 shows images from the borehole at well #1 (shown in Figure 1). These images show an obvious point at which groundwater is pouring out of the well wall, indicating the location of an aquifer. The water from these points flows directly to the bottom of the drilled well. Thus, it is important

that all aquifer positions are detected and sealed before the drilled wells reach the gobs.

When the gob has collapsed and the aquifers above the gob are sealed, the surface well used to drain the abandoned gob methane can be divided into three parts, as shown in Figure 3(a). In this case, the top part of the well is drilled through the topsoil overburden and enters the 10 m deep

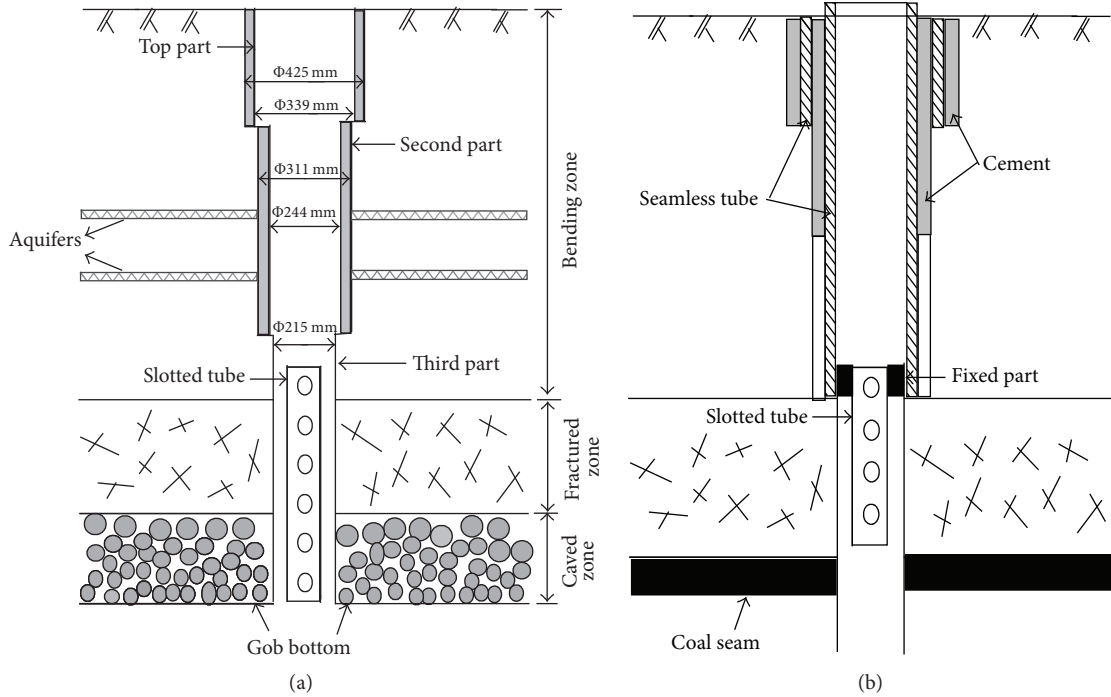


FIGURE 3: Sketch of two surface well structures: (a) surface well structure used in the Yongan mine area and (b) surface well structure used in the Chengzhuang mine area.

bedrock with a bore diameter of 425 mm, followed by introduction of a 339 mm diameter seamless tube, which is fixed to the well wall with high-strength, low-density cement. The second part of the well is drilled with a 311 mm bore diameter through all detected aquifers, followed by introduction of a 244 mm diameter seamless tube, which is sealed against the aquifers with cement. Finally, the third part of the well is drilled into the lower gob with a 215 mm bore diameter, followed by a slotted tube, which is used in case a well collapse blocks airflow passage in the gob.

Adopting this type of wellbore configuration can improve the efficiency of draining the abandoned gobs and reduce construction costs of the surface vertical wells. This configuration accounts for sealing of the aquifers without the unnecessary fixation of slotted tubes in the abandoned boreholes shown in Figure 3(b) [20].

Based on the proposed wellbore configuration and the geological conditions at the Yongan mine, the surface methane drainage system shown in Figure 4 was used for methane extraction. This surface methane drainage system consists of a pressure gauge, wellhead gate valve, one-way valve, tailrace, flame arrester, solenoid valve, temperature sensor, methane concentration sensor, oxygen concentration sensor, vacuum negative pressure gauge, panel, water-ring vacuum pump, screw supercharger, flow meter, air collector, master valve, and gathering station.

The six wells were closed and sealed after drilling was completed, and then pressure gauges (Figure 4) were installed at the upper part of each well to monitor the residual methane pressure in the abandoned mine gobs, as shown in Figure 5. The pressure measured at those wells was only 0.002–0.020 MPa, which is much lower than the original

methane pressure of 1.08 MPa. For comparison, the reported residual methane pressures at the Peyerimhoff abandoned mine in France and the Markham abandoned mine in England are between 0.050 MPa and 0.102 MPa [5].

The desorbed (released) methane in the gobs is extracted by utilizing the negative pressure at the well bottom produced by a water-ring vacuum pump. The methane is then pressurized to 0.2–0.3 MPa with a screw supercharger and transported to the air collector and gathering station. The methane extraction parameters are monitored with the methane concentration sensor, oxygen concentration sensor, temperature sensor, vacuum negative pressure gauge, and flow meter. The panel control program modulates the solenoid valve to adjust the methane extraction pressure, which directly affects the methane extraction concentration and flow. Owing to the low residual methane pressure in the abandoned gobs, the methane extraction pressure must be set to a micropositive pressure or micronegative pressure in the range of -7 to $+2$ kPa to ensure the stability of the methane production.

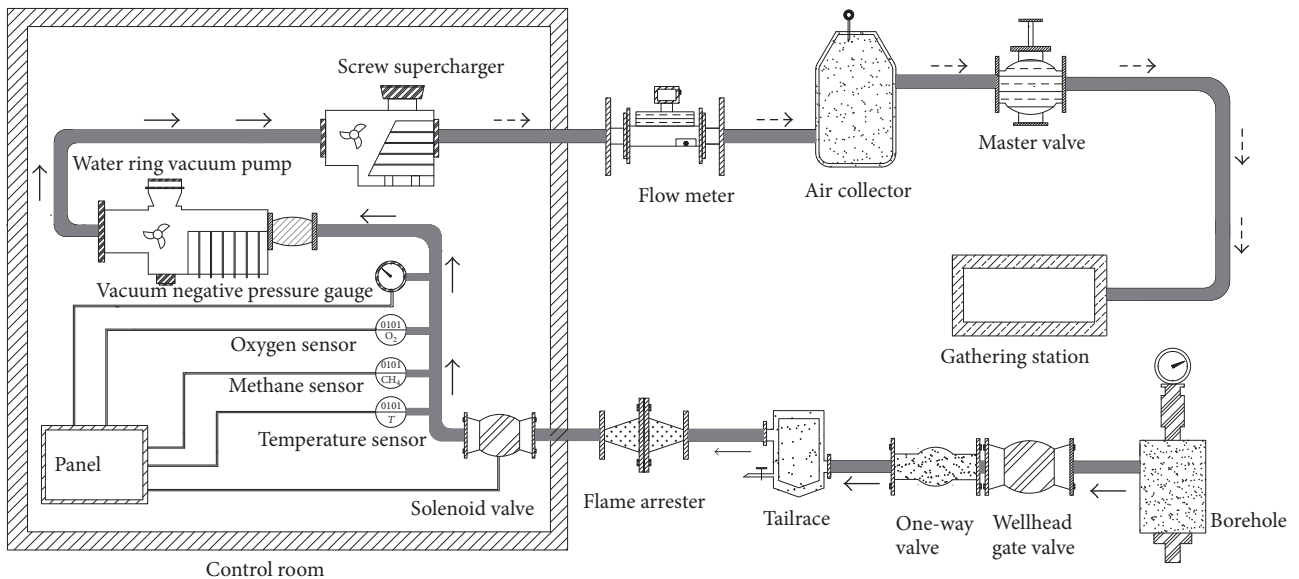
3.2. Location of the Well Bottom. Figure 6 shows a sketch of various surface well bottom locations. It is generally accepted that a well location in the fractured zone near the caved zone is most effective for gob methane drainage as this location is enriched by gob stress-relief methane [6]. Surface Well I, which has a well bottom located in the “O-ring” of the fractured zone, as shown in Figure 6, is typically used to drain the abandoned gob methane.

The methane flow in abandoned mine gobs can be described by Darcy’s law [24]:

$$u = -\frac{K_p}{\mu} \nabla P, \quad (1)$$



(a)



(b)

FIGURE 4: Surface methane drainage system: (a) physical image map and (b) schematic diagram.

where u is the relative velocity between the fluid and the solid structure, μ is the dynamic viscosity of the fluid, ∇P is the pressure gradient that acts as the driving force for fluid flow through the porous media, and K_p is the permeability.

Darcy's law indicates that Well I will only be suitable for use with a newly formed gob that has a relatively high residual methane pressure. There will be a relatively large pressure gradient between the lower area and the upper area of this type of gob after the free gob methane is extracted by the surface well, allowing the methane to flow easily into Well I.

However, the low methane pressure in an abandoned gob corresponds to a low negative pressure extraction, which

means that Well I has a small effective extraction range. The gob methane cannot easily flow into that small range in a reasonable amount of time owing to the very low pressure gradient. Therefore, it is necessary to change the conventional well bottom position for use in abandoned mine gobs. Well II has a bottom located near the residual coal and the gob bottom and should be used for quick and efficient extraction of the desorbed methane from the residual coal.

Occasionally, incomplete or inaccurate abandoned gob information may lead to a well being mistakenly drilled into the coal pillar around a gob. Because of the poor permeability of the original coal seam in the Yongan mine, the methane drainage flow from this well was poor and



FIGURE 5: Setup for field measurement of residual methane pressure in abandoned mine gob.

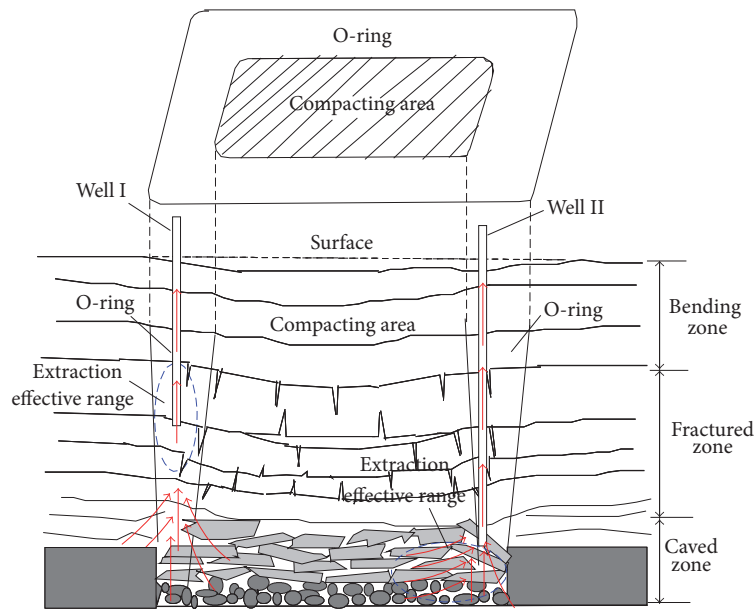


FIGURE 6: Sketch of different surface well bottom locations.

it had to be abandoned. Figure 7 shows that this well was mistakenly drilled into the coal pillar of coal seam #3. To reuse this abandoned well, drilling should continue until the well penetrates coal seams #9 and #15 located below coal seam #3. A hydraulic fracturing method [25–27] could then be used to increase the original permeability of the three coal seams and allow the abandoned well to be reused.

3.3. Intermittent Efficient Methane Drainage. The desorption rate of the residual coal in abandoned mine gob initially decreases sharply with increasing desorption time, after which it decreases more gradually [19]. As a result, the methane pressure in the abandoned gob decreases as the

gob methane is extracted. The free methane content can be obtained with Mariotte's law [28]:

$$V_g = \frac{\phi_r p T_0}{p_0 T Z}, \quad (2)$$

where V_g is the free methane volume in the normal state (m^3/t); ϕ_r is the residual pore volume (m^3/t); p is the methane pressure (MPa); p_0 and T_0 are the pressure in the normal state (0.101325 MPa) and absolute temperature (273 K), respectively; T is the reservoir temperature, which can be estimated by the depth; and Z is the methane compressibility factor, which can be obtained from generalized compressibility charts. During methane drainage, the methane pressure in an

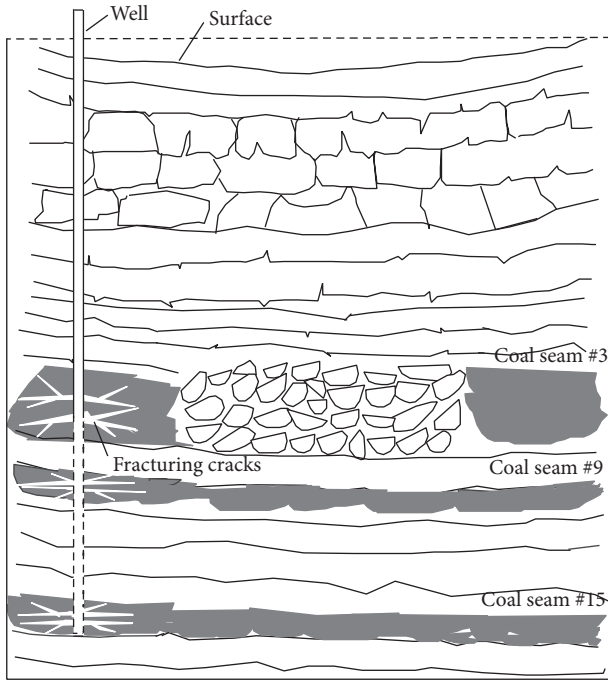


FIGURE 7: Schematic of the methane extraction through a coal pillar using hydraulic fracturing.

abandoned gob becomes relatively low, at which point the gob has a low free methane volume, as indicated by (2).

The adsorbed methane and desorbed methane in the coal are in a dynamic equilibrium. As the methane pressure successively decreases and increases, the coal will undergo corresponding successive desorption and adsorption processes. As the coal desorption rate and the free methane content decrease, the methane drainage flow will gradually decrease and become exhausted. At this point, it is advisable to cease drainage for a period to allow the methane in the coal pillar, roadway, or other gobs to gradually accumulate in the gob where the well is located; over time, the residual coal in this gob can thus gradually return to the initial methane pressure. When the methane extraction is restarted, the residual coal will undergo methane desorption at a relatively high rate again, enabling extraction of a high methane flow from the well. This technique could solve the problems of high energy consumption and low production efficiency that are experienced when the methane extraction flow of a well is low.

4. Field Application Results

As shown in Figure 1, wells #1 and #2 are located in adjacent gobs, which have similar geometrical and geological conditions. As a result, the two wells have similar gas adsorptions and flow conductivities. Moreover, the two wells have very similar well locations and methods of extraction. Therefore, wells #1 and #2 were selected to study the influence of the well bottom position on the methane production.

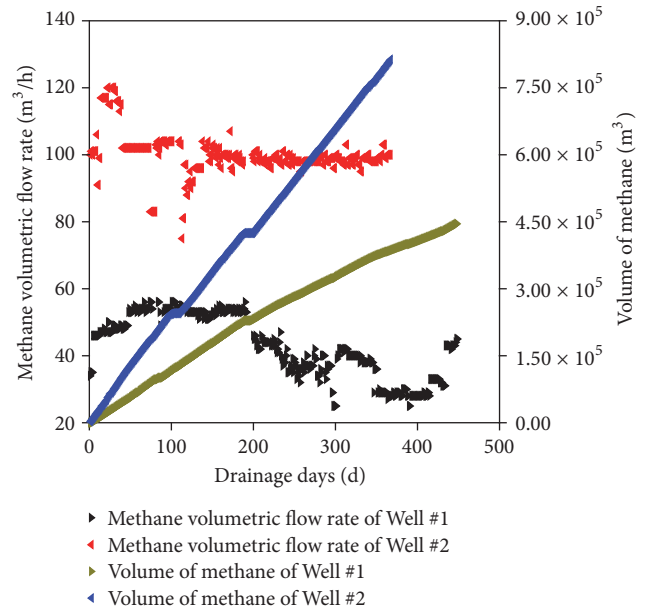


FIGURE 8: Comparison of methane extraction flow for different well locations.

The bottom of well #1 is located in the gob fractured zone approximately 40 m above the roof of coal seam #3, whereas the bottom of well #2 is located approximately 5 m below the floor coal seam #3. The methane volumetric flow rates and the methane volumes of the two wells are shown in Figure 8.

Figure 8 shows that there are some fluctuations for the initial methane volumetric flow rate, similar to the results obtained by Karacan (2015) [1], and then the overall trends of wells #1 and #2 are declining in the duration of the methane drainage, which are confirmed by EPA (2004) [17] and Palchik (2014) [19]. The average methane volumetric flow rate of well #1 was only 40 m³/h, whereas the average methane volumetric flow rate of well #2 was 100 m³/h, or 2.5 times greater than that of well #1. During the first 350 days of drainage, the methane volume in well #1 was 4.0 × 10⁵ m³, whereas the methane volume in well #2 was 7.5 × 10⁵ m³, which is nearly two times that of well #1. It is clear that methane extraction at well #2 was much more effective than at well #1. Therefore, it can be concluded that the methane extraction is better the closer the well bottom is to the bottom of the abandoned mine gob.

Well #3, shown in Figure 1, was chosen to investigate the impact of intermittent extraction on methane production. Figure 9 shows that, over 80 days of extraction at well #3, the methane volumetric flow rate decreased significantly from 325 m³/h to 130 m³/h, indicating the near exhaustion of methane in the gob. At this point, well #3 was closed for approximately 200 days to allow the methane from the surrounding gobs to flow into that gob, accumulating until the methane pressure returned to its original level.

When well #3 resumed extraction, the methane volumetric flow rate was initially relatively 380 m³/h high, which decreased sharply to approximately 150 m³/h 140 days later.

TABLE 2: Representative methane extraction effect of surface wells in the abandoned mine.

Methane extraction time (d)	Well number (#)	Average concentration Minimum~ maximum (%)	Average methane flow rate Minimum~ maximum (m ³ /h)	Cumulative methane flow (m ³)
1100	4	81 63~89	76 60~88	2.0×10^6
663	5	85 79~95	80 63~88	8.3×10^5
1016	6	83 77~95	159 139~210	4.4×10^6

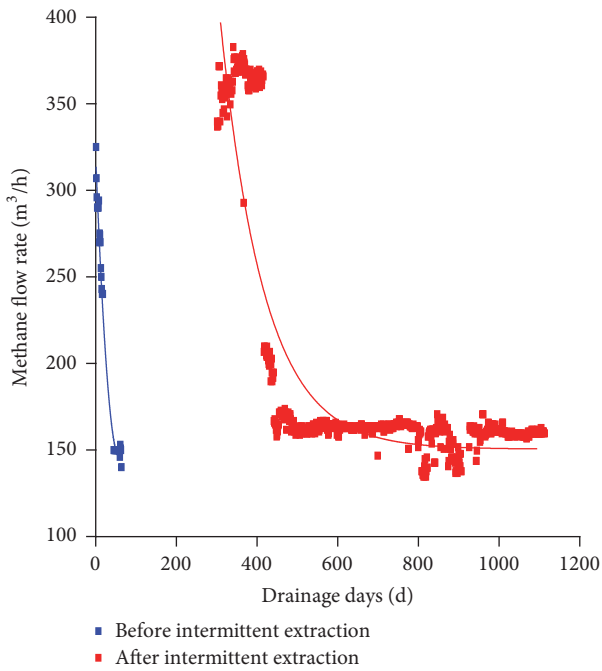


FIGURE 9: Methane extraction flows before and after intermittent extraction.

This suggests that the intermittent extraction method, that is, extraction-pause-extraction, can enable the well to continue extracting at a high methane volumetric flow rate and significantly reduce energy consumption, thereby improving the efficiency of the well.

Wells #4, #5, and #6 have the structure illustrated in Figure 3 and used the extraction system illustrated in Figure 4; the methane extraction results are summarized in Table 2. The minimum methane volumetric flow rate was $60 \text{ m}^3/\text{h}$, the maximum was $210 \text{ m}^3/\text{h}$, the average methane concentration was 83%, and the methane extraction time was 1100 days.

5. Conclusions

Abandoned mine methane can create various environmental, health, safety, and economic concerns. It is necessary to extract the methane from abandoned gobs, which can contain considerable methane resources. However, methane drainage

from abandoned mines in China is still in the exploratory stage compared to the stress-relief methane extraction employed during mining. This study evaluates technologies and engineering practices for surface vertical wells that are different from those used in stress-relief methane extraction, including a methane drainage system, well bottom locations, and intermittent drainage.

Aquifer positions above abandoned gobs were detected and sealed before drilled wells entered the gobs. A single well drainage system was used to control the negative methane extraction pressure at micropositive or micronegative pressures of -7 to $+2 \text{ kPa}$ to ensure stability of methane production. Because of the low gob methane pressure and low extraction pressures, the optimal well location to efficiently extract methane from the residual coal in a reasonable amount of time was near the bottom of the gob. An intermittent extraction method, that is, extraction-pause-extraction, could be used to enable wells to resume methane extraction at high flow rates. For wells drilled into coal pillars around gobs, it was suggested that the drilling should continue downwards until it has penetrated all the coal seams, after which hydraulic fracturing can be used to improve the low permeability of these coal seams.

The average methane volumetric flow rate at a well whose bottom is close to the gob bottom is 2.5 times greater than that of a well located in the gob fractured zone. When the methane volumetric flow rate at a well exhibited a drastic decrease from $325 \text{ m}^3/\text{h}$ to $130 \text{ m}^3/\text{h}$, it was closed for approximately 200 days. When the well resumed extraction after this pause, the methane volumetric flow rate had returned to a relatively high $380 \text{ m}^3/\text{h}$. In addition, a well that had been mistakenly drilled into coal pillars could be reused using hydraulic fracturing. The overall maximum methane volumetric flow rate, average concentration, and extraction span were $210 \text{ m}^3/\text{h}$, 83%, and 1100 days, respectively, with the proposed well structure and methane extraction system.

Conflicts of Interest

The authors declare that they have no conflicts of interest.

Acknowledgments

This research was supported by the National Natural Science Foundation of China (51504160, 51574172), the Coalbed

Methane Joint Research Foundation of Shanxi Province (2015012008), and the Joint Funds of the National Natural Science Foundation of China (U1710258, U1710121). This work is also a project funded by the innovative entrepreneurship projects for college students (CX090).

References

- [1] C. Ö. Karacan, "Modeling and analysis of gas capture from sealed sections of abandoned coal mines," *International Journal of Coal Geology*, vol. 138, pp. 30–41, 2015.
- [2] "Methane From Abandoned Coal Mines-A Solution for Controlling Emissions, DTI/Pub URN 04/933, 2004".
- [3] Z.-P. Meng, X.-C. Shi, S.-S. Liu, Y.-D. Tian, and C. Li, "Evaluation model of CBM resources in abandoned coal mine and its application," *Meitan Xuebao/Journal of the China Coal Society*, vol. 41, no. 3, pp. 537–544, 2016.
- [4] V. Palchik, "In situ study of intensity of weathering-induced fractures and methane emission to the atmosphere through these fractures," *Engineering Geology*, vol. 125, pp. 56–65, 2012.
- [5] J.-Q. Shi, R. M. Rubio, and S. Durucan, "An improved void-resistance model for abandoned coal mine gas reservoirs," *International Journal of Coal Geology*, vol. 165, pp. 257–264, 2016.
- [6] S. Sang, H. Xu, L. Fang, G. Li, and H. Huang, "Stress relief coalbed methane drainage by surface vertical wells in China," *International Journal of Coal Geology*, vol. 82, no. 3-4, pp. 196–203, 2010.
- [7] H. T. Sun, Y. R. Zheng, Q. T. Hu, and F. J. Liu, "Surface borehole casing coupling deformation mechanism," *Journal of China Coal Society*, vol. 36, pp. 823–829, 2011.
- [8] H. T. Sun, F. J. Liu, and J. Zhang, "Shear deformation model on surface drilling and its spatial analysis," *Journal of Mining and Safety Engineering*, vol. 28, pp. 72–76, 2011.
- [9] S. J. Schatzel, C. Ö. Karacan, H. Dougherty, and G. V. R. Goodman, "An analysis of reservoir conditions and responses in longwall panel overburden during mining and its effect on gob gas well performance," *Engineering Geology*, vol. 127, pp. 65–74, 2012.
- [10] H. Guo, C. Todhunter, Q. Qu, and Z. Qin, "Longwall horizontal gas drainage through goaf pressure control," *International Journal of Coal Geology*, vol. 150-151, pp. 276–286, 2015.
- [11] C. Ö. Karacan, "Analysis of gob gas venthole production performances for strata gas control in longwall mining," *International Journal of Rock Mechanics and Mining Sciences*, vol. 79, pp. 9–18, 2015.
- [12] C. Zhang, S. Tu, Q. Bai, G. Yang, and L. Zhang, "Evaluating pressure-relief mining performances based on surface gas venthole extraction data in longwall coal mines," *Journal of Natural Gas Science and Engineering*, vol. 24, pp. 431–440, 2015.
- [13] W. Qin, J. Xu, and G. Hu, "Optimization of abandoned gob methane drainage through well placement selection," *Journal of Natural Gas Science and Engineering*, vol. 25, pp. 148–158, 2015.
- [14] Q. Qu, H. Guo, and M. Loney, "Analysis of longwall goaf gas drainage trials with surface directional boreholes," *International Journal of Coal Geology*, vol. 156, pp. 59–73, 2016.
- [15] Y. Liu, S. Shao, X. Wang, L. Chang, G. Cui, and F. Zhou, "Gas flow analysis for the impact of gob gas ventholes on coalbed methane drainage from a longwall gob," *Journal of Natural Gas Science and Engineering*, vol. 36, pp. 1312–1325, 2015.
- [16] F. An, Z. Wang, H. Yang et al., "Application of directional boreholes for gas drainage of adjacent seams," *International Journal of Rock Mechanics and Mining Sciences*, vol. 90, pp. 35–42, 2016.
- [17] E.P.A, *Methane emissions from abandoned coal mines in the United States*, United States: EPA 430-R-04-001, 2004.
- [18] I. Leifer and K. Wilson, "The tidal influence on oil and gas emissions from an abandoned oil well: Nearshore Summerland, California," *Marine Pollution Bulletin*, vol. 54, no. 9, pp. 1495–1506, 2007.
- [19] V. Palchik, "Time-dependent methane emission from vertical prospecting boreholes drilled to abandoned mine workings at a shallow depth," *International Journal of Rock Mechanics and Mining Sciences*, vol. 72, pp. 1–7, 2014.
- [20] Q.-T. Hu and H.-T. Sun, "Graded optimization design method on surface gas drainage borehole," *Journal of the China Coal Society*, vol. 39, no. 9, pp. 1907–1913, 2014.
- [21] J. Liu, H. Sun, and Q. Hu, "Surface borehole synthesis tension deformation fracture time-space rule," *International Journal of Mining Science and Technology*, vol. 22, no. 4, pp. 465–470, 2012.
- [22] L. Yuan, H. Guo, P. Li, Y.-P. Liang, and B.-C. Liao, "Theory and technology of goaf gas drainage with large-diameter surface boreholes," *Journal of the China Coal Society*, vol. 38, no. 1, pp. 1–8, 2013.
- [23] H. Wang, Y. Jiang, S. Xue et al., "Assessment of excavation damaged zone around roadways under dynamic pressure induced by an active mining process," *International Journal of Rock Mechanics and Mining Sciences*, vol. 77, pp. 265–277, 2015.
- [24] Z. Zhu, Q. Wang, and Q. Wu, "On the examination of the Darcy permeability of soft fibrous porous media; new correlations," *Chemical Engineering Science*, vol. 173, pp. 525–536, 2017.
- [25] Q. Li, B. Lin, C. Zhai et al., "Variable frequency of pulse hydraulic fracturing for improving permeability in coal seam," *International Journal of Mining Science and Technology*, vol. 23, no. 6, pp. 847–853, 2013.
- [26] W. Wang, X. Li, B. Lin, and C. Zhai, "Pulsating hydraulic fracturing technology in low permeability coal seams," *International Journal of Mining Science and Technology*, vol. 25, no. 4, article 549, pp. 681–685, 2015.
- [27] J. Xu, C. Zhai, and L. Qin, "Mechanism and application of pulse hydraulic fracturing in improving drainage of coalbed methane," *Journal of Natural Gas Science and Engineering*, vol. 40, pp. 79–90, 2017.
- [28] A. Liu, X. Fu, K. Wang, H. An, and G. Wang, "Investigation of coalbed methane potential in low-rank coal reservoirs - Free and soluble gas contents," *Fuel*, vol. 112, pp. 14–22, 2013.

Research Article

A Numerical Simulation Study of the Migration Law of Water-Sand Two-Phase Flow in Broken Rock Mass

Feng Du,^{1,2} Guanghui Jiang ,³ and Zhanqing Chen ²

¹School of Energy Science and Engineering, Henan Polytechnic University, Jiaozuo, Henan 454000, China

²State Key Laboratory for Geomechanics and Deep Underground Engineering, China University of Mining and Technology, Xuzhou, Jiangsu 221008, China

³School of Mechanics and Civil Engineering, China University of Mining and Technology, Beijing 100083, China

Correspondence should be addressed to Guanghui Jiang; cumt_jgh@126.com

Received 26 October 2017; Accepted 19 December 2017; Published 21 January 2018

Academic Editor: Zhongwei Chen

Copyright © 2018 Feng Du et al. This is an open access article distributed under the Creative Commons Attribution License, which permits unrestricted use, distribution, and reproduction in any medium, provided the original work is properly cited.

When the upper parts of coal resources are exploited, the mining overburden separated strata may easily connect with the upper unconsolidated aquifers. This may cause the water-sand two-phase fluids in the aquifers to flow underground through the falling broken rock mass. It has been found that it is difficult to eliminate sand after it has entered a mine, which tends to severely restrict the restorations of mines and causes significant economic losses. This paper studied a seepage system dynamic model of water-sand two-phase fluids in broken rock mass based on related two-phase flow theories. In addition, using FORTRAN language, it established a numerical calculation program to study the migration law of water-sand two-phase fluids flowing into broken rock mass and determined the main influencing factors on the seepage characteristic parameters of water-sand two-phase fluids in broken rock mass and the amounts of sand losses.

1. Introduction

Water-sand inrush disasters are common occurrences during the mining of shallow coal seams in China's western mining areas. Since the coal seam is featured by shallow buried depths and thin base rock, it has been found that, following the exploitation of coal seams, the fallen broken rock mass becomes easily linked with the upper sand aquifers. The water-sand fluids flow underground through the broken rock mass of a mine. This may result in buried equipment on the working surfaces, and even casualties. These negative effects generate major threats to safety, as well as the efficient production of a mine. Figure 1 details the occurring principle of water-sand inrush disaster.

Many researchers have carried out studies which have focused on the water-sand inrush mechanism and have achieved significant results. In summary, the previous research studies were divided into two aspects as follows: first, the development laws of mining fissure or caving zones were examined, for example, the study of the flow channel development laws of water-sand fluids [1–7]. The second aspect

was the study of the water-sand inrush mechanism from the properties of the aquifers, which mainly focused on the examination of the water-rich characteristics of different aquifers and the critical hydraulic slopes of water-sand inrush [8, 9].

In actual situations, with the exception of the water-sand migration channels and the occurrence properties of the aquifers having influences on the water-sand inrush disasters, the migration laws of the water-sand two-phase fluids in broken rock mass are also of great importance for water-sand inrush disasters. These disasters must be studied thoroughly. There have been many previous research studies carried out regarding the seepage in broken rock mass. For example, Martins [10] computed the average seepage velocity of turbulent flow when the Reynolds number was larger than 300 in rubble structures. He studied the impacts of particle size, graduation, and the seepage sections on the seepage in rubble structures and also evaluated stability during seepage. Hansen et al. [11] analyzed the two-dimensional seepage in rubble dams using a one-dimensional non-Darcy seepage equation. Engelhardt and Finsterle [12] carried out hydraulic-temperature tests on broken rock mass mixtures as filling

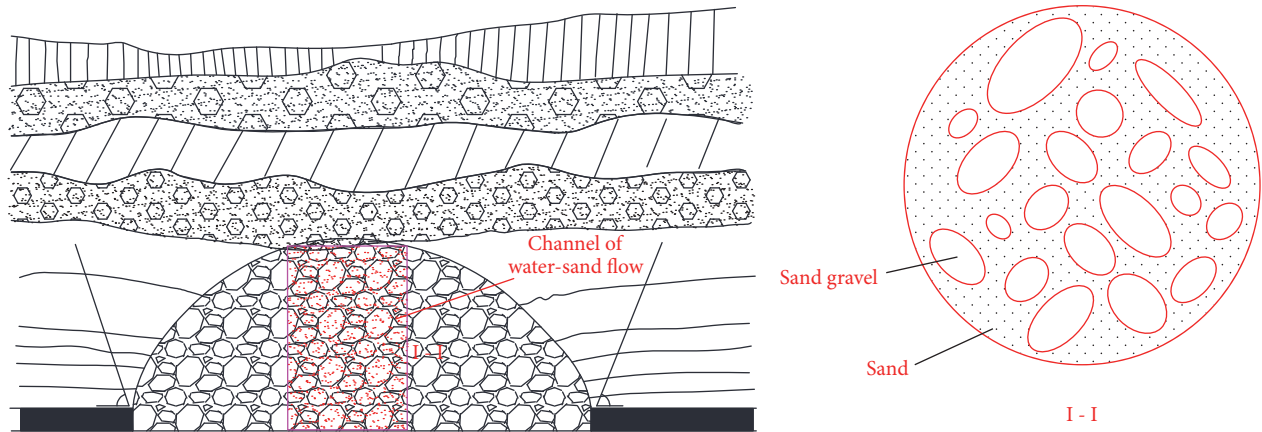


FIGURE 1: Schematic diagram of a water-sand inrush disaster.

materials for underground storage rooms for nuclear wastes and estimated the permeability, thermal conductivity, specific heat capacity, and other parameters of different broken rock mass mixtures by the reversed modeling method. Miao et al. [13] and Ma et al. [14, 15] examined the seepage characteristics of broken rock mass with different porosities using self-made testing devices on broken rock mass. Bai et al. [16] proposed a type of plug model when studying the water bursting mechanisms of collapse columns. In this model, the porosity of the broken rock mass was found to vary with mass exchange, and the changing rate of the mass varied according to the given laws. Yao et al. [17] took into account the dissolution of water on broken rock mass, along with the transport of water for fine particles in broken rock mass, and established a type of broken rock mass deformation-water seepage coupling dynamic model. In this model, the mass of the broken rock mass was found to vary with the water dissolution and transport, which gave rise to changes in the porosity and permeability. Furthermore, there have also been some research studies conducted regarding the flow laws of the solid-liquid phases using numerical calculations. For example, Presho and Galvis [18] proposed a type of multiscale and generalized finite element method for changed flux fields in order to research the two-phase flow in porous media. Barba et al. [19] and Monaghan [20] studied the complex flow of solid-liquid using smoothed particle hydrodynamics. Hai and Hong-yang [21] carried out studies on the basic laws of water-sand two-phase flow in broken rock mass utilizing lattice Boltzmann method and established a numerical calculation model of water-sand two-phase flow in broken rock mass.

The water-sand two-phase seepage problems in broken rock mass are very complex. For the convenience of research, this study took the broken rock mass as seepage material and sand and water as the seepage fluids and assumed that there were no significant changes in the structures of the broken rock mass during the water-sand seepage processes; the pores between the broken rock masses were occupied with water and sand; the volume fraction, the mass fraction, and volume concentration also varied with time. This study established a water-sand two-phase seepage dynamic model of the

broken rock mass based on such hypothesis and proposed a corresponding dynamic numerical computation method. Then, using FORTRAN language, a numerical calculation research was carried out on the seepage law of the water-sand two-phase fluids in the broken rock mass, which laid a theoretical foundation for the further study of the water-sand inrush mechanism during coal mining.

2. Water-Sand Two-Phase Flow Dynamic Model in a Broken Rock Mass

2.1. Motion Parameter Characteristics of the Water-Sand Two-Phase Flow. There are two phases of seepage fluids included in the water and sand phase of water-sand two-phase flow in broken rock mass. The space coordinates of any mass point in a broken rock mass will be identically equal to the material coordinates under the condition of not considering the structural deformation of the broken rock mass. Meanwhile, the space coordinates of the water-sand particles will vary with time. It was believed that any point in the space was occupied by both seepage material and fluid in poromechanics. In this way, there were three types of particles at any spatial point, which included broken rock mass particles, water particles, and sand particles, respectively. Their material coordinates were recorded as $X_1, X_2, X_3, X_1^1, X_2^1, X_3^1$, and X_1^2, X_2^2, X_3^2 , respectively. It was evident that the space coordinates x_1, x_2 , and x_3 of broken rock mass particles were identically equal to their material coordinates X_1, X_2 , and X_3 , while the space coordinates x_1^1, x_2^1 , and x_3^1 of the water particles and space coordinates x_1^2, x_2^2 , and x_3^2 of the sand particles vary with time.

In this study, since the deformation of the broken rock mass was not considered, its position and shape always overlapped with those of the control volume. The water and the sand were constantly flowing into the pores of the broken rock mass. Therefore, they had no certain overall position and shape and only partial position and shape, which corresponded to an infinitesimal element. Figure 2 illustrates the position and shape diagram of infinitesimal element, including the three types of infinitesimal media: broken rock mass, water, and sand at moment t and moment $t + dt$.

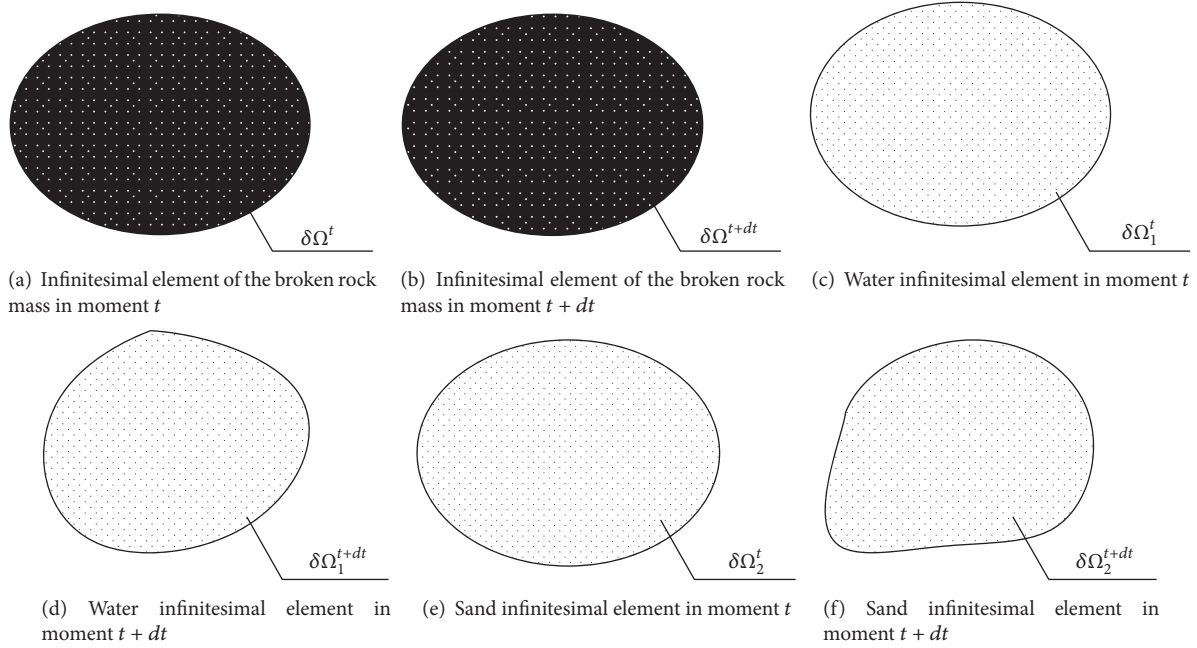


FIGURE 2: Position and shape diagram of infinitesimal element.

Figures 2(a) and 2(b) show the broken rock mass infinitesimal elements of the two moments, which had the same boundary and set of particles. However, the set of particles of the water and sand in its pores are obviously different. Therefore, strictly speaking, Figures 2(a) and 2(b) demonstrate the infinitesimal volume rather than the infinitesimal material. Figures 2(c) and 2(d) are the water infinitesimal element in moment t and moment $t+dt$, respectively. In Figures 2(c) and 2(d), it can be seen that the set of particles of the water are the same in infinitesimal element. However, the spatial position was different. Figures 2(e) and 2(f) are the sand infinitesimal element in moment t and moment $t+dt$, respectively. The set of particles of the sand were the same in infinitesimal element, but the spatial position was different.

The spatial positions of the broken rock mass infinitesimal element $\delta\Omega$, water infinitesimal element $\delta\Omega_1^t$, and sand infinitesimal element $\delta\Omega_2^t$ overlapped in moment t . The position and volume of the broken rock mass infinitesimal element remain unchanged after experiencing time dt . The water infinitesimal element occupied spatial area $\delta\Omega_1^{t+dt}$, and its size and shape were different from $\delta\Omega_1^t$. The sand infinitesimal element occupied spatial area $\delta\Omega_2^{t+dt}$, and its size and shape were different from $\delta\Omega_2^t$.

Due to the fact that the movement of $\delta\Omega_1$ boundary was caused by the water flow, the material derivative of $\delta\Omega_1$ was determined to be related to the speed of the water particles v_1 :

$$\frac{D}{Dt}\delta\Omega_1 = \frac{\partial v_1}{\partial x}\delta\Omega_1 \quad (1)$$

Similarly, the material derivative of $\delta\Omega_2$ was related to the speed of the sand particles v_2 :

$$\frac{D}{Dt}\delta\Omega_2 = \frac{\partial v_2}{\partial x}\delta\Omega_2 \quad (2)$$

Given that the porosity between the broken rock masses was ϕ , the mass densities of the water and sand were m_1 and m_2 , respectively; and the volume fractions of the water and sand phase were Y_1 and Y_2 , respectively. Then, the mass concentrations of the water and sand were as follows:

$$\begin{aligned} \rho_1 &= \phi Y_1 m_1 \\ \rho_2 &= \phi Y_2 m_2. \end{aligned} \quad (3)$$

The seepage velocities of the water and the sand were V_1 and V_2 , respectively, while the average velocities of the particles were v_1 and v_2 , respectively. Since the pores in the broken rock mass contained water and sand, the volume fraction was considered in the Dupuit-Forchheimer relation as follows:

$$\begin{aligned} V_1 &= \phi Y_1 v_1 \\ V_2 &= \phi Y_2 v_2. \end{aligned} \quad (4)$$

2.2. Mass Conservation Equations. During the seepage process, the water-sand flow displayed small changes in mass density, which were considered $\partial m_1/\partial t = 0$ and $\partial m_2/\partial t = 0$. Then, the water-sand phase mass conservation equations were, respectively, as follows:

$$\begin{aligned} \frac{\partial(\phi Y_1)}{\partial t} + \frac{\partial V_1}{\partial x} &= 0 \\ \frac{\partial(\phi Y_2)}{\partial t} + \frac{\partial V_2}{\partial x} &= 0. \end{aligned} \quad (5)$$

2.3. Momentum Conservation Equations. In this study, under the condition of ignoring the capillary force, the momentum exchange of the water-sand was reflected in the relationship

between the permeability parameter and volume fraction. In other words, the water phase permeability k_1 , non-Darcy flow factor β_1 , and acceleration coefficient c_{a1} were the functions of the volume fraction Y_1 , and the sand phase permeability k_2 , non-Darcy flow factor β_2 , and acceleration coefficient c_{a2} were the functions of the volume fraction Y_2 .

Water is considered to be a Newton fluid, and the momentum conservation equation is written on the basis of the Forchheimer relation as follows:

$$m_1 c_{a1} \frac{\partial V_1}{\partial t} = -\frac{\partial p}{\partial x} - \frac{\mu_1}{k_1} V_1 - m_1 \beta_1 V_1^2, \quad (6)$$

where p is the fluid pressure; μ_1 is the dynamic viscosity of the water; the other parameters were the same as mentioned above.

Wet sand is considered to be a power-law fluid [22]. In this study, the consistency coefficient of wet sand was set as C , the power exponent as n , the apparent viscosity as μ_{2a} , and the effective permeability as k_{2e} . Then, the momentum conservation equation was as follows:

$$m_2 c_{a2} \frac{\partial V_2}{\partial t} = -\frac{\partial p}{\partial x} - \frac{\mu_{2a}}{k_{2e}} V_2 - m_2 \beta_2 V_2^2. \quad (7)$$

Then, due to the relationship between the effective viscosity μ_{2e} and apparent viscosity μ_{2a} :

$$\mu_{2a} = \mu_{2e} V^{n-1}. \quad (8)$$

Equation (7) could then be written as

$$m_2 c_{a2} \frac{\partial V_2}{\partial t} = -\frac{\partial p}{\partial x} - \frac{\mu_{2e}}{k_{2e}} V_2^n - m_2 \beta_2 V_2^2. \quad (9)$$

By setting the fluidities of the water and sand as I_1 and I_2 , respectively, the following could be obtained:

$$I_1 = \frac{k_1}{\mu_1} \quad (10)$$

$$I_2 = \frac{k_{2e}}{\mu_{2a}}$$

Then, according to (8) and (10), (7) and (9) could be simplified as follows:

$$m_1 c_{a1} \frac{\partial V_1}{\partial t} = -\frac{\partial p}{\partial x} - \frac{1}{I_1} V_1 - m_1 \beta_1 V_1^2 \quad (11)$$

$$m_2 c_{a2} \frac{\partial V_2}{\partial t} = -\frac{\partial p}{\partial x} - \frac{1}{I_2} V_2^n - m_2 \beta_2 V_2^2.$$

2.4. Auxiliary Equations. Due to the fact that there were only two types of seepage fluids in the fractured rock pores, the water phase volume fraction Y_1 and sand phase volume fraction Y_2 met the following conditions:

$$Y_1 + Y_2 = 1. \quad (12)$$

The porosity evolution was determined by the porosity compressibility equation as follows:

$$\phi = \phi_{p0} [1 + c_\phi (p - p_0)], \quad (13)$$

where ϕ_{p0} represents the porosity when the pressure was ϕ_{p0} ; c_ϕ is the pore compressibility coefficient; p denotes the fluid pressure; p_0 represents the initial fluid pressure.

2.5. Permeability Parameters in the Water-Sand Two-Phase Flow in the Broken Rock Mass. During the water-sand two-phase flow in broken rock mass, the volume fractions of the water and the sand in the pores change with time. Therefore, fluidity, non-Darcy flow factor, and acceleration coefficient also change with time, and the change rule is affected by the sand grain size, graduation, and porosity. Therefore, the determinations of fluidity, non-Darcy flow factor, and acceleration coefficient are the key core elements to establishing the water-sand two-phase flow dynamic model in a broken rock mass.

According to the results of this study's laboratory testing [22], it was found that the fluidity I_1 , non-Darcy flow factor β_1 , and the acceleration coefficient c_{a1} of water phase and the effective fluidity I_{2e} , non-Darcy flow factor β_2 , and acceleration coefficient c_{a2} of sand phase all conformed with the following polynomial relations:

$$I_1 = a_{11} + a_{12}z + a_{13}z^2, \quad (14)$$

$$i = 1, 2, \dots, n_f, z \in [0, 1]$$

$$\lg \beta_1 = a_{21} + a_{22}z + a_{23}z^2, \quad (15)$$

$$i = 1, 2, \dots, n_f, z \in [0, 1]$$

$$\lg c_{a1} = a_{31} + a_{32}z + a_{33}z^2, \quad (16)$$

$$i = 1, 2, \dots, n_f, z \in [0, 1]$$

$$I_{2e} = a_{41} + a_{42}z + a_{43}z^2, \quad (17)$$

$$i = 1, 2, \dots, n_f, z \in [0, 1]$$

$$\lg \beta_2 = a_{51} + a_{52}z + a_{53}z^2, \quad (18)$$

$$i = 1, 2, \dots, n_f, z \in [0, 1]$$

$$\lg c_{a2} = a_{61} + a_{62}z + a_{63}z^2, \quad (19)$$

$$i = 1, 2, \dots, n_f, z \in [0, 1].$$

From (14) to (19), z represents the normalized volume fraction:

$$z = \frac{Y_2 - Y_2^l}{Y_2^r - Y_2^l}, \quad (20)$$

where Y_2^l and Y_2^r are the left and right limits of the sand phase volume fraction, respectively; a_{jk} ($j = 1, 2, \dots, 6$; $k = 1, 2, 3$) is the coefficient; Y_2^l, Y_2^r , and a_{jk} ($j = 1, 2, \dots, 6$; $k = 1, 2, 3$) change with the porosity; $z < 0$; the permeation parameters

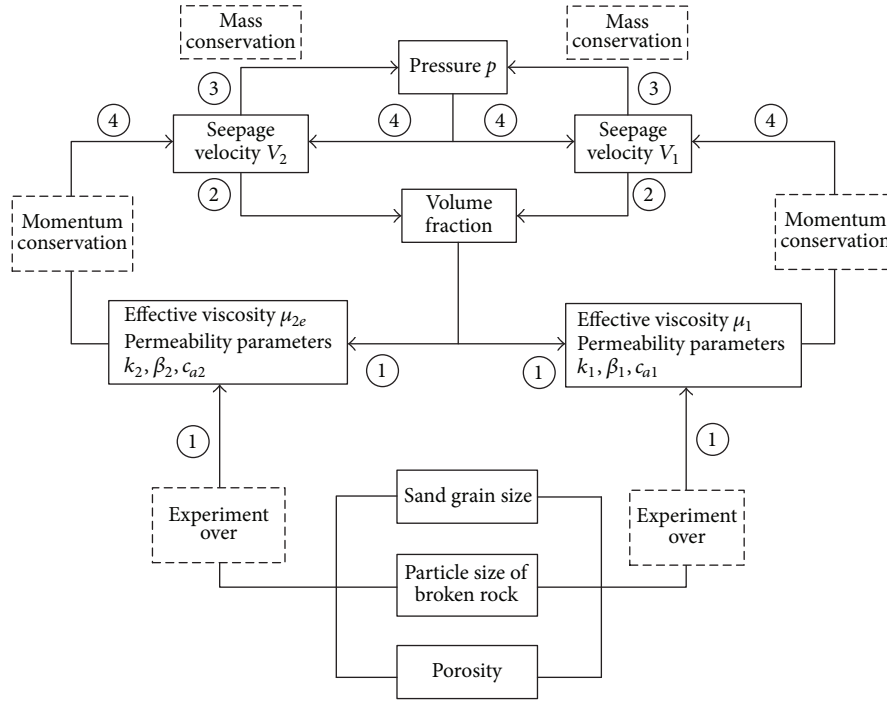


FIGURE 3: Relationship among all of the variables in the dynamic model.

when $z < 0$ and $z > 1$ ($Y_2 < Y_2^l$ and $Y_2 > Y_2^r$) could be calculated according to $z = 0$ and $z = 1$, respectively.

The relationship between the equations and physical quantities in the above dynamic model is shown in Figure 3. As can be seen in the figure, link ① is the calculation of the effective viscosities μ_1 and μ_{2e} and the permeability parameters of the water and sand phases, which were mainly obtained using calculations (16) to (20) on the basis of the tests [22]. Link ② is the calculation of the volume fractions Y_1 and Y_2 according to the mass conservation equations (5) and the auxiliary equation (12). Link ③ is the calculation of the pore pressure p according to the mass conservation equations (5) and the auxiliary equation (13). Link ④ is the calculation of the seepage velocities V_1 and V_2 according to momentum conservation equations (11).

3. Water-Sand Two-Phase Flow Dynamical Numerical Calculation in the Broken Rock Mass

3.1. Numerical Calculation Process. In this study, in order to further examine the water-sand migration rule in a broken rock mass, and in accordance with the abovementioned water-sand two-phase flow dynamic model, a numerical calculating program of the water-sand two-phase flow in a broken rock mass was programed using Fortran language program. Figure 4 illustrates its numerical calculating procedure. From the figure we can see that $k_1, \beta_1, c_{a1}, \mu_{2e}, k_{2e}, \beta_2,$ and c_{a2} were initially solved. This step was obtained through the basic calculations of the tests. At the same time, the effects of such factors as the grain sizes of the broken rock mass

and the grain sizes of the sand should be considered. Since this step only involved algebraic operations, there was no need to construct algorithms. At this point, the numerical solutions of the sand volume fraction Y_2 and the pore pressure p were, respectively, obtained by the numerical integration of the mass conservation equation. The algorithm was roughly the same. Finally, the numerical solutions of the seepage velocities V_1 and V_2 were obtained through the numerical integration of the momentum conservation equation. For the occurrences of water-sand inrush disasters during coal mining processes, the focus is usually on the variation rule of the sand mass loss amounts Q under different influencing factors. In this study, the sand mass loss amounts Q could be solved in accordance with the variation law of the seepage velocity V_2 of the sand in the model. As the sand flowed out of the broken rock mass, the mass of the sand in the broken rock mass continuously decreased, and the volume fraction decreased, accordingly. During the time period of $[0, t]$, the sand mass loss amounts Q flowing out of the broken rock mass were

$$Q_{\text{sand}}^{(t)} = \int_0^t m_2 V_2 \pi r^2 dt, \quad (t = 0, 1, 2, \dots, N), \quad (21)$$

where m_2 is the sand mass density; V_2 is the seepage velocity of the sand; and r denotes the width of the numerical model.

Through this study's numerical calculation results, not only could the loss law of sand in the broken rock mass under the different influencing factors be obtained, the variation law of the permeability characteristics in the broken rock mass could also be obtained. Therefore, in this study, a theoretical foundation for the study of the mechanism of water-sand

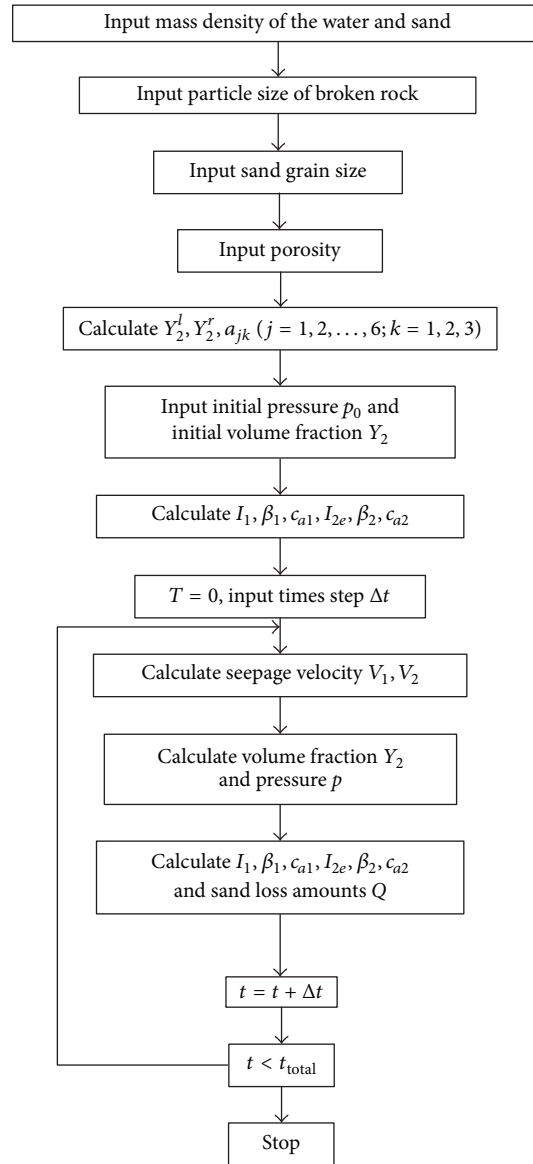


FIGURE 4: Technological process for the response calculations.

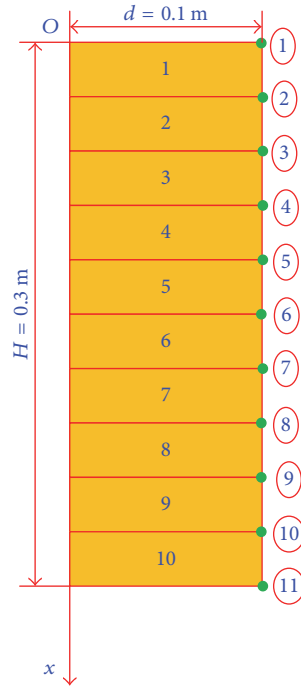
inrush disasters in shallow coal mining seams could be successfully laid.

3.2. Numerical Calculation Model

3.2.1. Establishment of the Model. In order to facilitate the study of the relationship between the sand grain flow, sand loss amounts and broken rock grain size, sand grain size, and porosity, it was proposed in this study to establish a cylindrical calculation model with a radius of $r = 0.05$ m and height of $H = 0.3$ m. The top interface of the model was used as the origin, and a plumb in a downward direction was used as the forward direction of Ox axis, in order to establish a numerical calculation coordinate system. Then, for the purpose of monitoring the change law of the sand grain flow in the model, the model was evenly divided into ten units, with a

total of eleven nodes. The node spacing was 0.03 m, as shown in Figure 5. It should be noted that, in order to compare with the results of the test, in this numerical calculation, the sand grain and broken rock mass were evenly mixed. Then, water was continuously added from the top of the model, which formed the water-sand two-phase fluid. Also, during the calculation process, the sand was no longer added.

In order to prove the theoretical model's reasonability with the experimental results shown in [22], the basic parameters of the model were set as follows: the mass density of the water was $m_1 = 1.0 \times 10^3$ kg/m³; dynamic viscosity of water was $\mu_1 = 1.01 \times 10^{-3}$ Pa·s; mass density of sand grain was $m_2 = 2.6 \times 10^3$ kg/m³; consistency coefficient was $C = 0.2436$; power exponent was $n = 0.11$; compressibility coefficient of the broken rock was $c_\phi = 1.0 \times 10^{-9}$ Pa⁻¹; and porosity was $\phi_{p0} = 0.6$ under the reference pressure $p_0 = 0$.



1–10: unit number; ①–⑪: node number

FIGURE 5: Unit and node number.

3.2.2. Numerical Calculation Scheme. (1) The variation law of the permeability parameters in the water-sand two-phase flow in broken rock mass has mainly been studied from the aspect of the variation law of sand phase seepage velocity V_2 and sand phase volume fraction Y_2 , as well as the variation of such parameters as the sand flow phase I_2 , acceleration coefficient c_{a2} , and the non-Darcy flow factors β_2 during the flow process of the water-sand two-phase flow in broken rock mass. In this scheme, the particle sizes of the broken rock mass were between 12 and 15 mm; the sizes of the sand grains were from 0.074 to 0.25 mm; the top pressure was $p_t = 3.0 \times 10^6$ Pa; the bottom pressure was $p_b = 0$ Pa.

(2) The factors, such as the particle size of the broken rock mass, sand grain size, and porosity, have important influences on inducing water-sand inrush disaster in a mine. Therefore, it has become very important to study the relationship between these factors and the amount of sand loss. This study's detailed scheme was as follows:

- ① *The influence of the particle size of the broken rock mass on the amount of sand loss:* the sand sizes were between 0.074 and 0.25 mm; with a top pressure of $p_t = 3.0 \times 10^6$ Pa, a bottom pressure of $p_b = 0$ Pa, and a porosity of $\phi = 0.585$. The particle sizes of the broken rock were 5 to 8 mm; 10 to 12 mm; and 12 to 15 mm.
- ② *The influence of the grain sizes of the sand on the amount of sand loss:* top pressure was $p_t = 3.0 \times 10^6$ Pa; bottom pressure was $p_b = 0$ Pa, with a porosity of $\phi = 0.585$; the particle sizes of the broken rock were 12 to 15 mm; the sand sizes were from 0.074 to 0.25 mm

(fine sand); 0.25 to 0.59 mm (medium sand); and 0.59 to 0.83 mm (coarse sand).

- ③ *The influence of the porosity on the amount of sand loss:* top pressure was $p_t = 3.0 \times 10^6$ Pa; bottom pressure was $p_b = 0$ Pa; the particle sizes of the broken rock were between 12 and 15 mm. The sand sizes were from 0.074 to 0.25 mm, and the porosity ϕ was 0.565, 0.575, and 0.585.

4. Results and Discussion

4.1. Variation Law of the Permeability Parameters in the Water-Sand Two-Phase Flow in the Broken Rock Mass

4.1.1. Variation Law of the Sand Flow. The variation laws of seepage velocity V_2 and volume fraction Y_2 of the sand phase are shown in Figure 6. The abscissa is the Ox axis of the model from top to bottom.

It can be seen from the figure that at $t = 0$ s, the seepage velocity V_2 of the sand was 0 m/s, which indicated that the sand had not been driven by water at the initial time. When $t = 30$ s and $t = 60$ s, the seepage velocity of the sand increased from the top of the model (0 to 0.03 m) to the lower part of the model (0.27 to 0.3 m) as a whole. However, the seepage velocity of the sand in the middle section of the model (0.06 to 0.24 m) remained essentially unchanged at 1.87×10^{-5} m/s, as shown in Figure 6(a). It can be seen that the phase volume fraction of the sand was evenly distributed in the model at $t = 0$ s, which accounted for 40% of the total volume. With the increasing seepage time, the volume

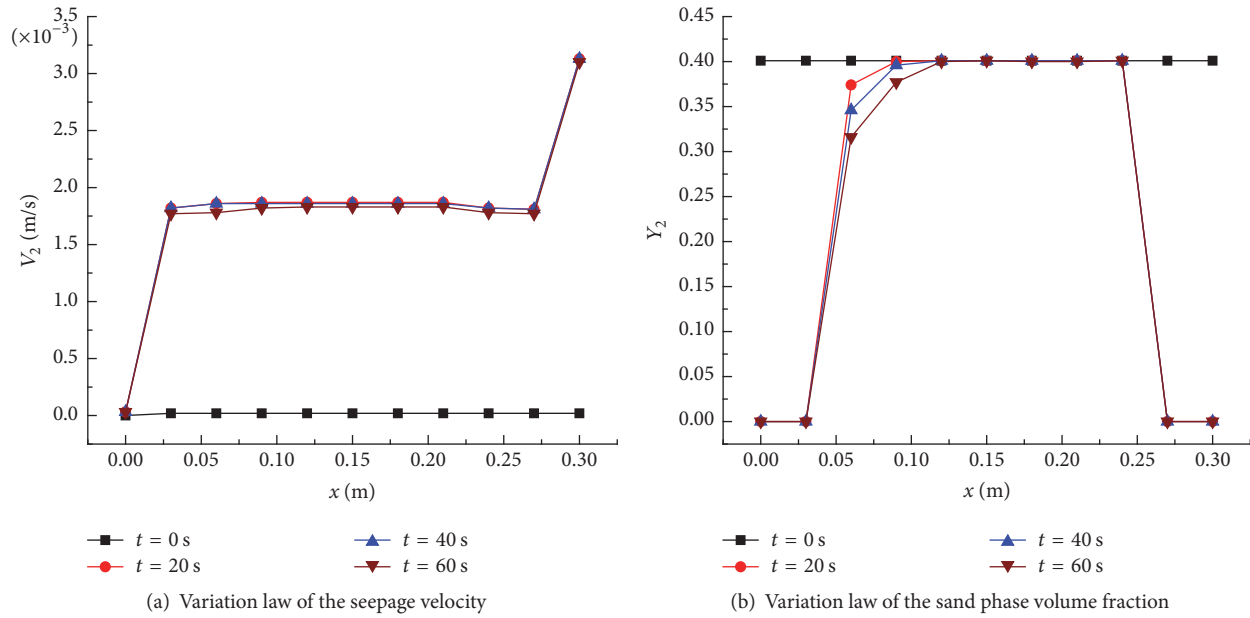


FIGURE 6: Variation law of seepage velocity V_2 and volume fraction Y_2 of the sand phase in the broken rock mass.

fractions at the top of the model (0 to 0.03 m) and the bottom (0.27 to 0.3 m) were reduced to 0%, while the sand volume fraction also decreased with the increase of time in the middle of the model between 0.06 and 0.12 m. The sand volume fraction remained basically unchanged between 0.12 and 0.24 m, which was determined to be not related to the seepage time, as shown in Figure 6(b).

4.1.2. Variation Law of the Permeability Parameters during the Sand Migration. As can be seen from the figure, the permeability parameters also showed large differences during the migration of the sand grains along the Ox axis. The sand fluidity I_2 actually reflected the change of the sand phase permeability during the sand migration process. At the top of the model, the sand grains were moving into the middle section, due to being driven by water. The sand content at the top became increasingly less, which resulted in a relative increase in the sand phase permeability. Likewise, the sand grains at the bottom of the model also flowed out quickly, and sand phase permeability at the bottom increased. However, due to the sand in the middle section being supplemented by the sand at the top, the result was that the sand phase permeability was almost unchanged in 60 s. Then, with the increase in time, the increasing range of the permeability continued to expand into the center of the model, as shown in Figure 7(a). The acceleration coefficient c_{a2} characterized the inertia force during the sand migration process. It was observed that as the volume fractions of the sand at the top and bottom decreased, the quality also decreased. The acceleration coefficient c_{a2} also showed the permeability characteristic of first being small at the top and bottom and basically unchanged in the middle. The acceleration coefficient of some nodes in the central part also displayed a decreasing trend with the increase in time, as

shown in Figure 7(b). The non-Darcy flow factor reflected the nonlinear feature of the sand's migration process, in which the higher the numerical value was, the more obvious the nonlinear characteristic would be. The degree of sand nonlinearity was found to be highest at the initial time, and the nonlinearity decreases rapidly with the loss of sand at the top and bottom. Meanwhile, in the middle section, the change of the volume fraction of the sand was not obvious, while the non-Darcy flow factor displayed little change and also had high nonlinear characteristics, as can be seen in Figure 7(c).

4.2. Analysis of the Main Influencing Factors of the Water-Sand Inrush Disasters

4.2.1. Effects of the Particle Sizes of the Broken Rock Mass. Figure 8(a) shows the numerical calculation results of the variation of the sand loss amounts with different grain sizes in the broken rock mass. The following can be seen in the figure. (1) As the grain sizes of the broken rock mass increased, the sand loss amounts also increased, and the mine became more prone to water-sand inrush disasters. (2) The relationship between the grain sizes of the broken rock mass and the sand loss amounts was nonlinear. When the particle sizes of the broken rock mass ranged from 12 to 15 mm, the sand loss amounts were 882 g in 60 s. When the particle sizes of the broken rock mass ranged from 10 to 12 mm, the sand loss amounts were 624 g. When the particle sizes of the broken rock mass ranged from 5 to 8 mm, the sand loss amounts were 487 g. When the particle sizes of the broken rock mass were between 12 and 15 mm, the increases of sand loss amounts were larger than those of the previous two particle sizes. Figure 8(b) displays the results of this study's indoor experiment [22]. It can be seen in the figure that as the particle sizes of the broken rock

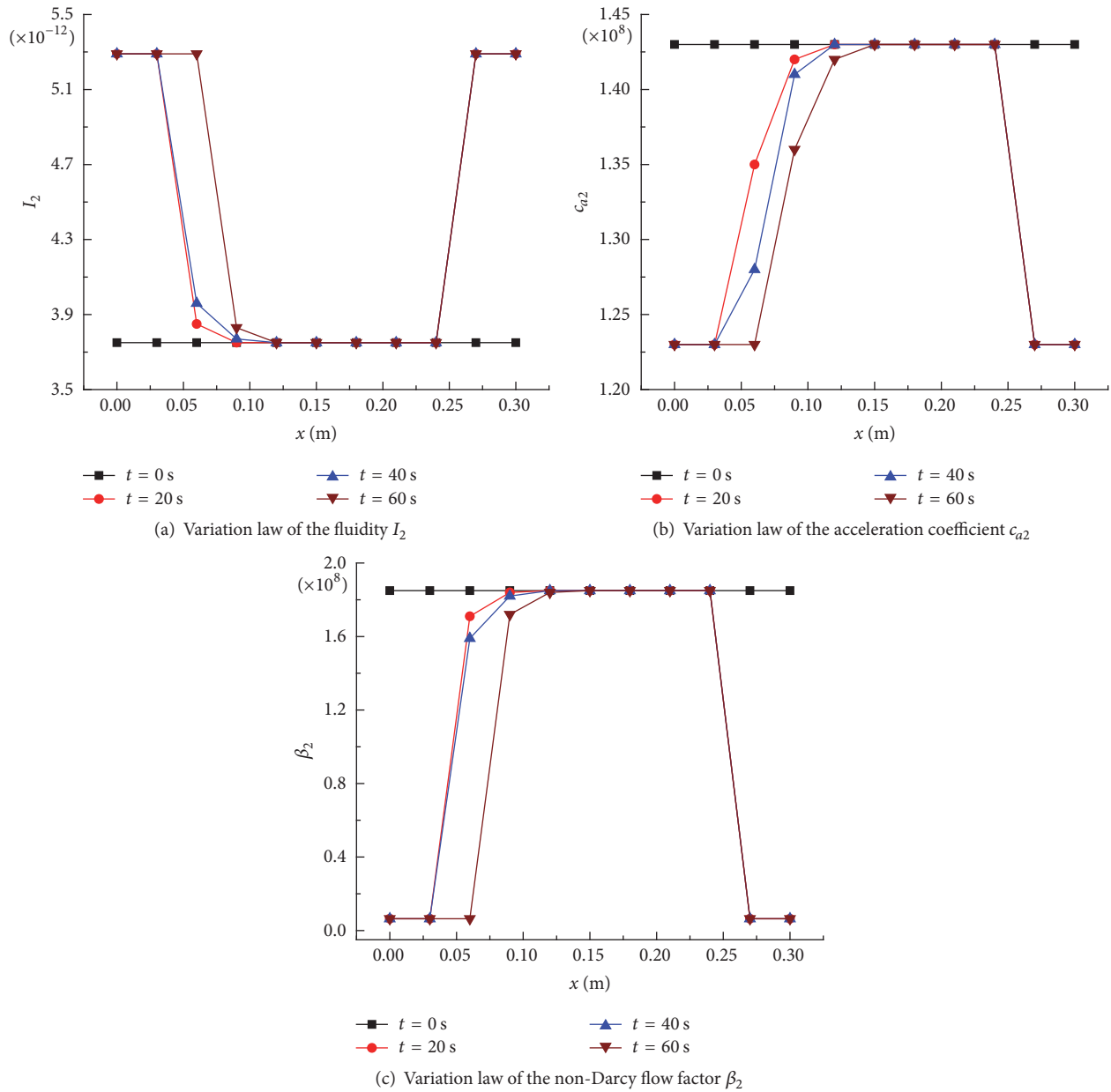


FIGURE 7: Variation laws of the water-sand two-phase permeability parameters in the broken rock mass.

mass increased, the sand loss amounts also increased, which was the same as the numerical calculation. However, the total sand loss amounts were determined to be smaller than the numerical calculation results. For example, when the particle sizes of the broken rock mass were between 12 and 15 mm, the total sand loss amounts were 489.9 g. When the particle sizes of the broken rock mass were between 10 and 12 mm, the total sand loss amounts were 298 g. When the particle sizes of the broken rock mass were between 5 to 8 mm, the total sand loss amounts were 15 g. This was mainly due to the fact that the test system needed to achieve the set porosity by displacement loading, and the gravel grains would be extruded and deformed during the process of the displacement loading. This resulted in major changes in the

gradation of the gravel, and the original pores became filled with the squeezed crushed grains. This caused the actual pores to be less than the theoretical calculation value, and the numerical calculation had effectively avoided this error.

4.2.2. *Effects of the Sand Sizes.* Figure 9 shows this study's numerical calculation results of the variations of the sand loss amounts for the different sand sizes. The following can be seen in the figure. (1) During the entire seepage process, the speed of the sand losses during the first 10 s was fast, and the losses of the three sand sizes displayed only slight differences (259 g, 251 g, and 231 g, respectively). Also, the differences among sand loss amounts with the three sand sizes became wider with the continuous increases in the seepage time. (2)

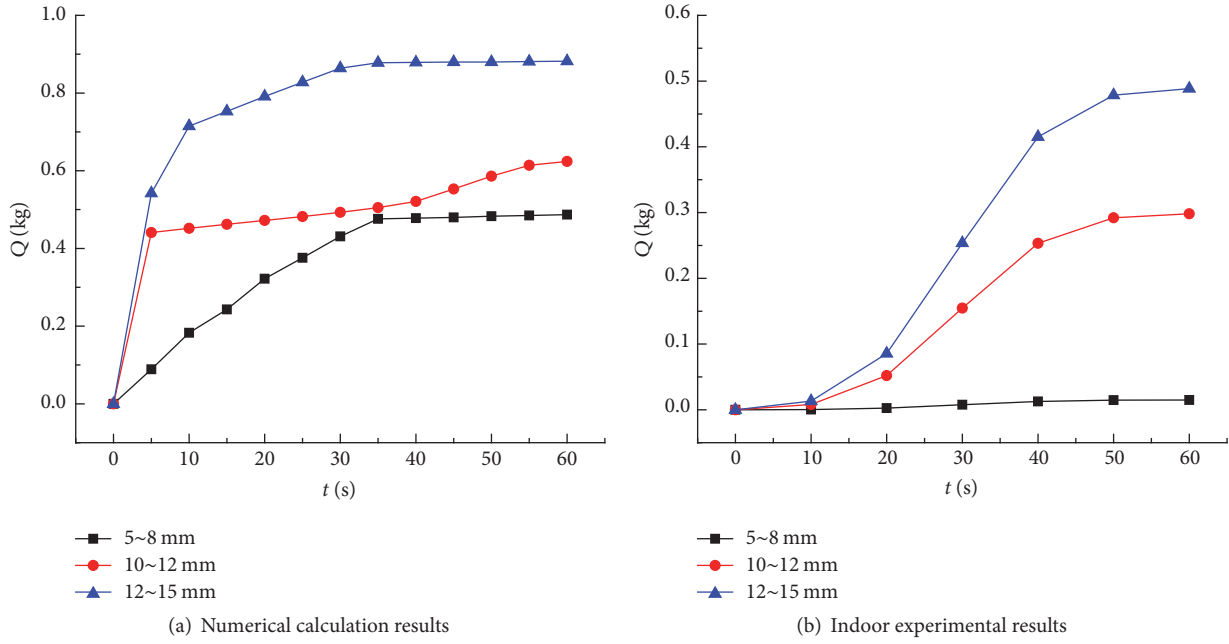


FIGURE 8: Variations in the sand loss amounts with the different particle sizes of the broken rock mass.

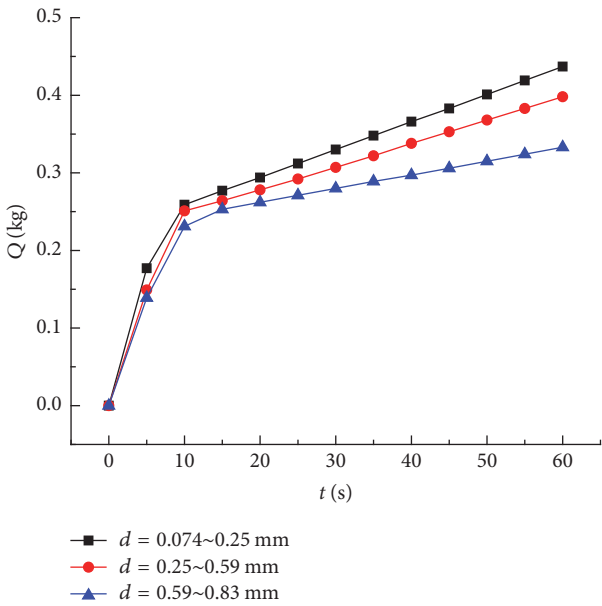


FIGURE 9: Variations of the sand losses in the different sand sizes.

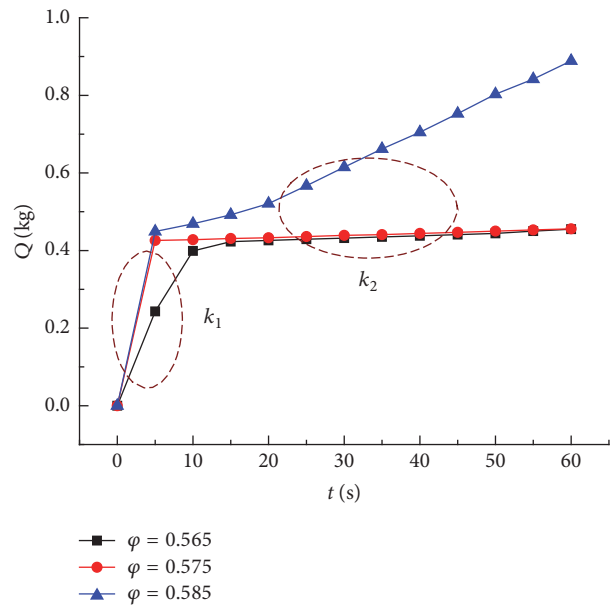


FIGURE 10: Variations of the sand loss amounts with the different porosities.

The sand with grain sizes from 0.074 to 0.25 mm had total loss amounts of 437 g in 60 s. The sand with grain sizes between 0.25 and 0.59 mm had total amounts of 398 g in 60 s. The sand with grain sizes between 0.59 and 0.83 mm had total amounts of 333 g in 60 s. Under the same condition, with the increases in the sand sizes, it was found that the smaller the sand loss amounts were, the easier it became for the water-sand inrush disasters of fine sand driven by water to occur in the mining of shallow coal seams. Therefore, prevention methods should be emphasized in the mining processes, and the drainage of

loose sand grain aquifers should be made in advance, in order to prevent fine sand being acted upon by flowing water.

4.2.3. *Effects of Porosity.* It can be seen in Figure 10 that the sand loss amounts with different porosities had the following rules:

(1) The speed of the sand grain loss in 10 s was significantly higher than that in the later periods. That is to say, the slope was $k_1 > k_2$, which was mainly due to the fact that the sands

at the bottom of the calculation model were close to the free face, and the sands, under the action of the water, flowed out very quickly and easily. As the time increased, the sand grains in the upper part of the model flowed into the middle section. In the cases of constant porosity, the sand grains in the middle were blocked, which led to slow losses of the sand grains. At the same time, it was found that there was a matching relationship between the sand sizes and the porosity. By taking $\phi = 0.585$ as an example, the sand loss amounts became reduced after 10 s. However, it was still higher than that of the other sand loss amounts with two low porosities.

(2) With the increases in the porosity, the sand loss amounts became larger. For example, in the case of $\phi = 0.585$, the total amount of sand loss was 889 g in 60 s. Meanwhile, at $\phi = 0.565$ and $\phi = 0.575$, the total amounts of sand losses were 455 g in 60 s. These results indicated that the larger the porosity of the broken rock mass was, the greater the probability of the water-sand inrush disasters and the amount of sand inrush would be. These findings were determined to be similar to the rule in the experiment, as well as the conclusions of the field observations [22].

5. Conclusions

In this research study, a basic examination of the nonlinear behavior of water-sand two-phase flow in the broken rock mass was carried out using both theoretical analysis and numerical calculation. This study mainly included the effects of porosity, particle sizes of the broken rock mass, sand sizes, sand content, and the lithology on the permeability parameters. The main conclusions which were obtained through the results of this study's research experiments were as follows:

(1) In accordance with the mass conservation law and the momentum conservation law of the water and sand phases, and the porosity compressibility equation of the broken rocks, basic equation, and partial auxiliary equations of the system were derived. A water-sand two-phase flow dynamic model in a broken rock mass was established, and the initial and boundary conditions of the model were discussed.

(2) An algorithm of dynamic response of the water-sand two-phase flow system in a broken rock mass was constructed. The relationships between the porosities, volume fractions, pore pressures, seepage velocities, and permeability parameters were examined. Furthermore, the influences of the particle sizes of the broken rock mass and the sand sizes on the permeability parameters were determined.

(3) A numerical calculation model of the water-sand two-phase flow in broken rock mass was established. By using this calculation model, the variation laws of the sand grain parameters (e.g., the seepage velocity V_2 , volume fraction Y_2), as well as the variation laws of the permeability parameters of sand phase (the non-Darcy flow factor β_2 ; acceleration coefficient c_{a2} , fluidity I_2 , etc.), were obtained. Due to the fact that the sand grains were not replenished in the numerical calculation, the sand grain in the upper part of the model gradually decreased with the increases in the seepage time. Also, the lower part of the model became rapidly reduced due to its closeness to the entrance. However, the sand grains

in the middle section of the model were observed to be relatively unchanged. At the same time, the corresponding law of the sand-phase permeability parameters was also produced. In other words, with the increases in the seepage time t , the sand-phase permeability parameters gradually decreased in the upper and lower ends of the model and basically remained constant in the middle. Also, the sand-phase nonlinear characteristic was higher in the middle than in the end sections.

(4) The particle sizes of the broken rock mass, sand sizes, porosity, and other factors were found to have important influences on the water-sand inrush disasters. Also, the sand loss amounts were greatly increased with the increases in the particle sizes of the broken rock mass and porosity and the decreases in sand sizes.

Conflicts of Interest

The authors declare that there are no conflicts of interest regarding the publication of this paper.

Acknowledgments

This paper was supported by the Research Fund of the State Key Laboratory of Coal Resources and Safe Mining, CUMT (13KF02); the National Natural Science Foundation of China (51704095 and 51774110); the Research Fund of the State Key Laboratory of Water Resources Protection and Utilization in Coal Mining, Shenhua Group (SHJT-16-30.11); the Research Fund of the State Key Laboratory for Geomechanics and Deep Underground Engineering, CUMT (SKLGDUEK1310); the Research Fund of the Henan Key Laboratory for Green and Efficient Mining and Comprehensive Utilization of Mineral Resources (Henan Polytechnic University) (S201619); the Key Project of Science and Technology of Department of Education of Henan Province (no. 14A440001).

References

- [1] J. Zhang and B. Shen, "Coal mining under aquifers in China: a case study," *International Journal of Rock Mechanics and Mining Sciences*, vol. 41, no. 4, pp. 629–639, 2004.
- [2] Q. Wu, M. Wang, and X. Wu, "Investigations of groundwater bursting into coal mine seam floors from fault zones," *International Journal of Rock Mechanics and Mining Sciences*, vol. 41, no. 4, pp. 557–571, 2004.
- [3] J.-A. Wang and H. D. Park, "Coal mining above a confined aquifer," *International Journal of Rock Mechanics and Mining Sciences*, vol. 40, no. 4, pp. 537–551, 2003.
- [4] G. Wang, M. Wu, R. Wang, H. Xu, and X. Song, "Height of the mining-induced fractured zone above a coal face," *Engineering Geology*, vol. 216, pp. 140–152, 2017.
- [5] D. Zhang, G. Fan, L. Ma, and X. F. Wang, "Aquifer protection during longwall mining of shallow coal seams: a case study in the Shendong coalfield of China," *International Journal of Coal Geology*, vol. 86, no. 2-3, pp. 190–196, 2011.
- [6] S. Peng, W. Ma M, and L. Zhong W, *Surface subsidence engineering[M]. Society for Mining, Metallurgy, and Exploration*, 1992.

- [7] X. Miao, X. Cui, J. Wang, and J. Xu, "The height of fractured water-conducting zone in undermined rock strata," *Engineering Geology*, vol. 120, no. 1-4, pp. 32–39, 2011.
- [8] W. Sun, W. Zhou, and J. Jiao, "Hydrogeological classification and water inrush accidents in China's coal mines," *Mine Water and the Environment*, vol. 35, no. 2, pp. 214–220, 2016.
- [9] State Administration of Coal Mine Safety, Analysis of China's coalmine accidents in 2013. Accident Investigation Division of State Administration of Coal Mine Safety, Beijing, China, 2014.
- [10] R. Martins, "Turbulent seepage flow through rockfill structures," *International Water Power & Dam Construction*, vol. 42, no. 3, pp. 41–44, 1990.
- [11] D. Hansen, V. K. Garga, and D. R. Townsend, "Selection and application of a one-dimensional non-Darcy flow equation for two-dimensional flow through rockfill embankments," *Canadian Geotechnical Journal*, vol. 32, no. 2, pp. 223–232, 1995.
- [12] I. Engelhardt and S. Finsterle, "Thermal-hydraulic experiments with bentonite/crushed rock mixtures and estimation of effective parameters by inverse modeling," *Applied Clay Science*, vol. 23, no. 1-4, pp. 111–120, 2003.
- [13] X. Miao, S. Li, Z. Chen, and W. Liu, "Experimental study of seepage properties of broken sandstone under different porosities," *Transport in Porous Media*, vol. 86, no. 3, pp. 805–814, 2011.
- [14] D. Ma, H. Bai, Z. Chen, and H. Pu, "Effect of particle mixture on seepage properties of crushed mudstones," *Transport in Porous Media*, vol. 108, no. 2, pp. 257–277, 2015.
- [15] D. Ma, M. Rezaia, H.-S. Yu, and H.-B. Bai, "Variations of hydraulic properties of granular sandstones during water inrush: effect of small particle migration," *Engineering Geology*, vol. 217, pp. 61–70, 2017.
- [16] H. Bai, D. Ma, and Z. Chen, "Mechanical behavior of ground-water seepage in karst collapse pillars," *Engineering Geology*, vol. 164, pp. 101–106, 2013.
- [17] B. Yao, J. Wei, D. Wang, D. Ma, and Z. Chen, "Numerical study on seepage property of karst collapse columns under particle migration," *CMES. Computer Modeling in Engineering & Sciences*, vol. 91, no. 2, pp. 81–100, 2013.
- [18] M. Presho and J. Galvis, "A mass conservative generalized multiscale finite element method applied to two-phase flow in heterogeneous porous media," *Journal of Computational and Applied Mathematics*, vol. 296, pp. 376–388, 2016.
- [19] L. A. Barba, A. Leonard, and C. B. Allen, "Advances in viscous vortex methods—meshless spatial adaption based on radial basis function interpolation," *International Journal for Numerical Methods in Fluids*, vol. 47, no. 5, pp. 387–421, 2005.
- [20] J. J. Monaghan, "Smoothed particle hydrodynamics and its diverse applications," *Annual Review of Fluid Mechanics*, vol. 44, pp. 323–346, 2012.
- [21] U. P. Hai and N. Hong-yang, "Characteristics of Water Sediment Two Phase Flows in Weakly Cemented Fractured Rock Mass Based on Lattice Boltzmann Method[C]," in *51st US Rock Mechanics/Geomechanics Symposium*, American Rock Mechanics Association.
- [22] F. Du, Z. H. Li, G. H. Jiang, and Z. Q. Chen, "Types and mechanism of water-sand inrush disaster in west coal mine," *Journal of China Coal Society*, vol. 42, no. 7, pp. 1846–1853, 2017 (Chinese).

Research Article

Lateral Percolation and Its Effect on Shale Gas Accumulation on the Basis of Complex Tectonic Background

Kun Zhang,^{1,2,3,4} Zhenxue Jiang ^{1,2}, Xuelian Xie,^{1,2} Zhiye Gao ^{1,2},
Tianlin Liu,^{1,2} Lishi Yin,^{1,2} Chengzao Jia,⁴ Yan Song,^{1,2,4} Chang'an Shan,⁵
Yinghui Wu,⁶ and Pengfei Wang⁷

¹State Key Laboratory of Petroleum Resources and Prospecting, China University of Petroleum, Beijing 102249, China

²Unconventional Natural Gas Research Institute, China University of Petroleum, Beijing 102249, China

³Unconventional Petroleum Collaborative Innovation Center, China University of Petroleum, Beijing 102249, China

⁴Research Institute of Petroleum Exploration and Development, Beijing 100083, China

⁵School of Earth Sciences and Engineering, Xi'an Shiyou University, Xi'an 710065, China

⁶School of Earth Sciences and Resources, China University of Geosciences, Beijing 100083, China

⁷Geoscience Documentation Center (CGS), Beijing 100083, China

Correspondence should be addressed to Zhenxue Jiang; jzxuecup@163.com and Zhiye Gao; gaozhiye@163.com

Received 18 September 2017; Accepted 13 November 2017; Published 11 January 2018

Academic Editor: Zhongwei Chen

Copyright © 2018 Kun Zhang et al. This is an open access article distributed under the Creative Commons Attribution License, which permits unrestricted use, distribution, and reproduction in any medium, provided the original work is properly cited.

As a result of complex tectonic background, shale gas in China exhibits differential enrichment. Choosing a favorable exploration target accurately is a crucial problem to be solved. In this study, the tests show that there is a superior transportation pathway within shale layer. Gas in the shale layer percolates much more in the direction parallel to the plane. Therefore, the accumulation pattern of shale gas indicates a complex tectonic background. Gas in the lower part of the structure diffuses and percolates in the vertical direction into the surrounding rock. Most gas percolates towards the high part of the structure in the direction parallel to the plane. When the shale was exposed, gas percolated along the parallel direction into the air. In the case of fracture development, if there is a reverse fault, gas would be enriched in the footwall. However, if there is an unsealed fault, it would become a pathway for gas migration. The above accumulation pattern was proved in several Areas. Also, this research presented a basis of evaluation units division. According to the buried depth, fractures, and structural position, Xiuwu Basin was divided into five evaluation units and Unit A3 is the most favorable exploration target.

1. Introduction

Unconventional oil and gas exploration, represented by the exploration of shale oil and gas, has been a great success in North America recently because of the change in exploration concepts and the development of hydraulic fracturing technology. Similarly, China also has huge unconventional oil and gas resources, especially shale gas [1, 2]. In 2010, Well Wei 201 drilled in the Weiyuan structure achieved an industrial breakthrough of shale gas in China. In 2016, a series of progressions in shale gas commercialization was made in Changning, Zhaotong, Jiaoshiba, and Anchang. The projected shale gas production in 2020 was supposed to be $30 \times 10^9 \text{ m}^3$ [3].

While the shale gas exploration of China has made progression, the gas content of the different blocks varied greatly. This indicates the need for further study by petroleum geologists of the shale gas accumulation mechanism. China and North America have different geological backgrounds. America was formed by a single plate, with a large area and high rigidity. The basins did not arise through multistage tectonic movements after the deposition of shale; shale gas accumulated continuously over a large area [4–6]. In contrast, China was formed by the union of multiple plates, such as the North China Plate, Yangtze Plate, and Cathaysia Plate. The Paleozoic marine shale of South China has experienced complex multiperiod tectonic and thermal evolution, and

the structural styles are variable which has resulted in the differential enrichment and accumulation of shale gas [7, 8]. When the total organic carbon (TOC) content, mineral composition, and structural evolution of similar circumstances differ, the shale gas content of adjacent blocks (or different evaluation units of the same blocks) varies greatly, due to the structural position, distance from faults, and other factors.

Yang et al. (2013) summarized two shale gas accumulation patterns: the Antrim shale gas accumulation pattern in the Michigan Basin (A-pattern) and the Barnett shale gas accumulation pattern in the Delaware Basin (B-pattern). The main feature of the A-pattern is that, from the shallow periphery to the deep Basin, biogenic gas, mixed gas, and thermogenic gas occur in sequence [9–11]. The main features of the B-pattern are that the shale gas is of thermogenic origin and is indigenously generated and accumulated. Shale gas of different genetic types occurs in areas with different thermal maturities. They suggest that the Barnett shale gas accumulation pattern (B-pattern) of the Delaware Basin is of greater significance for shale gas exploration in China. However, the Antrim shale gas accumulation pattern in the Michigan Basin (A-pattern) also cannot be ignored [6, 10].

Wang et al. [12] analyzed the conditions of shale gas accumulation and divided favorable areas using TOC content, organic-rich shale thickness, maturity, mineral composition, and depth. Guo [13] put forward a theory of two-factor enrichment of marine shale gas in South China. The development of high quality marine shale on a deep continental shelf constitutes a base of hydrocarbon generation of shale gas and excellent preservation is the key to accumulation and generation of shale gas. Wang et al. [14] put forward a theory of three-factor enrichment, whose cores include the conditions of hydrocarbon generation, reservoir conditions, and shale gas preservation conditions. Based on the exploration discoveries of shale gas and research progress in relevant geological theory, as well as “source-cap controlling hydrocarbon” theory, Nie et al. [15] analyzed the main controlling factors of shale gas enrichment in the Upper Ordovician Wufeng Formation and Lower Silurian Longmaxi Formation of Sichuan Basin and its periphery. The above theory played an important role in the evaluation of shale gas under the complex tectonic background of China. However, how to choose an evaluation unit in a potential block and how to reduce exploration risk are still important problems to be solved.

Previous studies on the reservoir characteristics and shale gas exploration potential of the Lower Cambrian used the organic-rich shale’s distribution characteristics, TOC, kerogen type, organic maturity, and reservoir characteristics to analyze the conditions of shale gas accumulation and to predict a favorable target area [16]. However, because the Xiuwu Basin experienced multiple depressions and extensions that caused the formation of a lot of fractures and complicated structural styles, it is hard to point a favorable and accurate exploration target simply using an index of hydrocarbon generating material basis or reservoir capacity [14, 17, 18]. In this study, a shale gas accumulation pattern was deduced and then proved through analysis of difference between the vertical and lateral permeability of shale. After

that, the evaluation units of the Xiuwu Basin were divided to indicate the next step in exploration.

2. Geological Setting

2.1. Tectonic and Sedimentary Characteristics. The Xiuwu Basin is located southeast of the Jiangnan Basin and north of the Jiangnan Uplift (Figure 1). The shale gas block, which is a part of Xiuwu Basin and includes shale gas exploration Well JiangYe 1 and JiangYe 2, is in the west part of the Xiushui-Wuning syncline. In the Sinian Period, the Xiuwu Basin was a craton basin, and in the Late Sinian, marine regression happened with the formation of the Piyuncun Formation, which consists of siliceous dolomite. The Wangyinpu Formation (thickness 45–50 m, organic-rich, and black siliceous shale) was deposited in the Early Cambrian while a large regression happened. Gradually, the water became shallow [19]. The clastic sedimentary system in the Early Cambrian developed into a carbonatite sedimentary system in the Middle-Late Cambrian. The sedimentary environment changed back to shallow marine in the Early-Middle Ordovician [20]. During the Late Ordovician-Early Silurian, due to the collision of the plate, the study area was a deep-water environment caused by the extrusion. The water became shallow again in the Middle Silurian. The land was uplifted to become ancient land in the Late Silurian [21, 22]. During the Devonian and Carboniferous, periods of uplift and precipitation (erosion) intersected incessantly and little sediment was deposited during that time. The Permian and Early-Middle Triassic were also times of major precipitation. In the Late Triassic, the Xiuwu Basin began to uplift but was impacted by the collision between the North China Plate and the South China Plate [14, 23]. Squeezed during the Early-Middle Jurassic, the study area turned into a syncline and a large number of thrust faults developed. During the Cretaceous, the squeezing stress environment of the Xiuwu Basin transferred to the extension. The stress properties of these thrust faults turned from extrusion to extension. The stress of the study area, influenced by the intrusion of the India-Australian plate onto the Eurasian plate, was changed from extension to extrusion again in the Neogene [24].

2.2. Stratigraphic Distribution. The Xiuwu Basin appears as a syncline with strata present from old to young, of the limbs to the core [25, 26]. From bottom-up, the Sinian, Cambrian, Ordovician, Middle and Lower Silurian, Upper Devonian, Upper Carboniferous, Middle and Upper Permian, and Lower Triassic were deposited. In the southeastern and southwestern parts of the study area, the Upper Cretaceous and Paleogene alluvial fan was overlain unconformably by the eroded strata. The Wangyinpu and Guanyintang Formations of the Lower Cambrian, Xiuwu Basin, which has high total organic carbon (TOC) content, thick organic-rich shale, high degree of thermal evolution, and type I kerogen, are the target layer of shale gas exploration [27]. The lithology of underlying strata, the Piyuncun Formation of Upper Sinian, is grey siliceous dolomite. The lithology of overlying strata, the Yangliugang Formation of Middle Cambrian, is grey

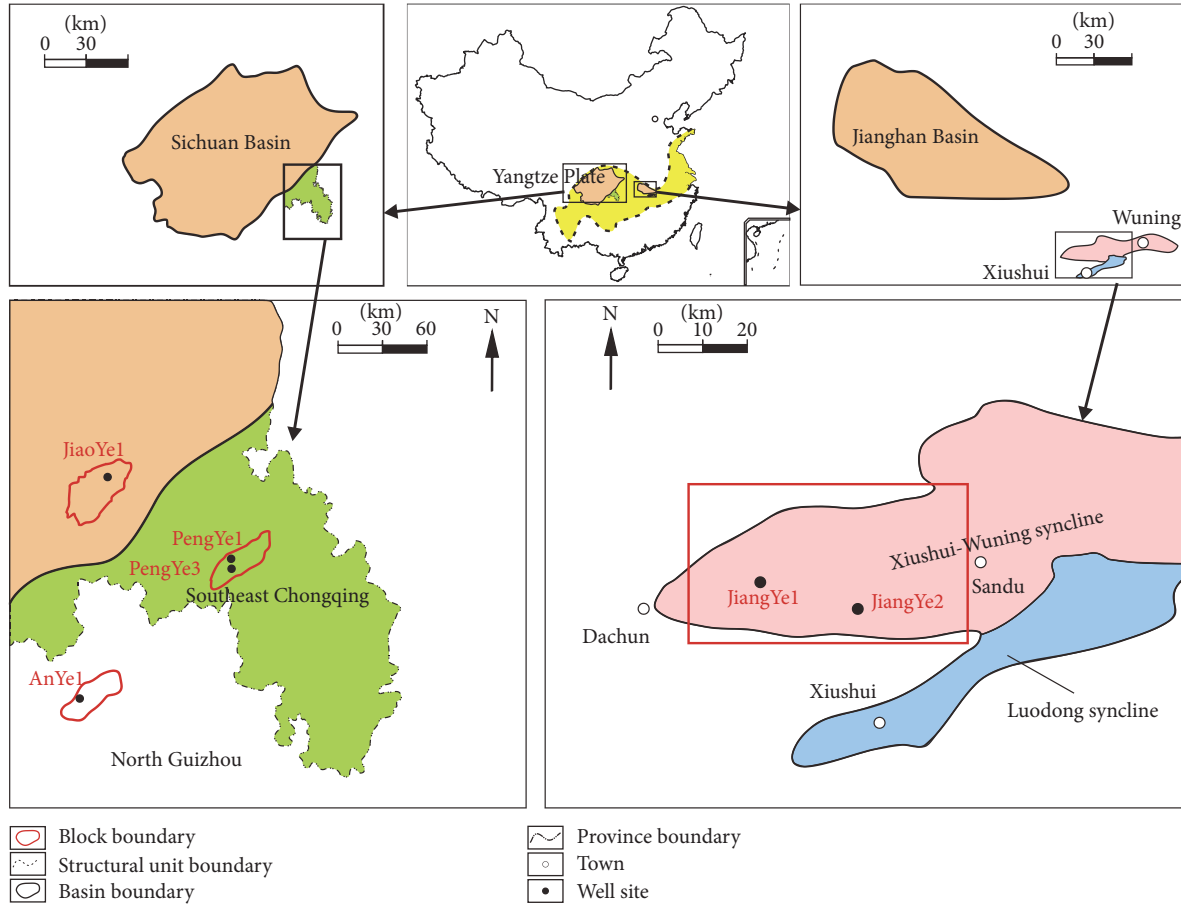


FIGURE 1: Geological map of Jiaoshiba, Anchang, Pengshui, and Xiuwu Basin with well locations.

microcrystalline limestone. Both of them are conformable contact. The stratigraphic column was shown in Figure 2.

3. Samples and Experiments

3.1. Permeability Test. In the Wangyinpu and Guanyintang Formations, from the bottom to the top in the Lower Cambrian of the Xiuwu Basin, 16 samples were taken from Lower Cambrian shale. 3 samples were from Well JiangYe 1, and 13 were from Well JiangYe 2 (Table 1). TEMCO Poro PDP-200 was used to analyze the vertical and lateral pulse permeability of full diameter core samples. The permeability test pressure was 1000 psi and the confining pressure 1500 psi. In the Longmaxi Formation, He et al. [28] have taken 12 samples from Lower Silurian shale of Pengshui Area, Well PengYe 1 (Table 2).

3.2. Core Immersion Test. At the drilling site of Well JiaoYe 1, Jiaoshiba Area, the core of Lower Silurian was immediately put into a sink when it was taken out of the wellhead. The size of the bubbles from the cylindrical surfaces and sections of the core, occurrence (continuous or discontinuous bubble), sound level, duration, and bubble position were all recorded.

4. Results

4.1. Experimental Result. The results of the permeability tests are shown in Figures 3 and 4, which illustrate that lateral permeability was 1–40 times that of the vertical permeability. This indicated the existence of a superior transportation pathway within the shale layers. The core immersion test of Lower Silurian of Well JiaoYe 1 also indicated that shale gas bubbles were mainly from a direction parallel to the plane (Figure 5). Bubbles from directions perpendicular to the plane were only a few. The results confirmed that gas in shale layers mainly percolates along the direction parallel to the plane.

4.2. Shale Gas Accumulation Pattern. For the characteristics of foliation development in shale, gas seepage has directional properties. With the compaction of shale, the sheet clay minerals tend to be parallel to the rock layer. And with the repeated superposition, plastic deformation, an excellent surface lamellation formed which made the stress in the bedding direction much weaker, and then the seepage rate increased. In the lamellation surface of organic-rich shale, the presence of microcracks increases the lateral permeability. As a result,

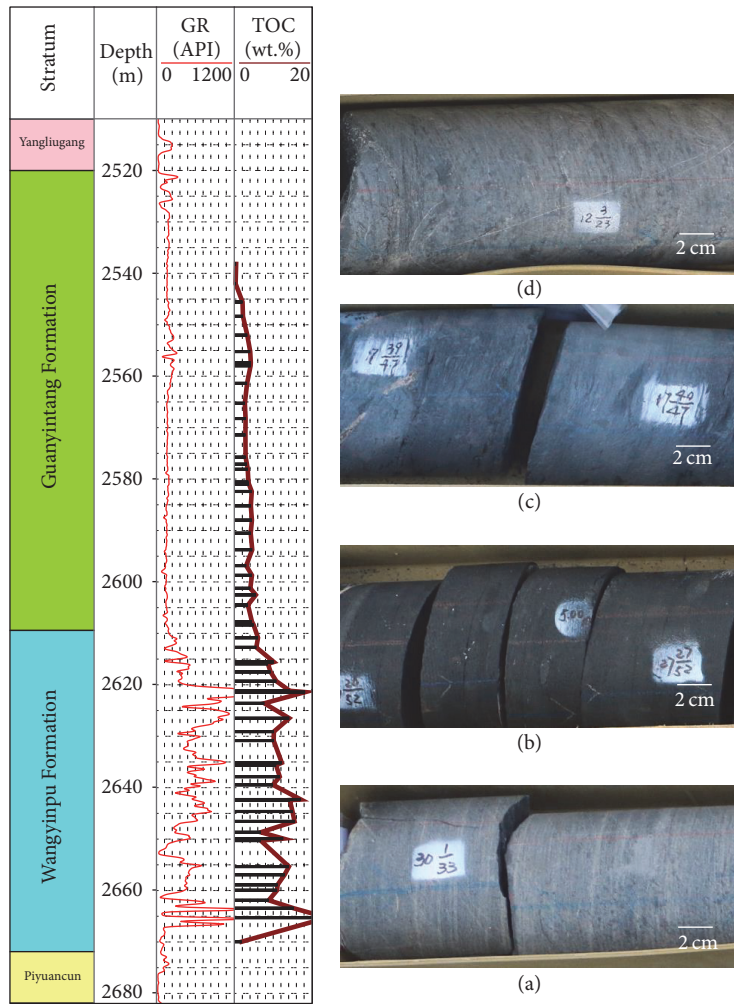


FIGURE 2: A stratigraphic column and core photos of Upper Ediacaran, Lower and Middle Cambrian of Jiangye-1 well. (a) Ediacaran Piyuancun Formation 2675 m, grey siliceous dolomite. (b) Lower Cambrian Wangyinpu Formation 2638 m, dark siliceous shale. (c) Lower Cambrian Guanyintang Formation 2546 m, dark grey siliceous shale. (d) Middle Cambrian Yangliugang Formation 2511 m, grey micrite. See Figure 1 for the location of the well site.

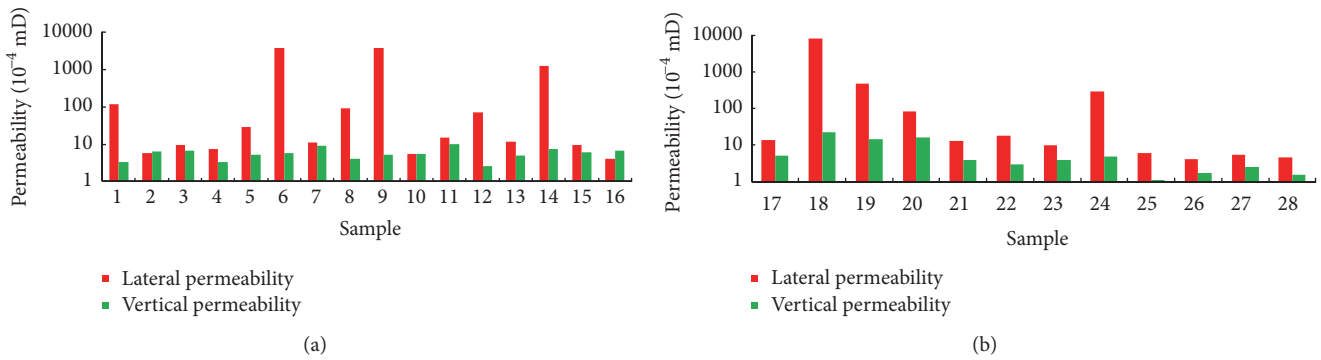


FIGURE 3: Lateral and vertical permeability histograms. (a) Samples of the Lower Cambrian shale, from Well JiangYe 1 and JiangYe 2. (b) Samples of the Lower Silurian shale, from Well PengYe 1. See Figure 1 for the well locations.

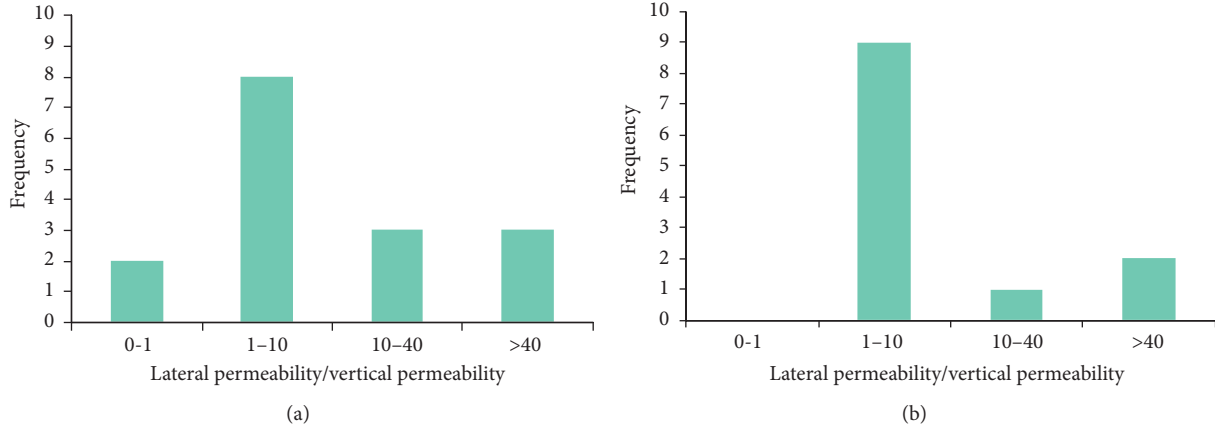


FIGURE 4: Ratio statistics between lateral and vertical permeability. (a) Samples of the Lower Cambrian shale, from Well JiangYe 1 and JiangYe 2. (b) Samples of the Lower Silurian shale, from Well PengYe 1. See Figure 1 for the well locations.

TABLE 1: Number, well, and formation of the permeability test samples.

Number	Well	Formation
(1)	JiangYe 1	Guanyintang
(2)	JiangYe 1	Wangyinpu
(3)	JiangYe 1	Wangyinpu
(4)	JiangYe 2	Guanyintang
(5)	JiangYe 2	Guanyintang
(6)	JiangYe 2	Guanyintang
(7)	JiangYe 2	Guanyintang
(8)	JiangYe 2	Guanyintang
(9)	JiangYe 2	Wangyinpu
(10)	JiangYe 2	Wangyinpu
(11)	JiangYe 2	Wangyinpu
(12)	JiangYe 2	Wangyinpu
(13)	JiangYe 2	Wangyinpu
(14)	JiangYe 2	Wangyinpu
(15)	JiangYe 2	Wangyinpu
(16)	JiangYe 2	Wangyinpu
(17)	PengYe 1	Longmaxi
(18)	PengYe 1	Longmaxi
(19)	PengYe 1	Longmaxi
(20)	PengYe 1	Longmaxi
(21)	PengYe 1	Longmaxi
(22)	PengYe 1	Longmaxi
(23)	PengYe 1	Longmaxi
(24)	PengYe 1	Longmaxi
(25)	PengYe 1	Longmaxi
(26)	PengYe 1	Longmaxi
(27)	PengYe 1	Longmaxi
(28)	PengYe 1	Longmaxi

the difference between vertical and lateral permeability leads to the diffusion rate of lateral much larger than that of vertical.

Curtis [9] indicated that shale gas migrates a short distance within shale layers. Researches about Jiaoshiba Areas revealed that there is no large range of migration in shale gas system. However, there must be a process of dynamic adjustment and balance in shale with high thermal maturity and complex evolution history [29–31]. When shale gas gathered in the high position, it would be lost naturally. Then, gas from the lower position would migrate a very short distance keeping the balance of accumulation and losing. Step-by-step migration of the adjacent pores has achieved the convergence of shale gas into the positive structure.

Hu et al. [32] used spontaneous imbibition experiments to study pore connectivity of shale. Gao and Hu [33] found that Barnett shale has low pore connectivity by conducting imbibition experiments. A number of previous researchers, Ji et al. [34, 35], Wang et al. [36, 37], Tang et al. [38–40], and Chen et al. [41], indicated that organic matter provided most of the connected pores and that the network consisting of interconnected organic pores, microcracks, and bedding plane provided the main percolation pathway of shale gas. The accumulation pattern was deduced in the comprehensive consideration of previous studies and the experimental results, as well as related tectonism (Figure 6).

Under the action of temperature, pressure, and catalyst, the organic matter matured and started to produce gas. When the shale formation was compressed by tectonic movements, the lateral permeability would be much higher than the vertical if there was no fault and unconformity. From the low part of the structure, most of the shale gas in free-state percolated to the high part along the bedding plane, while some would diffuse and percolate to surrounding rocks. In the high part of the structure, supplementary gas from the lower part of the structure led to higher shale gas content (Figure 6(C)). If the shale formation was exposed at the surface, shale gas would percolate in the direction parallel to the plane into the air, which would lead to low gas content (Figure 6(D)). In the case of fracture development, if there were a well-sealed reverse fault, shale gas would be enriched in the footwall (Figure 6(A)). However, if there were an

TABLE 2: Divisions of evaluation units.

Evaluation units	Secondary evaluation units	Buried depth	Structural position
A	A1	2000–3250 m	Slope
	A2	2000–3250 m	Gentle part and near to the large south structure
	A3	3250–4000 m	Gentle part
	A4	3250–4000 m	Slope with small fractures developed
B		<2000 m	Slope and near to outcrops
C		>4000 m	Depression part
D		South side	Large fractures developed and near to outcrops
E		North side	Large fractures developed and near to outcrops

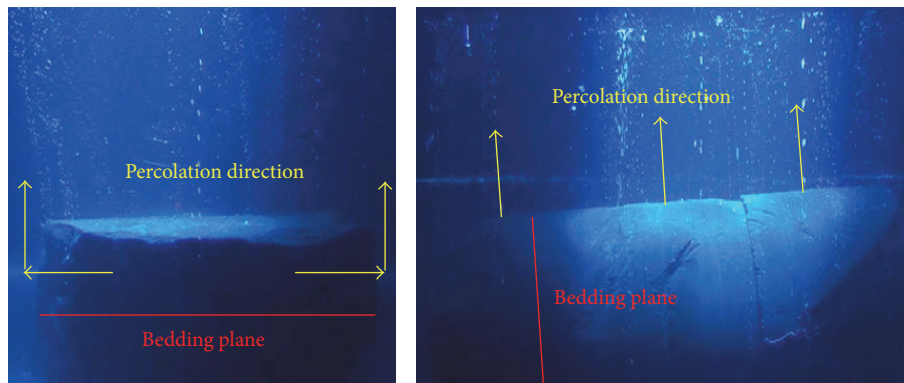


FIGURE 5: Core immersion test of Lower Silurian, from Well JiaoYe1, Jiaoshiba. See Figure 1 for the location.

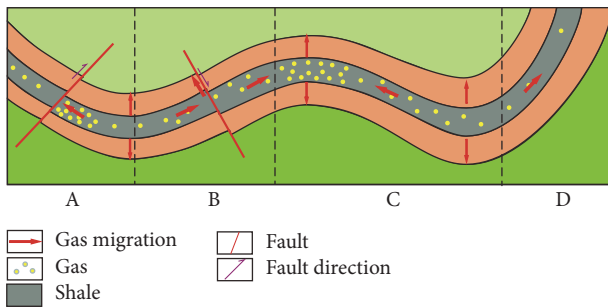


FIGURE 6: Shale gas accumulation pattern under complex tectonic background.

open fault, it would be a pathway for shale gas migration (Figure 6(B)).

5. Discussion

5.1. Validation of the Shale Gas Accumulation Pattern. Southeast Chongqing and North Guizhou are located in the internal-to-external transition zone of the Sichuan Basin. These areas developed anticlines, synclines, and other structural styles due to tectonic movements during the Cretaceous Period and are suitable areas to validate shale gas accumulation patterns, subjected to a complex tectonic background [42, 43]. The following validation took place in Jiaoshiba with

a typical anticline, Pengshui with an obvious syncline, and Anchang with well-sealed reverse faults.

Jiaoshiba, located on the inner side of the Sichuan Basin, is an anticline with a reverse fault on both sides. The area is well sealed because of not being subjected to tectonic extension. Thus in the direction parallel to the plane, there was little loss of shale gas (Zhou et al., 2010) [44]. According to the accumulation pattern, most of the shale gas would gather in place, except for a little diffusion and percolation into the surrounding rock. In the same time, supplementary gas rising from the lower part of the structure would increase the shale gas content (Figure 7).

Pengshui, southeast of Chongqing, located in the outside of Sichuan Basin, is a syncline as a whole with strata of both sides exposed [45–47]. According to the accumulation pattern, shale gas would migrate into the surrounding rock and then percolate to the slopes of the syncline resulting in a lower gas content than at Jiaoshiba. Although shale gas from the core would supply the limbs of the syncline, the gas would migrate through slopes because of surface exposures of the shale formation (Figure 8).

Anchang, North Guizhou, also located in the outside of the Sichuan Basin, is entirely a syncline with a reverse fault in the left limb. Analysis of the tectonic revolution showed that the well-sealed reverse faults were compressed throughout their history [46–48]. The accumulation of shale gas could be inferred on the basis of the accumulation pattern. Shale gas generated in the core would diffuse and percolate to the

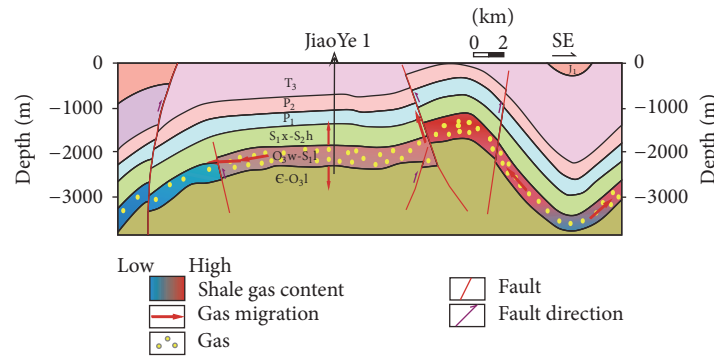


FIGURE 7: Shale gas accumulation diagram of the Jiaoshiba Area, Southeast Chongqing. See Figure 1 for the location.

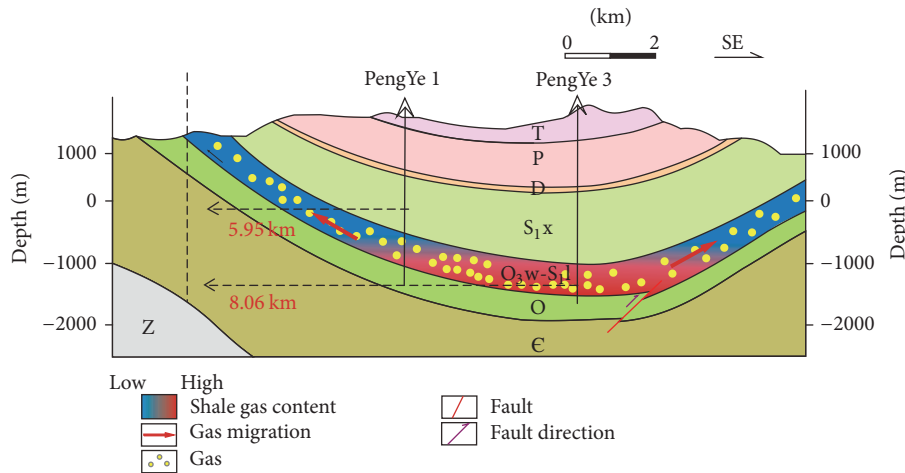


FIGURE 8: Shale gas accumulation diagram of the Pengshui Area, Southeast Chongqing. See Figure 1 for the location.

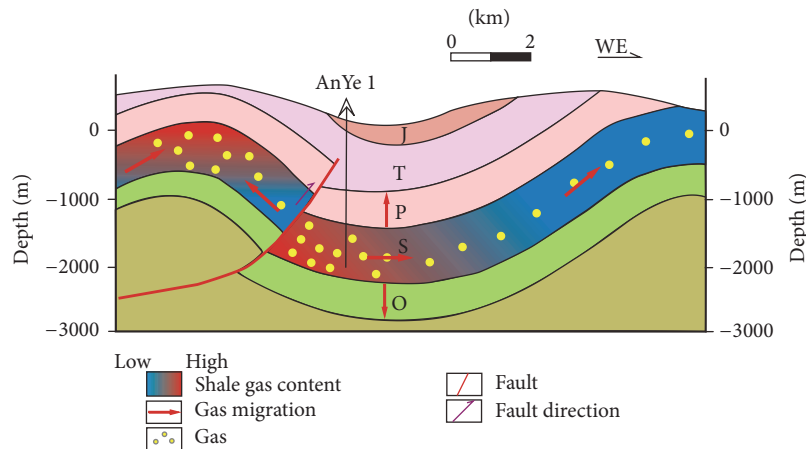


FIGURE 9: Shale gas accumulation diagram of Anchang Area, North Guizhou. See Figure 1 for the location.

limbs along the direction parallel to the plane, while a small part of it would diffuse vertically into the surrounding rock. Due to the good sealing property of the reverse fault in the left limb, shale gas would accumulate in the footwall of the fault. Due to exposure of the shale layer at the surface, gas of the right limb would be lost (Figure 9).

Well drilling in the Jiaoshiba, Anchang, and Pengshui Areas proved the above accumulation pattern. The gas content of Well JiaoYe 1 (Longmaxi Formation in Jiaoshiba) was $6.1 \text{ m}^3/\text{t}$, whereas the gas content of Well AnYe 1 (Longmaxi Formation) reached $6.49 \text{ m}^3/\text{t}$. However, the shale gas wells in the Pengshui Area were not in good condition. The gas

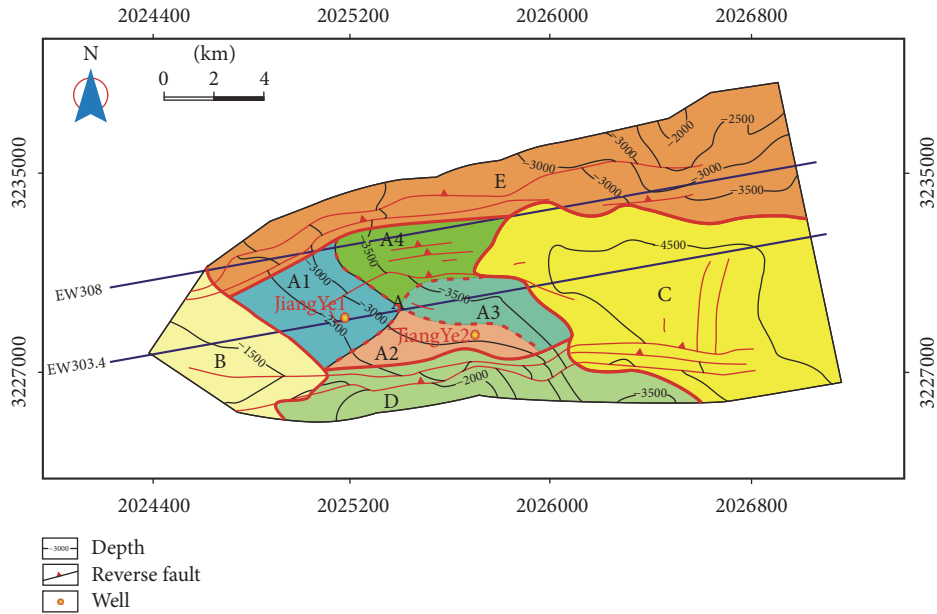


FIGURE 10: Division of evaluation units of the shale gas area, XiuWu Basin. See Figure 1 for the location.

content of Well PengYe 1 on the syncline slope was $1.99 \text{ m}^3/\text{t}$, and that of the Well PengYe 3 in the syncline depression was $2.79 \text{ m}^3/\text{t}$; both are less than Well JiaoYe 1 and Well AnYe 1.

5.2. Division of Evaluation Units in the Xiuwu Basin

5.2.1. Basis for Division of the Evaluation Units. The exploration practices showed that shale gas reservoirs with complex tectonic backgrounds are not large areas of continuous accumulation but are composed of both rich and damaged areas. To select a favorable exploration target accurately, division of the evaluation units of the shale gas area and analysis of accumulation conditions is essential. According to the accumulation pattern, combined with the tectonic background of the Xiuwu Basin and exploration costs, in this study, buried depth, fractures, and structural styles were chosen as the basis for dividing the evaluation units.

(1) Buried Depth. The chosen study area had a buried depth between 2000–4000 m. The reason is that the study area is a syncline with Lower Cambrian exposure in the limbs. If the buried depth was lower than 2000 m, dips of the strata would increase rapidly, which would make diffusion of the shale gas along the bedding plane much easier. However, the vertical depth of most shale gas wells in South China is less than 4000 m in consideration of costs. Therefore, the buried depth of potential targets should be lower than 4000 m.

(2) Fractures. Analysis of the tectonic evolution showed that the study area had a lot of thrust faults due to compression in Early and Middle Jurassic and was regionally stretched from Late Cretaceous to Paleogene. Although the properties of most of the thrust faults in the study area did not change, poor sealing in some faults led to the loss of shale gas along the fractures. For this reason, it was necessary to divide the

evaluation units according to the scale of fault development. The north and south sides of the Xiuwu Basin developed fractures, east-west strike, and connected to the surface.

(3) Structural Position. Figure 6 shows that there is a great difference in shale gas content in different structural positions. In the slope next to the surface, the shale gas cannot become enriched because of the large migration to the outcrop. In the gentle part of the structure, supplementary gas of the lower part increased the shale gas content and the amount of lateral migration was much more, both of which facilitated the enrichment of shale gas.

5.2.2. Division Results of Evaluation Units. Figure 10 and Table 2 show the results. The study area was divided into 5 parts. The buried depth of Unit B was lower than 2000 m and near an outcrop that provided easy diffusion. The buried depth of Unit C was deeper than 4000 m. Units D and E were on the south and east sides of the study area where regional fractures developed. Unit A had a moderate buried depth (2000–4000 m) and had fewer fractures that were more favorable than the other four units. In order to select the exploration target more accurately, Unit A was further divided into four secondary evaluation units.

6. Application and Favorable Area Prediction

Seismic line EW303.4 was deployed in the middle of the Xiuwu Basin and passed through Units A, B, C, and D. Seismic interpretation of the line and division results of the evaluation units is shown in Figure 11. The units were assessed based on the accumulation pattern of shale gas in a complex tectonic background: Unit C lies in the low part of the structure. On the one hand, shale gas would migrate to the surrounding rock along the direction vertical to the

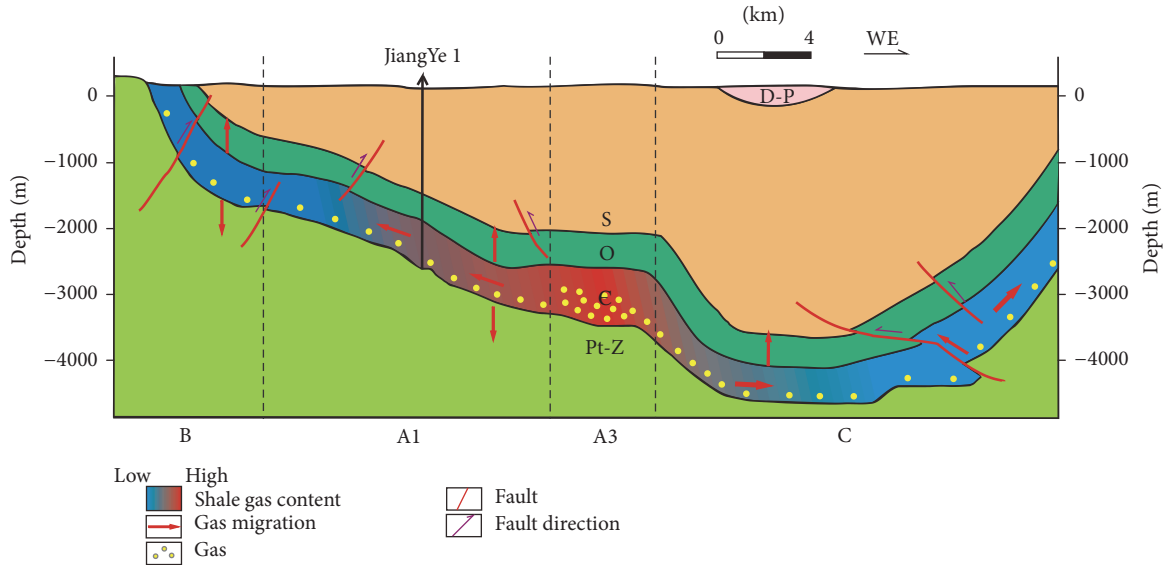


FIGURE 11: Evaluation units and shale gas accumulation diagram of seismic line EW303.4, Xiuwu Basin. See Figure 10 for the seismic line location.

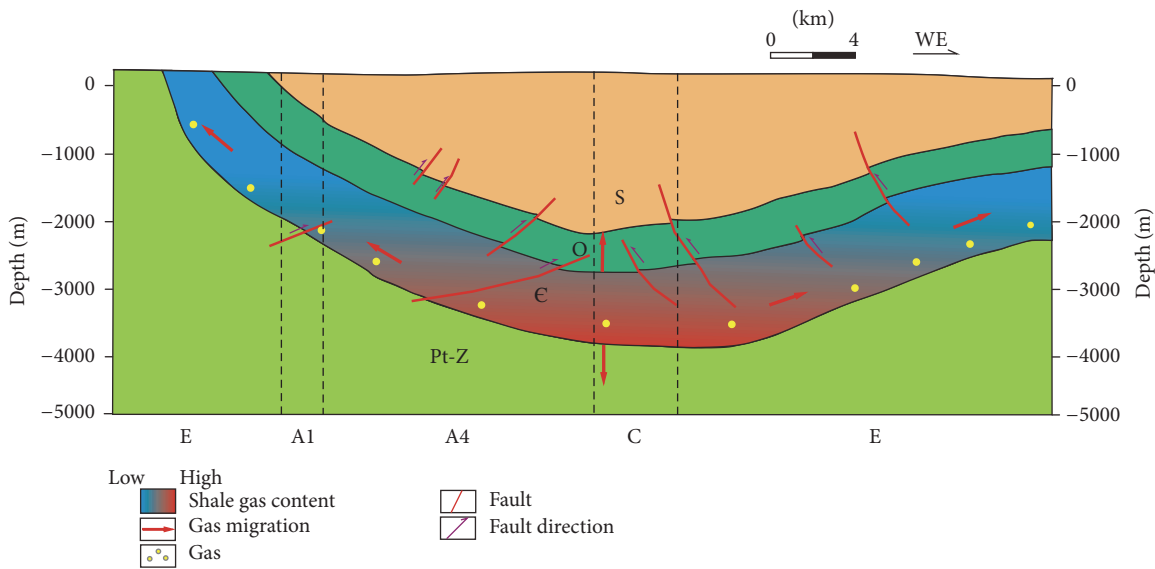


FIGURE 12: Evaluation units and shale gas accumulation diagram of seismic line EW308, Xiuwu Basin. See Figure 10 for the seismic location.

bedding plane. The opening structure would accelerate that process. On the other hand, shale gas would percolate along the bedding plane to both sides of the depression. In this process, a larger amount of shale gas would migrate to Unit A3 because of the steep slope of Unit C. Unit A3 lies in the gentle part. A small part of the shale gas would also migrate to the surrounding rock. In the direction parallel to the bedding plane, a large amount of gas would be supplied by Unit C and a little gas would migrate to Unit A1 due to the steep eastern slope and to the mild western slope that has high residual shale gas content. Units A1 and B occur on the slope of the structure. Shale gas would migrate to the surrounding rock and most of it would migrate to the outcrop

area since the slope is a pathway of shale gas loss. The shale gas content of Well JiangYe 1 of the Lower Cambrian in Unit A1 was $0.848 \text{ m}^3/\text{t}$ on average which confirmed that a slope connected to the outcrop would not be enriched with gas.

Due to the large fracture in the south of the southern study area, most parts of the gas lost when the extension occurred from Late Cretaceous to Paleogene. The shale gas content of Well JiangYe 2 of the Lower Cambrian in Unit A2 was $1.634 \text{ m}^3/\text{t}$ on average, which is still low, although higher than JY1.

Seismic line EW308 deployed in the northern Xiuwu Basin passed through Unit A1, A4, B, and E. Figure 12 shows that Unit A1, A4, and B are slopes that have less gas. The

extension made the fracture of Unit A4 a pathway which is a disadvantage for enrichment of the shale gas. The discussion above illustrated that Unit A3 is the most favorable area of the Xiuwu Basin.

7. Conclusions

Based on the difference between the vertical and lateral permeability and on the immersion test of drilling cores, it was concluded that the shale gas accumulation pattern indicated a complex tectonic background. It was proven in several areas and then applied in order to choose an exploration target of Xiuwu Basin. The conclusions are below.

(1) There is a superior transportation pathway within the shale layers. Gas percolates mainly along the direction parallel to the bedding plane and less in the direction perpendicular to the bedding plane.

(2) When the shale formation was compressed during tectonic movements and without development of faults and unconformity in the lower part of the structure, most of the shale gas percolated to the higher part along the bedding plane, while a small amount diffused and percolated to the surrounding rock. The higher part of the structure is full of shale gas because of the supplementary gas from the lower part of the structure, while a small amount of gas diffused and percolated into the surrounding rock.

(3) When the shale formation was exposed to the surface, shale gas percolated along the direction parallel to the bedding plane into the air, which resulted in low gas content. In the case of fracture development, if there was a reverse fault with good sealing, shale gas would be enriched in the footwall. However, if there was a tensioned normal fault with poor sealing, the fault would be a pathway for shale gas migration.

(4) According to buried depth, fractures, and structural position, the Xiuwu Basin was divided into 5 evaluation units; then Unit A was further divided into four secondary evaluation units. Unit A3 lies in the slope, had fewer fractures, and was a shale gas enrichment area because of the supplementary gas from Unit C on the steep slope and from Unit A1 on the gentle slope. Therefore, Unit A3 was the most favorable area for exploration of Xiuwu Basin.

Conflicts of Interest

The authors declare that they have no conflicts of interest.

Acknowledgments

This research was supported by the National Science and Technology Major Project (2017ZX05035-002), the Science Foundation of the Ministry of Land and Resources of China (no. 12120114046701), and the National Natural Science Foundation of China (no. 41472112).

References

- [1] D. Warlick, "Gas shale and CBM development in North America," *Oil & Gas Financial Journal*, vol. 3, no. 11, pp. 1–5, 2006.
- [2] C. Zou, D. Dong, S. Wang et al., "Geological characteristics and resource potential of shale gas in China," *Petroleum Exploration and Development*, vol. 37, no. 6, pp. 641–653, 2010.
- [3] W. Zhao, J. Li, T. Yang, S. Wang, and J. Huang, "Geological difference and its significance of marine shale gases in South China," *Petroleum Exploration and Development*, vol. 43, no. 4, Article ID 499510, pp. 499–510, 2016.
- [4] D. M. Jarvie, R. J. Hill, T. E. Ruble, and R. M. Pollastro, "Unconventional shale-gas systems: the Mississippian Barnett Shale of north-central Texas as one model for thermogenic shale-gas assessment," *AAPG Bulletin*, vol. 91, no. 4, pp. 475–499, 2007.
- [5] R. M. Pollastro, "Geologic framework of the Mississippian Barnett Shale, Barnett-Paleozoic total petroleum system, Bend arch-Fort Worth Basin, Texas," *AAPG Bulletin*, vol. 91, no. 4, pp. 405–436, 2007.
- [6] T. J. Kinley, L. W. Cook, J. A. Breyer, D. M. Jarvie, and A. B. Busbey, "Hydrocarbon potential of the Barnett Shale (Mississippian), Delaware Basin, west Texas and southeastern New Mexico," *AAPG Bulletin*, vol. 92, no. 8, pp. 967–991, 2008.
- [7] J. Zhang, H. Nie, B. Xu, S. Jiang, P. Zhang, and Z. Wang, "Geological condition of shale gas accumulation in Sichuan Basin," *Natural Gas Industry*, vol. 28, no. 2, pp. 151–156, 2008.
- [8] H. Nie, S. Bao, B. Gao et al., "A study of shale gas preservation conditions for the Lower Paleozoic in Sichuan Basin and its recently," *Earth Science Frontiers*, vol. 19, no. 3, pp. 280–294, 2012.
- [9] J. B. Curtis, "Fractured shale-gas systems," *AAPG Bulletin*, vol. 86, no. 11, pp. 1921–1938, 2002.
- [10] R. G. Loucks and S. C. Ruppel, "Mississippian Barnett Shale: Lithofacies and depositional setting of a deep-water shale-gas succession in the Fort Worth Basin, Texas," *AAPG Bulletin*, vol. 91, no. 4, pp. 579–601, 2007.
- [11] H. Nie and J. Zhang, "Shale gas reservoir distribution geological law, characteristics and suggestions," *Journal of Central South University (Science and Technology Edition)*, vol. 42, no. 2, pp. 1–9, 2010.
- [12] S. Wang, L. Wang, J. Huang, X. Li, and D. Li, "Accumulation conditions of shale gas reservoirs in Silurian of the upper Yangtze region," *Natural Gas Industry*, vol. 29, no. 5, pp. 45–50, 2009.
- [13] X. Guo, "Rules of twofactor enrichment for marine shale gas in Southern China, understanding from the Longmaxi Formation shale gas in Sichuan Basin and its surrounding area," *Acta Geologica Sinica*, vol. 88, no. 7, pp. 1209–1218, 2014.
- [14] G. Wang, Y. Ju, and K. Han, "Early Paleozoic shale properties and gas potential evaluation in Xiuwu Basin, western Lower Yangtze Platform," *Journal of Natural Gas Science and Engineering*, vol. 22, pp. 489–497, 2015.
- [15] H. Nie, Z. Jin, R. Bian, and W. Du, "The "source-cap hydrocarbon-controlling" enrichment of shale gas in Upper Ordovician Wufeng Formation-Lower Silurian Longmaxi Formation of Sichuan Basin and its periphery," *Shiyou Xuebao/Acta Petrolei Sinica*, vol. 37, no. 5, pp. 557–571, 2016.
- [16] W. Liu, J. Tian, X. Lin, J. Shi, C. Yang, and S. Peng, "Characteristics and significance of mineral compositions in Lower Cambrian black shale from Xiuwu Basin, Jiangxi, China," *Journal of Chengdu University of Technology (Science & Technology Edition)*, vol. 42, no. 1, pp. 90–97, 2015.
- [17] W. Qin, Q. Han, and J. Wang, "Shale gas reservoiring condition analysis in Xiuwu Basin," *Energy Research and Management*, vol. 3, no. 1, pp. 46–49, 2013.

- [18] G. He, "Geological characteristics of Lower Cambrian Shale in Xiuwu Basin," in *Proceedings of the Annual Meeting of Chinese Geoscience Union*, Beijing, China, October 19–23, 2014.
- [19] K. Xiao, H. Chen, Y. Wo, Y. Zhou, and Y. Zhang, "Impact of tectonic evolution on Paleozoic and Mesozoic petroleum systems in Jiangnan plain," *Oil and Gas Geology*, vol. 26, no. 5, pp. 688–693, 2005.
- [20] F. Guo, J. Kang, J. Sun, J. Lu, and X. Wang, "Tectonic evolution and hydrocarbon accumulation model for marine strata in Jiangnan Basin," *Lithologic reservoirs*, vol. 22, no. 1, pp. 23–29, 2010.
- [21] J. Yang, F. Yi, and L. Hou, "Genesis and petrogeochemistry characteristics of Lower Cambrian black shale series in northern Guizhou," *Acta Mineralogica Sinica*, vol. 24, no. 3, pp. 286–291, 2004.
- [22] Z. Feng, Y. Peng, Z. Jin et al., "Lithofacies paleogeography of the Cambrian in South China," *Journal of Paleogeography*, vol. 3, no. 1, pp. 1–14, 2001.
- [23] X. Qi, Q. Hu, X. Yi, and S. Zhang, "Shale gas exploration prospect of Lower Cambrian Wangyinpu formation in Xiuwu Basin," *China Mining Magazine*, vol. 24, no. 10, pp. 102–107, 2015.
- [24] Y. Wo, Y. Zhou, and K. Xiao, "The burial history and models for hydrocarbon generation and evolution in the marine strata in southern China," *Sedimentary Geology and Tethyan Geology*, vol. 27, no. 3, pp. 94–100, 2007.
- [25] L. Mei, D. Deng, C. Shen, and Z. Liu, "Tectonic dynamics and marine hydrocarbon accumulation of Jiangnan-Xuefeng Uplift," *Geological Science and Technology Information*, vol. 31, no. 5, pp. 85–93, 2012.
- [26] P. Wang, S. Li, X. Liu et al., "Yanshanian fold-thrust tectonics and dynamics in the Middle-Lower Yangtze River area, China," *Acta Petrologica Sinica*, vol. 28, no. 10, pp. 3418–3430, 2012.
- [27] F. Pang, S. Bao, S. Ren, S. Li, C. Tong, and L. Zeng, "Shale gas accumulation conditions and favorable areas of the Lower Cambrian in Xiuwu Basin," *Journal of Northeast Petroleum University*, vol. 38, no. 5, pp. 23–30, 2014.
- [28] X. He, Y. Gao, X. Tang, P. Zhang, and G. He, "Analysis of major factors controlling the accumulation in normal pressure shale gas in the southeast of Chongqing," *Natural Gas Geoscience*, vol. 28, no. 4, pp. 654–664, 2017.
- [29] T. Guo, "Evaluation of highly thermally mature shale-gas reservoirs in complex structural parts of the Sichuan Basin," *Journal of Earth Science*, vol. 24, no. 6, pp. 863–873, 2013.
- [30] T. Guo, "The Fuling Shale Gas Field-A highly productive Silurian gas shale with high thermal maturity and complex evolution history, southeastern Sichuan Basin, China," *Interpretation*, vol. 3, no. 2, pp. SJ25–SJ34, 2015a.
- [31] T. Guo and P. Zeng, "The structural and preservation conditions for shale gas enrichment and high productivity in the Wufeng-Longmaxi Formation, Southeastern Sichuan Basin," *Energy Exploration & Exploitation*, vol. 33, no. 3, pp. 259–276, 2015b.
- [32] Q. Hu, R. P. Ewing, and S. Dultz, "Low pore connectivity in natural rock," *Journal of Contaminant Hydrology*, vol. 133, pp. 76–83, 2012.
- [33] Z. Gao and Q. Hu, "Wettability of Mississippian Barnett Shale samples at different depths: Investigations from directional spontaneous imbibition," *AAPG Bulletin*, vol. 100, no. 1, pp. 101–114, 2016.
- [34] W. Ji, Y. Song, Z. Jiang, X. Wang, Y. Bai, and J. Xing, "Geological controls and estimation algorithms of lacustrine shale gas adsorption capacity: A case study of the Triassic strata in the southeastern Ordos Basin, China," *International Journal of Coal Geology*, vol. 134–135, pp. 61–73, 2014.
- [35] W. Ji, Y. Song, Z. Jiang et al., "Estimation of marine shale methane adsorption capacity based on experimental investigations of Lower Silurian Longmaxi formation in the Upper Yangtze Platform, south China," *Marine and Petroleum Geology*, vol. 68, pp. 94–106, 2015.
- [36] P. Wang, Z. Jiang, L. Chen et al., "Pore structure characterization for the Longmaxi and Niutitang shales in the Upper Yangtze Platform, South China: Evidence from focused ion beam-He ion microscopy, nano-computerized tomography and gas adsorption analysis," *Marine and Petroleum Geology*, vol. 77, pp. 1323–1337, 2016a.
- [37] P. Wang, Z. Jiang, W. Ji et al., "Heterogeneity of intergranular, intraparticle and organic pores in Longmaxi shale in Sichuan Basin, South China: Evidence from SEM digital images and fractal and multifractal geometries," *Marine and Petroleum Geology*, vol. 72, pp. 122–138, 2016b.
- [38] X. Tang, Z. Jiang, Z. Li et al., "The effect of the variation in material composition on the heterogeneous pore structure of high-maturity shale of the Silurian Longmaxi formation in the southeastern Sichuan Basin, China," *Journal of Natural Gas Science and Engineering*, vol. 23, pp. 464–473, 2015.
- [39] X. Tang, Z. Jiang, H. Huang et al., "Lithofacies characteristics and its effect on gas storage of the Silurian Longmaxi marine shale in the southeast Sichuan Basin, China," *Journal of Natural Gas Science and Engineering*, vol. 28, pp. 338–346, 2016.
- [40] X. Tang, Z. Jiang, S. Jiang, L. Cheng, and Y. Zhang, "Characteristics and origin of in-situ gas desorption of the Cambrian Shuijingtuo Formation shale gas reservoir in the Sichuan Basin, China," *Fuel*, vol. 187, pp. 285–295, 2017.
- [41] L. Chen, Z. Jiang, K. Liu et al., "Effect of lithofacies on gas storage capacity of marine and continental shales in the Sichuan Basin, China," *Journal of Natural Gas Science and Engineering*, vol. 36, pp. 773–785, 2016.
- [42] W. Zeng, W. Ding, J. Zhang et al., "Research on the fracture effectiveness of the Lower Cambrian Niutitang Shale in the southeastern Chongqing and northern Guizhou areas," *Earth Science Frontiers*, vol. 23, no. 1, pp. 096–106, 2016.
- [43] H. Bi, Z.-X. Jiang, P. Li et al., "Shale reservoir characteristics and its influence on gas content of Wufeng-Longmaxi Formation in the southeastern Chongqing," *Natural Gas Geoscience*, vol. 25, no. 8, pp. 1275–1283, 2014.
- [44] J. Liu, "Application of oil-based drilling fluid in third-open section of Qinye horizontal well," *Science & Technology Information*, vol. 10, no. 5, pp. 106–107, 2013.
- [45] E. Xu, Z. Li, and Z. Yang, "Thermal and hydrocarbon generation history of Wufeng and Longmaxi shales in Pengshui area, eastern Sichuan Basin: a well PY1 case study," *Petroleum Geology & Experiment*, vol. 37, no. 4, pp. 494–499, 2015.
- [46] J. Li, B. Yu, C. Liu, and M. Sun, "Clay Minerals of Black Shale and Their Effects on Physical Properties of Shale Gas Reservoirs in the Southeast of Chongqing: A Case Study from Lujiao Outcrop Section in Pengshui, Chongqing," *Geoscience*, vol. 26, no. 4, pp. 732–740, 2012.
- [47] J. Li, R. Xie, J. You, and L. Wang, "Reservoir forming condition and exploration prospect of shale-gas in Guizhou qianbei area," *China Mining Magazine*, vol. 21, no. 2, pp. 55–59, 2012.
- [48] J. He, Y. Duan, X. Zhang, B. Wu, and L. Xu, "Hydrocarbon Generation Conditions of the Shale in Niutitang Formation of Lower Cambrian, Southern Chongqing and Northern Guizhou," *Marine Geology Frontiers*, vol. 27, no. 7, pp. 34–40, 2011.

Research Article

Evolution of Friction and Permeability in a Propped Fracture under Shear

Fengshou Zhang,^{1,2} Yi Fang,³ Derek Elsworth,^{3,4} Chaoyi Wang,³ and Xiaofeng Yang⁵

¹Key Laboratory of Geotechnical & Underground Engineering of Ministry of Education, Tongji University, Shanghai 200092, China

²Department of Geotechnical Engineering, Tongji University, Shanghai 200092, China

³Department of Energy and Mineral Engineering, EMS Energy Institute and G3 Center, The Pennsylvania State University, University Park, PA 16802, USA

⁴Department of Geosciences, The Pennsylvania State University, University Park, PA 16802, USA

⁵School of Mechanics and Civil Engineering, China University of Mining and Technology (Beijing), Beijing 10083, China

Correspondence should be addressed to Yi Fang; yi.fang@utexas.edu

Received 15 September 2017; Accepted 9 November 2017; Published 4 December 2017

Academic Editor: Paolo Fulignati

Copyright © 2017 Fengshou Zhang et al. This is an open access article distributed under the Creative Commons Attribution License, which permits unrestricted use, distribution, and reproduction in any medium, provided the original work is properly cited.

We explore the evolution of friction and permeability of a propped fracture under shear. We examine the effects of normal stress, proppant thickness, proppant size, and fracture wall texture on the frictional and transport response of proppant packs confined between planar fracture surfaces. The proppant-absent and proppant-filled fractures show different frictional strength. For fractures with proppants, the frictional response is mainly controlled by the normal stress and proppant thickness. The depth of shearing-concurrent striations on fracture surfaces suggests that the magnitude of proppant embedment is controlled by the applied normal stress. Under high normal stress, the reduced friction implies that shear slip is more likely to occur on propped fractures in deeper reservoirs. The increase in the number of proppant layers, from monolayer to triple layers, significantly increases the friction of the propped fracture due to the interlocking of the particles and jamming. Permeability of the propped fracture is mainly controlled by the magnitude of the normal stress, the proppant thickness, and the proppant grain size. Permeability of the propped fracture decreases during shearing due to proppant particle crushing and related clogging. Proppants are prone to crushing if the shear loading evolves concurrently with the normal loading.

1. Introduction

Hydraulic fracturing has been a major well stimulation technique since the 1940s [1]. The process involves the injection of fracturing fluid into a targeted reservoir layer through a wellbore. The high pressure fluid drives the propagation of hydraulic fractures with proppant particles carried with the penetrating fluid along the fracture and into the reservoir formation [2]. Following the injection phase, the fracturing fluid flows back into the wellbore and the created hydraulic fractures will compact due to the release of fluid pressure. The proppant particles, typically made of sand, treated sand, or man-made ceramic materials, however hold the hydraulic fractures open, allowing the propped fractures to act as highly permeable flow paths for the extraction of hydrocarbons.

Over the past decade, massive hydraulic fracturing has been broadly applied for the extraction of tight gas, shale gas,

and other unconventional resources [3]. This broad application of horizontal drilling and stimulation, with multiple horizontal wells per pad, multiple fracturing stages per well, and multiple clusters per stage, has resulted in the successful recovery of hydrocarbons from ultralow permeability reservoirs. These include the recovery of unconventional resource from shales and tight sandstones [4]. Hydraulic fracturing in unconventional reservoirs can be significantly different from the hydraulic fracturing of conventional reservoirs. This is due to the presence of preexisting natural fractures or weak planes in the formation that may significantly affect the propagation of the fluid driven fractures. Based on various theories of conventional hydraulic fracturing, a bi-wing type fracture is typically assumed to result from the stimulation of a vertical well [5]. However, based upon field production data, as well as microseismic observations, it

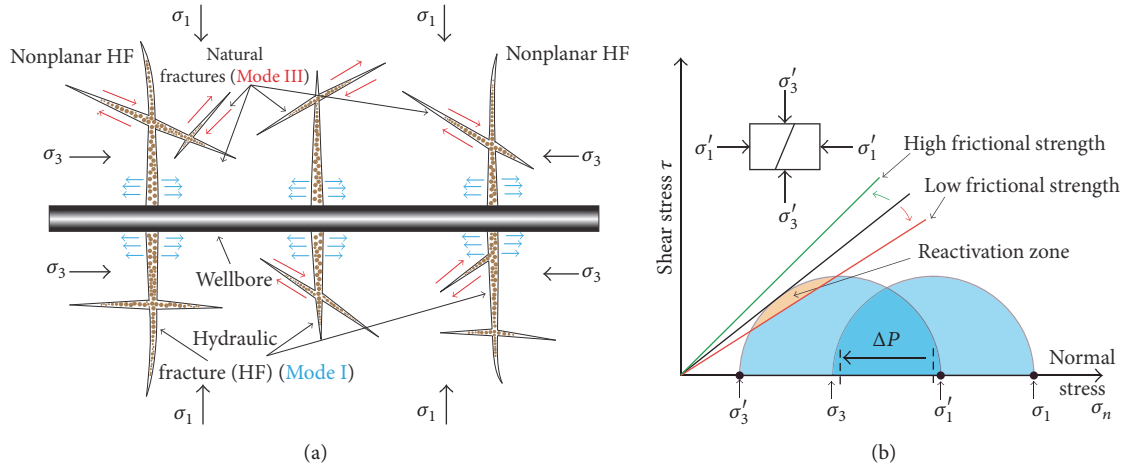


FIGURE 1: (a) Schematic of complex fracturing system filled with proppant after multistage hydraulic fracturing; (b) Mohr-Coulomb criterion for determining whether a preexisting fracture would be sheared after a combined effect of local stress reorientation and frictional alteration.

is believed that so-called “fracture complexity” may result from interactions between the created hydraulic fracture and preexisting natural fractures. This is especially prevalent in unconventional reservoirs where the contrast in permeabilities between matrix and natural fracture is very high [6–8]. When a propagating hydraulic fracture intersects a natural fracture, multiple scenarios for the form of the crossing are possible. These include direct crossing, hydraulic fracturing arrested by the natural fracture, crossing with an offset, or even more complicated scenarios when the third dimension is considered [9–16]. Therefore, fracture branching and the development of complex fracture networks are generally created during multistage hydraulic fracturing (Figure 1(a)) with implications for the state of stress applied on such oblique fractures (Figure 1(b)). Note that the near-wellbore tortuosity [17, 18] is not included in the schematic of Figure 1 but could greatly affect the fracture propagation and cause the increase of injection pressure.

Significant effort has been applied to understand mechanisms involved in creating hydraulic fracture networks in unconventional reservoirs [19]. Seismicity-permeability coupling relationship has been attempted in enhanced geothermal reservoir stimulation [20] and in the caprock for geological sequestration of CO_2 [21, 22]. However, less attention has been given to understanding the role of shear deformation (e.g., induced seismicity by hydroshearing) and permeability evolution of the complex fracture system that may evolve during long-term depletion. Injection-induced seismicity has been associated with both the operation of waste water reinjection [23] and hydraulic fracturing [24]. Nevertheless, whether induced seismicity can occur during long-term depletion of unconventional fractured reservoirs is of significant scientific interest but remains poorly understood. In the usual conceptual model of conventional hydraulic fracturing, the created fracture plane is perpendicular to the minimum stress direction; thus, there is no shear stress on the fracture as it propagates and before the depletion stage of reservoir production. After stimulation, additional shear

stresses induced during the depletion process should also be negligible for simple fracture geometry. Once depletion begins, considering the Mohr-Coulomb failure criterion, the gradual decrease in pore pressure will increase the effective clamping stress on the fracture plane (Biot coefficient < 1) and further stabilize the fracture planes [25]. Therefore, it can be concluded that the expectation of induced seismicity during conventional hydraulic fracturing is trivial.

However, for unconventional reservoirs, induced seismicity may result due to the more complex and oblique fracturing geometry. First, the hydraulic fracture planes are not necessarily aligned with the maximum horizontal stress, due to the presence of preexisting natural fractures and related fracture complexity. Second, nonuniform depletion due to heterogeneous permeability fields can cause stress reorientation and additional shear stress on the fracture planes due to poroelastic effects [26, 27]. Third, some field operations, such as the failure of diversion during refracturing and undesired well connection when fracturing a new well (i.e., cross-well communication or frac-hit), can lead to fluid leakage into the preexisting hydraulic fractures which have been under depletion and result in additional slip on preexisting fractures [28]. Fourth, reinjecting fluid into wells under depletion has been implemented in the field to boost the production under some circumstances, for example, if there is a sharp decline of production, or delineated depleted zone around the producing well [29]. Finally, numerous experimental studies show that the interaction between propagating hydraulic fractures and preexisting natural fractures is significantly influenced by differential stress and fracture orientation and frictional strength [9, 12]. As the frictional strength of propped fractures in the first fracturing phase may be altered, it may significantly influence the behavior of fracture propagation in the later refracturing phase. These circumstances make the potential for induced seismicity finite for unconventional resource recovery. Induced seismicity is governed by frictional behavior of the fracture surface contact [21]. Moreover, for both conventional and unconventional

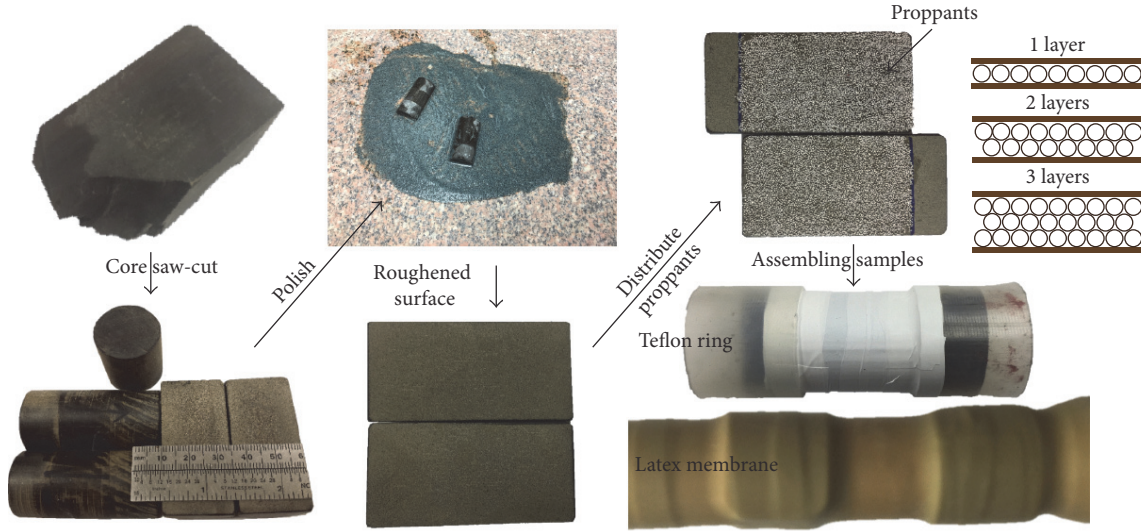


FIGURE 2: Procedures of sample preparation.

hydraulic fracturing, the main purpose is to create propped fractures and to increase the permeability of the formation. Thus, the evolution of permeability of the propped fractures is the key parameter that ultimately affects well production. In the course of production, the permeability of propped hydraulic fractures is expected to decrease due to the impacts of proppant embedment and crushing, concomitant with the gradual increase in the effective clamping stress (Zhang et al., 2015). Previous experimental studies only explored the shear behavior of joints filled with sandy granular materials [30, 31]. However, detailed coupling mechanisms involved in shearing and permeability evolution for propped fractures remain unclear. In this study, we explore the primary and secondary frictional and fluid transport response of propped fractures as the fundamental controlling parameters involved in the reactivation of preexisting fractures (Figure 1(b)). This experimental and analytical work reveals the coevolution of permeability with friction of a propped fracture under shear.

2. Experimental Methods

We explore the evolution of friction and permeability on propped fractures. We first present the procedure of sample preparation for the experiments. Then, we introduce the experimental setup and testing procedure implemented to explore the evolution of permeability and friction of a propped fracture under shearing. Finally, theories and methods to calculate the evolution of friction and permeability are discussed.

2.1. Sample Preparation. The experiments are completed on Green River shale (GRS) as an appropriate analogue of a shale reservoir. To provide a contrast in rock texture, Westerly granite (WG) was also used as a reference, because it has been extensively studied and is well suited for comparison due to its homogeneous and isotropic structure. The mineralogical compositions and mechanical properties of GRS and WG

TABLE 1: Mineralogical and mechanical properties of GRS and WG.

Mineral group	Green River shale	Westerly granite
Carbonates (%)	51.8	0
Tectosilicates (%)	45.9	5
Phyllosilicates (%)	2.3	95
Reference	[21]	[34]
Mechanical property	Green River shale	Westerly granite
Young's modulus (GPa)	3.2–3.8	76
Poisson ratio	0.345–0.365	0.27
Reference	[35]	[36]

are listed in Table 1. The rock samples were first cored to a length of 2 inches and diameter of 1 inch and then carefully saw-cut into two halves, representing a parallel plate model (Figure 2). The planar surfaces were uniformly polished with abrasive powder (#60 Grit carbide) to provide consistent surface roughness for all fracture analogues. To prevent the dislocation of proppant particles during the process of sample reassembly, a very thin layer of washable glue was placed on the fracture surfaces to temporarily fix the proppant particles. The proppant particles were uniformly and tightly placed on the surface of the fractures, forming a monolayer. To evaluate the effect of proppant thickness, samples with double and triple layers of proppants were also assembled and tested. The reassembled split samples, with proppants embedded, were packed within a latex membrane with an initial offset of 8 mm to accommodate the shear offset applied during shearing. To reduce the friction between the outer wall of the sample and the membrane, we used Teflon tape to cover the outer wall of the sample, through which the extra friction by the system can be significantly reduced.

In this experiment, we used commercial ceramic proppants. Three typical proppant sizes, that is, 40/80 mesh (180–425 μm), 30/50 mesh (300–600 μm), and 20/40 mesh (420–

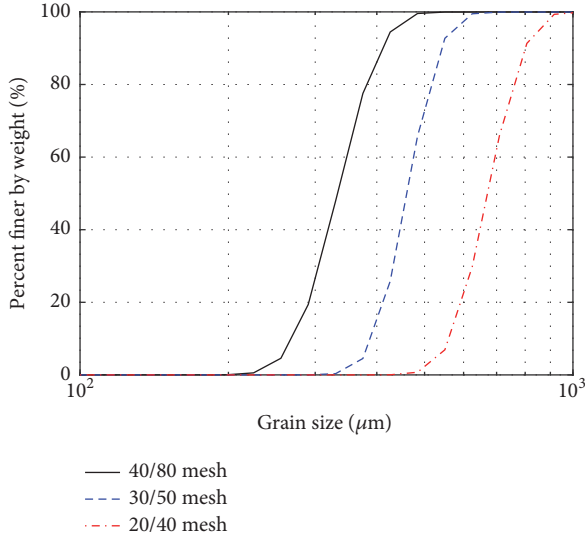


FIGURE 3: Grain size distributions of the three proppant types used in the experiments.

840 μm), were used in the experiments of this study. The proppant size is often referred to as the sieve cut and is typically in the range between 8 and 140 mesh (105 μm ~2.38 mm). The exact distributions of proppant grain size in this experiment are shown in Figure 3. The 40/80 mesh was used as a baseline for the purpose of comparison, while the 30/50 mesh and 20/40 mesh were utilized to study the effect of proppant size.

2.2. Experimental Setup and Testing Procedure. The experiments were performed in a triaxial testing apparatus that is able to independently apply confining pressure, pore pressure, and shear displacement at prescribed (constant) velocity. The evolution of fracture permeability during the experiments can also be concurrently monitored (Figure 4(a)). The packed sample was then assembled in the cylindrical vessel. The confining stress (normal stress in this configuration) was gradually applied until the desired magnitude was reached. With the desired normal stress applied, deionized water was circulated through the fracture with a constant upstream pressure for 5 mins to dissolve and remove the glue that was used to fix the proppant during sample assembly. Once a steady flow rate was attained, monotonic shearing at constant velocity was applied. The shear velocity was controlled at 3 $\mu\text{m/s}$ and the shearing was stopped after a displacement of 6 mm was reached. All experiments were performed at room temperature. The shear displacement was recorded by LVDT installed at the end of the displacing piston. Before and after experiment, samples were characterized by white light optical profilometry to observe the possible interaction (e.g., embedment or striations) between proppant particles and the shale surface due to shearing. White light profilometry was performed using a Zygo NewView 7300 profilometer with a 10x objective lens with data processed with Mx™ software (Figure 4(b)). Furthermore, to examine the shear-induced damage or crushing of proppants, the proppant particles were

scanned and sized both before and after experiment by a laser particle size analyzer.

2.3. Friction and Permeability Calculation. We calculated the coefficient of friction μ as a function of shear displacement using the ratio of measured shear stress to applied normal stress as $\mu = \tau/\sigma_n$ and ignoring cohesion. A parallel plate model for the cubic law is typically employed to describe fluid flow within a fracture [32]; however, as the number of proppant layers inside the fracture increases, the pattern of fluid flow experiences a transition from parallel plate flow to porous medium flow (Slichter, 1899; Kozeny, 1927; Carman, 1937; Li, 2017) (Figure 5). In the direct-shear experiment, the proppant particles may be dislocated, deform, and even break in shearing. Nevertheless, we define an equivalent hydraulic permeability k_f based on Darcy's law as follows:

$$k_f = \frac{Q(t) \mu_{\text{vis}} L(t)}{W b_e}, \quad (1)$$

where μ_{vis} (Pa·s) is the viscosity of fluid; $L(t)$ (m) is the contact length of the fracture surface; W (m) is the fracture width; $Q(t)$ (m^3/s) is the measured flow rate; and ΔP_f (Pa) is the differential pressure between the upstream and downstream extent of the fracture.

The permeability of a porous medium can be estimated based on the Kozeny-Carman equation [33] as follows:

$$k = \frac{1}{180} \frac{\epsilon^3}{(1 - \epsilon)^2} d_p^2. \quad (2)$$

The permeability is then related to the porosity of the packed bed ϵ and the particle diameter d_p .

3. Experimental Results

In this section, the results are presented to highlight key experimental observations related to the effects of normal stress, proppant thickness, proppant size, and rock texture on the friction-permeability relationships of propped fractures.

3.1. Effect of Normal Stress. Figures 6(a)–6(c) show the evolution of permeability, normalized permeability, and friction for the propped fracture during shearing under different normal stress, that is, 1 MPa, 3 MPa, and 5 MPa, respectively. A monolayer of proppant is present in all three cases with a corresponding proppant size in the range 0.18 mm to 0.425 mm (40/80 mesh). The total shear displacement is 5 mm. As expected, the initial permeability before shearing decreases with an increase in normal stress due to the combined influence of reduced porosity and fracture closure (Figure 6(a)). Permeability gradually declines during the shearing for all three cases. The normalized permeability indicates that the reduction in permeability is most profound for the case with the highest normal stress. At the end of loading, the permeability for the three cases decreases to be ~70%, 40%, and 20% of the initial values. A plausible mechanism for explaining this phenomenon is that the proppants crush the most during shearing for the case with

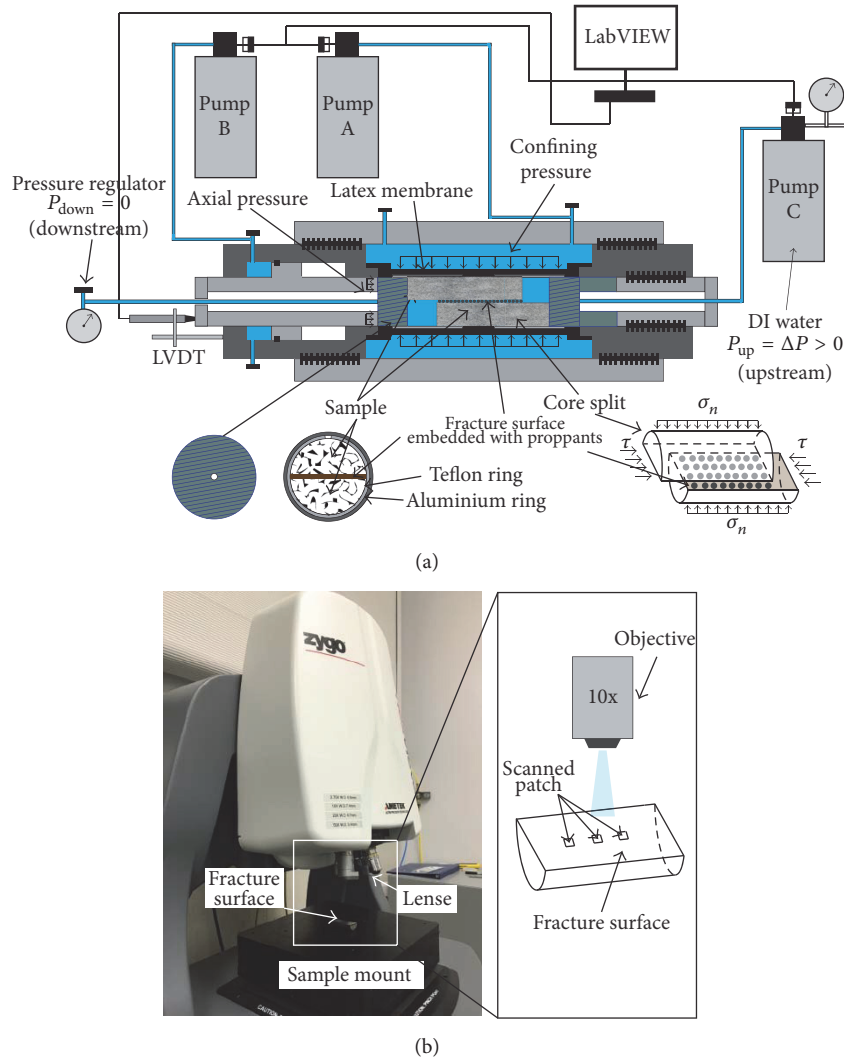


FIGURE 4: (a) Schematic of experimental arrangement for the measurement of evolution of permeability-friction. Pump A controls the confining pressure (normal stress) applied across the fracture. Pump B controls pressure that provides the source of shear stress applied to the fracture. Pump C injects the fluid at a prescribed flow rate or pressure, allowing the fluid source located at the origin of the fracture to flow along the fractures. (b) 3D optical surface profiler for characterizing statistical roughness of the fracture surface. The fracture surface is located ready for white light interferometric scanning.

the highest normal stress, which causes the largest relative decrease in apparent fracture aperture. Particle crushing is apparent from the grain size distributions collected before and after shearing shown in Figure 6(d), where the particle damage increases with normal stress, inferring its influence on permeability evolution. Note that, for the case of 1MPa normal stress, there is nearly no change in the grain size distribution before and after testing (i.e., no crushing of particles during shearing). Thus the grain size distribution of the initial proppant packing is not shown in the plot.

The frictional resistance of the propped fracture in Figure 6(c) also displays dependence on the normal stress. The coefficient of friction decreases as the normal stress increases, which is consistent with friction-normal stress relationships from previous experimental studies on simulated gouge [37, 38]. The reduction in frictional strength may be attributed

to two possible causes. First, at higher normal stresses, the normalized membrane restraint between the sample surface and the membrane is reduced. As the normal stress increases, the coefficient of friction converges to the actual value representing the contact behavior between proppant particles and the fracture surface. Second, higher normal stress will compact the proppant particles and result in the crushing and embedment of proppants, which changes the contact response at the interface between proppant particles and fracture surfaces. Figure 7 explicitly compares the topographies of the fracture surfaces both before and after slip and for different normal stresses. Each experiment is performed with a virgin fracture. A notable feature is that there are an increasing number of postshearing striations on the fracture surface as the normal stress increases. These striations result from the embedment of proppant particles into the fracture

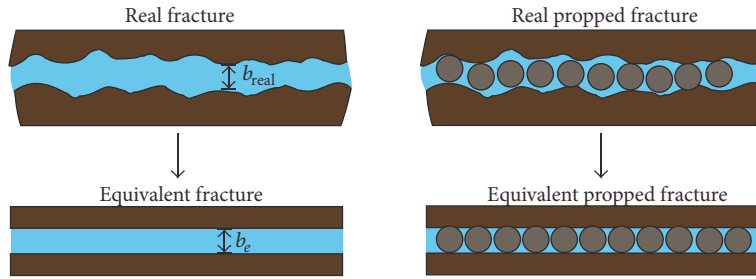


FIGURE 5: Simplified fracture models with parallel plate flow and porous medium flow.

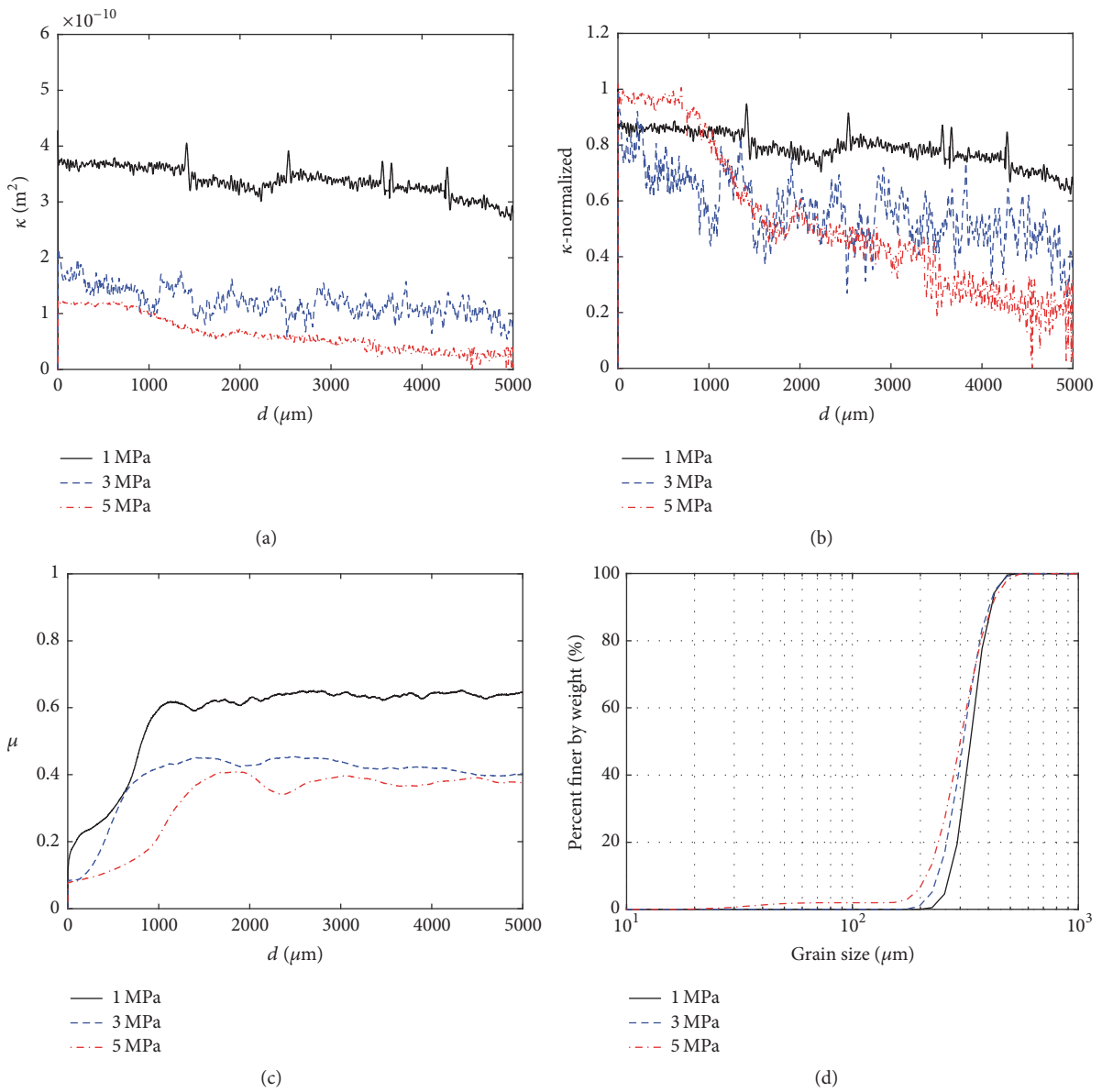


FIGURE 6: Evolution of (a) permeability, (b) normalized permeability (with respect to the initial permeability value), and (c) friction for the propped fracture during shearing under three different normal stresses of 1 MPa, 3 MPa, and 5 MPa with displacement; (d) particle size distributions of proppants after experiments: at 1 MPa, grain size distribution before and after testing does not change much; thus the distribution at 1 MPa is representative of the virgin particle distribution (i.e., 40/80 mesh).

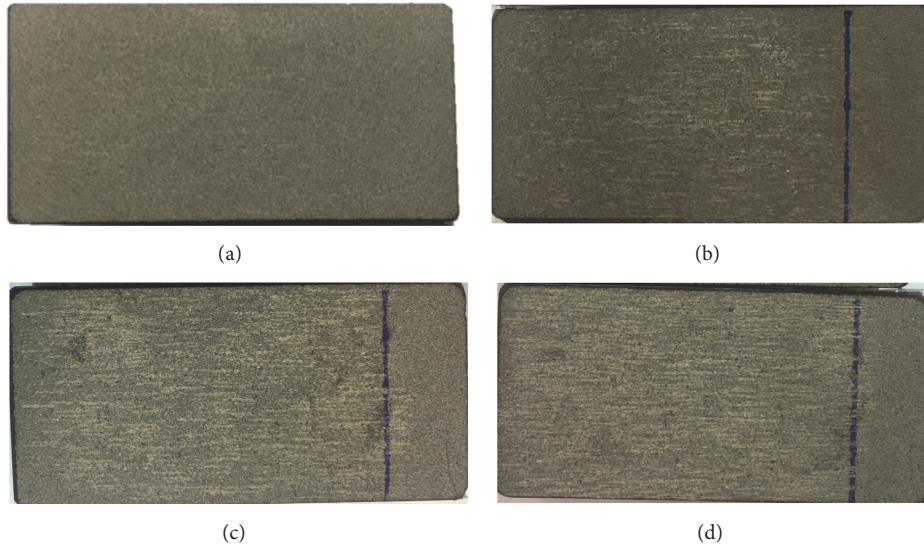


FIGURE 7: (a) Fracture surface before shearing, (b) fracture surface after shearing at a normal stress of 1 MPa, (c) fracture surface after shearing at a normal stress of 3 MPa, and (d) fracture surface after shearing at a normal stress of 5 MPa. The number of striations increases as the normal stress increases.

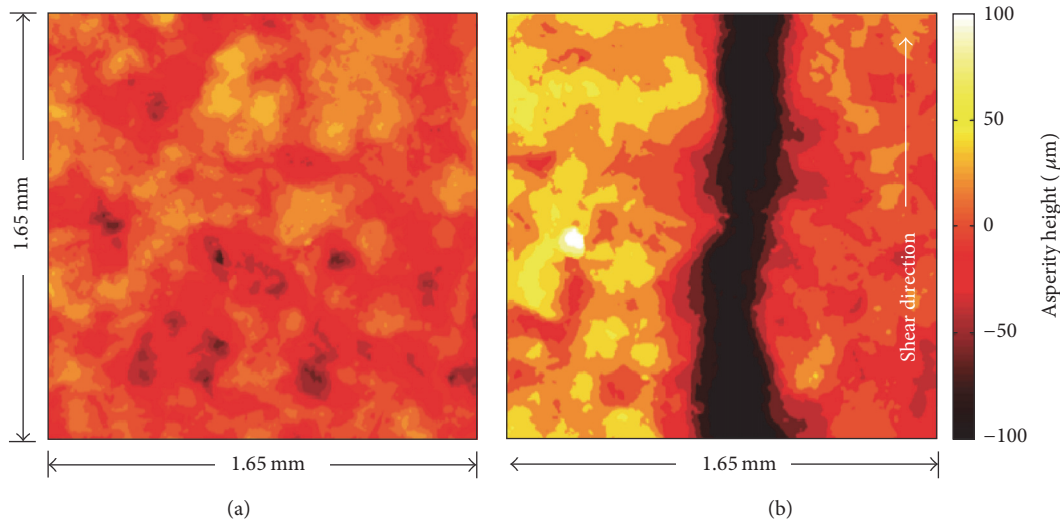


FIGURE 8: White light profilometry of fracture surface (a) before shearing (Figure 7(a)) and (b) after shearing at 5 MPa normal stress (Figure 7(d)). The dark channel represents a striation with a depth of $\sim 100 \mu\text{m}$.

surface with grooving owing to the shear loading. To further characterize the striations, the fracture surfaces were scanned with white light profilometry. Figure 8 compares the profiles of fracture surfaces both before and after shearing for the case of 5 MPa normal stress. The dark channel represents a striation with a depth of about $100 \mu\text{m}$. As the normal stress increases, the frictional behavior then gradually transits from being governed by the sliding of particles along the fracture surface to along the surface of striations. Since the surface of the striation is less rough than the initial fracture surface, the friction may decrease for the highest normal stress as shown in Figure 6(c).

3.2. Effect of Proppant Thickness. Figure 9 presents the evolution of permeability, normalized permeability, and friction during shearing for different proppant thickness as influenced by the number of proppant layers. Four cases are represented, showing the behavior for bare surfaces (i.e., no proppants embedded) and with monolayer and double and triple layers of proppant. The normal stress for all four cases is 3 MPa and the proppant size is 40/80 mesh. For idealized close-packing of monosized particles filled between two parallel plates, the monolayer structure has the largest porosity (0.3954) while the porosity approaches the minimum magnitude (0.2595) as the number of layers

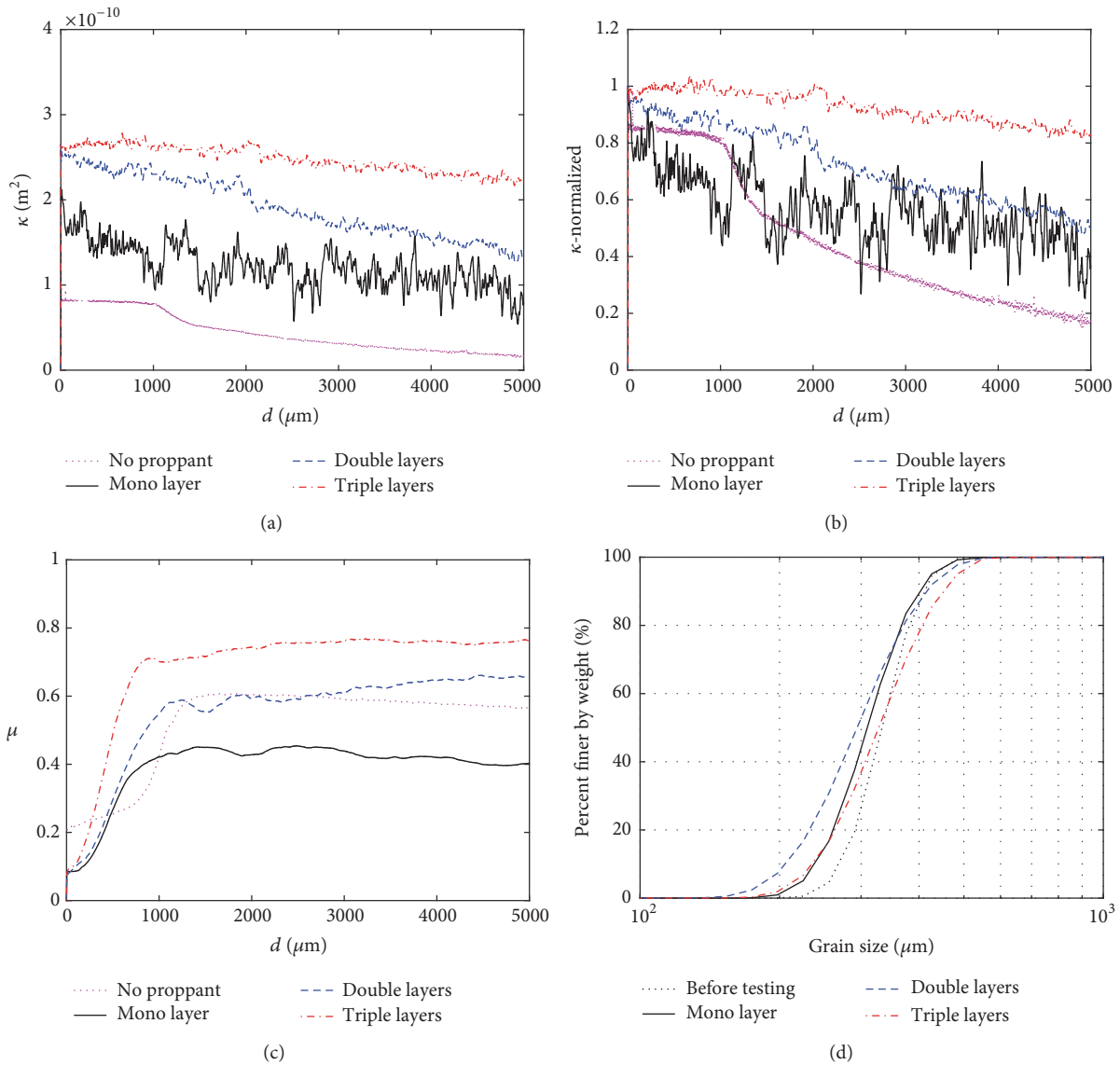


FIGURE 9: Evolution of (a) permeability, (b) normalized permeability (with respect to the initial permeability value), and (c) friction for the propped fracture during shearing under different proppant thickness, no proppant, monolayer, double layers, and triple layers with displacement; (d) grain size distributions of proppants before and after the experiments. The confining stress is 3 MPa and proppant size is 40/80 mesh for all cases.

increases and the aggregate conforms to a face-centered cubic (FCC) structure (Figure 10). From this rationale, and with monodisperse particle sizes, the permeability for a monolayer of proppant is expected to be the largest among all the cases. However, Figure 9(a) shows that the initial permeability of a monolayer of proppant is actually smaller than that for double and triple layers. This may be attributed to the permeability decrease due to proppant embedment where the case with a monolayer of proppant is affected the most. In the case of a monolayer, the fewer displacement degrees of freedom offered where the proppant is sandwiched between rigid faces, rather than compacting to the interior, result in a greater embedment.

Permeability gradually decreases during shearing for all four cases; however the mechanisms of permeability reduction between bare surfaces and proppant embedded surfaces are different. For the bare surfaces, the permeability decreases due to the generated wear products [21], while, for proppant embedded fractures, the permeability is reduced due to proppant crushing, embedment, and clogging during shearing. Furthermore, the normalized permeabilities indicate that the relative decrease in permeability increases as the proppant thickness decreases. The case without proppants has the largest permeability drop (i.e., more than 80%), while the case with triple-layer proppants has less than a 20% decrease in permeability. The grain size distributions of proppants, both

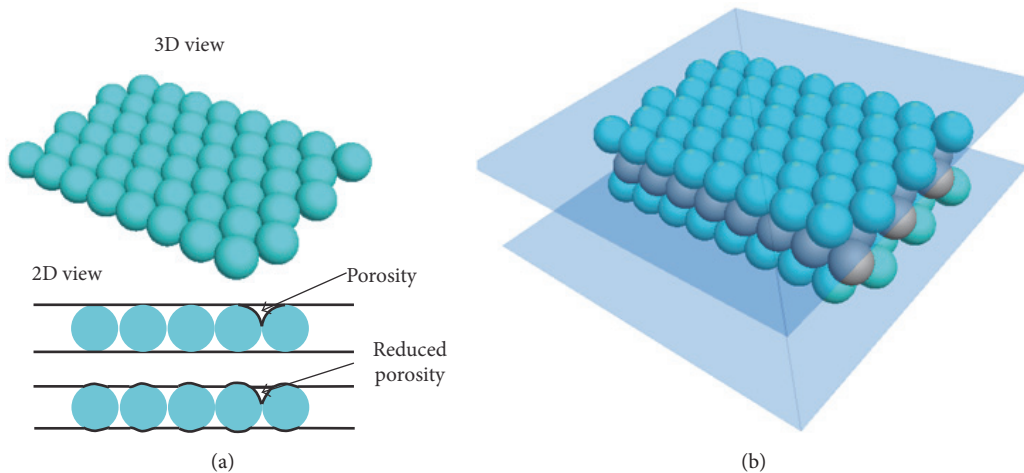


FIGURE 10: Idealized close-packing of monosized particles as (a) a monolayer and (b) multiple layers (FCC structure).

before and after the experiments (Figure 9(d)), indicate that the case with double-layer proppants has the most profound crushing of the proppant. However, the reason why the case with double-layer proppants exhibits the most particle crushing (relative to both single and triple layers) is not yet clear.

The friction of the propped fracture for these three cases with proppants shows a clear trend that more proppant layers result in an increase in frictional strength. This is possibly due to the increase in interlocking forces and jamming between particles when multiple proppant layers are present during shearing. The case without proppant exhibits a frictional strength similar to that of double-layer proppants but larger than the friction value for a monolayer of proppants.

3.3. Effect of Proppant Size. Figure 11 shows the evolution of permeability, normalized permeability, and friction for the propped fracture during shearing for the three different proppant sizes shown in Figure 3. All three cases are for a monolayer of proppant at a normal stress of 3 MPa. As expected, the initial permeability decreases as the proppant size decreases owing to the smaller initial apparent aperture and pore-throat size.

The normalized permeability for the 20/40 mesh proppant remains near constant during shearing, while that for the 30/50 mesh decreases by $\sim 20\%$ and that for the 40/80 mesh proppant decreases by $\sim 50\%$. To explain why the smaller proppant is subject to a larger permeability drop during shearing, Figure 11(d) plots the grain size distributions of the proppants both before and after the experiments for each proppant size. The smallest proppant size (40/80 mesh) shows significant particle crushing; however, particle crushing is not clearly identified with either the 30/50 mesh or 20/40 mesh proppants. While particle crushing could explain the severe permeability drop during shearing for the case with 40/80 mesh, it may not resolve the paradox of permeability drop for the 30/50 mesh proppant. Another possible reason for the permeability drop, besides that of particle crushing, is the potential reorganization of particles during shearing and

the possibility of particle clogging. Although not verified in the experiments, due to limitations of measurement, clogging is highly possible since the initial particle packing is relatively loose.

The friction of the propped fracture for these three cases is nearly identical which suggests that, given the identical normal stress, though the proppant size varies, the contact state between the proppant surface and the fracture surface is equivalent in each case. The results indicate that friction is mainly governed by the stress state as well as the degree of embedment between proppant particles and fracture surface.

3.4. Effect of Rock Texture. To investigate the effect of texture of the fracture surfaces and to eliminate the role of striation-formation on the response, the experiments were repeated with Westerly granite at 3 MPa normal stress and with a monolayer of proppant (40/80 mesh). Figures 12(a)–12(c) show the evolution of permeability, normalized permeability, and friction during shearing for the two different rock textures. The case with granite has a slightly larger initial permeability than that with shale, although both cases show a decrease in permeability during shearing. Granite is stiffer and of higher strength than shale; therefore the proppant embedment is smaller than shale under the same normal stress. This may explain the higher initial permeability for the granite before shearing. The permeability for both granite and shale sandwiching-fractures converges to similar magnitudes at the end of shearing. The normalized permeability indicates that the decrease in permeability for granite is slightly larger than that for shale. This is because there is more particle crushing in the case with granite than with shale, as apparent in the postexperiment reduction in the particle size distribution for granite (Figure 12(d)).

Friction of the propped fracture for granite is also slightly larger than that for shale, which could be attributed to the mineral-particle contact state (i.e., proppant-quartz for WG and proppant-calcite for GRS) and the larger amount of generated small particles as a result of particle crushing.

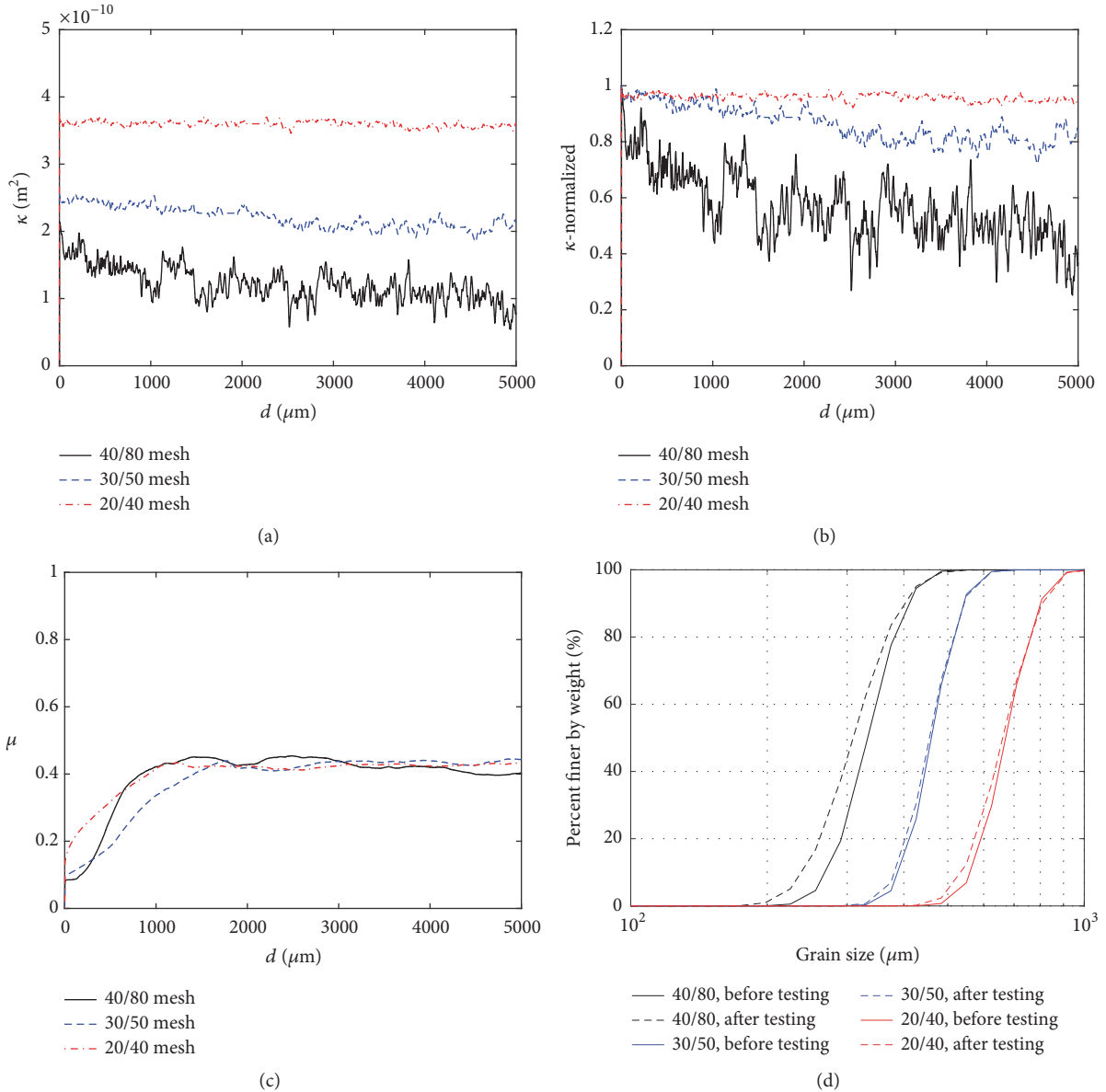


FIGURE 11: Evolution of (a) permeability, (b) normalized permeability (with respect to the initial permeability value), and (c) friction for the propped fracture during shearing for three different proppant sizes, namely, 40/80 mesh, 30/50 mesh, and 20/40 mesh with displacement; (d) particle size distributions of proppants both before and after shearing. The confining stress is 3 MPa for all cases.

4. Discussions

The experimental results show that the main factors controlling the frictional behavior of a propped fracture are the normal stress and proppant thickness. High normal stress results in the crushing of proppant particles, reducing the mean size of the proppant PSD (Figure 6(d)). However, this change in size has only limited impact on the frictional response of the encasing fractures (Figure 11(c)). Under high normal stress, the normalized membrane restraint between the sample surface and the membrane is reduced, implying that at higher normal stress this contributes proportionally less to the frictional resistance and yielding a strength closer to the real strength of the assemblage. This strength is

smaller than at lower stresses, due to the absence of the spurious shear restraint provided by the membrane. High normal stress also generates striations on the fracture surfaces during shearing, which allows a smoother contact between proppant particles and the fracture surface. As a result, the overall friction reduces as the normal stress increases. The proppant thickness also plays an important role in defining the friction of a propped fracture. Interlocking of particles and jamming are not expected between proppant particles for the monolayer proppant configuration. However, given the saw-cut fracture surface geometry, as the number of proppant layers increases from one to three, the interlocking forces between particles largely increase the friction of the propped fracture. The effects of proppant size and rock texture on

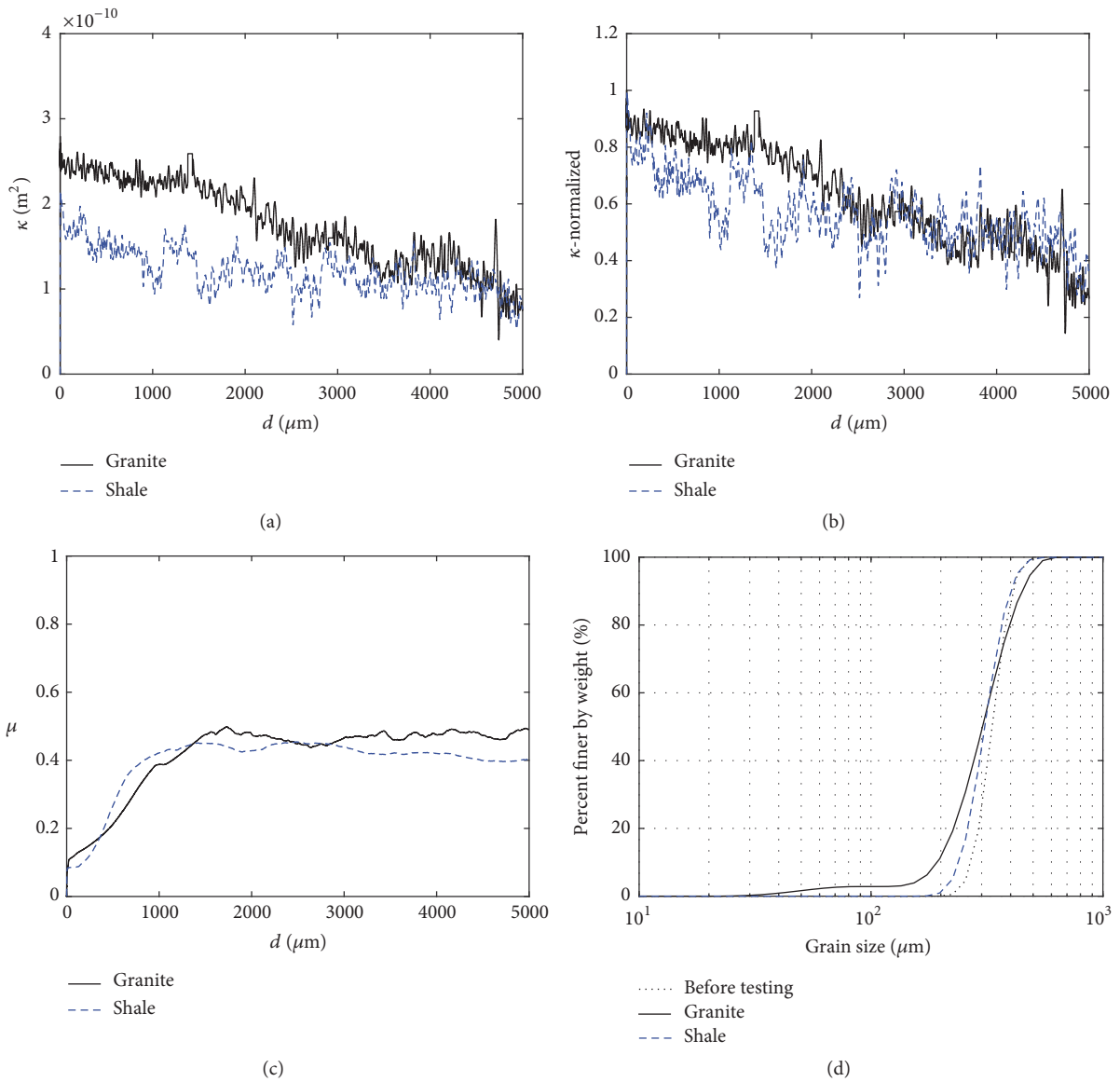


FIGURE 12: Evolution of (a) permeability, (b) normalized permeability (with respect to the initial permeability value), and (c) friction for the propped fracture during shearing for two different sandwiching fracture rock types: shale and granite with displacement; (d) particle size distributions (PSD) of proppants both before and after the experiments. The confining stress is 3 MPa and the proppant size is 40/80 mesh for both cases.

the friction of a propped fracture are secondary. In terms of the response of proppants in fractures, the friction of the fracture without proppant is significantly different from that with proppant (Figure 9(c)). For a single layer propped fracture, the reduced friction implies that, for refracturing in a propped fractured reservoir, the hydraulic fracture may be arrested by a propped fracture. It should be noted that the impact of fracture asperities on the friction of a propped fracture is ignored in this study. This particular fracture analogue comprises two flat surfaces with a uniform but minimal roughness (controlled by the PSD of the grinding powder), while, in reality, the resulting fracture surfaces may have considerably higher amplitude roughness.

The permeability of a propped fracture is mainly governed by the normal stress, the proppant thickness, and the proppant size. The normal stress controls the amount of proppant embedment and thus the dilation of the fracture aperture during shearing. High normal stress not only causes the compaction of the fracture and of the proppant bed, but also leads to the crushing of proppant particles that accelerates the fracture closure. Compared to the multilayered specimen, the monolayer case exhibits the smallest initial permeability due to proppant embedment. Although a larger proppant size favors a higher initial permeability of the propped fracture, the in-fracture transport of large diameter proppants during completion of slickwater fracturing is difficult; the issue of proppant size selection is beyond the scope of this study.

Except for the case with a monolayer of 20/40 mesh proppant, the permeability of the propped fracture decreases during the shearing process for all other cases. The comminution-related decline in permeability during shearing dominates over the effect of shear-induced dilation for a fracture with flat surface geometry. However, it is not excluded that permeability enhancement by shear slip of a fracture with high surface roughness would dominate over the proppant-crushing induced permeability decline. Another unexpected conclusion drawn from this study is that significant proppant crushing occurs during shearing even at a normal stress of 5 MPa. Since proppants are typically designed to withstand normal stresses as high as 50 MPa, they become vulnerable if the shear loading evolves concurrently with the normal loading.

It is also worth mentioning that there are some limitations in the experiments. First, the direct observations of proppant crushing and embedment are not feasible while keeping specimens in an in situ stress state. These results are indirectly reflected by the measurements of particle size and surface characteristics after the experiments. Second, the distribution of proppant after shearing cannot be measured; thus crucial information on proppant clogging is missing. The real time proppant clogging status may only be tested via the imaging techniques such as xCT scanning. Last, the normal stress applied by the apparatus is modulated by the strength of the aluminum ring (shown in Figure 4(a)) used to protect the void left by the offset distance between the two fractures. To prevent radial deformation of aluminum ring, the highest normal stress applied in the experiments is required to be less than 6 MPa. Although the normal stress in the experiments can be interpreted as the effective stress applied on the fracture wall, it is still lower than a typical magnitude in the field.

5. Conclusions

In this study, we explore the evolution of friction and permeability of a propped fracture using shearing-concurrent measurements of permeability during constant velocity shearing experiments. We separately examine the effects of normal stress (1 MPa, 3 MPa, and 5 MPa), proppant thickness (monolayer, double-layer, and triple-layer), proppant size (40/80 mesh, 30/50 mesh, and 20/40 mesh), and rock texture (Green River shale and Westerly granite) on the frictional and transport response of proppant packs confined between planar fracture surfaces. The results indicate that proppant-absent and proppant-filled fractures show different frictional strength, implying that proppants could change the friction of natural fractures and influence the potential for shear failure. For fractures with proppants, we observed the following: (1) the frictional response is mainly controlled by the normal stress and proppant thickness. High normal stress results in the crushing of proppant particles although this change in size has almost no impact on the frictional response of the proppant-fracture system. The observed postshearing striations on fracture surfaces suggest that the magnitude of proppant embedment is controlled by the applied normal stress. Moreover, under high normal stress, the reduced

friction implies that shear slip is more likely to occur for the propped fractures in deeper reservoirs. With this simple specific fracture configuration (i.e., saw-cut surface), the increase in the number of proppant layers, from monolayer to triple layers, significantly increases the friction of the propped fracture due to the interlocking of the particles and jamming, suggesting that high proppant density during emplacement would help stabilize the fractures during injection. (2) Permeability of the propped fracture is mainly controlled by the magnitude of the normal stress, the proppant thickness, and the proppant size. Permeability of the propped fracture decreases during shearing, which is plausibly due to proppant particle crushing and related clogging. Compared to the multilayered specimen, the monolayer case which has fewer displacement degrees of freedom exhibits the smallest initial permeability due to proppant embedment. Proppants become prone to crushing if the shear loading evolves concurrently with the normal loading. The above combined conclusions suggest the use of high-concentration proppants in the field, which not only provides high hydraulic conductivity for hydrocarbon production, but also may help to mitigate the risk of induced seismicity.

Disclosure

Yi Fang is now working at Institute for Geophysics, The University of Texas at Austin, Austin, TX 78712, USA.

Conflicts of Interest

The authors declare that they have no conflicts of interest.

Acknowledgments

The authors acknowledge the support provided by the Young 1000 Talent Program of China, Tongji Civil Engineering Peak Discipline Plan (CEPDP), National Natural Science Foundation of China under Grants 41772286 and 51674267, and US Department of Energy (DOE) under Grant DE-FE0023354. The useful discussions with Professor Chris Marone are also greatly appreciated.

References

- [1] M. Economides and K. Nolte, *Reservoir Stimulation*, Wiley, 3rd edition, 2000.
- [2] E. Detournay, "Mechanics of Hydraulic Fractures," *Annual Review of Fluid Mechanics*, vol. 48, no. 1, pp. 311–339, 2016.
- [3] G. E. King, "Thirty Years of Gas Shale Fracturing: What Have We Learned?" in *Proceedings of the SPE Annual Technical Conference and Exhibition*, Florence, Italy, 2010.
- [4] International Energy Agency (2014) World energy outlook 2014. International Energy Agency.
- [5] T. Perkins and L. Kern, "Widths of Hydraulic Fractures," *Journal of Petroleum Technology*, vol. 13, no. 09, pp. 937–949, 2013.
- [6] N. Warpinski, "Microseismic monitoring: inside and out," *Journal of Petroleum Technology*, vol. 61, no. 11, pp. 80–85, 2009.

- [7] S. C. Maxwell and C. L. Cipolla, "What does microseismicity tell us about hydraulic fracturing?" in *Proceedings of the SPE Annual Technical Conference and Exhibition*, Denver, CO, USA, 2011.
- [8] S. Maxwell, *Microseismic Imaging of Hydraulic Fracturing*, Society of Exploration Geophysicists, 2014.
- [9] T. L. Blanton, "An Experimental Study of Interaction Between Hydraulically Induced and Pre-Existing Fractures," in *Proceedings of the SPE Unconventional Gas Recovery Symposium*, Pittsburgh, Penn, USA, 1982.
- [10] M. J. Thiercelin, J. C. Roegiers, T. J. Boone, and A. R. Ingraffea, "An investigation of the material parameters that govern the behavior of fractures approaching rock interfaces," in *Proceedings of the 6th International Congress of Rock Mechanics*, International Society for Rock Mechanics, 1987.
- [11] N. Warpinski and L. Teufel, "Influence of geologic discontinuities on hydraulic fracture propagation," *Journal of Petroleum Technology*, vol. 39, no. 02, pp. 209–220, 2013.
- [12] C. E. Renshaw and D. D. Pollard, "An experimentally verified criterion for propagation across unbounded frictional interfaces in brittle, linear elastic materials," *International Journal of Rock Mechanics and Mining Sciences & Geomechanics Abstracts*, vol. 32, no. 3, pp. 237–249, 1995.
- [13] X. Zhang, R. G. Jeffrey, and M. Thiercelin, "Deflection and propagation of fluid-driven fractures at frictional bedding interfaces: A numerical investigation," *Journal of Structural Geology*, vol. 29, no. 3, pp. 396–410, 2007.
- [14] F. Zhang, E. Dontsov, and M. Mack, "Fully coupled simulation of a hydraulic fracture interacting with natural fractures with a hybrid discrete-continuum method," *International Journal for Numerical and Analytical Methods in Geomechanics*, vol. 41, no. 13, pp. 1430–1452, 2017.
- [15] A. Dahi-Taleghani and J. E. Olson, "Numerical modeling of multistranded-hydraulic-fracture propagation: accounting for the interaction between induced and natural fractures," *SPE Journal*, vol. 16, no. 3, pp. 575–581, 2011.
- [16] P. Fu, S. M. Johnson, and C. R. Carrigan, "An explicitly coupled hydro-geomechanical model for simulating hydraulic fracturing in arbitrary discrete fracture networks," *International Journal for Numerical and Analytical Methods in Geomechanics*, vol. 37, no. 14, pp. 2278–2300, 2013.
- [17] J. Romero, M. Mack, and J. Elbel, "Theoretical Model and Numerical Investigation of Near-Wellbore Effects in Hydraulic Fracturing," in *Proceedings of the SPE Annual Technical Conference and Exhibition*, Society of Petroleum Engineers, Dallas, TX, USA, 1995.
- [18] B. Lecampion, J. Desroches, X. Weng, J. Burghardt, and J. E. Brown, "Can we engineer better multistage horizontal completions? Evidence of the importance of near-wellbore fracture geometry from theory, lab and field experiments," in *Proceedings of the SPE Hydraulic Fracturing Technology Conference 2015*, pp. 539–557, February 2015.
- [19] X. Weng, "Modeling of complex hydraulic fractures in naturally fractured formation," *Journal of Unconventional Oil and Gas Resources*, vol. 9, pp. 114–135, 2015.
- [20] Y. Fang, D. Elsworth, and T. T. Cladouhos, "Reservoir permeability mapping using microearthquake data," *Geothermics*, vol. 72, pp. 83–100, 2018.
- [21] Y. Fang, D. Elsworth, C. Wang, T. Ishibashi, and J. P. Fitts, "Frictional stability-permeability relationships for fractures in shales," *Journal of Geophysical Research: Solid Earth*, vol. 122, no. 3, pp. 1760–1776, 2017.
- [22] C. Wang, D. Elsworth, and Y. Fang, "Influence of weakening minerals on ensemble strength and slip stability of faults," *Journal of Geophysical Research: Solid Earth*, vol. 122, no. 9, pp. 7090–7110, 2017.
- [23] K. M. Keranen, M. Weingarten, G. A. Abers, B. A. Bekins, and S. Ge, "Sharp increase in central Oklahoma seismicity since 2008 induced by massive wastewater injection," *Science*, vol. 345, no. 6195, pp. 448–451, 2014.
- [24] X. Bao and D. W. Eaton, "Fault activation by hydraulic fracturing in western Canada," *Science*, vol. 354, no. 6318, pp. 1406–1409, 2016.
- [25] M. A. Biot, "General solutions of the equations of elasticity and consolidation for a porous material," *Journal of Applied Mechanics*, vol. 23, pp. 91–96, 1956.
- [26] P. Segall and S. D. Fitzgerald, "A note on induced stress changes in hydrocarbon and geothermal reservoirs," *Tectonophysics*, vol. 289, no. 1-3, pp. 117–128, 1998.
- [27] N. P. Roussel and M. M. Sharma, "Role of stress reorientation in the success of refracture treatments in tight gas sands," *SPE Production and Operations*, vol. 27, no. 4, pp. 346–355, 2012.
- [28] C. Sardinha, C. Petr, J. Lehmann, J. Pyecroft, and S. Merkle, "Determining interwell connectivity and reservoir complexity through fracturing pressure hits and production-interference analysis," *Journal of Canadian Petroleum Technology*, vol. 54, no. 2, pp. 88–91, 2015.
- [29] T. Dohmen, J. Zhang, L. Barker, and J. P. Blangy, "Microseismic magnitudes and b-Values for delineating hydraulic fracturing and depletion," *SPE Journal*, 2017.
- [30] J. P. Pereira, "Rolling friction and shear behaviour of rock discontinuities filled with sand," *International Journal of Rock Mechanics and Mining Sciences & Geomechanics Abstracts*, vol. 34, no. 3-4, article 244-e1, 1997.
- [31] H. Jahanian and M. H. Sadaghiani, "Experimental study on the shear strength of sandy clay infilled regular rough rock joints," *Rock Mechanics and Rock Engineering*, vol. 48, no. 3, pp. 907–922, 2015.
- [32] P. A. Witherspoon, J. S. Y. Wang, K. Iwai, and J. E. Gale, "Validity of cubic law for fluid flow in a deformable rock fracture," *Water Resources Research*, vol. 16, no. 6, pp. 1016–1024, 1980.
- [33] J. Bear, "Dynamics of Fluids in Porous Media," *Soil Science*, vol. 120, no. 2, pp. 162–163, 1975.
- [34] R. M. Stesky, W. F. Brace, D. K. Riley, and P.-Y. F. Robin, "Friction in faulted rock at high temperature and pressure," *Tectonophysics*, vol. 23, no. 1-2, pp. 177–203, 1974.
- [35] L. T. O. Yildirim, *Evaluation of petrophysical properties of gas shale and their change due to interaction with water, [M.S. Thesis]*, The Pennsylvania State University, 2014.
- [36] S. L. Karner and C. Marone, "Frictional restrengthening in simulated fault gouge: Effect of shear load perturbations," *Journal of Geophysical Research: Solid Earth*, vol. 106, no. 9, pp. 19319–19337, 2001.
- [37] K. Mair and C. Marone, "Friction of simulated fault gouge for a wide range of velocities and normal stresses," *Journal of Geophysical Research: Solid Earth*, vol. 104, no. B12, pp. 28899–28914, 1999.
- [38] Y. Fang, S. A. M. den Hartog, D. Elsworth, C. Marone, and T. Cladouhos, "Anomalous distribution of microearthquakes in the Newberry Geothermal Reservoir: Mechanisms and implications," *Geothermics*, vol. 63, pp. 62–73, 2014.

Research Article

Research on Rapid Identification and Evaluation Technology for Gas Formation during Underbalanced Drilling

Hao Wu,^{1,2} Ping Chen,^{1,2} Xiangyu Fan,^{1,2} Hongquan Xia,^{1,2} Junrui Wang,²
Junli Wang,³ and Jian Wu³

¹State Key Laboratory of Oil and Gas Reservoir Geology and Exploitation, Southwest Petroleum University, Chengdu, Sichuan 610500, China

²School of Oil & Natural Gas Engineering, Southwest Petroleum University, Chengdu, Sichuan 610500, China

³Shu'nan Gas-Mine Field, PetroChina Southwest Oil and Gas Field Company, Luzhou, Sichuan 646000, China

Correspondence should be addressed to Ping Chen; chenping@swpu.edu.cn

Received 20 June 2017; Revised 12 October 2017; Accepted 26 October 2017; Published 15 November 2017

Academic Editor: Ming-Yao Wei

Copyright © 2017 Hao Wu et al. This is an open access article distributed under the Creative Commons Attribution License, which permits unrestricted use, distribution, and reproduction in any medium, provided the original work is properly cited.

The underbalanced drilling (UBD) technology has been widely implemented due to its advantages in drilling efficiency improvement and cost reduction. However, this advanced technology requires very special equipment and operational mechanism, which raises multiple challenges to traditional well logging techniques. In this study, a real-time logging system (MWD/LWD and mud logging) was developed and utilized during underbalanced drilling, to quickly identify and evaluate gas formation. This advanced system enables fast detection of gas formation and determining the formation type while drilling, by monitoring the changes in gas production. This real-time logging system provides a powerful technical support to the gas reservoir drilling and development. A case study has clearly shown that the interpretation and evaluation results based on the real-time logging data agree well with the results of conventional well logging. Therefore, this advanced real-time logging technique can be utilized as an effective guidance for field operation.

1. Introduction

Underbalanced drilling (UBD) is a process by which the bottom pressure of the well is maintained below the formation pressure and causes the formation fluid to flow into the wellbore and then to the surface under control [1]. With the increasing complexity of oil and gas reservoirs, the proportion of reservoirs with low porosity, permeability, pressure, and abundance increases annually. It is difficult to achieve expected targets with conventional drilling technology, but the use of UBD technology has been able to multiply production in this type of reservoir. However, there are also certain risks in UBD. When drilling into hydrocarbon reservoirs, especially gas reservoirs, kicks or blowout accidents may be caused if well control is handled poorly [2, 3]. Therefore, timely monitoring and control of the fluid production and appraising the hydrocarbon reservoir while drilling become particularly important.

The real-time evaluation of gas formation during UBD is very critical to gas reservoir exploration and development [4–6]. Currently, the most common approach is to monitor the changes of total hydrocarbon value and gas production in the real-time logging [7]. However, during UBD, formation gas constantly enters into the wellbore, which severely disturbs the background gas value. As a result, the conventional well logging approaches are not able to interpret gas formation accurately [8]. Bao and Chen (2005) discussed the method of identifying and evaluating the gas formation by analyzing the gas bearing condition of drilling cuttings with UBD. Xu et al. (2007) put forward the comprehensive discriminating and evaluating method of recognizing the gas formation by monitoring the drilling time, gas logging values, and the gas flow rate, observing the variation of drilling parameters, the change of the mud ditch surface, and the state of the torch combustion with UBD. This study has analyzed the real-time well logging measurements (MWD/LWD, mud logging) and

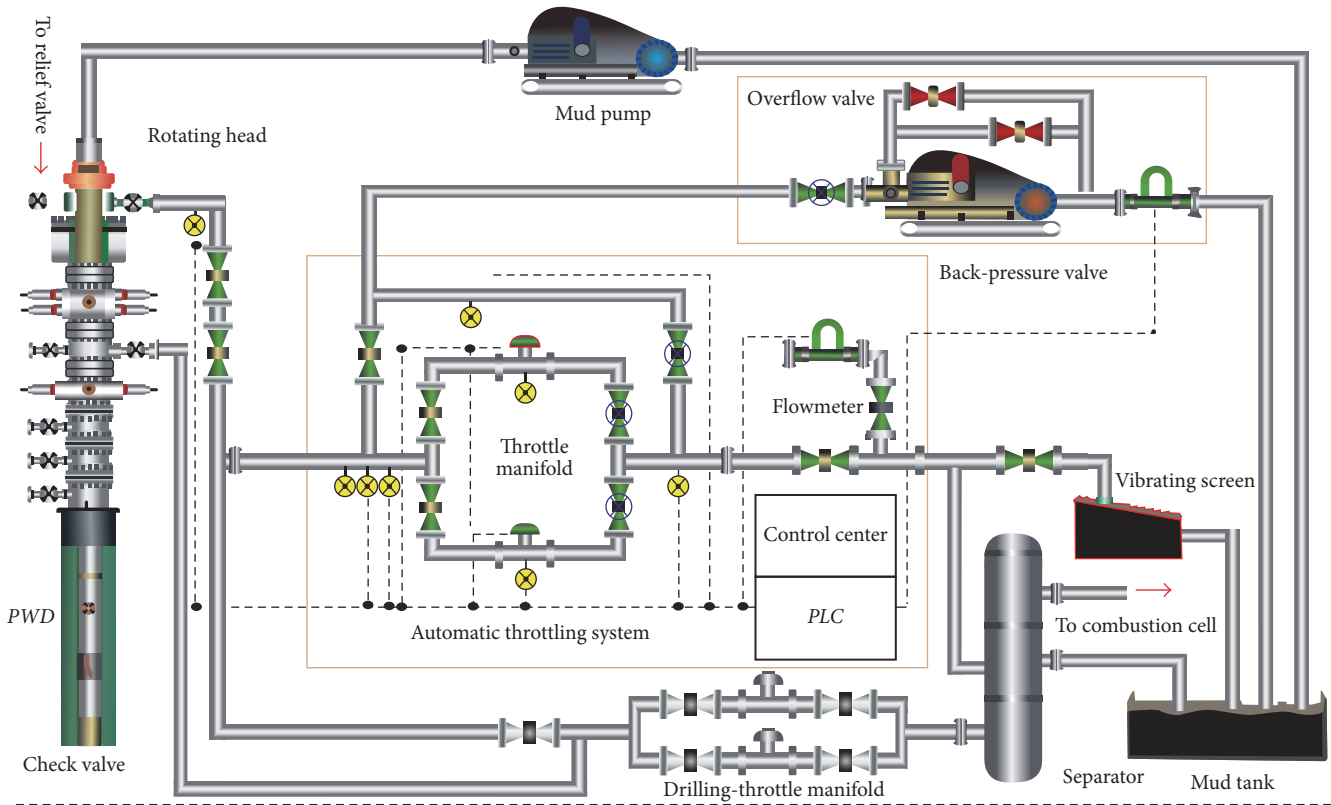


FIGURE 1: Flow chart of underbalanced drilling.

established a novel approach to identify and evaluate gas formation with underbalanced drilling. This new approach has provided significant improvement to the conventional well logging techniques. Meanwhile, it is also critical to a robust drilling program by rapidly evaluating gas formation and effectively guiding the site operation.

2. Measurement While Drilling in Underbalanced Drilling

To evaluate gas formation timely during UBD, a real-time surface monitoring system is necessary to monitor multiple variables during drilling process. In conventional drilling, this task is achieved by well logging system. However, the equipment and operation process of UBD is significantly different from that of conventional drilling (Figures 1 and 2). Thus, the well logging system is unable to monitor multiple parameters in UBD. To address these challenges, multiple instruments have been added to the original equipment, such as drilling mud performance sensor at the outlet, degasser, and gas sample collector [9].

The real-time well logging system is composed of data acquisition, signal processing, data transferring, monitoring, and data evaluation [10, 11] (Figure 3). The data acquisition sensors conduct multiple measurements of the mud system before the mud is injected and after the mud is returned. The preinjection measurements typically include determination of temperature, pressure, volume, and rheological parameters

of the mud. The return mud measurements (mud logging) include the total returned volume, gas flux, and rheological parameters at the outlet. The original analog signals are converted to digital signals using composite A/D signal adapter. Finally, the data signals are transferred to computer terminal wirelessly, and the interpretation results in the form of charts and diagrams can be visualized in real-time manner. This data processing and control system provides to field personnel capability of real-time monitoring and preventing the fluid loose/kick situation during UBD [12, 13].

When logging while drilling, there is a time difference (lag time) between the real data on the bit and the data on the wellhead sampled by log equipment. The lag time depends on the mud circling time and could be impacted by the circling speed and formation temperature. The theoretical lag time is expressed as

$$T = \frac{V}{Q_0} = \frac{\pi(D^2 - d^2)H}{4Q_0}, \quad (1)$$

where T is the lag time, min; Q_0 is mud flow rate, L/min; D is wellbore diameter, m; d is outer diameter of drill string, m; V is borehole annulus volume, m^3 ; H is well depth, m.

The drilling tool assembly uses English unit; for the convenience of field application, taking π value as 3.14 and

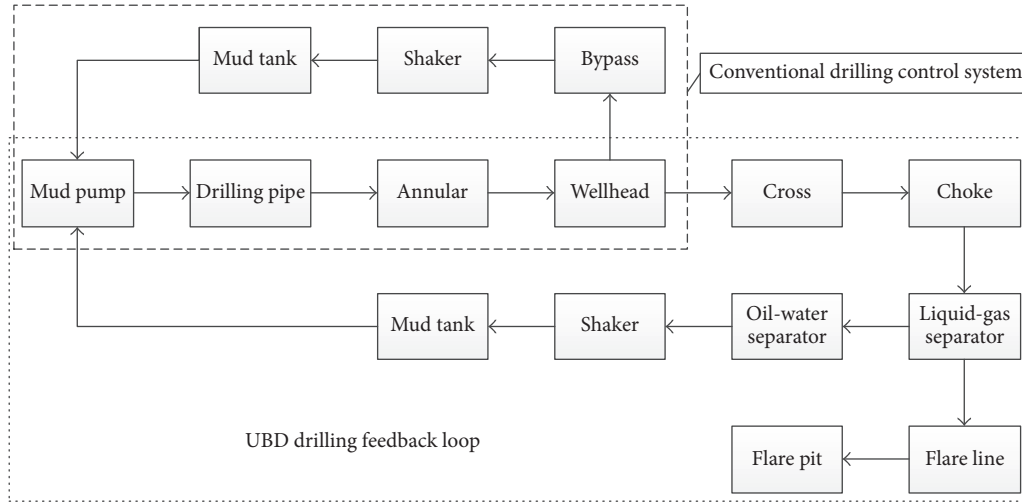


FIGURE 2: Control and feedback loop of underbalanced drilling.

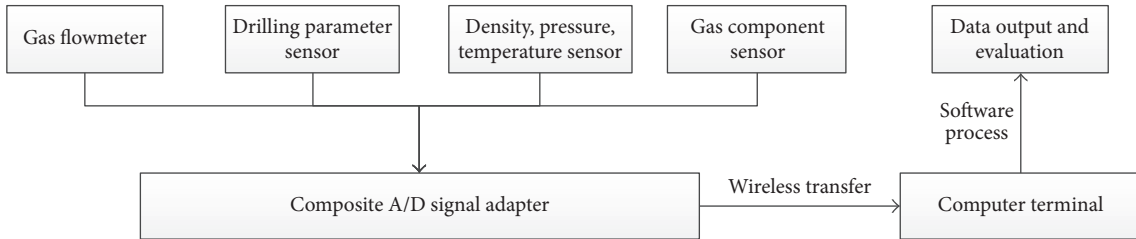


FIGURE 3: Organization chart of monitoring system.

converting from metric to English units, formula (1) can be written as

$$T = \frac{(D^2 - d^2) H}{118.5Q_0}, \quad (2)$$

where T , Q_0 , and H are the same as above, while D is wellbore diameter, inch; d is outer diameter of drill string, inch.

Due to the effect of gas effusion, the actual lag time is typically less than the theoretical value. The time difference can be further modified by humidity correction method [14].

3. Gas Zone Identification and Evaluation While Drilling

3.1. Quick Identification of Gas Zone. During UBD, the wellbore is at lower pressure compared with the formation. Hence, the higher pressure formation gas tends to flow into wellbore during and after drilling. This usually creates a significant noise and causes the measurement inaccuracy. The conventional well logging method is not able to evaluate gas zones accurately in this case. Thus, additional measurements and techniques are needed to quickly recognize gas zones [15, 16].

3.1.1. Monitoring Hydrocarbon Concentration in Return Mud. During UBD, since the hydrocarbon content in the gas

formation is much higher than that in the drilling mud, the hydrocarbon content in mud increases significantly after formation gas enters the wellbore and solubilizes (partially) in the drilling mud. Generally, when the hydrocarbon concentration in the return mud is increased by more than 3%, it indicates a gas zone is drilled.

3.1.2. Monitoring Drilling Time/Rate of Penetration (ROP). During UBD, the formation pressure is higher than the downhole pressure; thus the formation is easier to be drilled. When encountering porous or fracture-intensive formation, the drilling speed increases and the drilling time decreases noticeably. This becomes more obvious during liquid phase UBD; the ROP changes drastically when gas zone is encountered. However, when air drilling is applied in UBD, such change in ROP will not be so obvious. Hence, additional observations need to be made to detect gas zone.

3.1.3. Comprehensive Analysis of Drilling Parameters. When drilling into a new gas zone is determined by increased ROP and higher hydrocarbon content in the return mud, it is good practice to increase wellhead back pressure accordingly to prevent a kick. When exiting out of a gas zone, the wellhead back pressure is lowered again to create underbalance condition in wellbore, and thus ROP is increased. The adjustment of wellhead back pressure inevitably causes the changes in stand pipe pressure, casing pressure, gas flux, and so on.

When formation gas flows into annulus and goes up to wellhead, the stand pipe pressure drops significantly. If a significantly large volume of formation gas flows into the wellbore annulus, choke valves should be turned off. This operation controls the influx volume of formation gas and thus increases stand pipe pressure and casing pressure.

If stand pipe pressure decreases as the casing pressure increases, or both pressures fluctuate evidently, it suggests a gas zone is encountered in drilling. Additionally, since wellhead pressure drops significantly compared with bottom-hole pressure, formation gas expands quickly as it travels up to the wellhead, causing the volume of drilling mud increases. As a result, the density of the return mud drops. By monitoring the changes in the return mud density, the encountering of a gas zone can be determined.

In summary, a number of indicators have been found to be able to determine whether a gas zone is encountered while drilling, such as

- (i) the increase of ROP,
- (ii) the increase of total hydrocarbon content in return mud,
- (iii) the increase of casing pressure coupled with decreasing stand pipe pressure,
- (iv) the significant fluctuation of these pressures,
- (v) the reduced density of return mud,
- (vi) the increase of viscosity of the outlet drilling fluid,
- (vii) the increase of drilling fluid temperature,
- (viii) the decrease of the outlet electrical conductivity,
- (ix) the increase of gas flux volume.

Although some indicators mentioned above are not explicitly discussed in this study, those can provide additional evidence in the identification of the gas formation.

3.2. Detection of Gas Zone Medium. There is quite obvious difference in gas production while drilling the homogeneous gas layer and the fractured gas layer. The formation property of the gas layer could be identified in a real-time manner by interpreting the variation of gas production volume. In addition, the gas production rate from the gas zone drilled can also be estimated roughly. The gas production rates while drilling are expressed as

$$\begin{aligned} \text{Mud drilling: } Q &= \frac{L_1}{\eta L_2} T_g \cdot q \\ \text{Air drilling: } Q &= \frac{((L_1/\eta L_2) T_g)}{(1 - T_g)}, \end{aligned} \quad (3)$$

where Q is the gas production rate while drilling, L/min; q is the inlet volume flux, L/min; T_g is the total hydrocarbon value, %; L_1 is the gas extraction volume of the pump, mL/min; L_2 is the electrical degasser volume, mL/min; η is the electrical degasser efficiency, %.

Under stable operation environment, using the same instruments in the same operation, the pumping capacity

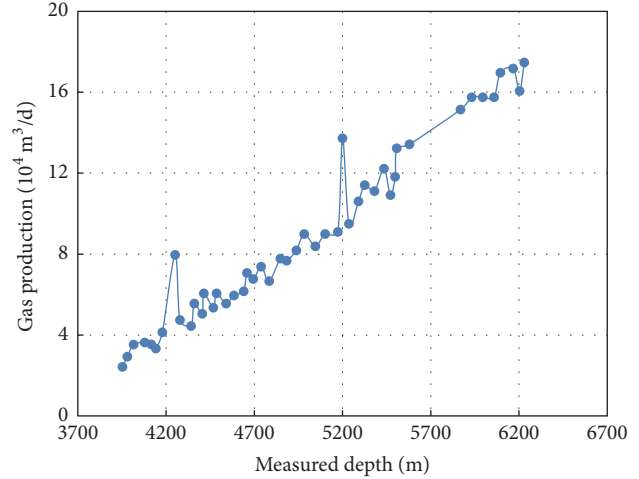


FIGURE 4: Gas production from a homogeneous sandstone while drilling.

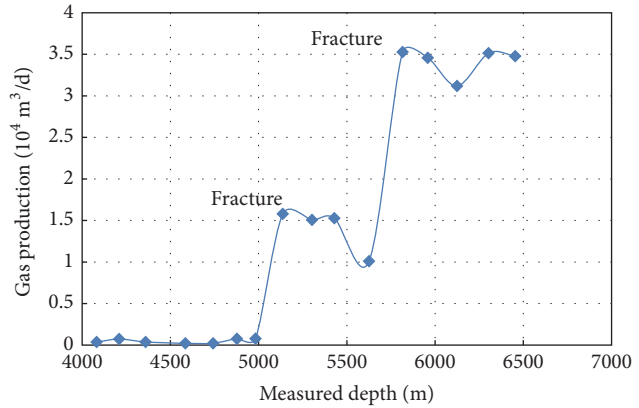


FIGURE 5: Gas production from a fractured reservoir while drilling.

and the electric degassing efficiency of sample pumps remain constant; thus, $L_1/\eta L_2$ is considered as a constant.

We are able to interpret formation type (homogeneous or fractured reservoirs) when gas production rate data is obtained while drilling. As seen in Figure 4, the gas production from a homogeneous sandstone formation changes linearly along the drilling depth. Figure 5 shows that the gas production is at various drilling depths in a fractured reservoir, where the gas production rate exhibits sudden change caused by the large permeability contrast between neighboring strata.

3.3. Evaluation and Interpretation Method of Gas Zone. During UBD, the flow of formation gas into wellbore causes the reduction of the density of drilling mud at outlet. Meanwhile, the release of formation gas from the drilling mud takes away the heat, causing the reduction of outlet temperature of drilling mud. Therefore, changes in the drilling fluid outlet density and temperature can be utilized as an indirect indicator to interpret the encountering of gas production zone. In addition, the responses of porosity logs to a gas

TABLE 1: Evaluation criteria for gas zone.

Effective porosity (%)	Density decrease (%)	Temperature decrease (%)	Result
>8	>15	>10	Gas zone
5–8	8–15	5–10	Poor gas zone
<5	3–8	3–5	Gas-water zone

formation are obvious; thus the drilling fluid outlet density and the temperature can be combined with logging porosity data to generate a better evaluation tool. Through the in-depth study of the characteristic parameters of the gas zone in the Peng Lai area (Shandong, China), based on mathematical statistics, a set of criteria for the evaluation of quality of the gas zone in Peng Lai area is summarized in Table 1.

In field practice, MWD/LWD data is usually used to identify the entrance of a gas zone. Then, this new set of evaluation criteria can be applied to interpret the type of gas zone. Finally, these interpretation results need to be studied, combining with the effective porosity log, to further verify the preliminary evaluation result.

4. Case Study

The PL133 well was designed to have a measured depth of 2769 m, and the main target layer was the Xujiahe Formation (T_3X_2). The low-density drilling fluid and underbalanced drilling technology were deployed in the well section between 1733 m and 2769 m MD. Through the analysis of the hydrocarbon in the adjacent wells, it was expected that the formation encountered in this well drilling would mainly be composed of gas, with some water saturation. According to the core analysis results, the average porosity of the Xujiahe Formation is 6.6% and the average permeability is 0.09 mD. The results have revealed that the formation in Penglai area has the extremely low porosity and low permeability characteristics. Underbalanced drilling technology was utilized in this well in order to detect and protect gas zone in a timely manner.

4.1. Rapid Identification of Gas Zone While Drilling. A comprehensive well logging interpretation result for the interval of PL113, 2520–2620 m MD, is shown in Figure 6. In the section above, 2532 m, the total hydrocarbon concentration stays at about 9.5% and no obvious increase is noticed. Meanwhile, the drilling time-curve shows the average drilling rate is larger than 13 min/m. Thus, the formation above 2532 m MD is considered as a nonreservoir formation. The total hydrocarbon value monitored is from the previously opened reservoir. In the 2532 m–2556 m interval, the total hydrocarbon value increases linearly from 10.04% to 16.22%. Meanwhile, the drilling time decreases from the average of 13 min/m to 7.5 min/m. The change of drilling parameters suggests the presence of a section of homogeneous gas formation. Below 2556 m MD, the total hydrocarbon value appears to drop significantly to 13.11%, while drilling rate gradually rises to about 10 min/m, which suggests an exit

of the gas zone. By applying the same method to the entire section, one can determine that gas bearing sections are present at 2564 m–2569 m, 2581 m–2584 m, 2593 m–2595 m, and 2613–2618 m MD.

As seen from Figure 6, the interpretation results from the traditional logging tools (borehole indication, porosity indication, and resistivity curve) and the newly added indicators (drilling indication, outlet indication, and gas logging indication) stay very consistent along each other. The results from traditional logging tools were obtained from well logging after drilling completion and the results from newly added indicators were obtained from logging while drilling. Therefore, it can be concluded that the real-time logging and monitoring data can be used to identify and evaluate the gas zones fast and accurately.

4.2. Interpretation of the Types of Gas Formation. From the drilling depth of 2532 m to 2556 m MD, the gas production rate increases from 0.59 m³/min to 1.03 m³/min, as seen in Figure 6. The relatively slow and also steady change of gas production rate indicates a homogeneous gas zone was encountered while drilling. At around 2564 m MD, the gas production increases sharply from 0.84 m³/min to 1.54 m³/min, which implies that a fractured gas zone might be drilled. From the gas production chart, the rapid surges at 2581 m–2584 m, 2593 m–2595 m, and 2613 m–2618 m are also indications of fractured gas zones, as shown in Figure 7. The conventional well logging results for PL 113 well reconfirm these assessments in Figure 7. In summary, a reasonably accurate interpretation of formation type of gas zone can be made by analyzing the changes in gas production rate while drilling.

4.3. Evaluation of Reservoir Property of a Gas Zone. The drilling fluid density, temperature, and gas zone's effective porosity of the PL113 well are presented in Figure 8. A significant decrease of density and temperature in the interval 2564–2569 m MD is observed. The percentages of these changes were calculated and showed in Table 2. This formation was initially identified as the gas zone during UBD. Using the proposed evaluation criteria (Table 1), we have interpreted this formation as a poor quality gas zone (Table 1). Similarly, the section 2581–2584 m MD is also classified as a poor quality gas zone. This interpretation agrees with the extremely low porosity and low permeability characteristics in this region. The mud density and temperature for 2613–2618 m MD interval indicate the presence of both gas and water, suggesting the possibility of water invasion in this zone. The conventional well log interpretation in Table 3 matches exactly the interpretation from Table 2, which further validates our interpretation.

Based on the analysis on the adjacent wells of the same formation and their well test results, it was found that the primary pay zone in this formation is gas zone and the pay is continuously distributed in the upper part of Xujiahe Formation (T_3X_2). Through comprehensive analysis in PL113 well, it was discovered that the favorable production zones are mainly located in the upper part of the Xujiahe Formation,

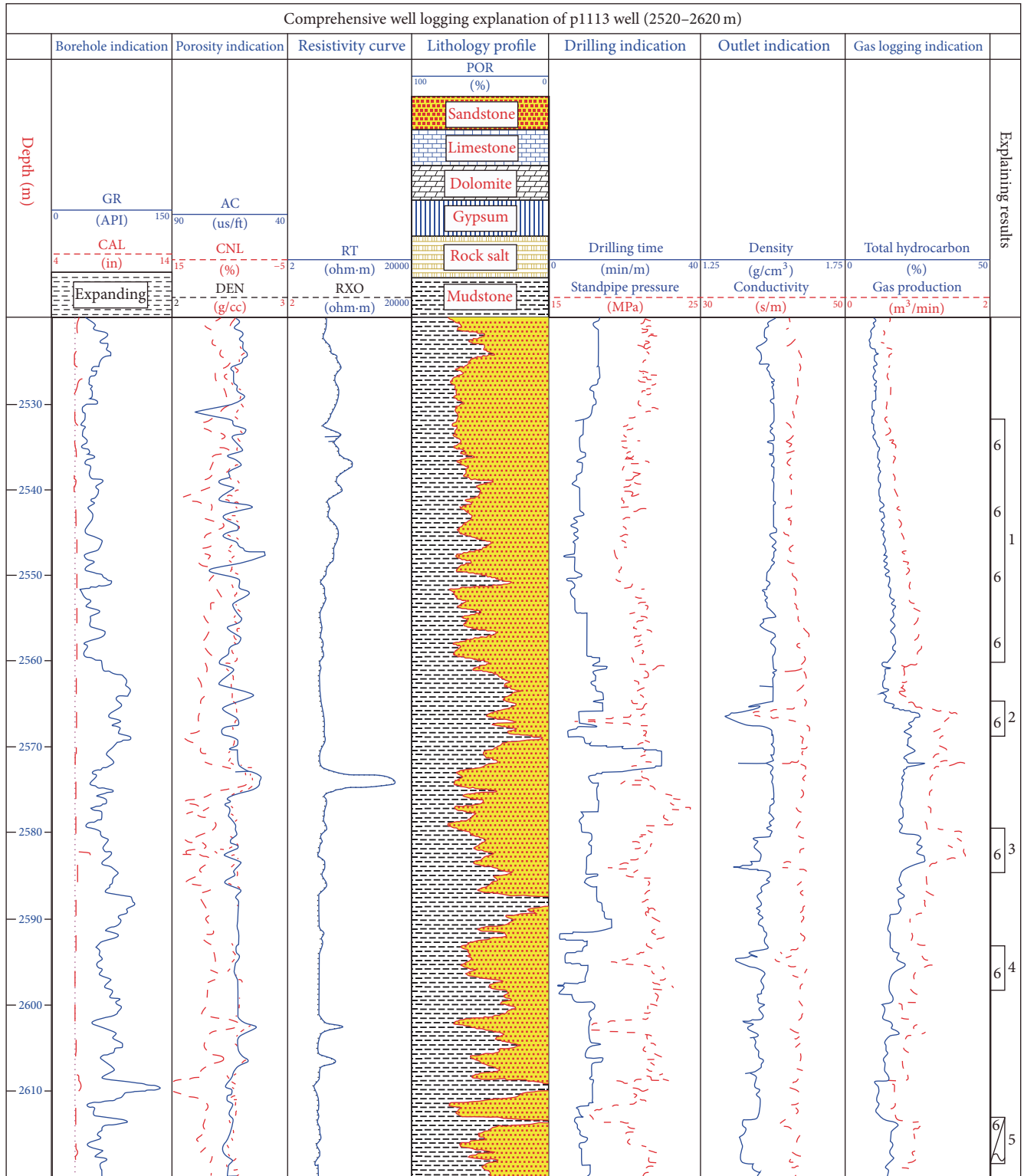


FIGURE 6: Comprehensive well logging of PL113 well (2520–2620 m).

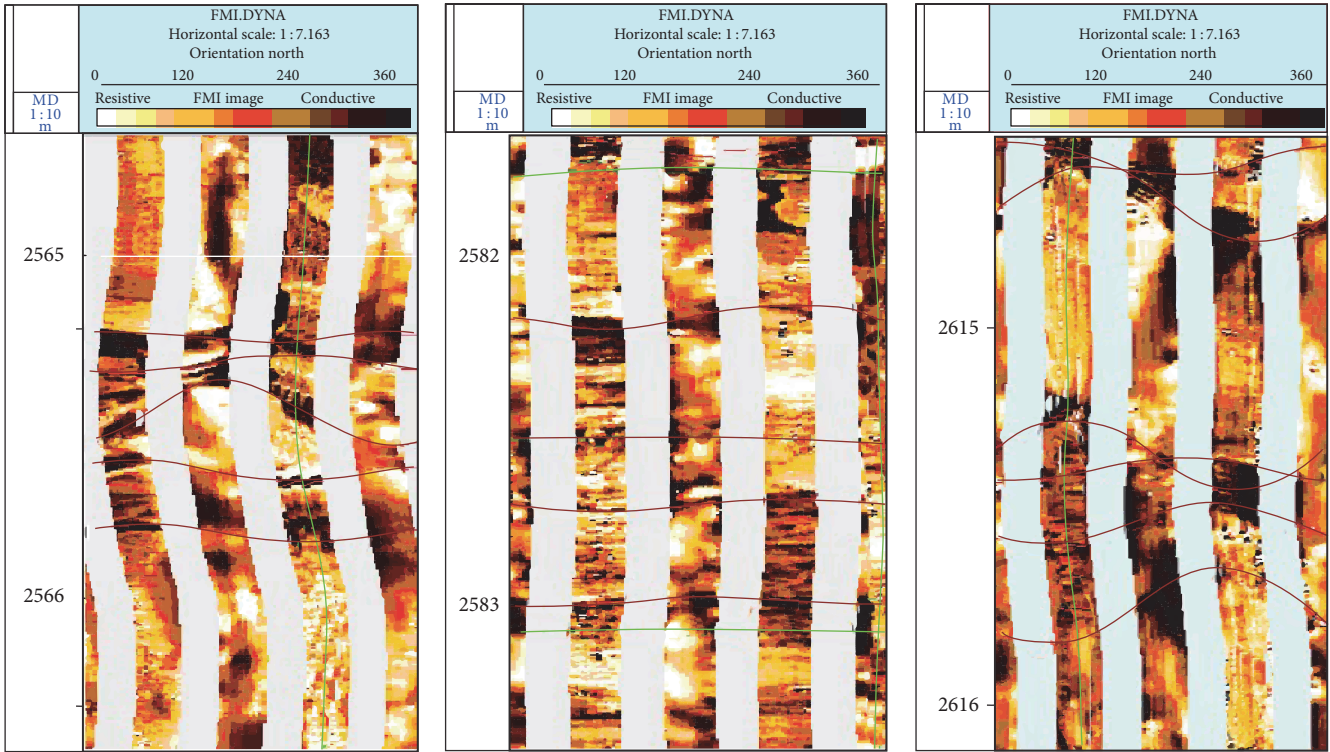


FIGURE 7: Depth imaging log in PL 113 well.

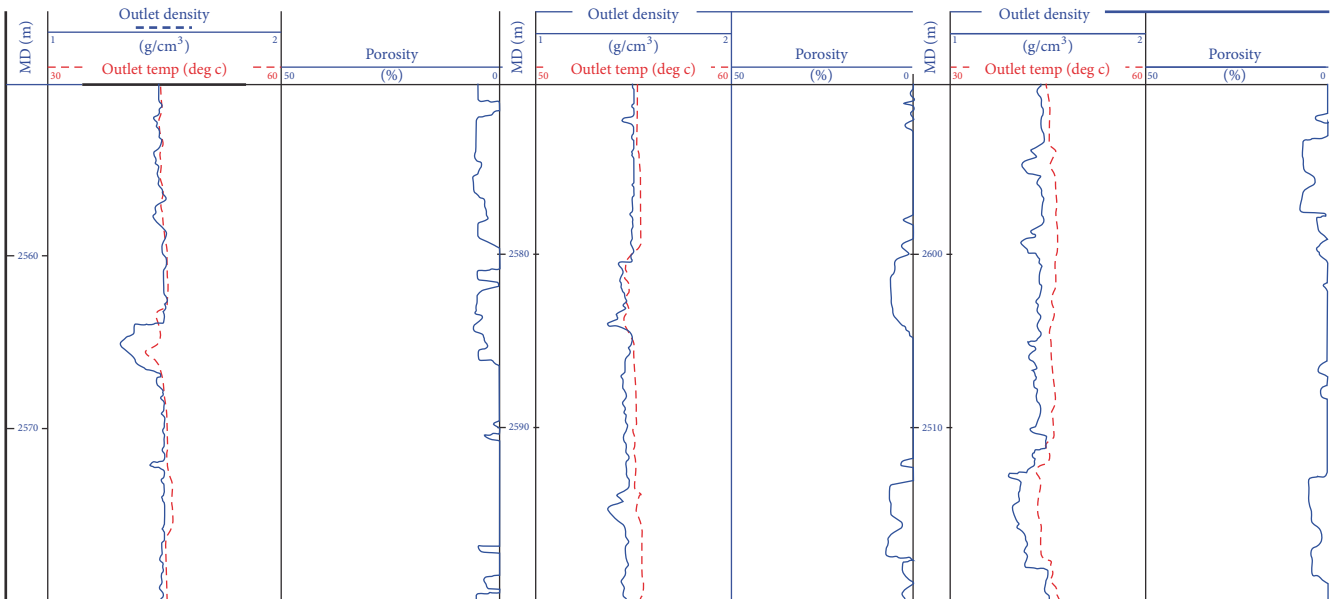


FIGURE 8: Changes in well log curves in gas zones, PL 113.

which should be considered during the later horizontal drilling design as well as reservoir development plan.

5. Conclusions

- (1) By utilizing of real-time logging data (MWD/LWD, mud logging), an accurate and timely identification of

gas zone in underbalance drilling becomes possible. In addition, the formation type and quality of gas zone could be determined using the change of gas production rate data along the depth. This new approach enables us to stay informed of the existence and quality of underground gas layers.

TABLE 2: Real-time logging interpretation results for PL113 well intervals.

MD (m)	Average effective porosity (%)	Outlet drilling fluid density		Outlet drilling fluid temperature		Interpreted result
		Variation (g/cm ³)	Drop (%)	Variation (°C)	Drop (%)	
2564–2569	6.07	1.50 to 1.31	12.67	45.47 to 42.71	6.07	Poor gas zone
2581–2584	6.36	1.49 to 1.37	8.05	46.33 to 43.57	5.96	Poor gas zone
2613–2618	5.18	1.46 to 1.36	6.84	46.05 to 44.51	3.34	Gas-water zone

TABLE 3: Conventional well logs interpretation results for PL113 well intervals.

MD (m)	Natural gamma ray (API)	Sonic log (us/ft)	Neutron log (P.U)	Density log (g/cm ³)	Deep lateral log (ohm-m)	Shallow lateral log (ohm-m)	Water saturation (%)	Interpreted result
2564.3–2568.6	45–114	59.1–67.9	7.6–10.1	2.52–2.66	23–38	23–38	31–49	Poor gas zone
2580.6–2584.5	43–83	59.5–67.5	7.2–13.7	2.37–2.58	18–37	16–35	31–47	Poor gas zone
2612.7–2618.1	44–86	59.0–66.5	9.2–12.8	2.47–2.62	16–22	15–23	59–88	Gas-water zone

- (2) With a deep understanding of real-time logging data from different types of gas formation, we have established a methodology to quickly identify and classify gas zones during the UBD. Applying the evaluation criteria to the logging data enables us to have a real-time evaluation of the gas zones in the field.
- (3) As the formation evaluation technique by monitoring and utilization of MWD data in the gas zone is still in its exploratory stage, hence, the proposed formation evaluation criteria in this study should be used cautiously and will be further refined.

Conflicts of Interest

The authors declare no conflicts of interest.

Acknowledgments

The authors gratefully acknowledge the financial support of the National Natural Science Foundation of China (Grant no. 51474185), the National Key Basic Research and Development Program (973 Program), China (Grant no. 2013CB228003), the Project of National First-Level Discipline in Oil and Gas Engineering, and Scientific Research Foundation of State Key Lab.

References

- [1] Y. Zhou and H. Zhai, *Underbalanced Drilling Technology and Application*, Petroleum Industry Press, 2003.
- [2] B. Rehm et al., *Underbalanced drilling: limits and extremes*, Elsevier, 2013.
- [3] L. W. Cooper, R. A. Hook, and B. R. Payne, "Air drilling techniques," in *Proceedings of the SPE Deep Drilling and Production Symposium*, SPE-6435-MS, Society of Petroleum Engineers, Amarillo, Tex, USA, April 1977.
- [4] R. Wang, *Study on Evaluation Technology of Underbalanced Drilling [MSc. thesis]*, Southwest Petroleum University, 2013.
- [5] H. Yang and L. Wang, *Basic Theory and Practice of Underbalanced Drilling*, Petroleum Industry Press, Beijing, China, 2009.
- [6] D. Brant, Bennion etc. Underbalance Drilling's Advantage & Danger [C]. SPE/IADC 23566: 653-660.
- [7] J. Tang, k. Hu, c. Li et al., "Characteristics and recognition methods of natural gas logging in sichuan field," *Natural Gas Industry*, vol. 27, no. 11, pp. 34–40, 2007.
- [8] C. Wang, C. Liu, and G. Chen, "Study and Application of Evaluation Method for Gas Interpretation of Sulige Gas Field," *Logging Engineering*, vol. 20, no. 2, pp. 7–10, 2009.
- [9] X. Xu and H. Liu, "Evaluation of gas collection and interpretation under underbalanced drilling conditions," in *Logging Engineering*, vol. 18, pp. 26–28, 3 edition, 2007.
- [10] K. Zhu, Y. Meng, X. Xu et al., "Evaluation of Underbalanced Logging Reservoirs in NP2-82 Well," *Drilling process*, vol. 33, no. 6, pp. 15–17, 2010.
- [11] L. Zhu, X. Wang, Y. Yan et al., "Monitoring technology of drilling and drilling in air drilling and its application," *Natural Gas Industry*, vol. 29, no. 1, pp. 64–66, 2009.
- [12] X. Fan, J. Wang, Q. Zhang, X. Zhou, and G. Yu, "An evaluation of porosity and permeability based on an unsteady seepage model in a reservoir while underbalanced drilling," *Journal of Petroleum Science and Engineering*, vol. 127, pp. 367–376, 2015.
- [13] X. Fan, Q. Zhang, J. Wang et al., "Mathematical methods for evaluating a reservoir based on gas dynamic monitoring during underbalanced drilling," *Journal of Natural Gas Science and Engineering*, vol. 26, pp. 1068–1079, 2015.
- [14] F. Li, "The calculation and correction for the lag time under the gas drilling conditions," *Mud Logging Engineering*, vol. 4, pp. 24–27, 2011.
- [15] J. Chen, "Rapid evaluation method and application of oil and gas stratum in drilling site," *Offshore Oil*, vol. 15, no. 1, pp. 26–30, 2001.
- [16] Z. Yan, H. Nia, Z. Tang et al., "Drilling Technology for Horizontal Wells in Long Horizontal Section of Low Porosity and Low Permeability Gas Field," *Special Oil & Gas Reservoirs*, vol. 17, no. 2, pp. 105–108, 2010.

Research Article

Back Analysis of Rock Hydraulic Fracturing by Coupling Numerical Model and Computational Intelligent Technology

Shaojun Li,¹ Hongbo Zhao,² Xiating Feng,¹ Quan Jiang,¹ and Qiancheng Sun¹

¹State Key Laboratory of Geomechanics and Geotechnical Engineering, Institute of Rock and Soil Mechanics, Chinese Academy of Sciences, Wuhan, Hubei 430071, China

²School of Civil Engineering, Henan Polytechnic University, Jiaozuo 454003, China

Correspondence should be addressed to Shaojun Li; sjli@whrsm.ac.cn

Received 17 June 2017; Revised 23 August 2017; Accepted 7 September 2017; Published 18 October 2017

Academic Editor: Zhongwei Chen

Copyright © 2017 Shaojun Li et al. This is an open access article distributed under the Creative Commons Attribution License, which permits unrestricted use, distribution, and reproduction in any medium, provided the original work is properly cited.

Hydraulic fracturing is widely used to determine in situ stress of rock engineering. In this paper we propose a new method for simultaneously determining the in situ stress and elastic parameters of rock. The method utilizing the hydraulic fracturing numerical model and a computational intelligent method is proposed and verified. The hydraulic fracturing numerical model provides the samples which include borehole pressure, in situ stress, and elastic parameters. A computational intelligent method is applied in back analysis. A multioutput support vector machine is used to map the complex, nonlinear relationship between the in situ stress, elastic parameters, and borehole pressure. The artificial bee colony algorithm is applied in back analysis to find the optimal in situ stress and elastic parameters. The in situ stress is determined using the proposed method and the results are compared with those of the classic breakdown formula. The proposed method provides a good estimate of the relationship between the in situ stress and borehole pressure and predicts the maximum horizontal in situ stress with high precision while considering the influence of pore pressure without the need to estimate Biot's coefficient and other parameters.

1. Introduction

Hydraulic fracturing is widely used in the recovery of oil, gas, geothermal, and mineral resources [1]. In petroleum engineering it is important to determine the in situ stresses and elastic parameters of the rock mass when using hydraulic fracturing in fracturing operations, wellbore stability analysis, and reservoir simulation [2]. While high accuracy is required for the values of the in situ stress and mechanical parameters of the rock mass, determination of these parameters is still one of the most challenging tasks in hydraulic fracturing.

Hydraulic fracturing tests are considered the most effective method for determining the in situ stress and mechanical parameters of rock mass [3–9]. The Hubbert and Willis hydraulic fracturing criterion and Haimson and Fairhurst's hydraulic fracturing criterion are the two classic formulae for hydrofracture breakdown ([10]; Hubbert et al., 1953). However, the pore pressure term, which is a significant

factor in deep boreholes, is ignored in Hubbert and Willis's hydraulic fracturing criterion. Modifications of the original equations were proposed to account for the pore pressure (Detournay et al., 1988; [1, 11–13]), but they have not been used in practice because it involves the Biot poroelastic parameters and Poisson's ratio which are difficult to obtain. Schmitt and Zoback built a more useful generalized form of the hydrofracture breakdown equation by considering the poroelastic effects [1]. It can be used to provide upper and lower bound to the maximum horizontal in situ stress because it depends on the specific pore and microcrack structure. However, this method requires the poroelastic coefficients which are difficult to determine in practice.

Owing to the limitations of the classic breakdown formulae and the complexity of hydraulic fracturing tests, laboratory and field tests have been commonly used to determine the in situ stress and mechanical parameters of rock mass (Algorithm 1). However, these tests may not always produce the poroelastic parameters or may provide inaccurate results

```

Sub MSVM()

Dim N As Integer      ' The number of training samples
Dim Dim_x As Integer ' The dimension of input variables
Dim Dim_y As Integer ' The number of output variables

Dim C As Double      ' Pentalty factor of SVM
Dim epsilon As Double
Dim sigma As Double

Dim X_input() As Double ' The input of training samples
Dim Y_output() As Double ' The output of traning samples

' The one sample
Dim xi() As Double
Dim xj() As Double
"The weights of MSVM
Dim W() As Double
Dim b() As Double
Dim W_k() As Double
Dim b_k() As Double
Dim W_s() As Double
Dim b_s() As Double

' the error of each sample
Dim u() As Double
Dim ai() As Double
Dim ui() As Double
Dim u_new() As Double

"The coefficient of matrix for computing Ws and bs
Dim A() As Double
Dim BB() As Double
Dim A_last_row() As Double
Dim B_last_row() As Double

"The Descending direction
Dim P_W() As Double
Dim P_b() As Double

Dim k() As Double
Dim D_a() As Double
Dim D_a.1() As Double
Dim kf() As Double

Dim I As Integer
Dim j As Integer
Dim l As Integer

"The step size eta_k
Dim eta As Double

"The control parameters of algorithm convergence
Dim delta_u As Double
Dim t As Integer

```

ALGORITHM 1: Continued.

```
"The value of the numbers of parameters of training samples
```

```
N = Range("N").Cells.Value
Dim_x = Range("Dim_x").Cells.Value
Dim_y = Range("Dim_y").Cells.Value
```

```
"The parameters of SVM
```

```
C = Range("_C").Cells.Value
epsilon = Range("epsilon").Cells.Value
sigma = Range("sigma").Cells.Value
```

```
ReDim X_input(1 To N, 1 To Dim_x) As Double
ReDim Y_output(1 To N, 1 To Dim_y) As Double
ReDim xi(1 To Dim_x) As Double
ReDim xj(1 To Dim_x) As Double
ReDim W(1 To Dim_y, 1 To N) As Double
ReDim b(1 To Dim_y) As Double
ReDim W_k(1 To Dim_y, 1 To N) As Double
ReDim b_k(1 To Dim_y) As Double
ReDim W_s(1 To Dim_y, 1 To N) As Double
ReDim b_s(1 To Dim_y) As Double
ReDim u(1 To N) As Double
ReDim ai(1 To N) As Double
ReDim ui(1 To Dim_y) As Double
ReDim u_new(1 To N) As Double
ReDim A(1 To N + 1, 1 To N + 1) As Double
'ReDim X(1 To N + 1, 1 To Dim_y) As Double
ReDim BB(1 To N + 1, 1 To Dim_y) As Double
ReDim A_last_row(1 To N) As Double
ReDim B_last_row(1 To Dim_y) As Double
ReDim P_W(1 To Dim_y, 1 To N) As Double
ReDim P_b(1 To Dim_y) As Double
ReDim k(1 To N, 1 To N) As Double
ReDim D_a(1 To N, 1 To N) As Double
ReDim D_a_1(1 To N, 1 To N) As Double
ReDim kf(1 To N) As Double
```

```
'Read the input of training samples
```

```
For I = 1 To N
  For j = 1 To Dim_x
    X_input(I, j) = Range("xi").Cells(I, j)
  Next
Next
```

```
'Read the output of training samples
```

```
For I = 1 To N
  For j = 1 To Dim_y
    Y_output(I, j) = Range("yi").Cells(I, j).Value
  Next
Next
```

```
' The initial value of Wk and bk
```

```
For I = 1 To Dim_y
  b(I) = 0
  For j = 1 To N
    W(I, j) = 0
  Next
Next
```

```
delta_u = 1
```

```

t = 0

'The iteration process of algorithm
While (delta_u > 0.001 And t < 100)

' Replace the value of Wk and bk by the New w and b
For I = 1 To Dim_y
  For j = 1 To N
    W_k(I, j) = W(I, j)
  Next
  b_k(I) = b(I)
Next

' Compute the value of ui and ai
For I = 1 To N
  u(I) = 0
  For j = 1 To Dim_x
    xi(j) = X_input(I, j)
  Next

  For ii = 1 To N
    For j = 1 To Dim_x
      xj(j) = X_input(ii, j)
    Next
    kf(ii) = kernel_fun(xi, xj, sigma)
  Next

  For ii = 1 To Dim_y
    ui(ii) = b_k(ii)
    For j = 1 To N
      ui(ii) = ui(ii) + W_k(ii, j) * kf(j)
    Next
  Next

  For j = 1 To Dim_y
    u(I) = u(I) + (Y_output(I, j) - ui(j))^2
  Next
  u(I) = Sqr(u(I))

  If (u(I) < epsilon) Then ai(I) = 0
  If (u(I) >= epsilon) Then ai(I) = 2 * C * (u(I) - epsilon)/u(I)
  ai(i) = 2 * C * (u(i) - epsilon)/u(i)
Next

'compute the Matrix K and Da
For I = 1 To N
  For j = 1 To N
    For l = 1 To Dim_x
      xi(l) = X_input(I, l)
      xj(l) = X_input(j, l)
    Next
    k(I, j) = kernel_fun(xi, xj, sigma)
    If (I = j) Then D_a(I, j) = ai(I) Else D_a(I, j) = 0
  Next
Next

For I = 1 To N
  For j = 1 To N
    If (I = j) Then A(I, j) = k(I, j) + 1/D_a(I, j) Else A(I, j) = k(I, j)
  Next
Next

```

```

    Next
Next

'Compute Transpose(a)*K
For I = 1 To N
    A_last_row(I) = 0
    For j = 1 To N
        A_last_row(I) = A_last_row(I) + ai(j) * k(j,I)
    Next
Next

A(N + 1, N + 1) = 0
For I = 1 To N
    A(N + 1, I) = A_last_row(I)
    A(N + 1, N + 1) = A(N + 1, N + 1) + ai(I)
    A(I, N + 1) = 1
Next

For I = 1 To Dim_y
    B_last_row(I) = 0
    For j = 1 To N
        B_last_row(I) = B_last_row(I) + ai(j) * Y_output(j, I)
    Next
Next

For I = 1 To N
    For j = 1 To Dim_y
        BB(I, j) = Y_output(I, j)
    Next
Next

For j = 1 To Dim_y
    BB(N + 1, j) = B_last_row(j)
Next

'Compute Ws and bs
With Application.WorksheetFunction
    x1 = .MMult(.MInverse(A), BB)
End With

For I = 1 To Dim_y
    For j = 1 To N
        W_s(I, j) = x1(j, I)
    Next
    b_s(I) = x1(N + 1, I)
Next

'Compute the descending direction
For I = 1 To Dim_y
    For j = 1 To N
        P_W(I, j) = W_s(I, j) - W_k(I, j)
    Next
    P_b(I) = b_s(I) - b_k(I)
Next

eta = 1
Dim delta_Lp As Double

```

```

Dim Lp_k_1 As Double
Dim Lp_k As Double

delta_Lp = 1

'Update the solution of W and b
While (delta_Lp > 0.0001)

  For I = 1 To Dim_y
    For j = 1 To N
      W(I,j) = (1 - eta) * W_k(I,j) + eta * P_W(I,j)
    Next
    b(I) = (1 - eta) * b_k(I) + eta * P_b(I)
  Next

  For I = 1 To N
    u_new(I) = 0

    For j = 1 To Dim_x
      xi(j) = X_input(I,j)
    Next

    For ii = 1 To N
      For j = 1 To Dim_x
        xj(j) = X_input(ii,j)
      Next
      kf(ii) = kernel_fun(xi, xj, sigma)
    Next

    For ii = 1 To Dim_y
      ui(ii) = b(ii)
      For j = 1 To N
        ui(ii) = ui(ii) + W(ii,j) * kf(j)
      Next
    Next

    For j = 1 To Dim_y
      u_new(I) = u_new(I) + (Y_output(I,j) - ui(j))^2
    Next

    u_new(I) = Sqr(u_new(I))

    If (u_new(I) < epsilon) Then ai(I) = 0
    If (u_new(I) >= epsilon) Then ai(I) = 2 * C * (u_new(I) - epsilon)/u_new(I)
    delta_u = delta_u + u_new(I)
  Next

  Lp_k_1 = 0
  Lp_k = 0

  For I = 1 To Dim_y
    For j = 1 To N
      Lp_k_1 = Lp_k_1 + W(I,j)^2/2
      Lp_k = Lp_k + W_k(I,j)^2/2
    Next
  Next

  For j = 1 To N
    If u_new(j) >= epsilon Then Lp_k_1 = Lp_k_1 + C * (u_new(j)^2 - 2 * u_new(j) * epsilon + epsilon^2)
    If u(j) >= epsilon Then Lp_k = Lp_k + C * (u(j)^2 - 2 * u(j) * epsilon + epsilon^2)
  Next

```

```

    Next

    delta_Lp = Lp_k.1 - Lp_k
    eta = 0.5 * eta
Wend

delta_u = 0
For I = 1 To N
    delta_u = delta_u + u_new(I)
Next

delta_u = delta_u/N

t = t + 1

Wend

For I = 1 To N
    For j = 1 To Dim_y
        Range("wi").Cells(I, j) = W(j, I)
    Next
Next

For j = 1 To Dim_y
    Range("bi").Cells(j) = b(j)
Next

End Sub
' Kernel function of RBF
Function kernel_fun(xx, yy, sigma2) As Double
Dim temp As Double
Dim temp1 As Double
Dim Dim_x As Integer

Dim_x = Range("Dim_x").Cells.Value
temp = 0
For I = 1 To Dim_x
temp = temp + (xx(I) - yy(I))^2
'temp = temp + xx(i) * yy(i)
Next I

temp1 = Sqr(temp)/(2 * sigma2^2)

kernel_fun = Exp(-temp1)
'Kf = (temp + 1)^sigma2

End Function

' Compute the performance function value using the MSVM
Sub Perffunc()
Dim I As Integer
Dim ii As Integer
Dim l As Integer
Dim j As Integer
Dim N As Integer
Dim Np As Integer
Dim sigma As Double

Dim xi() As Double

```

```

Dim xj() As Double
Dim W() As Double
Dim b() As Double
Dim Yy_p() As Double
Dim kf() As Double

N = Range("N").Cells.Value
Np = Range("Np").Cells.Value
Dim_x = Range("Dim_x").Cells.Value
Dim_y = Range("Dim_y").Cells.Value
sigma = Range("sigma").Cells.Value

ReDim xi(1 To Dim_x) As Double
ReDim xj(1 To Dim_x) As Double
ReDim W(1 To Dim_y, 1 To N) As Double
ReDim b(1 To Dim_y) As Double
ReDim Yy_p(1 To Np, 1 To Dim_y) As Double
ReDim kf(1 To N) As Double

For I = 1 To Dim_y
  For j = 1 To N
    W(I, j) = Range("wi").Cells(j, I)
  Next
  b(I) = Range("bi").Cells(I)
Next

For I = 1 To Np
  For j = 1 To Dim_x
    xi(j) = Range("x_p_input").Cells(I, j)
  Next

  For l = 1 To N
    For j = 1 To Dim_x
      xj(j) = Range("xi").Cells(l, j)
    Next
    kf(l) = kernel_fun(xi, xj, sigma)
  Next

  For ii = 1 To Dim_y
    Yy_p(I, ii) = b(ii)
    For j = 1 To N
      Yy_p(I, ii) = Yy_p(I, ii) + W(ii, j) * kf(j)
    Next
  Next
Next

For I = 1 To Np
  For j = 1 To Dim_y
    Range("y_p_output").Cells(I, j) = Yy_p(I, j)
  Next
Next

End Sub

```

ALGORITHM 1: The code of MSVM.

because of low-quality core samples [14]. Alternatively, back analysis, associated with the “in situ” approach, has been widely used to determine the mechanical parameters of rock mass in rock engineering [15–20]. Zhang and Yin proposed a back analysis method which combined a neural network and a genetic algorithm to simultaneously identify the in situ stresses and elastic parameters [2]; however, this method did not consider the poroelastic effect. To overcome this difficulty, in this paper we extend our proposed displacement back analysis method to determine the in situ stress and mechanical parameters of a rock mass based on measured borehole pressure. The borehole pressure can be easily measured in the field with a pressure gauge installed inside the borehole [21]. Back analysis is implemented following an optimization strategy based on the multioutput support vector machine (MSVM) and artificial bee colony algorithm (ABC) model, which is effective in multiple parameter identification [22].

The rest of this paper is organized as follows. The classic breakdown formula is presented in detail in Section 2. The formulation and procedure of back analysis based on borehole pressure are presented in detail in Section 3. In Section 4, a numerical example is used to verify the proposed method, and our conclusions are presented in Section 5.

2. Hydraulic Breakdown Equations

Hydraulic fracturing is a widely accepted technology used for determining in situ stress magnitude and direction. The principal stress σ_v has a magnitude equal to the overburden pressure in the vertical direction. The smallest horizontal principal stress σ_{hmin} is usually determined directly in the experiment from the shut-in pressure. The greatest horizontal principle stress σ_{Hmax} must be calculated using a breakdown formula derived from an appropriate hydraulic fracturing model. Hubbert and Willis proposed a classic breakdown formula (1) to calculate σ_{Hmax} for hydraulic fracturing in non-porous impermeable rocks [23], ignoring the pore pressure term.

$$P_b = 3\sigma_{hmin} - \sigma_{Hmax} + T, \quad (1)$$

where T is the rock tensile strength.

Equations (2) and (3) are the breakdown formulae of porous impermeable rocks and porous permeable rocks, respectively, including the pore pressure [24]:

$$P_b = 3\sigma_{hmin} - \sigma_{Hmax} + T - P_p \quad (2)$$

$$P_b = \frac{3\sigma_{hmin} - \sigma_{Hmax} + T - \alpha((1-2\nu)/(1-\nu))P_p}{2 - \alpha((1-2\nu)/(1-\nu))}, \quad (3)$$

where P_b is the breakdown pressure, P_p is the pore pressure, α is the Biot poroelastic parameter, and ν is Poisson's ratio. Although (3) may best describe the conditions under which hydraulic fracturing is conducted from an open borehole, (2) is used in practice because of the difficulty of determining α and ν . Schmitt and Zoback proposed a more generalized form

for the equations of hydrofracture breakdown for porous impermeable rocks and porous permeable rocks [1]:

$$P_b = 3\sigma_{hmin} - \sigma_{Hmax} + T - \beta P_p \quad (4)$$

$$P_b = \frac{3\sigma_{hmin} - \sigma_{Hmax} + T - \alpha((1-2\nu)/(1-\nu))P_p}{1 + \beta - \alpha((1-2\nu)/(1-\nu))}, \quad (5)$$

where β is the poroelastic effect parameter.

3. Back Analysis Model Based on Borehole Pressure

The in situ stress can be estimated based on borehole pressure using the hydraulic breakdown equations (Section 2). However, these equations present some limitations in practice. Therefore, we propose a back analysis method that combines a numerical method and an intelligent computational method. A multioutput support vector machine (MSVM) is used to map the complex, nonlinear relationship between the in situ stress, elastic parameters, and borehole pressure. The numerical method provides the training samples for the MSVM. It is important to use an optimization method in back analysis. Here, we use the ABC algorithm to find the best-fit in situ stress and elastic parameters by comparing the measured pressure data and the MSVM predicted pressure.

3.1. Nonlinear Relationships between Pressure and Geomechanical Parameters. The relationship between the borehole pressure and geomechanical parameters can be derived by the MSVM. The basic idea of MSVM is to extend the single-output support vector machine to a multidimensional output case. Given a set of training samples $\{(X_1, Y_1), (X_2, Y_2), \dots, (X_N, Y_N)\}$, $X_i \in R^n$, $Y_i \in R^Q$, the MSVM model can be built by solving the following optimization problem based on an iterative reweighted least-square algorithm [25].

$$L'_p(W, b) = \frac{1}{2} \sum_{j=1}^Q \|W_j\|^2 + \frac{1}{2} \sum_{i=1}^N a_i u_i^t + \tau \quad (6)$$

$$a_i = \begin{cases} 0 & u_i^t < \varepsilon \\ 2C(u_i^t - \varepsilon)u_i^t & u_i^t \geq \varepsilon, \end{cases}$$

where N is the number of input, Q is the number of output, W is the weight, b and C are constants, τ is the sum of constant terms that do not depend on either W or b , ε is the tolerant error, and t denotes the t th iteration. A brief description and the MSVM algorithm can be found in the literature [22]. The MSVM model can be expressed as

$$Y(X) = \sum_{k=1}^n \mathbf{W}k(X, X_k) + \mathbf{b}. \quad (7)$$

Based on the above MSVM model, the nonlinear relationship between the borehole pressure and geomechanical parameters can be described as

$$\begin{aligned} \text{MSVM}(\mathbf{X}) : R^n &\longrightarrow R^Q \\ \mathbf{Y} &= \text{MSVM}(\mathbf{X}), \end{aligned} \quad (8)$$

where $\mathbf{X} = (x_1, x_2, \dots, x_n)$ is the n -dimensional vector of the identified parameter, for example, the in situ stress, Young's modulus, or Poisson's ratio. $\mathbf{Y} = (y_1, y_2, \dots, y_Q)$ is the Q -dimensional vector of the borehole pressure.

To build the MSVM model, the necessary training or learning samples are constructed and the MSVM parameters are determined. The samples are constructed by numerical analysis which computes the corresponding borehole pressure for a given set of tentative determined parameters. The MSVM parameters have a strong influence on the performance of the MSVM. In this study, we determined these parameters using the formulation presented by Meza et al. [26].

3.2. Optimization Method. The back analysis ABC algorithm, developed by Karaboga [27], was adopted to search for the optimal geomechanical parameters of the rock mass. In the algorithm, the colony of artificial bees consists of three groups: employed bees, onlookers, and scouts. The ABC algorithm involves a cycle of four phases: the initialization phase, employed bees phase, onlooker bee phase, and scout bee phase.

In the initialization phase, the ABC generates a randomly distributed initial population of SN solutions and calculates the fitness of each solution.

$$x(i, j) = x_{\min}^j + \text{rand}(0, 1) (x_{\max}^j - x_{\min}^j), \quad (9)$$

where $x(i, j)$ is the candidate solution of the problem; $i = 1, 2, \dots, \text{SN}/2$ and $\text{SN}/2$ denotes the size of the population; $j = 1, 2, \dots, D$ and D is the dimension number of each solution; $\text{rand}(0, 1)$ is a random number between $[0, 1]$; x_{\min}^j and x_{\max}^j are the upper and lower bounds of each solution.

Once initialization is completed, the employed bees search for a solution and calculate the fitness value (see Section 3.3) in the employed bees phase. A candidate solution is produced according to the following equation:

$$v(i, j) = x(i, j) + \varphi_{ij} (x(i, j) - x(k, j)), \quad (10)$$

where k is different from i and is a randomly chosen index from $\{1, 2, \dots, \text{SN}/2\}$, j is also an index randomly chosen from $\{1, 2, \dots, D\}$, and φ_{ij} is a random number in the range $[-1, 1]$ that controls the generation of food sources around $x(i, j)$ and represents the comparison of two food positions seen by a bee.

In the onlooker bee phase, the onlooker bees choose a solution based on the fitness value, determine which solution will be abandoned, and allocate its employed bees as scout bees. The probability of being selected for each fitness value can be expressed as

$$p_i = \frac{\text{fitness}_i}{\sum_{n=1}^{\text{SN}} \text{fitness}_n}, \quad (11)$$

where fitness_i is the fitness value of the solution.

Finally, in the scout bee phase the scout bees randomly search for a new solution in the determined ranges. A solution that cannot be improved further through a predetermined number of cycles is assumed to be abandoned by the onlookers.

3.3. The Fitness Function. In order to find the optimal solution, it is necessary to build the fitness function for the ABC algorithm; that is,

$$\text{fitness} = \sqrt{\frac{\|\text{MSVM}(X) - Y\|^2}{Q}}, \quad (12)$$

where $\text{MSVM}(X)$ is the predicted pressure using the MSVM model, Y is the vector of the monitored pressure, and Q is the number of monitored points.

3.4. Procedure of the MSVM-ABC Based Method. If the MSVM model can establish the nonlinear relation between the borehole pressures and determined parameters, the model can be used to predict the borehole pressures. Then, the ABC algorithm is utilized to find the optimal parameters through error minimization between the pressures predicted by the MSVM model and the measured pressures. The back analysis flowchart is shown in Figure 1 and the algorithm is described as follows.

Step 1. Determine the general information and data such as the unknown (determined by back analysis) and known parameters of the numerical model, the MSVM and ABC algorithm parameters, and the range of parameters to be determined.

Step 2. Generate the combination of determined parameters, calculate the borehole pressure for each combination, and then build the learning samples for MSVM.

Step 3. Based on the learning samples of Step 2, construct the MSVM model using the MSVM algorithm and activate the ABC algorithm.

Step 4. Search for the optimal determined parameters based on the monitored pressure.

4. Validation and Application

To verify the proposed method, a numerical example is adopted to determine the in situ stress and elastic mechanical parameters of the elastic rock. The numerical experiment is conducted based on 2D hydraulic fracturing model of water injection into a hypothetical deep formation. Further details of the physical and numerical model can be found in the literature published by Schmitt and Zoback [1].

The parameters to be determined are the maximum and minimum horizontal in situ stress $\sigma_{H\max}$ and $\sigma_{H\min}$, respectively, Young's modulus E , and Poisson's ratio ν . The rock mass in all the zones is considered to be elastic. The mechanical parameters of the joints and the permeability

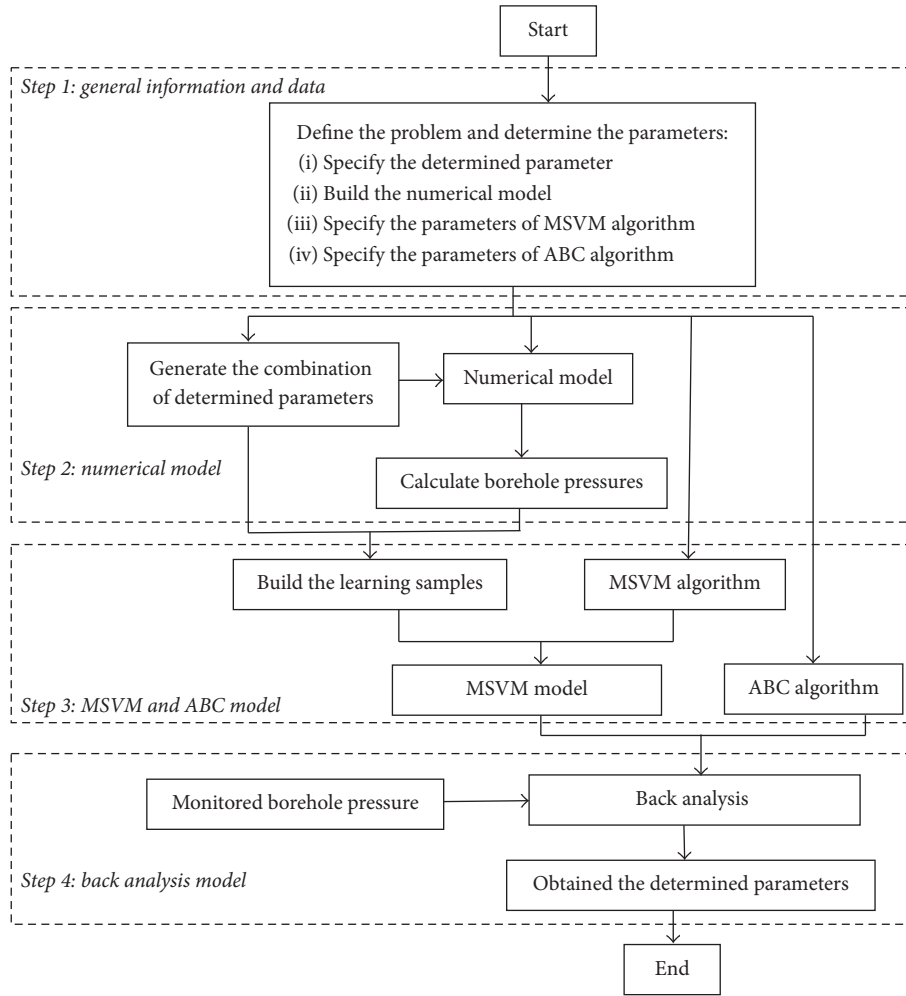


FIGURE 1: Flowchart of the back analysis process to obtain the rock parameters.

of the rock mass are known; the parameter values can be seen in the literature published by Schmitt and Zoback [1]. Thirty sets of training samples and ten testing samples derived in previous studies [1, 2] were selected. Based on the MSVM algorithm, the MSVM code was written in Excel and VBA. The MSVM parameters and some of the weight w_i and constant b_i values and samples are shown in Figure 2. Good agreement between the measured data and the pressures estimated by the MSVM is shown in Figure 3, indicating the good performance of the MSVM model. Thus, the proposed model can accurately estimate the borehole pressures, replacing the existing numerical analysis method for calculating borehole pressures. The results also confirm that the MSVM model provides an accurate representation of the nonlinear relationship between the pressures and the determined parameters.

The ABC code is also written in Excel and VBA. The parameters of the ABC algorithm and the calculation results are shown in Figure 4. Based on the proposed method for determining the in situ stress and mechanical parameters of rock mass, the results are shown in Table 1. we obtained the

values of σ_{Hmax} , σ_{hmin} , E , and ν as 24.46 MPa, 14.33 MPa, 44.02 GPa, and 0.25, respectively. The elastic mechanical parameters of the rock agree with the results calculated by the Genetic Algorithm-Neural Network (ANN-GA) [2]. A comparison of in situ stress values calculated using four different formulations is shown in Figure 5. σ_{hmin} agrees well with the value estimated by ANN-GA, (1), and (2). The relative error is only 1.07%. σ_{Hmax} agrees well with the value estimated by (2), which considers the pore pressure, but differs considerably from the values calculated by (1) and ANN-GA which do not consider the poroelastic effects. The relative error is up to 31.8%. Using (4), we obtain the upper and lower limits of the maximum horizontal in situ stress σ_{Hmax} (14.95–34.55 MPa). The value 24.46 MPa is within this range. Thus, the proposed method can be used in back analysis as an alternative numerical analysis method, which considers the poroelastic effects and provides rational, high-precision results. Note that the proposed method can determine the maximum horizontal in situ stress without estimating the poroelastic coefficient, which is a difficult parameter to obtain.

TABLE 1: Comparison of in situ stresses and mechanical parameters between MSVM model and other preexisted models.

Model	σ_H (MPa)	σ_h (MPa)	Young's modulus E (GPa)	Poisson's ratio ν
MSVM	24.46	14.33	44.02	0.25
ANN-GA [#]	35.83	14.968	39.92	0.26
Eq. (1) [*]	34.549	15.637		
Eq. (2) [*]	24.749	15.637		

[#]The model proposed by Zhang and Yin [2]. ^{*}The model proposed by Hubbert and Willis [23].

Multioutput support vector machine

Parameters of MSVM			Training samples			Testing or predicting samples			
σ	ϵ	C	Number of samples	Dimension of input	Dimension of output	Number of samples			
5	1E-05	300	30	4	4	40			

Models of MSVM
wi & bi (The first row)

Training samples		Output(y_i)				wi & bi (The first row)					
Input(x_i)											
		25.51749	41.53803	25.30404	22.62262						
1	44.9 34.1 40.0 0.2	39.778	66.733	40.377	37.482	32.69383	61.6205	28.92746	36.87203		
2	43.8 30.9 42.0 0.3	35.882	60.069	37.09	32.905	-5.799298	-0.497959	2.342793	-6.83015		
3	43.2 15.7 25.0 0.3	19.425	25.968	18.394	16.293	-2.643523	-11.87645	-8.24627	-8.16457		
4	42.9 20.0 30.0 0.2	21.183	30.267	22.859	20.486	-26.79601	-28.7827	-8.93134	-5.26611		
5	42.3 33.0 40.0 0.2	37.403	61.538	37.959	34.59	-7.965503	-24.82346	-13.728	-8.95032		
6	41.9 28.5 42.0 0.3	33.423	54.845	34.099	30.028	-10.14168	5.245473	-15.5702	-11.6237		
7	41.0 17.8 26.0 0.3	21.578	27.741	20.437	18.33	14.51593	-10.42965	2.294206	4.102865		
8	40.4 31.3 47.0 0.3	37.074	60.791	37.452	33.623	13.77002	10.75531	13.80466	12.93566		
9	39.8 27.0 38.0 0.2	32.056	43.779	33.969	28.521	2.65743	-51.59696	23.6693	0.200652		
10	39.2 11.3 28.0 0.2	14.387	21.38	13.928	11.916	-15.18197	-8.023748	-11.0173	-10.7767		
11	38.9 29.9 41.0 0.3	35.089	57.713	35.694	31.699	2.148607	37.66816	0.857885	4.119908		
12	38.1 18.9 35.0 0.3	23.467	30.347	22.057	19.47	7.290676	-2.550754	-4.21743	-2.08841		
13	37.6 27.4 27.0 0.3	31.439	51.838	32.584	28.979	9.948569	50.389	14.00926	11.58154		
14	36.5 14.9 37.0 0.2	19.223	27.261	18.048	15.485	0.180288	14.13271	-0.47812	-2.10495		
15	35.5 25.1 39.0 0.2	30.255	39.013	28.688	26.052	-3.420387	-48.26779	-22.4071	-7.36326		
16	34.6 12.8 24.0 0.3	16.305	23.295	15.414	13.331	-3.60225	1.880641	-2.63221	-3.7458		
17	33.8 28.9 42.0 0.3	34.409	55.727	34.523	30.596	9.328942	61.70773	16.13344	9.398126		
18	33.2 17.9 32.0 0.3	22.06	28.912	20.846	18.474	4.171029	8.203456	4.833736	4.764868		
19	32.5 10.3 36.0 0.2	13.789	20.18	13.122	10.948	-16.877	-20.59279	-12.9272	-11.6762		
20	31.5 24.9 21.0 0.2	28.983	45.886	29.211	25.937	12.27877	38.88137	15.94925	12.30997		
21	31.1 16.9 24.0 0.3	20.342	26.571	19.426	17.392	-1.505729	-21.8008	-2.46657	0.202625		
22	30.5 22.7 35.0 0.3	27.216	35.282	25.95	23.289	-1.505308	3.553947	-0.44801	-0.55972		
23	29.5 25.1 40.0 0.2	29.886	39.043	28.714	26.014	1.008502	-27.74127	0.52993	3.700371		
24	28.4 13.6 28.0 0.2	17.67	24.647	16.346	14.127	6.005568	17.7538	1.352429	-0.47782		
25	27.8 20.2 32.0 0.2	24.602	30.77	23.131	20.661	0.912869	-3.943866	0.386886	0.365483		
26	27.2 15.8 26.0 0.3	19.189	26.153	18.522	16.371	-6.679902	8.441547	3.515295	2.837635		
27	26.9 13.1 43.0 0.3	17.573	24.725	16.366	13.71	-13.40561	-17.60743	-13.6856	-14.2492		
28	26.3 20.6 27.0 0.3	24.947	30.101	23.283	21.048	8.177915	-25.86171	0.189852	2.768714		
29	25.7 21.3 38.0 0.2	26.112	33.84	24.708	21.888	6.515285	9.419643	6.692563	4.489202		
30	25.1 11.1 21.0 0.3	14.721	20.638	13.348	11.579	-16.08006	-25.25597	-18.7337	-16.7728		

FIGURE 2: Parameters and model of MSVM in the Excel VBA platform.

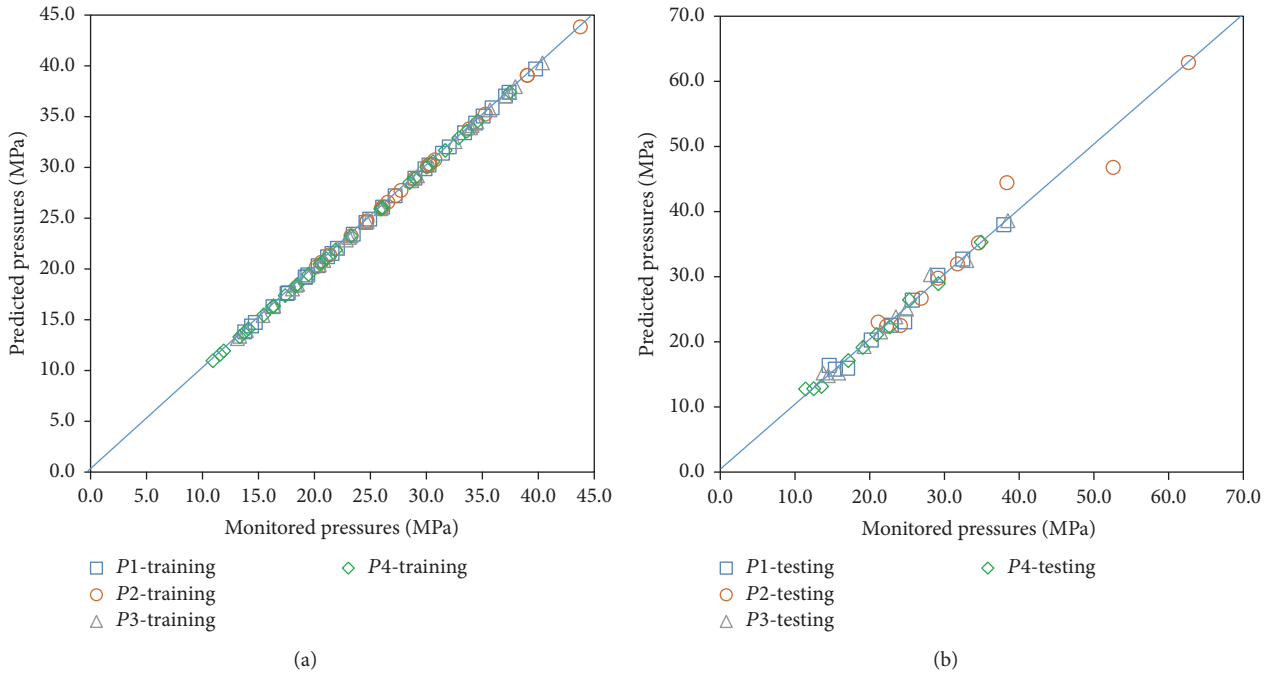


FIGURE 3: Comparison of pressure data estimated by MSVM and borehole measured data.

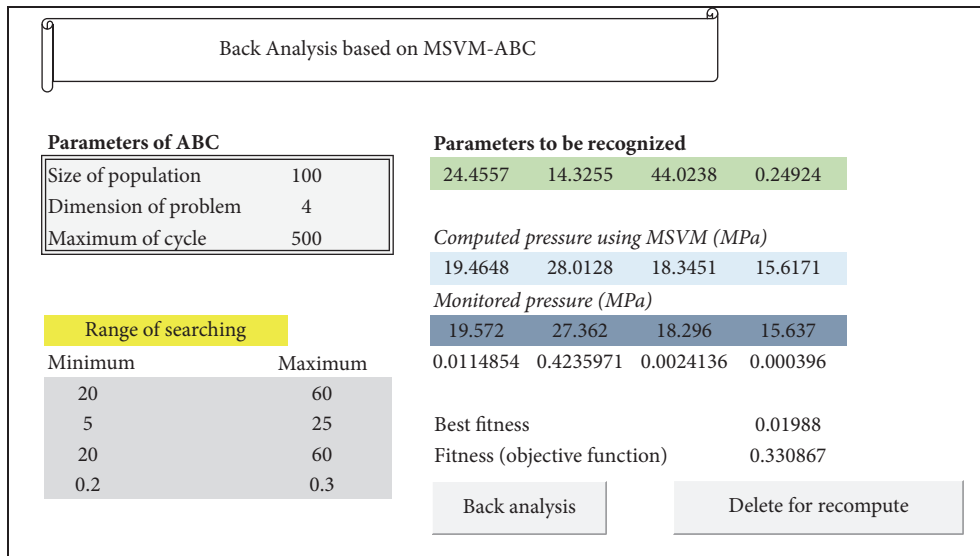


FIGURE 4: MSVM-ABC-based back analysis, its parameters, and results in the Excel VBA platform.

Moreover, there are four borehole pressures, namely, formation breakdown pressure (FBP) $P1$, fracture propagation pressure (FPP) $P2$, instantaneous shut-in pressure (ISIP) $P3$, and leak-off pressure (LOP) $P4$. A comparison of back analysis on borehole pressures obtained by three different methods is presented in Figure 6. The borehole pressure calculated by the proposed MSVM method is very close to the measured pressure. The relative error is less than 3%. On the other hand, the convergence processes of the algorithm and fitness variations are shown in Figures 7 and 8. Initially, the data was distributed randomly in the searching space

(Figure 8) and then converged to the solution of the problem in the 500th generation. This indicates that the proposed method can determine both the in situ stress and elastic mechanical parameters of the elastic rock with excellent converging performance.

5. Conclusions

In this paper, a new borehole pressure-based back analysis approach to determine the stress and mechanical parameters of rock mass is proposed. The method combines a coupling

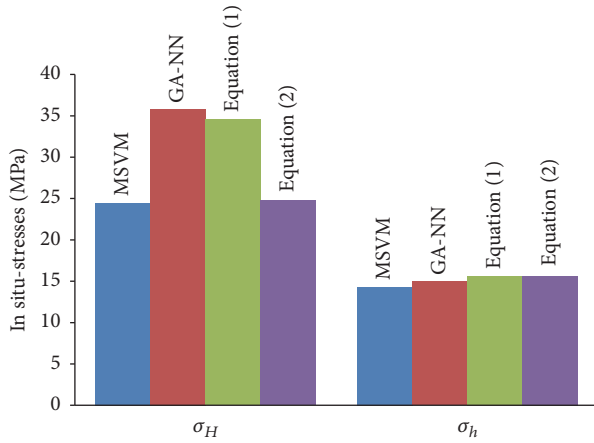


FIGURE 5: Comparison of recognized in situ stress using different models (σ_H , σ_h are the maximum and minimum in situ stress).

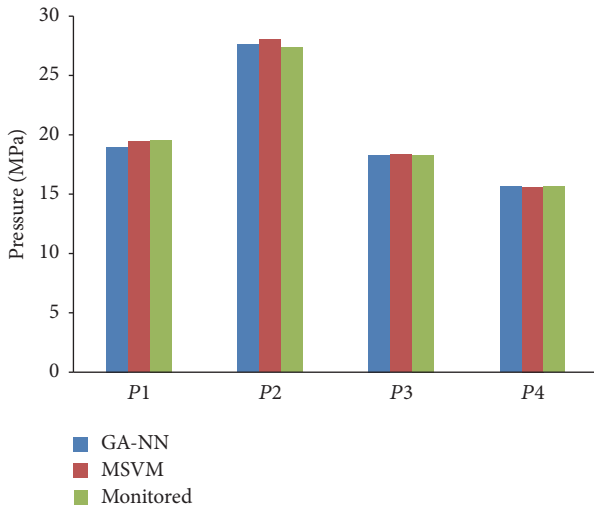


FIGURE 6: Comparison of borehole pressures obtained by different prediction methods and monitored data.

numerical model of hydraulic fracturing and a computational intelligent method. The method is applied to a numerical example to successfully determine both the in situ stress and mechanical parameters of a rock mass. In this approach, the MSVM is adopted to represent the nonlinear relationship between the borehole pressure and mechanical parameters of the rock mass, proving more efficient than existing numerical models. The ABC algorithm is used to search for the optimal parameters in the search space. The proposed approach is implemented in Excel with VBA.

In the classic breakdown formula, it is difficult in practice to determine the maximum horizontal in situ stress while considering the poroelastic coefficient. The proposed back analysis method can predict the maximum horizontal in situ stress based on the borehole pressures without the need to obtain the poroelastic coefficient. Thus, it is a more practical method for determining the in situ stress from hydraulic fracturing. The proposed method is practical and accurate and can be conveniently applied to simultaneously determine

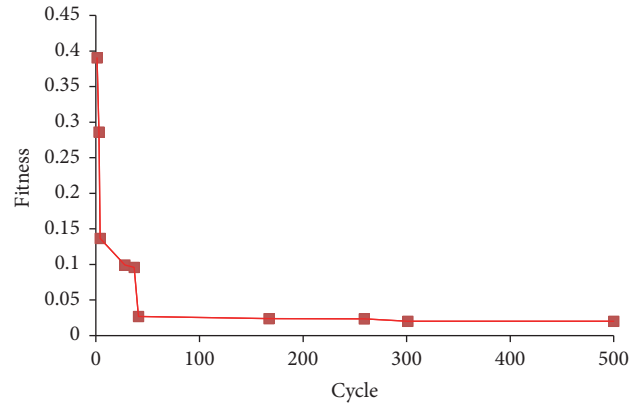


FIGURE 7: Fitness variation with increased cycles in the ABC analysis.

the in situ stress and mechanical parameters of rock from hydraulic fracturing.

Symbols

σ_v :	Principal stress in y direction
σ_{Hmax} :	The greatest horizontal principle stress
σ_{hmin} :	The smallest horizontal principal stress
ν :	Poisson's ratio
β :	Poroelastic effect parameter
W :	The weight vector
MSVM(X):	The predicted pressure using the MSVM model
C :	Hyper parameter that determines trade-off between the regularization and the error reduction term
ϵ :	Tolerant error
Q :	Number of output
φ_{ij} :	A random number in the range $[-1, 1]$
b :	A constant for classification threshold
P_b :	Breakdown pressure
P_p :	Pore pressure
E :	Young's modulus
α :	Biot poroelastic parameter
T :	Rock tensile strength
N :	Number of input
τ :	Sum of constant terms that do not depend on either W or b
rand(0, 1):	A random number between $[0, 1]$
fitness:	Fitness value of the solution.

Conflicts of Interest

The authors declare that they have no conflicts of interest.

Acknowledgments

The authors gratefully acknowledge the National Natural Science Foundation of China (Grant no. 41372315), the State Key Research Development Program of China (Grant

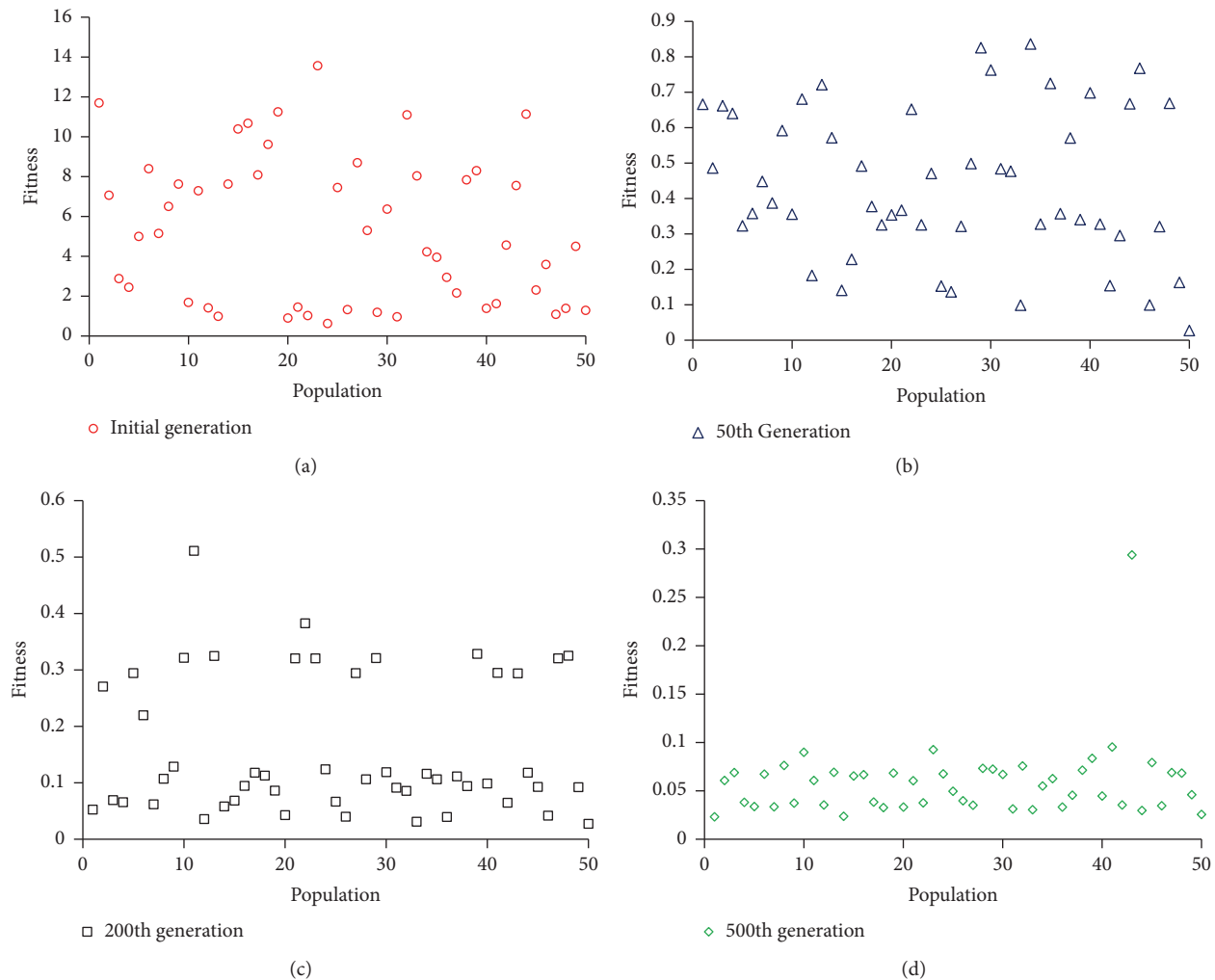


FIGURE 8: Fitness distribution in the searching space at different cyclic stages.

no. 2016YFC0600702), and Innovative Research Team (in Science and Technology) in University of Henan Province (no. 15IRTSTHN029).

References

[1] D. R. Schmitt and M. D. Zoback, “Poroelastic effects in the determination of the maximum horizontal principal stress in hydraulic fracturing tests-A proposed breakdown equation employing a modified effective stress relation for tensile failure,” *International Journal of Rock Mechanics and Mining Sciences and*, vol. 26, no. 6, pp. 499–506, 1989.

[2] S. Zhang and S. Yin, “Determination of in situ stresses and elastic parameters from hydraulic fracturing tests by geomechanics modeling and soft computing,” *Journal of Petroleum Science and Engineering*, vol. 124, pp. 484–492, 2014.

[3] Z. Fang and A. Khaksar, “Complexity of minifrac tests and implications for in-situ horizontal stresses in coalbed methane reservoirs,” in *Proceedings of the International Petroleum Technology Conference*, Bangkok, Thailand, 2011.

[4] B. C. Haimson and C. Fairhurst, “In-situ stress determination at great depth by means of hydraulic fracturing,” in *Proceedings of the 11th U.S. Symposium on Rock Mechanics (USRMS)*, pp. 559–584, Berkeley, CA, USA, 1969.

[5] B. C. Haimson, “The hydrofracturing stress measuring method and recent field results,” *International Journal of Rock Mechanics and Mining Sciences and*, vol. 15, no. 4, pp. 167–178, 1978.

[6] B. C. Haimson, “The hydraulic fracturing method of stress measurement: theory and practice,” in *Comprehensive Rock Engineering*, J. A. Hudson, Ed., vol. 3, pp. 395–412, Pergamon Press, Oxford, 1993.

[7] J. W. Puller, K. W. Mills, R. G. Jeffrey, and R. J. Walker, “In-situ stress measurements and stress change monitoring to monitor overburden caving behaviour and hydraulic fracture pre-conditioning,” *International Journal of Mining Science and Technology*, vol. 26, no. 1, pp. 103–110, 2016.

[8] A. J. White, M. O. Traugott, and R. E. Swarbrick, “The use of leak-off tests as means of predicting minimum in-situ stress,” *Petroleum Geoscience*, vol. 8, no. 2, pp. 189–193, 2002.

[9] H. Xu, S. Sang, J. Yang et al., “In-situ stress measurements by hydraulic fracturing and its implication on coalbed methane development in Western Guizhou, SW China,” *Journal of Unconventional Oil and Gas Resources*, vol. 15, pp. 1–10, 2016.

- [10] B. Haimson and C. Fairhurst, "Initiation and extension of hydraulic fractures in rocks," *Society of Petroleum Engineers Journal*, vol. 7, no. 03, pp. 310–318, 2013.
- [11] W. Medlin and L. Masse, "Laboratory investigation of fracture initiation pressure and orientation," *Society of Petroleum Engineers Journal*, vol. 19, no. 02, pp. 129–144, 2013.
- [12] J. R. Rice and M. P. Cleary, "Some basic stress diffusion solutions for fluid saturated elastic porous media with compressible constituents," *Reviews of Geophysics*, vol. 14, no. 2, pp. 227–241, 1976.
- [13] A. E. Scheidegger, "Stresses in the Earth's crust as determined from hydraulic fracturing data," *Geol. Bauwes*, pp. 45–53, 1962.
- [14] I. Ocaik and S. E. Seker, "Estimation of elastic modulus of intact rocks by artificial neural network," *Rock Mechanics and Rock Engineering*, vol. 45, no. 6, pp. 1047–1054, 2012.
- [15] X. T. Feng, H. B. Zhao, and S. J. Li, "A new displacement back analysis to identify mechanical geo-material parameters based on hybrid intelligent methodology," *Int. J. Num. Anal. Methods Geomech*, pp. 28–1141, 2004.
- [16] G. Gioda and L. Jurina, "Numerical identification of soil structure interaction pressures," *International Journal for Numerical and Analytical Methods in Geomechanics*, pp. 33–56, 1981.
- [17] S. Li, H. Zhao, Z. Ru, and Q. Sun, "Probabilistic back analysis based on Bayesian and multi-output support vector machine for a high cut rock slope," *Engineering Geology*, vol. 203, pp. 178–190, 2016.
- [18] P. Oreste, "Back-analysis techniques for the improvement of the understanding of rock in underground constructions," *Tunnelling and Underground Space Technology*, vol. 20, no. 1, pp. 7–21, 2005.
- [19] B. Pichler, R. Lackner, and H. A. Mang, "Back analysis of model parameters in geotechnical engineering by means of soft computing," *International Journal for Numerical Methods in Engineering*, vol. 57, no. 14, pp. 1943–1978, 2003.
- [20] S. Sakurai and K. Takeuchi, "Back analysis of measured displacements of tunnels," *Rock Mechanics and Rock Engineering*, vol. 16, no. 3, pp. 173–180, 1983.
- [21] G. D. Cooper, S. G. Nelson, and M. D. Schopper, "Improving fracturing design through the use of a on-site computer system," in *Proceedings of the SPE12063 presented at the 1983 SPE Annual Technical Conference Exhibition*, San Francisco, CA, 1983.
- [22] H. Zhao and S. Yin, "Inverse analysis of geomechanical parameters by the artificial bee colony algorithm and multi-output support vector machine," *Inverse Problems in Science and Engineering*, vol. 24, no. 7, pp. 1266–1281, 2016.
- [23] M. K. Hubbert and D. G. Willis, "Mechanics of hydraulic fracturing," *Trans. AIME*, vol. 210, pp. 153–163, 1957.
- [24] E. Detournay and H. D. Cheng, "Poroelastic response of a borehole in a non-hydrostatic stress field," *Int. J. Rock Mech. Min. Sci. Geomech. Abstr*, pp. 171–182, 1988.
- [25] D. Tuia, J. Verrelst, L. Alonso, F. Perez-Cruz, and G. Camps-Valls, "Multioutput support vector regression for remote sensing biophysical parameter estimation," *IEEE Geoscience and Remote Sensing Letters*, vol. 8, no. 4, pp. 804–808, 2011.
- [26] A. M. Á. Meza, G. D. Santacoloma, C. D. Acosta Medina, and G. C. Domínguez, "Parameter selection in least squares-support vector machines regression oriented, using generalized cross-validation," *DYNA (Colombia)*, vol. 79, no. 171, pp. 23–30, 2012.
- [27] D. Karaboga, "An idea based on honey bee swarm for numerical optimization," Technical Report-TR06, Erciyes University, Engineering Faculty, Computer Engineering Department, 2005.

Research Article

Real-Time Pore Pressure Detection: Indicators and Improved Methods

Jincai Zhang^{1,2} and Shangxian Yin²

¹Geomech Energy, Houston, TX, USA

²North China Institute of Science and Technology, Yanjiao, Beijing, China

Correspondence should be addressed to Jincai Zhang; zhangjincai@yahoo.com and Shangxian Yin; yinshx03@126.com

Received 6 June 2017; Accepted 1 August 2017; Published 27 September 2017

Academic Editor: Fengshou Zhang

Copyright © 2017 Jincai Zhang and Shangxian Yin. This is an open access article distributed under the Creative Commons Attribution License, which permits unrestricted use, distribution, and reproduction in any medium, provided the original work is properly cited.

High uncertainties may exist in the predrill pore pressure prediction in new prospects and deepwater subsalt wells; therefore, real-time pore pressure detection is highly needed to reduce drilling risks. The methods for pore pressure detection (the resistivity, sonic, and corrected d -exponent methods) are improved using the depth-dependent normal compaction equations to adapt to the requirements of the real-time monitoring. A new method is proposed to calculate pore pressure from the connection gas or elevated background gas, which can be used for real-time pore pressure detection. The pore pressure detection using the logging-while-drilling, measurement-while-drilling, and mud logging data is also implemented and evaluated. Abnormal pore pressure indicators from the well logs, mud logs, and wellbore instability events are identified and analyzed to interpret abnormal pore pressures for guiding real-time drilling decisions. The principles for identifying abnormal pressure indicators are proposed to improve real-time pore pressure monitoring.

1. Introduction

Many deep sedimentary formations have abnormal pore fluid pressures or overpressures. Abnormal pore pressures may cause serious drilling incidents (e.g., fluid influx, kicks, and even blowouts), if these abnormal pressures are not accurately predicted in predrill stage or detected in real-time drilling. Pore pressure analysis mainly includes three aspects, that is, predrill pore pressure prediction, real-time pore pressure detection, and postwell analysis. If predrill pore pressure prediction has big uncertainty, real-time pore pressure detection is needed to update predrill pore pressure prediction and advise drilling operations in real-time to adjust the mud weight to reduce drilling risks. Real-time pore pressure detection generally relies on the following available data for analyses and interpretations when they are available: logging-while-drilling (LWD), measurement-while-drilling (MWD), measured pore pressures, drilling parameters, and mud logging data.

2. Methods of Real-Time Pore Pressure Detection

Different methods for pore pressure prediction have been proposed based on resistivity, sonic transit time (or interval velocity), and other petrophysical data (e.g., [1–10]). This paper will not focus on pore pressure prediction but on real-time detection. For real-time pore pressure detection, the pore pressure calculating methods need to be adapted to fit the real-time needs. In the following sections, methods for real-time pore pressure detection are implemented based on the shale properties with improved normal compaction trend lines.

2.1. Resistivity Method. Resistivity logging data can be used to calculate pore pressure in shales. Eaton [2] proposed the following empirical equation to estimate pore pressure:

$$P_{pg} = OBG - (OBG - P_{ng}) \left(\frac{R}{R_n} \right)^n, \quad (1)$$

where P_{pg} is the pore pressure gradient; P_{ng} is the normal pore pressure gradient; R is the measured shale resistivity; OBG is the overburden stress gradient; R_n is the shale resistivity in the normal pressure condition; n is an exponent (may vary from 0.6 to 1.5 and normally $n = 1.2$).

To use Eaton's resistivity method for real-time pore pressure calculation, we need to determine the shale resistivity in the normal compaction condition. The following depth-dependent equation can be used to calculate the normal compaction trend (NCT):

$$R_n = R_0 e^{bZ}, \quad (2)$$

where R_0 is the resistivity value when $Z = 0$; b is a compaction parameter; Z is the true vertical depth below the mudline (i.e., the surface level for onshore drilling or the sea floor in offshore drilling).

Determining the NCT is critically important for the real-time pore pressure detection. A case study [9] is used here to illustrate how to obtain the depth-dependent NCT parameters for real-time applications (Figure 1). We firstly calculate the NCT based on (2) and then estimate the pore pressure from Eaton's equation (see (1)), as shown in Figure 1. The calculated pore pressure needs to be calibrated to the measured pore pressure data (e.g., the RTF in Figure 1). Based on this calibration we can adjust the parameters R_0 and b . When the calculated pore pressure matches the measured pore pressure, it indicates that the NCT (i.e., the parameters R_0 and b) is applicable for the real-time pore pressure detection in this area. Certainly, this NCT is also needed to adjust based on the pore pressure indicators in the real-time drilling, which will be discussed later. Therefore, prior to the real-time pore pressure detection, a critical step is to determine the NCT from the offset wells. The formation resistivity may be affected by salinity, anisotropy, and temperature; therefore, corrections are needed when these effects are profound.

It should be noted that the NCT may have different set of calibration parameters for different offset wells. In this case, the calibration parameters in the closer well or wells should be used for the real-time well and then be adjusted based on the pore pressure indicators shown in the real-time drilling.

2.2. Sonic Velocity Method. Pore pressure gradient can also be calculated from the sonic method [11]:

$$P_{pg} = \text{OBG} - (\text{OBG} - P_{ng}) \left(\frac{\Delta t_n}{\Delta t} \right)^m, \quad (3)$$

where Δt is the transit time in shales obtained from the well log; Δt_n is the transit time in shales at the normal pressure condition; m is an exponent, and normally the exponent $m = 3$ can be applied in the case that the overpressure was generated by undercompaction without any secondary mechanism of pore pressure generation.

The normal compaction trend or the transit time (Δt_n) in normal pressure condition needs to be obtained in order to apply Eaton's sonic method. The following depth-dependent NCT equation can be used [9]:

$$\Delta t_n = \Delta t_m + (\Delta t_{ml} - \Delta t_m) e^{-cZ}, \quad (4)$$

where Δt_m is the transit time in the shale matrix; Δt_{ml} is the transit time in the mudline (e.g., the transit time value when $Z = 0$); Z is the depth below the mudline; c is the compaction parameter.

Alternatively, other sonic methods can be used for pore pressure calculation (e.g., [5, 9]). The following sonic method can also be used to calculate pore pressure gradient [9]:

$$P_{pg} = \text{OBG} - (\text{OBG} - P_{ng}) \frac{\ln(\Delta t_{ml} - \Delta t_m) - \ln(\Delta t - \Delta t_m)}{cZ}. \quad (5)$$

The geothermal gradient fuels the clay diagenesis reaction that takes place as the clay minerals of smectites transform to illite (e.g., [12, 13]). Therefore, shales in some areas (e.g., the Gulf of Mexico shelf) have different clay minerals as the burial depth increases. For example, the shale in a certain basin is mainly composed of smectite at a shallower depth, but the illite dominated at a deeper depth. The smectite to illite conversion (*S-I*) causes abnormal pressures [14]. Therefore, the normal compaction trends of the transit time should be different at different depths to account for the *S-I* conversion. Equation (4) can be used to obtain the multisegmental NCTs which have different compaction parameters (c_s and c_i), as shown in Figure 2; that is,

$$\text{for smectite: } \Delta t_s = \Delta t_m + (\Delta t_{ml} - \Delta t_m) e^{-c_s Z}$$

$$\text{for illite: } \Delta t_i = \Delta t_m + (\Delta t_{ml} - \Delta t_m) e^{-c_i Z}$$

$$\text{for a linear } S-I \text{ transition: } \Delta t_t = ((Z - Z_1)\Delta t_i + (Z_2 - Z)\Delta t_s)/(Z_2 - Z_1),$$

where c_s , c_i are the compaction parameters for the smectite and illite, respectively; Z_1 is the depth of the smectite; Z_2 is the depth of the illite; Z_1 and Z_2 can be determined from mineral test results in offset wells or from the regional temperature profile which is associated with *S-I* transitions.

Again, prior to applying the sonic method to the real-time detection, the normal compaction trend (NCT) needs to be obtained from (4) and (5) and to be calibrated to the offset well data. Then, this NCT is ready for the real-time application.

2.3. Corrected *d*-Exponent Method. It has been found that the rate of penetration (ROP) increases when drilling into an undercompacted shale or a shale with an abnormal pore pressure. That is, an increased rate of penetration may be indicative of an abnormal increase in pore pressure. However, there are also many other factors affecting ROP, such as the lithology, differential pressure, weight of the bit, rotating speed, torque, bit type, and change of bits. Therefore, the ROP is too random to be used as a detection method for abnormal pore pressure [15]. Instead, *d*-exponent can be used as one of the real-time pore pressure detection methods. Jorden and Shirley [16] proposed the following *d*-exponent equation:

$$D_x = \frac{\log(\text{ROP}/60N)}{\log(12W/10^6D)}, \quad (6)$$

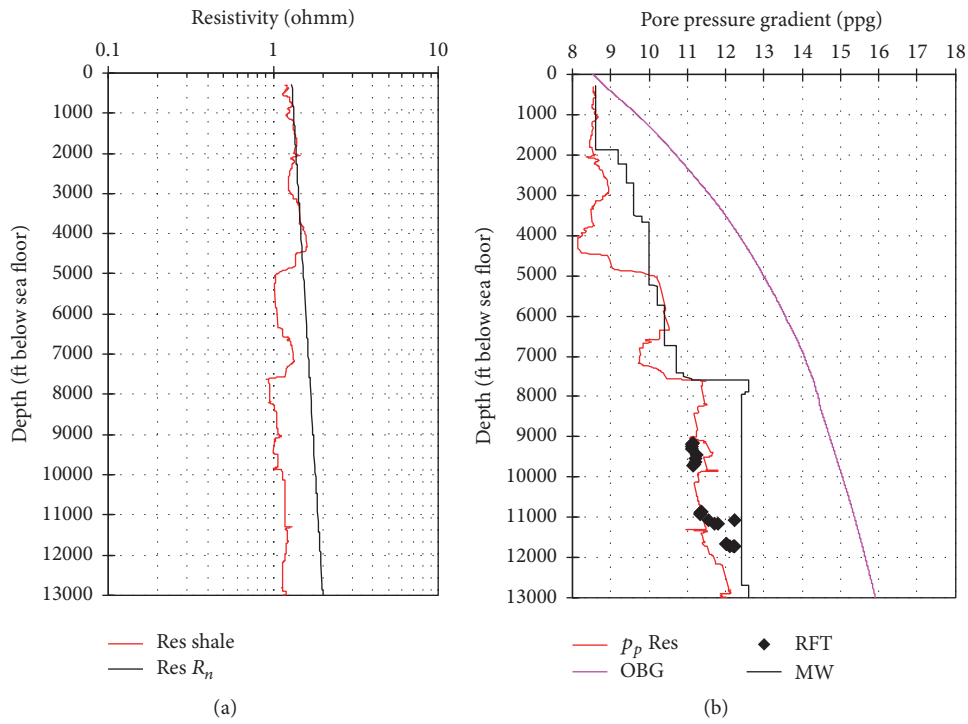


FIGURE 1: Measured and calculated pore pressure gradient and NCT calculated from the resistivity method ((1)-(2)).

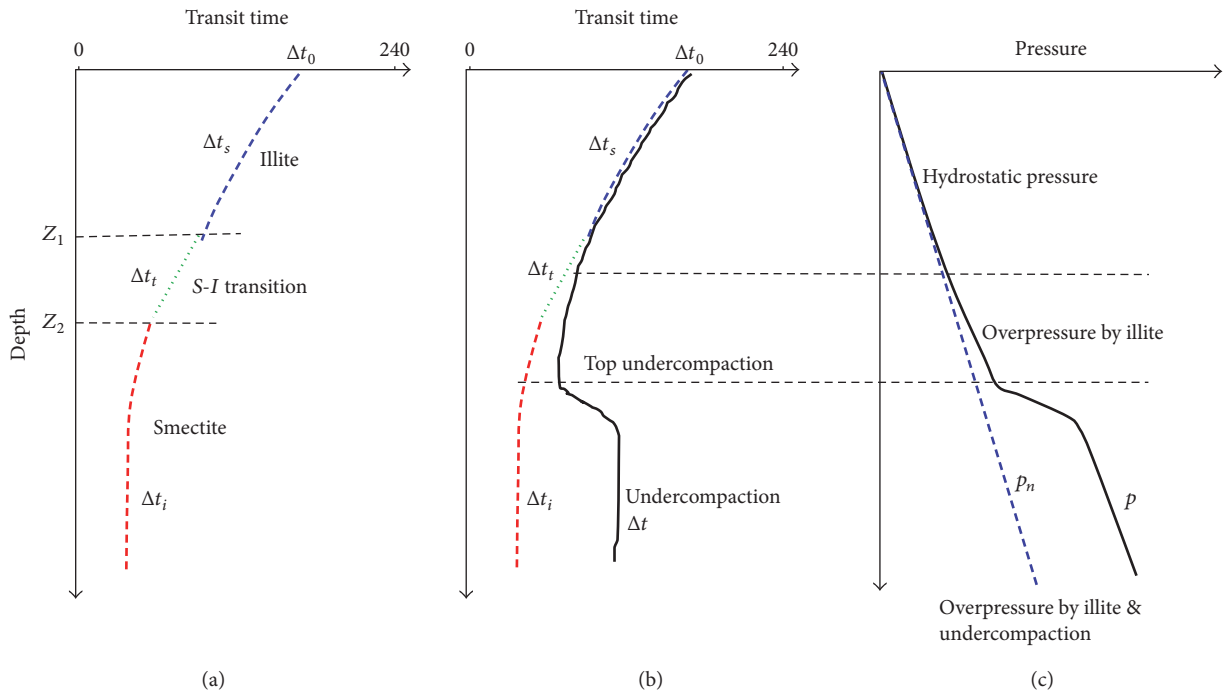


FIGURE 2: NCTs in the transit time versus the depth for the shale composed of the smectite and illite. (a) Composite NCT; (b) composite NCT and transit time; (c) overpressures caused by smectite to illite conversion and undercompaction.

where D_x is the d -exponent equation; ROP is the rate of penetration (ft/hr); N is the rotary speed (rpm); W is the weight on bit (lbs); D is the hole diameter (inches).

The d -exponent is highly dependent on the differential pressure, that is, the difference of mud pressure and pore pressure. If mud weight is changed, then the d -exponent will change. Therefore, d -exponent needs to be corrected to reflect the change of mud weight. Rehm and McClendon [17] suggested the following correction:

$$D_{xc} = D_x \frac{P_{ng}}{P_{MW}}, \quad (7)$$

where D_{xc} is the corrected d -exponent equation; P_{MW} is the downhole mud weight, and the equivalent circulating density (ECD) is recommended for P_{MW} in pore pressure calculation; P_{ng} is the hydrostatic pore pressure gradient.

Using the corrected d -exponent, the empirical equation [11] for pore pressure estimate can be written in the following form, which is similar to the resistivity method:

$$P_{pg} = OBG - (OBG - P_{ng}) \left(\frac{D_{xc}}{D_n} \right)^n, \quad (8)$$

where D_n is the shale d -exponent in the normal pressure condition; n is the exponent, and normally $n = 1.2$.

It should be noted that the d -exponent method initially was used for the rolling cutter bits. However, the PDC bits are widely used in the drilling industry. Because the PDC-type bits cut rocks with a shear cutting action instead of the chipping action that Jordan and Shirley [16] assumed in their chip-hold down model, the corrected d -exponent plots will differ from tricone or bicone bits in the same formation. Therefore, a careful calibration is needed prior to real-time applications of the corrected d -exponent method.

Determining normal d -exponent (D_n) is a key step for using this method to calculate pore pressure in the real-time. We propose the following depth-dependent equation of the NCT for the corrected d -exponent:

$$D_n = D_0 + dZ, \quad (9)$$

where D_0 is the shale d -exponent in the mudline; d is the calibration parameter; Z is the depth below the mudline. It should be noted that if the hole size, weight of bit, and other parameters change, the normal compaction trend may change.

For a normally compacted formation, porosity usually has an exponential relationship with depth [18]. Therefore, the following depth-dependent exponential equation of the NCT can also be used for the corrected d -exponent:

$$D_n = D_0 e^{d_e Z}, \quad (10)$$

where d_e is a calibration constant.

In the same lithology, the corrected d -exponent gives a good indication of the state of compaction and pore pressure [15]. To reduce lithology effect in different lithologies, we only use the corrected d -exponents in shales for the pore pressure detection. Figure 3 presents a shale gas well for

applying the corrected d -exponent method to estimate pore pressure by using the proposed depth-dependent NCT. After calibrations, this NCT can be used for the real-time pore pressure detection.

The big advantage of this method is that the parameters needed for calculation are obtained or measured from the drill bit (the BHA). Therefore, the pore pressure obtained from the corrected d -exponent method reflects the pore pressure near the bottom of the hole. The other advantage is that it can be used even in the case where there is no LWD data. It should be noted that this method is not applicable for the controlled drilling (e.g., controlled ROP). Based on the limitation of the d -exponent (highly dependent on ROP, lithology, bits, and hole size), this method should be associated with other methods for the real-time pore pressure detection.

3. Abnormal Pore Pressure Indicators and Detection in Real-Time Drilling

Well influx (including kicks, blowouts) and mud losses are potential risks for drilling operations, particularly for the well with a narrow mud weight window. Real-time pore pressure monitoring can constrain and update the predrill model to reduce uncertainties of pore pressure prediction and reduce drilling risks. Real-time pore pressure detection can be performed either on the rig site or remotely with the access of the real-time data. The real-time data for pore pressure detection mainly include LWD resistivity and sonic transit time, mud gas log, and drilling parameters (for calculating D_{xc}). The pore pressure measurement while drilling is important for calibrating real-time pore pressure model. The other calibration data includes mud logging data and drilling monitoring data, such as gas monitoring (total gas, trip gas, and connection gas), ROP, PWD (pressure while drilling), ECD (equivalent circulation density), ESD (equivalent static density) monitoring, hole fill monitoring, torque and drag, cuttings and cavings, well flow, and mud losses. Abnormal changes in these data may be related to an abnormal pore pressure, but they could also be caused by other factors (e.g., changes of lithology, salinity, temperature, hole size, and mud weight). Therefore, it is necessary to use all available data to analyze and interpret the indicators of abnormal pore pressure.

3.1. Procedures of Real-Time Pore Pressure Detection. For real-time pore pressure detection and monitoring, the following steps can be performed:

- (1) Construct predrill petrophysical and pore pressure model as introduced in Section 2 and calibrate the predrill model to offset wells if they are available. The model includes methods of resistivity, sonic, D_{xc} , and so on. The model should include uncertainties and address drilling challenges and potential issues.
- (2) Apply the model to the real-time well. It particularly needs to have a calibrated NCT for each method.
- (3) Connect the model to real-time data (e.g., use ConnectML WITS and ConnectML WITSML to connect

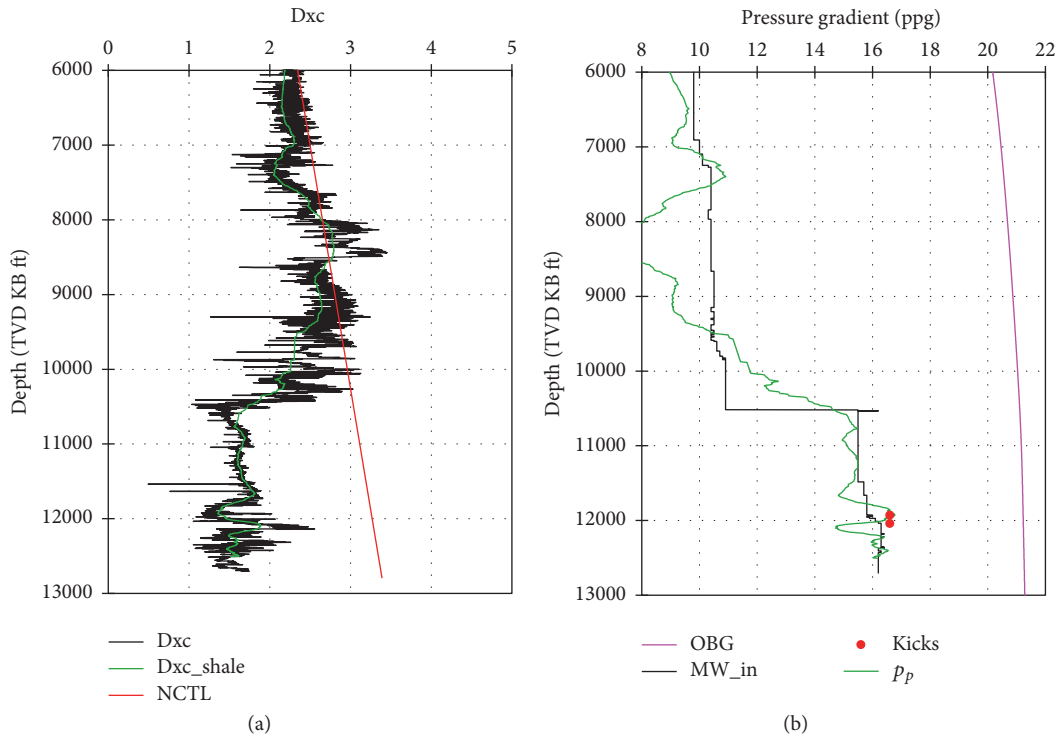


FIGURE 3: Pore pressure obtained from the corrected d -exponent method with depth-dependent compaction trend line in a shale gas well. (a) plots the corrected d -exponent in shale and the normal corrected d -exponent calculated from (9) with $D_0 = 1.5$ and $d = 0.00015$. (b) shows the overburden gradient, mud weight, kicks, and pore pressure gradient calculated from the corrected d -exponent (see (8)).

- LWD and MWD tools), so that the real-time data can be automatically loaded to the model. The model can then automatically calculate pore pressures based on the NCT using the real-time LWD and MWD data.
- (4) Compare the real-time calculated pore pressure to downhole mud weight (ESD, ECD); to determine if the mud weight is sufficient, particularly it needs to identify whether or not the mud weight is less than the pore pressure gradient. Only comparing the real-time calculated pore pressure gradient to the mud weight is not enough to conclude an underbalanced drilling status. Therefore, it also needs to combine to other real-time indicators of pore pressures.
 - (5) Adjust the models (mainly NCTs) based on the following data if they are available: real-time pore pressure measurement, well influx, mud pit gains, kicks, mud gas data, mud losses, drilling parameters, and borehole instability events (e.g., cavings, torque, fills, and pack-offs).
 - (6) Alert and inform the rig for action when the pore pressure is lower (underbalanced) or close to the downhole mud weight.
 - (7) Liaise with technical expert group on all issues related to unplanned drilling operations, ECD, and pore pressures.
 - (8) Make postwell knowledge capture and transfer within the appropriate organizations and systems.

The real-time monitoring should ensure that

- (1) pore pressure is continuously monitored and indicators of the abnormal pressures are identified;
- (2) real-time pore pressure methods, estimates, and updates are discussed routinely with all involved monitoring parties to provide a consistent interpretation to the rig operations;
- (3) abnormal pore pressure events are identified as soon as possible;
- (4) the abnormal events, including significant observations, changes, or updates in pore pressure estimates, if they are occurring or imminent, need to be communicated to the operations (e.g., operation geologist and drilling engineer) quickly;
- (5) the appropriate actions of operations (e.g., raising mud weight when the pore pressure gradient is lower than the downhole mud weight) are taken quickly.

3.2. Indicators from LWD Logs. The primary methods for real-time pore pressure calculation are the well-logs-based methods (i.e., from LWD resistivity and sonic transit time) as described in the previous section, and the resistivity log is normally available in the real-time. General rule for LWD-based prediction is that the decrease in resistivity or increase in transit time (which is not caused by the hydrocarbon presence) compared to the NCT is indicative of pore pressure increase. The normal compaction trends (NCT) are very

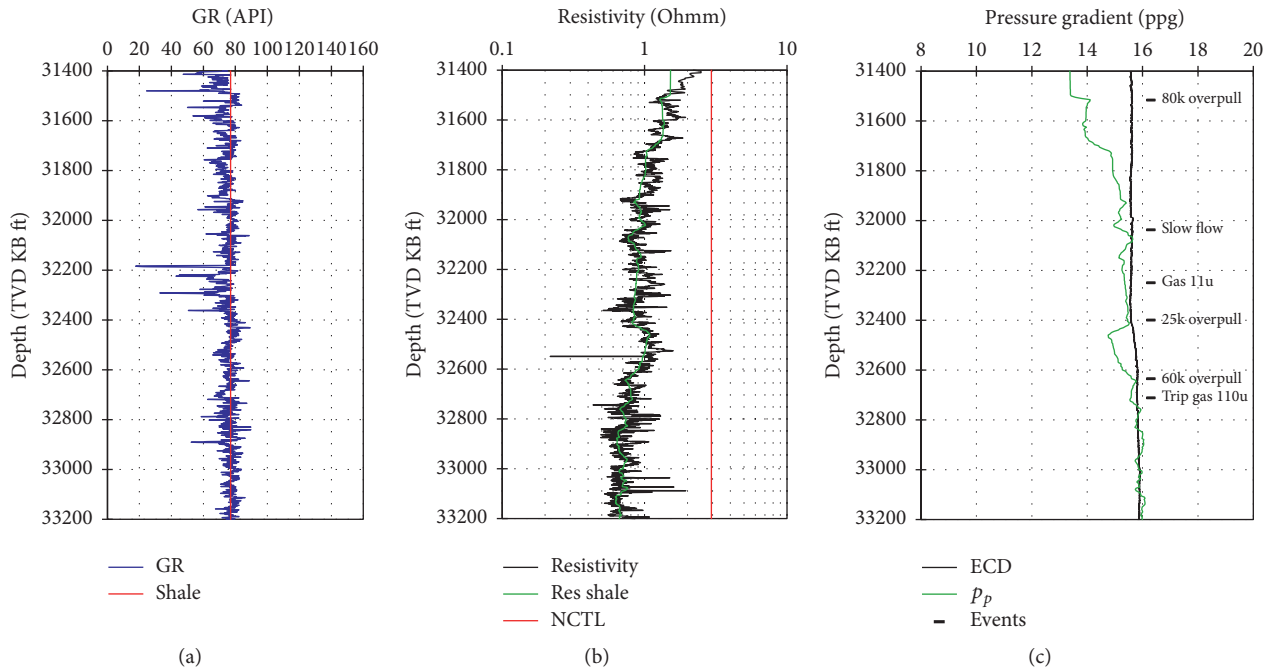


FIGURE 4: Real-time pore pressure detection from LWD resistivity. (a) shows the real-time gamma ray and shale lines; (b) presents the resistivity (red curve), picked shale resistivity (green curve), and NCT (red line); (c) plots the real-time calculated pore pressure (green curve), ECD, and drilling events (overpull, well influx, and mud gas indicators).

critical for applying these methods. The NCT should be properly calibrated from the offset wells prior to drilling. A fine adjustment of the NCT may be needed in real-time based on real-time pore pressure indicators. It should be noted that the LWD sensors have certain distances behind the bit (e.g., 20–100 ft, depending on the tools and BHA). Normally, the resistivity tool is closer to the drill bit than the sonic tool. Even using the resistivity data, the detected pore pressure from LWD logs is not the one at the bottom hole. Therefore, the log-based methods should be combined to other methods (e.g., Dxc method, in which the parameters are obtained from the bit measurements) to determine the pore pressure at the bit.

Figure 4 presents an example of real-time pore pressure monitoring from LWD resistivity in a deepwater well in the Gulf of Mexico, in which the NCT is obtained from the offset wells by using (2) and the pore pressure is calculated from (1) based on the NCT and real-time shale resistivity. The pore pressure result was used to guide drilling engineers for real-time mud weight adjustments. Wellbore fluid flow and trip gas below 32000 ft in Figure 4 were due to a lower downhole MW (or ECD) than the formation pore pressure. The real-time calculated pore pressure was close to or higher than the ECD (Figure 4), meaning, in the permeable formation, that the formation fluid flow into the wellbore occurs. This is consistent with the abnormal pressure indication (well flow and trip gas show) observed in real-time.

3.3. Direct Indicators of Pore Pressure: Well Influx and Mud Losses. Well flow, mud pit gain because of well influx, and kicks are, normally, direct indicators of a higher pore pressure

than the applied mud weight. In these cases, increasing the mud weight is needed. It should be noted that in these cases a well may not have fluid flow if the formations are impermeable (e.g., shales). In the impermeable formations, other indicators of underbalanced drilling status may be noticeable, such as wellbore instability (e.g., tight hole, caving, and pack-off). These indicators need to be analyzed to determine whether or not it is in underbalanced drilling status. If mud losses or lost circulation is observed, it normally indicates that the applied mud weight is higher than the fracture gradient (excluding mud losses into open fractures or vuggy zones); more details can be found in Zhang and Yin [19]; therefore, it may need to reduce the mud weight. When the hole ballooning occurs, it normally indicates that the mud weight is very close to the fracture gradient.

3.4. Indicators from the Mud Gas. Mud gas is an important indicator of the abnormal pore pressure in drilling operations, particularly in shale formations because of lack of good methods to measure the pore pressure in the shale. If large amounts of formation gas flow into the wellbore, the downhole mud weight is reduced because of the nature of low density of gas. This is “gas cut mud,” indicating that the actual density of the mud coming out of the hole is less than the density of the mud being pumped into the hole. If the gas influx is large, the gas cut mud can cause a marked reduction of the downhole mud weight, and this could result in a gas kick or blowout. Therefore, the gas cut mud is an important indicator of the abnormal pore pressure. Connection and total gas measurements in mud logging have been used qualitatively for decades in drilling

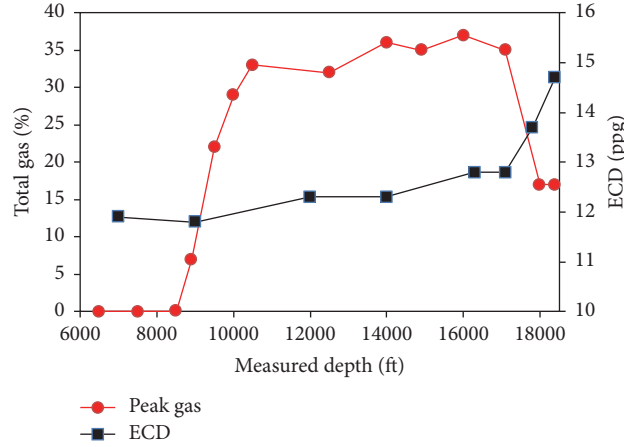


FIGURE 5: The total gas versus the downhole mud weight in a horizontal well (the estimated pore pressure from DFIT is 14.6 ppg).

oil and gas wells to identify overbalanced, underbalanced, or near underbalanced pressure conditions. Figure 5 plots the relationship of the downhole mud weight (ECD) and the peak total gas in a shale gas formation for an underbalanced drilling. The well was drilled horizontally when the borehole reached the shale gas formation at the vertical depth of 8500 ft. Figure 5 shows that when the ECD was at 12–12.7 ppg, the maximum total gas reached 37%. When the ECD was increased and exceeded the pore pressure gradient (14.6 ppg), the total gas reduced markedly to 17%. Therefore, mud gas data from mud logs can be used as an indicator of the abnormal pore pressure. General rule for the mud gas is that an increase in the mud gas relative to the background gas is an indication of pore pressure increasing. The drawback of this method is that mud gas data have a lag time behind the bit. That is, they are only available after the mud circulating the gas from the bottom hole (or the gas-bearing formation) to the surface, and the lag time can have several hours of delay depending on the hole depth. Six principles were proposed to quantitatively interpret mud gases relative to formation pore pressure [20]. These principles for total gas displays are restated as follows:

- (i) normal background and no reported connection gases, then $P_p < \text{Swab} < \text{ESD} < \text{ECD}$,
- (ii) normal background and sporadic connection gases, then $\text{Swab} < P_p < \text{ESD} < \text{ECD}$,
- (iii) normal background and consistent connection gases, then $\text{Swab} < \text{ESD} < P_p < \text{ECD}$,
- (iv) elevated background and either sporadic or consistent connection gases, then $\text{Swab} < \text{ESD} < \text{ECD} < P_p$,
- (v) greatly elevated background and difficult to recognize connection gases, then $\text{Swab} < \text{ESD} < \text{ECD} \ll P_p$,
- (vi) total gas drops in response to an ECD increase, then $P_p > \text{ECD}$,

where Swab is the downhole swab pressure resulting from the drill string movement; P_p is the pore pressure gradient; ESD is the equivalent static mud density; ECD is the equivalent circulating mud density.

3.5. Pore Pressure Calculation from the Connection Gas. Since mud gas is highly related to the pore pressure, we propose a new relationship to estimate pore pressure from the mud gas data based on Darcy's law. If the formation gas flows from the formation into the wellbore, then the formation pore pressure should be greater than the downhole mud pressure. We assume that the gas flow rate and the pressures follow Darcy's law; that is, they have the following linear relationship:

$$q \propto \frac{kA}{\mu} (p_p - p_{MW}), \quad (11)$$

where q is the gas flow rate; k is the permeability; A is the cross-sectional area of the flow; μ is the fluid viscosity; p_p is the formation pore pressure; p_{MW} is the downhole mud pressure.

Not only is gas flow dependent on differential pressure as described by Darcy's law, but it may be also dependent on gas absorption and other factors. Here we adopt a simplified approach; that is, use (11) to describe gas flow from the formation into the wellbore. Assuming the connection gas is the gas flow, (11) can be simplified as the following form:

$$p_p = aQ_c + p_{MW}, \quad (12)$$

where Q_c is the connection gas; a is a calibration parameter.

If the total gas is very high, the connection gas may not be observed; however, elevated background gas may happen, and this indicates that the pore pressure is greater than the downhole mud pressure. Therefore, we can use the following equation to estimate pore pressure:

$$p_p = cQ_b + p_{MW}, \quad (13)$$

where Q_b is the elevated background gas; c is a calibration parameter.

Figure 6 presents a case of pore pressure calculation from the connection gas in a gas-bearing formation using (12). When the calibration data are available, constant a or c can be obtained; therefore, pore pressure can be estimated using the connection gas or elevated background gas.

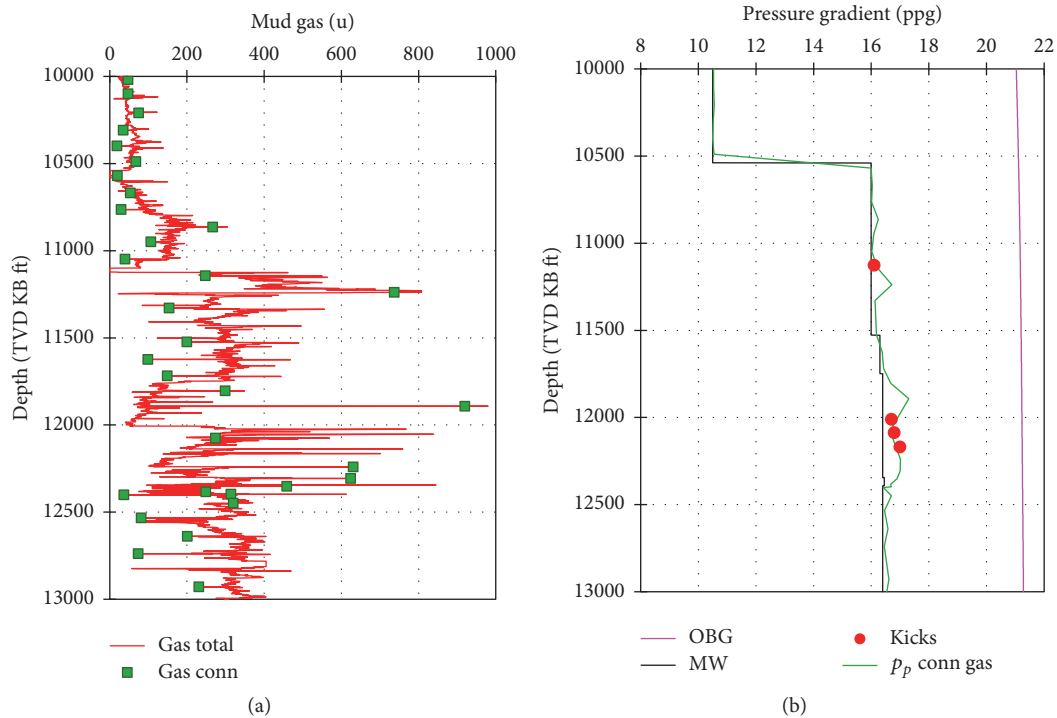


FIGURE 6: The pore pressure estimated from the connection gas using (12) in a shale gas well. (a) shows the total gas and connection gas (Gas conn); (b) presents the calculated pore pressures compared to the kicks, mud weight (MW), and overburden stress (OBG).

It should be noted that (12) and (13) describe the case where the downhole mud weight is lower than the pore pressure; that is, the borehole has gas influx from the formation (e.g., connection gas). Therefore, (12) and (13) can be applicable only if the downhole mud weight is lower than the pore pressure. Since natural gas is a compressible fluid, (11)–(13) are the approximate solutions for estimating pore pressures, and the calibration from other pore pressure methods or the observed data is needed. It should also be noted that the total gas and connection gas have lag time (depending on the depth). The lag time is the time from the gas coming out the formation at the bottom hole to be circulated with the mud to the gas trap (gas collector) on the drilling deck, and this lag time needs to be corrected for the pore pressure estimate.

3.6. Indicators from PWD. Identifying whether an underbalanced drilling status occurs or not is a key technique for real-time pore pressure detection. In the real-time measurements, the downhole mud weight data (ECD or ESD) can be obtained. The underbalanced drilling status can be identified through comparing the pore pressure gradient to the mud weight. A kick can be identified from the pressure while drilling (PWD) measurements—an abrupt increase in downhole pressure and temperature because the formation fluid flowing into the wellbore has a higher pressure than the mud pressure and a higher temperature than the mud temperature. Figure 7 shows that a shale gas well was drilled with a constant surface mud weight and a near-constant

downhole mud weight (ECD) initially. However, the PWD increases rapidly owing to a kick, in which the formation fluid flows into wellbore with a much higher formation pressure than the downhole mud pressure and a much higher formation temperature than the downhole mud temperature. Therefore, well influx can be identified through analyzing the downhole measured mud pressure and temperature.

3.7. Indicators from Wellbore Instability. When the mud weight is inappropriate, wellbore instability events occur while drilling, which can help to diagnose the overpressure and to adjust mud weight in real-time drilling operations. Wellbore instability can be classified into two categories: shear and tensile failures. When the downhole mud weight is less than the shear failure gradient (SFG, or borehole collapse pressure gradient), the wellbore experiences shear failure [21, 22]. Shear failure is mainly caused by the condition in which the applied mud weight is lower than the SFG. The indicators of shear failures while drilling include hole enlargement (borehole breakout), hole closure, tight hole (overpull), high torque, hole fill after trip, hole bridging, hole pack-off, and hole collapse [23]. Some of these indicators may be caused by a swelling shale when the water-based mud is used because of the chemical reaction between the mud and the shale formation. Therefore, it needs to identify the causes of the failures.

Here we use a vertical well as an example to illustrate the relationship of wellbore instability and pore pressure. Based on Mohr-Coulomb failure criterion, the minimum

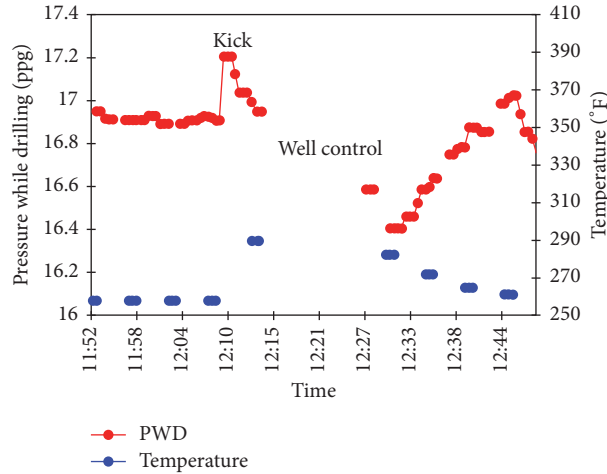


FIGURE 7: Well influx/kick detected from pressure while drilling showing an abrupt increase in measured downhole pressure (PWD or ECD) and temperature.

mud weight to avoid borehole shear failure can be obtained from the following equation [21]:

$$p_m = \frac{1 - \sin \varphi}{2} (3\sigma_H - \sigma_h - \text{UCS}) + p_p \sin \varphi, \quad (14)$$

where p_m is the minimum mud pressure or collapse (shear failure) pressure, φ is the angle of friction of the rock; UCS is the rock uniaxial compressive strength; σ_H , σ_h are the maximum and minimum horizontal stresses, respectively. The horizontal stresses are most important parameters for analyzing wellbore stability, which can be obtained from either field measurements or calculations (e.g., [24]).

Equation (14) shows that the shear failure is directly related to the pore pressure; a higher pore pressure needs a heavier mud weight to keep the wellbore from the shear failure. Therefore, wellbore instability can be used as an indicator of an overpressured formation.

Tensile failure, however, occurs when the mud pressure exceeds the capacity of the near-wellbore rock to bear tensile stress. If the downhole mud weight is higher than the fracture gradient, the formation will be fractured to create hydraulic fractures (or drilling-induced tensile fractures). Real-time indicators of drilling-induced tensile failures include hole ballooning, drilling mud losses, and lost circulation. Reducing mud weight, adding lost circulation materials (LCM), or applying wellbore strengthening technique are possible cures for the drilling-induced tensile failures.

3.8. Indicators from Abnormal Cuttings. General rule is that the insufficient mud weight produces more and larger cuttings. There are generally four types of cuttings—normal cuttings, cuttings from preexisting fractures, cuttings owing to underbalanced drilling, and cuttings owing to shear failures.

(1) *Normal Cuttings.* If the mud weight is appropriate, that is, higher than pore pressure and collapse pressure but lower than the fracture gradient, the wellbore is in a good condition.

In this case, normal cuttings are generated with PDC cutting marks when a PDC bit is used, as shown in Figure 8(a).

(2) *Cuttings from Preexisting Fractures.* In a formation with preexisting fractures or in a faulted section, the rock may have a lower compressive strength and lower fracture gradient. In this case, it may generate blocky cuttings in which the naturally fractured planes may be observed; therefore, mud losses probably occur in the preexisting fractures. Figure 8(b) presents a picture of blocky cuttings in a subsalt formation where mud losses occurred.

(3) *Cuttings Owing to Underbalanced Drilling.* If the downhole mud weight is less than the formation pore pressure gradient, the wellbore experiences splintering failure or spalling. In this case, spiky and concaved cavings are generalized, as shown in Figure 9, and wellbore collapse and fluid kick (if a permeable formation is encountered) may occur.

(4) *Cuttings Owing to Shear Failures.* Shear failures cause angular or splintered cavings in the wellbore. In this case, the rock failure of the wellbore is similar to a triaxial compressive core test, where angular or splintered rock pieces are formed, as shown in Figure 10.

3.9. Summary of Real-Time Indicators for Abnormal Pore Pressures. As stated in the previous sections, Table 1 summarizes the indicators of abnormal pore pressures in the real-time monitoring. These indicators can be used to identify abnormal pore pressures and to calibrate and update the real-time pore pressure models.

4. Conclusions

For the real-time pore pressure detection, a real-time pore pressure model needs to firstly be built based on all available data in offset wells, and then all real-time abnormal pressure indicators need to be incorporated to calibrate the model. The real-time pore pressure model mainly includes LWD-based

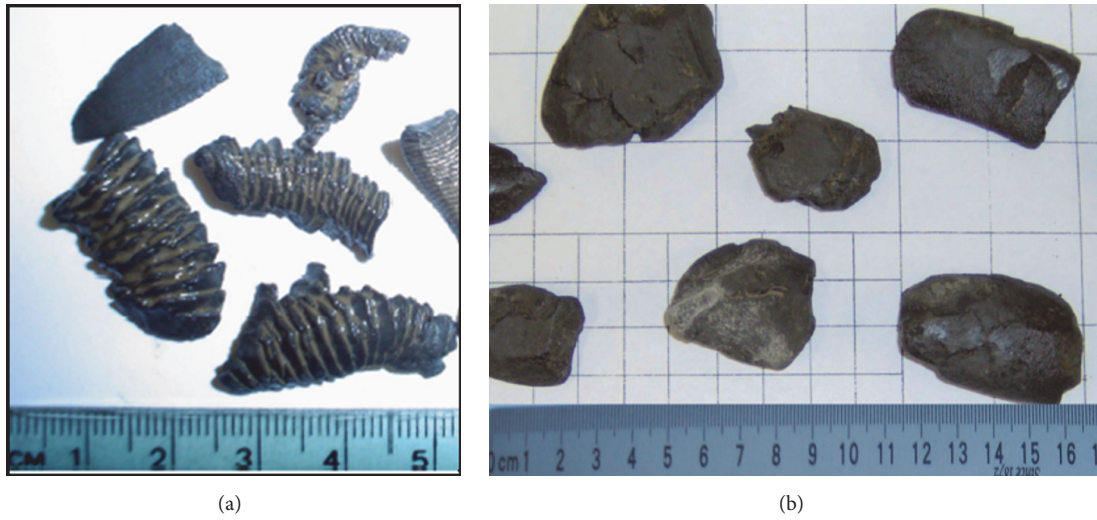


FIGURE 8: Drilling cuttings. (a) Normal PDC cuttings of shales; (b) blocky cuttings from a formation with preexisting fractures.

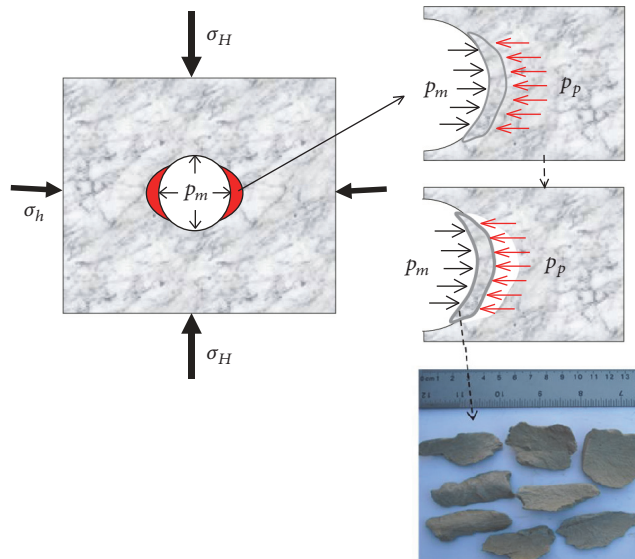


FIGURE 9: Schematic representation of wellbore spalling/chips for a higher pore pressure than the mud pressure (underbalanced drilling condition) in a vertical borehole. Upper part illustrates the high pore pressure that blows rock chips into wellbore; the bottom picture shows spiky and concaved cuttings resulting from the insufficient mud weight.

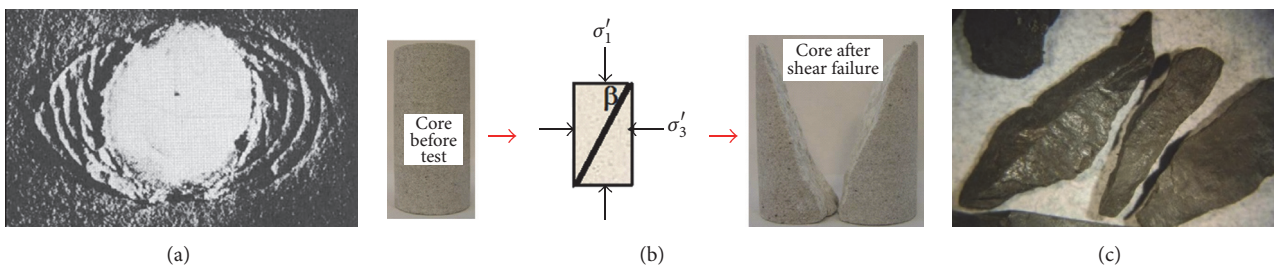


FIGURE 10: Angular or splintered cavings caused by shear failures: a case of lower mud weight than the shear failure gradient. (a) Borehole breakout from shear failure in a laboratory test [25]; (b) triaxial compressive core test creating angular rock pieces; (c) angular/splintered cavings from a subsalt borehole.

TABLE 1: Real-time indicators of abnormal pore pressures.

Indicators	General behaviors
Total gas	Total gas should increase when an underbalanced drilling occurs in a gas-bearing formation.
Background gas	Background gas should increase with ROP. For a constant ROP, background gas is expected to increase as the pore pressure increases.
Connection gas and pump-off gas	Connection gas, swab gas, or pumps-off gas occurring may indicate that the pore pressure is higher than the ESD.
Gas cut mud	Gas cut mud is a sign of abnormal pore pressure and underbalanced drilling.
ROP	ROP increase may indicate the pore pressure gradient increasing.
Dxc	Gradual decrease in Dxc compared to its NCT may indicate the pore pressure gradient increasing (Figure 11).
Resistivity	Gradual decrease in resistivity compared to its NCT may indicate the pore pressure gradient increasing (Figure 11).
DT	Gradual increase in sonic transit time (DT) compared to its NCT may indicate pore pressure gradient increasing (Figure 11).
PWD and temperature	Sudden increase in PWD with increase of MWD temperature may indicate an influx or kick.
Mud volume	Mud pit volume increasing may indicate a kick.
Cuttings	Increase in percentage of cuttings may indicate wellbore instability or abnormal pore pressure. Splintery cavings may indicate underbalanced drilling, and large amounts of splintery and angular cavings indicate a wellbore collapse.
Hole fill	Hole fills (i.e., cavings falling in) after connections indicate wellbore instability and it may need to increase the mud weight.
High torque, overpull, tight hole, pack-off	Hole pack-off, overpull, tight hole, and increasing torque and drag are likely to be caused by a higher collapse pressure or higher pore pressure than the mud weight. It needs to increase the mud weight.

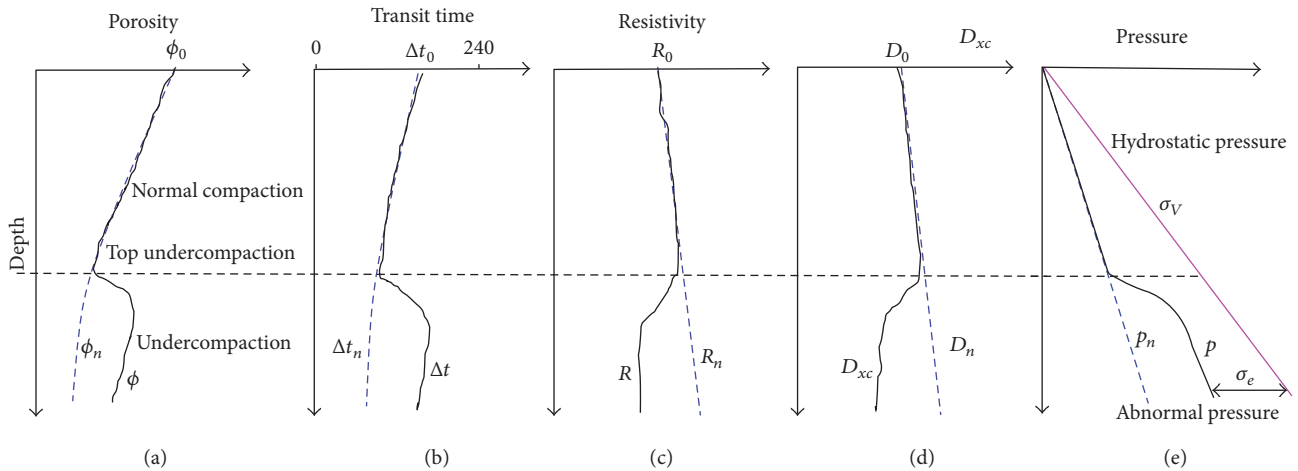


FIGURE 11: Generalized normal compaction trends (NCTs) and abnormal pressures caused by undercompaction. From (a) to (e): porosity, transit time, resistivity, D -exponent, and pore pressure plots.

(e.g., resistivity and sonic transit time) and MWD-based (e.g., Dxc) pore pressure detection methods. To apply these methods, the normal compaction trends are the key parameters. The new depth-dependent equations of the normal compaction trends for resistivity, sonic transit time, and Dxc are proposed, which provide a quantitative way to handle normal compaction trend lines. The normal compaction trend lines need to be calibrated to both offset data and the real-time measured pore pressures and other indicators to finalize the trend lines. To reduce uncertainties, the pore pressure model needs to integrate with the real-time measurements and

indicators, such as real-time pore pressure measurements, well influx and kicks, mud logging (total gas, trip gas, and connection gas), MWD, ROP, ECD/ESD measurements, and borehole instability events (e.g., abnormal torque and drag, tight hole, abnormal cuttings or cavings, hole enlargement or breakout, hole fill, and pack-off).

A new method is proposed to calculate pore pressure from the connection gas and background gas. It can be used for real-time pore pressure interpretation, particularly for shale gas formations. It should be noted that some real-time measurements have lag time, for example, drill gas in

mud logging and cuttings on the surface. The LWD sensors (such as resistivity and sonic tools) also have certain distances behind the drill bit. These disadvantages make it difficult for the real-time monitoring to detect the pore pressure at the bit (excluding Dxc). However, if a formation follows a certain compaction or undercompaction trend, then, the pore pressure at the bit can be interpolated.

Disclosure

Jincai Zhang is now with Sinopec Tech, Houston, USA.

Conflicts of Interest

The authors declare that there are no conflicts of interest regarding the publication of this paper.

Acknowledgments

This work was partially supported by the Program for Innovative Research Team in University sponsored by Ministry of Education of China (IRT-17R37), "Shisan Wu" China National Key R&D Project (2017YFC0804108), and Natural Science Foundation of Hebei Province of China (D2017508099).

References

- [1] G. Dickinson, "Geological aspects of abnormal reservoir pressures in gulf coast louisiana," *AAPG Bulletin*, vol. 37, no. 2, pp. 410–432, 1953.
- [2] B. A. Eaton, "The effect of overburden stress on geopressure prediction from well logs," *Journal of Petroleum Technology*, vol. 24, no. 08, pp. 929–934, 1972.
- [3] G. L. Bowers, "Pore pressure estimation from velocity data: accounting for overpressure mechanisms besides undercompaction," *SPE Drilling & Completion*, vol. 10, no. 2, pp. 89–95, 1995.
- [4] M. Traugott, "Pore pressure and fracture gradient determinations in deepwater," *World Oil*, 1997.
- [5] G. L. Bowers, "Determining an appropriate pore-pressure estimation strategy," in *Proceedings of the Offshore Technology Conference*, Offshore Technology Conference, Houston, Tex, USA, 2001.
- [6] P. B. Flemings, B. B. Stump, T. Finkbeiner, and M. Zoback, "Flow focusing in overpressured sandstones: Theory, observations, and applications," *American Journal of Science*, vol. 302, no. 10, pp. 827–855, 2002.
- [7] M. R. P. Tingay, R. R. Hillis, R. E. Swarbrick, C. K. Morley, and A. R. Damit, "Origin of overpressure and pore-pressure prediction in the Baram province, Brunei," *AAPG Bulletin*, vol. 93, no. 1, pp. 51–74, 2009.
- [8] S. Li, J. George, and C. Purdy, "Pore-pressure and wellbore-stability prediction to increase drilling efficiency," *Journal of Petroleum Technology*, vol. 64, no. 2, pp. 98–101, 2012.
- [9] J. Zhang, "Pore pressure prediction from well logs: Methods, modifications, and new approaches," *Earth-Science Reviews*, vol. 108, no. 1–2, pp. 50–63, 2011.
- [10] J. Zhang, "Effective stress, porosity, velocity and abnormal pore pressure prediction accounting for compaction disequilibrium and unloading," *Marine and Petroleum Geology*, vol. 45, pp. 2–11, 2013a.
- [11] B. A. Eaton, "The equation for geopressure prediction from well logs," in *Proceedings of the Fall Meeting of the Society of Petroleum Engineers of AIME*, Society of Petroleum Engineers, Dallas, Tex, USA, 1975.
- [12] W.-L. Huang, J. M. Longo, and D. R. Pevear, "An experimentally derived kinetic model for smectite-to-illite conversion and its use as a geothermometer," *Clays and Clay Minerals*, vol. 41, no. 2, pp. 162–177, 1993.
- [13] R. Lahann, W. Lahann, D. McCarty, and J. Hsieh, "Influence of clay diagenesis on shale velocities and fluid-pressure," in *Proceedings of the Offshore Technology Conference*, Offshore Technology Conference, Houston, Tex, USA, 2001.
- [14] R. W. Lahann and R. E. Swarbrick, "Overpressure generation by load transfer following shale framework weakening due to smectite diagenesis," *Geofluids*, vol. 11, no. 4, pp. 362–375, 2011.
- [15] J.-C. Mouchet and A. Mitchell, *Abnormal Pressures While Drilling*, Editions TECHNIP, Paris, France, 1989.
- [16] J. Jorden and O. Shirley, "Application of drilling performance data to overpressure detection," *Journal of Petroleum Technology*, vol. 18, no. 11, pp. 1387–1394, 2013.
- [17] B. Rehm and R. McClendon, "Measurement of formation pressures from drilling data," *Paper SPE*, p. 3601, 1971.
- [18] L. F. Athy, "Density, porosity, and compaction of sedimentary rocks," *AAPG Bulletin*, vol. 14, no. 1, pp. 1–24, 1930.
- [19] J. Zhang and S. Yin, "Fracture gradient prediction: an overview and an improved method," *Petroleum Science*, pp. 1–11, 2017.
- [20] M. Alberty and K. Fink, in *Proceedings of the SPE Annual Technical Conference and Exhibition*, Society of Petroleum Engineers, New Orleans, La, USA, 2013.
- [21] J. Zhang, "Borehole stability analysis accounting for anisotropies in drilling to weak bedding planes," *International Journal of Rock Mechanics and Mining Sciences*, vol. 60, pp. 160–170, 2013b.
- [22] J. Zhang, J. Lang, and W. Standifird, "Stress, porosity, and failure-dependent compressional and shear velocity ratio and its application to wellbore stability," *Journal of Petroleum Science and Engineering*, vol. 69, no. 3–4, pp. 193–202, 2009.
- [23] J. Lang, S. Li, and J. Zhang, "Wellbore stability modeling and real-time surveillance for deepwater drilling to weak bedding planes and depleted reservoirs," in *Proceedings of the SPE/IADC Drilling Conference and Exhibition*, 2011.
- [24] Y. Zhang and J. Zhang, "Lithology-dependent minimum horizontal stress and in-situ stress estimate," *Tectonophysics*, vol. 703–704, pp. 1–8, 2017.
- [25] M. Addis, N. Barton, S. Bandis, and J. Henry, "Laboratory studies on the stability of vertical and deviated boreholes," in *Proceedings of the SPE Annual Technical Conference and Exhibition*, Society of Petroleum Engineers, New Orleans, La, USA, September 1990.